

STRUCTURE AND BONDING

136

Series Editor D. M. P. Mingos
Volume Editor Gerard Parkin

Metal-Metal Bonding

 Springer

136

Structure and Bonding

Series Editor: D. M. P. Mingos

Editorial Board:

**P. Day · X. Duan · L.H. Gade · K.R. Poeppelmeier
G. Parkin · J.-P. Sauvage**

For further volumes:

<http://www.springer.com/series/430>

Structure and Bonding

Series Editor: D. M. P. Mingos

Recently Published and Forthcoming Volumes

Metal-Metal Bonding

Volume Editor: Gerard Parkin
Vol. 136, 2010

Functional Phthalocyanine Molecular Materials

Volume Editor: Jianzhuang Jiang
Vol. 135, 2010

Data Mining in Crystallography

Volume Editors: Hofmann, D. W. M.,
Kuleshova, L. N.
Vol. 134, 2010

Controlled Assembly and Modification of Inorganic Systems

Volume Editor: Wu, X.- T.
Vol. 133, 2009

Molecular Networks

Volume Editor: Hosseini, M. W.
Vol. 132, 2009

Molecular Thermodynamics of Complex Systems

Volume Editors: Lu, X., Hu, Y.
Vol. 131, 2009

Contemporary Metal Boron Chemistry I

Volume Editors: Marder, T. B., Lin, Z.
Vol. 130, 2008

Recognition of Anions

Volume Editor: Vilar, R.
Vol. 129, 2008

Liquid Crystalline Functional Assemblies and Their Supramolecular Structures

Volume Editor: Kato, T.
Vol. 128, 2008

Organometallic and Coordination Chemistry of the Actinides

Volume Editor: Albrecht-Schmitt, T. E.
Vol. 127, 2008

Halogen Bonding

Fundamentals and Applications
Volume Editors: Metrangolo, P., Resnati, G.
Vol. 126, 2008

High Energy Density Materials

Volume Editor: Klapötke, T. H.
Vol. 125, 2007

Ferro- and Antiferroelectricity

Volume Editors: Dalal, N. S.,
Bussmann-Holder, A.
Vol. 124, 2007

Photofunctional Transition Metal Complexes

Volume Editor: V. W. W. Yam
Vol. 123, 2007

Single-Molecule Magnets and Related Phenomena

Volume Editor: Winpenny, R.
Vol. 122, 2006

Non-Covalent Multi-Porphyrin Assemblies

Synthesis and Properties
Volume Editor: Alessio, E.
Vol. 121, 2006

Recent Developments in Mercury Science

Volume Editor: Atwood, David A.
Vol. 120, 2006

Layered Double Hydroxides

Volume Editors: Duan, X., Evans, D. G.
Vol. 119, 2005

Metal-Metal Bonding

Volume Editor: Gerard Parkin

With contributions by

B.B. Averkiev · J.F. Berry · A.I. Boldyrev · T. Cadenbach ·
M.H. Chisholm · R.A. Fischer · G. Frenking · C. Gemel ·
S. Gonzalez-Gallardo · M.S. Hill · v. Hopffgarten ·
C. Ni · G. Parkin · P.P. Power · G. Prabusankar ·
A.P. Sergeeva · C.A. Tsipis

Prof. Dr. Gerard Parkin
Columbia University
Dept. Chemistry
3000 Broadway
New York NY 10027
USA
parkin@columbia.edu

ISSN 0081-5993 e-ISSN 1616-8550
ISBN 978-3-642-05242-2 e-ISBN 978-3-642-05243-9
DOI 10.1007/978-3-642-05243-9
Springer Heidelberg Dordrecht London New York

Library of Congress Control Number: 2009943436

© Springer-Verlag Berlin Heidelberg 2010

This work is subject to copyright. All rights are reserved, whether the whole or part of the material is concerned, specifically the rights of translation, reprinting, reuse of illustrations, recitation, broadcasting, reproduction on microfilm or in any other way, and storage in data banks. Duplication of this publication or parts thereof is permitted only under the provisions of the German Copyright Law of September 9, 1965, in its current version, and permission for use must always be obtained from Springer. Violations are liable to prosecution under the German Copyright Law.

The use of general descriptive names, registered names, trademarks, etc. in this publication does not imply, even in the absence of a specific statement, that such names are exempt from the relevant protective laws and regulations and therefore free for general use.

Cover design: KünkelLopka GmbH, Heidelberg, Germany

Printed on acid-free paper

Springer is part of Springer Science+Business Media (www.springer.com)

Series Editor

Prof. D. Michael P. Mingos

Principal

St. Edmund Hall

Oxford OX1 4AR, UK

michael.mingos@st-edmund-hall.oxford.ac.uk

Volume Editor

Prof. Dr. Gerard Parkin

Columbia University

Dept. Chemistry

3000 Broadway

New York NY 10027

USA

parkin@columbia.edu

Editorial Board

Prof. Peter Day

Director and Fullerian Professor
of Chemistry

The Royal Institution of Great Britain

21 Albermarle Street

London W1X 4BS, UK

pday@ri.ac.uk

Prof. Xue Duan

Director

State Key Laboratory

of Chemical Resource Engineering

Beijing University of Chemical Technology

15 Bei San Huan Dong Lu

Beijing 100029, P.R. China

duanx@mail.buct.edu.cn

Prof. Lutz H. Gade

Anorganisch-Chemisches Institut

Universität Heidelberg

Im Neuenheimer Feld 270

69120 Heidelberg, Germany

lutz.gade@uni-hd.de

Prof. Dr. Kenneth R. Poeppelmeier

Department of Chemistry

Northwestern University

2145 Sheridan Road

Evanston, IL 60208-3133

USA

krp@northwestern.edu

Prof. Gerard Parkin

Department of Chemistry (Box 3115)

Columbia University

3000 Broadway

New York, New York 10027, USA

parkin@columbia.edu

Prof. Jean-Pierre Sauvage

Faculté de Chimie

Laboratoires de Chimie

Organo-Minérale

Université Louis Pasteur

4, rue Blaise Pascal

67070 Strasbourg Cedex, France

sauvage@chimie.u-strasbg.fr

Structure and Bonding

Also Available Electronically

Structure and Bonding is included in Springer's eBook package *Chemistry and Materials Science*. If a library does not opt for the whole package the book series may be bought on a subscription basis. Also, all back volumes are available electronically.

For all customers who have a standing order to the print version of *Structure and Bonding*, we offer the electronic version via SpringerLink free of charge.

If you do not have access, you can still view the table of contents of each volume and the abstract of each article by going to the SpringerLink homepage, clicking on "Chemistry and Materials Science," under Subject Collection, then "Book Series," under Content Type and finally by selecting *Structure and Bonding*.

You will find information about the

- Editorial Board
- Aims and Scope
- Instructions for Authors
- Sample Contribution

at springer.com using the search function by typing in *Structure and Bonding*.

Color figures are published in full color in the electronic version on SpringerLink.

Aims and Scope

The series *Structure and Bonding* publishes critical reviews on topics of research concerned with chemical structure and bonding. The scope of the series spans the entire Periodic Table and addresses structure and bonding issues associated with all of the elements. It also focuses attention on new and developing areas of modern structural and theoretical chemistry such as nanostructures, molecular electronics, designed molecular solids, surfaces, metal clusters and supramolecular structures. Physical and spectroscopic techniques used to determine, examine and model structures fall within the purview of *Structure and Bonding* to the extent that the focus

is on the scientific results obtained and not on specialist information concerning the techniques themselves. Issues associated with the development of bonding models and generalizations that illuminate the reactivity pathways and rates of chemical processes are also relevant.

The individual volumes in the series are thematic. The goal of each volume is to give the reader, whether at a university or in industry, a comprehensive overview of an area where new insights are emerging that are of interest to a larger scientific audience. Thus each review within the volume critically surveys one aspect of that topic and places it within the context of the volume as a whole. The most significant developments of the last 5 to 10 years should be presented using selected examples to illustrate the principles discussed. A description of the physical basis of the experimental techniques that have been used to provide the primary data may also be appropriate, if it has not been covered in detail elsewhere. The coverage need not be exhaustive in data, but should rather be conceptual, concentrating on the new principles being developed that will allow the reader, who is not a specialist in the area covered, to understand the data presented. Discussion of possible future research directions in the area is welcomed.

Review articles for the individual volumes are invited by the volume editors.

In references *Structure and Bonding* is abbreviated *Struct Bond* and is cited as a journal.

Impact Factor in 2008: 6.511; Section “Chemistry, Inorganic & Nuclear”:
Rank 2 of 40; Section “Chemistry, Physical”: Rank 7 of 113

Preface

Despite the fact that compounds that feature metal–metal bonds have been known for many decades, interesting discoveries continue to be made at a rapid pace. The purpose of this volume is to highlight some of these recent advances in both main group and transition metal chemistry, and an overview of the topics covered is provided here.

Berry describes transition metal compounds in which there are chains of metal atoms. Such compounds are often considered as potential molecular wires for molecular electronic applications and the conductance of these compounds at the molecular level is discussed. In addition to compounds that feature homometallic chains, those with heterometallic chains are also described.

Chisholm describes a different approach to linking together metal centers, namely one in which quadruply bonded dimolybdenum and ditungsten moieties are electronically coupled *via* a conjugated π -system of an organic bridging ligand. The types of structures obtained include loops, triangles and squares of the dinuclear moieties.

Ni and Power describe the use of sterically demanding terphenyl ligands to synthesize transition metal dinuclear compounds of type ArMMAr that have exceptionally short M–M bonds and high M–M bond orders. For example, ArCrCrAr is described as possessing a quintuple Cr–Cr bond.

The evaluation of the metal–metal bond order is often an important component in the description of compounds with metal–metal bonds, and Parkin evaluates the various electron-counting procedures that are used to predict metal–metal bond orders in transition metal compounds that feature bridging hydride and alkyl ligands.

At the interface of main group and transition metal chemistry, Frenking, Fischer et al. describe recent developments in which monovalent gallium species can serve as ligands for transition metals, thereby affording a variety of compounds that feature M–Ga bonds. Furthermore, many of these compounds with M–Ga bonds can be converted into compounds that feature M–Zn bonds. Also, with respect to main group chemistry, Hill discusses catenated compounds of Group 13–15 elements, which feature chains of M–M bonds.

Finally, the concept of aromaticity and antiaromaticity in compounds that feature rings of metal atoms is discussed by Tsipis, who focuses on rings of main group metal atoms, and by Boldyrev et al., who focus on transition metal compounds.

New York
January 2010

Gerard Parkin

Contents

Metal–Metal Bonds in Chains of Three or More Metal Atoms: From Homometallic to Heterometallic Chains	1
J.F. Berry	
Electronically Coupled MM Quadruple Bonded Complexes of Molybdenum and Tungsten	29
Malcolm H. Chisholm	
Transition Metal Complexes Stabilized by Bulky Terphenyl Ligands: Application to Metal–Metal Bonded Compounds	59
Chengbao Ni and Philip P. Power	
Metal–Metal Bonding in Bridging Hydride and Alkyl Compounds	113
Gerard Parkin	
Structure and Bonding of Metal-Rich Coordination Compounds Containing Low Valent Ga(I) and Zn(I) Ligands	147
Sandra Gonzalez-Gallardo, Ganesan Prabusankar, Thomas Cadenbach, Christian Gemel, Moritz von Hopffgarten, Gernot Frenking, and Roland A. Fischer	
Homocatenation of Metal and Metalloid Main Group Elements	189
Michael S. Hill	
Aromaticity/Antiaromaticity in “Bare” and “Ligand-Stabilized” Rings of Metal Atoms	217
Constantinos A. Tsipis	
All-Transition Metal Aromaticity and Antiaromaticity	275
Alina P. Sergeeva, Boris B. Averkiev, and Alexander I. Boldyrev	
Index	307

Metal–Metal Bonds in Chains of Three or More Metal Atoms: From Homometallic to Heterometallic Chains

J.F. Berry

Abstract Extended metal atom chains (EMACs) have attracted attention for their unique structural and bonding features. They allow for a systematic study of metal–metal bonding in discrete, oligomeric, polymetallic one-dimensional molecules. Because of their shape and bonding patterns, these complexes are often considered potential molecular wires for molecular electronic applications. As such, the electronic structure of the simplest EMACs, i.e., those that consist of three metals linked together, the ligand systems that have been used to support EMACs, and preliminary work on the conductance of EMACs at the molecular level are discussed. New heterometallic EMACs have also been recently synthesized and are discussed here. While these molecules may be of interest in molecular electronic applications, they also serve as a testing ground for studying the nature of heterometallic electronic effects.

Keywords Electronic structure · Extended metal atom chains · Heterometallic compounds · Metal–metal bonds · Molecular wires · Single-molecule conductance

Contents

1	Introduction	2
2	Electronic Structure	3
	2.1 Trichromium Species	3
	2.2 Tricobalt Species	5
	2.3 Trinickel Species	9
	2.4 Tricopper Species	10
	2.5 Triruthenium Species	11
	2.6 Spectroscopic Developments	12
3	New Ligands for EMACs	12
	3.1 Axial Ligands	13
	3.2 Equatorial Ligands	14

4	Molecular Conductance Measurements.....	21
5	Heterometallic EMACs.....	23
6	Conclusions and Outlook.....	26
	References	26

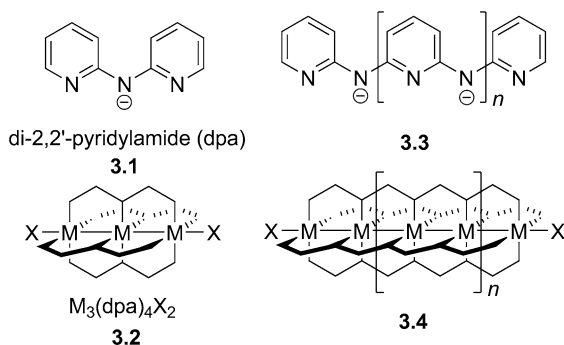
1 Introduction

One-dimensional (1D) molecular entities have captured the imagination of chemists and physicists for many years. The simplest 1D species, diatomic molecules, have played an important part in the development of chemical bonding theories, including the description of metal–metal bonds. Aligning three or more metal atoms into a linear chain has been possible by using supporting bridging ligands such as the family of oligopyridylamine ligands shown in Scheme 1.

The prototypical oligopyridylamine ligand is di-2,2'-pyridylamine (Hdpa), shown in its anionic form as **3.1**; extended metal atom chain (EMAC) complexes of this ligand have structures that are shown schematically as in **3.2**. Extended ligands such as **3.3** have been synthesized, and their complexes, **3.4**, are known with $n = 0, 1, 2,$ and 3 corresponding to tri-, penta-, hepta-, and nona-nuclear chains, respectively. The chemistry of these fascinating compounds was reviewed by me in 2005 [1] and by Peng in 2006 [2]. The focus of this chapter is therefore on developments in the field since then, which can be classified into four broad categories:

1. Computational and spectroscopic work to improve our understanding of the electronic structure of EMACs
2. Expanding EMAC chemistry to new ligand systems
3. Measurement of charge transport through EMAC molecules
4. Synthesis and characterization of heterometallic chains

The four topics will be dealt with in the sections that follow.



Scheme 1 Molecular structures of **3.1–3.4**

2 Electronic Structure

Because of their relative simplicity, trinuclear $M_3(dpa)_4X_2$ species have been the main focus of efforts to understand the electronic structure and bonding in EMACs. For these systems, the d orbital manifold consists of bonding, nonbonding, and antibonding combinations of orbitals with σ , π , and δ symmetry. The σ set is formed by d_{z^2} -type metal orbitals, which are the most widely separated in energy; the d_{xz} and d_{yz} orbitals form a set of π orbitals that are less spread out in energy. There are two sets of orbitals with δ symmetry: a low-energy set is formed by interactions between the d_{xy} orbitals, and a second set is formed by interactions between $d_{x^2-y^2}$ orbitals. The second set is higher in energy than all of the other orbitals in the manifold because these orbitals have significant antibonding overlap with the lone pairs of the N atoms in the equatorial ligand. These σ^* interactions also limit the δ overlap between these orbitals. The general sequence of these molecular orbitals is shown in Fig. 1 [3].

Simply filling in this orbital manifold with the appropriate number of metal-based electrons yields the ground state electron configurations for $M_3(dpa)_4Cl_2$ complexes shown in Table 1 [4]. Recent work has shown that various aspects of this table require modification, as detailed later.

2.1 Trichromium Species

A major experimental effort was made in 2004 to elucidate the electronic structure of $Cr_3(dpa)_4X_2$ molecules [5]. One of the major structural problems associated with these molecules is how to distinguish between a symmetrical Cr_3 chain (**3.5**) and an unsymmetrical species (**3.6**). This problem is compounded experimentally in the crystal structures of species such as **3.6**, which typically exhibit crystallographic disorder in the metal atom positions such that a crystal contains roughly equal amounts of $Cr \equiv Cr \cdots Cr$ and $Cr \cdots Cr \equiv Cr$ molecular orientations. The geometric average of these two orientations is equivalent to a symmetrical molecule, **3.5**. Thus, careful crystallographic work is necessary in order to properly determine the molecular structures of these compounds. In fact, many of the early crystal structures of $Cr_3(dpa)_4Cl_2$ were found to be incorrect in this respect: symmetrical structures were initially claimed [6], but were subsequently found to be unsymmetrical and disordered upon re-refinement of the crystallographic data [5] (Scheme 2).

A fascinating structural result was obtained through the study of a series of $Cr_3(dpa)_4X_2$ compounds with various X anions (see Table 2). The Cr–Cr bond distances were found to depend strongly on the nature of X. Ligand substitution at the X position was even found to lead to symmetrical (**3.5**) structures in some cases. Very weak X ligands such as tetrafluoroborate or nitrate lead to strongly unsymmetrical molecules with $Cr \equiv Cr$ bonds as short as 1.93 Å. Strong σ donors such as CN^- , however, favor a symmetrical Cr–Cr–Cr chain with longer Cr–Cr distances (>2.35 Å). The reason for this switch in the molecular structure of the compounds

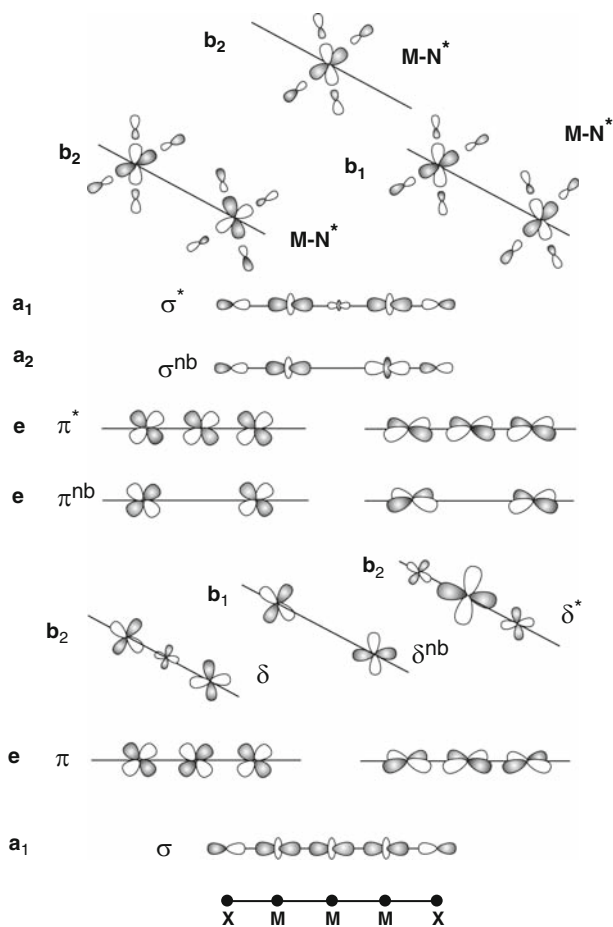
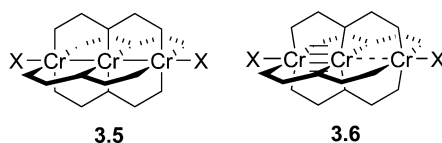


Fig. 1 Shapes, symmetries, and relative energies of molecular orbitals for a trinuclear $M_3(dpa)_4X_2$ species

Table 1 Ground state electron configurations and spin states for $M_3(dpa)_4Cl_2$ species based on the orbital manifold given in Fig. 1

Compound	Electron configuration	Ground spin state
$Cr_3(dpa)_4Cl_2$	$\sigma^2 \pi^4 \delta^2 \delta_{nb}^1 \delta^{*1} \pi_{nb}^2$	$S = 2$
$Co_3(dpa)_4Cl_2$,	$\sigma^2 \pi^4 \delta^2 \delta_{nb}^2 \delta^{*2} \pi_{nb}^4 \pi^{*4} \sigma_{nb}^1$	$S = 1/2$
$Rh_3(dpa)_4Cl_2$		
$Ni_3(dpa)_4Cl_2$	$\sigma^2 \pi^4 \delta^2 \delta_{nb}^2 \delta^{*2} \pi_{nb}^4 \pi^{*4} \sigma_{nb}^2 \sigma^{*2}$	$S = 0$
$Cu_3(dpa)_4Cl_2$	$\sigma^2 \pi^4 \delta^2 \delta_{nb}^2 \delta^{*2} \pi_{nb}^4 \pi^{*4} \sigma_{nb}^2 \sigma^{*2} \delta^1 \delta_{nb}^1 \delta^{*1}$	$S = 1/2$
$Ru_3(dpa)_4Cl_2$	$\sigma^2 \pi^4 \delta^2 \delta_{nb}^2 \delta^{*2} \pi_{nb}^4 \sigma_{nb}^2$	$S = 0$

**Scheme 2** Molecular structures of **3.5** and **3.6****Table 2** Metal–metal bond lengths in $\text{Cr}_3(\text{dpa})_4\text{X}_2$ compounds [5, 7]

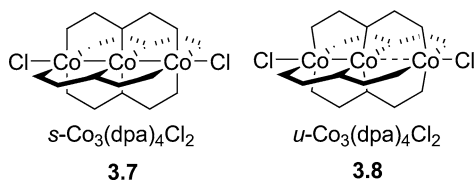
X	$\text{Cr} \equiv \text{Cr}$, Å	$\text{Cr} \cdots \text{Cr}$, Å
NO_3^-	1.93	2.64
BF_4^-	1.96	2.59
NCCH_3	2.14	2.46
I^-	2.18	2.48
NCS^-	2.22	2.47
Br^-	2.22	2.48
Cl^-	2.24	2.48
NCO^-	2.26	2.48
CN^-	2.37	Symmetrical
$\text{C} \equiv \text{CPh}^-$	2.43	Symmetrical

is that, in the symmetrical case, the strong σ donors can donate to the σ_{nb} *nonbonding* orbital, whereas in the unsymmetrical case, strong σ donors would necessarily destabilize the more localized $\text{Cr} \equiv \text{Cr} \sigma$ bond [5].

The unsymmetrical structure of $\text{Cr}_3(\text{dpa})_4\text{Cl}_2$ has thus far not been reproduced by computation. Rohmer and Bénard have found that spin unrestricted density functional theory (DFT) computations on $\text{Cr}_3(\text{dpa})_4\text{Cl}_2$ reveal a rather shallow potential energy surface, leading to several local minimum geometries with $S = 2$ that are within $\sim 40 \text{ kJ mol}^{-1}$ of each other [8]. The most stable of these states adopts a symmetrical structure with $\text{Cr}–\text{Cr}$ lengths of 2.35 Å; a slightly unsymmetrical state ($\Delta(\text{Cr}–\text{Cr}) = 0.106 \text{ Å}$) lies very close in energy, as does a strongly unsymmetrical state ($\Delta(\text{Cr}–\text{Cr}) = 0.679 \text{ Å}$). Regardless of their geometry, these states all involve an electronic structure with ten unpaired electrons, nine of which are localized in sets of three on each of the Cr atoms and are antiferromagnetically coupled ($\uparrow\uparrow\uparrow \cdots \downarrow\downarrow\downarrow \cdots \uparrow\uparrow\uparrow$). The last unpaired electron takes part in a *three-center three-electron* σ bond that spans all three Cr atoms [9]. The coexistence of spin-coupling and delocalized bonding is a unique feature of the electronic structure of these trichromium species.

2.2 Tricobalt Species

The tricobalt molecule $\text{Co}_3(\text{dpa})_4\text{Cl}_2$ has been the subject of extensive experimental and computational work because the molecule crystallizes in a number of different solvates that have strikingly different structural and magnetic properties [10]. In particular, crystallization of $\text{Co}_3(\text{dpa})_4\text{Cl}_2$ from CH_2Cl_2 solutions produces



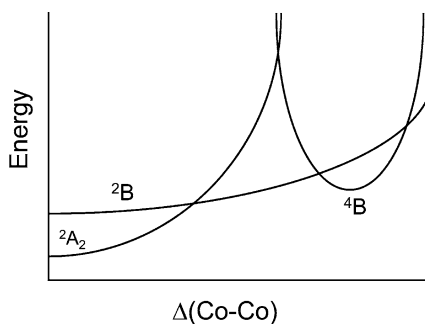
Scheme 3 Molecular structures of **3.7** and **3.8**

crystals of two different morphologies: an orthorhombic form, space group $Pnn2$ with composition $\text{Co}_3(\text{dpa})_4\text{Cl}_2 \cdot \text{CH}_2\text{Cl}_2$, and a tetragonal form, space group $I\bar{4}$ with composition $\text{Co}_3(\text{dpa})_4\text{Cl}_2 \cdot 2\text{CH}_2\text{Cl}_2$. The difference in the molecular structures found in these two crystals is remarkable. The former contains a *symmetrical* tricobalt chain with Co–Co bond distances of 2.34 Å (**3.7**), and the latter crystal contains an *unsymmetrical* tricobalt chain with Co–Co distances of 2.30 and 2.47 Å (**3.8**) [10] (Scheme 3).

The observation of both *s* and *u* forms of $\text{Co}_3(\text{dpa})_4\text{Cl}_2$ suggests that these compounds may be *bond stretch isomers*, two molecules that are different only in the length of one or more bonds [11–13]. Computational work was performed on $\text{Co}_3(\text{dpa})_4\text{Cl}_2$ using DFT in order to support the claim of bond-stretch isomerism as well as to determine the electronic basis for the unusual structural behavior of this molecule. The first computational work on this compound determined that the spin doublet potential energy surface is shallow with respect to geometric distortions of the type that can interchange **3.7** and **3.8** [14]. Only one potential energy minimum was found on the doublet surface, of symmetry 2A_2 (D_4 symmetry), corresponding to a symmetric structure like that in **3.7**. No unsymmetrical doublet state was found. Instead, the structural variability of the compound was seen in two different excited quartet states, the unsymmetrical 4A state (C_4 symmetry) and the symmetrical 4B state. The observed structural variations in $\text{Co}_3(\text{dpa})_4\text{Cl}_2$ were therefore attributed to spin crossover into one of these two excited states. Compound **3.7** derived from population of the 4B state, and **3.8** from population of the 4A state. Thus, it was suggested [14] that **3.7** and **3.8** were better described as spin-state isomers than as bond-stretch isomers.

However, the spin-state isomerism description does not fully explain the unusual structural changes seen in the unsymmetric molecule by variable-temperature X-ray crystallography [10]. In order to explain these anomalous features, McGrady has recently re-examined the electronic structure of the $\text{Co}_3(\text{dpa})_4\text{Cl}_2$ potential energy landscape and found several new features that do indeed account for the observed structural features [15]. These features are a new, unsymmetrical 4B state that is lower in energy than the unsymmetrical 4A state found by Bénard and Rohmer, and a new excited doublet state, 2B , which is capable of providing a smooth energetic pathway between the symmetric ground 2A_2 and the unsymmetric excited 4B [15]. The ground state, 2A_2 , is adequately described by the electron configuration given in Table 1; the 2B state may be roughly described as containing a high-spin Co(II) ion attached to a *high-spin* Co–Co bonded unit. Antiferromagnetic coupling between the former ($S = 3/2$) and the latter ($S = 1$) species yields the total S value of $1/2$

Fig. 2 Potential energy diagram for $\text{Co}_3(\text{dpa})_4\text{Cl}_2$ showing the states discussed in the work of McGrady [15]



for the ^2B state. A spin-flip within the Co–Co bonded unit transforms the ^2B state into the ^4B state, which has a high-spin Co(II) species attached to a *low-spin* Co–Co bonded unit.

Though the ground state geometry of the ^2B state is symmetrical, the potential energy of this state is less dramatically affected by changes in $\Delta(\text{Co–Co})$ than the ^2A state. Thus, as shown in Fig. 2, the ^2B state allows for a smooth transition between ^2A and ^4B . Since the main difference in the electronic structure of ^2A vs ^2B or ^4B is the presence of an unpaired electron in a Co $d_{x^2-y^2}$ orbital in the latter cases, the variable temperature structural data of **3.8** may be modeled by increasing the population of this $d_{x^2-y^2}$ orbital to represent the increase in temperature. These data are shown in Fig. 3, where all of the trends in bond distances are remarkably well reproduced by theory [15].

McGrady has also investigated the origin of the magnetic and structural features of the $[\text{Co}_3(\text{dpa})_4\text{Cl}_2]^+$ cation [16], which are unusual in that the salt $[\text{Co}_3(\text{dpa})_4\text{Cl}_2][\text{BF}_4]$ has been shown to undergo *two* stepwise spin transitions ($S = 0 \rightarrow S = 1 \rightarrow S = 2$). Variable temperature X-ray crystallography has shown that the geometry of the $[\text{Co}_3(\text{dpa})_4\text{Cl}_2]^+$ cation is symmetrical and insensitive to temperature changes, despite the population of singlet, triplet, and quintet spin states at different temperatures [17]. The original proposal for the electronic structure of this cation was that the ground state could be described by removal of one electron from the a_2 SOMO of $\text{Co}_3(\text{dpa})_4\text{Cl}_2$, yielding the symmetrical $^1\text{A}_1$ state shown on the left in Fig. 4 [17]. This electron configuration corresponds to a $\text{Co}^{2.5+}\text{–Co}^{2+}\text{–Co}^{2.5+}$ formal oxidation state assignment for the cation, which is in agreement with the symmetrical structure. The shortcoming of this proposed electronic structure is that promotion to a triplet state will necessarily populate the a_2 orbital. Although this situation would not strongly affect the Co–Co bond distances, population of the a_2 orbital would be expected to lengthen the Co–Cl bonds due to the Co–Cl antibonding character of this orbital. Since Co–Cl bond elongation is not observed experimentally, it appears that the $^1\text{A}_1$ ground state assignment does not adequately explain all of the experimental details. Instead, another possible singlet state, $^1\text{B}_1$, was considered in which the b_2 orbital mainly localized on the central Co atom is the site of oxidation. This formally leads to a $\text{Co}^{2+}\text{–Co}^{3+}\text{–Co}^{2+}$ ground state with an open-shell singlet configuration and one unpaired electron in each of the a_2 and

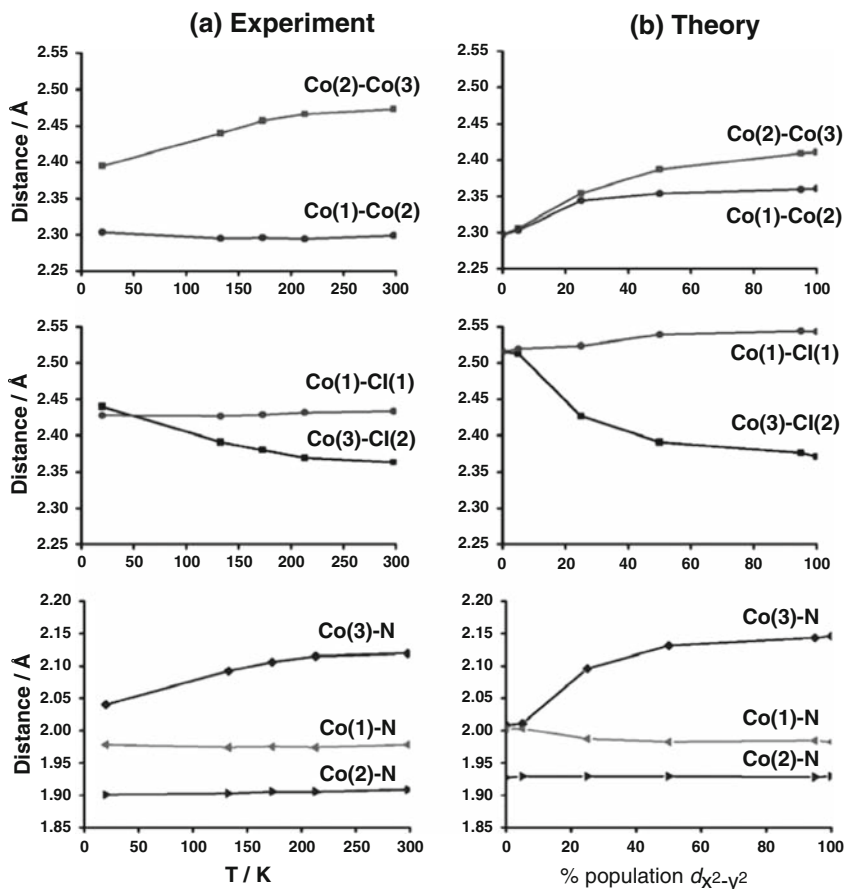
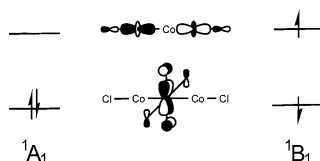


Fig. 3 Experimental (a) structural changes in $\text{Co}_3(\text{dpa})_4\text{Cl}_2$, and a theoretical model (b) of these changes discussed earlier

Fig. 4 Possible singlet states for the $[\text{Co}_3(\text{dpa})_4\text{Cl}_2]^+$ cation



b_2 orbitals (Fig. 4). These two electrons are weakly antiferromagnetically coupled, yielding the singlet ground state and low-lying triplet excited state. Since there is no change in the electron distribution between these two states, no change in the geometry of the molecule is to be expected. Interestingly, the only quintet state of low enough energy to be considered as viable was a 5E state with an unsymmetrical geometry ($\Delta(\text{Co}-\text{Co}) = 0.12 \text{ \AA}$). This state is best considered as consisting of a

high-spin Co(II) ion ferromagnetically coupled to an $S = 1/2$ Co_2^{5+} group [16]. Since this configuration only accounts for $\sim 18\%$ of the bulk sample used in the X-ray crystallographic determination at 300 K, there are currently no major structural features that can confirm the geometry of this state.

2.3 Trinickel Species

The molecule $\text{Ni}_3(\text{dpa})_4\text{Cl}_2$ has been described as having two high-spin terminal Ni(II) ions that couple to each other antiferromagnetically yielding a singlet ground state [18,19]. This description presumes a total lack of Ni–Ni bonding. The nature of the spin coupling in this molecule has recently been refined by Bénard and Rohmer through the use of broken symmetry DFT calculations [20]. In this work, two singlet states were examined: the diamagnetic singlet having an electron configuration similar to that in Table 1, and the open-shell singlet calculated through broken symmetry techniques. Only the open-shell singlet reproduces the geometric features of $\text{Ni}_3(\text{dpa})_4\text{Cl}_2$, suggesting that the diamagnetic singlet state, which lies $\sim 80\text{--}100$ kJ mol $^{-1}$ higher in energy, is not observed [20].

In the open-shell singlet state, four magnetic orbitals are important to the description of bonding: the $\sigma(\text{nb})$ a_2 orbital, the σ^* a_1 orbital, and the two $b_1 \pm b_2$ combinations of the lowest-lying δ ($d_{x^2-y^2}$) orbitals. Since each of these four molecular orbitals is singly occupied, there is a significant contribution to Ni–Ni bonding through the delocalization of the σ orbitals: the σ^* orbital is only *half*-filled, and does not completely cancel the bonding effect of the filled σ bonding a_1 orbital, which is much lower in energy [20].

Thus, despite a major decrease in Ni–Ni distances of 0.15 Å that occurs upon oxidation of $\text{Ni}_3(\text{dpa})_4\text{Cl}_2$, the one-electron oxidized species, $[\text{Ni}_3(\text{dpa})_4](\text{PF}_6)_3$, has the same *formal* bond order as the neutral species. The dramatic shortening of the Ni–Ni bond distances is mainly an effect of the loss of the strongly donating axial chloro ligands [20].

The electronic structure of $\text{Ni}_3(\text{dpa})_4\text{Cl}_2$ has also been compared to that of the hypothetical heterometallic $\text{NiPdNi}(\text{dpa})_4\text{Cl}_2$ [21]. The magnetic orbitals and the antiferromagnetic coupling in both cases are the same: coupling of the spins of the a_1 and a_2 electrons occurs through direct exchange (i.e., through the central metal atom), and coupling of the b_1 and b_2 electrons occurs via superexchange (through the bridging ligand). The spin coupling was determined using broken symmetry techniques, and is reported as $2J$, based on the Heisenberg Hamiltonian $\hat{H} = -2J\hat{S}_A \cdot \hat{S}_B$, where S_A and S_B are the spins of the two terminal high-spin Ni(II) ions. For $\text{Ni}_3(\text{dpa})_4\text{Cl}_2$, $2J$ was calculated as -91 cm $^{-1}$, in reasonable agreement with the experimental value of -216 cm $^{-1}$ [21]. For the NiPdNi species, $2J$ was calculated to be roughly three times larger than for the Ni_3 case, suggesting that either direct exchange via the central Pd atom or ligand-mediated superexchange could be more efficient in the heterometallic case [21]. A further computational comparison of Ni_3 complexes to the as yet unknown Pd_3 complexes has been

undertaken, and the Pd₃ complexes are predicted to be diamagnetic regardless of which equatorial or axial ligands are used [22].

2.4 Tricopper Species

The tricopper species Cu₃(dpa)₄Cl₂ and its one-electron oxidized cationic form, [Cu₃(dpa)₄Cl₂]⁺, have both been synthesized and are well characterized [4]. The neutral species has magnetic properties consistent with antiferromagnetic coupling between three linearly aligned Cu(II) ions. Broken symmetry DFT calculations with approximate spin projections were recently used to determine the electronic structure and mechanism of antiferromagnetic coupling in this compound [3]. The electronic structure of Cu₃(dpa)₄Cl₂ features an unpaired electron in each of the high-energy d_{x²-y²} orbital combinations (*b*₂, *b*₁, and *b*₂). There is no significant overlap between these δ-type orbitals due to the long Cu⋯Cu separations of 2.52 Å, and since all of the bonding and antibonding combinations of σ- and π-type orbitals are also filled, there is no net Cu–Cu bonding.

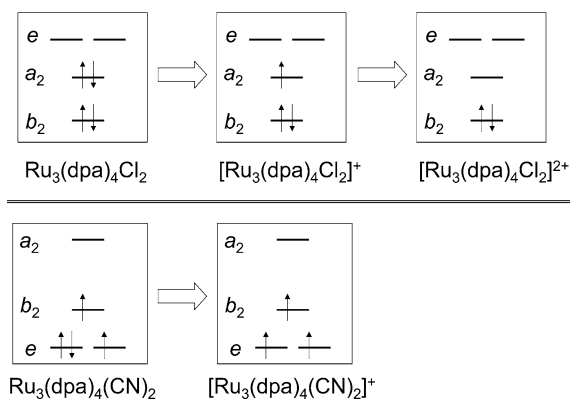
The mechanism of antiferromagnetic coupling in Cu₃(dpa)₄Cl₂ was also investigated and was found to occur mainly via a superexchange pathway through the bridging dpa ligands [3]. This pathway is similar to the well-known superexchange pathway in dicopper carboxylates [23]. One-electron oxidation of Cu₃(dpa)₄Cl₂ removes an electron from the highest-energy orbital of *b*₂ symmetry, resulting in a Cu²⁺⋯Cu³⁺⋯Cu²⁺ electron distribution with a d_{x²-y²}-based unpaired electron on each of the terminal Cu²⁺ ions. The mechanism of antiferromagnetic coupling between these two electrons is similar to that in the neutral molecule, but since there is no unpaired electron on the central Cu³⁺ ion, the magnitude of the coupling is smaller (Table 3) [3]. The hypothetical molecule Ag₃(dpa)₄Cl₂ and its one-electron oxidized cation [Ag₃(dpa)₄Cl₂]⁺ were also examined using these computational methods. Though the Ag⋯Ag separations were computed to be longer than those in the Cu₃ compounds (see Table 3), a similar electronic structure was found. Interestingly, the magnetic exchange interactions become stronger by an order of magnitude when the heavier Ag atoms replace the lighter Cu ones [3].

Table 3 Experimental and calculated metal–metal separations and isotropic exchange constants for [M₃(dpa)₄Cl₂]^{*n*+} (M = Cu, Ag; *n* = 0, 1) [3]

	$2J$ (calc), cm ⁻¹	$2J$ (exp), cm ⁻¹	M⋯M (calc), Å	M⋯M (exp), Å
Cu ₃ (dpa) ₄ Cl ₂	-437	-373	2.53	2.48
[Cu ₃ (dpa) ₄ Cl ₂] ⁺	-64	-34	2.57	2.51
Ag ₃ (dpa) ₄ Cl ₂	-1270	-	2.68	-
[Ag ₃ (dpa) ₄ Cl ₂] ⁺	-265	-	2.70	-

Table 4 Triruthenium compounds [24]

	Compound	Spin state	Compound	Spin state
Ru_3^{6+}	$\text{Ru}_3(\text{dpa})_4\text{Cl}_2$	0	$\text{Ru}_3(\text{dpa})_4(\text{CN})_2$	1
Ru_3^{7+}	$[\text{Ru}_3(\text{dpa})_4\text{Cl}_2](\text{BF}_4)$	$1/2$	$[\text{Ru}_3(\text{dpa})_4(\text{CN})_2](\text{BF}_4)$	$3/2$
Ru_3^{8+}	$[\text{Ru}_3(\text{dpa})_4\text{Cl}_2](\text{BF}_4)_2$	0		

**Fig. 5** Electron configurations for the $[\text{Ru}_3(\text{dpa})_4\text{Cl}_2]^{0/+ / 2+}$ electron transfer series (*top*) and for the $[\text{Ru}_3(\text{dpa})_4(\text{CN})_2]^{0/+}$ series (*bottom*)

2.5 Triruthenium Species

Several new Ru_3 complexes have been synthesized that have enabled a clear picture of their electronic structure to be elucidated [24]. The compounds and their spin states are displayed in Table 4. Interestingly, replacement of the axial chloride ions in $\text{Ru}_3(\text{dpa})_4\text{Cl}_2$ by cyanide ligands prompts the compounds to adopt high-spin states [24]. Four key molecular orbitals can be used to rationalize this effect and all of the available information about the spin states of the compounds. These orbitals are the δ^* combination (b_2), the doubly degenerate π^* set (e), and the nonbonding σ_{nb} combination (a_2).

The molecule $\text{Ru}_3(\text{dpa})_4\text{Cl}_2$ has an electron configuration similar to that given in Table 1, but the ordering of the orbitals is such that the frontier orbitals are those shown in Fig. 5: e (LUMO) $>$ a_2 (HOMO) $>$ b_2 (HOMO–1) [24]. This ordering is different from the ordering seen for the first-row transition metal compounds due to the larger Ru 4d orbitals that lead to stronger π and δ interactions. As shown in Fig. 5, one- and two-electron oxidation successively removes electrons from the HOMO. Since this orbital has Ru–Ru nonbonding character and Ru–Cl antibonding character, oxidations of $\text{Ru}_3(\text{dpa})_4\text{Cl}_2$ cause very little change in the Ru–Ru bond distances, but do lead to a dramatic shortening of the Ru–Cl bond distances [24].

The ordering of the frontier orbitals in $\text{Ru}_3(\text{dpa})_4(\text{CN})_2$ is different from that in the chloro analog (Fig. 5). Specifically, the e orbitals are significantly lower in

energy and the a_2 orbital is significantly higher in energy in the cyano complex than in the chloro species. The reason for this adjustment is due to the special properties of the cyanide ligand as a strong σ donor and a π acid. Thus, the a_2 orbital is destabilized due to increased σ interactions with CN^- , and the e set is stabilized due to π interactions with the unfilled C–N π^* orbitals [24]. Interestingly, these changes lead to *high-spin* ground states for both $\text{Ru}_3(\text{dpa})_4(\text{CN})_2$ and its one-electron oxidized cation (Fig. 5). The electron configuration for $\text{Ru}_3(\text{dpa})_4(\text{CN})_2$ leads to an orbitally degenerate ^3E ground state, which may be Jahn-Teller active. It is possible that there is a Jahn-Teller distortion in the form of a “kink” in the Ru–Ru–Ru axis, causing a 10° deviation from linearity. This deviation is, however, also found in the $\text{Ru}_3(\text{dpa})_4\text{Cl}_2$ series.

2.6 Spectroscopic Developments

In addition to the computational work mentioned earlier, there have been several specific spectroscopic studies that should be mentioned here. The first involves chromatographic separation of the enantiomers of several EMACs and determination of their specific rotation by circular dichroism techniques [25, 26]. Another spectroscopic study involves the full assignment of vibrational modes of Ni_3 and Co_3 EMACs by combined IR and resonance Raman spectroscopy [27]. The compounds $\text{Cr}_3(\text{dpa})_4\text{Cl}_2$ and $\text{Cr}_3(\text{dpa})_4(\text{NCS})_2$ have been examined by combined IR/Raman/surface-enhanced Raman spectroscopy, and bands at 570 cm^{-1} and 346 cm^{-1} have been assigned to the $\text{Cr}\equiv\text{Cr}$ stretch of **3.6** and the asymmetric Cr–Cr–Cr stretch of **3.5**, respectively [28]. Interestingly, the 570 cm^{-1} band increases in intensity with increased temperature relative to a $[\text{Cr}_3(\text{dpa})_4\text{Cl}_2]\text{PF}_6$ standard, suggesting that the $\text{Cr}_3(\text{dpa})_4\text{Cl}_2$ molecule undergoes a temperature-dependent structural change. In this case, the *symmetrical* form of the molecule would be the ground state and the *unsymmetrical* form is an excited state. Temperature-dependent measurements of the *symmetrical* \rightleftharpoons *unsymmetrical* equilibrium constants yielded the following thermodynamic parameters: $\Delta H = 46\text{ kJ mol}^{-1}$, $\Delta S = 138\text{ J mol}^{-1}\text{ K}^{-1}$ [28]. This ΔH value nicely matches the energy difference between the symmetrical ground state of $\text{Cr}_3(\text{dpa})_4\text{Cl}_2$ and one of its unsymmetrical excited states as calculated by Bénard and Rohmer [8].

3 New Ligands for EMACs

There are two major ways to adjust the properties and functionality of EMACs through chemical methods, which involve the alteration of either the axial or the equatorial ligands. Thus far, compounds with new axial ligands have been developed in order to add new functionality to previously known systems. The design of

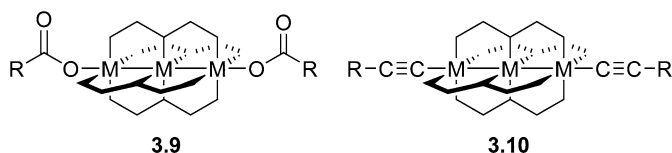
new equatorial ligands has allowed for the preparation of new chain lengths with different metals and new oxidation states for the resulting complexes.

3.1 Axial Ligands

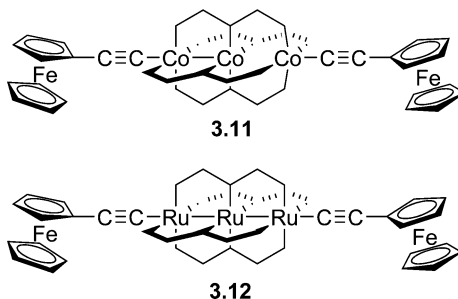
As exemplified by the example of $\text{Ru}_3(\text{dpa})_4\text{Cl}_2$ and $\text{Ru}_3(\text{dpa})_4(\text{CN})_2$ discussed earlier [24], the identity of the axial ligands can have a major impact on the electronic structure of EMAC complexes. Since halide ligands are often included in EMACs as a result of their initial synthesis, substitution of these ligands with other moieties is a primary method by which these complexes can be functionalized. For example, carboxylates have been employed as axial ligands (**3.9** in Scheme 4), allowing the resulting trinickel complexes to engage in hydrogen bonding [29].

In 2004, a general method for the preparation of acetylide-ligated EMACs (**3.10**) was reported [7]. This methodology has allowed compounds to be prepared that bear redox-active ferrocenyl end-groups, as in the tricobalt [30] and triruthenium [31] species shown in Scheme 5. Interestingly, **3.11** adopts an unsymmetrical structure with respect to the Co–Co separations, whereas the triruthenium species **3.12** is symmetric. The electrochemical properties of the two compounds are slightly different. The difference in the redox potential for the two Fe sites ($\Delta E_{1/2}$) has been measured for both species; $\Delta E_{1/2}$ is 75 mV for **3.11** (in THF solution) and 100 mV for **3.12** (in CH_2Cl_2). These values are related to the stability of the mixed-valence $\text{Fe}^{2+} \cdots \text{Fe}^{3+}$ form of the compound.

An important comparison between trinickel complexes of type **3.9** and **3.10** has been made in studying the luminescent properties of the compounds in which $\text{R} = \text{anthracyl}$ [32]. The ethynyl-linked complex shows strong green-blue luminescence



Scheme 4 Molecular structures of **3.9** and **3.10**



Scheme 5 Molecular structures of **3.11** and **3.12**

upon irradiation at 370 nm that is clearly due to excitation of the anthracene groups. The carboxylate group, however, shows no significant luminescence, which is attributed to the lack of sufficient π conjugation between the metals and the anthracene group in this complex [32].

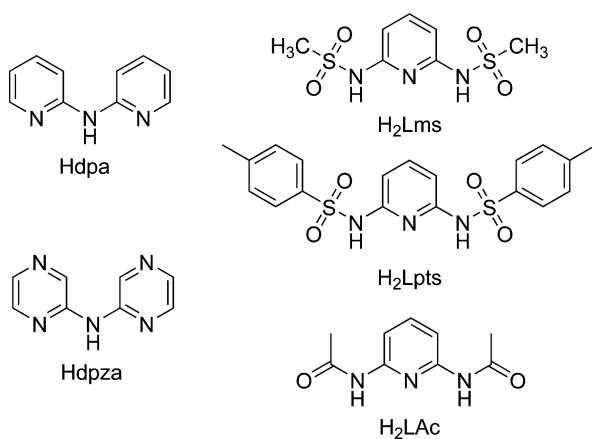
Other axial ligands for EMACs that have been recently reported include thiolate groups [33] and PF_6^- [34]. The former may be of use in linking EMACs to electrode surfaces to study their potential electron transport properties as discussed more fully in Sect. 4.

3.2 Equatorial Ligands

The design and synthesis of new polydentate organic ligands for the purpose of synthesizing novel EMACs has recently been an active area of study. The new ligands and their complexes will be presented here in comparison to their polypyridylamine prototypes, and the ligands will be discussed in the order of increasing denticity. Though they are obviously nontrivial and quite important, the synthetic organic aspects of ligand design and synthesis will not be discussed here.

3.2.1 Tridentate Ligands

New ligands that have been specifically designed to support linear trimetallic species are shown in Scheme 6, along with the prototypical *dpa* ligand. For the sake of consistency, the ligand abbreviations shown are the same as those given in the original literature. These new ligands fall into two general classes: those that will form EMACs as anions, and those that will be dianions.



Scheme 6 Molecular structures of tridentate ligands

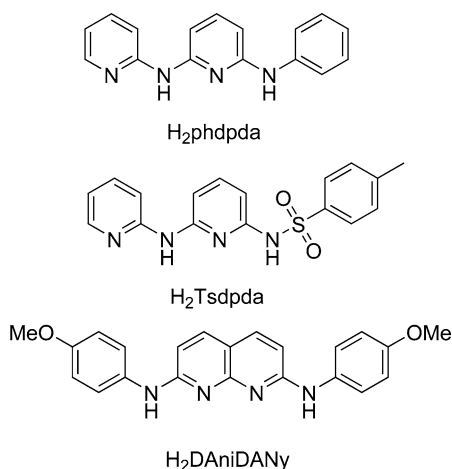
The former class is represented by the ligand dpza, which is structurally very similar to dpa, but has pyrazine rings instead of pyridine rings. The dpza ligand has been used to synthesize one Cr₃ compound and two Ni₃ compounds: Cr₃(dpza)₄Cl₂, Ni₃(dpza)₄Cl₂, and Ni₃(dpza)₄(NCS)₂ [35]. In contrast to the analogous dpa compound, Cr₃(dpza)₄Cl₂ adopts a perfectly symmetrical structure with equal Cr–Cr bond lengths of 2.39 Å. The structures of the trinickel complexes are more closely related to those of dpa.

The dpza ligand strongly affects the redox properties of these trimetallic complexes. As compared to the dpa analogs, oxidation of the dpza complexes occurs at higher potentials. However, new redox processes are observed at –0.4 to –1.1 V vs ferrocene that are attributed to reductions of the molecules from the M₃⁶⁺ to the M₃⁵⁺ oxidation states [35].

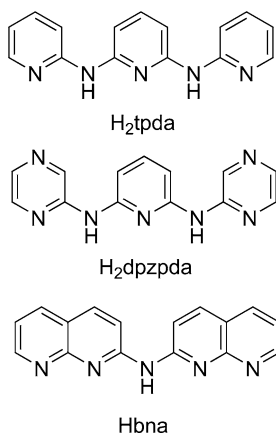
The three ligands shown in the right-hand side of Scheme 6 have been used to synthesize the first mixed equatorial ligand systems in compounds of the type Ni₃(dpa)₂(L)₂, where L denotes either Lms, Lpts, or Lac [36]. These three complexes, which all exist in the *trans* geometry, have different numbers of axial ligands, and, therefore, different magnetic properties. Ni₃(dpa)₂(Lpts)₂ has no axial ligands and is thus diamagnetic, containing three square-planar Ni(II) ions. This compound can be oxidized by NOBF₄ to the Ni₃⁷⁺ form, which a significant shortening of the Ni–Ni distances from 2.38 to 2.31 Å, consistent with partial Ni–Ni bond formation. With the Lms ligand, the mono-aquo species Ni₃(dpa)₂(Lms)₂(H₂O) is formed, which has two unpaired electrons from the single high-spin square pyramidal Ni(II) ion. In Ni₃(dpa)₂(Lac)₂, the oxygen atoms from the acetyl groups of both ligands bind axially, resulting in a complex that, like Ni₃(dpa)₄Cl₂, has an open-shell singlet ground state with antiferromagnetic coupling between the two high-spin outer Ni atoms. The trinickel complexes of these *N*-sulfonyl-based ligands have been examined computationally [37]. The sulfonyl *N*-donors have been found to be less basic than nonsulfonated amines, and their Ni complexes are expected to prefer high-spin states [37].

3.2.2 Tetradentate Ligands

The first ligand that was successfully used to support tetranuclear EMACs was the phdpda ligand, shown in Scheme 7 [38]. Now, two new ligands have been prepared that also support tetranuclear nickel compounds: Tsdpda and DAniDANy [39]. Though Ni₄(phdpda)₄ is diamagnetic and has no axial ligands, the tetranickel complex of Tsdpda, Ni₄(Tsdpda)₄(H₂O)₂, binds two axial water molecules. This causes the two outer Ni ions to be high-spin, and thus the magnetic properties of this complex are best described as involving antiferromagnetic coupling between the two terminal high-spin Ni(II) ions. Chemical oxidation of Ni₄(Tsdpda)₄(H₂O)₂ with AgBF₄ yields the Ni₄⁹⁺ complex [Ni₄(TSDpda)₄]BF₄ that has no axial ligation. The Ni–Ni distances are slightly shorter in the one-electron oxidized species, consistent with both the removal of axial ligands and Ni–Ni bond formation.



Scheme 7 Molecular structures of tetradentate ligands



Scheme 8 Molecular structures of pentadentate ligands

$\text{Ni}_4(\text{DAniDANy})_4$, like $\text{Ni}_4(\text{phdpda})_4$, has no axial ligands and is therefore diamagnetic.

3.2.3 Pentadentate Ligands

The tpda ligand (Scheme 8) has been used to form pentametallic complexes with the metals Cr [40], Co [41], Ni [41], and Ru [42]. To date, two new analog ligands have been shown to stabilize pentametallic chains. The dpzppda ligand contains pyrazine rings on the periphery of the molecule instead of pyridine rings; the bna ligand uses naphthyridine groups instead of pyridylamido groups. The dpzppda ligand has been used to synthesize new pentacobalt complexes [43]. Analogous to the trinuclear dpza complexes described earlier, reversible reductions of $\text{Co}_5(\text{dpzppda})_4\text{Cl}_2$

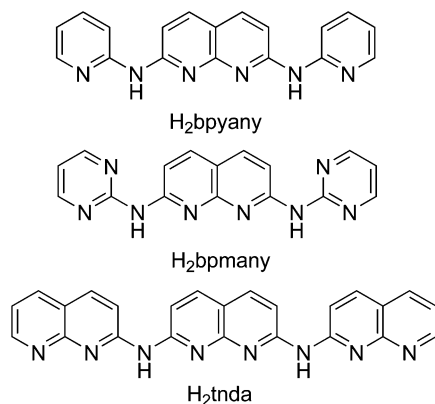
and $\text{Co}_5(\text{dpzpd})_4(\text{NCS})_2$ are accessible [43]. One-electron reduction of these complexes has been achieved through their reaction with hydrazine, yielding the corresponding $[\text{Co}_5(\text{dpzpd})_5(\text{X})_2]^-$ anions.

Reduction of the Co_5^{10+} core to Co_5^{9+} causes several important geometrical changes to occur in these molecules. The Co–X (X = axial ligand) bond distances become longer by about 0.05 Å upon reduction, as do the “inner” Co–Co bond lengths, though the lengthening here is to a lesser extent, ~ 0.02 Å. The outer Co–Co distances are not perturbed by reduction of the complex. Computational work was undertaken in order to rationalize these results. Because of the complexity of the system, however, extended Hückel methods were used, the results from which were not particularly informative [43].

Pentanickel complexes $[\text{Ni}_5(\text{bna})_4\text{Cl}_2](\text{PF}_6)_2$, $[\text{Ni}_5(\text{bna})_4\text{Cl}_2](\text{PF}_6)_4$, and $[\text{Ni}_5(\text{bna})_4(\text{NCS})_2](\text{NCS})_2$ have been synthesized using the bna ligand [44]. The naphthyridine groups in this ligand allow these complexes to be isolated in unprecedented low oxidation states with a Ni_5^{8+} group. The electronic structure of the Ni_5^{8+} units can be thought of as something between a localized Ni(II)–Ni(I)–Ni(II)–Ni(I)–Ni(II) system and a delocalized $(\text{Ni}_2)^{3+}$ –Ni(II)– $(\text{Ni}_2)^{3+}$ species. This formulation is consistent with the observation of a broad intervalence charge transfer band at 1,186 nm for the complexes.

3.2.4 Hexadentate and Octadentate Ligands

One of the most important recent results in the field has been the synthesis of higher-nuclearity even-numbered chains of six or eight metal atoms. The rational design of ligands that can support chains of six or eight metal atoms necessitated a slightly different approach from previously employed ligands. The key strategy involved utilizing naphthyridine groups to ensure that even-numbered chains would result. Thus, the ligands shown in Scheme 9 employ a mix of naphthyridine and pyridylamine groups to achieve the desired result.



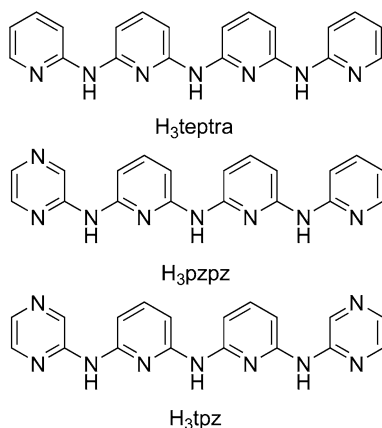
Scheme 9 Molecular structures of hexadentate and octadentate ligands

Hexacobalt and hexanickel complexes have been synthesized using the bpyany ligand [45, 46]. In both cases, the M_6^{12+} and M_6^{11+} oxidation states have been found to be stable. In contrast to the case of the pentacobalt complexes, reduction of the $[Co_6(bpyany)_4]^{4+}$ core does not have a significant effect on either the Co–Co or Co–ligand bond distances [45]. A different scenario takes place in the $[Ni_6(bpyany)_4]^{4+/3+}$ complexes. Here, the one-electron reduction is localized on the central $Ni_2(\text{naphthyridine})_4$ unit, and this Ni–Ni bond distance shrinks by almost 0.1 to 2.20 Å upon one-electron reduction [46]. This view of the electronic structure is in agreement with the well-known mixed-valence Ni(I)–Ni(II) naphthyridine complexes [47]. Similar effects are seen in the $[Ni_6(bpmany)_4]^{4+/3+}$ species [48].

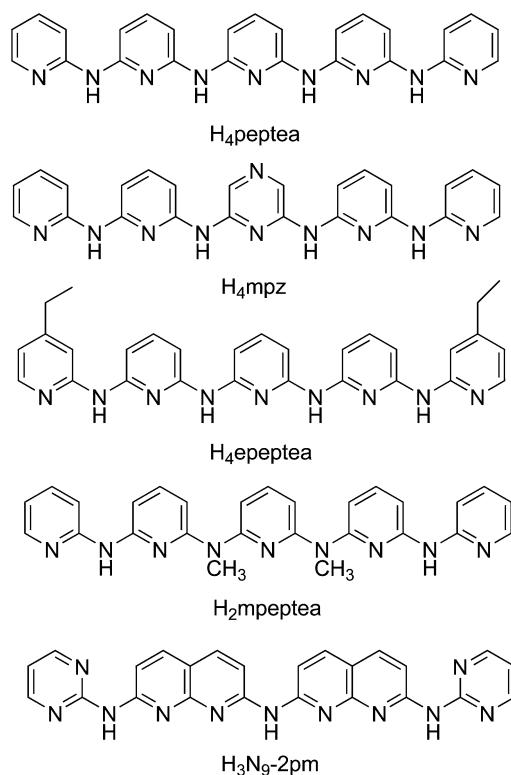
With the tnda ligand, the EMAC-forming reaction yields $[Ni_8(\text{tnda})_4Cl_2](ClO_4)_3$, a mixed-valent Ni_8^{13+} species that formally contains three Ni(I) ions [49]. The “extra” electrons in the complex are presumed to be evenly distributed among the three $Ni_2(\text{naphthyridine})_4$ sites, such that the electronic structure can be approximated as $(Ni_2)^{3+}-Ni(II)-(Ni_2)^{3+}-Ni(II)-(Ni_2)^{3+}$. This complex has been shown to undergo two successive one-electron oxidations, first at the central $Ni_2(\text{naphthyridine})_4$ site, then at one of the two terminal $Ni_2(\text{naphthyridine})_4$ sites [49].

3.2.5 Heptadentate and Nonadentate Ligands

In addition to the prototypical teptra ligand (Scheme 10), two new heptadentate ligands have been shown to stabilize heptametallc EMACs: pzp and tpz. These new ligands contain one and two terminal pyrazine groups, respectively. To date, the only $M_7(\text{teptra})_4X_2$ species that are known are the heptanickel [38] and heptachromium species [50]. By using the pyrazine derivatives, heptacobalt species $Co_7(L)_4X_2$ with $L = \text{pzp}$ or tpz and $X = \text{Cl}$ and NCS have become accessible [51]. All four complexes have been crystallographically characterized and show remarkably short Co–Co bond distances less than 2.0 Å throughout the entire chain. The complexes show rich electrochemistry, displaying two available oxidations and



Scheme 10 Molecular structures of heptadentate ligands



Scheme 11 Molecular structures of nonadentate ligands

a reversible reduction. The magnetic behavior of these complexes is not yet well understood.

The prototypical nonadentate ligand, pep tea (Scheme 11), has thus far led to the isolation of one EMAC compound, Ni₉(pep tea)₄Cl₂ [52]. The new derivatives shown in Scheme 10 were designed to target new nonmetallic EMACs. This has only been possible for two of the new ligands so far: mpz and N₉-2pm. The mpz ligand has been used to synthesize the first Cr₉ complexes, Cr₉(mpz)₄Cl₂ and Cr₉(mpz)₄(NCS)₂ [53]. As one would expect, these complexes have an unsymmetrical X–Cr≡Cr⋯Cr≡Cr⋯Cr≡Cr⋯Cr≡Cr⋯Cr–X structure.

Two nickel EMACs were synthesized with the N₉-2pm ligand, which are both shown in Fig. 6 [54]. Interestingly, although this ligand is nonadentate, a nonanickel and an octanickel complex were formed, both in the same reaction mixture. The nonanickel species, [Ni₉(N₉-pm)₄Cl₂](PF₆)₂, is a mixed-valence compound with seven Ni(II) and two Ni(I) ions. The Ni(I) ions are suggested to occupy the naphthyridine sites, similar to the hexanickel and octanickel species described earlier. The proposed electronic structure can therefore be approximated by the following: Cl–Ni(II)⋯Ni(II)⋅(Ni₂)³⁺⋯Ni(II)⋯(Ni₂)³⁺⋯Ni(II)⋯Ni(II)–Cl. The two outer Ni(II)–Cl ions will be paramagnetic because they are five-coordinate and high-spin, whereas all of the other Ni(II) ions will be square planar and diamagnetic.

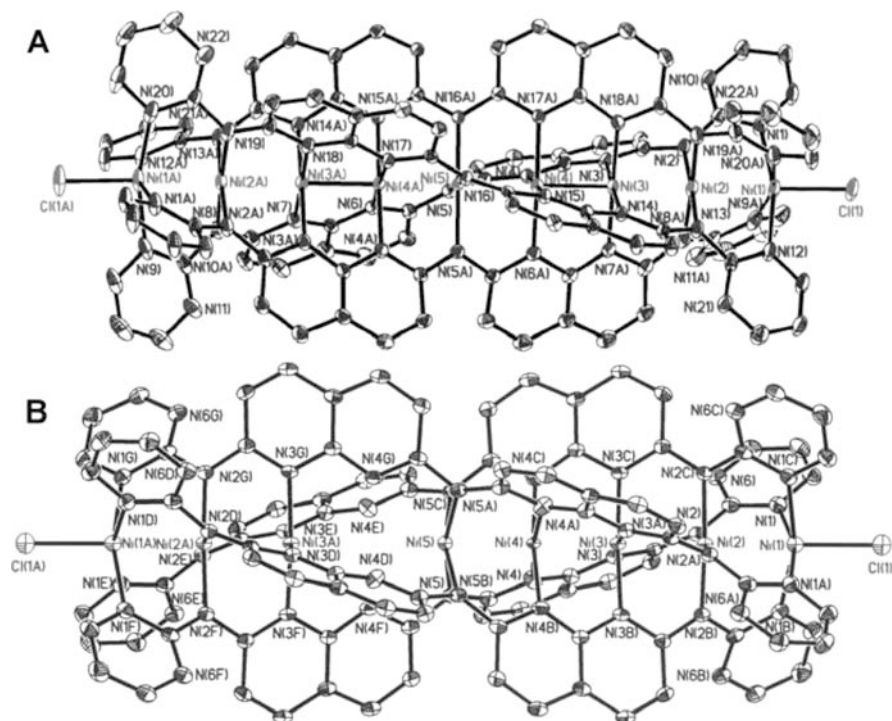
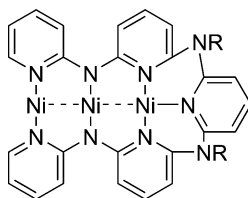


Fig. 6 Molecular structures of (a) $[\text{Ni}_9(\text{N}_9\text{-2pm})_4\text{Cl}_2]^{2+}$ and (b) $[\text{Ni}_8(\text{N}_9\text{-2pm})_4\text{Cl}_2]^{2+}$



Scheme 12 Coordination mode of epeptea and mpeptea

Each of the $(\text{Ni}_2)^{3+}$ units will also contain one unpaired electron, so this complex possesses six unpaired electrons unevenly distributed among four magnetic centers [54].

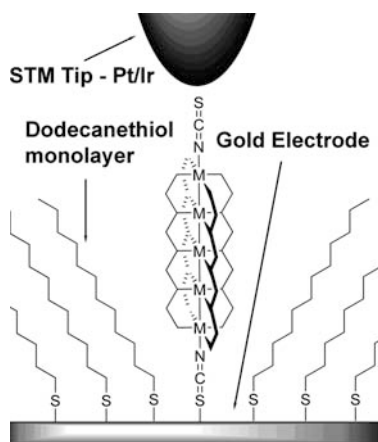
The octanickel species, $[\text{Ni}_8(\text{N}_9\text{-2pm})_4\text{Cl}_2](\text{PF}_6)_2$, contains what is described as a “defective” structure where one of the central Ni atoms is missing (see Fig. 6b). The Ni_8^{16+} core therefore consists entirely of Ni(II) ions, and only the outer two are paramagnetic and couple antiferromagnetically with each other.

The ligands epeptea and mpeptea also adopt nontraditional coordination modes. Instead of forming nonanuclear EMACs, both ligands support complexes of the formula $\text{Ni}_3(\text{L})_2$, in which each of the two ligands wraps around a linear trinickel chain binding equatorially and axially as shown in Scheme 12 [55]. These molecules behave in all respects exactly like the trinuclear EMACs described earlier.

4 Molecular Conductance Measurements

One of the most exciting developments in the field of EMACs has been the execution of experiments to test their electron transport capability at the molecular level. The basic design elements for these experiments have been the synthesis of devices in which a single EMAC molecule, or several EMAC molecules, is trapped in direct contact between two electrodes. There are many different ways to do these experiments that provide different types of information, and numerous challenges that arise making interpretation of the results nontrivial. For example, since it is virtually impossible to obtain detailed structural information about hybrid {electrode–molecule–electrode} junctions, the exact molecular orientations in two different junctions are, statistically speaking, very likely to be different from one another. Considering that molecular charge transport properties may depend strongly on molecular orientation, this effect could drastically influence the results one obtains. It is therefore often necessary to perform a statistical analysis on as many distinct measurements as possible if meaningful, reproducible data are desired.

A systematic study of $M_5(\text{tpda})_4(\text{NCS})_2$ complexes was made in which the pentametallallic molecules were adhered to a gold surface through the thiocyanate sulfur atom [56]. In order to isolate the molecules from one another and to provide a non-conductive background for current measurements, an alkane–thiol monolayer was also used. Electron transfer through the molecules was probed using a scanning tunneling microscopy (STM) measurement as shown in Scheme 13. The EMAC/alkane thiol surface was scanned such that the height of the STM tip above each point on the surface is adjusted to give a constant current response. This way, a point on the surface that is more conducting than the background will have a larger topographical height, Δh .



Scheme 13 STM molecular conductance experimental design

High points on the EMAC-containing surfaces were attributed to the presence of EMAC molecules, and by preparing the surfaces with different molecules, a comparison of the observed Δh values in each case allows for a qualitative comparison of the conductance. The observed Δh values were found to increase from $\text{Ni}_5(\text{tpda})_4(\text{NCS})_2$ to $\text{Co}_5(\text{tpda})_4(\text{NCS})_2$ to $\text{Cr}_5(\text{tpda})_4(\text{NCS})_2$ surfaces, roughly following the trend of increasing overall bond order in the molecules. Moreover, surfaces were made containing one-electron oxidized forms of these pentanuclear complexes; for these surfaces, significant changes in the magnitude of Δh were observed for the Ni_5 and Cr_5 compounds. In the former case, the observed spots became more conductive in the oxidized form, and in the latter case, lesser conductance was observed [56].

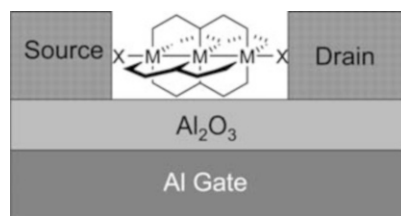
A similar experiment involving statistical analysis of thousands of individual measurements of M_3 and M_5 compounds has been recently reported [57, 58]. In this case, quantitative values of the single molecular resistance, R , were measured. As anticipated from the previous results, the R values drop from $24\text{ M}\Omega$ to $10\text{ M}\Omega$ to $3\text{ M}\Omega$ on going from Ni_5 to Co_5 to Cr_5 comecules. An analogous measurement for $\text{Ru}_5(\text{tpda})_4(\text{NCS})_2$ has also been made, yielding an R value of $\sim 5\text{ M}\Omega$, placing the Ru_5 species between Co_5 and Cr_5 in terms of the efficiency of charge transport [42]. The R values for M_3 species were also measured and were found to be much lower than those for the M_5 complexes. The compound $\text{Cr}_3(\text{dpa})_4(\text{NCS})_2$ has the lowest R value of $0.9\text{ M}\Omega$, followed by $\text{Co}_3(\text{dpa})_4(\text{NCS})_2$, and then $\text{Ni}_3(\text{dpa})_4(\text{NCS})_2$ ($R = 1.9\text{ M}\Omega$ and $3.4\text{ M}\Omega$, respectively) [57, 58]. The trends in molecular conductance in the trinuclear molecules have been examined theoretically, and nonequilibrium Green's function methods have been shown to reproduce the experimentally determined values rather well [59].

The method outlined earlier has also been used to measure R for the mixed-valence $[\text{Ni}_5(\text{bna})_4(\text{NCS})_2]^{2+}$ species (see Sect. 3.3.2.3). The determined R value, $\sim 18\text{ M}\Omega$, is distinctly lower than in the case of the homovalent $\text{Ni}_5(\text{tpda})_4(\text{NCS})_2$, signifying greater electron mobility in the mixed-valent species [44].

Reproducible current vs potential (I - V) data have been collected on the M_3 and M_5 compounds using another experimental architecture. In this case, EMACs were bound on an alkane-thiol/gold substrate, and then gold nanoparticles were added that are presumed to attach themselves to the available terminal NCS linkage. Conductance is then measured by making an electrical connection between an STM tip and the gold nanoparticle [57, 58]. In a statistical analysis of many measurements, $\text{Cr}_5(\text{tpda})_4(\text{NCS})_2$ has been found to produce I - V data in two characteristic regimes: sometimes the molecules show high conductance, reaching currents of $\sim 400\text{ nA}$ at a potential of 1 V , and sometimes a modest potential of $\sim 50\text{ nA}$ is achieved [57, 58]. Moreover, for a given device, stochastic switching from the conductive to the nonconductive form and back is observed [57, 58]. The proposed cause for this unusual behavior is a suggested change from a $\text{SCN-Cr}\equiv\text{Cr}\cdots\text{Cr}\equiv\text{Cr}\cdots\text{Cr-NCS}$ (nonconducting) structure to a $\text{SCN-Cr}=\text{Cr}=\text{Cr}=\text{Cr}=\text{Cr-NCS}$ (conducting) form [57, 58].

A single-molecule transistor design (Fig. 7) was used to shed some light on the mechanism of charge transport through single trimetal molecules [60]. This

Fig. 7 Experimental design of a single-trimetal molecule transistor



experiment involved trapping a single trimetal molecule ($\text{Ni}_3(\text{dpa})_4\text{Cl}_2$ and $\text{Cu}_3(\text{dpa})_4\text{Cl}_2$ were both used) between a nanometer-sized gap between two gold electrodes mounted on top of an aluminum gate electrode. In the devices measured, distinct steps in the I–V curves were observed due to the Coulomb blockade effect, whereby electrostatic effects prevent current from passing through a molecule until the potential is modulated such that an oxidation state change takes place. In addition to these Coulomb blockade effects, major peaks in differential conductance ($\partial I/\partial V$) were observed having energies in the range of tens of meVs. These excitations were attributed to symmetric and asymmetric metal–metal stretching modes of the trimetal molecules. Thus, it was determined that the mechanism of conductance through these trimetal EMACs was one in which electron transport through the molecule was coupled to metal–metal vibrational excitations [60].

5 Heterometallic EMACs

For EMACs, like any other polynuclear molecules, specific synthesis of heterometallic species is generally more difficult than homometallic ones. Only recently have synthetic breakthroughs been reported that allow the design and synthesis of specific hetero-trimetallic compounds with the dpa ligand. So far, two types of heterometallic species have been synthesized that have the metals in an $\text{M}_A\text{--M}_B\text{--M}_A$ or an $\text{M}_A\text{--M}_A\text{--M}_B$ arrangement. In order to distinguish between potentially isomeric compounds, the formulas for these compounds will always be written in such a way as to emphasize the metal connectivity (e.g., $\text{NiPdNi}(\text{dpa})_4\text{Cl}_2$ instead of $\text{Ni}_2\text{Pd}(\text{dpa})_4\text{Cl}_2$ and $\text{CrCrFe}(\text{dpa})_4\text{Cl}_2$ instead of $\text{Cr}_2\text{Fe}(\text{dpa})_4\text{Cl}_2$). I recommend the general adoption of this formulation.

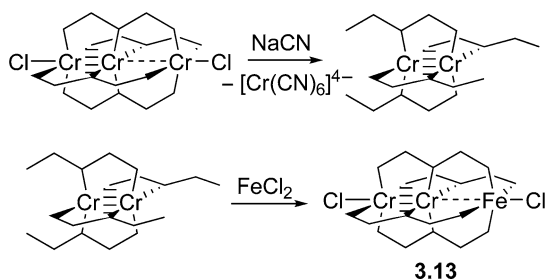
The first type of molecules have been anticipated by computational work on hypothetical $\text{NiPdNi}(\text{dpa})_4\text{Cl}_2$ [21, 22]. The synthesis and DFT calculations on a similar complex, $\text{CoPdCo}(\text{dpa})_4\text{Cl}_2$, were subsequently reported [61]. The compound was made by heating the Hdpa ligand with a 2:1 mixture of CoCl_2 and PdCl_2 . Variable temperature magnetic susceptibility measurements are complicated by the presence of first-order spin-orbit coupling within the two Co(II) ions as well as exchange interactions between them. Computational analysis of several potential ground state electron configurations shows that the antiferromagnetic singlet due to coupling of two high-spin Co(II) ions is the lowest in energy. An estimate of

the (isotropic) exchange parameter was made from broken-symmetry calculations, yielding a value of -113 cm^{-1} for $2J$ ($H = -2JS_1 \cdot S_2$), which is energetically very similar to the spin-orbit coupling parameter for Co(II), $\lambda = -172 \text{ cm}^{-1}$. A full analysis of the magnetic properties taking into account both J and λ has not yet been possible [61].

The compounds $\text{CuPdCu}(\text{dpa})_4\text{Cl}_2$ and $\text{CuPtCu}(\text{dpa})_4\text{Cl}_2$ have also been reported and are best described as containing two terminal Cu(II) ions having one unpaired electron each joined by a central square planar diamagnetic d^8 ion [62]. The antiferromagnetic coupling of the two unpaired electrons in the molecule has been investigated. Interestingly, the $2J$ values in the CuPdCu and CuPtCu complexes, -7 cm^{-1} and $<1 \text{ cm}^{-1}$, respectively, are significantly smaller than that of the isoelectronic $[\text{Cu}_3(\text{dpa})_4\text{Cl}_2]^+$ cation. Computational analysis of this phenomenon suggests that the magnitude of $2J$ is highly dependent on the spin population of the central metal atom. Pd and Pt do not accept spin density as easily as does Cu, so the $2J$ values for those compounds are correspondingly lower.

My group has begun a project focused on synthesis and characterization of heterometallic species of the type $\text{M}_A\text{M}_A\text{M}_B(\text{dpa})_4\text{X}_2$. As opposed to the work of other groups, which is guided by the potential applications of EMACs in molecular circuitry, we are interested in gaining a fundamental understanding of how metal atoms in close proximity to each other affect each other's electronic structure. This work is motivated by the observation of successful heterometallic species in many important catalytic applications, from heterometallic enzyme active sites to alloys or mixed metal oxides in heterogeneous catalysis. Our methods of study involve the synthesis of $\text{M}_A\text{M}_A\text{M}_B(\text{dpa})_4\text{X}_2$ compounds using a diamagnetic M_AM_A pair so that we can determine the electronic structure of M_B and compare it with other known systems.

For example, the prototypical molecule from our lab, $\text{CrCrFe}(\text{dpa})_4\text{Cl}_2$ (**3.13**, Scheme 14), was synthesized so that we could understand how the presence of an axial heterometallic $\text{Cr} \cdots \text{Fe}$ interaction affects the electronic structure of the Fe(II) ion [63]. This molecule could be synthesized via a general two-step strategy from $\text{Cr}_3(\text{dpa})_4\text{Cl}_2$. $\text{Cr}_3(\text{dpa})_4\text{Cl}_2$ and excess sodium cyanide react to extract one of the Cr atoms from the trinuclear chain to yield $\text{Cr}_2(\text{dpa})_4$, which can then react with another metal source, here FeCl_2 is used, to produce the heterometallic complex [63].



Scheme 14 Preparative route to **3.13**

Oxidation of the Fe center from Fe^{2+} to Fe^{3+} was studied by cyclic voltammetry. Interestingly, the redox potential of the $\text{Fe}^{2+/3+}$ wave in **3.13** was much more accessible than in other pyridine-ligated Fe(II) complexes, suggesting that the $\text{Cr}\cdots\text{Fe}$ interaction helps to stabilize the higher oxidation state [63].

The analogous $\text{CrCrCo}(\text{dpa})_4\text{Cl}_2$ and $\text{MoMoCo}(\text{dpa})_4\text{Cl}_2$ molecules have also been recently reported, which show unusual structural and magnetic features [64]. In both complexes, an unsymmetric $\text{M}\equiv\text{M}\cdots\text{Co}$ structure is observed; since the quadruply bonded $\text{M}\equiv\text{M}$ unit is considered to a first-order approximation to be diamagnetic, the Co(II) ion is the only paramagnetic center of the molecule and will be responsible for its magnetic properties. Whereas the Co(II) ion in $\text{MoMoCo}(\text{dpa})_4\text{Cl}_2$ is high-spin at all temperatures, $\text{CrCrCo}(\text{dpa})_4\text{Cl}_2$ displays spin-crossover behavior and achieves a low-spin $S = 1/2$ ground state at low temperatures. Thus, the heterometallic $\text{M}\cdots\text{Co}$ interaction clearly has an important effect on the magnetism of the Co center [64].

The MoMoCo and CrCrCo compounds also have different structural features. The crystal structure of $\text{CrCrCo}(\text{dpa})_4\text{Cl}_2$ was measured at 100 K and at room temperature, providing structural information about both the low-spin and high-spin states of the molecule, respectively. As one would expect, the Co–L bond distances change dramatically because of the spin-state change. However, while the Co–N bonds get shorter as the molecule becomes low-spin, the Co–Cl bond distances *increases* by ~ 0.2 Å and the $\text{Cr}\cdots\text{Co}$ distance shrinks from 2.62 to 2.49 Å. This change in the $\text{Cr}\cdots\text{Co}$ and Co–Cl bond distances has been attributed to an unusually large *trans* influence of the $\text{Cr}\cdots\text{Co}$ heterometallic interaction [64]. Another notable feature of the two CrCrCo structures is that on going from high-spin to low-spin, the Cr–N bond distances for the terminal Cr atom become shorter, though not to the same extent that the Co–N bond lengths change. This observation suggests that some of the spin density in the compound is delocalized onto the $\text{Cr}\equiv\text{Cr}$ unit and not solely isolated on the Co(II) ion [64].

Peng has also recently reported heterometallic RuRuNi and RuRuCu complexes that have been synthesized by reaction of Hdpa with a stoichiometric mixture of $\text{Ru}_2(\text{OAc})_4\text{Cl}$ and MCl_2 under reducing conditions [65]. Combined spectroscopic/DFT studies have shown that the electronic structures of these compounds are unusual. Instead of the anticipated $\text{Ru}(\text{II})\text{–Ru}(\text{II})\text{–M}(\text{II})$ formulation, these complexes adopt an $\text{Ru}_2^{5+}\text{–M}^+$ electron configuration. Thus, $\text{RuRuCu}(\text{dpa})_4\text{Cl}_2$ has magnetic properties similar to many other Ru_2^{5+} complexes: an $S = 3/2$ ground state with large zero-field splitting of > 50 cm^{-1} . No contribution from the diamagnetic Cu^+ ion is seen. One-electron oxidation of these complexes involves oxidation of the M^+ ions to M^{2+} [65].

It should be mentioned that the work described earlier on $\text{M}_A\text{M}_A\text{M}_B$ systems represents an extension of the conceptual design first described by Mashima for complexes containing phosphine derivative ligands and mainly second- or third-row transition metals [66–77]. By changing from P-donor ligands to N-donors, the new EMAC complexes of first-row metals can exist in high-spin configurations and are more relevant to the types of heterometallic active sites observed in metalloproteins.

6 Conclusions and Outlook

In some respects, the chemistry of EMACs is entering maturity. For example, our understanding of the electronic structure of homonuclear trimetallic compounds is becoming quite good. There are new emerging areas, such as single-molecule conductance and heterometallic electronic effects, where we still have a lot to learn. For the future of this field, I think we can expect to see new synthetic procedures developed that will produce new types of EMACs, both homometallic and heterometallic, that will challenge our understanding of the nature of metal–metal bonds. We may also anticipate a combined experimental/theoretical approach to understanding the basis for molecular conductance and how it relates to metal–metal bonding. Another important synthetic goal that has yet to be realized is the fabrication of a *functional* molecular device containing EMACs and the use of these devices in molecule-scale computing. We are on the threshold of these discoveries.

Acknowledgment and Dedication I am very grateful to the National Science Foundation for their support of my research group's work on heterometallic electronic effects (CHE-0745500). I would like to dedicate this review to the memory of my graduate mentor, F. Albert Cotton (1930–2007). His untimely death has been a major blow to this field and to the chemical community at large. He would have been intrigued and impassioned by some of the latest results reviewed herein.

References

1. Berry JF (2005) In: Cotton FA, Murillo CA, Walton RA (ed) Multiple bonds between metal atoms. Springer Science, New York
2. Yeh C-Y, Wang C-C, Chen C-H, Peng S-M (2006) In: Hirao T (ed) Redox systems under nano-space control. Springer, Berlin
3. Bénard M, Berry JF, Cotton FA, Gaudin C, López X, Murillo CA, Rohmer M-M (2006) *Inorg Chem* 45:3932
4. Berry JF, Cotton FA, Daniels LM, Murillo CA, Wang X (2003) *Inorg Chem* 42:2418
5. Berry JF, Cotton FA, Lu T, Murillo CA, Roberts BK, Wang X (2004) *J Am Chem Soc* 126:7082
6. Clérac R, Cotton FA, Daniels LM, Dunbar KR, Murillo CA, Pascual I (2000) *Inorg Chem* 39:748
7. Berry JF, Cotton FA, Murillo CA, Roberts BK (2004) *Inorg Chem* 43:2277
8. Benbellat N, Rohmer M-M, Bénard M (2001) *Chem Commun* 2368
9. Rohmer M-M, Bénard M (2002) *J Cluster Sci* 13:333
10. Clérac R, Cotton FA, Daniels LM, Dunbar KR, Kirschbaum K, Murillo CA, Pinkerton AA, Schultz AJ, Wang X (2000) *J Am Chem Soc* 122:6226
11. Parkin G, Hoffmann R (1994) *Angew Chem Int Ed Eng* 33:1462
12. Parkin G (1993) *Chem Rev* 93:887
13. Parkin G (1992) *Acc Chem Res* 25:455
14. Rohmer M-M, Strich A, Bénard M, Malrieu JP (2001) *J Am Chem Soc* 123:9126
15. Pantazis DA, McGrady JE (2006) *J Am Chem Soc* 128:4128
16. Pantazis DA, Murillo CA, McGrady JE (2008) *Dalton Trans* 608
17. Clérac R, Cotton FA, Dunbar KR, Lu TB, Murillo CA, Wang X (2000) *J Am Chem Soc* 122:2272
18. Clérac R, Cotton FA, Dunbar KR, Murillo CA, Pascual I, Wang X (1999) *Inorg Chem* 38:2655
19. Berry JF, Cotton FA, Murillo CA (2003) *Dalton Trans* 3015

20. Kiehl P, Rohmer M-M, Bénard M (2004) *Inorg Chem* 43:3151
21. López X, Bénard M, Rohmer M-M (2006) *J Mol Struct Theochem* 777:53
22. López X, Rohmer M-M, Bénard M (2008) *J Mol Struct* 890:18
23. Kahn O (1993) *Molecular magnetism*. Wiley, New York
24. Kuo CK, Liu IPC, Yeh CY, Chou CH, Tsao TB, Lee G-H, Peng S-M (2007) *Chem Eur J* 13:1442
25. Armstrong DW, Cotton FA, Petrovic AG, Polavarapu PL, Warnke MM (2007) *Inorg Chem* 46:1535
26. Warnke MM, Cotton FA, Armstrong DW (2007) *Chirality* 19:179
27. Lai SH, Hsiao CJ, Ling JW, Wangb WZ, Peng S-M, Chen IC (2008) *Chem Phys Lett* 456:181
28. Hsiao CJ, Lai SH, Chen IC, Wang W-Z, Peng S-M (2008) *J Phys Chem A* 112:13528
29. Li H, Yan J, Xu YY, Gao WG, Lee G-H, Peng S-M (2007) *J Coord Chem* 60:2731
30. Berry JF, Cotton FA, Murillo CA (2004) *Organometallics* 23:2503
31. Kuo CK, Chang JC, Yeh CY, Lee G-H, Wang C-C, Peng S-M (2005) *Dalton Trans* 3696
32. Cotton FA, Chao H, Li Z, Murillo CA, Wang QS (2008) *J Organomet Chem* 693:1412
33. Cotton FA, Murillo CA, Wang QS (2007) *Inorg Chem Commun* 10:1088
34. Cotton FA, Murillo CA, Wang QS, Young MD (2008) *Eur J Inorg Chem* 5257
35. Ismayilov RH, Wang W-Z, Lee G-H, Wang RR, Liu IPC, Yeh C-Y, Peng S-M (2007) *Dalton Trans* 2898
36. Huang MY, Yeh CY, Lee G-H, Peng S-M (2006) *Dalton Trans* 5683
37. López X, Bénard M, Rohmer M-M (2007) *Inorg Chem* 46:5
38. Lai SY, Lin TW, Chen YH, Wang CC, Lee G-H, Yang MH, Leung MK, Peng S-M (1999) *J Am Chem Soc* 121:250
39. López X, Huang MY, Huang GC, Peng S-M, Li FY, Bénard M, Rohmer M-M (2006) *Inorg Chem* 45:9075
40. Cotton FA, Daniels LM, Lu TB, Murillo CA, Wang X (1999) *J Chem Soc Dalton Trans* 517
41. Shieh SJ, Chou CC, Lee GH, Wang CC, Peng S-M (1997) *Angew Chem Int Ed Eng* 36:56
42. Yin CX, Huang GC, Kuo CK, Fu MD, Lu HC, Ke JH, Shih KN, Huang YL, Lee GH, Yeh CY, Chen CH, Peng S-M (2008) *J Am Chem Soc* 130:10090
43. Wang WZ, Ismayilov RH, Wang RR, Huang YL, Yeh CY, Lee GH, Peng S-M (2008) *Dalton Trans* 6808
44. Liu IPC, Bénard M, Hasanov H, Chen IWP, Tseng WH, Fu MD, Rohmer M-M, Chen CH, Lee GH, Peng S-M (2007) *Chem Eur J* 13:8667
45. Chien CH, Chang JC, Yeh CY, Lee GH, Fang JM, Peng S-M (2006) *Dalton Trans* 2106
46. Chien CH, Chang JC, Yeh CY, Lee GH, Fang JM, Song Y, Peng S-M (2006) *Dalton Trans* 3249
47. Bencini A, Berti E, Caneschi A, Gatteschi D, Giannasi E, Invernizzi I (2002) *Chem Eur J* 8:3660
48. Tsao TB, Lo SS, Yeh CY, Lee GH, Peng S-M (2007) *Polyhedron* 26:3833
49. Hasan H, Tan UK, Lee GH, Peng S-M (2007) *Inorg Chem Commun* 10:983
50. Chen YH, Lee CC, Wang CC, Lee GH, Lai SY, Li FY, Mou CY, Peng S-M (1999) *Chem Commun* 1667
51. Wang WZ, Ismayilov RH, Lee GH, Liu IPC, Yeh CY, Peng S-M (2007) *Dalton Trans* 830
52. Peng S-M, Wang CC, Jang YL, Chen YH, Li FY, Mou CY, Leung MK (2000) *J Magn Magn Mater* 209:80
53. Ismayilov RH, Wang WZ, Wang RR, Yeh CY, Lee GH, Peng S-M (2007) *Chem Commun* 1121
54. Ismayilov RH, Wang WZ, Wang RR, Huang YL, Yeh CY, Lee GH, Peng S-M (2008) *Eur J Inorg Chem* 4290
55. Cotton FA, Chao H, Murillo CA, Wang QS (2006) *Dalton Trans* 5416
56. Lin SY, Chen IWP, Chen CH, Hsieh MH, Yeh CY, Lin TW, Chen YH, Peng S-M (2004) *J Phys Chem B* 108:959
57. Chen IWP, Fu MD, Tseng WH, Yu JY, Wu SH, Ku CJ, Chen CH, Peng S-M (2006) *Angew Chem Int Ed* 45:6244
58. Chen I-WP, Fu MD, Tseng WH, Yu JY, Wu SH, Ku CJ, Chen C-H, Peng S-M (2006) *Angew Chem Int Ed* 45:6244
59. Hsu LY, Huang QR, Jin BY (2008) *J Phys Chem C* 112:10538

60. Chae DH, Berry JF, Jung S, Cotton FA, Murillo CA, Yao Z (2006) *Nano Lett* 6:165
61. Rohmer M-M, Liu IPC, Lin JC, Chiu MJ, Lee CH, Lee G-H, Bénard M, López X, Peng S-M (2007) *Angew Chem Int Ed* 46:3533
62. Liu IPC, Lee G-H, Peng S-M, Bénard M, Rohmer M-M (2007) *Inorg Chem* 46:9602
63. Nippe M, Berry JF (2007) *J Am Chem Soc* 129:12684
64. Nippe M, Victor E, Berry JF (2008) *Eur J Inorg Chem* 5569
65. Huang GC, Bénard M, Rohmer M-M, Li LA, Chiu MJ, Yeh CY, Lee GH, Peng S-M (2008) *Eur J Inorg Chem* 1767
66. Kitagawa Y, Nakano S, Kawakami T, Mashima K, Yamaguchi K (2003) *Polyhedron* 22:2019
67. Mashima K, Nakano H, Mori T, Takaya H, Nakamura A (1992) *Chem Lett* 185
68. Mashima K, Nakano H, Nakamura A (1993) *J Am Chem Soc* 115:11632
69. Nakano H, Nakamura A, Mashima K (1996) *Inorg Chem* 35:4007
70. Mashima K, Nakano H, Nakamura A (1996) *J Am Chem Soc* 118:9083
71. Mashima K, Tanaka M, Tani K, Nakamura A, Takeda S, Mori W, Yamaguchi K (1997) *J Am Chem Soc* 119:4307
72. Mashima K, Tanaka M, Kaneda Y, Fukumoto A, Mizomoto H, Tani K, Nakano H, Nakamura A, Sakaguchi T, Kamada K, Ohta K (1997) *Chem Lett* 411
73. Tanaka M, Mashima K, Nishino M, Takeda S, Mori W, Tani K, Yamaguchi K, Nakamura A (2001) *Bull Chem Soc Japan* 74:67
74. Mashima K, Fukumoto A, Nakano H, Kaneda Y, Tani K, Nakamura A (1998) *J Am Chem Soc* 120:12151
75. Ruffer T, Ohashi M, Shima A, Mizomoto H, Kaneda Y, Mashima K (2004) *J Am Chem Soc* 126:12244
76. Mashima K, Shimoyama Y, Kusumi Y, Fukumoto A, Yamagata T, Ohashi M (2007) *Eur J Inorg Chem* 235
77. Ohashi M, Shima A, Ruffer T, Mizomoto H, Kaneda Y, Mashima K (2007) *Inorg Chem* 46:6702

Electronically Coupled MM Quadruple Bonded Complexes of Molybdenum and Tungsten

Malcolm H. Chisholm

Abstract The synthesis, molecular and electronic structures of covalently linked dinuclear units having MM quadruple bonds ($M = \text{Mo}$ or W) are described together with their attendant spectroscopies. Particular attention is paid to compounds where $M_2\delta$ to bridge π bonding generates strongly coupled M_2 centers whose mixed valence ions formed upon one electron oxidation traverse the Class II/III border.

Keywords Molybdenum · Tungsten · MM Quadruple Bonds · Electronic Coupling · Mixed Valence · Spectroscopy

Contents

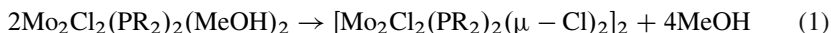
1	Introduction	30
2	Syntheses	31
3	Molecular Structures	32
4	Electronic Coupling: Frontier Molecular Orbital Interactions and Electronic Structure Calculations	37
	4.1 Oxalate Bridges	37
	4.2 $O_2C-X-CO_2$ Bridges	39
	4.3 Other Related Bridges	40
5	Electrochemical Studies	42
6	EPR Spectroscopy	45
7	Optical Spectra	47
	7.1 IVCT and Charge Resonance Bands	47
	7.2 Metal-to-Bridge Charge Transfer Bands	48
8	Steady-State Emission and Transient Absorption Spectroscopy	50
9	Resonance Raman Spectra	51
10	Molecular Loops, Triangles, and Squares	52
11	Concluding Remarks	54
	References	54

M.H. Chisholm
Department of Chemistry, The Ohio State University, Columbus, OH 43210, USA
e-mail: chisholm@chemistry.ohio-state.edu

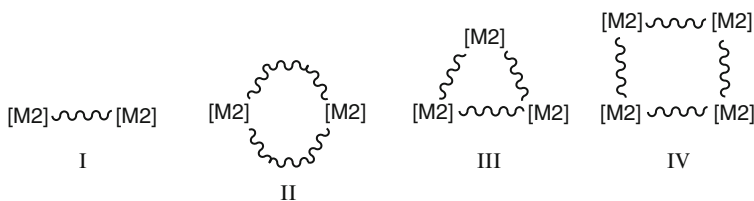
* In memory of Professor F.A. Cotton.

1 Introduction

The first example of the linking of two MM quadruple bonds was discovered by McCarley who found that two Mo_2 units could be linked together by bridging halides if there were attendant ligands that were labile as shown in (1) [1–3].



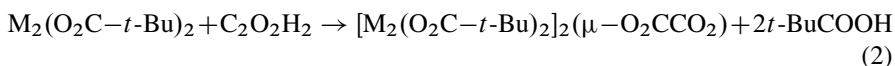
The molecular structure of the tetramolecular molybdenum complex consisted of a planar rectangular Mo_4 unit with short and long distances indicative of only weak MM bonding interactions between the two Mo_2^{4+} centers. Indeed, with iodide bridges the long Mo to Mo distances were clearly nonbonding. These types of compounds along with those M_4 clusters (squares, butterflies, diamonds, and bisphe-noids) derived from the linking of MM triple bonds with bridging halide or alkoxide ligands are not discussed in this study. They have been the topic of a recent view [4]. Rather here we are concerned with MM quadruple bonds that are linked together by the agency of an organic bridging ligand. These are now referred to as “dimers of dimers,” molecular loops, molecular triangles, and squares, and are schematically represented by the drawings given in **I**, **II**, **III**, and **IV**, respectively.



In these drawings the $\sim\sim\sim$ represents an organic bridging group which is covalently bonded to each dinuclear center. The electronic coupling of the two M_2 units thus arises from their mutual coupling to the bridge. The dominant mechanism of coupling involves the frontier orbitals of the M_2 center and the bridge, specifically the $\text{M}_2\delta$ orbitals and the bridge π system. If the bridge lacks a conjugated π system and is saturated, the two M_2 centers are electronically isolated: the bridge acts as an insulator. Since MM quadruple bonds of configuration $\sigma^2\pi^4\delta^2$ are redox-active and very often undergo reversible one-electron oxidations to give $[\text{M}_2]^{5+}$ centers with configuration $\sigma^2\pi^4\delta^1$ [5], the oxidation of the dimer of dimers, molecular loops and triangles and squares leads to mixed valence complexes. Depending upon the degree of electronic coupling through the bridge these may be classified on the Robin and Day Scheme [6] as valence-trapped, class I, fully delocalized, class III or somewhere in between, class II, a situation which often depends upon the time scale of the measurement. Probing the nature of the electronic coupling in the neutral and mixed-valence ions has been a focus of attention in the study of these complexes.

2 Syntheses

Two synthetic approaches have been prevalent in the preparation of these dinuclear coupled complexes. The first involves the reaction between a dimetal tetracarboxylate and a bridging ligand that contains two active protons such as a dicarboxylic acid. This has been extensively used by the Chisholm group in the synthesis of dimers of dimers, compounds of type I [7, 8]. In reactions of this type the formation of the dimer of dimers is achieved by its preferential precipitation from solution. The most simple example of this type of reaction is seen in the reactions of oxalic acid with the dimetal pivalates shown in (2) ($M = Mo$ or W).

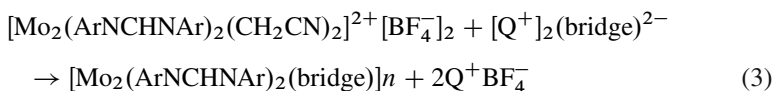


In this reaction the formation of the oxalate bridged compound is indicated by a striking color change. The starting $M_2(O_2C-t-Bu)_4$ compounds are yellow and the oxalate bridged compounds are maroon and blue when $M = Mo$ and W , respectively. In general, strong electronic coupling between the M_2 centers and the bridge is signaled by intense absorptions in the visible region of the spectrum that arise from metal-to-bridge charge transfer.

In reactions of the type shown in (2) which are equilibria reactions, several problems can arise in the isolation of the desired product including, if the dimer of dimers is soluble, the formation of mixtures involving higher oligomers. This problem notwithstanding, the Chisholm group have prepared numerous compounds of type I in this manner.

An alternative approach that has been used extensively and to good effect by the Cotton group involves salt metathesis reactions. For example, the reaction between the cationic molybdenum complex $[Mo_2(\text{formamidinate})_3(CH_3CN)_2]^+BF_4^-$ and the sodium or tetra-*n*-butylammonium salt of a bridge(2-) anion leads cleanly to the formation of the bridged complex $[Mo_2(\text{formamidinate})_3]_2(\text{bridge})$ [9, 10]. Typically the Cotton group have employed the formamidinate *p*-MeOC₆H₄NCHNC₆H₄-*p*-OMe. These attendant ligands provide access to soluble and crystallizable products.

The dicationic complexes $[Mo_2(ArNCHNAr)_2(CH_3CN)_4]^{2+}[BF_4^-]_2$ contain a *cis*-templating $Mo_2(\text{formamidinate})_2$ unit and when these are allowed to react with the stoichiometry shown in (3), then molecular loops, **II** ($n = 2$), triangles, **III** ($n = 3$), or squares, **IV** ($n = 4$) can be formed. ($Ar = p\text{-MeOC}_6\text{H}_4$; $Q = Na$ or $n\text{-Bu}_4N$) [11].



Rigid planar bridges such as oxalate and 1,4-terephthalate favor the formation of molecular squares, while flexible bridges may more readily be accommodated in

molecular loops. In some instances equilibria have been observed involving these species and this matter is discussed later.

Another route to dimers of dimers employed by the Cotton group has involved the use of the Mo_2^{5+} -containing compound $\text{Mo}_2(\text{ArNCHNAr})_3\text{Cl}_2$ in its reactions with salt metathesis bridge reagents in the presence of zinc metal or NaHBEt_3 as a reducing agent [10].

Salt metathesis reactions involving the pivalate cations $[\text{Mo}_2(\text{O}_2\text{C}-t\text{-Bu})_3(\text{CH}_3\text{CN})_2]^+$ and $[\text{Mo}_2(\text{O}_2\text{C}-t\text{-Bu})_2(\text{CH}_3\text{CN})_4]^{2+}$ have also been examined. The monocations have been found to yield dimers of dimers, but the dications have not led to the isolation of discrete molecular triangles or squares but rather to insoluble materials that are most likely polymeric.

The approaches taken by the Chisholm and Cotton groups each have their advantages and limitations. The use of the formamidinate supported Mo_2^{4+} centers has led to well-characterized crystalline compounds that are kinetically persistent even in their oxidized forms. However, this synthetic approach is limited to molybdenum compounds. The use of pivalate or related carboxylate ancillary ligands often leads to kinetically labile compounds in solution due to ligand-scrambling reactions. However, for the complexes that can be isolated in a pure form a direct comparison of electronic coupling is possible for both molybdenum- and tungsten-containing complexes. Since their ionic/covalent radii are of almost identical size, this has allowed the examination of M_2 to bridge coupling in the 4d and 5d analogues and even complexes containing the MoW quadruple bond.

It is not the purpose of this chapter to provide a comprehensive review concerning every compound synthesized in these manners but rather to focus on the various interesting properties that have emerged from these syntheses.

3 Molecular Structures

Illustrative examples of dicarboxylate bridged compounds supported by the *p*-anisoleformamidinate ligands are shown in Fig. 1 where the formamidinate ligand is abbreviated to its NCN metal-bound component. For the dimer of dimers the Mo_2 units are not required to be aligned in a parallel manner though, as will be described later, this geometry maximizes the potential for $\text{Mo}_2\delta - \text{bridge}\pi - \text{Mo}_2\delta$ communication. For molecular loops, triangles, and squares the parallel arrangement is required and only small deviations may arise due to crystal packing. In all of these compounds the MoMo distance within each Mo_2^{4+} unit is essentially that of a typical MoMo quadruple bond, namely $\sim 2.10 \text{ \AA}$.

Another interesting class of bridging ligands is seen in the structures of those bearing dioxalene dianions [13] and tetraazatetracene [14]. These bridges are planar and enforce parallel Mo_2 units with Mo_2 to Mo_2 distances of $\sim 7 \text{ \AA}$. They affect strong coupling between the Mo_2 centers and the products of both one- and two-electron oxidations have been structurally characterized. Each successive oxidation brings about a lengthening of each Mo–Mo bond in the dinuclear units by

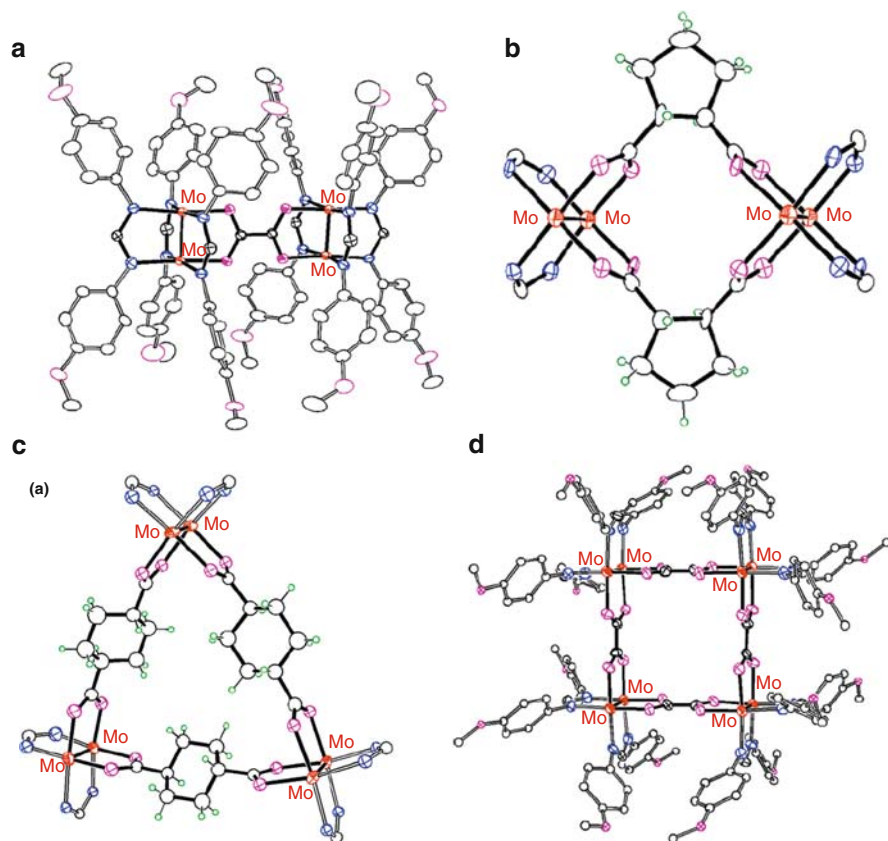
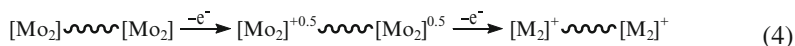


Fig. 1 Examples of a dimer of dimers (**a**); a molecular loop (**b**) a molecular triangle (**c**) and a molecular square (**d**). In (**b**) and (**c**) the p-anisole groups have been omitted. Adapted from [12]

$\sim 0.02 \text{ \AA}$ which provides clear structural evidence for electron delocalization of the type represented by (4).



The structure of the neutral tetraazatetracene bridged compound is shown in Fig. 2.

The *N, N'* diaryloxaamidinate bridge leads to two isomers both of which have been structurally characterized [15]. One isomer has a planar bridged structure involving six-membered MoMoOCCN rings, while the other has a twisted geometry with five-membered MoMoOCN rings as shown schematically in **V** and **IV**, respectively.

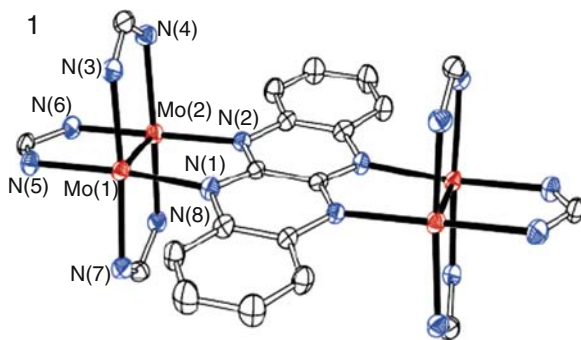
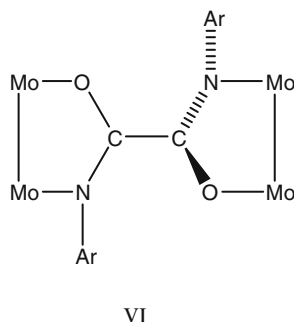
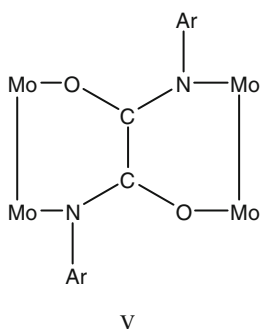
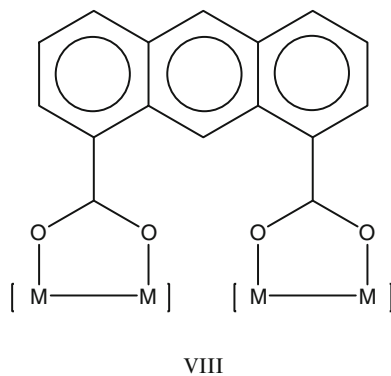
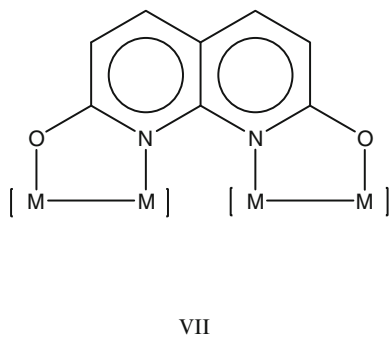


Fig. 2 A bridging tetraazatetracene ligand uniting two $\text{Mo}_2(\text{p-anisoleNCHN-p-anisole})_3$ units. Adapted from [14]



These isomers show very different degrees of electronic communication as evidenced by their electrochemical properties and this matter will be discussed later.

The bridging ligands derived from deprotonation of 2,7-dihydroxynaphthyrine and 1,8-anthracenedicarboxylic acid, shown in **VII** and **VIII**, align the metal atoms in a linear or chain-like manner.



The two bridges shown in **VII** and **VIII** can be viewed as being stereochemically correspondent with respect to the central Mo to Mo distance though only the

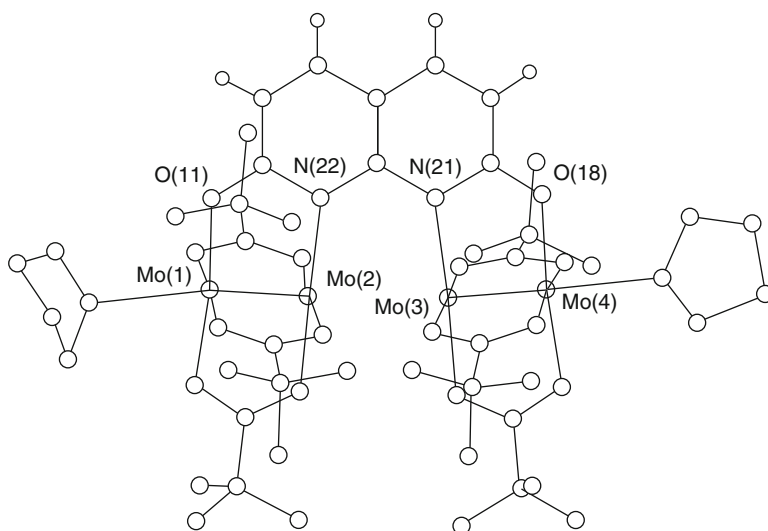
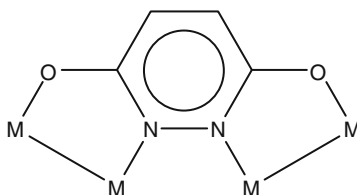


Fig. 3 A drawing of the $[\text{Mo}_2(\text{O}_2\text{C}-t\text{-Bu})_3]_2(\mu\text{-C}_8\text{H}_4\text{N}_2\text{O}_2)\cdot 2\text{THF}$ molecule. Adapted from [8]

compound $[\text{Mo}_2(\text{O}_2\text{C}-t\text{-Bu})_3]_2(\mu\text{-C}_8\text{H}_4\text{N}_2\text{O}_2)$ has been structurally characterized [16]. A view of this molecule is given in Fig. 3. The molecule adopts a slightly twisted geometry in the solid state where the alignment of the two MoMo axes is offset. This allows for minimization of O to O repulsions of the pivalate's oxygens and for weak internal $\text{Mo}\cdots\text{O}$ bonding interactions. Within the Mo_4 chain there are short 2.11-Å and long 3.2-Å distances corresponding to localized MM quadruple bond distances and nonbonding distances. The Mo_2 units are, however, brought much closer together in this arrangement than in those noted before.

There is little doubt that the 1,8-anthracenedicaboxylate bridged tetranuclear compounds adopt a related structure in the solid state involving this type of C_2 symmetry where the two MoMo units are offset from one another. Indeed, by low-temperature ^1H NMR spectroscopy one can freeze out three pivalate signals in the ratio 1:1:1, but at room temperature these appear in the ratio 2:1 corresponding to a time-averaged structure with respect to the bridge, namely cis and trans pivalates and a linear M_4 unit [8].

Another bridge of interest is the 3,6-dioxypyridazine shown in **IX**. Here the central metal atoms are brought close together ~ 3.5 Å and are united by just two nitrogen atoms.



IX

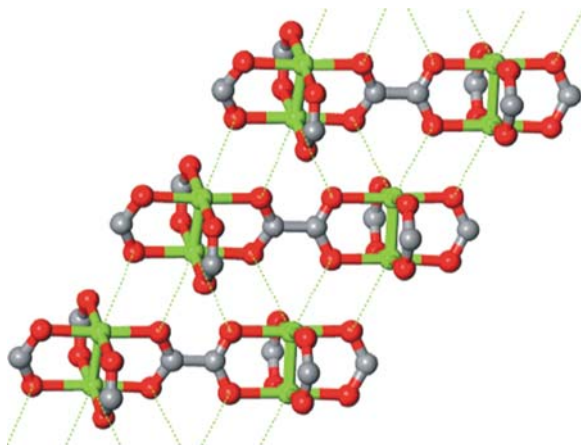


Fig. 4 Drawing of a section of the infinite chain structure found for $[(t\text{-BuCO}_2)_3\text{Mo}_2]_2(\mu\text{-O}_2\text{CCO}_2)$. The *t*-Bu groups are omitted for clarity. Adapted from [18]

The molecular structure of the tungsten-containing compound $[(t\text{-BuCO}_2)_3\text{W}_2]_2(\mu\text{-C}_4\text{H}_2\text{N}_2\text{O}_2)$ was determined in its neutral and singly oxidized forms [17]. Each W_2 unit was crystallographically independent in each redox state, but the average lengthening of the WW distance upon oxidation was $\sim 0.02 \text{ \AA}$ consistent with a delocalized mixed-valence ion with WW bond orders of 3.75.

Many other compounds have been made which are structurally related to the ones noted earlier, and as mentioned the use of the *p*-anisole formamidinates has yielded crystalline materials well suited for single-crystal X-ray studies. With attendant carboxylate ligands microcrystalline powders are often obtained, and in some cases their structures have been examined by powder X-ray diffraction and direct space methods. This involves employing a model structure within the unit cell to simulate the observed powder pattern. Accurate bond distances and angles cannot be obtained but the arrangements and ordering of the molecules in the solid state can be well established. In this way the compounds $[(t\text{-BuCO}_2)_3\text{M}_2]_2(\mu\text{-X})$ where $\text{M} = \text{Mo}$ or W and $\text{X} = \text{oxalate}$ [18] and 1,4-terephthalate [19] have been determined. In the solid state these form infinite chain structures due to weak intermolecular oxygen to metal interactions along the MM axis. A representation of this is shown in Fig. 4 for the Mo_4 -oxalate compound.

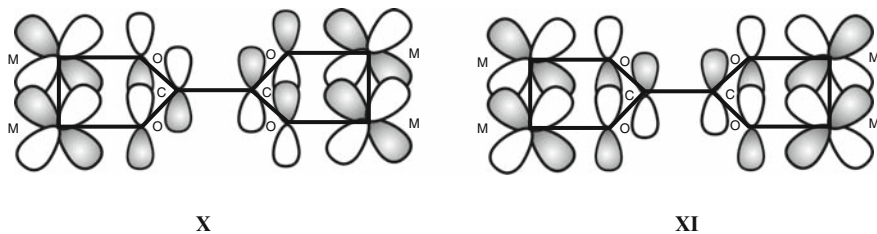
The formamidinates do not tend to associate in this manner because of both steric and electronic factors, but the molecular squares often pack to form channels that can trap solvent molecules.

4 Electronic Coupling: Frontier Molecular Orbital Interactions and Electronic Structure Calculations

The electronic coupling between the two dinuclear centers arises from the frontier orbital interactions of the M_2 centers and the bridge. Simple symmetry arguments aided by considerations of orbital energies and overlap provide an invaluable first step in understanding the bonding in these complexes. These chemically intuitive approaches can then be aided by electronic structure calculations employing density functional theory, DFT, and time-dependent density functional theory, TDDFT, with the aid of commercial program packages. The calculations most often are applied to model compounds where ancillary ligands, but not the bridge, are reduced in size to minimize computational time and resources. For example, an H atom may substitute for an alkyl or aryl group.

4.1 Oxalate Bridges

After forming C–C, C–O, and O–M σ bonds, planar oxalate has just six π molecular orbitals and only two of these have the appropriate energy and symmetry match to interact with the $MM\delta$ orbital. These orbital interactions are schematically represented by **X** and **XI**.



Of these the in-phase combination of the two $M_2\delta$ orbitals with the oxalate π^* orbital, **XI**, is by far the most important. (The filled CO_2 π bonding orbitals lie several eV below the energy of the $M_2\delta$ orbitals). Effectively, the filled $M_2\delta$ orbitals back-bond to the oxalate π^* system and stabilize the planar O_2CCO_2 unit by placing electron density in an orbital which has C–C π bonding character. The free oxalate dianion has the twisted D_{2d} geometry which minimizes oxygen lone pair repulsions.

Calculations on the model compounds $[(HCO_2)_3M_2]_2(\mu-O_2CCO_2)$, where formate substitutes for pivalate, employing DFT support this view and the frontier MOs are shown in Fig. 5.

The splitting of the energies of the HOMO and HOMO-1 is a measure of the degree of electronic coupling. As can be seen from an inspection of Fig. 5 this is greater for $M = W$ than for $M = Mo$. The greater interaction arises because the $W_2\delta$ orbital is higher in energy than the $Mo_2\delta$ and the $W5d\pi$ -overlap with the oxalate π^* orbital is greater than that for $Mo4d\pi$.

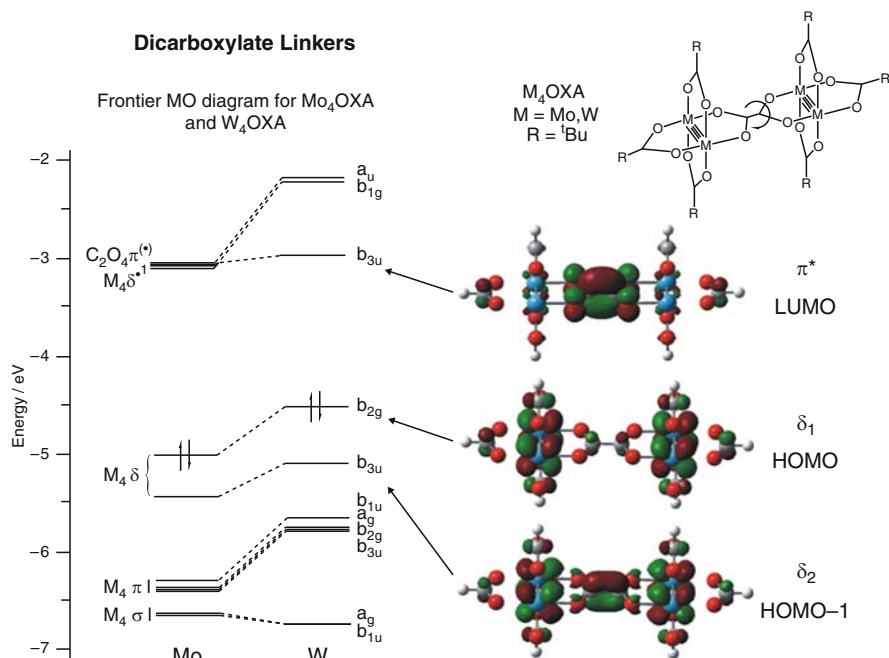


Fig. 5 Frontier orbital energy diagram and Gausview plots of the model compounds $[(HCO_2)_3M_2]_2(\mu\text{-oxalate})$, where M = Mo or W. Adapted from [18]

It is, of course, possible to calculate the orbital energies and the absolute energies of the molecules for various dihedral angles involving the two oxalate CO_2 planes. When the dihedral angle θ is 0° , i.e., the molecule contains a planar $M_2O_2CCO_2M_2$ unit, the energy is a minimum, indicating a ground-state geometry and that with $\theta = 90^\circ$ is a maximum. In this way a barrier to rotation about the oxalate C–C bond can be estimated for M = Mo to be $\sim 5 \text{ kcal mol}^{-1}$ and for M = W, $\sim 9 \text{ kcal mol}^{-1}$ [18]. This leads to the prediction that rotation about the central C–C bond should be possible with room temperature thermal energy and that a Boltzmann distribution of rotamers with $\theta = 0 \rightarrow 90^\circ$ will exist in solution. A simple Walsh diagram indicating the changes to the FMOs with dihedral angle θ is given in Fig. 6. This very clearly indicates that only the $M_2\delta$ and oxalate π^* orbitals are really affected. The $M_2\pi$, σ , and δ^* orbitals are essentially unchanged in energy, and this reinforces the value of the simple considerations of orbital symmetry and energy. When $\theta = 90^\circ$ the two $M_2\delta$ combinations are degenerate as are the two oxalate π^* orbitals. Indeed, in terms of electronic coupling the limiting position of $\theta = 0^\circ$ (D_{2h} symmetry) and $\theta = 90^\circ$ (D_{2d} symmetry) represents fully “on and off” positions of a molecular rheostat. Also it can be seen from the Walsh diagram and Fig. 5 that the HOMO to LUMO electronic transition represents a metal-to-bridge charge transfer. In D_{2h} symmetry this is g to u and is fully allowed. The Walsh diagram also indicates that the energy of this transition increases as θ increases

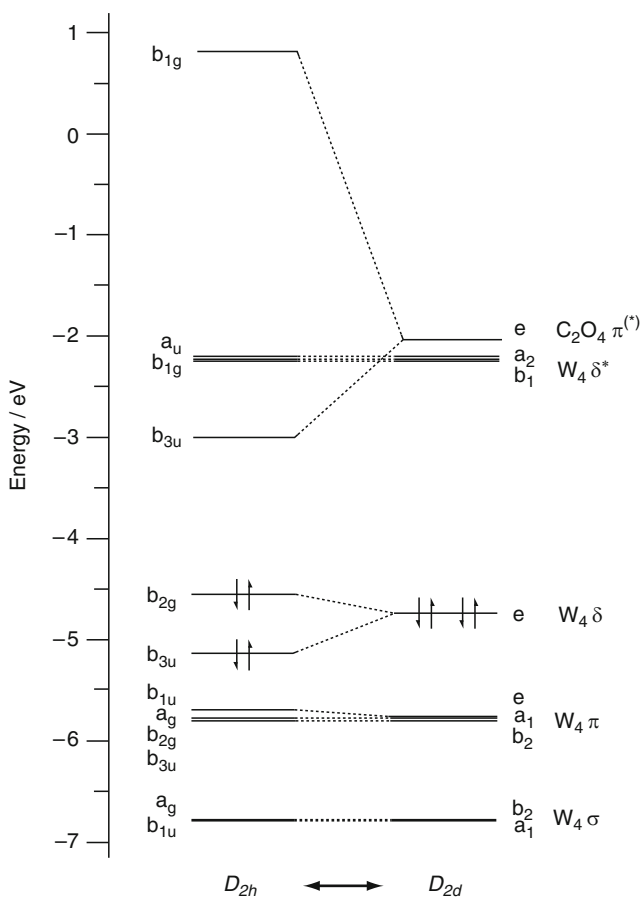


Fig. 6 A Walsh diagram for the oxalate bridged complex $[(\text{HCO}_2)_3\text{W}_2]_2(\mu\text{-oxalate})$ for the planar bridge, D_{2h} , and its twisted D_{2d} form. Adapted from [18]

from 0° . TDDFT calculations on the model compounds provide further predictions that can be compared with experimental data relating to electronic and vibrational spectroscopy and these will be mentioned later.

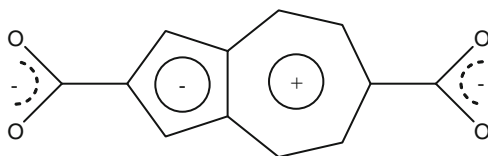
4.2 $\text{O}_2\text{C}-\text{X}-\text{CO}_2$ Bridges

The simple orbital considerations of oxalate can readily be extended to longer extended chains $\text{O}_2\text{C}-\text{X}-\text{CO}_2$ where X provides some group entering into conjugation, e.g., $-\text{C}_6\text{H}_4-$ or $(\text{CH}=\text{CH})_n$. With increasing distance between the M_2 centers the magnitude of the electronic coupling decreases. This was nicely seen for a series of $[\text{Mo}_2]$ units linked by $\text{O}_2\text{C}-(\text{CH}=\text{CH})_n-\text{CO}_2$ groups, where $n = 1, 2, 3$, and 4,

by Cotton and coworkers [9, 20]. When $X = C_6X_4$ as in 1,4-terephthalate the electronic coupling can be modulated by the substituents X which determine the energy of the LUMO and the favored ground-state geometry [21]. For example, for $X = H$ or F the ground state is the planar $M_2O_2CC_6CO_2M_2$ geometry. The electronic coupling is greater for $X = F$ than for $X = H$ because the fluorine substituents lower the energy of the LUMO. For $X = Cl$, steric factors disfavor that planar central core and with a dihedral angle between the O_2C and C_6 planes at $\sim 54^\circ$ the coupling is significantly reduced.

It must be emphasized that while lowering the energy of the LUMO favors electronic coupling, the magnitude of the electronic coupling always decreases with increasing M_2 to M_2 distance. The energy gap between the HOMO and the LUMO provides an indicator of the 1MLCT transition in the electronic absorption spectrum but not the energy splitting of the HOMO and HOMO-1. This is nicely exemplified by the properties of a series α -, α' -linked thienyl dicarboxylates $[(t\text{-BuCO}_2)_3M_2]_2(\mu\text{-O}_2C(\text{Th})_n\text{CO}_2)$ where $\text{Th} = C_4H_2S$ and $n = 1, 2,$ and 3 . Increasing n decreases the energy of the 1MLCT and also decreases M_2 to M_2 coupling as indicated by the calculated energy difference between the HOMO and HOMO-1 and experimental observations based on electrochemistry and EPR spectroscopy [22].

While electronic structure calculations employing DFT are extremely useful they do not allow one to make firm predictions of the properties of the mixed-valence ions formed upon one-electron oxidation. For example, with a 2,6-azulenedicarboxylate bridge the polarity of the bridge resulting from the resonance structure shown in **XII** naturally leads to a splitting of the two $M_2\delta$ orbitals [23]. However, it rests with experimental data to determine whether the singly



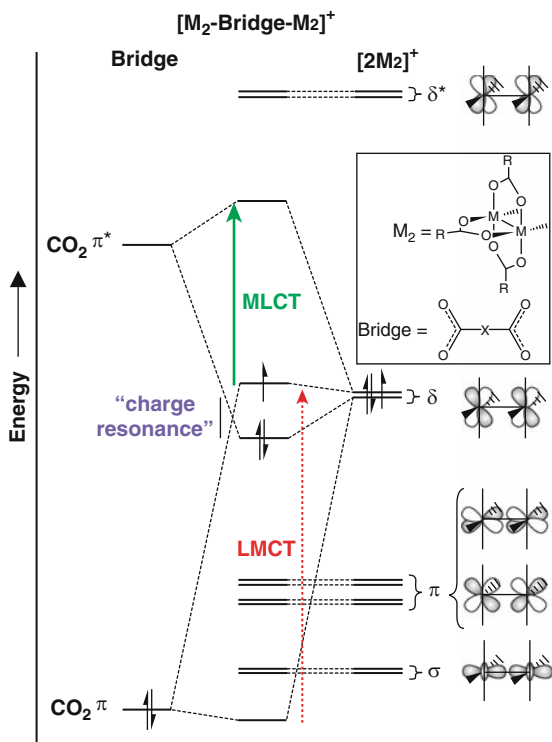
XII

oxidized radical cations should be classified as valence-trapped or as delocalized over the two M_2 centers.

4.3 Other Related Bridges

Just as simple bonding considerations for the oxalate bridge based on the orbital interactions shown in **X** and **XI** can be extended to $O_2C-X-CO_2$ bridges, so can the substitution of O by NR or O by S be anticipated. The $NRp\pi$ and $S3p\pi$ orbital energy are higher in energy than the $O2p\pi$ and consequently the filled bridge π and the filled $M_2\delta$ orbital interaction becomes more important. The $C-S\pi$ bond is

Fig. 7 Schematic MO energy level diagram showing the possible electronic transitions in a mixed-valence bridged complex of the form $[M_2\text{-bridge-M}_2]^+$. Adapted from [26]



notably weaker than the C–O π bond and as a consequence the C–S π^* is lower in energy. Thus thiocarboxylate linkers show greater $M_2\delta$ to bridge back-bonding relative to their carboxylate analogues, and this in turn leads to enhanced $M_2\delta$ to $M_2\delta$ coupling [24, 25].

In many ways the electronic coupling in both the neutral and the mixed-valence compounds can be reduced to the simple orbital diagram depicted in Fig. 7 [26]. In the neutral complex only the 1MLCT transition is observed, but for the singly oxidized radical cations three electronic transitions are possible: the LMCT, the IVCT (in a fully delocalized compound this is better described as charge resonance transition), and an LMCT. For carboxylate linkers the LMCT is not observed because the $CO_2 \pi$ orbitals are too low in energy, but substitution of O by S or NR raises the energy of this filled π orbital.

Of course, MO energy level diagrams are only a starting point in predicting electronic spectra. In reality the electronic transitions occur between states and these may mix many orbital interactions. However, this MO approach has proved remarkably useful in accounting for the lowest energy intense bands which for the neutral complexes are metal-to-bridge charge transfer and involve the HOMO and LUMO. In strongly coupled mixed valence cations the low energy IR band can also be correlated with the single electron transition between the SOMO and HOMO, the charge resonance band as expressed in Fig. 7.

5 Electrochemical Studies

The MM quadruple bond of configuration $\sigma^2\pi^4\delta^2$ is well known to undergo reversible oxidation to generate the MM^{5+} -containing cation of configuration $\sigma^2\pi^4\delta^1$ [5]. The structural change that accompanies this electron removal is small but readily detectible by X-ray studies that reveal a lengthening of the MM distance by $\sim 0.05 \text{ \AA}$ and a slight shortening of the metal–ligand distances as a result of the increase in positive charge on the metal center, and, in the case of ligands with filled $p\pi$ orbitals, the removal of an electron from the δ orbital which provides an antibonding filled–filled interaction. The chemical potential of this oxidation is dependent on the metal and the attendant ligands [5]. For otherwise identical compounds the substitution of Mo_2 by W_2 lowers the oxidation by 0.5 V. Nitrogen donor ligands such as formamidinates are better electron donors than oxygen donor ligands such as carboxylates. In general, the dimers of dimers show two oxidation potentials corresponding to the successive removal of electrons from the complex, and studies of these complexes by both cyclic voltammetry and differential pulse voltammetry allow the determination of the separation of the two redox processes. The separation of these two oxidations in mV, $\Delta E_{1/2}$, can be related to the relative stability of the mixed-valence ion, K_c , by the (5) [8, 27].

$$[M_2] \text{---} [M_2] + \{[M_2] \text{---} [M_2]\}^{2+} = 2 \{[M_2] \text{---} [M_2]\}^{1+}; K_c \quad (5)$$

$$K_c = \exp(\Delta E_{1/2}/25.69)$$

The larger the value of $\Delta E_{1/2}$ in mV, the larger the value of K_c , and the greater the stability of the mixed-valence ion in (5). Large values of K_c indicate strongly coupled M_2 centers.

There are some important points to recognize when using electrochemical methods to determine the magnitude of electronic coupling. (1) $\Delta E_{1/2}$ and K_c are thermodynamic parameters and are greatly influenced by the solvent and the counter anion. (2) They do not distinguish between electronic coupling and electrostatic effects (3) Both oxidation processes should be fully reversible and both should be metal centered (In some instances the bridge may be redox active).

With these caveats in mind, the redox properties of closely related compounds employing the same solvent and counter ion have been very useful – though they cannot alone distinguish between class II and class III behavior on the Robin and Day Scheme [6].

Table 1 summarizes some electrochemical data for bridged tetranuclear complexes supported by *p*-anisoleformamidinates. The $\Delta E_{1/2}$ values and K_c rapidly drop off with increasing distance as was nicely shown for the series $\mu\text{-O}_2\text{C}(\text{CH} = \text{CH})_n\text{CO}_2$ where $n = 0, 1, 2, 3$, and 4.

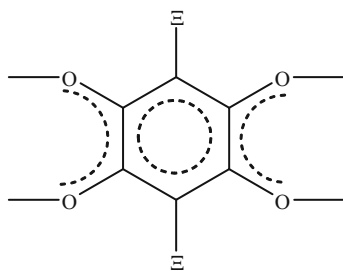
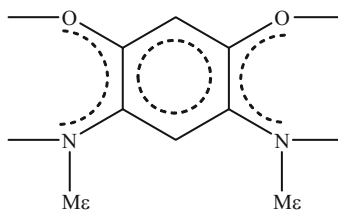
The *N,N'*-diaryloxamidate bridged complexes which exist in two isomers have very different redox properties. The so-called α -isomers that have the twisted geometry shown in VI have small $\Delta E_{1/2}$ (~ 190 mV) and K_c values ($\sim 10^3$), while the

Table 1 Summary of electrochemical data for selected bridged compounds of formula $[\text{Mo}_2(\text{p-MeOC}_6\text{H}_4\text{NCHNC}_6\text{H}_4\text{-p-OMe})_3]_2(\text{bridge})^{0/+/+2}$

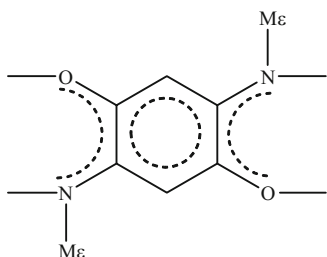
Bridge ²⁻	$\Delta E_{1/2}$ (mV)	K_c	d (Å)	References
	212	3.8×10^3	7.0	[28]
	145	2.0×10^2	7.7	[29]
	105	60	11.6	[29]
	75	19	13.9	[29]
	100	49	11.2	[28]
	416	1.1×10^7	7.2	[30]

planar geometry shown in **V**, the so-called β -isomers, are more strongly coupled with $\Delta E_{1/2} \sim 520\text{--}540$ mV and $K_c \sim 10^9$ (Ar = C_6H_5 or $p\text{-MeC}_6\text{H}_4$) [15].

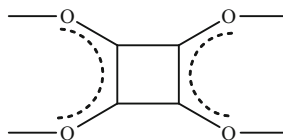
The anionic bridges of dioxolene **XIII** [13], and deprotonation of dihydroxy (1,5- or 1,4-)dimethylamino (2,4- or 2,5-) benzene, **XIV** and **XV** show extremely strong coupling as evidenced by $\Delta E_{1/2} \sim 800$ mV and $K_c \sim 10^{13}$ [30, 31], while the squarate bridge, **XVI**, yields very weak coupling, and in the doubly oxidized ion the two single electrons are only weakly antiferromagnetically coupled with $J = -121 \text{ cm}^{-1}$ [32].

XIII (X = H, Cl, NO₂)

XIV



XV



XVI

In all of these cases the magnitude of the electronic coupling can be correlated with the bonding of the $Mo_2\delta$ orbitals to the bridge π -system and is nicely quantified by electronic structure calculations.

Electrochemical data for selected bridged tetranuclear complexes supported by pivalate ligands are given in Table 2. These data nicely demonstrate the importance of energies of the $MM\delta$ orbitals. In the series of oxalate bridged complexes, where the MM unit is Mo_2 , MoW , and W_2 , the $\Delta E_{1/2}$ and K_c values increase with tungsten content. In the series of 1,4-CO₂ vs. 1,4-COS-C₆H₄ bridges the replacement of oxygen by sulfur brings about a significant enhancement in coupling as evidenced by K_c values.

Also in comparing the data for the bridges shown in **VII** and **VIII** that align the two MM units with a very short distance ~ 3.1 Å, the K_c value for **VIII** is negligible while that for **VII** is large providing a clear indication of the importance of the bridge in coupling the MM centers. Indeed, the coupling in the oxalate bridged tungsten complex is larger than that in the 3,6-dioxopyradazine bridged complex despite their respective W to W distances being ~ 7 and 3.3 Å [17].

Collectively the electrochemical data support the view that the nature of the bridge dominates the magnitude of the $\Delta E_{1/2}$ and K_c and that by large measure these correlate with the degree of electronic coupling based on MO calculations. However, as mentioned earlier they cannot uniquely distinguish between class II and class III.

Table 2 Electrochemical data for selected bridged compounds of the formula $[(\text{Bu}^t\text{CO}_2)_3\text{M}_2]_2(\text{bridge})^{0/+/+2}$ (M = Mo or W)

Bridge ²⁻	M	$\Delta E_{1/2}$ (mV)	K_c	d (Å)	References
	Mo W	280 717	5.4×10^4 1.3×10^{12}	7.0 7.0	[12] [12]
	Mo W	65 285	13 6.6×10^4	11 11	[12] [12]
	Mo W	184 518	1.3×10^3 5.7×10^8	11 11	[18] [18]
	Mo W	280 630	5.4×10^4 4.5×10^{10}	 3.3	[23] [23]
	Mo	389	3.8×10^6	3.1	[12]
	Mo W	0 156	4 4.3×10^2	3.1 3.1	[12] [12]

6 EPR Spectroscopy

Oxidation of the MM quadruply bonded center leads to a metal-centered radical that is easily detected by EPR spectroscopy. Both molybdenum and tungsten have various nuclei, the majority of which are spin inactive. However, ^{95}Mo and ^{97}Mo have $I = 5/2$ and very similar magnetic moments. Thus the isotropic EPR spectrum of the Mo_2^{5+} cations consists of a central resonance, $g \sim 1.9$, flanked by a six-line hyperfine spectrum: $A \sim 28 \text{ G}$. The isotope ^{183}W has $I = 1/2$ and 15% natural abundance and so the EPR spectrum of the W_2^{5+} cation consists of a central

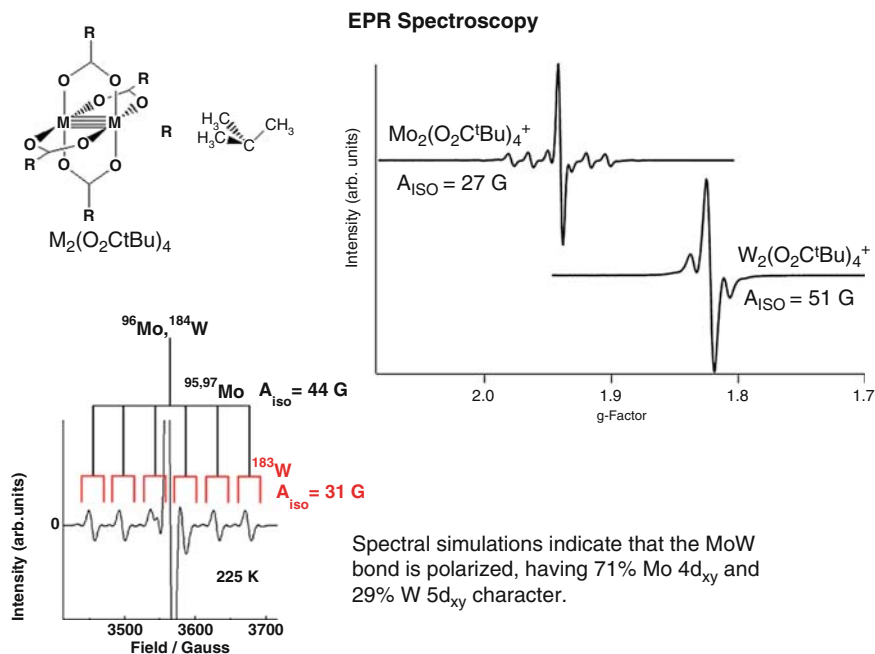


Fig. 8 EPR spectra of MM radical cations with the electronic configuration $\sigma^2\pi^4\delta^1$. Adapted from [33]

resonance $g \sim 1.8$ G flanked by satellites with $A_0 \sim 56$ G. At higher magnification the hyperfine spectrum due to two spin active nuclei in the MM^{5+} unit can be detected. These g values are notably reduced from the free electron value due to spin-orbit coupling. The mixed metal cation MoW^{5+} has a single electron in a $MoW\delta$ orbital that is polarized toward molybdenum, and the satellite spectrum reveals this with coupling to $^{95/97}Mo$, $A_0 = 44$ G and ^{183}W , $A_0 = 31$ G. The spectra of the $MM(O_2C-t-Bu)_4^+$ cations are shown in Fig. 8 [33].

Related spectra for the oxalate and terephthalate bridged Mo_4 -containing compounds supported by pivalate ligands are shown in Fig. 9. Here it is clearly evident that on the EPR time scale, $\sim 10^9$ s $^{-1}$, the oxalate cation involves complete delocalization of the positive charge over all four Mo atoms. The single electron in the HOMO sees equally all four Mo atoms. Here the presence of two spin active nuclei in the M_4^+ center is more easily seen. In contrast, the EPR spectrum of the terephthalate radical cation is localized on one Mo_2 center: the mixed-valence ion is valence-trapped [34].

For tungsten terephthalate bridged compounds the radical cations show delocalization over the four W centers, once again revealing the greater electronic coupling with the 5d element.

A particularly interesting example of electron delocalization is seen for the 2,6-azulenedicarboxylate bridge, previously shown in XII. The W_4 -containing cation, $[(t-BuCO_2)_3W_2]_2(\mu\text{-bridge})^+$, has a central resonance, $g \sim 1.81$, and is flanked by

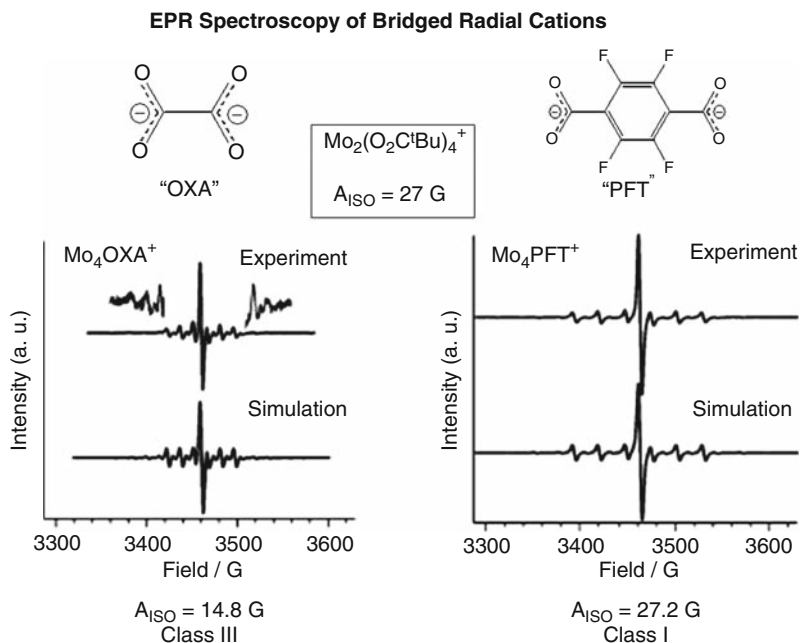


Fig. 9 EPR spectra of the radical cations $[(t\text{-BuCO}_2)_3\text{Mo}_2]_2(\text{bridge})^+$, where bridge = oxalate and 1,4-terephthalate

two sets of satellites due to ^{183}W with $A_0 \sim 20$ and 40 G indicative of a delocalized but polarized SOMO consistent with polar nature of the azulene [23]. Here the W_2 to W_2 distance is close to 14 \AA and still the single electron is delocalized over the four tungsten centers via coupling through the bridge.

7 Optical Spectra

7.1 IVCT and Charge Resonance Bands

Strongly coupled M_2 centers upon oxidation yield mixed-valence ions that are classified as class III and show low energy absorptions in the NIR. These absorptions are solvent independent and relatively narrow. The magnitude of the electronic coupling is essentially one-half of the λ_{max} in cm^{-1} . An interesting and informative example of this type of behavior is seen in the spectra shown in Fig. 10 for the cations $[(t\text{-BuCO}_2)_3\text{MM}]_2(\mu\text{-O}_2\text{CCO}_2)^+$ where $\text{MM} = \text{W}_2, \text{MoW},$ and Mo_2 [29]. The magnitude of the coupling follows the order $\text{MM} = \text{W}_2 > \text{MoW} > \text{Mo}_2$ which is the same trend seen from the electrochemical data discussed earlier. It is also apparent that while the shape of the band is symmetrical for the complexes where $\text{MM} = \text{W}_2$ and MoW , the shape of the absorption for $\text{MM} = \text{Mo}_2$ is

Electronic Absorption Spectra of M_4OXA^+ Radical Cations

Compound	ν_{\max}	$\Delta\nu_{1/2}$ (exp)	$\Delta\nu_{1/2}$ (calc)	H / cm^{-1}
Mo_4OXA	4050	2196	3059	2025
$(MoW)_2OXA$	5110	1191	3436	2555
W_4OXA	6000	877	3722	3000

$$\Delta\nu_{1/2}(\text{calc}) = [2310\nu_{\max}]^{1/2}$$

(for a Class II system, assuming a Gaussian shaped band)

$$\nu_{\max} = 2H$$

(For a Class III system)

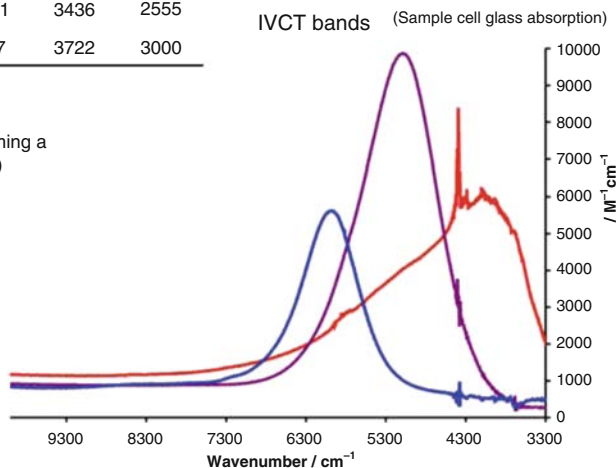


Fig. 10 Electronic absorption spectra for the radical cations $[(t\text{-BuCO}_2)_3MM]_2(\mu\text{-O}_2\text{CC}_2)^+$, where $MM = Mo_2, MoW,$ and W_2 , showing the IVCT/charge resonance bands in THF solution at 298 K

highly asymmetric having a relatively sharp rise at the low energy side and a long tail to higher energy. This is, in fact, entirely in line with predictions based on mixed-valence ions that are close to the class II/III boarder [35].

The spectra for the cations $[(t\text{-BuCO}_2)_3MM]_2(2,5\text{-(OH)}_2\text{-C}_6\text{H}_2\text{-1,4(CO)}_2)^+$ are shown in Fig. 11 [21]. Here the substituted terephthalate bridge separates the two MM centers by ca 11 Å in contrast to ~ 7 Å for the oxalate. The spectra for $MM = Mo_2$ and W_2 are now very different. For the molybdenum complex there is a very broad electronic transition which is at a much higher energy when compared to the sharp and narrow absorption at $\sim 3,000 \text{ cm}^{-1}$ for the tungsten complex. Once again these spectra are consistent with expectations based on current theories for mixed-valence ions. The molybdenum complex ion is class II and shows spectral features predicted by Hush [36], while the tungsten analogue is class III.

7.2 Metal-to-Bridge Charge Transfer Bands

As was noted earlier, the dominant mode of electronic coupling for dicarboxylate bridged compounds involves the π^* orbitals of the bridge and the $MM\delta$ orbitals. Thus complexes of this type show intense 1MLCT bands that typically fall in the visible region of the spectrum. Once again the oxalate bridged series of complexes

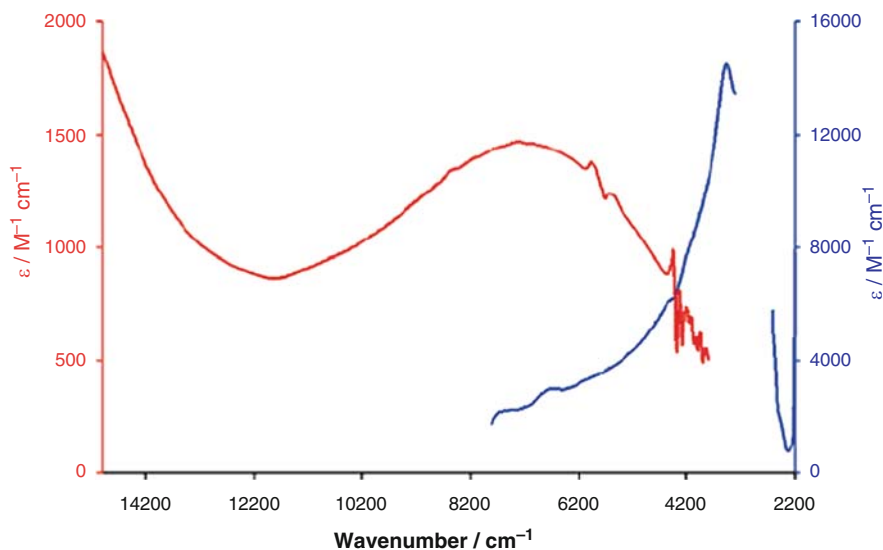


Fig. 11 Electronic absorption spectra for the radical cations $[(t\text{-BuCO}_2)_3\text{M}_2](\mu\text{-}2,5\text{-}(\text{OH})_2\text{-C}_6\text{H}_4\text{-}1,4\text{-}(\text{CO}_2)_2)^+$ showing the IVCT bands. Adapted from [21]

$[(t\text{-BuCO}_2)_3\text{MM}]_2(\mu\text{-O}_2\text{CCO}_2)$ are particularly informative and illustrative of this. The spectra are shown in Fig. 12 for $\text{MM} = \text{Mo}_2, \text{MoW}, \text{and W}_2$ [29]. The energy of this electronic transition moves to lower energy with increasing W content which is consistent with expectations based on the redox properties of the $\text{MM}\delta$ orbital and the HOMO–LUMO gap.

It is also apparent that the tungsten complex has a strong vibronic progression. When the spectra of the $[(t\text{-BuCO}_2)_3\text{W}_2]_2(\mu\text{-O}_2\text{CCO}_2)$ complex are recorded in 2-methyltetrahydrofuran in the temperature range from 300 to 2K the vibronic features become notably better resolved with decreasing temperature. Indeed, two progressions are seen and both are sensitive to isotopic substitution of $\text{O}_2^{13}\text{C}^{13}\text{CO}_2$ for natural abundance oxalate [18]. These progressions are undoubtedly associated with the symmetric vibrations of the oxalate bridge in the photo excited state of the molecule.

One other important feature is seen in the variable temperature spectra of the tungsten oxalate bridged complex, namely that the onset of the absorption moves to lower energy and sharpens [18]. This is shown in Fig. 13. This can be understood in terms of the thermal population of molecules with varying $\text{O}_2\text{C} - \text{CO}_2$ dihedral angles. As noted earlier, the ground state has a planar oxalate bridge, but the barrier to rotation is relatively small: 5-9 kcal mol⁻¹. Thus in lowering the temperature the Boltzmann population of molecules with planar or near-planar oxalate geometries increases and as noted in the Walsh diagram (Fig. 6), this lowers the HOMO–LUMO gap and the corresponding ¹MLCT absorption.

Since the electronic coupling between the M_2 centers is dependent upon the conjugation within the bridge this may be modulated by both steric and electronic

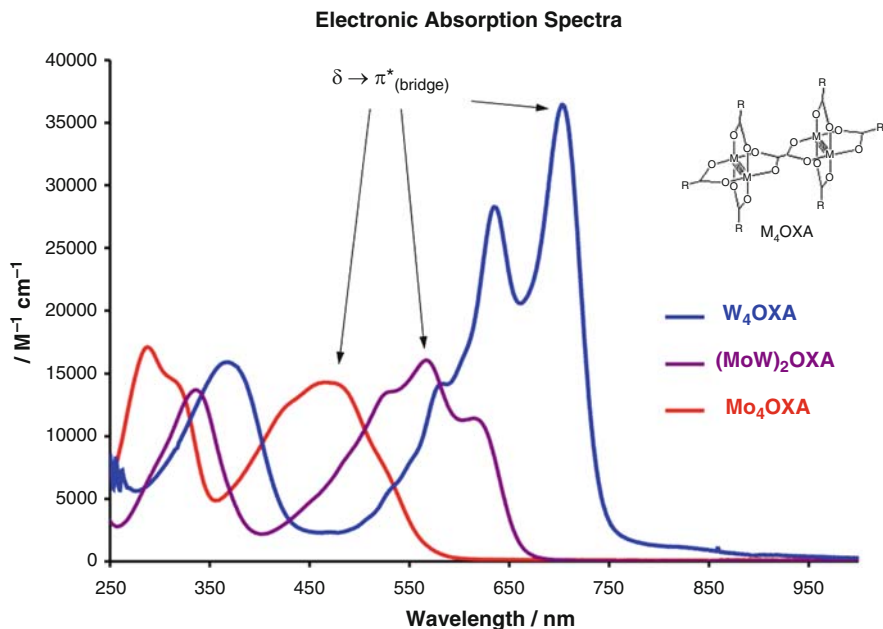


Fig. 12 Electronic absorption spectra showing the ¹MLCT Bands in the series of compounds [(*t*-BuCO₂)₃MM]₂(μ-O₂CCO₂), where MM = Mo₂, MoW, and W₂

factors. This was nicely demonstrated for a series of 1,4-substituted terephthalate bridge compounds where the substituents were H, F, Cl, and OH [21].

Upon oxidation to the mixed-valence ion, the ²MLCT involving the bridge sharpens and loses much of its vibronic features [37]. This is a general phenomenon and is particularly striking for ions such as [(*t*-BuCO₂)₃W₂]₂(μ-O₂CCO₂)⁺. This change can be understood in terms of enhanced electronic coupling of the two dinuclear centers, with a planar geometry and the greater nesting of the ground and excited state potential energy surfaces in the oxidized radical cations.

8 Steady-State Emission and Transient Absorption Spectroscopy

A number of α,α'-linked thienyl dicarboxylates and fused thienylcarboxylate-containing compounds have been found to show interesting emissive properties as have extended oligomers of the formula [Mo₂(TiPB)₂(O₂C(Th)₃CO₂)_{*n*}] [38, 39], where TiPB = 2,4,6-triisopropylbenzoate. These molybdenum compounds show dual emission: fluorescence is from the ¹MLCT state and phosphorescence is from the ³MMδδ* state. Evidence for the latter comes from both the fact that unlike the solvent-dependent ¹MLCT emission the ³MMδδ state is solvent independent

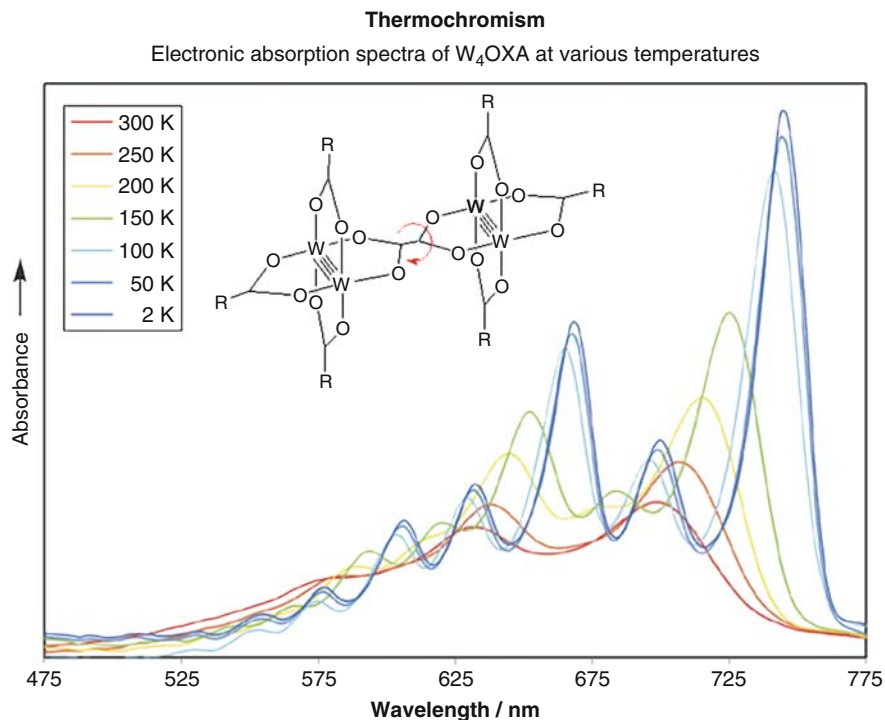


Fig. 13 Electronic absorption spectra of the compound $[(t\text{-BuCO}_2)_3W_2]_2(\mu\text{-O}_2\text{CCO}_2)$ recorded in 2-methyltetrahydrofuran at various temperatures. Adapted from [18]

at 1,100 nm and at 77 K shows striking vibronic features associated with $\nu(\text{MM}) \sim 400\text{ cm}^{-1}$. The tungsten compounds showed only emission from the S_1 , $^1\text{MLCT}$ state.

When examined by both fs and ns transient absorption spectroscopy with excitation into either the ^1LCT or $^1\text{MLCT}$ the molybdenum compounds showed similar excited state dynamics corresponding to short-lived S_1 states ($^1\text{MLCT}$) with $\tau \sim 10\text{ ps}$ and long-lived T_1 states ($^3\text{MM}\delta\delta^*$) $\tau \sim 50\text{ }\mu\text{s}$. The related tungsten compounds also have S_1 ($^1\text{MLCT}$) states with lifetimes on the order 5 ps, but the triplet states were notably shorter lived than the $^3\text{MM}\delta\delta^*$ states for molybdenum. The shorter-lived T_1 states are believed to be due to $^3\text{MLCT}$ which lie at a lower energy and are not, or only very weakly emissive. A Jablonski diagram for the compounds $[(t\text{-BuCO}_2)_3M_2]_2(\mu\text{-O}_2\text{C(Th)}_2\text{CO}_2)$ is given in Fig. 14.

9 Resonance Raman Spectra

As noted earlier these bridged compounds show intense $^1\text{MLCT}(M_2\delta\text{ to bridge } \pi^*)$ absorptions that typically fall in the visible region of the spectrum. With excitation into these bands the compounds show very significant resonance enhancement

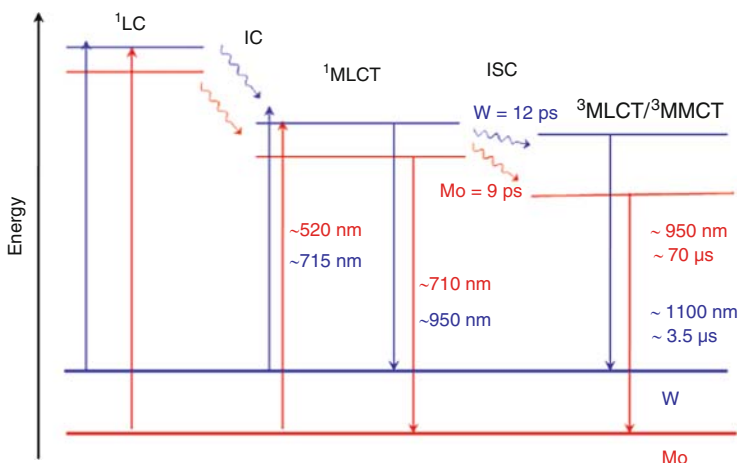


Fig. 14 A Jablonski diagram for the bithienyl carboxylate bridged compounds $[(t\text{-BuCO}_2)_3\text{M}_2]_2(\mu\text{-O}_2\text{C(Th)}_2\text{CO}_2)$, where $M = \text{Mo}$ and W

of the symmetric Raman active modes of the bridge and the metal–metal stretch [17–19, 22]. This has been seen for a number of compounds involving bridges with thienyl and aromatic rings but is most pronounced for the simple oxalate bridges as shown in Fig. 15. Here one can readily identify $\nu(\text{MM})$, and ν_1 , ν_2 , and ν_3 of the oxalate together with an extensive series of overtones and combination modes. The calculated values for the model compounds $[(\text{HCO}_2)_3\text{M}_2]_2(\mu\text{-O}_2\text{CCO}_2)$ based on time-dependent DFT agree well with those observed for the pivalate supported compounds [18].

10 Molecular Loops, Triangles, and Squares

In general, much less is known about the chemistry and spectroscopy of molecular loops, triangles, and squares.

As noted earlier, molecular loops are formed with flexible bridges and cis ancillary ligands such as the *p*-anisoleformamidinates, DAniF, employed in the reaction shown in (3). Cotton, Murillo, and their coworkers prepared a series of loops with the flexible $\text{O}_2\text{C}-(\text{CF}_2)_n-\text{CO}_2$ bridges, where $n = 2, 3, \text{ or } 4$: $[(\text{DAniF})_2\text{Mo}_2]_2(\text{bridge})_2$ [40]. These were characterized by single-crystal X-ray crystallography and by both ^1H and ^{19}F NMR spectroscopy. Interestingly while the compounds where $n = 2$ and 4 were stable in solution the compound with $n = 3$ was shown to exist in an equilibrium with a molecular triangle: $[(\text{DAniF})_2\text{Mo}_2(\text{O}_2\text{C}(\text{CF}_3)_3\text{CO}_2)]_3$. From a concentration- and temperature-dependent study, Cotton and coworkers were able to show that the triangle was enthalpically favored $\Delta H^\circ = -41.9 \text{ kJ mol}^{-1}$ but entropically disfavored: $\Delta S^\circ = -82 \text{ J mol}^{-1} \text{ K}^{-1}$ [40].

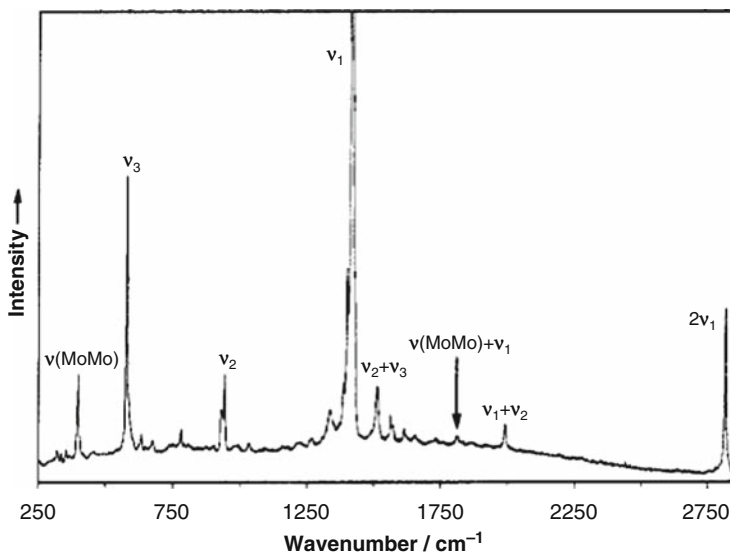


Fig. 15 Resonance Raman spectra of a solid sample of $[(t\text{-BuCO}_2)_3\text{Mo}_2](\mu\text{-O}_2\text{CCO}_2)$ with excitation at 671.4 nm

In a somewhat related study Cotton, Murillo, and coworkers also prepared and structurally characterized a molecular triangle and a square having a perfluoroterephthalate bridge: $[(\text{DAniF})_2\text{Mo}_2(\text{O}_2\text{CC}_6\text{F}_4\text{CO}_2)]_n$, where $n = 3$ and 4 [41]. This work clearly showed that, even for a bridge that is well known as a linear connector in the construction of metallo-organic frameworks and coordination polymers and for a Mo_2^{4+} unit that has a rigid paddlewheel motif, there is sufficient flexibility within the bridge and the dinuclear unit to accommodate a geometry that ideally requires 60° angles, **III**, rather than the 90° of the square, **IV**. For the equilibrium involving the conversion of 3 moles of squares to 4 moles of triangle the equilibrium constant K was $1.98(7) \times 10^{-4}$ at 24°C . This conversion was enthalpically disfavored $\Delta H^\circ = -23.5 \text{ kJ mol}^{-1}$ but entropically favored ($\Delta H^\circ = +8.2 \text{ JK}^{-1}\text{mol}^{-1}$) [41].

It is interesting to speculate upon how a molecular loop and triangle or a triangle and square manage to equilibrate and apparently so readily. One can perhaps consider a catalytic process involving some impurity, and Cotton suggested that water may play a key role in these interconversions.

These species are known to be redox active and molecular squares have been shown to exhibit two or three oxidation waves by cyclic voltammetry [42]. However, little is known concerning the nature of the oxidized species. No molecular square or triangle has been prepared for W_2^{4+} units, and for Mo_2^{4+} units it is likely that the oxidized species are valence-trapped. Nevertheless these mixed-valence ions should have interesting properties. Indeed, charged species in the form of a square have been predicted to be appropriate for quantum computing [43], and

it is interesting to contemplate the interconversion of the mixed valence isomers schematically represented in (4), where O represents an M_2 center.



Bursten et al. have considered the bonding in a series of molecular squares of formula $[(HCO_2)M_2(\mu-O_2CCO_2)]_4$, where $M = Mo, W, Tc, Ru,$ and Rh [28]. For the quadruply bonded units where $M = Mo$ or W the $M_2\delta$ orbitals mix with the oxalate π system to form a metal based set of δ combinations of $a_{1g}, e_u,$ and b_{2g} symmetry in the D_{4h} point group. The a_{1g} is bonding, the e_u nonbonding, and the b_{2g} weakly antibonding. Given the interesting spectroscopic properties of the oxalate bridged dimers of dimers in both their neutral and oxidized forms, the possibilities for the oxalate bridge square are quite fascinating.

11 Concluding Remarks

As was noted in the introduction, it was not the purpose of this chapter to be comprehensive but rather to introduce the reader to the rich structural and spectroscopic properties of these linked MM quadruply bonded species. Cotton, Murillo, and their coworkers have prepared many related compounds, dimers of dimers, molecular loops, triangles, and squares involving Rh_2^{4+} and Ru_2^{4+} units, but their chemistries have been less developed [12, 44–48]. Also of note has been the elegant syntheses and spectroscopies of Ren and his coworkers on Ru_2^{n+} -linked units [49–52]. These too are fascinating because of electronic communication between redox active centers. They do not contain MM quadruple bonds and so have not been discussed either.

References

1. Cotton FA, Shang M (1991) The structure of the molybdenum tetranuclear cluster complex $Mo_4Cl_8(PEt_3)_4$: how unrecognized disorder previously reduced the quality of the refinement. *J Cluster Sci* 2:121–129
2. McGinnis RN, Ryan TR, McCarley RE (1978) Reactions of activated quadruply bonded molybdenum dimers. Formation of new rectangular clusters containing the tetrametal analog of cyclobutadiyne. *J Am Chem Soc* 100:7900–7902
3. Ryan TR, McCarley RE (1982) Synthesis and characterization of rectangular tetranuclear cluster complexes of molybdenum(II) by condensation of quadruply bonded dimers. *Inorg Chem* 21:2072–2079
4. Chisholm MH, MacIntosh AM (2005) Linking multiple bonds between metal atoms: clusters, dimers of “dimers”, and higher ordered assemblies. *Chem Rev* 105:2949–2976
5. Cotton FA, Murillo CA, Walton RA (2005) Multiple bonds between metal atoms. Springer Science, Berlin, Germany

6. Robin MB, Day P (1967) Mixed valence chemistry. a survey and classification. *Adv Inorg Chem Radiochem* 10:247–422
7. Cayton RH, Chisholm MH (1989) Electronically coupled bonding between covalently linked metal-metal quadruple bonds of molybdenum and tungsten. *J Am Chem Soc* 111:8921–8923
8. Cayton RH, Chisholm MH, Lobkovsky EB (1991) Metal-metal multiple bonds in ordered assemblies. 1. Tetranuclear molybdenum and tungsten carboxylates involving covalently linked metal-metal quadruple bonds. Molecular models for subunits of one-dimensional stiff-chain polymers. *J Am Chem Soc* 113:8709–8724
9. Cotton FA, Donahue JP, Murillo CA (2003) Polyunsaturated dicarboxylate tethers connecting dimolybdenum redox and chromophoric centers: syntheses, structures, and electrochemistry. *J Am Chem Soc* 125:5436–5450
10. Cotton FA, Lin C, Murillo CA (1998) Coupling Mo_2^{n+} units via dicarboxylate bridges. *Dalton Trans* 3151–3154
11. Cotton FA, Daniels LM, Lin C, Murillo CA (1999) Square and triangular arrays based on Mo_2^{4+} and Rh_2^{4+} units. *J Am Chem Soc* 121:4538–4539
12. Cotton FA, Lin C, Murillo CA (2001) Supramolecular arrays based on dimetal building block. *Acc Chem Res* 34:759–771
13. Cotton FA, Murillo CA, Villagrán D, Yu R (2006) Uniquely strong electronic communication between $[\text{Mo}_2]$ units linked by dioxolene dianions. *J Am Chem Soc* 128:3281–3290
14. Cotton FA, Li Z, Lin CY, Murillo CA, Villagrán D (2006) Strong electronic interaction between two dimolybdenum units linked by tetraazatetracene. *Inorg Chem* 45:767–778
15. Cotton FA, Lin CY, Murillo CA, Villagrán D, Wang X (2003) Modifying electronic communication in dimolybdenum units by linkage isomers of bridged oxamidate dianions. *J Am Chem Soc* 125:13564–13575
16. Cayton RH, Chisholm MH, Huffman JC, Lobkovsky EB (1991) 1,8-Naphthyridinyl-2,7-dioxo bridged quadruply bonded molybdenum-molybdenum system, an insight into the nature of a linear rigid chain polymer [M-M...M-M]. *Angew Chem Int Edit* 30:862–864
17. Chisholm MH, Clark RJH, Gallucci JC, Hadad CM, Patmore NJ (2004) Electronically-coupled tungsten-tungsten quadruple bonds: comparisons of electronic delocalization in 3,6-dioxypyridazine and oxalate bridged compounds. *J Am Chem Soc* 126:8303–8313
18. Bursten BE, Chisholm MH, Clark RJH, Firth S, Hadad CM, MacIntosh AM, Wilson PJ, Woodward PM (2002) Oxalate bridged complexes of dimolybdenum and ditungsten supported by pivalate ligands: $(\text{t-BuCO}_2)_3\text{M}_2(\mu\text{-O}_2\text{CCO}_2)\text{M}_2(\text{O}_2\text{C-t-Bu})_3$. Correlation of the solid-state, molecular and electronic structures with Raman, resonance Raman and electronic spectral data. *J Am Chem Soc* 124:3050–3063
19. Bursten BE, Chisholm MH, Clark RJH, Firth S, Hadad CM, Wilson PJ, Woodward PM (2002) Perfluoroterephthalate bridged complexes with MM quadruple bonds: $(\text{t-BuCO}_2)_3\text{M}_2(\mu\text{-O}_2\text{CCF}_4\text{CO}_2)\text{M}_2(\text{O}_2\text{C-t-Bu})_3$, where M = Mo or W. Studies of solid-state, molecular and electronic structure and correlations with electronic and Raman spectra data. *J Am Chem Soc* 124:12244–12254
20. Cotton FA, Donahue JP, Murillo CA (2003) Polyunsaturated dicarboxylate tethers connecting dimolybdenum redox and chromophoric centers: absorption spectra and electronic structures. *J Am Chem Soc* 125:5486–5492
21. Chisholm MH, Feil F, Hadad CM, Patmore NJ (2005) Electronically coupled MM quadruply-bonded complexes (M = Mo or W) employing terephthalate bridges: toward molecular rheostats and switches. *J Am Chem Soc* 127:18150–18158
22. Byrnes MJ, Chisholm MH, Clark RJH, Gallucci JC, Hadad CM, Patmore NJ (2004) Thienyl-carboxylate ligands bound to and bridging MM quadruple bonds, M = Mo or W: models for polythiophenes incorporating MM quadruple bonds. *Inorg Chem* 43:6334–6344
23. Barybin MV, Chisholm MH, Dalal NS, Holovics TH, Patmore NJ, Robinson R, Zipse DJ (2005) Long range electronic coupling of MM quadruple bonds (M = Mo or W) via a 2,6-azulenedicarboxylate bridge. *J Am Chem Soc* 127:15182–15190
24. Chisholm MH, Patmore NJ (2006) Electronic coupling in 1,4 - $(\text{COS})_2\text{C}_6\text{H}_4$ linked MM quadruple bonds (M = Mo or W): the influence of S for O substitution. *Dalton Trans* 3164–3169

25. Chisholm MH, Singh N (2009) Are tetrathiooxalate and diborinate bridge MM quadruply bonded complexes related to oxalate bridged complexes? *Dalton Trans* 5867–5872
26. Chisholm MH, Patmore NJ (2007) Studies of electronic coupling and mixed valency in metal-metal quadruply bonded complexes linked by dicarboxylate and closely related ligands. *Acc Chem Res* 40:19–27
27. Richardson DE, Taube H (1981) Determination of E'_2-E' in multistep charge transfer by stationary-electrode pulse and cyclic voltammetry: application to binuclear amines. *Inorg Chem* 20:1278–1285
28. Bursten BE, Chisholm MH and D'Acchioli JS (2005) Oxalate bridged dinuclear M_2 units: dimers of dimers, cyclotetramers (squares) and extended sheets [$M = Mo, W, Tc, Ru$ and Rh]. *Inorg Chem* 44:8476–8480
29. Chisholm MH, Patmore NJ (2009) Oxalate bridged heteronuclear compounds containing MM quadruple bonds ($MM = Mo_2, MoW$ and W_2) and their radical cations. *Can J Chem* 87:1–7
30. Cotton FA, Jin J-Y, Zhong L, Murillo CA, Reibenspies JH (2008) Exceptionally strong electronic coupling between $[Mo_2]$ units linked by substituted quinones. *Chem Commun* 211–213
31. Cotton FA, Donahue JP, Murillo CA, Perez LM, Yu R (2003) Cyclic polyamidato dianions as bridges between Mo_2^{4+} units. Synthesis, crystal structures, electrochemistry, absorption spectra and electronic structures. *J Am Chem Soc* 125:8900–8910
32. Cotton FA, Murillo CA, Young MD, Yu R, Zhao Q (2008) Very large differences in electronic communication of dimetal species with heterobiphenylene and heteroanthracene units. *Inorg Chem* 47:219–229
33. Chisholm MH, D'Acchioli JS, Pate BD, Patmore NJ, Dalal NS, Zipse DJ (2005) Cations $M_2(O_2C-t-Bu)_4^+$, where $M = Mo$ and W and $MoW(O_2C-t-Bu)_4^+$. Theoretical, spectroscopic and structural investigations. *Inorg Chem* 44:1061–1067
34. Chisholm MH, Pate BD, Wilson PJ, Zalesk JM (2002) On the electronic delocalization in the radical cations formed by oxidation of MM quadruple bonds linked by oxalate and perfluoroterephthalate bridges. *Chem Commun* 1084–1085
35. Brunschwig BS, Creutz C, Sutin N (2002) Optical transitions of symmetrical mixed-valence systems in the class II-III transition regime. *Chem Soc Rev* 31:168–184
36. Hush NS (1967) Intervalence-transfer absorption. II. Theoretical considerations and spectroscopic data. *Progr Inorg Chem* 8:381–444
37. Lear BJ, Chisholm MH (2009) Oxalate Bridged MM Quadruply Bonded Complexes as Test Beds for Current Mixed Valence Theory: Looking Beyond the IVCT Transition. *Inorg Chem* 48:10954–10971
38. Burdzinski G-T, Chisholm MH, Chou P-T, Chou Y-H, Feil F, Gallucci JC, Ghosh Y, Gustafson TL, Ho M-L, Liu Y, Ramnauth R and Turro C (2008) The remarkable influence of the $M_2\delta$ to thienyl π conjugation in oligothiophenes incorporating MM quadruple bonds. *Proc Nat Acad Sci U S A* 105:15247–15252
39. Chisholm MH, Chou P-T, Chou Y-H, Ghosh Y, Gustafson TL, Ho M-L (2008) Preparations and photophysical properties of fused and non-fused thienyl bridged MM ($M = Mo$ or W) quadruply bonded complexes. *Inorg Chem* 47:3415–3425
40. Cotton FA, Murillo CA, Yu R (2006) An equilibrium between a loop and a triangle containing Mo_2^{4+} species and perfluorodicarboxylate linkers. *Inorg Chim Acta* 359:4811–4820
41. Cotton FA, Murillo CA, Yu R (2006) Dynamic equilibrium between cyclic oligomers. Thermodynamic and structural characterization of a square and a triangle. *Dalton Trans* 3900–3905
42. Cotton FA, Liu CY, Murillo CA, Wang X (2006) Dimolybdenum-containing molecular triangles and squares with diamidate linkers: structural diversity and complexity. *Inorg Chem* 45:2619–2626
43. Lent CS (2006) *Quantum cellular automata*. Imperial College Press, London
44. Angaridis P, Berry JF, Cotton FA, Lei P, Lin C, Murillo CA, Villagrán D (2004) Dicarboxylato-bridged diruthenium units in two different oxidation states: the first step towards the synthesis of Creutz-Taube analogs with dinuclear Ru_2^{n+} species. *Inorg Chem Commun* 7:9–13

45. Angaridis P, Berry JF, Cotton FA, Murillo CA, Wang X (2003) Molecular squares with paramagnetic diruthenium corners: synthetic and structural challenges. *J Am Chem Soc* 125:10327–10334
46. Cotton FA, Murillo CA, Lin C (2002) The use of dimetal building blocks in convergent synthesis of large array. *Proc Nat Acad Sci U S A* 99:4810–4813
47. Cotton FA, Daniels LM, Lin C, Murillo CA, Y S-Y (2001) Supramolecular squares with Rh_2^{4+} corners. *Dalton Trans* 502–504
48. Cotton FA, Lin C, Murillo CA (2001) The first dirhodium-based supramolecular assemblies with interlocking lattices and double helices. *Dalton Trans* 499–501
49. Chen W-Z, Ren T (2006) Symmetric and unsymmetric “dumbbells” of Ru_2 -alkynyl units via C-C bond formation reactions. *Inorg Chem* 45:9175–9177
50. Xi B, Ren T (2009) Wire-like diruthenium σ -alkynyl compounds and charge mobility therein. *Compt Rend Chim* 12:321–331
51. Xu G-L, Wang C-W, Ni Y-H, Goodson TG, Ren T (2005) Iterative synthesis of oligoynes capped by a $Ru_2(ap)_4$ -terminus and their electrochemical and optical properties. *Organometallic* 24:3247–3254
52. Hurst SK, Ren T (2002) Synthesis, characterization and electrochemistry of diruthenium complexes linked by aryl acetylide bridges. *J Organomet Chem* 660:1–5

Transition Metal Complexes Stabilized by Bulky Terphenyl Ligands: Application to Metal–Metal Bonded Compounds

Chengbao Ni and Philip P. Power

Contents

1	Introduction	60
2	Terphenyl Ligands	60
3	Terphenyl Metal Halide Derivatives of Transition Metals	61
3.1	Group 3 Terphenyl Metal Halide Precursors	61
3.2	Terphenyl Chromium Halides	64
3.3	Terphenyl Manganese Halides	67
3.4	Terphenyl Iron and Cobalt Halide Complexes	70
4	Homoleptic, Two-Coordinate Terphenyl Transition Metal Complexes	72
5	Terphenyl Transition Metal Complexes with Amido Coligands	73
5.1	Quasi-Two-Coordinate Amido Complexes $Ar'M-NHAr^{\#}$	73
5.2	Terphenyl Transition-Metal Complexes of the Parent Dialkylamide- NMe_2	77
6	Terphenyl Metal Halide Reactions with Acetylides	80
7	Reduction of Terphenyl Metal Halides	83
7.1	Terphenyl Stabilized Metal(I) Dimers $ArMMAr$ ($M = Cr, Fe, \text{ and } Co$)	83
7.2	Terphenyl Ligand Substituent Effects in Chromium Complexes	86
7.3	Reduction of the Terphenyl Metal Halides in the Presence of PMe_3	90
7.4	Arene Complexed Terphenyl Metal Species	93
8	Reactivity Studies of Terphenyl Metal(I) Species	95
8.1	Reactivity of $Ar'CrCrAr'$	95
8.2	Reactivity of $3,5\text{-}^iPr_2\text{-}Ar^*Fe(C_6H_6)$	97
8.3	Reactivity Studies of $3,5\text{-}^iPr_2\text{-}Ar^*Co(\eta^6\text{-}C_7H_8)$	101
9	Terphenyl Derivatives of Group 11 Elements	102
10	Conclusion	106
	References	106

Chengbao Ni and P.P. Power (✉)
Department of Chemistry, University of California, Davis One Shields Avenue,
CA 95616, USA
e-mail: pppower@ucdavis.edu

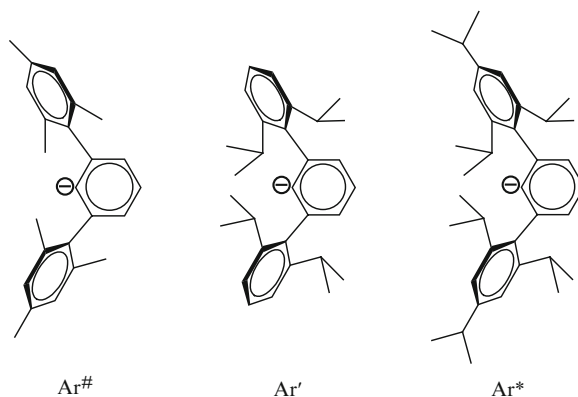
1 Introduction

A wide variety of monodentate, sterically encumbering ligands have been used to stabilize low coordination numbers in both main group and transition element compounds [1]. In recent years, the very crowded *m*-terphenyls have emerged as a particularly effective class of bulky ligand for the stabilization of numerous main group element compounds with unusual bonding and electron configurations [2, 3]. These include, for example, the first compounds with formal triple bonds between group 13 [4, 5] and group 14 metals [6, 7], as well as a stable crystalline heavier main group radical species [8]. In contrast, transition metal terphenyl derivatives have received less attention and most of the work has been performed within the last 5 years. This account focuses on these recently discovered transition metal species.

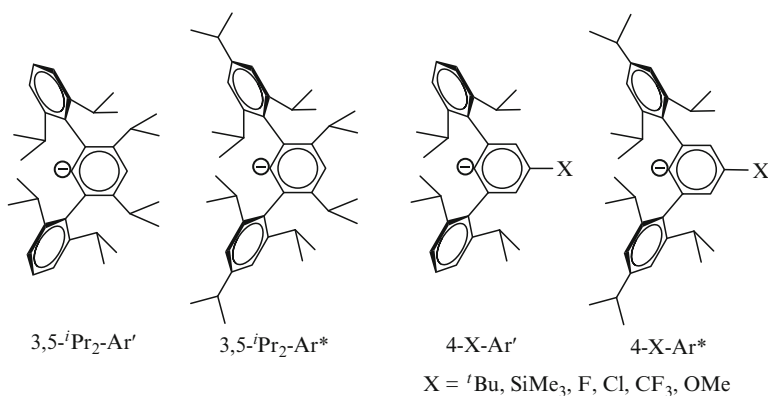
2 Terphenyl Ligands

The terphenyl ligands most often employed in the recent studies are of the general form $-\text{C}_6\text{H}_3-2, 6\text{-Ar}_2$ (Scheme 1). The flanking aryl rings (Ar) usually carry substituents at their *ortho* and sometimes *para* positions so that they are constrained to maintain an almost perpendicular orientation with respect to the central aryl ring. This generates a protective steric pocket that is often sufficient to shield a reactive metal center. The preparation of terphenyl ligands is best achieved through a one-pot routine developed by Hart and coworkers and the author's group [9–11].

Terphenyl ligands modified by substitution at the *meta* or *para* positions of the central ring have been introduced [12] (Scheme 2). These substitutions can alter the steric or crystallization characteristics of their derivatives. Furthermore, the more hindered rotation of the flanking-induced substituents by *meta* substitution further increases the steric protection of attached reactive metal centers. Examples of the modified terphenyl ligands are illustrated in Scheme 2.



Scheme 1 Commonly used terphenyl ligands

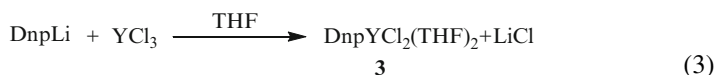
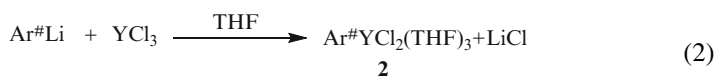
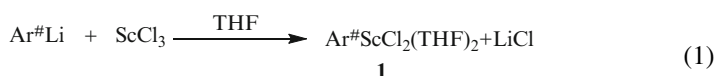


Scheme 2 Modified terphenyl ligands

3 Terphenyl Metal Halide Derivatives of Transition Metals

3.1 Group 3 Terphenyl Metal Halide Precursors

The exploration of the chemistry of terphenyl derivatives of the group 3 metals is due mainly to Rabe and coworkers [13–18]. The ligands used were of the formula $\text{C}_6\text{H}_3\text{-2,6-Ar}_2$ ($\text{Ar} = \text{C}_6\text{H}_5$, $\text{C}_6\text{H}_2\text{-2,4,6-Me}_3$, 1-naphthyl, or 3-MeO- C_6H_4). The halide complexes **1–3** could readily be obtained by simple salt metathesis from the reaction of the terphenyl lithium with anhydrous metal trichlorides MCl_3 ($\text{M} = \text{Sc}$ or Y) in THF at room temperature [13, 14]. The yttrium complexes **2** and **3** were isolated in moderate yield (ca. 50%); however, only a low yield of the scandium complex **1** could be obtained, most likely because of C–H bond activation as indicated by NMR spectroscopy. These metatheses reactions did not proceed in aromatic solvents or hexanes probably as a result of the low solubility of the reactants in these media. Complex **1** decomposes slowly in THF solution, while **2** and **3** are considerably more stable.

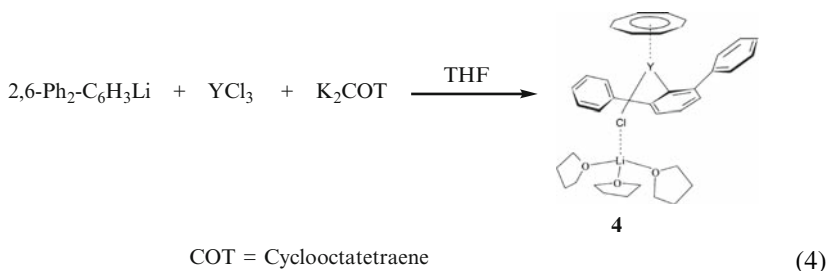


Dnp = 2,6-bis(1-naphthyl)phenyl

The structure of **1** shows that it is a monomer in which the metal has a distorted trigonal bipyramidal coordination geometry. The axial positions are occupied by two chlorides; two oxygen donor atoms and the ipso carbon of the terphenyl group bind in the equatorial positions. The O–Sc–O plane and the plane of the terphenyl aryl central ring are almost coplanar (deviation ca. 4.6°). The Sc–C(*ipso*) bond length is 2.247(3) Å. The two Sc–O distances of 2.162(2) and 2.168(2) Å are almost identical, and are similar to those in the five-coordinate complex ScPh₃(THF)₂ (2.183(2) Å) [15]. The Sc–Cl distances of 2.422(1) and 2.404(1) Å are also very close.

Although complexes **1** and **2** feature the same terphenyl ligand, the metals have different coordination geometries because of the different metal sizes (Fig. 1) [13, 14]. In **2**, the metal has distorted octahedral coordination geometry (cf. 5-coordination in **1**), and the molecular structure can be described as the *mer* isomer because of the location of the three THF donors. In contrast, the yttrium in the 2,6-bis(1-naphthyl) phenyl derivative **3** has a distorted trigonal-bipyramidal coordination which is very similar to that of scandium in **1**. In this case the lower coordination number can be attributed to the slightly larger size of the Dnp substituent. The Y–C(*ipso*) and Y–Cl distances in **2** and **3** are comparable; however in **2**, the bond length for Y–O(1) (which is *trans* to the terphenyl ligand) is ca. 0.2 Å longer than the other two Y–O distances.

The cyclooctatetraenyl terphenyl derivative **4** [16] was obtained from the one-pot reaction of equimolar amounts of K₂COT, YCl₃, and 2,6-Ph₂-C₆H₃Li in THF at room temperature.



Complex **4** is monomeric and the yttrium is η^1 - σ bound to the terphenyl ligand, η^8 bound to the cyclooctatetraenyl ligand, as well as to a chloride which bridges the yttrium and lithium ions. The average Y–C_{cot} distance is 2.564 Å with a Y–centroid distance of 1.80(4) Å.

Rabe and coworkers also used donor-functionalized terphenyl ligands which feature the donor group (OMe) at the *ortho* positions of the flanking aryl substituents [17, 18]. In addition to acting as chelating Lewis base donors, the two methoxy groups are useful NMR spectroscopic markers. The donor-functionalized ligand, 2,6-(C₆H₄-2-OMe)₂-C₆H₃ (Danip), enabled two yttrium derivatives to be synthesized and structurally characterized.

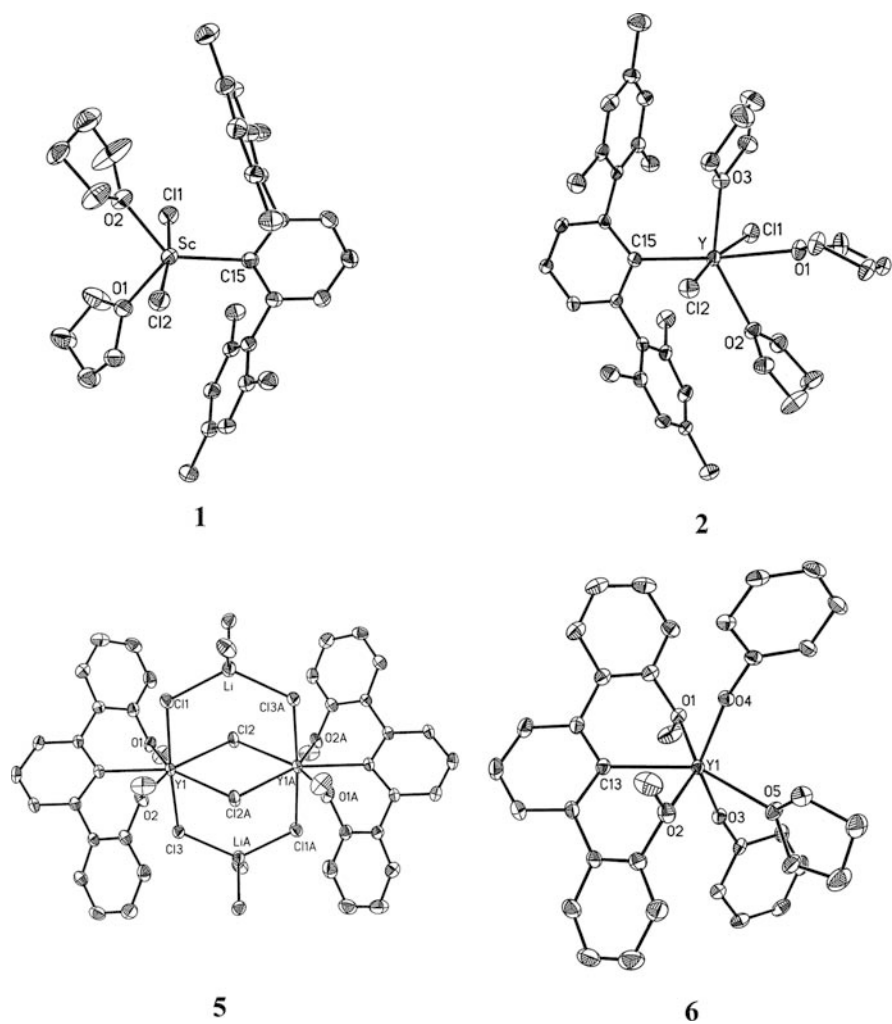
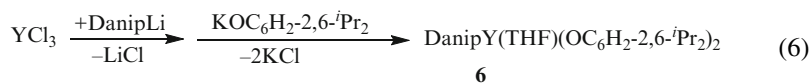
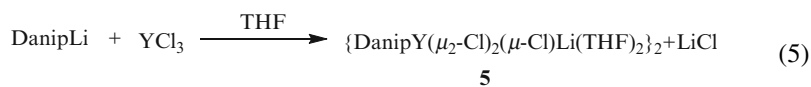


Fig. 1 Selected structures without H atoms (carbon atoms of THF in **5** and *i*Pr substituents in **6** are not shown) [13–18]



The chloride species $\{\text{DanipY}(\mu_2\text{-Cl})_2(\mu\text{-Cl})\text{Li}(\text{THF})_2\}_2$ (**5**) was synthesized by metathesis of YCl_3 with the lithium salt [17]. Complex **5** features a dimeric

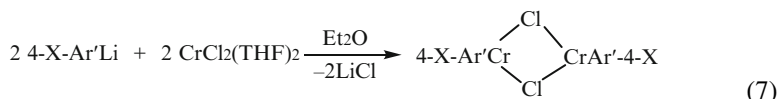
centrosymmetric heterobimetallic cage-like framework, which consists of two yttriums, each coordinated by a chelating Danip ligand, two Li atoms, and six chlorides. Two μ_2 -Cl atoms bridge the two yttriums directly (Y–Cl 2.9929(8) Å ave.) and four μ_2 -Cl atoms bridge the yttrium (Y–Cl 2.6456(5) Å ave.) and Li⁺ ions, which are also coordinated to two THF donor ligands. In addition, each yttrium is coordinated to two oxygen (Y–O = 2.449(2) Å) atoms of the MeO groups on the *ortho* position of the flanking rings.

Complex **6** was prepared by reaction of K(OC₆H₂-2, 6-*i*Pr₂) with in situ generated **5**. It is monomeric and the yttrium is coordinated to the terphenyl ligands via the ipso carbon and two oxygen atoms of the *ortho* MeO groups, the oxygen from OC₆H₂-2, 6-*i*Pr₂ and a THF donor.

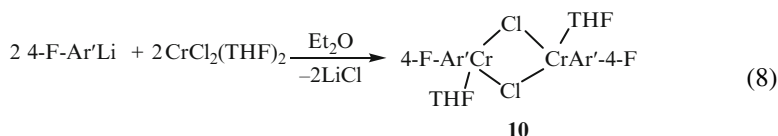
3.2 Terphenyl Chromium Halides

In 2005, it was shown that the reduction of the aryl chromium(II) chloride species, Ar'CrCl, with KC₈ afforded the Cr(I)–Cr(I) dimer Ar'CrCrAr' [19], in which the chromium atoms are linked by a fivefold metal–metal interaction. The effects of different terphenyl ligands on the quintuple Cr–Cr bonding in ArCrCrAr (Ar = 4-X–Ar', X = H, F, MeO or SiMe₃) dimers were also studied (see Sect. 7.2), and these dimers were similarly prepared by reduction of the corresponding aryl chromium chlorides [20].

The aryl chromium chloride species were synthesized in good yield (ca. 70 – 80%) by simple addition of one equivalent of ArLi (Ar = 4-X–Ar', X = H, F, MeO, SiMe₃) to CrCl₂(THF)₂ in ether at 0°C [21]. The reaction proceeded smoothly with complete elimination of LiCl to yield either blue or greenish blue crystals of the dimers {4-X–Ar'Cr(μ–Cl)}₂ (X = H (**7**), MeO (**8**), SiMe₃(**9**)), or {4-F–Ar'Cr(μ–Cl)(THF)}₂ (**10**). Donor molecules such as THF can also be incorporated depending on the substituents on the *para* position of the central ring.



X = H (**7**), OMe (**8**), SiMe₃(**9**)



Complexes **7–10** are dimerized through bridging of the terphenyl bound chromiums by the chlorides. For **9** and **10**, the bridging chloride positions are contaminated with iodide due to its inclusion as a LiI impurity in the ArLi salt. The structures

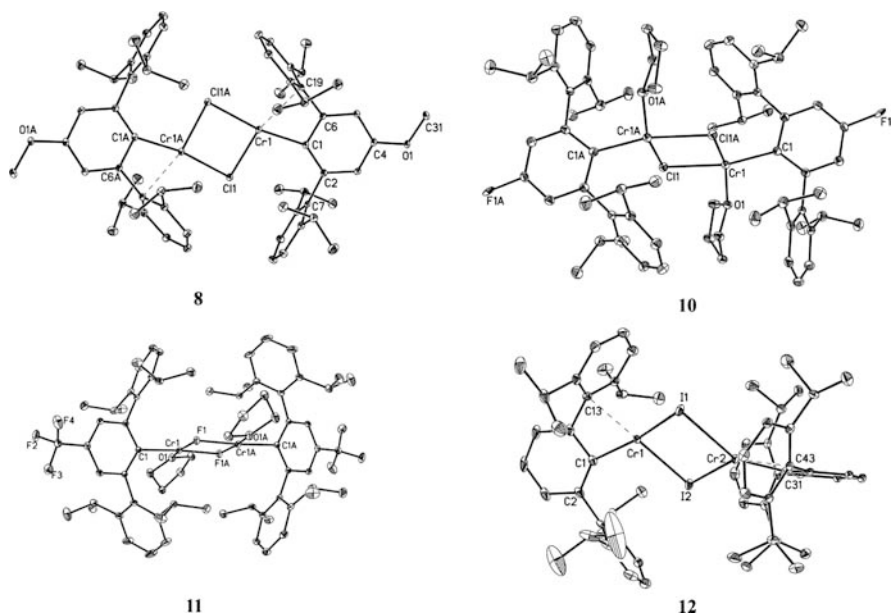
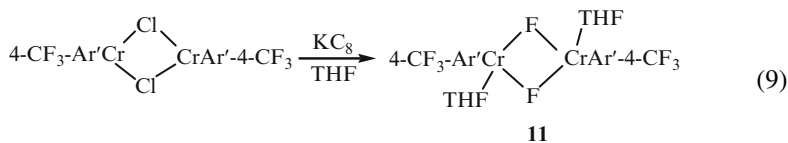


Fig. 2 Selected structures of terphenyl chromium halides without H atoms [21, 22]

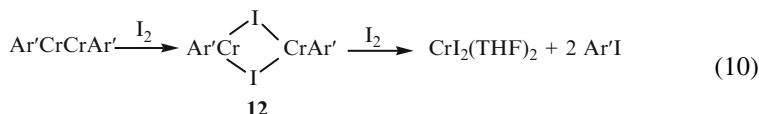
of **7**, **9**, and **10** are characterized by inversion centers midway between the two chromiums and they all display planar Cr_2Cl_2 cores (Fig. 2). In contrast, the structure of **8** has a mirror plane passing through the two chlorides and the Cr_2Cl_2 moiety has a fold angle of 154.0° along the Cr–Cr axis. This is considerably wider than that observed in the Cp^* ($\text{Cp}^* = \text{C}_5\text{Me}_5$) stabilized Cr(II) complex $(\text{Cp}^*\text{Cr}(\mu\text{-Cl}))_2$ (124.8°) [23]. The Cl–Cr–Cl and Cr–Cl–Cr angles are $87.51(2)$ and $89.56(2)^\circ$, respectively.

In **7–9**, there is a further interaction of the metal with an *ipso* carbon of one of the flanking $\text{C}_6\text{H}_3\text{-2, 6-}^i\text{Pr}_2$ rings of the terphenyl group. Thus, the chromium atoms can be considered to have a *quasi*-four-coordinate, square-planar environment. In **10**, no such Cr–C interaction was observed due to the coordination of a THF molecule to the metal which also gives a distorted square-planar metal environment. In each structure, the Cr–Cl distances are in the range of 2.32 to 2.46 Å, the average of which is similar to the 2.388 Å observed in the square-planar Cr(II) complex $\{\text{HC}(\text{CMeNDipp})_2\text{Cr}(\mu\text{-Cl})_2(\text{Dipp} = \text{C}_6\text{H}_3\text{-2, 6-}^i\text{Pr}_2)\}$ [24]. Magnetic studies of **7** indicated weak antiferromagnetic Cr(II)–Cr(II) exchange with coupling constant of $J = -7.0(1) \text{ cm}^{-1}$.

Binuclear difluoro-bridged chromium complexes are rare and the only well-characterized previous example is the multidentate Cr(III) derivative $\{[N, N''\text{-}(2\text{-O-3, 5-}^t\text{Bu}_2\text{-C}_6\text{H}_2\text{-CH}_2)_2\text{-1, 2-NHCH}_2\text{CH}_2\text{NH}]\text{Cr}(\mu\text{-F})_2\}$ [25]. The terphenyl stabilized chromium fluoride $\{4\text{-CF}_3\text{-Ar}'\text{Cr}(\mu\text{-F})_2\}$ (**11**) was obtained by decomposition during the reduction of $\{4\text{-CF}_3\text{-Ar}'\text{Cr}(\mu\text{-Cl})_2\}$ with KC_8 in THF. Unlike the generally blue color observed for the chlorides, **11** has a pale purple color.



The structure of **11** is very similar to that of **10**. It has a crystallographically required inversion center between the two metal atoms. Thus, the Cr_2F_2 moiety is planar. Like **10**, the chromium center in **11** is coordinated to two bridging fluorides, one terphenyl ligand, and one THF molecule, and has a distorted square planar geometry. The Cr–F distances of 1.970(2) and 2.104(2) Å are different, and may be compared to that observed (1.975 Å) [25] in $\{[(N,N'-(2\text{-O-}3,5\text{-}^t\text{Bu}_2\text{-C}_6\text{H}_2\text{-CH}_2)_2\text{-1,2-NHCH}_2\text{CH}_2\text{NH}]\text{Cr}(\mu\text{-F})\}_2$. Due to the THF coordination to the chromium atom, no Cr–Dipp interaction was observed. Magnetic studies were consistent with the expected antiferromagnetically exchange-coupled Cr(II)–Cr(II) dimer with a fitted coupling constant J of 2.5 m^{-1} .



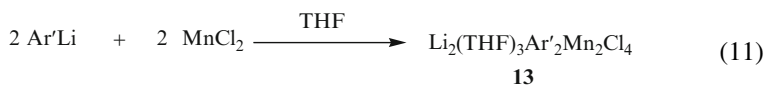
Structurally characterized chromium complexes with bridging iodides are also scarce and only a handful of examples are known [26–28]. The complex $\{\text{Ar}'\text{Cr}(\mu\text{-I})\}_2$ (**12**) was not synthesized by metathesis, but by the reaction of $\text{Ar}'\text{CrCrAr}'$ with one equivalent of iodine [22], which oxidizes the chromiums to Cr(II) and cleaves the quintuple bond. Reaction with a further equivalent of I_2 afforded the $\text{CrI}_2(\text{THF})_2$ complex with $\text{Ar}'\text{I}$ elimination. In **12** two chromiums are bridged by two iodides and the Cr–I distances are in the range of 2.674 to 2.775 Å, which is comparable to that in $\{\text{CpCr}(\mu\text{-I})\}_2$ (2.6678(5) and 2.6592(5) Å) [28]. One of the chromiums (Cr(1)) interacts with the $\text{C}_6\text{H}_3\text{-}2, 6\text{-}^i\text{Pr}_2$ ring but for Cr(2) the central ring of the Ar' ligand is oriented perpendicularly to the metal coordination plane and displays no secondary Cr–C interaction. This difference may be due to the reduced crowding in **12** as a result of the longer Cr–I bonds.

In summary, it is clear that the aryl chromium halide derivatives generally prefer distorted square-planar geometry by coordination of THF in complexes **10** and **11**, or by an interaction with the *ipso* carbon of the flanking $\text{C}_6\text{H}_3\text{-}2, 6\text{-}^i\text{Pr}_2$ rings in **7–9** and **12**. The square planar geometry is, no doubt, favored by the d^4 configuration of the Cr^{2+} ions. The Cr–Cr separation increases from 3.109(2) Å in the fluoride (**11**) [20], to 3.301(2) Å in the chloride (**3**) [21], and to 3.774 Å in the iodide derivative (**12**) [22], due to the increasing sizes of the bridging atoms. The Cr–C(*ipso*) distances range from 2.035(6) to 2.058(2) Å in **7–9** and **12** and are somewhat longer (2.125(3) and 2.117(2) Å) in **10** and **11**. The latter distances are similar to the 2.124(6) Å in the square planar Cr(II) complex $\text{Mes}_2\text{Cr}(\text{PMe}_3)_2$ [29]. This is a result of THF complexation and also, perhaps, the presence of an electron-withdrawing group [30] at the *para* position of the central rings in

10 and **11**. The Cr–C interactions in **7–9** and **12** range from 2.413 to 2.489 Å, which are on average 0.4 Å longer than the Cr–C(*ipso*) distances. The interaction of the flanking C₆H₃–2,6-*i*Pr₂ rings with the metal centers is also evident in the distortion of the bond angles at the *ipso* carbon. Thus, in **7–9** and **12**, the Cr–C(1)–C(2) angle is about 40° narrower than the Cr–C(1)–C(6) angle, while the difference of such angles is only about 4° in complexes **10** and **11**.

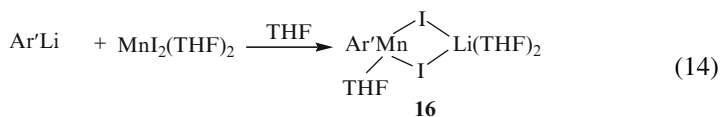
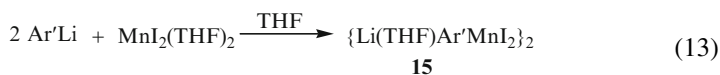
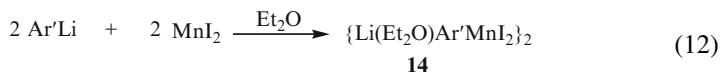
3.3 Terphenyl Manganese Halides

The reaction of anhydrous MnCl₂ with Ar'Li in THF was performed by following the same routine used for the preparation of the chromium chlorides. However, instead of the simple chloride-bridged species “{Ar'Mn(μ-Cl)}₂”, colorless crystals of the LiCl inclusion complex {(Ar'MnCl)₂Li₂Cl₂(THF)₃} (**13**) [31] were isolated.



X-ray crystallography revealed that **13** has a cuboidal structure featuring three types of bridging chloride (Fig. 3). These are: Cl(2), which μ₂-bridges the Mn atoms; Cl(1), which μ₃-bridges two Mn atoms and one Li; Cl(3) and Cl(4), which bridge two Li and one of the Mn atoms. The two lithiums in the structure are four-coordinate; one is coordinated to three μ₃-chlorides and THF, whereas the other is coordinated to two μ₃-chlorides and two THF molecules. Each manganese atom is bonded to one terminal terphenyl ligand and three bridging chlorides to afford distorted tetrahedral metal coordination. The differences in the Mn–Cl distances can be rationalized on the basis of the coordination geometries of the Cl, Mn, and Li centers and are in the range of 2.464(3) to 2.694(4) Å, which is considerably longer than the average Mn–Cl distance of 2.326 Å in the Mn(II) complex {HC(CMeNDipp)₂Mn(μ-Cl)}₂ [32].

Similarly, the reaction of MnI₂ with one equivalent Ar'Li in diethyl ether did not eliminate LiI; instead {Li(Et₂O)Ar'MnI₂}₂ (**14**) [21] was obtained.



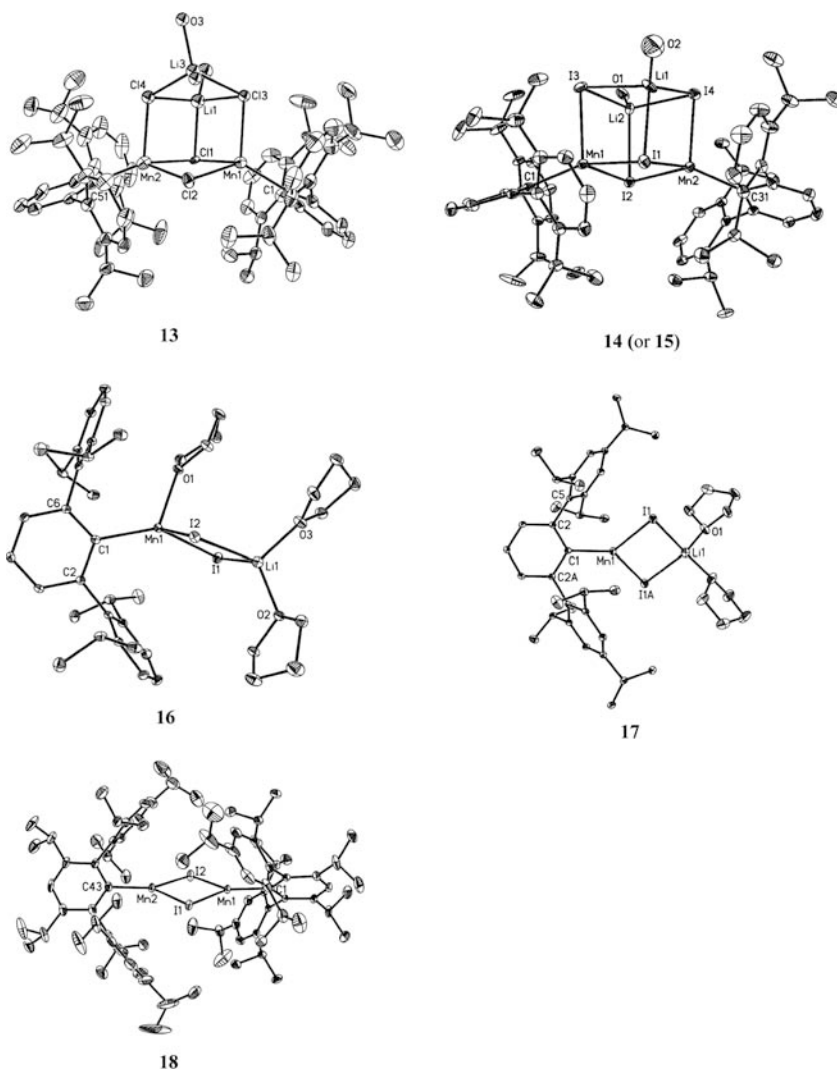


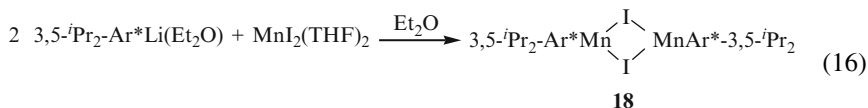
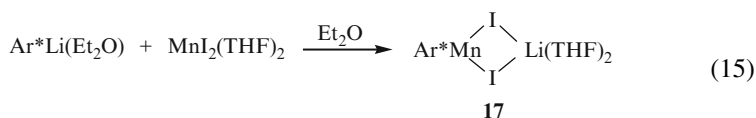
Fig. 3 Selected structures of terphenyl manganese halides without H atoms (carbon atoms of THF or Et₂O in **13–15** are also not shown) [21, 31]

Unlike the cuboidal structure of its chloride analog **13**, **14** has a cubane structure in which all twelve edges are bonding interactions. All the iodides in **14** are μ_3 -coordinated to metal ions and each lithium ion is coordinated to one diethyl ether molecule and three bridging iodides.

When the reaction of Ar'Li with one equivalent of MnI₂(THF)₂ was carried out in THF, two types of crystals, {Li(THF)Ar'MnI₂}₂ (**15**) and Ar'Mn(μ -I)₂Li(THF)₃ (**16**), were isolated [31]. Like the structure of **14**, **15** has a cubane structure with one THF molecule coordinated to each of the lithium ions (Fig. 3). Complex **16**

cocrystallizes with half an equivalent of $\{\text{LiI}(\text{THF})_2\}$, which is separate from the manganese complex. Unlike the dimanganese structures of **13–15**, **16** features just one manganese, which is bridged by two iodides to the lithium ion. The manganese atom is also coordinated to a terminal terphenyl ligand and a THF molecule (Mn–O 2.1731(13) Å), and has distorted tetrahedral geometry, similar to that observed in **13–15**. The MnI_2Li moiety has a fold angle of 172.9° along the I–I axis, which is somewhat wider than that of 164.4° observed in $\{\text{HC}(\text{CMeNDipp})_2\text{Mn}(\mu\text{-I})_2\text{Li}(\text{Et}_2\text{O})_2\}$ [33]. The Mn–I distances of 2.7716(3) and 2.7896(3) Å in **16**, are comparable to those in $\{\text{HC}(\text{CMeNDipp})_2\text{Mn}(\mu\text{-I})_2\}$ (2.7688(7) and 2.7484(8) Å) [34], and are slightly shorter than those of 2.793(5) and 2.847(2) Å in **15**, which has μ_3 bridging iodides.

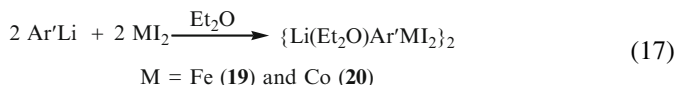
The bulkier ligands Ar^* and 3, 5-*i*Pr₂– Ar^* (cf. Schemes 1 and 2) were also used to prepare the terphenyl manganese iodide derivatives. For Ar^* , LiI was not eliminated and the monomeric complex $\text{Ar}^*\text{Mn}(\mu\text{-I})_2\text{Li}(\text{THF})_2$ (**17**) [31] obtained is very similar to **16**, except that the manganese in **17** is three-coordinate and has a trigonal planar geometry as a result of the greater bulk of the Ar^* ligand. However, with the even bulkier ligand 3, 5-*i*Pr₂– Ar^* , the by-product LiI was completely eliminated and the three-coordinate dimeric Mn(II) complex $\{3, 5\text{-}i\text{Pr}_2\text{-Ar}^*\text{Mn}(\mu\text{-I})_2\}$ (**18**) was obtained [31].



In summary, with increasing size of the terphenyl ligands, the geometries of the ArMnX ($X = \text{Cl}$ or I) derivatives change from distorted tetrahedral geometry, in the case of Ar' ligand, to distorted trigonal planar geometry with the bulkier Ar^* and 3, 5-*i*Pr₂– Ar^* ligands. The Mn–C(*ipso* carbon of the aryl ring) distances in **13–18** are in the narrow range of 2.068(4) to 2.134(7) Å, and are similar to those in the two-coordinate homoleptic derivatives $\text{Mn}(\text{Mes}^*)_2$ (2.108(2) Å) [35, 36] and four-coordinate heteroleptic cationic Mn(II) species $[\text{MesMn}(\text{Et}_2\text{O})_3]^+ [\text{BPh}_4]^-$ (2.111(8) Å) [37]. Notably, the Mn–C(*ipso*) bond distances in four-coordinate Mn complexes (2.109(1) Å in **14**, 2.1327(18) Å in **15** and 2.1327(18) Å in **16**) are slightly longer than those of the three-coordinate manganese atoms (2.093(2) Å) in **17** (2.093(2) Å) and **18** (2.084(2) Å). Similarly, the Mn–I distances in three-coordinate **17** and **18** are slightly shorter than those in the four-coordinated **14–16**. Unlike the chromium halide species, which show a secondary M–C interaction with the flanking aryl ring, the three-coordinate manganese iodide species showed no evidence of such interactions.

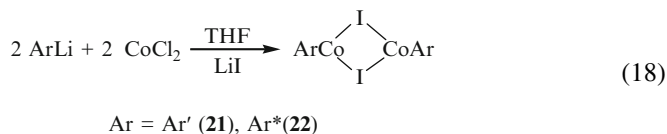
3.4 Terphenyl Iron and Cobalt Halide Complexes

The iron(II) and cobalt(II) terphenyl metal halide complexes have very similar structures to those of their manganese analogs. The reaction of Ar'Li with one equivalent of MI₂ (M = Fe and Co) readily afforded {Li(Et₂O)Ar'MI₂}₂ (M = Fe(**19**) or Co(**20**)) [21], which are isostructural to **14**. Each metal ion is coordinated to a terminal terphenyl ligand and three μ₃ bridging iodides and thus has a distorted tetrahedral geometry.



In **19**, the Fe–C bond lengths (2.044(3) and 2.038(4) Å) are similar to that in Fe(Mes^{*})₂ (2.058(6) Å) [35]. The Fe–I bonds are in the range of 2.7341(7) to 2.7769(7) Å and are similar to the Fe–I bond lengths in {Ph₃PSFeI(μ-I)}₂ (2.732 and 2.644 Å) [38].

The preparation of the terphenyl iron and cobalt chloride complexes afforded products that crystallized poorly. For iron, the simple products {Ar'Fe(μ-Cl)}₂ or {Ar'Fe(μ-I)}₂ could not be completely characterized. The metathesis using the bulkier ligand 3, 5-ⁱPr₂-Ar^{*} afforded {3, 5-ⁱPr₂-Ar^{*}Fe(μ-X)}₂ [31] (X = partial Cl and I), due to the incorporation of LiI in the Li(3, 5-ⁱPr₂-Ar^{*}) starting material. A similar problem was encountered in the reactions of CoCl₂. When using the ligands Ar' and Ar^{*} with CoCl₂, the only isolated crystals were of {ArCo(μ-I)}₂ (Ar = Ar' (**21**) and Ar^{*} (**22**)) [31] in which, the chloride is completely exchanged with the iodide according to X-ray crystallography.



Like the structure of **18**, complexes **21** and **22** are dimerized through bridging iodides. However, unlike the planar geometry observed for the Mn₂I₂ moiety in **18**, the Co₂I₂ units in **21** and **22** have a slight fold angle of ca. 5.4°. The Co–C distances in **21** (1.953(3) Å) and **22** (1.964(3) Å) are quite similar and are slightly longer than those in **20** (1.998(5) and 2.004(5) Å), in which the cobalts have higher coordination numbers. The Co–I distances (range from 2.587(3) to 2.609(3) Å) in **22** are similar to those in {Ph₃POCoI(μ-I)}₂ (2.6230(4) Å) [39] and are significantly shorter than the 2.6755(7) to 2.7141(8) Å observed in **20** owing to the lower coordination number of the cobalt in **22**.

The unusual cobalt iodide derivative {Ar[#]Co(μ-I)(CH₃-N=CH₂)}₂ (**23**) was obtained by the reaction of {Ar[#]Co(μ-I)}₂ with LiNMe₂ (see Sect. 5.2) [40]. It is dimerized through the two bridging iodides (2.6898(4) and 2.6825(4) Å). Each

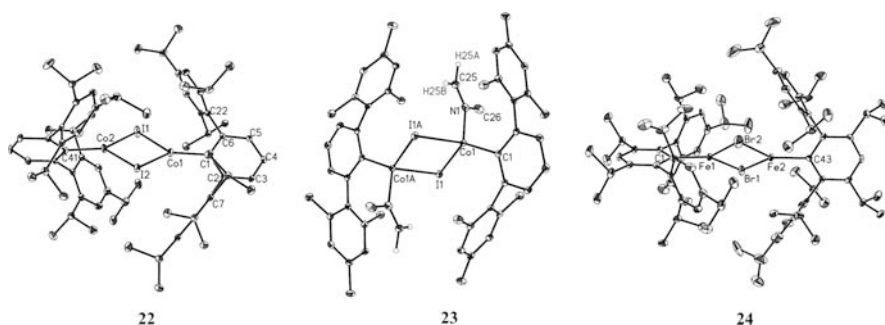
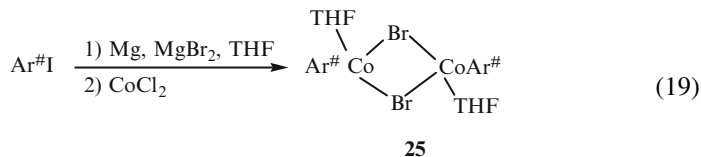


Fig. 4 Selected structures of terphenyl iron and cobalt halides without H atoms (except those of the $\text{HN}=\text{CH}_2$ ligand in **23**) [31, 40, 41]

cobalt atom is also coordinated to a terphenyl ligand (Co–C 2.012(2) Å) and a neutral imine molecule $\text{CH}_3\text{N}=\text{CH}_2$ via the nitrogen lone pair (Co–N 2.0472(19) Å) to give a distorted tetrahedral geometry.

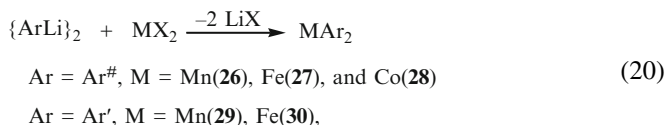
Terphenyl iron and cobalt bromide derivatives were studied with a view to improving yields and crystallinity. The iron species $\{\text{Li}(\text{Et}_2\text{O})\text{Ar}^*\text{FeBr}_2\}_2$ was obtained as an amber powder from hexanes or benzene, but it did not crystallize well. However, $\{3, 5\text{-}i\text{-Pr}_2\text{-Ar}^*\text{Fe}(\mu\text{-Br})\}_2$ (**24**) was prepared by the reaction of $3, 5\text{-}i\text{-Pr}_2\text{-Ar}^*\text{Li}$ with FeBr_2 in diethyl ether and structurally characterized. This complex could also be obtained by oxidizing the half sandwich Fe(I) complex $3, 5\text{-}i\text{-Pr}_2\text{-Ar}^*\text{Fe}(\eta^6\text{-C}_6\text{H}_6)$ with $\text{BrN}(\text{SiMe}_3)_2$ [41] (Fig. 4). For further details see Sect. 8.2.

The only known terphenyl cobalt bromide derivative is $\{\text{Ar}^\# \text{Co}(\mu\text{-Br})(\text{THF})\}_2$ (**25**), which was the first well-characterized terphenyl derivative of a transition metal. It was prepared by reaction of $\text{Ar}^\#\text{I}$ with activated magnesium (a mixture of magnesium metal and MgBr_2) and then with CoCl_2 in THF [42]. Halogen exchange occurred during the reaction and the bromide-bridged species was isolated instead of the chloride. The structure of **25** bears some resemblance to that of **23**. The cobalts are bridged by two bromides with Co–Br distances of 2.480(2) and 2.495(2) Å, which are very similar to that observed in the four-coordinate Co(II) complex $[\text{Co}(\mu\text{-Br})\{\text{C}(\text{SiMe}_3)_2(\text{SiMe}_2\text{NMe}_2)\}_2]$ (2.478(2) Å) [43]. In addition, each cobalt is coordinated to the terphenyl ligand (2.053(8) Å) and a THF molecule (Co–O 2.023(8) Å) and has a distorted tetrahedral coordination geometry.



4 Homoleptic, Two-Coordinate Terphenyl Transition Metal Complexes

Since the first stable, open-shell, two coordinate crystalline dialkyl species $\text{Mn}\{\text{C}(\text{SiMe}_3)_3\}_2$ was reported in 1985 [44], two-coordinate open shell transition metal complexes have attracted considerable interest. The related bulky aryl ligands have also played an important role in the stabilization of low coordination numbers at transition metals. Coordinatively unsaturated transition metal aryls tend to form oligomers [45–47]; however, the use of the very bulky Mes^* ($\text{Mes}^* = \text{C}_6\text{H}_2-2,4,6\text{-Bu}_3^t$) ligand afforded the two-coordinate transition metal derivatives MMes_2^* ($\text{M} = \text{Mn}$ or Fe) [35, 36]. Recently, Kays' group synthesized $\text{MAr}_2^\#$ ($\text{M} = \text{Mn}$ (**26**), Fe (**27**), or Co (**28**)) [48] Complexes **26–28** were obtained by reaction of $\{\text{LiAr}^\#\}_2$ with one equivalent of the metal dihalide in a mixture of THF and toluene. They were isolated as colorless (**26**), yellow–green (**27**), and dark purple (**28**) crystals, respectively, from hexanes.



Complexes **26–28** are monomeric and the metal centers are coordinated to two $\text{Ar}^\#$ ligands. Their crystals are isomorphous and feature two crystallographically independent molecules. The C–M–C angles of the two molecules differ by an average of ca. 7° and are in the range of $162.8(1)$ to $173.0(1)^\circ$. Similarly, the two-coordinate derivatives MAr'_2 ($\text{M} = \text{Mn}$ (**29**), Fe (**30**)) [31, 49] were obtained by the reaction of metal dihalides with LiAr' . Interestingly, the color of **30** is orange, which differs from the yellow of FeMes_2^* [35, 36] or yellow–green of $\text{FeAr}_2^\#$ [48].

Complexes **29** and **30** are isostructural and their crystallographic metrical parameters are almost identical (Fig. 5). There is only half of a molecule in the asymmetric unit due to the crystallographic mirror plane that passes through the metal centers. The M–C distances are very similar to those in the Mes^* and $\text{Ar}^\#$ analogs. The C–M–C angles in **29** and **30** are $160.19(9)$ and $159.34(6)^\circ$, respectively, which are similar to those in MMes_2^* ($\text{M} = \text{Mn}$, $159.66(10)^\circ$; $\text{M} = \text{Fe}$, $157.9(2)^\circ$) [35, 36], but somewhat narrower than those in $\text{MAr}_2^\#$ ($\text{M} = \text{Mn}$, $166.4(2)$ and $173.0(2)^\circ$; $\text{M} = \text{Fe}$, $164.4(2)$ and $171.1(2)^\circ$). It was proposed that the bending in the complexes MMes_2^* is due to weak interactions between the metal and the *tert*-butyl *ortho*-CH groups of the ligands and the bending in $\text{MAr}_2^\#$ complexes is a result of the secondary interaction between the metal centers and the *ipso* carbon of the flanking mesityl ring. However, no secondary interactions were observed in **29** or **30**. Thus, the bending in these complexes may be governed by packing effects. In addition, there is a ca. 17.7° angle between the M–C bond and the plane of the central aryl ring of the ligand a distortion that is not observed in the $\text{Ar}^\#$ analogs. Magnetic studies of **26–28** show that they have magnetic moments of 5.89, 4.90 and $3.81 \mu_B$

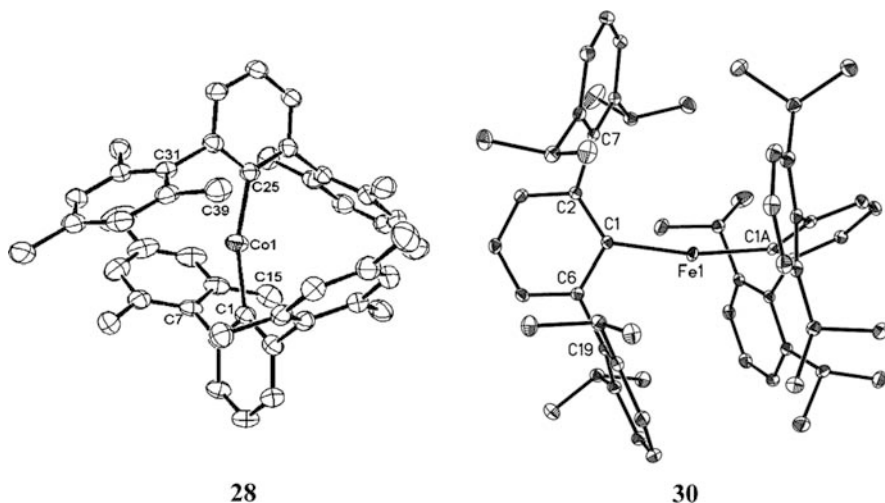


Fig. 5 Selected structures of homoleptic M(II) complexes without H atoms [48, 49]

respectively [48]. These values are close to the spin only values and indicate the presence of five, four, and three unpaired electrons.

5 Terphenyl Transition Metal Complexes with Amido Coligands

5.1 Quasi-Two-Coordinate Amido Complexes $Ar'M-NHAr^{\#}$

Numerous other heteroleptic transition metal terphenyl complexes, in which the halide is replaced by a variety of groups, are also possible. For example, amido ligands are of interest because of their ability to combine steric flexibility, good metal–ligand bond strength, and relatively straightforward synthetic accessibility. These attributes have led to their pioneering use in the synthesis of a wide variety of homoleptic, low (2 or 3) coordinate open shell ($d^1 - d^9$) complexes [50–57]. However, there are very few examples of heteroleptic two-coordinate complexes containing amido ligands or indeed heteroleptic, open shell two-coordinate species of any kind. A rare example is $\{(Me_3Si)_2N\}Fe(SAr^{\#})$ [58], which features a bulky terphenyl thiolate and an amido ligand. A major obstacle to the synthesis of the heteroleptic complexes was the scarcity of suitable starting materials that would afford two-coordinate complexes upon derivatization with amido or organo groups. The isolation of well-characterized terphenyl transition metal halides discussed in Sect. 3 provides a very useful entry to heteroleptic complexes in general. The reaction of the aryl metal halides with $LiN(H)Ar^{\#}$ in hexanes at room temperature yielded the aryl metal amido complexes $Ar'MN(H)Ar^{\#}$ ($M = Mn$ (**31**), Fe (**32**), Co (**33**)) with the elimination of LiX . Complexes **31–33** were isolated in moderate yield as pale yellow, bright red, and deep purple crystals, respectively [59].

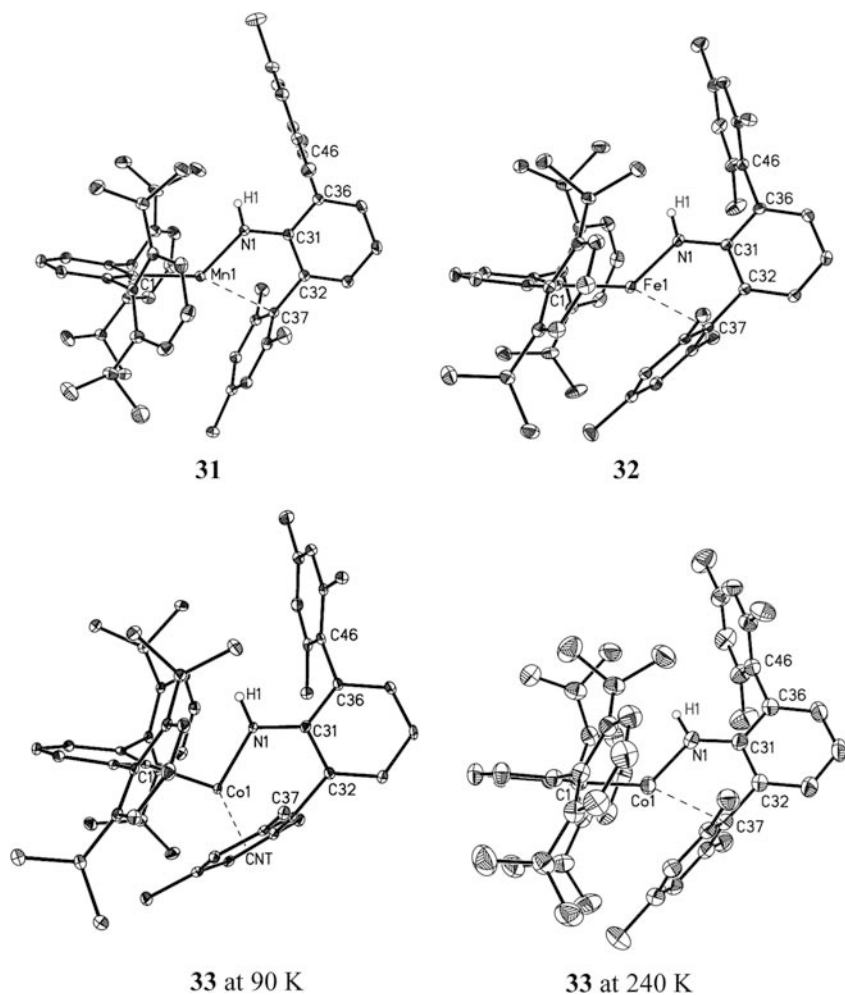
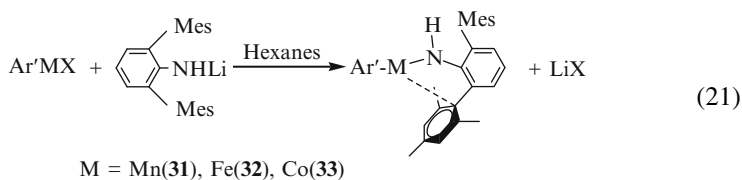


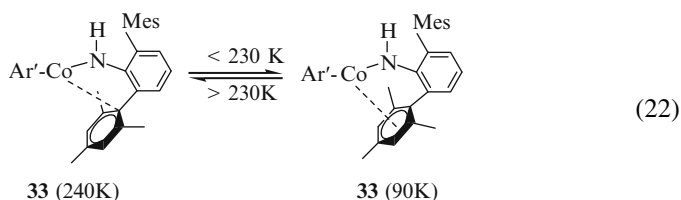
Fig. 6 Structures of complexes **31**–**33** without H atoms (except the N–H) [59]

The structures of **31** and **32** (Fig. 6) are very similar. In each complex, the metal is coordinated to the terphenyl ligand and the amido ligand. The M–C(1) σ -bonded distances are essentially the same as those in the homoleptic two-coordinate complexes **26** and **27**, respectively. The Mn–N distance (1.9807(12) Å) in **31** is similar to those in $\text{Mn}\{\text{N}(\text{SiMePh}_2)_2\}_2$



(1.989(3) Å) [59], but somewhat shorter than those in $\text{Mn}\{\text{NMesBMes}_2\}_2$ (2.046(4) Å) [60]. The Fe–N distance (1.9324(12) Å) in **32** is similar to those in $\text{Fe}\{\text{NMesBMes}_2\}_2$ (1.938(2) Å) [61] and $\text{Fe}\{\text{N}(\text{SiMePh}_2)_2\}_2$ (1.917(2) Å) [62]. The C(1)–M–N angles are 132.58(5) and 134.97(5)°, respectively, which deviate from linearity due to the interaction between M(II) and the *ipso* carbon(C(37)) of the flanking $-\text{C}_6\text{H}_2-2, 4, 6-\text{Me}_3$ ring. The M–C(37) distance is ca. 0.5 Å longer than the M–C(1) bond length. Similar interactions were also observed in the amido complexes $\text{M}\{\text{NMesBMes}_2\}_2$ (M = Mn [60] or Fe [61]). For each complex, the magnetic properties are fully consistent with the presence of the expected high-spin manganese(II) and iron(II) ions. The μ_{eff} for **32** is 5.36 μ_{B} , which is significantly more than the spin only value of 4.90 μ_{B} ($S = 2$) and suggests a considerable orbital contribution to the effective magnetic moment.

The structure of **33** was determined by X-ray crystallography at both 90(2) K and 240(2) K (Fig. 6). The structure obtained at 240(2) K is isostructural to those of **31** and **32**. The cobalt atom is coordinated to the terphenyl ligand and the amido ligand and has secondary interaction with the *ipso* carbon of the Mes ring (Co–C 2.393(2) Å). However, the structure at 90(2) K shows that there is a very strong η^6 interaction with one of the flanking Mes rings instead of the M–C secondary interaction seen at 240 K. The Co-centroid distance is 1.636(3) Å, which is considerably shorter than that in $\text{Ar}'\text{CoCoAr}'$ (see later) (1.7638(16) Å) [63], but lies within the expected range of 1.561 to 1.766 Å¹. The strong interaction causes the C(1)–Co–N(1) bending angle of 101.75(11)° at 90(2) K to be much narrower than the 133.90(6)° observed at 240(2) K. The strong Co – η^6 -arene bonding is consistent with calculations for first row transition metal–arene interactions, which show that they are often stronger for cobalt [64–66]. The Co–C(1) σ -bonded distances at both temperatures (1.977(1) and 1.992(2) Å) are essentially the same and are similar to that in **28**. The Co–N distances (1.875(3) and 1.880(2) Å) are somewhat shorter than those in the quasi-two coordinate complexes $\text{Co}\{\text{NMesBMes}_2\}_2$ (1.910(3) Å) [61] and $\text{Co}[\text{N}(\text{SiMePh}_2)_2]_2$ (1.901(3) Å) [62].



The structural changes in **33** are consistent with its magnetic properties, which indicate that the cobalt(II) ion undergoes an electronic spin-state transition from the low-spin, $S = 1/2$, state below 229 K to the high-spin, $S = 3/2$, state above this temperature (22). As is often the case for an electronic spin-state crossover,

¹ Co-centroid distance of 31 Co-arene (benzene or toluene) complexes from Cambridge database (version 5.29, February 2008).

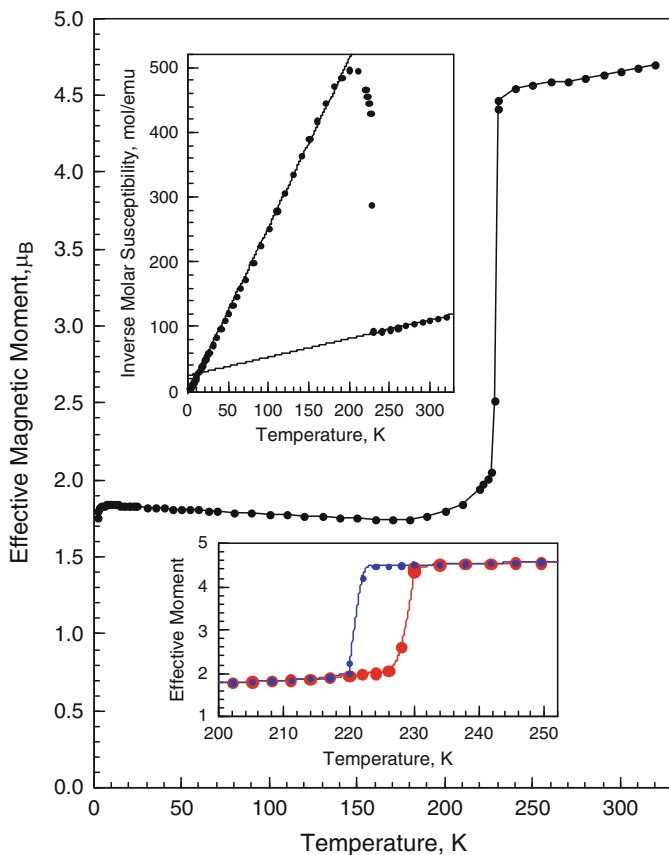


Fig. 7 The temperature dependence of the effective magnetic moment of **33** obtained upon warming. Upper inset: the inverse molar magnetic susceptibility of **33** obtained upon warming and its corresponding Curie–Weiss law fit. Lower inset: The hysteresis in the effective magnetic moment of **33** observed upon warming, *red*, and cooling, *blue* [59]

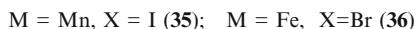
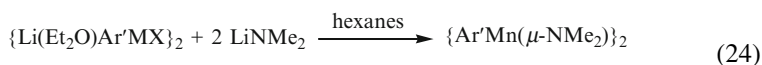
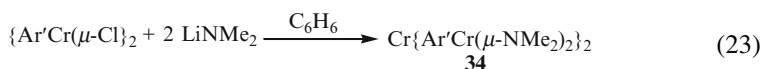
the transition exhibits hysteresis upon warming and cooling, which is shown in the lower inset to Fig. 7. Spin crossover in cobalt(II) systems has been well studied. However, the majority of the complexes concern multidentate ligand complexes with six-coordination or less commonly five-coordination at cobalt [67].

In **31–33**, all the σ -bond lengths involving the transition metals (M –C(*ipso* carbon of the aryl) and M –N) decrease in the sequence $Mn > Fe > Co$, which is in agreement with the decrease in the size of these metal ions [68]. The C(32)–C(37) distances in **33** as well as in **31** and **33** are essentially the same and show no significant change from that of C(36)–C(46), which is the corresponding C–C distance of the non-interacting flanking $-C_6H_2-2,4,6-Me_3$ ring. Although the secondary M –C interactions in the three structures induce considerable bending in their geometries, there is little effect on other structural parameters. For instance, there is no appreciable lengthening of the M –C or M –N σ -bonds. Also, the M –C interaction with

the flanking rings produces little structural change within the interacting rings. The reaction of $\{\text{Ar}'\text{CrCl}\}_2$ with $\text{LiN(H)Ar}^\#$ was also attempted and the blue solution of $\{\text{Ar}'\text{CrCl}\}_2$ turned deep red at low temperature, but changed to dark brown in about 30 min when it was warmed above ca. -40°C . No pure product was isolated at room temperature, however.

5.2 Terphenyl Transition-Metal Complexes of the Parent Dialkylamide-NMe₂

The reactions of LiNMe_2 with the corresponding aryl metal halides in hexanes or benzene readily afforded the dimethyl amido complexes **34–36** [40].



The complex **34** exhibits an unusual trinuclear structure. Several attempts were made to prepare the dimeric $\{\text{Ar}'\text{Cr}(\mu\text{-NMe}_2)\}_2$ analogous to **35** or **36**; however, **34** was the only isolated product. The molecule has a crystallographically imposed inversion center at the central chromium(II) ion which has a distorted square planar coordination geometry and is bound to four bridging NMe₂ ligands with N(1)–Cr(2)–N(2) and N(1)–Cr(2)–N(2A) angles of $97.38(7)^\circ$ and $82.62(7)^\circ$, respectively. The two outer chromium(II) ions are coordinated to two of the NMe₂ groups that bridge to the central chromium as well as to a terminal aryl ligand. These chromium(II) ions are three coordinate with distorted T-shaped coordination environment with a large C(1)–Cr(1)–N(1) angle of $163.55(8)^\circ$, and narrow C(1)–Cr(1)–N(2) and N(1)–Cr(1)–N(2) angles of $110.11(7)$ and $86.21(8)^\circ$. The coordination geometry at Cr(1) and Cr(1A) is thus highly unusual and may be contrasted with the *quasi*-square planar geometry in **7–9**, in which the chromium(II) ions interact with the *ipso* carbon from one of the flanking aryl rings. This *quasi*-T-shaped geometry at chromium(II) appears to be preceded only by that in the alkoxide $[\text{Cr}\{\text{OC}^t\text{Bu}_3\}_2(\text{Cl})\text{Li}(\text{THF})_2]$ [69] and is generally not found for chromium(II) amides, where the distorted trigonal planar geometry in complexes such as $\{\text{Cr}(\text{NRR}')(\mu\text{-NRR}')\}_2$ (R = 3,5-Me₂-C₆H₃, R' = adamantyl) [70] and $\{\text{Cr}(\text{N}^i\text{Pr}_2)(\mu\text{-N}^i\text{Pr}_2)\}_2$ [71] is normal. The Cr–N distances are in the narrow range of 2.005(2) to 2.113(2) Å, with Cr(outer)–N distances slightly shorter than those to the central chromium(II) ion, perhaps because of the lower coordination number of Cr(1) and Cr(1A). The Cr₂N₂ core in **34** is folded along the Cr–Cr axis with a fold angle of $34.11(4)^\circ$, which is similar to, but larger than, the $24.0(3)^\circ$ observed in $\{\text{Cr}(\text{NRR}')(\mu\text{-NRR}')\}_2$ [70]. The Cr–Cr separation in **34** is 2.9515(3) Å, which lies between the 2.838(2) Å in $\{\text{Cr}(\text{NCy}_2)(\mu\text{-NCy}_2)\}_2$ [72] and the 3.150(1) Å observed

in $\{\text{Cr}(\mu\text{-NPh}_2)(\text{NPh}_2)(\text{THF})\}_2$ [72], but is significantly longer than the 2.67(1) Å in *trans*- $\{(\eta^5\text{-C}_5\text{H}_5)\text{Cr}(\text{NO})(\mu\text{-NMe}_2)\}_2$ [73]. This might be due to the steric effect of the bulky terphenyl ligand on the terminal metal centers. The effective magnetic moment of **34** is 2.13 μ_{B} and because of the intramolecular exchange interactions, it is significantly below the spin only μ_{eff} of 4.90 μ_{B} expected for isolated chromium(II) ions.

Complexes **35** and **36** were prepared following the same synthetic route as **34**. In these cases the straightforward dimeric complexes with bridging NMe₂ groups were obtained in good yield. Crystals of **35** and **36** are isomorphous and the structures of the two complexes are very similar and are characterized by a crystallographically imposed inversion center between the metal ions. Dimerization occurs through almost symmetric bridging of the metal ions by the -NMe₂ groups. The Ar' group is terminally bound to each metal to yield a distorted, almost planar, trigonal coordination geometry (Fig. 8). For **35**, The Mn-N distances (2.0938(8) and 2.1247(9) Å) are somewhat shorter than those found in the three coordinate manganese(II) amido bridging complexes, such as $\{\text{Mn}(\text{N}^i\text{Pr}_2)(\mu\text{-N}^i\text{Pr}_2)\}_2$ (2.139(5) Å) [74] and $[\text{Mn}\{\text{N}(\text{SiMe}_3)_2\}\{\mu\text{-N}(\text{SiMe}_3)_2\}]_2$ (2.174(3) Å) [75] possibly for steric reasons. Although the Mn₂N₂ core is symmetric and almost perfectly square, the external N-Mn-C angles differed by over 21°. This difference is also probably steric in origin as a result of transannular terphenyl-terphenyl interactions. The Mn-Mn separation is 2.9479(3) Å, indicating very weak metal interactions. For **36**, The Fe-N distances of 2.0206(18) and 2.0354(19) Å are longer than those in $\{i\text{PrPDEA}\}\text{Fe}(\mu\text{-NMe}_2)\text{M}\}$ (*i*PrPDEA = (2, 6-*i*Pr₂-C₆H₃N=CMe₂)₂C₅H₃N, M = Li, K) (1.9773(16) Å) [76] and the NH₂-bridged complex $\{\text{Fe}(\text{CO})_3(\mu\text{-NH}_2)\}_2$ (1.98(2) Å) [77]. The distortion in the C-Fe-N angles (C(1)-Fe(1)-N(1) 138.53(8)° and C(1)-Fe(1)-N(1A) 124.99(8)°) is not as large as it is in **35**, but the Fe-Fe separation of 2.7241(6) Å is similar to the 2.715(1) Å and 2.663(1) Å observed in $\{\text{Fe}(\text{NR}_2)(\mu\text{-NR}_2)\}_2$ (R = Ph or SiMe₃) [78].

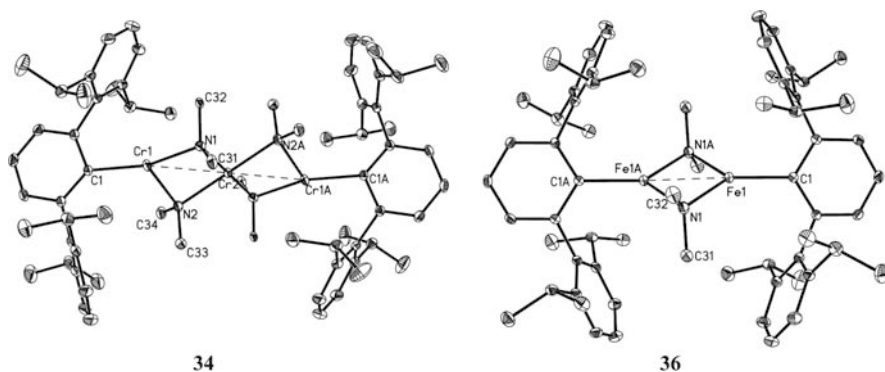
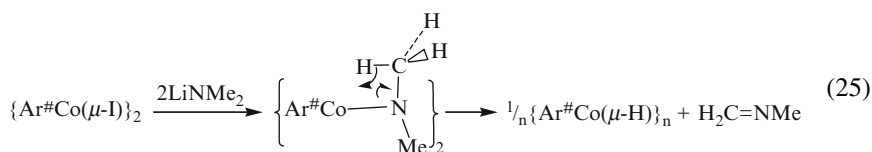


Fig. 8 Structures of **34** and **36** without hydrogens [40]

The magnetic properties of compounds **35** and **36** are similar. A fit of the temperature dependence of **35** with $g = 2$ and $S = 5/2$ yields $J = -38(1) \text{ cm}^{-1}$ and indicates a corresponding manganese(II) spin-only μ_{eff} of $5.92 \mu_{\text{B}}$. A fit of the temperature dependence of **36** with $g = 2$ and $S = 2$ yields $J = -75(3) \text{ cm}^{-1}$ and $N\alpha = 0.00110(8) \text{ emu/mol Fe}$ and a corresponding spin-only iron(II) μ_{eff} of $4.90 \mu_{\text{B}}$.

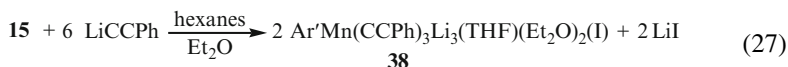
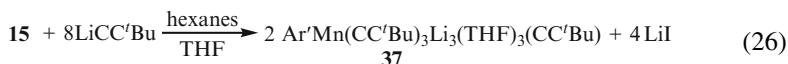
The reaction of $\{\text{Ar}'\text{Co}(\mu\text{-Cl})\}_2$ with two equivalents of LiNMe_2 was also attempted, but no amido product was obtained in this case, perhaps due to decomposition of the desired product. As a consequence, the less bulky aryl metal halide $\{\text{Ar}^\# \text{Co}(\mu\text{-I})\}_2$ was employed; only **23** ($\{\text{Ar}^\# \text{Co}(\mu\text{-I})(\text{CH}_3\text{NCH}_2)\}_2$), (see Fig. 4) could be isolated from the reaction mixture. In contrast to **35** and **36**, the reaction proceeded without elimination of lithium halide and the iodide-bridged species **23** was isolated in low yield.



The mechanism by which **23** is produced during the course of the reaction is unknown. However, it is possible that an amide intermediate $\text{Ar}^\# \text{CoNMe}_2$ is produced initially. Then the smaller size of the $\text{Ar}^\#$ ligand relative to Ar' may permit decomposition. The released $\text{H}_2\text{C}=\text{NMe}$ may then be trapped by unreacted $\{\text{Ar}^\# \text{Co}(\mu\text{-I})\}_2$ to form **23**, while the presumably unstable cobalt hydride decomposes to unidentified products. The structure of **23** bears a resemblance to that of $\{\text{Ar}^\# \text{Co}(\mu\text{-Br})(\text{THF})\}_2$ (**25**), and is dimerized through the two bridging iodides and is characterized by an inversion center midway between the cobalt(II) ions as in **35** and **36**. Thus, the Co_2I_2 unit is planar. Each cobalt is also bound to a terminal $\text{Ar}^\#$ group and a $\text{CH}_2=\text{NCH}_3$ ligand, which is coordinated through the nitrogen lone pair to afford distorted tetrahedral coordination geometry at cobalt. The $\text{Co}\text{-I}$ distances of $2.6898(4)$ and $2.6825(4) \text{ \AA}$ are comparable to those in $[\{\text{Ph}_3\text{POCoI}(\mu\text{-I})\}_2]$ (2.647 and 2.652 \AA) [39]. The $\text{Co}\cdots\text{Co}$ separation is $3.628(3) \text{ \AA}$, which is consistent with the absence of bonding interaction between the two cobalts and the magnetic properties of the complex. The $\text{Co}\text{-N}$ distance of $2.0472(19) \text{ \AA}$ is within the range of bond distances for numerous cobalt(II) imino complexes. The $\text{N}(1)\text{-C}(25)$ bond length of $1.262(3) \text{ \AA}$ is considerably shorter than the $\text{N}(1)\text{-C}(26)$ distance of $1.451(3) \text{ \AA}$, and is consistent with $\text{N}\text{-C}$ double bonding. The dehydrogenation of NMe_2 was also observed in $(\text{PMe}_2\text{Ph})\text{Cl}_2\text{W}(\mu\text{-NMe}_2)\text{-}(\mu\text{-}\sigma, \eta^2\text{-CHCH}_2)(\mu\text{-}\eta, \sigma\text{-CH}_2\text{NMe})\text{WCl}(\text{NMe}_2)(\text{PMe}_2\text{Ph})$ [79, 80], but unlike the $\mu\text{-}\sigma$ and η^2 coordination mode in that complex, the ligand adopts a σ only coordination through the lone pair on nitrogen. This may be due to the tendency of cobalt(II) complexes to prefer tetrahedral coordination. Currently, the chemistry of these NMe_2 complexes is under investigation.

6 Terphenyl Metal Halide Reactions with Acetylides

The acetylide group ($-\text{C}\equiv\text{CR}$) ligand is an extremely versatile one, which can bond to transition metals in a variety of coordination modes, and donate up to 5 electrons [81–84]. The reaction of $\{(\text{THF})\text{Li}\}_2\text{Mn}_2\text{Ar}'_2\text{I}_4$ (**15**) with two equivalents of LiCCR ($\text{R} = \text{}^t\text{Bu}$ or Ph) in a mixture of hexanes and THF or diethyl ether afforded $\text{Ar}'\text{Mn}(\text{CC}^t\text{Bu})_3\text{Li}_3(\text{THF})_3(\mu_3\text{-CC}^t\text{Bu})$ (**37**) or $\text{Ar}'\text{Mn}(\text{CCPh})_3\text{Li}_3(\text{THF})(\text{Et}_2\text{O})_2(\mu_3\text{-I})$ (**38**) [31]. The reaction of **15** with LiCC^tBu was attempted with different stoichiometric ratios of **15** to LiCC^tBu ; however, **37** was the only isolated product irrespective the ratio of the reactants. In contrast, **15** reacts with six equivalents of LiCCPh and **38** could be obtained, regardless the stoichiometric ratio of **15** to LiCCPh .



In **37**, the manganese is coordinated to three $-\text{CC}^t\text{Bu}$ groups through the β -carbons of the acetylide groups and one terphenyl ligand, and thus has a distorted tetrahedral geometry. In addition, three lithium ions coordinated by THF bridge the three acetylide groups by π -complexation and one μ_3 -bridging acetylide group through σ -donation. Thus, the oxidation state of the manganese in **37** remains +2, which was further conformed by magnetic studies (Fig. 9). Examples of alkali metal ions capped by the electron rich acetylide groups in manganese complexes were quite rare and the known examples are the Mn(I) complexes $\{\text{Mn}(\text{dmpe})_2(\text{CCSiMe}_3)_2\}[\text{M}]$ ($\text{M} = \text{Li}$ or Na , $\text{dmpe} = 1,2\text{-bis}(\text{dimethylphosphino})\text{ethane}$) [86]. The Mn–C(β -carbon of the $-\text{CC}^t\text{Bu}$ group) bond lengths are essentially identical, with an average distance of 2.192(3) Å. Due to the coordination of the triple bond in the acetylide groups to the Li ions, the Mn–C distances in **37** are considerably longer than the average Mn–C distances of 2.075 Å in the heterocubane structure of the phosphoraneiminato complex $\{\text{Mn}(\text{CCSiMe}_3)(\text{NPEt}_3)\}_4$ [87]. Magnetic studies indicated that the Mn(II) center has a high-spin configuration with five unpaired electrons.

The structure of **38** is very similar to that of **37** with the manganese center coordinated to three $-\text{CCPh}$ groups and one terphenyl ligand and lithium ions complexed between the acetylide groups. However, instead of a μ_3 coordination through the α -carbon of an acetylide group, there is a μ_3 -iodide bridged to three lithium ions in **38**. Only mixed base donors (diethyl ether and THF coordinating to Li) afforded crystalline products. Magnetic studies showed that **38** had five unpaired electrons with $S = 5/2$, which is normal for high-spin Mn(II) complexes.

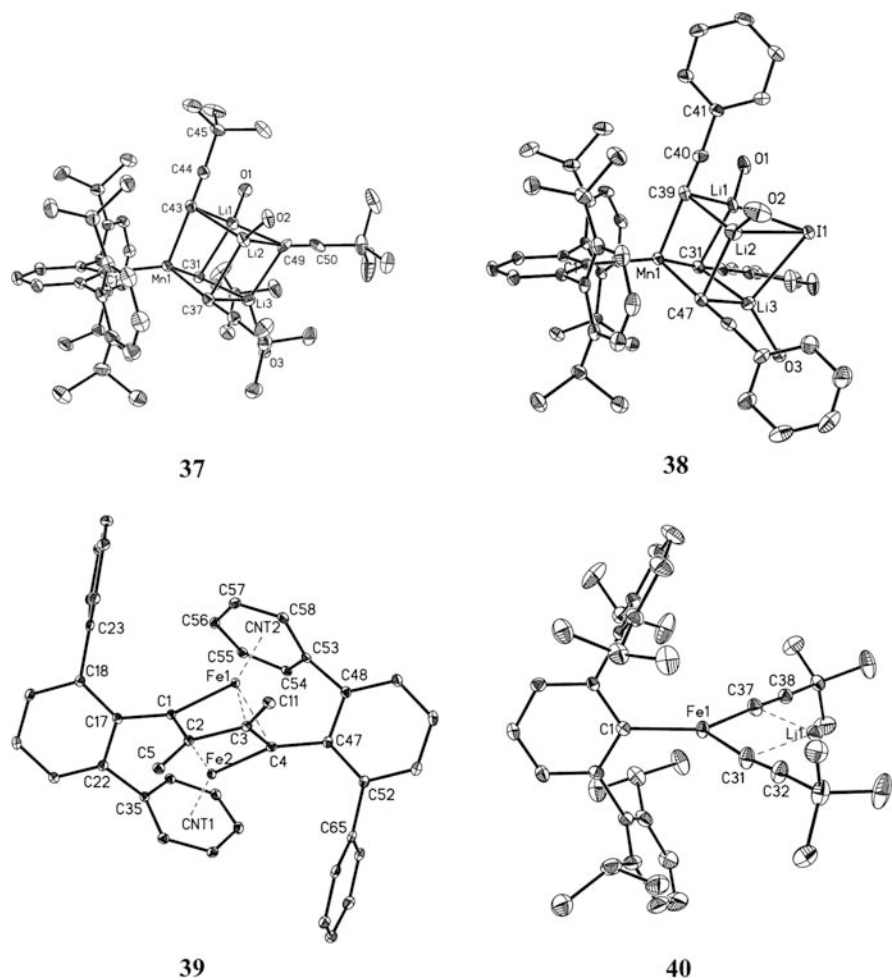
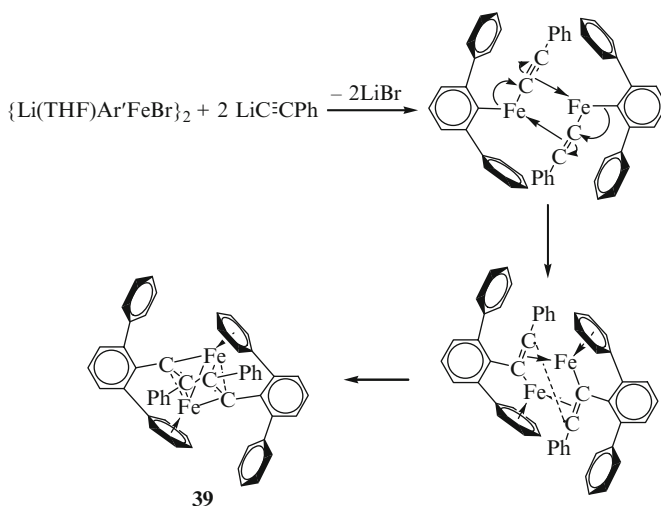


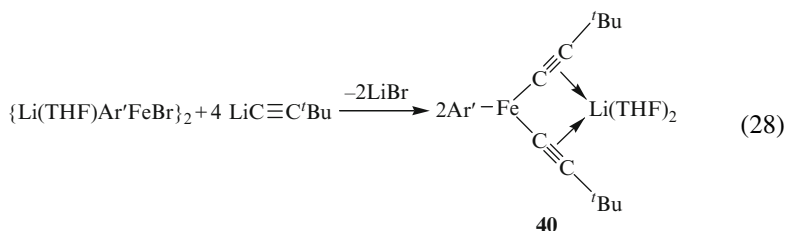
Fig. 9 Structures of **37–40** without H atoms (carbons of THFs in **37** and **38**, Prⁱ groups in **39** and THF molecule in **40** are not shown) [49, 85]

The reactions of $\{\text{Li}(\text{Et}_2\text{O})\text{Ar}'\text{FeBr}_2\}_2$ with the lithium acetylide reagents afforded very different results (Scheme 3) from those obtained for manganese [85]. It is possible that the initial step involves elimination of LiBr to give the intermediate “Ar'Fe–C \equiv CPh,” which may associate through the π -donation of the electron rich acetylide group to the iron center. In concert with η^6 -complexation of the iron by a flanking aryl ring, the Ar' group then migrates from the iron with reduction of the metal to +1 with generation of radical character at the α -carbon of the acetylide group. Radical coupling then leads to dimerization and formation of a C–C bond to afford complex **39**. Radical coupling of aryl-substituted acetylides is known for alkali metal derivatives related to **39** [88].



Scheme 3 Proposed mechanism for the formation of **39**. ⁱPr groups are not shown [85]

X-ray crystallography revealed that complex **39** is a 1,3-butadiene ligand stabilized binuclear transition metal complex with a metal–metal interaction. The Fe–Fe distance is 2.5559(3) Å, which is slightly longer than the sum, 2.48 Å, of the single bond covalent radii for iron [89]. The chemical environments of the two irons are very similar, so the following discussion focuses on Fe(1). The Fe(1) atom is η^1 - σ -bonded to C(1), η^2 - π -bonded to C(3) and C(4) of the 1,3-butadiene moiety. In addition, it is η^6 -bonded to one of the flanking $-\text{C}_6\text{H}_3-2, 6\text{-Pr}_2^i$ rings of the Ar' unit attached to C(4). The Fe–C(1) σ -bonded distance is 1.965(2) Å. The Fe– η^2 interactions with the double bonded carbon atoms C(3) and C(4) are slightly different (2.128(2) and 2.058(2) Å). It is noteworthy that the single bond (C(2)–C(3)) and the double bonds (C(1)–C(2) and C(3)–C(4)) within the 1,3-butadiene ligand are elongated by ca. 0.07 Å, in comparison to uncomplexed 1,3-butadiene [90–92]. The Fe–centroid distances are 1.589(3) and 1.595(3) Å, which are considerably shorter than those in the Fe(I) complexes, Ar'FeFeAr' (1.733(2) and 1.763(2) Å) (see later) [63], ($\eta^6\text{-C}_6\text{H}_6$)FeAr*–3, 5-Pr₂ⁱ (Ar*–3, 5-Pr₂ⁱ = C₆H–2, 6-(C₆H₂–2, 4, 6-Pr₃ⁱ)₂–3, 5-Pr₂ⁱ) (1.643(2) Å) [93], and [$\{(\text{C}_6\text{H}_3-2, 6\text{-Pr}_2^i)\text{NC}(\text{Me})\}_2\text{CH}\}\text{Fe}(\eta^6\text{-C}_6\text{H}_6)$] (1.6245(8) Å) [94]. The Fe–C(aryl ring) distances are in the range of 2.050(2) to 2.192(2) Å and the C–C distances involving C(53) (1.445(2) and 1.436(2) Å) are on average ca. 0.03 Å longer than the other C–C distances within the same aryl ring. The strengths of the metal–carbon interactions to C(53) and C(56) are reflected in their deviation from the C54–C55–C57–C58 plane by ca. 0.146 and 0.076 Å, respectively, with the result that the C₆H₃–2, 6-ⁱPr₂ ring has a distorted boat geometry. Similar distortions are also observed in the central aryl ring of the terphenyl ligands.



The ion pair complex **40** was prepared similarly; however, no insertion or coupling was observed for the acetylide groups. This may be due to the bulky substituent (*t*Bu) on the α -carbon of the acetylide group, which hinders Ar' migration and radical formation on the α -carbon and disfavors coupling of the acetylide group. Instead, two acetylides become coordinated to the iron and a lithium ion is complexed by THF and two alkyne moieties. Thus, the oxidation state of Fe in **40** is +2. The iron is coordinated to the terphenyl group Ar' and two acetylide groups through the β -carbon atoms, and has a distorted trigonal planar coordination geometry. The Fe–C(1) bond length of 2.039(2) Å is very similar to the terminal Fe–C distance in the three-coordinate Fe(II) complex {MesFe(μ -Mes)}₂ (2.023(5) Å) (Mes = C₆H₂–2, 4, 6-Me₃) [95]. The Fe–C(acetylide) distances (2.029(3) and 2.033(2) Å) are very close, and are slightly longer than those in other three-coordinate Fe(II) complexes, such as HC[C'*t*BuN(2, 6-*i*Pr₂–C₆H₃)]₂FeCCR (R = SiMe₃ 1.961(6) Å [96] and R = Ph, 2.000(2) Å [97]). Due to the coordination of the acetylide group to the lithium ion, the Fe(1)–C(31)–C(32) angle of 172.5(3)° deviates slightly from linearity. Magnetic studies showed that it had a high-spin d⁶ configuration with *S* = 2.

Similar reactions for the chromium species were also attempted. The blue solution of {Ar'Cr(μ -Cl)}₂(**7**) becomes deep red when treated with the acetylide reagents and the color of the solutions changed to dark brown upon warming. Unfortunately, no crystals could be isolated.

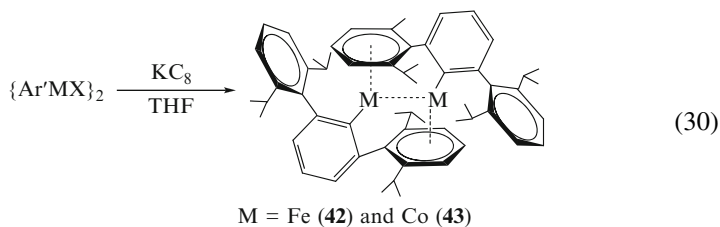
7 Reduction of Terphenyl Metal Halides

7.1 Terphenyl Stabilized Metal(I) Dimers ArMMAr (M = Cr, Fe, and Co)

Since the landmark [Re₂Cl₈]²⁻ dianion was structurally characterized in 1964 [98], the topic of multiple bonding between metal–metal centers has been a very active research area in inorganic chemistry [99]. In particular, the “paddle-wheel” complexes of the type [M₂L₄L'₀₋₂] (L = bridging bidentate ligand; L' = axial ligand), which have quadruple bonds formed by the overlap of σ , 2 π , and δ orbitals, have been intensely investigated. Beginning in the mid-1970s, however, theoretical and spectroscopic investigations of diatomic transition-metal species M₂ (M = Cr

between two d^5 chromium(I) centers. A simplified molecular orbital(MO) diagram could be used to explain the nature of the fivefold Cr–Cr interaction, namely, one σ (d_z^2 overlap; A_g symmetry), two π (d_{yz} and d_{xz} ; B_u symmetry), and two δ ($d_{x^2-y^2}$ and d_{xy} ; B_g symmetry) with 10 valence electrons. The actual bonding situation is more complex because mixing between orbitals of the same symmetry can occur. Theoretical studies on the simplified species PhCrCrPh and HCrCrH have confirmed the very short Cr–Cr bond length and the overall trans-bent geometry observed in **41** [113, 114]. The publication of **41** has sparked considerable further interest in quintuple bonded species [113–117]. Several dichromium complexes including ArCrCrAr (Ar = modified terphenyl) [20], $Cr_2(Ar^1N=CHCHN=Ar^1)_2$ ($Ar^1 = C_6H_3-2, 6-Pr_2^i$) [118], $Cr_2\{2-(NMe_3)-5-Trip-pyridine\}_2$ (Mes = $C_6H_2-2, 4, 6-Me_3$, Trip = $C_6H_2-2, 4, 6-Pr_3^i$) [119], and $[K(\text{crypt}[2, 2, 2])][Cr_2(\{N(\text{Xyl})\}_2CH)_3]$ (Xyl = $C_6H_3-2, 6-Me_2$) [120] have been reported. All these complexes contain five orbital interactions and featured very short Cr–Cr bond lengths that range from 1.7397(9) to 1.8351(4) Å [20, 118–120].

In order to explore M–M bonding in first row transition metals further, the reduction of iron halide $\{Li(OEt_2)_2Ar'FeI_2\}_2$ (**19**) or $\{Li(THF)Ar'FeBr_2\}_2$ and the cobalt halide $\{Li(OEt_2)_2Ar'CoI_2\}_2$ (**20**) or $\{Ar'Co(\mu-Cl)\}_2$ with KC_8 in tetrahydrofuran was performed. The reductions afforded $Ar'FeFeAr'$ (**42**) and $Ar'CoCoAr'$ (**43**) in low yield [63].



Both **42** and **43** also display trans-bent $C_{ipso}-M-M-C_{ipso}$ core configurations, which appear to resemble that observed in **41**. In a manner which also appears to be similar to **41**, the iron and cobalt atoms are η^1 -bonded to an *ipso*-carbon from the central aryl ring of the terphenyl ligand and also interact with a flanking ring of a terphenyl ligand attached to the other metal within the dimer. However, in **42** and **43** these flanking ring interactions are very much stronger than those in **41** as indicated by a 0.5 Å shortening of the metal–centroid distances. Thus, in **42** the Fe–flanking ring centroid distances are 1.733(2) and 1.763(2) Å and in **43** the Co–centroid distance is similar at 1.764(2) Å. These lengths, which may be compared to 2.203(6) Å observed in **41**, are similar to the Fe- and Co-centroid distances in the η^6 -aryl complexes $[HC\{C(Me)N(C_6H_3-2, 6-Pr_2^i)\}_2Fe(\eta^6-C_6H_6)]$ [94], $[3, 5-Pr_2^iAr^*Fe(\eta^6-C_6H_6)]$ [93], $[HC\{C(Me)N(C_6H_6-2, 6-Me_2)\}Co(\eta^6-C_7H_8)]$ [121].

The most prominent structural parameters in **42** and **43** are the Fe–Fe and Co–Co distances which present an even greater contrast to the chromium structure. The Fe–Fe (2.515(9) Å) and Co–Co (2.8033(5) Å) separations greatly exceed the

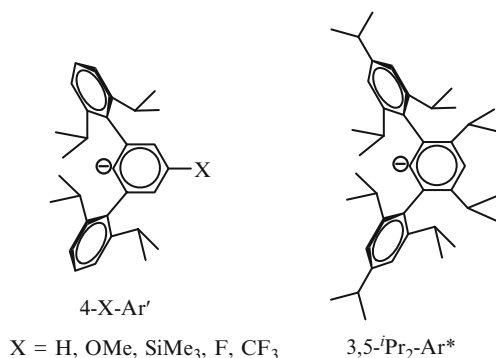
1.8351(4) Å observed in **41**. The Fe–Fe distance, is very similar to the Fe–Fe separation in **39** and is very close to the sum, 2.48 Å, of the single bond covalent radii for iron [89], whereas the Co–Co separation is over 0.3 Å longer than the 2.46 Å distance predicted for a cobalt–cobalt single bond [89]. On the basis of these distances, an iron–iron single bond might be expected for **42** whereas the cobalts in **43** are expected to be weakly bonded or non-bonded. However, magnetic studies of **42** show that it is paramagnetic and has two high-spin, $S = 3/2$, Fe(I) ions and that there is little antiferromagnetic coupling between them. In contrast, magnetic data for solid and solution samples of **43** show that it is essentially diamagnetic. The magnetic data for **43** suggest that the two Co(I), d^8 centers are either very strongly antiferromagnetically coupled or that they each have a diamagnetic, non-bonded low-spin d^8 configuration. DFT calculations suggest that there is little or no bonding between the cobalt or the iron centers in **42** and **43** in agreement with the experimental data.

Attempts to synthesize $Ar'MnMnAr'$ were also made by reduction of the corresponding manganese halide $\{Li(OEt)_2Ar'MnI_2\}_2$ (**14**) with KC_8 in tetrahydrofuran; however, no crystals were isolated from the resulting red brown solution.

7.2 Terphenyl Ligand Substituent Effects in Chromium Complexes

Following the initial report of **41**, the first compound with a quintuple bond between two Cr centers, it was decided to explore how changes in the steric and electronic properties of the terphenyl ligand might affect the metal–metal bonding. Thus, we developed a series of ligands related to Ar' with different electronic and steric properties (Scheme 4) and prepared a series of chromium(II) halide precursors for further study (cf Sect. 3.2).

Reduction of the chromium(II) halide precursors $\{4-X-Ar'Cr(\mu-Cl)\}_2$ ($X = MeO$ (**8**), $SiMe_3$ (**9**)) or $\{4-F-Ar'Cr(\mu-Cl)(THF)\}_2$ (**10**) (**31**) in THF readily afforded



Scheme 4 Modified terphenyl ligands related to Ar' and Ar^* for the stabilization of M(I) complexes ($M = Cr, Mn, Fe, \text{ or } Co$)

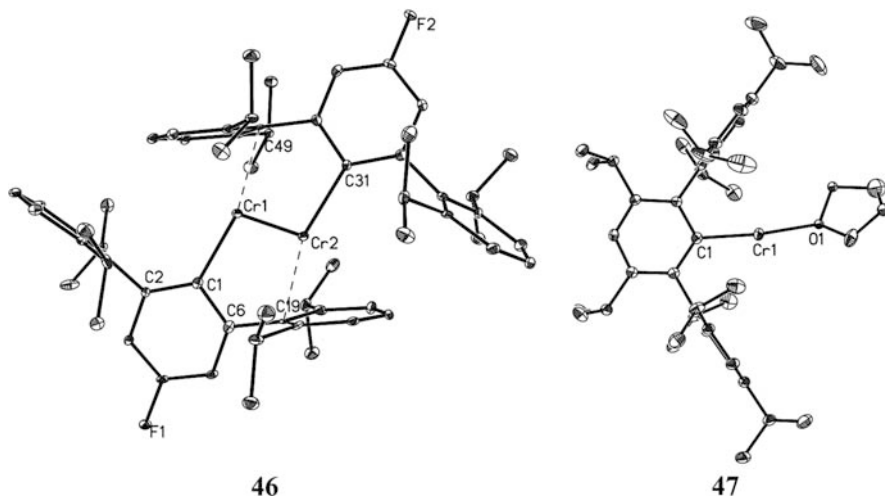
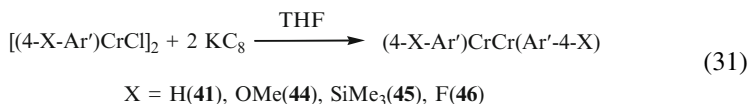


Fig. 11 Structures of **46** and **47** without H atoms [20, 122]

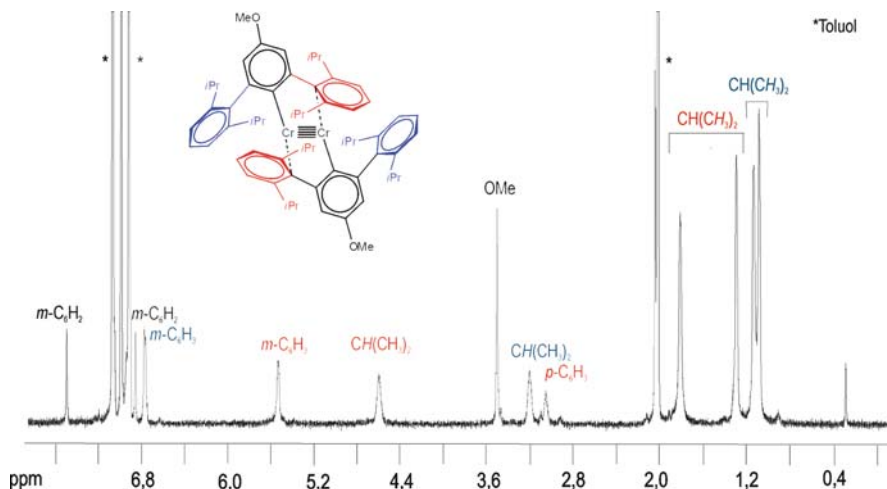


4-X-Ar'CrCrAr'-4-X (X = MeO (**44**), SiMe₃ (**45**), or F (**46**)) [20]. Complexes **44–46** are all deep red and pyrophoric like **41**. The low-temperature X-ray crystal structures revealed similar, *trans*-bent dimeric structures with short Cr–Cr distances ranging from 1.8077(7) to 1.8351(4) Å. While **41**, **44** and **45** reside on a crystallographic inversion center, and hence display strictly *anti*-periplanar conformations, this is not the case for **46**, which shows a slightly twisted arrangement of its C_{ipso}–Cr–Cr–C_{ipso} core [C(1) – Cr(1) – Cr(2) – C(31) = 172.8°] with little change in the overall geometry of the molecule (Fig. 11). The C_{ipso}–Cr–Cr angles in **41** and **44–46** are almost invariant and in the range of 101.65(6) – 102.78(1)°. A notable feature of the structures is the close approach of one of the C₆H₃–2, 6-*i*Pr₂ substituents of each terphenyl ligand to one of the chromium(I) ions. The Cr–C(*ipso*) distances of the affected flanking aryl rings range from 2.294(1) to 2.322(2) Å, which is approximately ca. 0.18 Å or 8% longer than the Cr–C(*ipso*) bonds of the central aryl rings. The remaining Cr–C distances exceed 2.41 Å. Because of the similar structure of these complexes, **41** and **44–46** all show temperature-independent paramagnetism with χ_M values of 0.00112(5), 0.00150(10), 0.00088(3), and 0.00062(3) emu/mol Cr respectively (Table 1).

The ¹H NMR spectrum of (4-MeO-Ar')CrCr(Ar'-4-OMe) (**44**) is representative of the four complexes. The spectrum features four diastereotopic methyl resonances in the usual range, one signal for the MeO group, as well as two signals for the protons in the *meta* positions of the flanking aryl ligand. Two multiplets at 3.21 and 4.62 ppm correspond to tertiary CH resonances of the ¹Pr groups. The spectrum is

Table 1 Selected bond lengths (Å) and angles (°) of **41** and **44–46** [20]

	41	44	45		46
Cr(1)–Cr(1a)	1.8351(4)	1.8160(5)	1.8077(7)	Cr(1)–Cr(2)	1.831(2)
Cr(1)–C(1)	2.131(1)	2.131(2)	2.136(2)	Cr(1)–C(1)	2.132(6)
				Cr(2)–C(31)	2.138(6)
Cr(1)–C(7a)	2.294(1)	2.311(2)	2.322(2)	Cr(1)–C(49)	2.307(6)
				Cr(2)–C(19)	2.294(6)
C(1)–Cr(1)–Cr(1a)	102.78(1)	102.25(4)	101.65(6)	Cr(1)–Cr(2)–Cr(31)	102.7(2)
				Cr(1)–Cr(2)–Cr(1)	102.3(2)
C(7)–Cr(1a)–Cr(1)	94.19(3)	95.37(4)	95.73(5)	C(19)–Cr(2)–Cr(1)	94.6(2)
				C(49)–Cr(1)–Cr(2)	94.3(2)
C(1)–Cr(1)–Cr(1a)–C(1a)	180.0	180.0	180.0	C(1)–Cr(1)–Cr(2)–C(31)	172.8

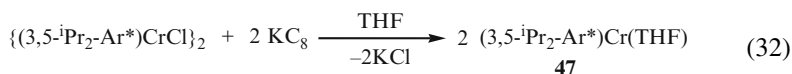
**Fig. 12** ^1H NMR spectrum of (4-MeO-Ar')CrCr(Ar'-4-OMe) (**44**) in C_7D_8 at -50°C (*denotes signals of solvent toluene) [20]

consistent with C_{2h} symmetry, indicating the presence of two inequivalent flanking C_6H_3 –2, 6- $i\text{Pr}_2$ substituents due to restricted rotation about the Cr–C(ipso) bond (Fig. 12). An unusual feature of the spectrum is the dramatically shielded signal of the *para* hydrogen atom of one of the flanking aryl rings. The signal for the corresponding *meta* hydrogens is also shifted to lower frequency. This observation is explained by the proximity of the respective hydrogens to a flanking aryl ring of the opposite terphenyl ligand, inducing a diamagnetic shift of these resonances. These signals may be assigned to the flanking ring closest to chromium. DFT calculations predict that on the model compounds (4-X- C_6H_4)CrCr(C_6H_4 –4-X) (X = H, SiMe₃, OMe, or F) have almost identical geometries in the gas phase and this is in agreement with the experimental results.

The related Ar'-4-CF₃ ligand, which has a strong electron-withdrawing group CF₃ on the *para* position of the central aryl ring, was also developed

and the reduction of $\{(4\text{-F}_3\text{C-Ar}')\text{CrCl}\}_2$ was carried out analogously to the synthesis of **41** with the aim of preparing the metal–metal bonded dimer $(4\text{-F}_3\text{C-Ar}')\text{CrCr}(\text{Ar}'\text{-4-CF}_3)$. Initially, the reaction mixture assumed a deep-red color typical for the other ArCrCrAr complexes; however, the color of the THF solution changed to purple in about half an hour, even with the exclusion of light, indicating decomposition. After workup, purple crystals $\{(4\text{-F}_3\text{C-Ar}')\text{Cr}(\mu\text{-F})(\text{THF})\}_2$ (**11**) were isolated. The structure of **11** was discussed in Sect. 3.2.

To assess the effects of increased steric congestion, initial attention was focused on the Ar^* ligand. This differs from Ar' in that it has $i\text{Pr}$ groups instead of hydrogens at the *para* positions of the flanking rings. Unfortunately, the attempted synthesis of $\text{Ar}^*\text{CrCrAr}^*$ has not led to characterizable products to date. Instead, the related ligand $3,5\text{-}i\text{Pr}_2\text{-Ar}^*$, which has two additional $i\text{Pr}$ groups at the *meta* positions of the central aryl ring, was investigated. This substitution improves the crystallization characteristics of its derivatives. In addition, hindered rotation of the flanking $\text{C}_6\text{H}_2\text{-2,4,6-}i\text{Pr}_3$ substituents further increases the steric protection of attached, reactive metal centers. Surprisingly, reduction of $\{3,5\text{-}i\text{Pr}_2\text{-Ar}^*\text{CrCl}\}_2$ with KC_8 in THF did not generate the deep red solution initially; instead, the blue solution became dark orange. After workup, orange crystals were obtained and were shown by X-ray crystallography to be the monomeric chromium(I) complex $3,5\text{-}i\text{Pr}_2\text{-Ar}^*\text{Cr}(\text{THF})$ (**47**) (Fig. 11) [20, 122]. The chromium is coordinated to the terphenyl ligand and a THF molecule. The coordination geometry is nearly linear with a wide C-Cr-O angle of $173.7(2)^\circ$. The Cr-C bond length of $2.087(3)\text{Å}$ is comparable to those observed in the quintuple bonded species. All other Cr-C contacts exceed 3.0Å and indicate no other Cr-C interactions. The effective magnetic moment of $5.95\mu_{\text{B}}$ indicates high-spin Cr(I) with a $3d^5$ electronic configuration as predicted by theoretical calculations. **47** represents the first example of a two coordinate chromium(I) complex.

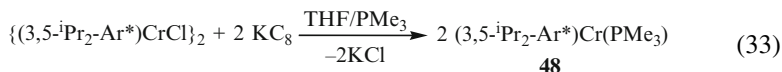


Disproportionation of **47** into a Cr(II)/Cr(0) complex was obtained when **47** was stored in toluene and its structure will be discussed in Sect. 7.4.

In short, by modifying the Ar' ligand on the *para* position with substituents of different electronic properties, further examples of the quintuple bond species $(4\text{-X-Ar}')\text{CrCr}(\text{Ar}'\text{-4-X})$ ($\text{X} = \text{H, MeO, SiMe}_3, \text{F}$) could be isolated. They all show similar and very short Cr-Cr distances and it is suggested that the changes induced in the Cr-Cr bond length by the different substituents X in the *para* position of the central aryl ring of the terphenyl ligand are probably a result of packing rather than electronic effects. In the case of $4\text{-CF}_3\text{-Ar}'$, the desired product is unstable. Although the steric bulk of the Ar' ligand is necessary for the stabilization of Cr-Cr bond, the extremely bulky ligand $3,5\text{-}i\text{Pr}_2\text{-Ar}^*$ creates sufficient steric pressure to prevent Cr-Cr bond formation and coordination to donor molecule such as THF or PMe_3 (see Sect. 7.3) is preferred to dimerization.

7.3 Reduction of the Terphenyl Metal Halides in the Presence of PMe_3

The reduction of $\{3, 5\text{-}^i\text{Pr}_2\text{-Ar}^*\text{CrCl}\}_2$ with KC_8 in THF in the presence of excess PMe_3 afforded the complex $3, 5\text{-}^i\text{Pr}_2\text{-Ar}^*\text{Cr}(\text{PMe}_3)$ (**48**) [20, 122], which was obtained as orange red crystals from hexanes. Like its THF-substituted analog **47**, the chromium is almost linearly coordinated to the terphenyl ligand and a PMe_3 molecule with a C-Cr-P angle of $167.39(4)^\circ$, which is similar to that observed in **47** (Fig. 13).



Following this report, the isolation of analogous Lewis base complexes of univalent later metals was attempted in order to obtain other two-coordinate $\text{M}(\text{I})$ species of the type Ar-M-L ($\text{L} = \text{donor molecule}$). No crystalline products were obtained with use of the $\text{Ar}^*\text{-}3, 5\text{-}^i\text{Pr}_2$ group. Instead, use of the less bulky ligand $3, 5\text{-}^i\text{Pr}_2\text{-Ar}'$ led to a series of halides, $\{3, 5\text{-}^i\text{Pr}_2\text{-Ar}'\text{MX}\}_2$ ($\text{M} = \text{Mn, Fe, or Co}$), which upon reduction with KC_8 in THF in the presence of excess PMe_3 afforded the iron and cobalt phosphine complexes $3, 5\text{-}^i\text{Pr}_2\text{-Ar}'\text{Fe}(\text{PMe}_3)$ (**49**) and $\text{Co}(\eta^3\text{-}\{1\text{-(H}_2\text{C)}_2\text{C-C}_6\text{H}_3\text{-}2\text{-(C}_6\text{H}_2\text{-}2, 4\text{-Pr}_2^i\text{-}5\text{-(C}_6\text{H}_3\text{-}2, 6\text{-}^i\text{Pr}_2)\text{-}3\text{-}^i\text{Pr}\})\text{PMe}_3)_3$ (**50**) as orange-red and orange crystals as shown in (34) and (35) [123].

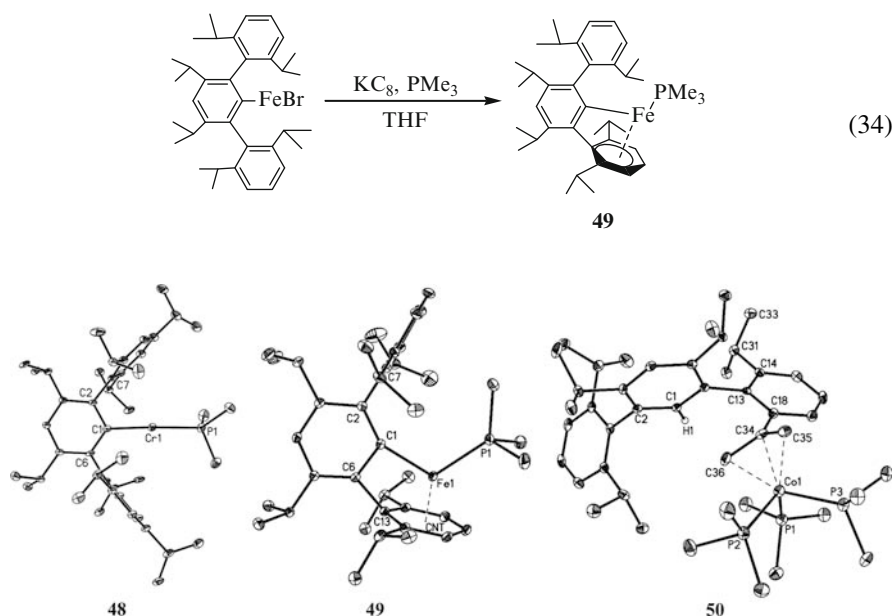
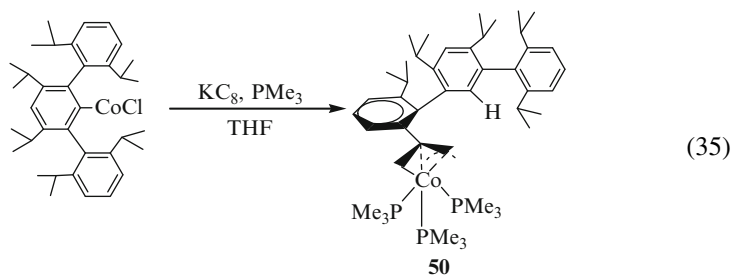


Fig. 13 Structures of **48–50** without H atoms (except C1-H in **50**) [122, 123]

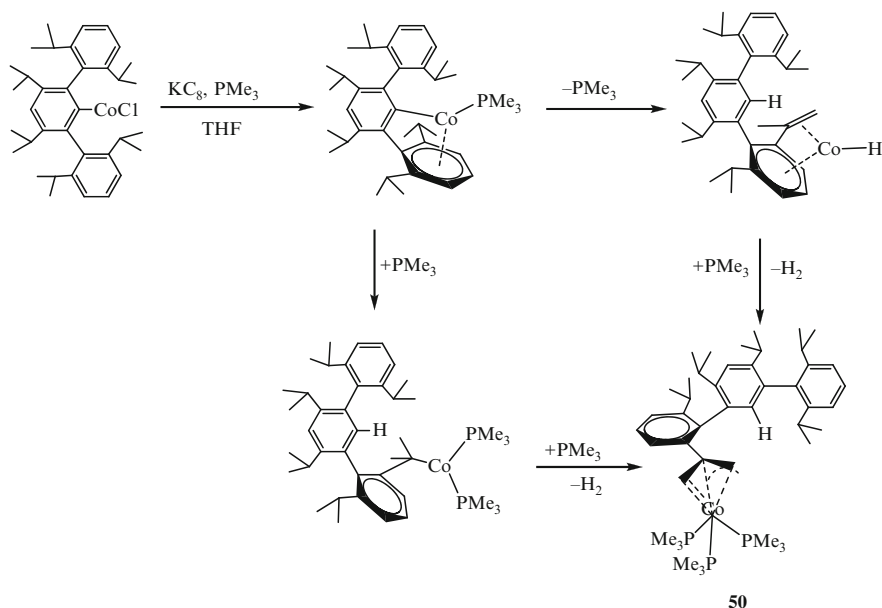


In **49**, the iron is coordinated to the *ipso* carbon of the aryl ligand and one PMe_3 molecule. Unlike the almost linear two-coordinate Cr(I) complex **48**, the iron in **49** has a strongly bent coordination geometry with a strong η^6 interaction with one of the flanking C_6H_3 -2, 6- Pr^i rings of the terphenyl ligand (Fig. 13). The Fe-centroid distance of 1.574(2) Å is similar to those in $\{\text{Fe}(\eta^6\text{-C}_{10}\text{H}_8)(1, 2\text{-bis}(\text{dicyclohexylphosphino})\text{ethane})\}$ (1.597(6) Å) [124] and in $\{(\text{C}_6\text{H}_{11}\text{-N}=\text{CH})_2(\eta^6\text{-C}_7\text{H}_8)\text{Fe}\}$ (1.542 Å) [125]. Because of the strong η^6 interaction with the flanking aryl ring, the terphenyl ligand exhibits a very distorted geometry, for example, at the *ipso*-carbon, the Fe(1)–C(1)–C(6) and Fe(1)–C(1)–C(2) angles differ by over 42° and the angles involving the flanking rings (C(1)–C(6)–C(13) $103.10(11)^\circ$, C(1)–C(2)–C(7) $121.56(12)^\circ$) are also very dissimilar. The Fe–P distance of 2.2509(5) Å lies in the range of 2.157 Å to 2.471 Å², observed in numerous iron phosphine complexes. The strong η^6 –arene interaction exhibited by **49** and other putatively low-coordinate late transition metal complexes is supported by calculations [66].

In sharp contrast to **49**, the reduction of $\{3, 5\text{-}^i\text{Pr}_2\text{-Ar}'\text{CoCl}\}_2$ under similar conditions did not afford a product analogous to either **49** or the linear structure of **48**; instead, the highly unusual conversion of the terphenyl group into an η^3 -allyl ligand was observed and the unexpected product **50** (Fig. 13) was isolated in low yield after the separation of 3, 5- $^i\text{Pr}_2\text{-Ar}'\text{-H}$. It is proposed that the formation of **50** involves two intermediates. The proposed mechanism is shown in Scheme 5.

The similarities of the reduction of $\{\text{Ar}'\text{MX}\}_2$ ($\text{M} = \text{Fe}$ or Co) in THF [63] and the reduction of $\{3, 5\text{-}^i\text{Pr}_2\text{-Ar}^*\text{MX}\}_2$ in aromatic solvents [93, 126] suggest the initial formation of the PMe_3 adduct, which is similar to **49** and has an 18-electron configuration. However, it has a geometry more strained than that of **49** owing to the smaller size of cobalt. The strain may lead to cleavage of the Co–C σ -bond of the PMe_3 complex with formation of an alkene/hydride intermediate via replacement of the $\eta^1\text{-PMe}_3$ ligand by the η^2 -alkene group and concomitant abstraction of two hydrogen atoms from an ^iPr group. Under the influence of excess PMe_3 , this intermediate could rearrange to give **50** with elimination of H_2 . This dehydrogenation of inert alkyl groups via remote C–H activation has been observed in $\text{Pd}(\text{OAc})_2$ -mediated systems [127]. A possible alternative mechanism involves the formation of the PMe_3 adduct initially. Under the influence of excess PMe_3 , the

² The Fe–P distance of iron center to PMe_3 molecule of 118 compounds from Cambridge database (version 5.29, February 2008).



Scheme 5 Proposed mechanism of formation of **50** [123]

cobalt center could move to the central carbon atom of the isopropyl group first. Upon complexation of a PMe_3 molecule and elimination of H_2 gas, **50** could be formed.

Similarly, reduction of the less crowded cobalt species $\{\text{Ar}'\text{CoCl}\}_2$ with KC_8 in the presence of excess PMe_3 afforded the related compound $\text{Co}(\eta^3\text{-}\{1\text{-(H}_2\text{C)}_2\text{C-C}_6\text{H}_3\text{-2-(C}_6\text{H}_4\text{-3-(C}_6\text{H}_3\text{-2, 6-Pr}^i\text{))}\text{-3-Pr}^i\text{}}\text{)})(\text{PMe}_3)_3$ (**51**); however, when the reduction was attempted with the significantly smaller $\text{Ar}^\#$ ligand, which has methyl instead of isopropyl groups on the flanking rings, a brown solution was obtained and no crystalline product was isolated. Complexes **50** and **51** were isolated in low but reproducible yields.

The structures of **50** and **51** are very similar. The cobalt is no longer bound to the *ipso* carbon of the central ring of the aryl ligand. Instead it has become coordinated to three-carbon atoms that were originally part of an isopropyl group from a flanking aryl ring. The coordination geometry at the central carbon of the allyl group becomes planar and the C—C distances lie in the range of 1.420(5)–1.437(2) Å, consistent with a C—C bond order near 1.5. These distances are slightly longer than those bonds in other Co-allyl complexes, such as $\{[(\text{CH}_3\text{O})_3\text{P}](\text{CO})_2\text{Co}\{(\text{CH}_2)_2\text{CCH}_2\}\}_2(\text{CO})$ (1.408 Å) [128]. The Co—C distances in **50** and **51** are in the range of 1.974(4) to 2.034(4) Å, which is also similar to that observed in the allyl complexes mentioned earlier and are within the range of Co—C distance of 1.911 to 2.11 Å in allyl cobalt complexes in general³. The three Co—P distances are very similar with

³ The Co—C distance of Co-allyl compounds from Cambridge database (version 5.29, February 2008).

an average Co–P value of 2.156(4) Å, which is close to those in the related complex [Co(PhCCC₅H₁₁)(PMe₃)₃]⁺[B(Ph)₄][−] (2.161(2) Å average) [129].

In short, reduction of {ArMX}₂ (M = Cr, Fe, or Co) with KC₈ in THF in the presence of excess PMe₃, afforded M(I) complexes with very different geometries from the original chromium species **48**, which has linear coordination. In contrast, the iron species **49** has a very bent geometry with a very strong Fe–η⁶ interaction to a flanking aryl ring. In sharp contrast, the η³–allyl complexes **50** and **51** were formed by dehydrogenation of an isopropyl group of the flanking ring.

7.4 Arene Complexed Terphenyl Metal Species

When toluene was added to the crude product obtained from the reduction of {(3, 5-*i*Pr₂–Ar*)CrCl}₂ with KC₈ at room temperature, an immediate color change was observed and the mixed-valent dinuclear complex [(3, 5-*i*Pr₂–Ar*)Cr(η³:η⁶-CH₂Ph)Cr(Ar*–1-H-3, 5-*i*Pr₂)] (**52**) was isolated [20]. Although the structural arrangement of **52** is superficially similar to that of {Cr[HC(CMeNDipp)]₂}₂ (η⁶:η⁶-PhCH₃) [130], a striking difference is that in **52**, a C–H bond of toluene has been activated and the proton has been transferred to an Ar*–1-H-3, 5-*i*Pr₂ ligand. Thus, the structure contains an *anionic* (CH₂Ph)[−] group whose bridging coordination mode resembles that in the Cr(I)/Cr(III) complex [Cp*Cr(η¹-CH₂Ph)(η³:η⁶-CH₂Ph)CrCp*] (Cp* = C₅Me₅) which was formed by thermal rearrangement of [Cp*Cr(η¹-CH₂Ph)(η³:η⁶-CH₂Ph)CrCp*] [131]. However, in **52** one chromium, Cr(1), is bonded to two anionic ligands [(3, 5-*i*Pr₂–Ar*)[−] and (CH₂Ph)[−]] and is assigned the +2 oxidation state. In contrast, Cr(2), which closely resembles the sandwich structure of (bis)benzene chromium and related compounds [132], is assigned the zero oxidation state. The reaction may thus be regarded as a valence disproportionation of the Cr(I) complex (3, 5-*i*Pr₂–Ar*)Cr(THF) (**47**). The observation of a deprotonated CH₂ group in the benzyl anion is supported by the relatively short C–C distance of 1.459(4) Å, and by the observation of two hydrogen atoms bound to C(7) in the X-ray structure. The strong interaction between Cr(1) and the benzylic carbon atom, C(7), is reflected in the bending of C(7) away from the plane of the phenyl ring [(C(7)–C(1)–centroid) = 169.3°]. The benzyl ligand is bound in an allylic fashion with bonding parameters similar to [Cp*Cr(η¹-CH₂Ph)(η³:η⁶-CH₂Ph)CrCp*] [131], and {Cp*Cr(C₆F₅)(η³-CH₂Ph)} [133], which appear to be the only other structurally characterized complexes of chromium with an η³-coordinated benzyl ligand. The protonation of the second terphenyl ligand was confirmed by the observation of a hydrogen atom bound to the *ipso* carbon of its central aryl ring. The magnetic properties of **52** are consistent with the presence of both Cr(0) and Cr(II) as is indicated by the structural and spectroscopic results. It was suggested that the first step in the formation of **52** very likely involves the interaction of **47**, present in the reaction mixture, with toluene. Coordinative unsaturation at a chromium center may then induce the migration of a methyl proton from toluene to one of the (3, 5-*i*Pr₂–Ar*)[−] ligands.

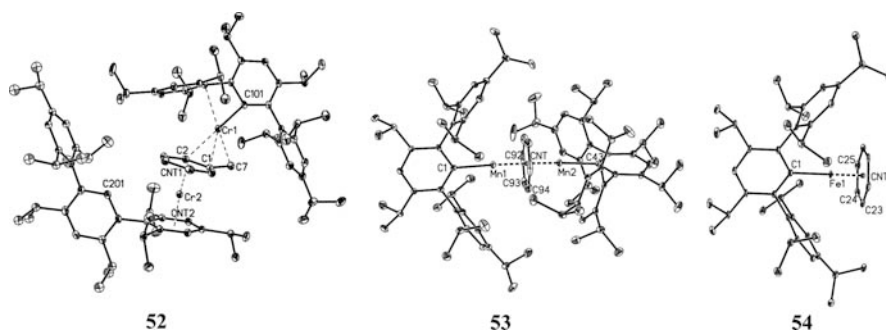
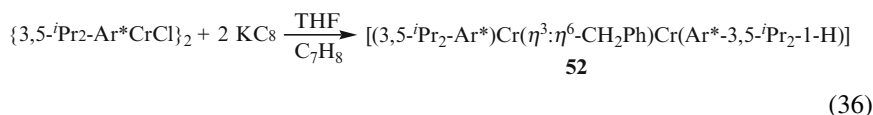
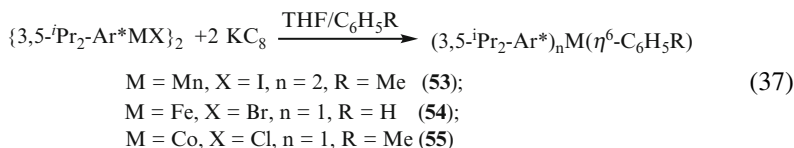


Fig. 14 Structures of **52**–**54** without H atoms [20, 93]

However, other possible mechanisms cannot be excluded definitively at present due to the difficulty in isolating the labile intermediates in this reaction (Fig. 14).



Although the attempted preparation of the $3,5\text{-}i\text{Pr}_2\text{-Ar}^*\text{M(L)}$ ($\text{L} = \text{THF}$ or PMe_3 , $\text{M} = \text{Mn}$, Fe , or Co) failed to produce characterizable products, the arene stabilized complexes $\{3,5\text{-}i\text{Pr}_2\text{-Ar}^*\text{Mn}\}_2(\eta^6\text{-C}_7\text{H}_8)$ (**53**) [93], $3,5\text{-}i\text{Pr}_2\text{-Ar}^*\text{Fe}(\eta^6\text{-C}_6\text{H}_6)$ (**54**) [93], and $3,5\text{-}i\text{Pr}_2\text{-Ar}^*\text{Co}(\eta^6\text{-C}_7\text{H}_8)$ (**55**) [126] were easily obtained upon the addition of C_6H_6 or toluene.



Complex **53** is a rare example of an inverted-sandwich complex. The two $3,5\text{-}i\text{Pr}_2\text{-Ar}^*\text{Mn}$ moieties are bridged by a toluene molecule with Mn–centroid distances of 1.7815(12) and 1.7798(12) Å and a Mn–centroid–Mn angle of 178°. The Mn–centroid distances are longer than the usual range found in complexes having η^6 -coordination to arene rings⁴, due probably to the bridging nature of the interacting toluene in **53**. In agreement with the long Mn–centroid distances, the average C–C bond length within the bridging toluenes is essentially the same as it is

⁴ The Mn–centroid (benzene or toluene) of 79 manganese complexes in the Cambridge Crystal Structure Database (Version 5.28, August 2006) range from 1.546 to 1.765 Å.

in the uncomplexed molecule [134]. In **53**, each manganese is present in a highly distorted coordination environment as Mn(I) with a nominal $3d^6 t_2^4 e^2$ electronic ground state, and $S = 2$. Magnetic studies showed that the effective magnetic moment is $5.17 \mu_B$ per manganese(I) ion, which is in agreement with $5.2 \mu_B$ expected for two d^6 Mn(I) centers with no Mn–Mn bonding or any magnetic exchange.

In contrast to **53**, reduction of $\{3, 5\text{-}^i\text{Pr}_2\text{-Ar}^*\text{FeCl}\}_2$ in the presence of benzene afforded the orange half-sandwich complex **54**. The iron is coordinated to the *ipso* carbon of the terphenyl ligand and a benzene in an η^6 fashion. The C(1)–Fe–centroid is strictly linear and the Fe(1)–centroid distance of $1.6427(13) \text{ \AA}$ is similar to the Fe–centroid distance of $1.6245(8) \text{ \AA}$ in the related β -diketiminato Fe(I) complex $[\{(C_6H_3-2, 6\text{-Pr}^i_2)NC(Me)\}_2CH]Fe(\eta^6\text{-C}_6\text{H}_6)$ [94], but is shorter than the $1.733(2)$ and $1.763(2) \text{ \AA}$ in $\text{Ar}'\text{FeFeAr}'$ (**42**). Magnetic studies showed that the Fe(I) center adopts a high-spin configuration with three unpaired electrons.

Similar to **54**, reduction of $\{3, 5\text{-}^i\text{Pr}_2\text{-Ar}^*\text{CoCl}\}_2$ in toluene afforded the green half-sandwich complex **55**, which is related to that of $(HC\{C(Me)NC_6H_3-2, 6\text{-Me}_2\}_2)Co(\eta^6\text{-C}_7\text{H}_8)$ [135]. The C(1)–Co–centroid angle is 167.6° and the Co–centroid distance is $1.659(1) \text{ \AA}$, which is comparable to the corresponding distance of 1.602 \AA in the Co(I) complex $Co(PMe_3)_2(BPh_4)$ [136], where cobalt interacts with a phenyl ring in an η^6 fashion. The ^1H NMR spectrum of **55** exhibits paramagnetically shifted resonances between 20 and -70 ppm, suggesting a high-spin d^8 ($S = 1$) electronic configuration for the cobalt(I) center, which was further confirmed by the study of its magnetic properties.

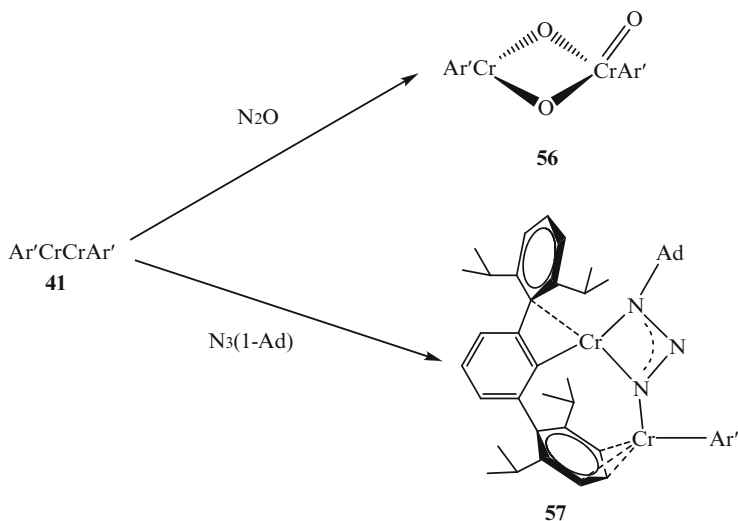
8 Reactivity Studies of Terphenyl Metal(I) Species

8.1 Reactivity of $\text{Ar}'\text{CrCrAr}'$

Although $\text{Ar}'\text{CrCrAr}'$ (**41**) is extremely sensitive to air and moisture, it shows no reactivity toward H_2 , elemental S_8 and PMe_3 . This may be due to the steric effects of the bulky terphenyl ligands. However, it reacts with $t\text{BuNC}$ and CyNC ($\text{Cy} = \text{C}_6\text{H}_{11}$) to afford red brown solutions; however, no crystals have been isolated so far.

Reactions of **41** with the cumulenes N_2O (excess) and $\text{N}_3(1\text{-Ad})$ ($\text{Ad} = \text{adamantyl}$) led to cleavage of the Cr–Cr bond and the formation of the products of $\text{Ar}'\text{Cr}(\mu\text{-O})_2\text{Cr}(O)\text{Ar}'$ (**56**) and $\text{Ar}'\text{Cr}(\mu_2\text{-}\eta^1, \eta^3\text{-N}_3(1\text{-Ad}))\text{CrAr}'$ (**57**) (Scheme 6) [137].

Exposure of **41** to excess N_2O afforded **56**, which was obtained as dark green crystals from hexanes. The two CrAr' units are bridged by two oxygens and Cr(2) is also bound to a terminal oxygen, whereas Cr(1) interacts with the *ipso* carbon of a flanking $\text{-C}_6\text{H}_3 - 2, 6\text{-}^i\text{Pr}_2$ ring (Cr(1)–C(13) $2.358(4) \text{ \AA}$) of its terphenyl ligand. Thus, the molecule contains chromium in the +3 (Cr(1)) and +5 (Cr(2)) oxidation states. The Cr(1) atom has distorted trigonal pyramidal coordination, whereas Cr(2) has a distorted tetrahedral geometry. The difference in metal



Scheme 6 Preparation of **56** and **57** [137]

oxidation state is discernible in the bridging Cr–O distances, which are on average more than 0.03 Å longer for Cr(1) than for Cr(2). Unlike the planar Cr₂O₂ cores observed in the Cr(III) complex {Cr(NRR')₂(μ-O)}₂ (R = 3, 5-Me₂-C₆H₃, R' = adamantyl) [138] or the symmetric Cr(V) complex {(η⁵-C₅H₅)Cr(O)(μ-O)}₂ [139], the Cr₂O₂ moiety in **56** (Cr–Cr = 2.5252(8) Å) has a fold angle of 163.7(4)°, which is similar to the 159.9° in the dianionic Cr(V) complex {OCr(PFP)(μ-O)}₂²⁻ (PFP = perfluoropinacolate) [140]. The Cr(2)–O(terminal) distance of 1.575(3) Å is considerably shorter than the Cr–O (bridging) distances and indicates strong multiple bonding. It is also somewhat shorter than those in Cr(V) complexes, such as {(η⁵-C₅H₅)Cr(O)(μ-O)}₂ (1.594(3) Å) [139] and HC[C(Me)N(Dipp)]₂Cr(O)₂ (1.600(4) Å) [141]. The magnetic properties indicate that both the distorted tetrahedral trivalent Cr(2) and the pentavalent Cr(1) have the expected one unpaired electron with *S* = 1/2 for each ion; there is little if any intramolecular exchange and the observed effective magnetic moment is 1.97 μ_B per chromium.

The reaction of **41** with one equivalent of N₃(1-Ad) afforded **57** (Fig. 15). Unusually, no N₂ was eliminated [130, 142]. Instead, there was insertion of the azido group between the two chromiums with cleavage of the Cr–Cr quintuple bond to yield **57**. The Cr(1) atom is coordinated to two nitrogens from the azido group and to a terminal aryl ligand through the central *ipso* carbon. There is also an interaction with the *ipso* carbon of the flanking –C₆H₃–2, 6-*i*Pr₂ ring. The C(61)–Cr(1)–C(1)–N(1)–N(2)–N(3)–Cr(2)–C(31) atoms are coplanar so that the metal has a very distorted square planar geometry. The Cr(2) atom has an unusual heteroleptic, *quasi*-two-coordinate geometry. The angle in the N(3)–Cr(2)–C(31) unit is 101.49(8)°, which is narrower than the 112.3(3)° and 110.8(1)° angles in the homoleptic *quasi*-two-coordinate Cr(II) amido complexes Cr{NMesBMes₂}₂ [143] and Cr{NPhBMes₂}₂ [61]. The greater distortion is probably caused by the weak interaction of Cr(2)

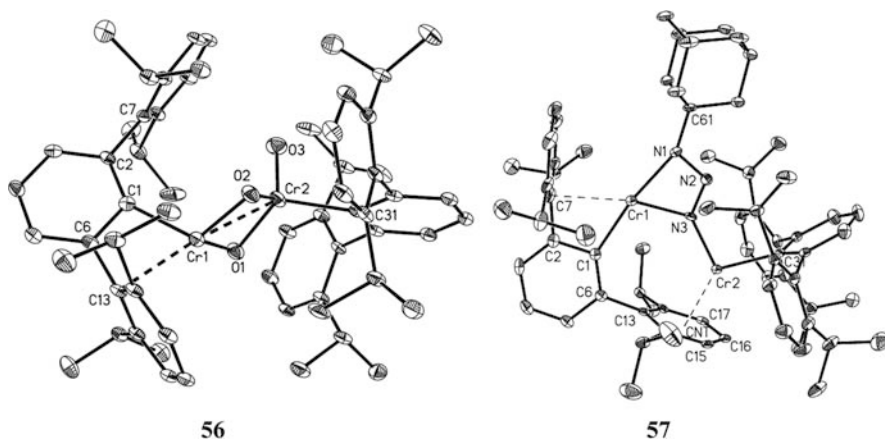


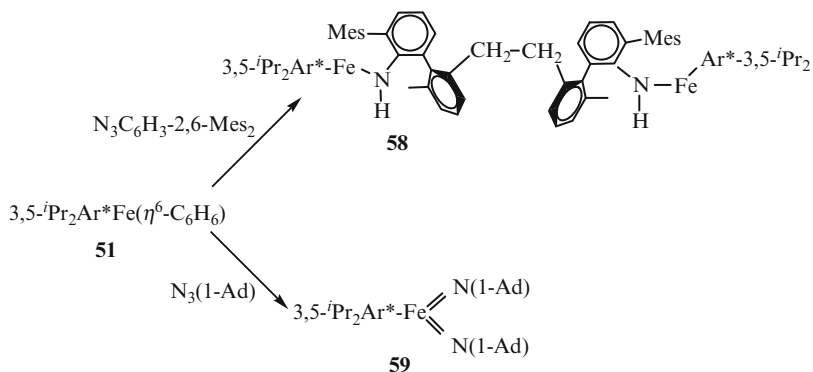
Fig. 15 Structures of **56** and **57** without H atoms [138]

with a flanking $-C_6H_3-2,6-Pr_2^i$ ring from the Ar' group attached to Cr(1). The interaction primarily involves C(15) at 2.477(2) Å, C(16) at 2.358(2) Å, and C(17) at 2.453(2) Å. Within the bridging azide unit, the N–N distances of 1.329(3) and 1.305(3) Å, and the N(1)–N(2)–N(3) angle of 109.8(2)° are similar to those in other triazene complexes⁵. Thus, the 1-Ad–N₃–Cr(2)– Ar' moiety may be viewed as a bidentate triazene anionic ligand for Cr(1). As a result, the oxidation state of each chromium ion is +2. The magnetic properties indicate that each of the 3d⁴ chromium(II) ions has an $S = 1$ ground state. This unexpected ground state presumably results from the highly distorted coordination environment of each ion. A fit of the results indicates the presence of weak intramolecular ferromagnetic coupling between the two chromium(II) ions with $J = 7.8(7) \text{ cm}^{-1}$ and an average g -value of 2.40(2). The reaction of **41** with one equivalent of iodine in hexanes could readily afford the iodide-bridged complex $\{Ar'Cr(\mu-I)\}_2$ (**12**) (see Sect. 3.2) in which the chromium ions in $Ar'CrCrAr'$ are oxidized to Cr(III) and the quintuple bond is cleaved.

8.2 Reactivity of 3,5- i Pr₂– Ar^* Fe(C₆H₆)

A variety of reagents were used to investigate the reactivity of 3,5- i Pr₂– Ar^* Fe(C₆H₆) (**54**) (Scheme 7).

⁵ The N–N distances are typically 1.26 to 1.35 Å and the N–N–N angles are typically 99.1 to 111.9° in the 54 triazene complexes reported in the Cambridge Crystallographic Database (version 5.29, February 2008) in which one metal is coordinated to two nitrogen atoms of the triazene ligand.



Scheme 7 Preparation of **58** and **59** [144]

With the intention to synthesize a two-coordinate Fe(III) imide of formula $3,5\text{-Pr}^i\text{Ar}^*\text{-Fe}=\text{N}(\text{C}_6\text{H}_3\text{-2,6-Mes}_2)$, the reaction of **54** with $\text{Ar}^\# \text{N}_3$ was performed, but complex **58** [144] was the only product isolated (46% yield) from the reaction mixture. Complex **58** is dimerized through an intermolecular C–C bond involving ortho methyl groups from the flanking mesityl rings. Such behavior is similar to that of the reported β -diketiminato $[\text{HC}\{\text{C}(\text{Me})\text{N}(\text{C}_6\text{H}_3\text{-2,6-}^i\text{Pr}_2)\}_2\text{FeN}(1\text{-Ad})]$ which, in the presence of a pyridine donor, undergoes intramolecular hydrogen abstraction from the ortho isopropyl group to afford an iron amide [145]. The formation of **58** also resembles the behavior of the unstable Co(III) terminal imido complexes $\{\text{HB}(\text{pyrazolyl-3-R-5-Me})_3\}\text{CoN}(\text{SiMe}_3)$ ($\text{R} = ^i\text{Pr}$ or ^tBu) which rearranges by hydrogen atom abstraction from a ^iPr or ^tBu group to form, in the case of the ^iPr -substituted species, a product dimerized through a C–C bond [146]. In a similar way, the first step in the formation of **58** may be hydrogen abstraction from an *ortho*-methyl group of a flanking mesityl ring of the imido group $-\text{C}_6\text{H}_3\text{-2,6-Mes}_2$ by the nitrogen center. The radical thus generated may dimerize intermolecularly rather than interact with the metal which may be sterically less favorable. The iron(II) centers in **58** have a bent ($\text{N}(1)\text{-Fe}(1)\text{-C}(1) = 138.91(8)^\circ$) two-coordinate geometry, the bending is accompanied with a moderately close interaction ($\text{Fe}\text{-C}(49) = 2.8666(2) \text{ \AA}$) with the ipso-carbon of one of the flanking mesityl rings. The magnetic properties indicated the μ_{eff} of $5.29 \mu_{\text{B}}$ per Fe atom, which is consistent with a high-spin d^6 electron configuration.

Reaction of the orange solution of **54** with $\text{N}_3(1\text{-Ad})$ in hexanes afforded dark red crystals of $3,5\text{-}^i\text{Pr}_2\text{-Ar}^*\text{Fe}(\text{N-Ad})_2$ (**59**) [144] (Fig. 16). It is noteworthy that **59** was the only isolated product when variable molar ratios of $\text{N}_3(1\text{-Ad})$ to **54** were attempted. It is notable not only because it is the first stable Fe(V) imide, but it is also a very rare example of a well-characterized Fe(V) molecular species of any kind [147]. The iron has a planar three-coordinate geometry with interligand angles that have a maximum deviation of only ca. 1.4° from the idealized 120° trigonal planar value. The coordination planes at the imido nitrogens are almost coincident (maximum deviation: 7.2°) with the central $\text{C}(1)\text{Fe}(1)\text{N}(1)\text{N}(2)$ plane.

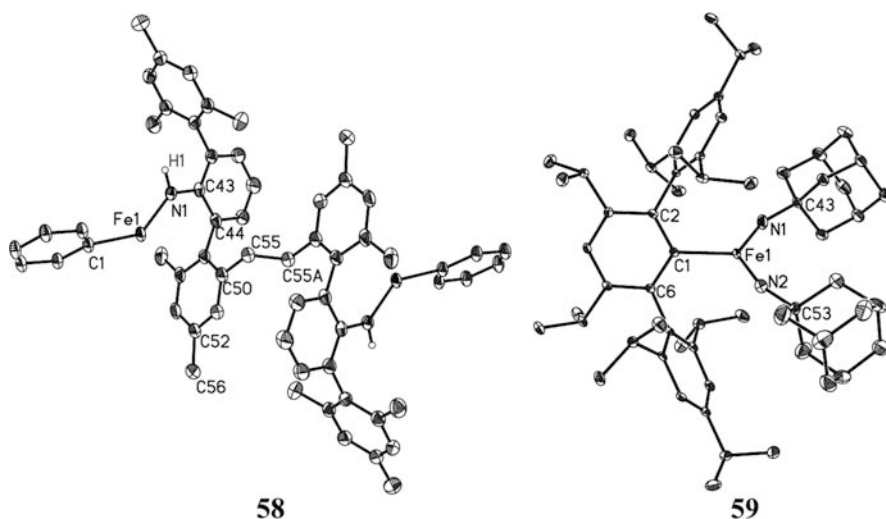


Fig. 16 Structures of **58** and **59** without H atoms (except N–H) [144]

However, the plane of the central aryl ring of the terphenyl ligand subtends an angle of ca. 55° with respect to the metal plane. The Fe–C distance is marginally shorter than that in **59**, whereas the iron nitrogen bond lengths, Fe(1)–N(1) = 1.642(2) or Fe(1)–N(2) = 1.618(2) Å, are considerably shorter than the single Fe–N bond (1.909(2) Å) in **58**. The shorter Fe–N bond length is associated with the wider Fe–N–C bending angle. The shortest Fe–N bond length in **59** is 1.618(2) Å and this distance approaches the ca. 1.61 Å recently reported for the Fe(V) nitride [*trans*–(cyclam–OAc)FeN]⁺ [148], although it is ca. 0.05 Å longer than the Fe–N bond length of 1.57 Å measured by Wieghardt and coworkers EXAFS in the unique Fe(VI) nitride species [(Me₃–cyclam–OAc)FeN]²⁺ [149, 150] and considerably longer than the ca. 1.51–1.55 Å Fe–N distance determined for in Fe(IV) nitrides by Meyer, Peters, and their coworkers [151, 152]. Magnetic studies of **59** afford a μ_{eff} value, which decreases linearly from 2.74 μ_{B} at 8 K to 2.43 μ_{B} at 320 K. A plot of $1/\chi_{\text{M}}$ versus temperature is not strictly linear but the data indicate a low-spin d^3 configuration. The $S = 1/2$ ground state is consistent with a previous finding for [*trans*–(cyclam–OAc)FeN]⁺ which is also low spin [148].

The reaction of **54** with (Me₃Si)₂NBr afforded the bromide-bridged complex {3, 5-*i*Pr₂Ar*Fe(μ-Br)}₂ (**21**) [41]. This is in sharp contrast to reaction of the M(II) amido complexes M{N(SiMe₃)₂}₂ (M = Mn, Fe) with (Me₃Si)₂NBr, which led to the isolation of the M(III) complexes M{N(SiMe₃)₂}₃ [153]. The structure of **24** (See Sect. 3.2) resembles the structure of its manganese analog {3, 5-*i*Pr₂Ar*Mn(μ-I)}₂ (**18**). The Fe₂Br₂ core is planar and has torsion angles of ca. 48.6 and 44.6° to the two central aryl rings of the terphenyl ligands. The Fe–Fe separation of ca. 3.289 Å is similar to the Fe(III) complex {Fe(μ-Br)[(C₆H₂–2, 4, 6-Me₃)NSiMe₂]₂O}₂ (3.232(3) Å) [154]. The Fe–Br distances are in the range

of 2.403(5) to 2.477(4) Å, which is comparable to those in the Fe(II) complex {1, 3, 4-*t*Bu₃C₅H₂Fe(μ-Br)}₂ (2.4746(12) to 2.5110(13) Å) [155].

Complex **54** does not react with PhSSPh at room temperature; however, heating the toluene solution to 80°C overnight led to cleavage of the S–S single bond and formation of the heteroleptic, dimeric, aryl arylthiolato complex {3, 5-*i*Pr₂Ar*Fe(μ-SPh)}₂ (**60**) [41], which is dimerized through two bridging phenylthiolato groups. Each iron displays a distorted trigonal planar geometry and the Fe₂S₂ core is planar. The phenyl substituents on the thiolate sulfur atoms are oriented above and below from the Fe₂S₂ plane. The C(85)–S(1) and C(92)–S(2) bonds subtend angles of ca. 50.2 and 27.3° with respect to the Fe₂S₂ core. The different orientations of the phenyl substituents on the thiolate sulfur ligand may be due to the steric effect of the bulky terphenyl ligand. The Fe–Fe separation is 3.481(3) Å and the Fe–S distances are very similar with an average of 2.3844(8) Å, which is comparable to the Fe–S bridging distances in other Fe(II) complexes [156–159].

The reaction of **54** with N₂O in hexanes led to a dramatic color change from orange to deep red even at –78°C (Fig. 17). Deep red plates of {3, 5-*i*Pr₂Ar*OFe(μ-O)}₂ (**61**) [41] were obtained in low yield from hexanes. X-ray crystallography revealed that there is a planar Fe₂O₂ core in which two oxygen atoms bridge two 3, 5-*i*Pr₂Ar*OFe moieties. The latter shows that an oxygen has also been inserted into the Fe–C(*ipso*) bond. In addition, each iron interacts with one of the flanking C₆H₂–2, 4, 6-*i*Pr₃ rings (Fe(1)–C(14) 2.458(3) Å). The coordination environment at iron can thus be viewed as distorted tetrahedral. Structurally characterized complexes bearing an Fe₂(μ-O)₂ core, such as [Fe₂(μ-O)₂(6-Me₃-TPA)₂](ClO₄)₂, [160, 161] [Fe₂(μ-O)₂(6-Et₃-TPA)₂](ClO₄)₃ [162], and [Fe₂(μ-O)₂(6-(NH₂)₃-TPA)₂](ClO₄)₂ [163], are stabilized by multidentate neutral ligands tris(2-pyridylmethyl)amine (abbreviated as TPA) and are usually in the ionic form, which is different from **61**. The Fe–Fe distance, 2.4818(7) Å, in **61** is significantly shorter than those observed in Fe(III) complexes [Me₃-TPA)₂](ClO₄)₂(2.714(2) Å) [160] and [Fe₂(μ-O)₂(6-(NH₂)₃-TPA)₂](ClO₄)₂ (2.706(3) Å) [163], or even the Fe(III)/

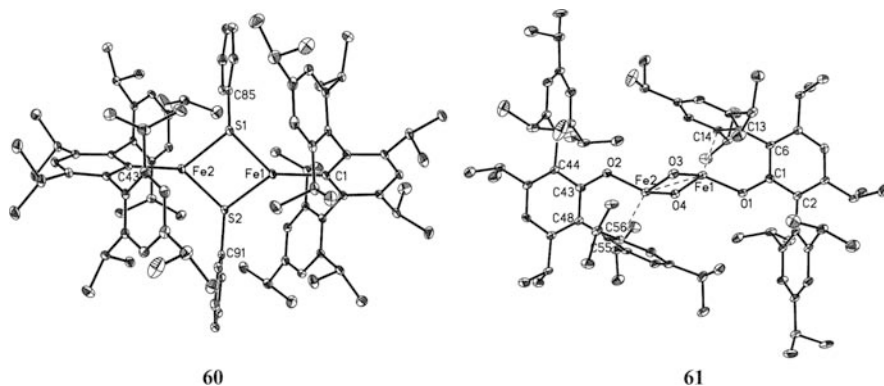


Fig. 17 Structures of **60** and **61** without H atoms [41]

Fe(IV) complex $[\text{Fe}_2(\mu\text{-O})_2(6\text{-Et}_3\text{-TPA})_2](\text{ClO}_4)_3(2.683(1)\text{ \AA})$ [162]. We attribute this to the lower coordination number of the Fe centers in **61**. The Fe– μ –O distances are quite similar and are in the range of 1.818(2) to 1.829(2) Å, which is comparable to the normally observed values for Fe(III)– μ –O distances (range 1.73 – 1.83 Å) [164]. The Fe–O(terminal) distance of 1.869(2) Å is longer than the Fe–O terminal distance of 1.822(5) Å in $\{\text{Fe}(\text{OMes}^*)(\mu\text{-OMes}^*)\}_2$ [165], and the lengthening is probably due to the steric effect and the interaction of the irons with the flanking rings in **61**.

8.3 Reactivity Studies of 3, 5-*i*Pr₂–Ar*Co(η^6 -C₇H₈)

The cobalt species 3, 5-*i*Pr₂–Ar*Co(η^6 -C₇H₈) (**55**) also yielded interesting products when reacted with small molecules such as CO and NO [126]. The reaction of **55** with excess CO proceeded smoothly and within minutes produced the new acyl/carbonyl complex 3, 5-*i*Pr₂–Ar*C(O)Co(CO) (**62**) as red crystals. The X-ray structure (Fig. 18) showed that the cobalt was coordinated to an acyl group, which was formed by insertion of a CO molecule into the Co–C(ipso) bond, as well to a terminal carbonyl group. In addition, the cobalt has a strong η^6 -interaction with one of the flanking aryl rings with a Co–centroid distance of 1.599(2) Å. The Co–C(1) and C(1)–O(1) distances are 1.739(5) and 1.162(5) Å, respectively. These are similar to those in $\{\text{PhB}(\text{CH}_2\text{PPh}_2)_3\}\text{Co}(\text{CO})_2$ (Co–C = 1.729(5) and 1.744(5) Å; C–O = 1.170(5) and 1.140(5) Å) [166]. The relatively short Co–C and C(1)–O(1) distances indicate strong back-bonding between the cobalt and the terminal carbonyl [167], which is consistent with the CO stretching band observed at 1965 cm⁻¹. Complex **62** has an 18-valence electron configuration and it is further confirmed by ¹H NMR spectroscopy, which shows no broadening or shifting of the signals. The possible mechanism of the formation of **62** may involve carbonyl coordination with elimination of toluene, followed by migratory insertion of a carbonyl into the Co–C(aryl) bond.

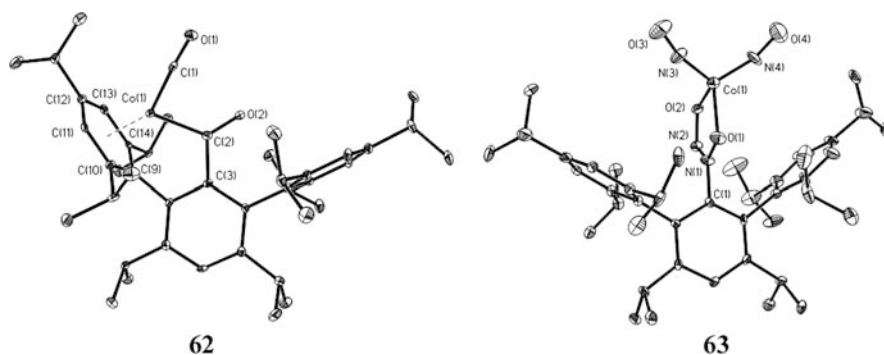


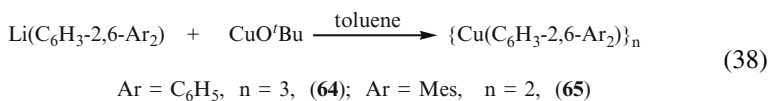
Fig. 18 Structures of **62** and **63** without H atoms [126]

The reaction of **55** with excess NO in hexanes afforded reddish-brown crystal of 3, 5-*i*Pr₂-Ar**N*(NO)OC_o(NO)₂ (**63**) in low yield. In **63**, the metal center displays a distorted tetrahedral geometry with coordination to two terminal NO ligands through the nitrogen atoms and to a bidentate [3, 5-*i*Pr₂-Ar**N*(NO)O]⁻ ligand, which was formed by insertion of NO into the Co–C σ-bond with concomitant NO coupling and N–N bond formation which resembles that of Cupferron [PhN(NO)O]NH₄ [168–170]. Such double NO insertion is rare for late transition metals [171], but is more common in early transition metal alkyl or aryl complexes, such as (η⁵-C₅H₅)₂Zr(CH₂Ph)₂ [172] and WMe₆ [173]. The large Co–N–O (terminal NO) angles of 164.37(11) and 159.8(11)° indicate the terminal NO ligands are three-electron donors, which is consistent with the N–O bands at 1660 and 1720 cm⁻¹ in IR. Thus, **63** has an 18-electron configuration and is diamagnetic, which was further confirmed by ¹H NMR study. In summary, **55** readily undergoes addition/migratory insertion reactions with CO or double insertion and N–N coupling reaction with NO.

9 Terphenyl Derivatives of Group 11 Elements

Organocopper reagents are of major importance for C–C bond formation in organic synthesis [174–177]. Thus, bulky terphenyl derivatives of Cu(I) are of significant interest. Many of the Cu(I) derivatives of terphenyls have come from the group of Niemeyer.

The reaction of the terphenyl lithium salts with CuO^{*t*}Bu in a 1:1 ratio led to the complexes {Cu(C₆H₃-2, 6-Ph₂)₃} (**64**) and {CuAr[#]}₂ (**65**) [178].



Complex **64** is a trimer (Fig. 19), in which two terphenyl ligands bridge two coppers via their *ipso* carbons of the central rings and the third terphenyl ligand bridges two coppers via its *ipso* carbon of the central ring and one of the flanking aryl rings by an η²-π interaction. The Cu–C(bridging) distances range from 1.989(3) to 2.085(3) Å, which is significantly longer than the Cu–C(terminal) distance of 1.924(3) Å. The Cu–C distances within the Cu–η²-π interaction are 2.158(3) and 2.232(4) Å. The angles involving two-coordinate coppers are almost linear (170.8 and 171.3°). In contrast, with the bulkier terphenyl ligand Ar[#], which has mesityl groups in the flanking positions, a dimeric complex **65** was obtained. In **65**, each copper atom is coordinated to the *ipso* carbon of the terphenyl ligand and has η²-π interaction with flanking aryl ring of the terphenyl ligand attached to the other metal center. The Cu–C distances in **65** are very similar to those involving Cu(3) in **64**.

The tetranuclear copper derivative {(Ar[#]Cu)₂(CuI)(CuO^{*t*}Bu)}₂ (**66**) [179] was obtained as a by-product of the synthesis of **65**. The core structure of **66** is an

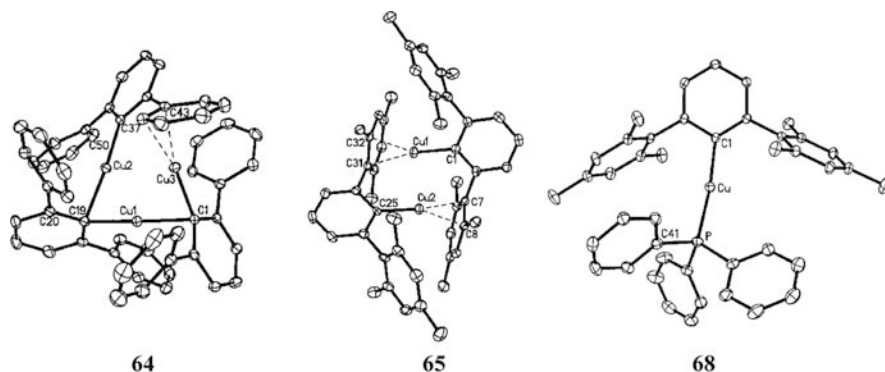
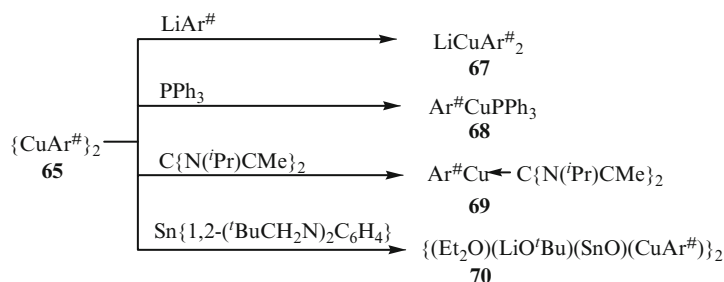


Fig. 19 Structures of **64**, **65**, and **68** without H atoms [178]

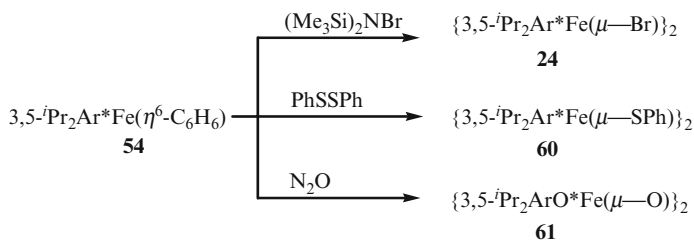


Scheme 8 Reactions of **65**

eight-membered C₂Cu₄OI ring, in which the four Cu atoms are bridged by two terphenyl ligands, an O^{*t*}Bu ligand, and an iodide. The Cu–Cu distances bridged by terphenyls are 2.3761(7) and 2.3766(7) Å, which are ca. 0.4 Å shorter than the bridging distances of 2.7227(8) and 2.8578(8) Å observed for iodide and oxygen.

Reactions of **65** with LiAr[#] and various donor molecules were also carried out (Scheme 8). Complex **65** reacted with a further equivalent of LiAr[#] to afford the lithium cuprate complex LiCuAr[#]₂ (**67**) [178], which was the first example of a neutral monomeric cuprate with the simple LiCuR₂ formula. In **67**, the Cu atom is coordinated to the two terphenyl ligands via ipso carbons and has a C–Cu–C angle of 171.1(2)°. The lithium ion is stabilized by η¹ coordination of the ipso carbon of one terphenyl ligand and η⁶ interaction with a flanking ring of the other terphenyl ligand. The reaction of LiAr[#] with CuO^{*t*}Bu in a 2:1 ratio, also afforded **67**.

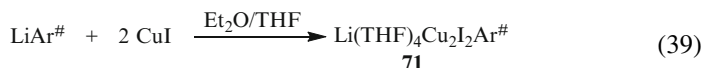
Reaction of **65** with PPh₃ and C{N(*i*Pr)CMe}₂ afforded the complexes Ar[#]CuPPh₃ (**68**) [180] and Ar[#]Cu←C{N(*i*Pr)CMe}₂ (**69**) [180]. Complexes **68** and **69** have two-coordinate coppers with wide C–Cu–E (E = P or C) angles of 168.82(8) and 178.23(11)°, respectively. The Cu–C(ipso) distances in **68** and **69** are very similar (Scheme 9). The Cu–P distance is 2.1891(11) Å in **68**. In **69**, the Cu–C(32) distance is 1.902(3) Å, which is similar to the Cu–C(ipso) distance of 1.910(2) Å.



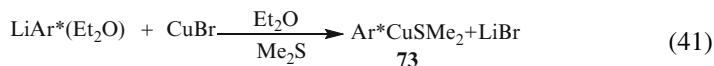
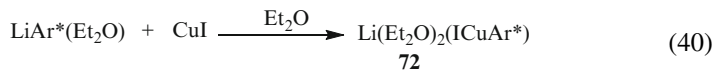
Scheme 9 Preparation of **24**, **60**, and **61**

In contrast, the reaction of **65** with the stannediyl $\text{Sn}\{1, 2\text{-}(t\text{BuCH}_2\text{N})\text{C}_6\text{H}_4\}$, followed by hydrolysis and treatment with LiO^tBu , afforded the unstable copper derivative $\{(\text{Et}_2\text{O})(\text{LiO}^t\text{Bu})(\text{SnO})(\text{CuAr}^\#)\}_2$ (**70**) [181]. The core structure of **70** involves a $\text{Sn}_2\text{O}_4\text{Li}_2$ array. The two $\text{Ar}^\#\text{Cu}$ units are coordinated to the oxygen atoms, which share a face with the Sn atoms. The Cu–O distance is 1.848(2) Å and the C1–Cu–O angle of $178.23(14)^\circ$ is almost linear.

Organocopper(I) terphenyls were also prepared by reaction of an organolithium reagent with copper halide. Reaction of CuI with $\text{LiAr}^\#$ with a ratio of 2:1 in THF/ Et_2O afforded the ionic species $[\text{Li}(\text{THF})_4][\text{Ar}^\#\text{Cu}_2\text{I}_2]$ (**71**) (39) [182]. Complex **71** crystallizes as separate ion pairs. Within the anion $[\text{Ar}^\#\text{Cu}_2\text{I}_2]^-$, the terphenyl ligand bridges two copper iodide units through an ipso-carbon with a Cu–C distance of 1.968(13) Å. The Cu–Cu separation is 2.391(3) Å, which is very similar to those observed in complex **66** [179]. The C–Cu–I angles ($164.1(4)$ and $166.8(4)^\circ$) deviate somewhat from linearity.



Similarly, reaction of the $\text{Ar}^*\text{Li}(\text{OEt}_2)$ with one equivalent of CuI afforded the contact ion-pair species $\text{Li}(\text{Et}_2\text{O})_2(\text{ICuAr}^*)$ (**72**) (40) [182]. In **72**, the copper atom is coordinated to the terphenyl ligand and an iodide, which bridges one lithium ion. However, when the reaction $\text{Ar}^*\text{Li}(\text{OEt}_2)$ with CuBr was performed in Et_2O , followed by addition of Me_2S , the neutral species $\text{Ar}^*\text{CuSMe}_2$ (**73**) was obtained [183]. In **73**, the Cu–C distance is 1.894(6) Å and the Cu–S bond length is 2.177(2) Å, and there is a C–Cu–S angle of $176.3(2)^\circ$.



Reaction of LiAr with CuCN afforded the cyanoorganocuprate complexes $\text{Ar}^\#\text{CuC}\equiv\text{NLi}(\text{THF})_3$ (**74**) [184] and $\{\text{Ar}^*\text{CuC}\equiv\text{NLi}(\text{THF})_2\}_2$ (**75**) (42, 43) [185]. Complex

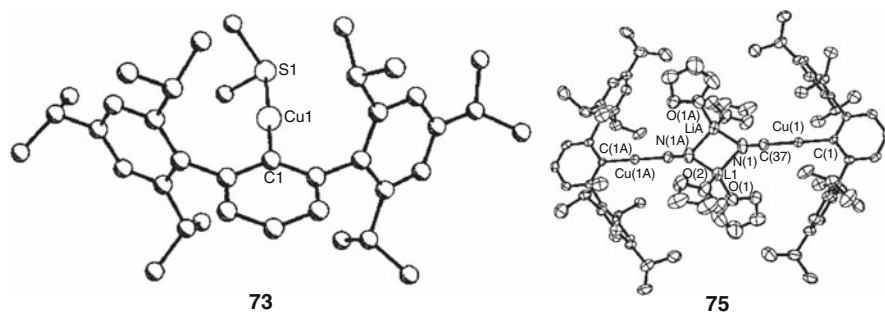
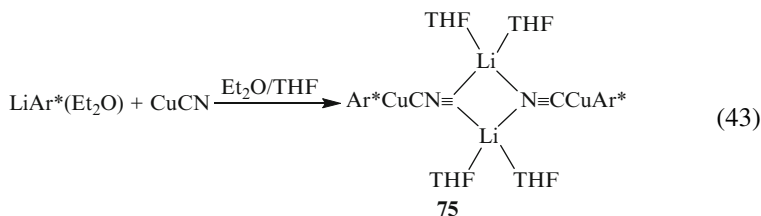
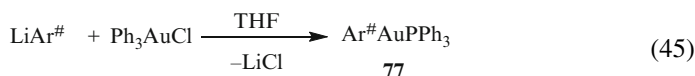


Fig. 20 Structures of copper complexes **73** and **75** without H atoms [183, 185]

74 is monomeric, in which the C≡N group bridges the copper atom and lithium atom in a η^2 fashion. In contrast, **75** is Dimeric (Fig. 20). The Ar^{*}Cu unit is terminally bound to the C≡N ligand via the carbon atoms. In addition, the nitrogen atoms of the C≡N ligands bridge two Li(THF)₂ units. In both complexes, the copper atoms are two-coordinate with almost linear interligand angles.



Structurally characterized silver and gold terphenyl derivatives are rare. The silver derivative [Li(THF)₄][AgAr₂[#]] (**76**) [186] was prepared (44) by reaction of LiAr[#] with AgOCN in THF/Et₂O with exclusion of light and obtained as colorless crystals in relatively low yield (38%). The structure of **76** consists of well-separated cation and anions. The [AgAr₂[#]]⁻ anion has silver bound to two aryl ligands through their *ipso*-carbon atoms with almost linear C–Ag–C angles of 176.7(4) and 176.8(8)°. The Ag–C distances are in the range of 2.048(15) to 2.112(19) Å, which is comparable to the average Ag–C distances observed in the anions [Li₂Ag₃Ph₆]⁻ (2.13 Å) [187].



The reaction of $\text{LiAr}^\#$ with Ph_3PAuCl in a 1:1 ratio in THF at room temperature afforded the gold derivative $\text{Ar}^\#\text{AuPPh}_3$ (**77**), which is the first and, this far, the only structurally authenticated terphenyl gold complex [188]. The monomeric structure features a two-coordinate gold atom with a wide angle of $174.21(8)^\circ$. The Au–C distance is $2.046(3) \text{ \AA}$ and the Au–P distance is $2.296(2) \text{ \AA}$. These can be compared with the corresponding distances in $\text{Ph}_3\text{PAu}\{\text{C}_6\text{H}_3\text{-}2, 6\text{-(CH}_2\text{NMe}_2)_2\}$ (Au–C = $2.045(9) \text{ \AA}$; Au–P = $2.282(2) \text{ \AA}$, P–Au–C = $178.6(3)^\circ$) [189].

10 Conclusion

The application of the sterically hindered terphenyl ligands(Ar) to transition metal elements has led to the synthesis and characterization of a series of monoaryl transition metal halides. With the availability of these halide precursors, a variety of transition metal complexes with unusual bonding, particularly the quintuple bonded complex ArCrCrAr or the nonbonded analogs ArMMAr (M = Fe and Co), along with the two-coordinate complexes $\text{Ar}^\#\text{MN(H)Ar}^\#$ (M = Mn, Fe, and Co) and $3, 5\text{-}^i\text{Pr}_2\text{-Ar}^\#\text{Cr(L)}$ (L = PMe_3 or THF) and arene-stabilized complexes ($3, 5\text{-}^i\text{Pr}_2\text{-Ar}^\#\text{Mn}$)($\eta^6\text{-C}_7\text{H}_8$), $3, 5\text{-}^i\text{Pr}_2\text{-Ar}^\#\text{Fe}$ ($\eta^6\text{-C}_6\text{H}_6$), $3, 5\text{-}^i\text{Pr}_2\text{-Ar}^\#\text{Co}$ ($\eta^6\text{-C}_7\text{H}_8$), could be prepared. Reactivity studies of some of these complexes have been carried out and further studies will help to understand the bonding within these species in greater detail. With the exception of yttrium, silver, and gold, all published work with transition metal terphenyls has concerned first-row elements. Even in the first row, however, there is the notable absence of titanium, vanadium, and metal derivatives. The synthesis of these and a range of second- and third-row derivatives can be anticipated.

Acknowledgements The authors are grateful to the National Science Foundation for financial support. In addition, we thank the many talented and dedicated coworkers who are named in the references for their crucial role in advancing the chemistry described in this review.

References

1. Power PP (2004) *J Organomet Chem* 689:3904
2. Twamley B, Haubrich ST, Power PP (1999) *Adv Organomet Chem* 44:1
3. Clyburne JAC, McMullen N (2000) *Coord Chem Rev* 210:73
4. Su J, Li X-W, Crittendon RC, Robinson GH (1997) *J Am Chem Soc* 119:5471
5. Wright RJ, Fettinger JC, Power PP (2006) *Angew Chem Int Ed* 45:5953
6. Stender M, Philips AD, Wright RJ, Power PP (2002) *Angew Chem Int Ed* 41:1785
7. Philips AD, Wright RJ, Olmstead MM, Power PP (2002) *J Am Chem Soc* 124:5930
8. Power PP (2003) *Chem Rev* 103:789
9. Du C-JF, Hart H, Ng K-KD (1986) *J Org Chem* 51:3162
10. Saednya A, Hart H (1996) *Synthesis* 1455
11. Simons RS, Haubrich ST, Mork BV, Niemeyer M, Power PP (1998) *Main group chemistry* 2:275
12. Stanciu C, Richards AF, Fettinger JC, Brynda M, Power PP (2006) *J Organomet Chem* 691:2540

13. Rabe GW, Brub CD, Yap B, Lam K-C, Concolino TE, Rheingold AL (2002) *Inorg Chem* 41:1446
14. Rabe GW, Berube CD, Yap GPA (2001) *Inorg Chem* 40:2682
15. Putzer MA, Bartholomew GP (1999) *Z Anorg Allg Chem* 625:1777
16. Rabe GW, Zhang-Presse M, Riederer FA, Incarvito CD, Golen JA, Rheingold AL (2004) *Acta Cryst* 60:1442
17. Rabe GW, Berube CD, Yap GPA (2001) *Inorg Chem* 40:4780
18. Rabe GW, Zhang-Presse M, Riederer FA, Yap GPA (2003) *Inorg Chem* 42:3527
19. Nguyen T, Sutton AD, Brynda M, Fettinger JC, Long GJ, Power PP (2005) *Science* 310:844
20. Wolf R, Ni C, Nguyen T, Brynda M, Long GJ, Sutton AD, Fischer RC, Fettinger JC, Hellman M, Pu L, Power PP (2007) *Inorg Chem* 46:11277
21. Sutton AD, Ngyuen T, Fettinger JC, Olmstead MM, Long GJ, Power PP (2007) *Inorg Chem* 46:4809
22. Ni C, Ellis BD, Power PP unpublished work
23. Heintz RA, Ostrander RL, Rheingold AL, Theopold KH (1994) *J Am Chem Soc* 116:11387
24. Gibson VC, Newton C, Redshaw C, Solan GA, White AJP, Williams DJ (2001) *Eur J Inorg Chem* 1895
25. Sanzenbacher R, Bottcher A, Elias H, Huber M, Haase W, Glerup J, Jensen TB, Neuburger M, Zehnder M, Springborg J, Olsen CE (1996) *Inorg Chem* 35:7493
26. Handy LB, Ruff JK, Dahl LF (1970) *J Am Chem Soc* 92:7327
27. Morse DB, Rauchfuss TB, Wilson SR (1990) *J Am Chem Soc* 112:1860
28. Burin ME, Smirnova MV, Fukin GK, Baranov EV, Bochkarev MN (2006) *Eur J Inorg Chem* 351
29. Hermes AR, Morris RJ, Girolami GS (1988) *Organometallics* 7:2372
30. Dillon KB, Gibson VC, Howard JAK, Redshaw C, Sequeira L, Yao JW (1997) *J Organomet Chem* 528:179
31. Ni C, Fettinger JC, Long GJ, Power PP submitted for publication 2009
32. Chai J, Zhu H, Roesky HW, He C, Schmidt H-G, Noltemeyer M (2004) *Organometallics* 23:3284
33. Prust J, Most K, Muller I, Stasch A, Roesky HW, Uson I (2001) *Eur J Inorg Chem* 1613
34. Chai J, Zhu H, Most K, Roesky HW, Vidovic D, Schmidt H-G, Noltemeyer M (2003) *Eur J Inorg Chem* 4332
35. Mueller H, Seidel W, Goerls H (1995) *Angew Chem Int Ed* 34:325
36. Wehmschulte RJ, Power PP (1995) *Organometallics* 14:3264
37. Solari E, Musso F, Gallo E, Floriani C, Re N, Chiesi-Villa A, Rizzoli C (1995) *Organometallics* 14:2265
38. Saak W, Haase D, Pohl SZ (1988) *Naturforsch B Chem Sci* 43:289
39. Gorter S, Hinrichs W, Reedijk J, Rimbault J, Pierrard JC, Hugel RP (1985) *Inorg Chim Acta* 105:181
40. Ni C, Fettinger JC, Long GJ, Grandjean F, Power PP (2009) *Inorg Chem* 48:11594
41. Ni C, Ellis BD, Fettinger JC, Long GL, Power PP, unpublished work
42. Ellison JJ, Power PP (1996) *J Organomet Chem* 526:263
43. Al-Juaid SS, Eaborn C, El-Hamruni SM, Hitchcock PB, Smith JD, Can SES (2002) *J Organomet Chem* 549:121
44. Buttrus NH, Eaborn C, Hitchcock PB, Smith JD, Sullivan AC *Chem Comm* 1985:1380
45. Gambarotta S, Floriani C, Chiesi-Villa A, Gaustini C (1983) *J Chem Soc Chem Comm* 1128
46. Klose A, Floriani C, Chiesi-Villa A, Rizzoli C, Re N (1994) *J Am Chem Soc* 116:9123
47. Theopold KH, Silvestre J, Byrne EK, Richeson DS (1989) *Organometallics* 8:2001
48. Kays DL, Cowley AR (2007) *Chem Comm* 1053
49. Ni C, Power PP (2009) *Chem Comm* 5543
50. Lappert MF, Power PP, Sanger AR, Srivastava RC (1980) *Metal and metalloid amides*. Ellis Horwood, Chichester, UK
51. Bradley DC (1975) *Chem Brit* 11:393
52. Bradley DC, Chisholm MH (1976) *Acc Chem Res* 9:273
53. Eller PG, Bradley DC, Hursthouse MB, Meek DW (1977) *Coord Chem Rev* 24:1

54. Cummins CC (1998) *Prog Inorg Chem* 47:685
55. Alvarez S (1999) *Coord Chem Rev* 13:193
56. Power PP (1989) *Comments Inorg Chem* 8:177
57. Power PP (1994) *Chemtracts Inorg Chem* 6:181
58. Ellison DJ, Ruhlandt-Senge K, Power PP (1994) *Angew Chem Int Ed* 33:1178
59. Ni C, Fettinger JC, Long GJ, Power PP (2009) *Inorg Chem* 48:2443
60. Bartlett RA, Feng X, Olmstead MM, Power PP, Weese KJ *J Am Chem Soc* (1987) 109:4851
61. Chen H, Bartlett RA, Olmstead MM, Power PP, Shoner SC (1990) *J Am Chem Soc* 112:1048
62. Bartlett RA, Power PP (1987) *J Am Chem Soc* 109:7563
63. Nguyen T, Merrill A, Ni C, Lei H, Fettinger JC, Ellis BD, Long GJ, Brynda M, Power PP (2008) *Angew Chem Int Ed* 47:9115
64. Pandey R, Rao BK, Jena P, Blanco MA (2001) *J Am Chem Soc* 123:3799
65. Jaeger TD, van Heijnsbergen D, Klippenstein SJ, von Helden G, Meijer G, Duncan MAJ (2004) *Am Chem Soc* 126:10981
66. La Macchia G, Gagliardi L, Power PP, Brynda M (2008) *J Am Chem Soc* 130:5105
67. Goodwin HA (2004) *Top Curr Chem* 234:23
68. Emsley J (1998) *The elements*. Oxford University Press, Oxford
69. Hvoslef J, Hope H, Murray BD, Power PP (1983) *Chem Comm* 1438
70. Ruppia KBP, Feghali K, Kovacs I, Aparna K, Gambarotta S, Yap GPA, Bensimon C (1998) *J Chem Soc Dalton Trans* 8:1595
71. Edema JJH, Gambarotta S, Spek AL (1989) *Inorg Chem* 28:811
72. Edema JJH, Gambarotta S, Meetsma A, Spek AL, Smeets WJJ, Chiang MY (1993) *J Chem Soc Dalton Trans* 789
73. Bush MA, Sim GA (1970) *J Chem Soc A* 611
74. Belforte A, Calderazzo F, Englert U, Strähle J, Wurst K (1991) *J Chem Soc Dalton Trans* 2419
75. Murray BD, Power PP (1984) *Inorg Chem* 23:4564
76. Bouwkamp MW, Lobkovsky E, Chirk JP (2006) *Inorg Chem* 45:2
77. Dahl LF, Costello WR, King RB (1968) *J Am Chem Soc* 90:5422
78. Olmstead MM, Power PP, Shoner SC (1991) *Inorg Chem* 30:2547
79. Ahmed KJ, Chisholm MH, Foltling K, Huffman JC (1985) *J Chem Soc Chem Comm* 152
80. Ahmed KJ, Chisholm MH, Foltling K, Huffman JC (1986) *J Am Chem Soc* 108:989
81. Nast R (1982) *Coord Chem Rev* 47:89
82. Carty AJ (1982) *Pure Appl Chem* 54:113
83. Sappa E, Tiripicchio A, Braunstein P (1985) *Coord Chem Rev* 65:219
84. Raithby PR, Rosales MJ (1986) *Adv Inorg Chem Radiochem* 29:169
85. Ni C, Long GJ, Power PP (2009) *Organometallics* 28:5012
86. Fernandez FJ, Alfonso M, Schmalle HW, Berke H (2001) *Organometallics* 20:3122
87. Riese U, Neumuller B, Faza N, Massa W, Dehnicke KZ (1997) *Anorg Allg Chem* 623:351
88. Pauer F, Power PP (1994) *J Organomet Chem* 474:27
89. Pauling L (1976) *Proc Natl Acad Sci U S A* 73:4290
90. Yamaguchi S, Endo T, Uchida M, Izumizawa T, Furukawa K, Tamao K (2000) *Chem-Eur J* 6:1683
91. Bats JW, Urschel B (2006) *Acta Crystallogr Sect E* 62:748
92. Jaroschik F, Nief F, Goff X-FL, Ricard L (2007) *Organometallics* 26:1123
93. Ni C, Fettinger JC, Long GJ, Power PP (2008) *Chem Comm* 1014
94. Smith JM, Sadique AR, Cundari TR, Rodgers KR, Lukat-Rodgers G, Lachicotte RJ, Flaschenriem CJ, Vela J, Holland PL (2006) *J Am Chem Soc* 128:756
95. Muller H, Seidel W, Gorls H (1993) *J Organomet Chem* 445:133
96. Vela J, Smith JM, Yu Y, Ketterer NA, Flaschenriem CJ, Lachicotte RJ, Holland PL (2005) *J Am Chem Soc* 127:7857
97. Eckert NA, Smith JM, Lachicotte RJ, Holland PL (2004) *Inorg Chem* 43:3306
98. Cotton FA, Curtis NF, Harris CB, Johnson BFG, Lippard SJ, Mague JT, Robinson WR, Wood JS (1964) *Science* 145:1305

99. Cotton FA, Murillo LA, Walton RA (Eds) *Multiple bonds between metal atoms*, 3rd ed. Springer, Berlin, 2005
100. Kundig EP, Moskovits M, Ozin GA (1975) *Nature* 254:503
101. Klotzbucher W, Ozin GA (1977) *Inorg Chem* 16:984
102. Norman JG, Kolari HJ, Gray HB, Trogler WC (1977) *Inorg Chem* 16:987
103. Bursten BE, Cotton FA, Hall MB (1980) *J Am Chem Soc* 102:6349
104. Morse MD (1986) *Chem Rev* 86:1049
105. Barden CJ, Rienstra-Kiracofe JC, Schaefer HF (2000) *J Chem Phys* 113:690
106. Yanagisawa S, Tsuneda T, Hirao K (2000) *J Chem Phys* 112:545
107. Boudreaux EA, Baxter E (2001) *Int J Quantum Chem* 85:509
108. Gutsev GL, Bauschlicher CW (2003) *J Phys Chem A* 107:4755
109. Roos BO, CollectCzech (2003) *Chem Comm* 68:265
110. Jules JL, Lombardi JR (2003) *J Phys Chem A* 107:1268
111. Boudreaux EA, Baxter E (2004) *Int J Quantum Chem* 100:1170
112. Cotton FA, Koch SA, Millar M (1978) *Inorg Chem* 17:2084
113. Brynda M, Gagliardi L, Widmark PO, Power PP, Roos BO (2006) *Angew Chem Int Ed* 45:3804
114. Landis CR, Weinhold F (2006) *J Am Chem Soc* 128:7335
115. Frenking G (2005) *Science* 310:796
116. Radius U, Breher F (2006) *Angew Chem Int Ed* 45:3006
117. Merino G, Donald KJ, D'Acchioli JS, Hoffmann R (2007) *J Am Chem Soc* 129:15295
118. Kreisel KA, Yap GPA, Dmitrenko O, Landis CR, Theopold KH (2007) *J Am Chem Soc* 129:14162
119. Noor A, Wagner FR, Kempe R (2008) *Angew Chem Int Ed* 47:7264
120. Tsai Y-C, Hsu C-W, Yu J-SK, Lee GH, Wang Y, Kuo T-S (2008) *Angew Chem Int Ed* 47:7250
121. Dai X, Kapoor P, Warren TH (2004) *J Am Chem Soc* 126:4798
122. Wolf R, Brynda M, Ni C, Long GJ, Power PP (2007) *J Am Chem Soc* 129:6076
123. Ni C, Ellis BE, Fettinger JC, Long GJ, Power PP *Dalton Trans*, 5041
124. Kubo H, Hirano M, Komiya S (1998) *J Organomet Chem* 556:89
125. Le Floch P, Knoch F, Kremer F, Mathey F, Scholz J, Scholz W, Thiele K-H, Zenneck U (1998) *Eur J Inorg Chem* 119
126. Lei H, Ellis BD, Ni C, Grandjean F, Long GJ, Power PP (2008) *Inorg Chem* 47:10205
127. Giri R, Mangel N, Foxman BM, Yu J-Q *Organometallics* (2008) 27:1667 and references therein
128. Cann K, Riley PE, Davis RE, Pettitt R (1978) *Inorg Chem* 21:1421
129. Bouayad A, Dartiguenave M, Menu M-J, Dartiguenave Y, Belanger-Gariepy F, Beauchamp AL (1989) *Organometallics* 8:629
130. Tsai Y-C, Wang P-Y, Chen S-A (2007) *J Am Chem Soc* 129:8066
131. Thomas BJ, Mitchell JF, Theopold KH, Leary JA (1988) *J Organomet Chem* 348:333
132. Seyferth D *Organometallics* (2002) 21:1520, 2800
133. Mani G, Gabbar FP (2004) *Angew Chem Int Ed* 43:2263
134. Madelung (Ed) (1987) *Landolt-Bornstein: numerical data and functional relationships in science and technology*, Vol 15. Springer, Berlin
135. Dai X, Kapoor P, Warren TH (2004) *J Am Chem Soc* 126:4798
136. Carlos Ananias de Carvalho L, Dartiguenave M, Dartiguenave Y, Beauchamp AL (1984) *J Am Chem Soc* 106:6848
137. Ni C, Ellis BD, Long GJ, Power PP (2009) *Chem Comm* 2332
138. Rupp KBP, Feghali K, Kovacs I, Aparna K, Gambarotta S, Yap GPA, Bensimon C (1998) *J Chem Soc Dalton Trans* 1595
139. Herberhold M, Kremnitz W, Razavi A, Schollhorn H, Thewalt U (1985) *Angew Chem Int Ed* 24:601
140. Nishino H, Kochi JK (1990) *Inorg Chim Acta* 174:93
141. Monillas WH, Yap GPA, MacAdams LA, Theopold KH (2007) *J Am Chem Soc* 129:8090
142. Edwards NY, Eikey RA, Loring MI, Abu-Omar MM (2005) *Inorg Chem* 44:3700
143. Bartlett RA, Chen H, Power PP (1989) *Angew Chem Int Ed* 28:316

144. Ni C, Fettinger JC, Long GJ, Brynda M, Power PP (2008) *Chem Commun* 6045
145. Eckert NA, Vaddadi S, Stoian S, Lachiotte RJ, Cundari TR, Holland PL (2006) *Angew Chem Int Ed* 45:8868
146. Thyagarajan S, Shay DT, Incarvito CD, Rheingold AL, Theopold KH (2003) *J Am Chem Soc* 125:4440
147. Cotton FA, Wilkinson G, Murrillo CA, Bochman M *Advanced inorganic chemistry*, 6th ed. Wiley, New York, p 794
148. Aliagra-Alcalde N, George S de B, Mienert B, Bill E, Wiegardt K, Neese F (2005) *Angew Chem Int Ed* 44:2908
149. Berry JF, Bill E, Bothe E, George S de B, Mienert B, Neese F, Wiegardt K (2006) *Science* 312:1937
150. Chirik P *Angew Chem Int Ed* (2006) 45:6956
151. Rohde J-U, Betley TA, Jackson TA, Saouma CT, Peters JC, Que L (2007) *Inorg Chem* 46:5720
152. Vogel C, Heinemann FW, Sutter J, Anthon C, Meyer K (2008) *Angew Chem Int Ed* 47:1
153. Ellison JJ, Power PP, Shoner SC (1989) *J Am Chem Soc* 111:8044
154. Das AK, Moatazedi Z, Mund G, Bennet AJ, Batchelor RJ, Leznoff DB (2007) *Inorg Chem* 46:366
155. Wallasch M, Wolmershauser G, Sitzmann H (2005) *Angew Chem Int Ed* 44:2597
156. MacDonnell FM, Ruhlandt-Senge K, Ellison JJ, Holm RH, Power PP (1995) *Inorg Chem* 34:1815
157. Hauptmann R, Kliss R, Schneider J, Henkel G (1998) *Z Anorg Allg Chem* 624:1927
158. Komuro T, Kawaguchi H, Tatsumi K (2002) *Inorg Chem* 41:5083
159. Vela J, Smith JM, Yu Y, Ketterer NA, Flaschenriem CJ, Lachicotte RJ, Holland PL (2005) *J Am Chem Soc* 127:7857
160. Zang Y, Dong Y, Que L Jr, Kauffmann K, Munck E (1995) *J Am Chem Soc* 117:1169
161. Zheng H, Zang Y, Dong Y, Young VG Jr, Que L Jr (1999) *J Am Chem Soc* 121:2226
162. Hsu H-F, Dong Y, Shu L, Young VG Jr, Que L Jr (1999) *J Am Chem Soc* 121:5230
163. Honda Y, Arii H, Okumura T, Wada A, Funahashi Y, Ozawa T, Jitsukawa K, Masuda H (2007) *Bull Chem Soc Jan* 80:1288
164. Kurtz DM Jr (1990) *Chem Rev* 90:585
165. Bartlett RA, Ellison JJ, Power PP, Shoner SC (1991) *Inorg Chem* 30:2888
166. Jenkins DM, Betley TA, Peters JC (2002) *J Am Chem Soc* 124:11238
167. Hocking RK, Hambley TW (2007) *Organometallics* 26:2815
168. Popov AI, Wendlandt WW (1954) *Anal Chem* 26:883
169. Wendlandt WW (1955) *Anal Chem* 27:1277
170. Elving PJ, Olson EC (1955) *Anal Chem* 27:1817
171. Puiiu SC, Warren TH (2003) *Organometallics* 22:3974
172. Fochi G, Floriani C, Chiesi-Villa A, Guastini C (1986) *J Chem Soc Dalton Trans* 445
173. Fletcher SR, Skapski AC (1973) *J Organomet Chem* 59:299
174. Bahr G, Burba P (1970) *Houben-Weyl Methoden der Organischen Chemie*, Vol 13/1. Muller E (ed.) Georg Thieme, Stuttgart. pp 735–761
175. Posner GH (1980) *An introduction to synthesis using organocopper reagents*. Wiley, New York
176. Taylor RJK (Ed) (1994) *Organocopper reagents: a practical approach*. Oxford University Press, Oxford
177. Lipshutz BH (1995) *Comprehensive organometallic chemistry*, Vol 12, Chap 3.2. In: Abel EW, Stone FGA, Wilkinson G (Eds). Pergamon Press, Oxford
178. Niemeyer M (1998) *Organometallics* 17:4649
179. Niemeyer M (2001) *Acta Crystallogr Sect E Struct Rep Online* 57:m416
180. Niemeyer M (2003) *Z Anorg Allg Chem* 629:1536
181. Niemeyer M (2004) *Z Anorg Allg Chem* 630:252
182. Hwang C-S, Power PP (1999) *Organometallics* 18:697
183. Schiemenz B, Power PP (1996) *Organometallics* 16:958
184. Hwang C-S, Power PP (2003) *Bull Korean Chem Soc* 24:605
185. Hwang C-S, Power PP (1998) *J Am Chem Soc* 120:6409

186. Hwang C-S, Power PP (1999) *J Organomet Chem* 589:234
187. Chiang MY, Bohlem E, Bau R (1985) *J Am Chem Soc* 107:1679
188. Rabe GW, Mitzel NW (2001) *Inorg Chim Acta* 316:132
189. Contel M, Stol M, Casado MA, van Klink GPM, Ellis DD, Spek AL, van Koten G (2002) *Organometallics* 21:4556
190. Chen H, Bartlett RA, Dias HVR, Olmstead MM, Power PP (1989) *J Am Chem Soc* 111:4338

Metal–Metal Bonding in Bridging Hydride and Alkyl Compounds*

Gerard Parkin

Abstract A theoretical analysis of the bonding in a series of dinuclear compounds that feature bridging hydride or alkyl ligands indicates that the direct metal–metal bond order is best predicted by an electron-counting procedure in which 3-center-2-electron M–H–M and M–R–M interactions are represented by the μ -LX “half-arrow” method. In contrast, an electron-counting procedure which apportions half of the valence electron of H or R to each metal center results in direct metal–metal bond orders that are not in accord with theory.

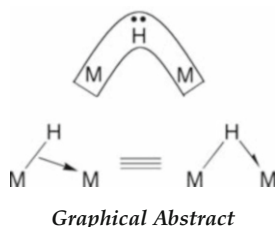
Keywords Alkyl · Bond order · Hydride · Metal · Metal–metal bond · 3-Center-2-electron interaction

Contents

1	Introduction	114
2	Electron-Counting Procedures and the Origin of M–M Bond Order Ambiguities in the Presence of Bridging Hydride and Alkyl Ligands	115
3	Overview of 3-Center-2-Electron [M(μ -H)M] Interactions	118
4	Analysis of the Bonding in Dinuclear Molybdenum Compounds with Bridging Methyl and Hydride Ligands as a Representative Study	122
	4.1 Bond Length and Bond Order	123
	4.2 Theoretical Calculations	123
5	Application of the μ -LX “Half-Arrow” Electron-Counting Method to Other Compounds	128
	5.1 Dinuclear Compounds with Single Hydrogen Bridges	129
	5.2 Dinuclear Compounds with Double Hydrogen Bridges	132
	5.3 Dinuclear Compounds with Triple Hydrogen Bridges	136
	5.4 Dinuclear Compounds with Quadruple Hydrogen Bridges	139
6	Conclusions	141
	References	143

G. Parkin
Department of Chemistry, Columbia University, New York, New York 10027, USA
e-mail: parkin@columbia.edu

* Dedicated to three people who have had a profound influence concerned with providing an understanding of the bonding in bridging hydride complexes, namely Malcolm Green, Larry Dahl, and Roald Hoffmann.



1 Introduction

By comparison to organic compounds, the assignment of bond orders in inorganic compounds is often nontrivial and is sometimes contentious. Although a theoretical analysis of a molecule naturally provides the best description of the nature of a bonding interaction between a pair of elements, the first-order assessment of such interactions is often obtained by simple electron-counting formalisms. For example, on the basis that the carbon atoms in $[\text{CH}_3]$, $[\text{CH}_2]$, and $[\text{CH}]$ moieties possess electronic configurations with 7, 6, and 5 electrons in the valence shell, application of the octet rule predicts the existence of C–C single, double, and triple bonds in $\text{H}_3\text{C}-\text{CH}_3$, $\text{H}_2\text{C}=\text{CH}_2$, and $\text{HC}\equiv\text{CH}$, respectively. Likewise, for dinuclear transition metal compounds, the nature of the metal–metal (M–M) bonding interaction is typically obtained by (1) evaluating the electronic nature of the uncoupled metal centers in the absence of any $\text{M}\cdots\text{M}$ interaction and (2) determining which bond order would then be consistent with a *reasonable* electronic configuration for the molecule. For example, the 18-electron rule [1, 2] is often invoked as a guide in assigning the M–M bond orders in dinuclear *organometallic* compounds. Thus, $(\text{OC})_5\text{MnMn}(\text{CO})_5$ is predicted to have an Mn–Mn bond order of one on the basis that each $[\text{Mn}(\text{CO})_5]$ moiety possesses a 17-electron configuration, such that the formation of a single Mn–Mn bond enables each manganese center to achieve an 18-electron configuration.

However, while an 18-electron configuration is often viewed as a target, it must be emphasized that the number of M–M bonds cannot exceed the number of available valence electrons on the metal fragment [3]. As an illustration, $\text{R}_3\text{M}\equiv\text{MR}_3$ ($\text{M} = \text{Mo}, \text{W}$) [4, 5] possesses a triple bond with each metal having a 12-electron configuration because the metal center of the $[\text{R}_3\text{M}]$ fragment has only three valence electrons available for bonding.

Although there is little controversy concerning the M–M bond orders for molecules such as $(\text{OC})_5\text{MnMn}(\text{CO})_5$ and R_3MMR_3 , problems may arise if the metal centers are bridged by ligands. For example, $\text{Os}_3(\text{CO})_{10}(\mu_2\text{-H})_2$ has been represented in the literature with at least *six* bonding descriptions in which the $\text{Os}\cdots\text{Os}$ bond order for the bridged pair varies from zero to two (Fig. 1) [6]. Furthermore, with the use of “dotted lines” to represent certain bonds, it is evident that some of the bonding descriptions for $\text{Os}_3(\text{CO})_{10}(\mu_2\text{-H})_2$ are ill defined and ambiguous. It is, therefore, apparent that there are problems with the application of simple

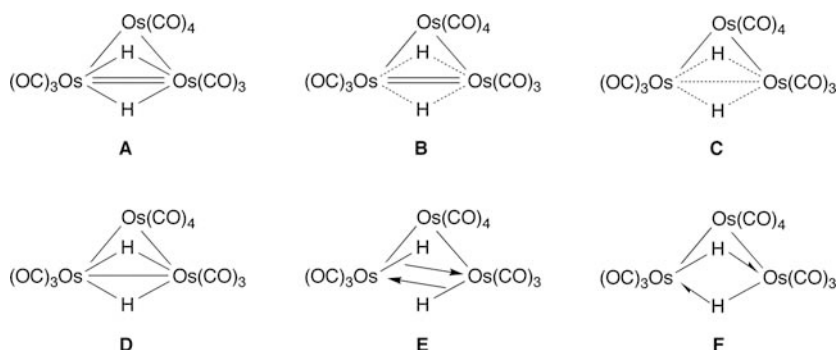


Fig. 1 Structural representations for $\text{Os}_3(\text{CO})_{10}(\mu_2\text{-H})_2$ (see [6])

electron-counting procedures for compounds with certain types of bridging ligands (such as H and R), and the purpose of this article is to review the various methods and evaluate which predicts M–M bond orders that are more in accord with the results of theoretical calculations.

2 Electron-Counting Procedures and the Origin of M–M Bond Order Ambiguities in the Presence of Bridging Hydride and Alkyl Ligands

Adopting a “neutral ligand” formalism, the electron count at a metal center is simply the sum of (1) the number of valence electrons of the metal atom and (2) the number of electrons donated by all of the ligands in their neutral form, with the sum being modified appropriately to take account of the charge on the molecule [1]. A selection of ligands and the number of electrons that they contribute when binding to a single metal center are provided in Table 1, which also includes the $[\text{L}_l\text{X}_x\text{Z}_z]$ designation according to Green’s Covalent Bond Classification method, where L, X, and Z, respectively, correspond to 2-electron, 1-electron, and 0-electron *neutral* ligand functions (Fig. 2) [1, 7]. For situations in which the ligand bridges two metal centers, however, further consideration of the bonding is required to evaluate the electron donor number of the ligand.

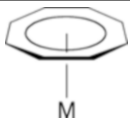
For example, due to the availability of a lone pair on trivalent phosphorus, a compound that features a bridging PR_2 ligand can be represented in terms of simple resonance structures that feature two 2-center-2-electron bonds (Fig. 3). Thus, the bridging PR_2 ligand serves as a one-electron (M–X) donor to one metal and as a two-electron ($\text{M}\leftarrow\text{L}$) donor to the other metal, such that it is overall a three-electron $\mu\text{-LX}$ donor ligand. For such situations, the derived electron count at each metal center enables one to predict an M–M bond order that is in accord with theoretical calculations and the result is noncontroversial.

Table 1 Number of electrons provided by various neutral ligands and their CBC descriptions

Ligand	Metal-Ligand interaction	No. of electrons donated (neutral ligand formalism)	CBC Description
H	$M-H$	1	X
R	$M-R$	1	X
CR ₂ (Schrock alkylidene)		2	\bar{X}_2
CR(X) (Fischer carbene)		2	L
CR	$M\equiv C-R$	3	\bar{X}_3
$\eta^2-C_2H_4$		2	LZ'^a
$\eta^3-C_3H_5$		3	LX
$\eta^3-C_4H_6$		4	$L_2Z'^a$
$\eta^3-C_3H_3$		3	X ₃
$\eta^4-C_4H_4$		4	LX ₂
$\eta^5-C_5H_5$		5	L ₂ X
$\eta^6-C_6H_6$		6	$L_3Z'^a$
$\eta^7-C_7H_7$		7	L ₂ X ₃

(continued)

Table 1 (continued)

Ligand	Metal–Ligand interaction	No. of electrons donated (neutral ligand formalism)	CBC Description
$\eta^8\text{-C}_8\text{H}_8$		8	L_3X_2
CO	$\text{M} \leftarrow \text{CO}$	2	LZ'^a
PR_3	$\text{M} \leftarrow \text{PR}_3$	2	L

^aThe Z' backbonding component is undetermined

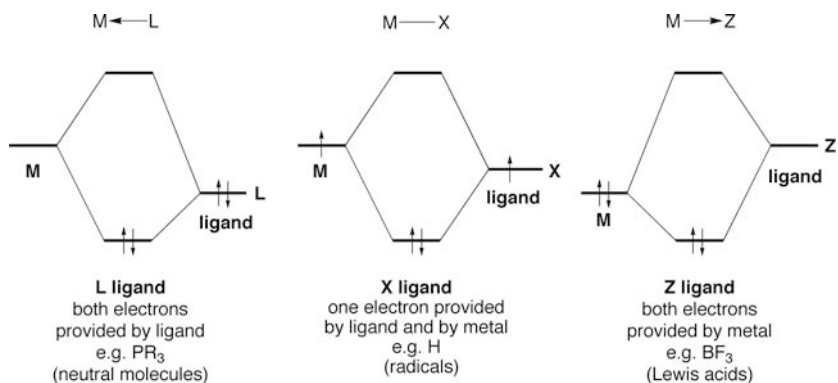


Fig. 2 Molecular orbital representations of the three fundamental types of 2-center-2-electron interactions

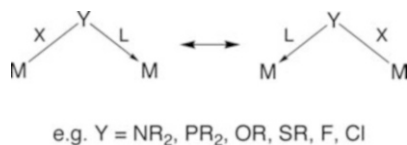


Fig. 3 Two 2-center-2-electron bonds in situations where the bridging atom has a lone pair

On the other hand, since a hydrogen atom in an M–H moiety does not possess a lone pair, a compound that features a bridging hydride ligand cannot be represented in terms of two 2-center-2-electron M–H bonds. Rather, the $[\text{M}(\mu\text{-H})\text{M}]$ interaction must be described as a 3-center-2-electron bond. However, while simple M–X “line” and $\text{M} \leftarrow \text{L}$ “arrow” representations of normal covalent and dative covalent bonds provide a convenient means to evaluate the electron count of a metal center, there are many varied representations for 3-center-2-electron $[\text{M}(\mu\text{-H})\text{M}]$ interactions in the literature (Fig. 4). As a consequence, the derived electron count and resulting M–M bond order depends upon one’s interpretation of the 3-center-2-electron $[\text{M}(\mu\text{-H})\text{M}]$ interaction. In such cases, the derived M–M bond order may be controversial.

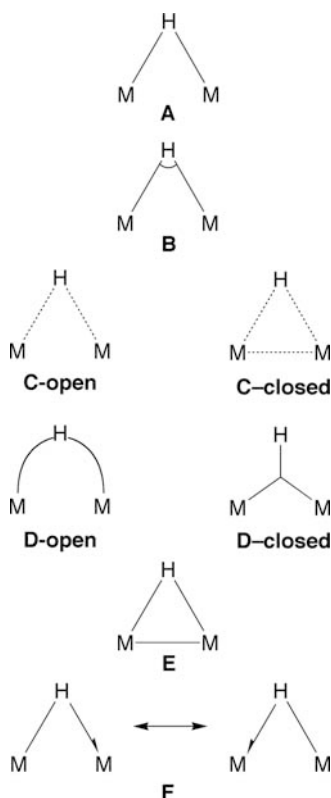


Fig. 4 Representations of 3-center-2-electron M–H–M interactions presented in the literature

Similar problems are also encountered for symmetrically bridging alkyl groups for which the $[M(\mu\text{-R})M]$ interactions are also of the 3-center-2-electron type.

3 Overview of 3-Center-2-Electron $[M(\mu\text{-H})M]$ Interactions

A simplified molecular orbital representation of a 3-center-2-electron $[M(\mu\text{-H})M]$ interaction is illustrated in Fig. 5, in which the three atomic orbitals combine to give three molecular orbitals that have M–H bonding, nonbonding, and antibonding character [8, 9]. While this figure emphasizes the interaction between the metal centers and the hydrogen atom, it is important to note that there is also a degree of interaction between the two metals. The amount of this interaction depends on the geometry of the system and the extremes are often referred to as “open” and “closed” (Fig. 6) [10, 11].

Despite the fact that the molecular orbital representation of the 3-center-2-electron $[M(\mu\text{-H})M]$ interaction is straightforward, a large variety of graphical representations have been used to depict the bonding situation (Fig. 4). Unfortunately,

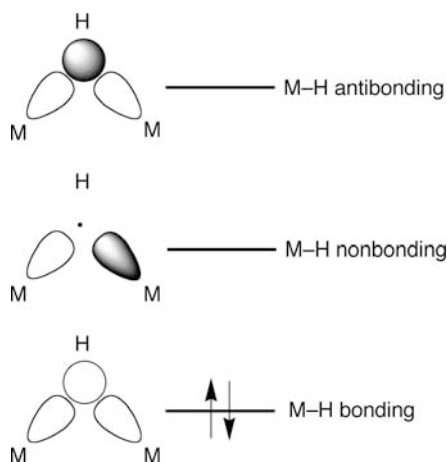


Fig. 5 Simplified MO diagram for a 3-center-2-electron interaction (taken from reference 6)

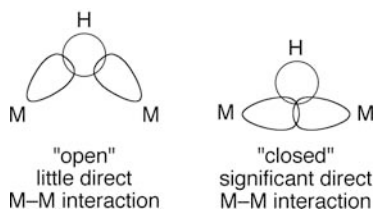


Fig. 6 “Open” and “closed” 3-center-2-electron interactions with varying degrees of $M \cdots M$ interaction (taken from reference 6)

many of these representations are not useful for electron-counting purposes. For example, Dahl originally formulated $[M(\mu\text{-H})M]$ interactions with two solid lines between M and H (**A**) [12–14], but this representation can give the mistaken impression that the two “bonds” attached to hydrogen are independent 2-center-2-electron bonds. A simple modification of this representation is to join the two bonds by a curved line around the hydrogen atom (**B**), thereby indicating that the two bonds are not independent, a notation which was first introduced by Parry for B–H–B interactions [15, 16]. A “dashed-bond” depiction of the 3-center-2-electron bond was employed by Churchill, who also emphasized the possible “open” (**C-open**) and “closed” (**C-closed**) nature of the interactions [17–20]. Other variants for “open” and “closed” 3-center-2-electron $[M(\mu\text{-H})M]$ interactions bonds are the “bent” (**D-open**) and “Y” (**D-closed**) representations used by Bau, Koetzle, and Kirtley [10, 11]. While the “dashed-bond” depiction (**C-closed**) is a good representation for a 3-center-2-electron $[M(\mu\text{-H})M]$ interaction, Dahl has noted that a problem which has arisen is that others have redrawn the dashed lines as solid lines (**E**), thereby resulting in the incorrect notion that there is a separate M–M 2-center-2-electron bond in addition to the 3-center-2-electron M–H–M interaction [13]. The 3-center-2-electron M–H–M interaction has also been described as a protonated metal–metal



Fig. 7 Representations of the 3-center-2-electron B–H–B interaction in diborane which emphasizes the octet configuration of boron

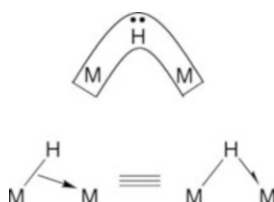


Fig. 8 The “half-arrow” representation of a 3-center-2-electron M–H–M interaction, which may be viewed as donation of a pair of electrons associated of the M–H sigma bond into a vacant orbital on the other M

bond of the anionic $[M-M]^-$ moiety [19]. While this is a perfectly good description of the interaction, it must be emphasized that the “metal–metal bond” is no longer the same as that in the hypothetical anionic $[M-M]^-$ fragment.

In addition to the ambiguous interpretation of M–M bond orders, it is evident that representations (A) to (E) shown in Fig. 4 are not particularly useful for electron-counting purposes. It is, therefore, significant that Green introduced an approach for counting electrons in systems that possess 3-center-2-electron interactions (F). Consider, for example, diborane, the archetype of 3-center-2-electron bonding. The bonding in this molecule is often simply described as involving donation of the σ -bond electron density of the B–H bond of one BH_3 fragment into an empty orbital on boron of the other fragment (Fig. 7). Green’s simple modification of this representation is to draw a “half-arrow” from the bridging hydrogen atom rather than a “full arrow” from the midpoint of the M–H bond (Fig. 8) [21, 22]. The “half-arrow” notation can also be applied to other examples of 3-center-2-electron interactions as present in, for example, bridging alkyl and agostic alkyl complexes [23].

Despite the different appearance of the two representations, the “half-arrow” conveys exactly the same information as that involving an arrow from the center of the bond, with $M-H \rightarrow M'$ depicting that the pair of electrons associated with the M–H σ -bond is donated into a vacant orbital on M' , such that the hydride ligand may be viewed as a μ -LX ligand. The principal advantage of the “half-arrow” notation is that it is less cumbersome for drawing molecules with multiple bridging groups because the arrow is drawn between atoms, rather than between the center of a bond and an atom. A second advantage is that the notation is similar to that using a “full arrow” from an atom to represent interactions involving bridging ligands that possess a lone pair, such as PR_2 or Cl (*vide supra*). The essential distinction between the “half-arrow” and “full arrow” representations, however, is that the former implies donation of a *bond* pair, while the latter implies donation of a *lone*

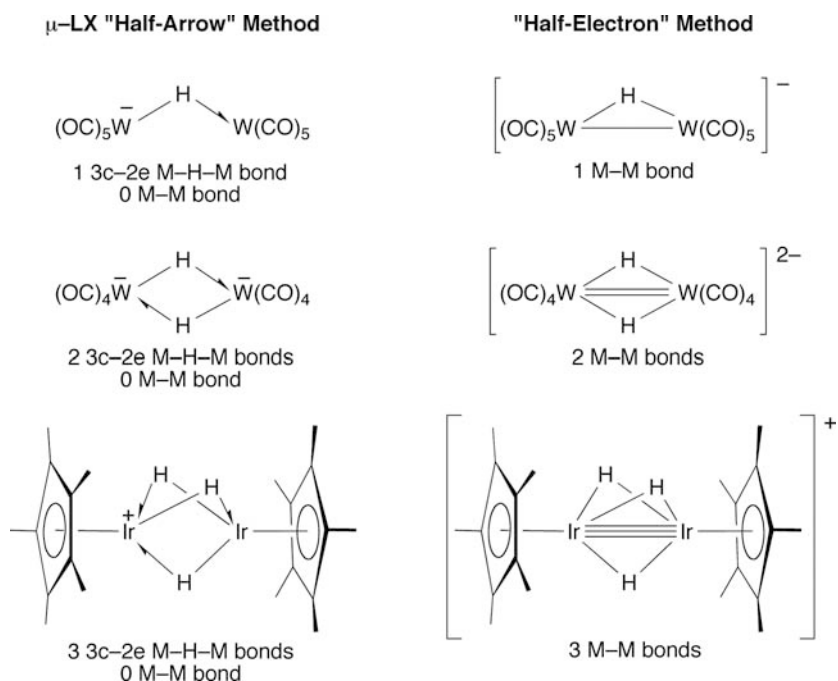


Fig. 9 Different descriptions of the metal–metal bond orders in some dinuclear complexes with bridging hydride ligands according to the electron-counting method. The “half-electron” method does not explicitly take into account the 3-center-2-electron nature of the M–H–M interaction and thus results in a greater M–M bond order than would be predicted theoretically. In contrast, the “half-arrow” method treats the 3-center-2-electron nature of the M–H–M interactions explicitly and thereby predicts an M–M bond order which is in accord with theory

pair. It is also important to emphasize that the absence of a “line” between the two metal atoms in the “half-arrow” notation does *not* imply that there is no interaction between these atoms. Rather, the “half-arrow” notation merely indicates that any $M \cdots M$ interaction that does exist is one that is mediated by the bridging atom, i.e., a 3-center-2-electron interaction.

In addition to the “half-arrow” μ -LX description of the bonding for evaluating M–M bond orders, an alternative method merely apportions the electron associated with each hydride ligand equally to both metals (the “half-electron” method) [24–27]. Specifically, the M–M bond order is obtained by application of the formula $m = (18n - N)/2$, where m is the number of 2-center-2-electron M–M bonds, n is the number of M atoms, and N is the total electron count assuming that each bridging hydride ligand contributes one electron. For example, the “half-electron” method predicts an Re = Re double bond for $[(CO)_4Re]_2(\mu-H)_2$ [25].

An important consequence of the different ways in which the two methods treat the bridging hydride ligands is that the “half-electron” and “half-arrow” electron-counting procedures predict different M–M bond orders. For example, a selection of compounds and their assigned M–M bond orders is provided in Fig. 9, from

which it is evident that the “half-electron” method consistently predicts greater M–M bond orders than does the “half-arrow” method. Obviously, the actual M–M bond order must be independent of the electron-counting procedure employed, and the following sections correlate the results of theoretical calculations on a variety of systems with the bond orders predicted by the two electron-counting procedures. These comparisons indicate that the “half-arrow” method predicts M–M bond orders that are more in accord with theoretical analyses than those predicted by the “half-electron” method.

4 Analysis of the Bonding in Dinuclear Molybdenum Compounds with Bridging Methyl and Hydride Ligands as a Representative Study

$[\text{Cp}^*\text{Mo}(\mu\text{-O}_2\text{CMe})_2(\mu\text{-PMe}_2)(\mu\text{-Me})]$ is an example of a dinuclear molybdenum compound which has been shown by X-ray diffraction to possess a methyl group that bridges the two molybdenum centers in a symmetric manner [28]. In the absence of an Mo···Mo interaction, application of the “half-arrow” formalism predicts an electron count of 17 electrons for each metal center, such that an Mo–Mo single bond is required for each metal center to achieve an 18-electron configuration in the diamagnetic molecule (Fig. 10). On the other hand, application of the formula $m = (18n - N)/2$ for the “half-electron” method predicts an Mo = Mo double bond (Fig. 10).

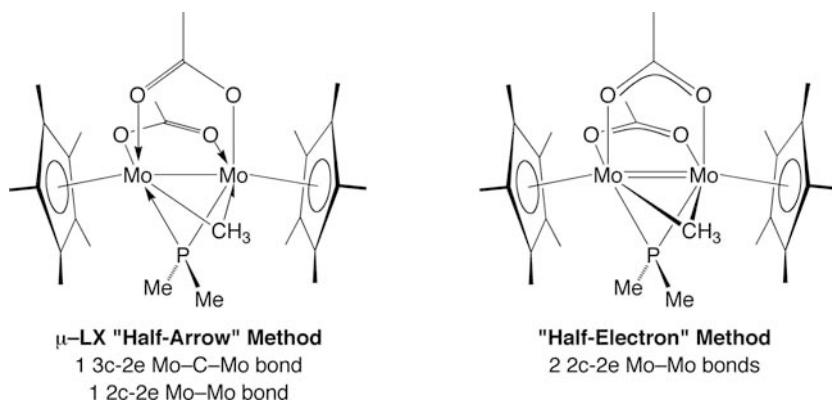


Fig. 10 Predicted Mo–Mo bond orders for $[\text{Cp}^*\text{Mo}(\mu\text{-O}_2\text{CMe})_2(\mu\text{-PMe}_2)(\mu\text{-Me})]$ using two different electron-counting procedures

Table 2 Typical M–M bond lengths (Å) in unbridged dinuclear molybdenum and tungsten compounds

	Molybdenum	Tungsten	References
M–M	2.88–3.32	2.65–3.33	[29–32]
M=M	–	2.44–2.49	[31, 32, 34, 35]
M≡M	2.17–2.26	2.25–2.34	[35]
M≡M	2.06–2.17	2.16–2.38	[35, 36]

4.1 Bond Length and Bond Order

In principle, one would expect that experimental evidence for the bond order within $[\text{Cp}^*\text{Mo}(\mu\text{-O}_2\text{CMe})_2(\mu\text{-PMe}_2)(\mu\text{-Me})]$ could be obtained from the observed Mo–Mo bond length. For example, Mo–Mo bond lengths span a substantial range of at least 2.06 Å to 3.32 Å, and the ranges for Mo–Mo single and multiple bonds in *unbridged* dinuclear compounds are reasonably distinct, as illustrated in Table 2 [29–37]. However, a serious problem is encountered in situations where the two metal centers are also linked by a bridging ligand. Specifically, it is well known that the steric and electronic requirements of bridging groups cause a metal–metal distance to be either *shorter* or *longer* than that in the absence of the bridge [38–41]. For example, while protonation of an M–M bond often leads to an increase in $\text{M}\cdots\text{M}$ separation [42], there are several examples where the M–M distance decreases slightly upon protonation [43–46]. Furthermore, in some cases, the metal–metal separation in dinuclear complexes with bridging ligands and *no* metal–metal bond may be shorter than that in unbridged complexes with a metal–metal bond [47]. Assigning an Mo–Mo bond order on the basis of the bond length is, therefore, fraught with difficulty.

Nevertheless, despite this caveat, comparison of the Mo–Mo bond length of 2.8447(5) Å for $[\text{Cp}^*\text{Mo}(\mu\text{-O}_2\text{CMe})_2(\mu\text{-PMe}_2)(\mu\text{-Me})]$ with the data for other structurally related dinuclear cyclopentadienyl molybdenum compounds (Table 3) indicates that the value is much more in accord with that of an Mo–Mo single bond than that of an Mo=Mo double bond. For example, of the compounds listed in Table 3, molecules with Mo–Mo single bonds have bond lengths in the range 2.62–3.24 Å, while those with Mo=Mo double bonds have bond lengths in the range 2.58–2.62 Å.

4.2 Theoretical Calculations

While the Mo–Mo bond length of $[\text{Cp}^*\text{Mo}(\mu\text{-O}_2\text{CMe})_2(\mu\text{-PMe}_2)(\mu\text{-Me})]$ is consistent with a single bond, thereby supporting the $\mu\text{-LX}$ “half-arrow” electron-counting method for evaluating M–M bond orders, the serious limitations associated with bond length/bond order correlations in systems with bridging ligands mean

Table 3 Mo–Mo bond lengths and formal bond orders in dinuclear cyclopentadienyl molybdenum complexes and related derivatives (compiled data taken from reference 6)

	$d_{\text{Mo}\cdots\text{Mo}}/\text{\AA}$	Mo–Mo bond order: [μ -LX] “half- arrow” method	Mo–Mo bond order: “half-electron” method
[CpMo(CO) ₂] ₂ (μ -PMe ₂)(μ -H)	3.267(2)	0	1
[CpMo(CO) ₂] ₂ (μ -PBu ₂ ^t)(μ -H)	3.247(1)	0	1
[CpMo(CO) ₂] ₂ (μ -PPh ₂)(μ -H)	3.244(1)	0	1
[CpMo(CO) ₂] ₂ (μ -PPhEt)(μ -H)	3.278(1)	0	1
[CpMo(CO) ₂] ₂ (μ -P{C ₆ H ₂ Bu ₂ ^t - CMe ₂ CH ₃ })(μ -H)	3.250(1)	0	1
[CpMo(CO) ₃] ₂	3.235(1)	1	1
{[CpMo(CO) ₂] ₂ (μ -PMe ₂)} ⁻	3.157(2)	1	1
{[CpMo(CO) ₂] ₂ (μ -PPh ₂)} ⁻	3.185(1)	1	1
[Cp*Mo(μ -O ₂ CMe)] ₂ (μ -PMe ₂)- (μ -Me)	2.8447(5)	1	2
[Cp ^{i-Pr} Mo(μ -Cl)] ₂	2.607(1)	1	1
[Cp*Mo(μ -Br)] ₂	2.643(2)	1	1
[Cp*Mo(μ -I)] ₂	2.708(3)	1	1
[(C ₅ Me ₄ Et)Mo] ₂ (μ -Cl) ₃ (μ -PPh ₂)	2.6388(8)	1	1
[CpMo(μ -SMe)] ₂	2.603(2)	1	1
[(Cp ^{Me₄Et})Mo(μ -SMe)] ₂	2.616(1)	1	1
[(Cp ^{Me})Mo(μ -S)(μ -SMe)] ₂	2.582(1)	2	2
[Cp*Mo(μ -S)(μ -SH)] ₂	2.573(1)	2	2
[Cp*Mo(μ -S)(μ -SMe)] ₂	2.573(1)	2	2
[CpMo(μ -S)] ₂ (μ -SPR ⁱ)(μ -PPh ₂)	2.623(2)	2	2
[CpMo(CO)] ₂	2.448(1)	3	3
[IndMo(CO)] ₂	2.500(1)	3	3

that it is essential to analyze the Mo–Mo bond order by using theoretical methods. Therefore, calculations were performed on [Cp*Mo(μ -O₂CMe)]₂(μ -PMe₂)(μ -Me) and the computationally simpler [CpMo(μ -O₂CH)]₂(μ -PH₂)(μ -H) compound in which all methyl groups were replaced by hydrogen atoms [6]. For comparison purposes, the chloride derivative [CpMo(μ -O₂CH)]₂(μ -PH₂)(μ -Cl) was also investigated because it represents a compound with an unambiguous (in the sense that both electron-counting methods predict the same bond order) Mo–Mo single bond.

4.2.1 Bond Order Calculations

A variety of protocols exist for evaluating bond orders in molecules [48] and the bonding in [Cp*Mo(μ -O₂CMe)]₂(μ -PMe₂)(μ -Me) and [CpMo(μ -O₂CH)]₂(μ -PH₂)(μ -X) was assessed using the Mayer bond order [49], that has also been used in other inorganic systems [50, 51]. The Mayer bond orders for a series of dimolybdenum compounds are summarized in Table 4, which provide several important comparisons. Firstly, the Mayer bond order of 0.72 for [Cp*Mo-

Table 4 Comparison of calculated bond orders for a series of dinuclear molybdenum compounds with those predicted by two alternative electron-counting methods. In each case, the bond order predicted by the $[\mu\text{-LX}]$ “half-arrow” method corresponds exactly to that derived by consideration of the orbital occupations, whereas the “half-electron” method fails for compounds with bridging hydride and methyl ligands. Data taken from reference 6

	$d_{\text{Mo}\cdots\text{Mo}}$ /Å	Mayer bond index <i>M</i>	Mo–Mo configuration and calculated bond order	electron count bond order: $[\mu\text{-LX}]$ “half- arrow” method	electron count bond order: “half-electron” method
$\{[\text{CpMo}(\mu\text{-O}_2\text{CH})_2(\mu\text{-PH}_2)(\mu\text{-H})]^{2-}$	3.07	0.45	$\sigma^2\delta^2\delta^{*2}\pi^{*2}$, BO = 0	0	1
$[\text{Cp}^*\text{Mo}(\mu\text{-O}_2\text{CMe})_2(\mu\text{-PMe}_2)(\mu\text{-Me})$	2.88	0.72	$\sigma^2\delta^2\delta^{*2}$, BO = 1	1	2
$[\text{CpMo}(\mu\text{-O}_2\text{CH})_2(\mu\text{-PH}_2)(\mu\text{-H})$	2.77	0.97	$\sigma^2\delta^2\delta^{*2}$, BO = 1	1	2
$[\text{CpMo}(\mu\text{-O}_2\text{CH})_2(\mu\text{-PH}_2)(\mu\text{-Cl})$	2.91	0.78	$\sigma^2\delta^2\delta^{*2}$, BO = 1	1	1
$\{[\text{CpMo}(\mu\text{-O}_2\text{CH})_2(\mu\text{-PH}_2)]^-$	2.64	1.53	$\sigma^2\delta^2\pi^2\delta^{*2}$, BO = 2	2	2
$\{[\text{Cp}^*\text{Mo}(\mu\text{-O}_2\text{CMe})_2(\mu\text{-PMe}_2)(\mu\text{-Me})]^{2+}$	2.81	1.17	$\sigma^2\delta^2$, BO = 2	2	3
$\{[\text{CpMo}(\mu\text{-O}_2\text{CH})_2(\mu\text{-PH}_2)(\mu\text{-H})]^{2+}$	2.67	1.52	$\sigma^2\delta^2$, BO = 2	2	3
$\{[\text{CpMo}(\mu\text{-O}_2\text{CH})_2(\mu\text{-PH}_2)(\mu\text{-Cl})]^{2+}$	2.83	1.23	$\sigma^2\delta^2$, BO = 2	2	2
$\{[\text{CpMo}(\mu\text{-O}_2\text{CH})_2(\mu\text{-PH}_2)]^+$	2.35	2.38	$\sigma^2\delta^2\pi^2$, BO = 3	3	3

$(\mu\text{-O}_2\text{CMe})_2(\mu\text{-PMe}_2)(\mu\text{-Me})$ is comparable to the value of 0.97 for the bridging hydride derivative $[\text{CpMo}(\mu\text{-O}_2\text{CH})_2(\mu\text{-PH}_2)(\mu\text{-H})$, both of which are too low to be considered as double bonds. Secondly, the Mayer bond order for $[\text{CpMo}(\mu\text{-O}_2\text{CH})_2(\mu\text{-PH}_2)(\mu\text{-Cl})$ is 0.78, which serves as a reference point for an undisputed formal Mo–Mo single bond. On this basis, the Mayer bond orders support the assignment of a single Mo–Mo bond to each of these complexes and thus indicate that the Mo–Mo bond order is best predicted by using the $\mu\text{-LX}$ “half-arrow” electron-counting protocol.

Additional evidence for the assignment of formal Mo–Mo single bonds to $[\text{Cp}^*\text{Mo}(\mu\text{-O}_2\text{CMe})_2(\mu\text{-PMe}_2)(\mu\text{-Me})$, $[\text{CpMo}(\mu\text{-O}_2\text{CH})_2(\mu\text{-PH}_2)(\mu\text{-H})$ and $[\text{CpMo}(\mu\text{-O}_2\text{CH})_2(\mu\text{-PH}_2)(\mu\text{-Cl})$ is provided by comparison with $\{[\text{CpMo}(\mu\text{-O}_2\text{CH})_2(\mu\text{-PH}_2)]^-\}$, a convenient reference point for an Mo=Mo double bond since both electron-counting methods assign the same bond order. Thus, the Mayer bond order for $\{[\text{CpMo}(\mu\text{-O}_2\text{CH})_2(\mu\text{-PH}_2)]^-\}$ (1.53) is notably greater than the values for $[\text{Cp}^*\text{Mo}(\mu\text{-O}_2\text{CMe})_2(\mu\text{-PMe}_2)(\mu\text{-Me})$ (0.72), $[\text{CpMo}(\mu\text{-O}_2\text{CH})_2(\mu\text{-PH}_2)(\mu\text{-H})$ (0.97), and $[\text{CpMo}(\mu\text{-O}_2\text{CH})_2(\mu\text{-PH}_2)(\mu\text{-Cl})$ (0.78). Correspondingly, the cation $\{[\text{CpMo}(\mu\text{-O}_2\text{CH})_2(\mu\text{-PH}_2)]^+\}$, provides a reference point for an undisputed formal Mo \equiv Mo triple bond and, as expected, the Mayer bond order for

$\{[\text{CpMo}(\mu\text{-O}_2\text{CH})_2(\mu\text{-PH}_2)]_2\}^+$ (2.38) is substantially greater than that for $\{[\text{CpMo}(\mu\text{-O}_2\text{CH})_2(\mu\text{-PH}_2)]_2\}^-$ (1.53).

In addition to a progressive increase in Mayer bond order across the series of compounds with well-defined Mo–Mo single, double, and triple bonds, the Mo–Mo bond lengths decrease in the same sequence: $[\text{CpMo}(\mu\text{-O}_2\text{CH})_2(\mu\text{-PH}_2)(\mu\text{-Cl})]$ (2.91 Å), $\{[\text{CpMo}(\mu\text{-O}_2\text{CH})_2(\mu\text{-PH}_2)]_2\}^-$ (2.64 Å), and $\{[\text{CpMo}(\mu\text{-O}_2\text{CH})_2(\mu\text{-PH}_2)]_2\}^+$ (2.35 Å). The same inverse relationship between Mayer bond order and bond length is also observed upon comparing dianionic, neutral, and dicationic forms of $\{[\text{CpMo}(\mu\text{-O}_2\text{CH})_2(\mu\text{-PH}_2)(\mu\text{-H})]_2\}^{\text{Q}\pm}$, namely $\{[\text{CpMo}(\mu\text{-O}_2\text{CH})_2(\mu\text{-PH}_2)(\mu\text{-H})]_2\}^{2-}$ (0.45, 3.07 Å), $[\text{CpMo}(\mu\text{-O}_2\text{CH})_2(\mu\text{-PH}_2)(\mu\text{-H})]$ (0.97, 2.77 Å), and $\{[\text{CpMo}(\mu\text{-O}_2\text{CH})_2(\mu\text{-PH}_2)(\mu\text{-H})]_2\}^{2+}$ (1.52, 2.67 Å), which have formal Mo–Mo bond orders of 0, 1, and 2, respectively.

4.2.2 Molecular Orbital Analyses

Molecular orbital (MO) analyses also provide a useful means to establish M–M bond orders. Prior to discussing the hydride-bridged compound, $[\text{CpMo}(\mu\text{-O}_2\text{CH})_2(\mu\text{-PH}_2)(\mu\text{-H})]$, however, it is first instructive to evaluate the deprotonated species $\{[\text{CpMo}(\mu\text{-O}_2\text{CH})_2(\mu\text{-PH}_2)]_2\}^-$ for which an Mo=Mo double bond is predicted by both electron-counting methods. In this regard, it is significant that the Mo...Mo interaction in $\{[\text{CpMo}(\mu\text{-O}_2\text{CH})_2(\mu\text{-PH}_2)]_2\}^-$ corresponds to a $\sigma^2(\delta)^2(\pi)^2(\delta^*)^2$ configuration (Figs. 11 and 12), i.e., a formal Mo=Mo double bond consisting of one σ and one π bond.

The molecular orbital diagram for the bridging hydride complex may be formally constructed by protonating $\{[\text{CpMo}(\mu\text{-O}_2\text{CH})_2(\mu\text{-PH}_2)]_2\}^-$. In this analysis, only the π bonding molecular orbital [MO <59>] of $\{[\text{CpMo}(\mu\text{-O}_2\text{CH})_2(\mu\text{-PH}_2)]_2\}^-$ has the appropriate symmetry and sufficient overlap with the empty 1s orbital of the proton fragment to give a significant electronic interaction, thereby giving rise to a 3-center Mo–H–Mo bonding orbital [MO <46>] and an antibonding orbital [MO <69>] (Fig. 13).

Since the π bonding molecular orbital [MO <59>] of $\{[\text{CpMo}(\mu\text{-O}_2\text{CH})_2(\mu\text{-PH}_2)]_2\}^-$ becomes involved in the 3-center Mo–H–Mo interaction, only three metal-dominated MOs remain occupied in $[\text{CpMo}(\mu\text{-O}_2\text{CH})_2(\mu\text{-PH}_2)(\mu\text{-H})]$, as shown in Fig. 11, resulting in a $\sigma^2(\delta)^2(\delta^*)^2$ configuration that is most consistent with an Mo–Mo *single* bond, in accord with that predicted by using $\mu\text{-LX}$ “half-arrow” electron-counting method.

Consideration of Fig. 11 indicates how the π -bond component of the double bond in $\{[\text{CpMo}(\mu\text{-O}_2\text{CH})_2(\mu\text{-PH}_2)]_2\}^-$ is destroyed as a consequence of removal of the π -bond electron density upon protonation. In this regard, 3-center-2-electron M–H–M interactions are often referred to as protonated metal–metal bonds. However, with respect to the last description, it must be emphasized that the “metal–metal bond” component is no longer the same as that in the deprotonated fragment, i.e., it is *not* a 2-center-2-electron bond. A simplified MO diagram which illustrates the concept that protonation reduces the M–M bond order for a general situation is provided in Fig. 14.

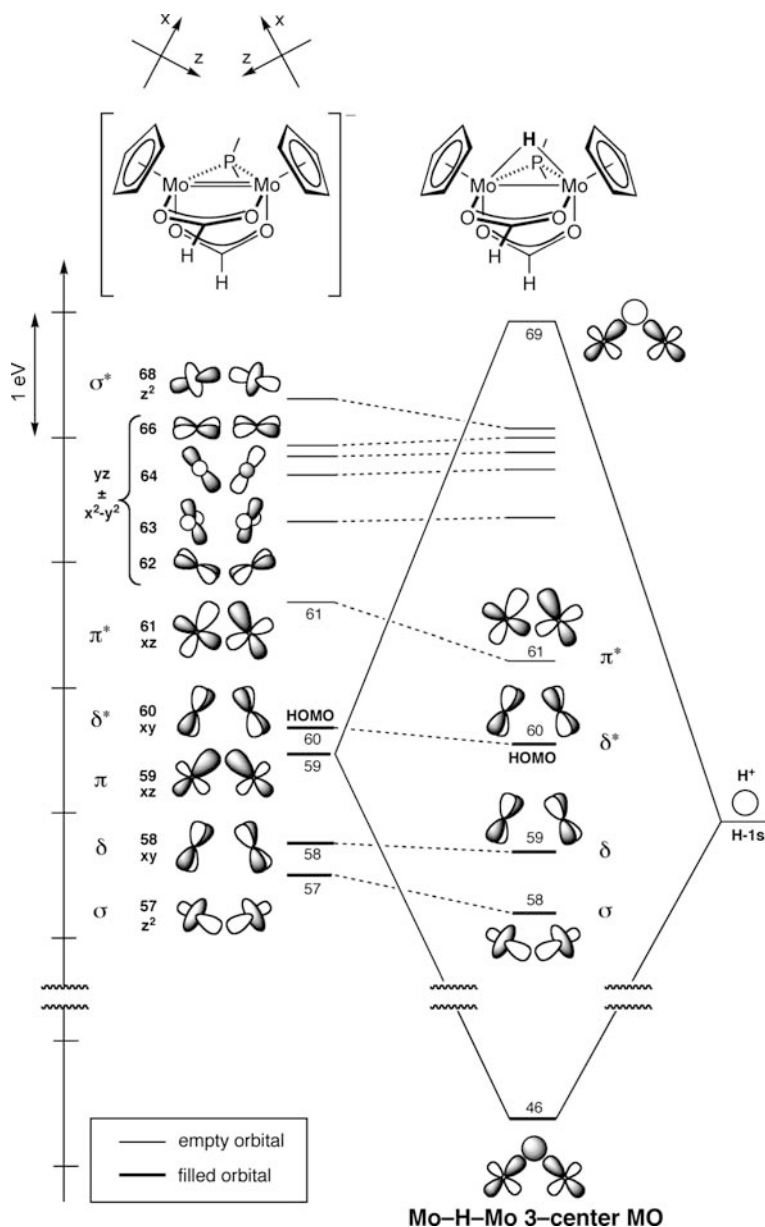


Fig. 11 MO diagram for $[\text{CpMo}(\mu\text{-O}_2\text{CH})_2(\mu\text{-PH}_2)(\mu\text{-H})]$ derived from $\{[\text{CpMo}(\mu\text{-O}_2\text{CH})_2(\mu\text{-PH}_2)]^-\}$ and H^+ fragments. Modified from reference 6

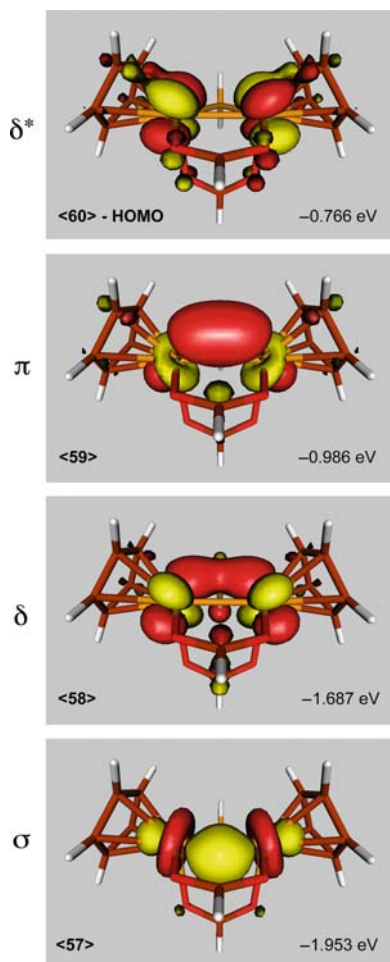


Fig. 12 Molecular orbitals corresponding to the direct Mo–Mo interaction in $\{[\text{CpMo}(\mu\text{-O}_2\text{CH})_2(\mu\text{-PH}_2)]\}^-$. The $\sigma^2(\delta)^2(\pi)^2(\delta^*)^2$ configuration corresponds to a formal Mo=Mo double bond. Taken from reference 6

5 Application of the μ -LX “Half-Arrow” Electron-Counting Method to Other Compounds

Consideration of both the Mayer bond order analysis and the molecular orbital analysis indicates that the Mo–Mo bond order predicted by the μ -LX “half-arrow” method for $[\text{CpMo}(\mu\text{-O}_2\text{CH})_2(\mu\text{-PH}_2)(\mu\text{-H})]$ is much more in accord with the theoretical calculations than is the bond order of two predicted by the “half-electron” method. A variety of other studies support the use of the μ -LX “half-arrow” electron-counting method for predicting M–M bond orders in dinuclear compounds [52–59]. In particular, Hoffmann and Albright have used MO theory to analyze the

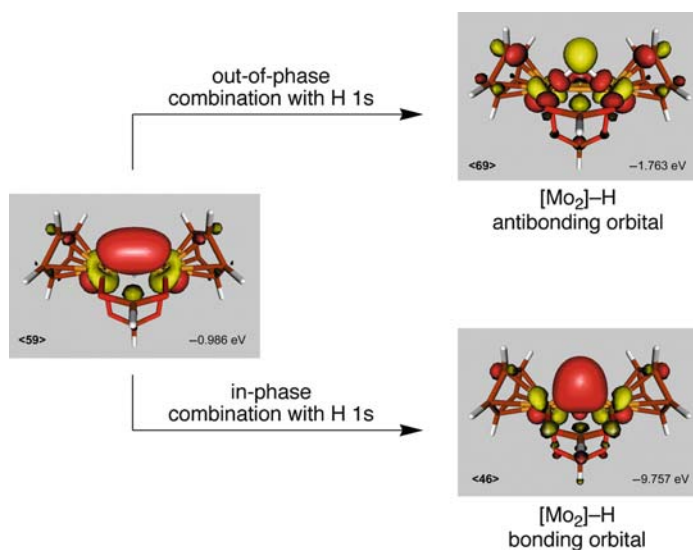


Fig. 13 Mo–H Bonding and antibonding orbitals derived by interaction of the H^+ 1s orbital with the Mo–Mo π -bonding orbital of $\{[\text{CpMo}(\mu\text{-O}_2\text{CH})_2(\mu\text{-PH}_2)]^-\}$. Taken from reference 6

bonding in dinuclear compounds that contain two, three, and four bridging hydride ligands [52, 53]. Illustrative MO diagrams are presented in Figs. 15–17, from which it is evident that the direct M–M bond orders are in accord with those predicted by the $\mu\text{-LX}$ “half-arrow” electron-counting method. For example, the MO diagram of $\{[(\text{CO})_4\text{W}(\mu\text{-H})_2]^{2-}\}$, with two 3-center-2-electron W–H–W bridges, indicates that the direct W–W interaction possesses a $\pi^2(\delta)^2(\delta^*)^2(\pi^*)^2$ configuration (Fig. 15), which corresponds to a formal bond order of zero and not the bond order of two that is predicted by the “half-electron” method. Subsequent calculations on a series of isoelectronic $[(\text{CO})_4\text{M}(\mu\text{-H})_2]^{Q\pm}$ compounds agree with the assigned bond order of zero: “there is practically no direct M–M bond in the chromium, molybdenum, manganese [*sic*], rhenium and tungsten carbonyl dimers with double hydrogen bridges. The metal atoms are bonded exclusively through the hydrogen bridge” [55]. The following sections describe the analysis of the M–M bond order in a variety of dinuclear compounds that are classified according to the number of bridging hydride ligands.

5.1 Dinuclear Compounds with Single Hydrogen Bridges

$\{[(\text{CO})_5\text{M}]_2(\mu\text{-H})\}^-$ ($\text{M} = \text{Cr}, \text{Mo}, \text{W}$) [11] represents a classic series of complexes with single 3-center-2-electron M–H–M interactions for which the “half-electron” method predicts an M–M single bond, whereas the $\mu\text{-LX}$ “half-arrow” method

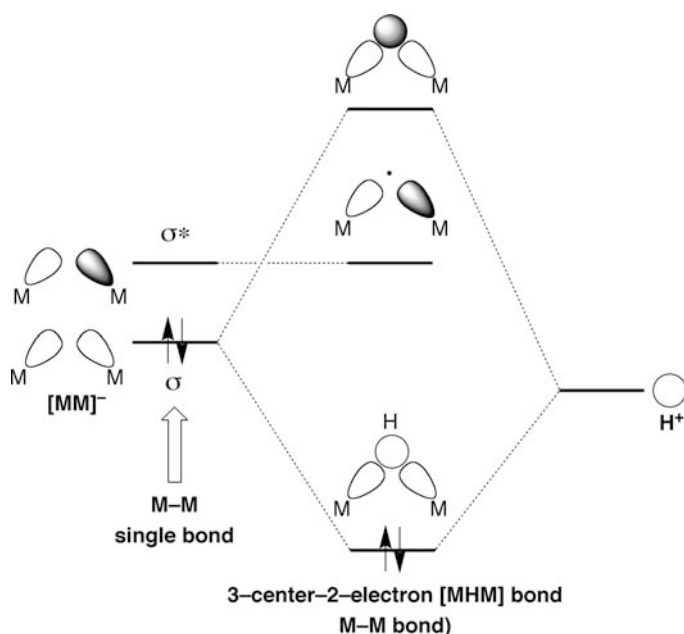


Fig. 14 Molecular orbital description of a [MHM] species derived by interaction of $[M_2]^-$ and H^+ fragments in which each atom uses a single orbital. Protonation of the $[M_2]^-$ fragment results in the interaction of the H 1s orbital with the M–M bonding orbital, thereby forming the 3-center-2-electron M–H–M bonding and antibonding orbitals. The M–M antibonding orbital does not have the appropriate symmetry to interact with the H 1s orbital and thus remains M–H nonbonding. If the $[M_2]^-$ fragment possesses two electrons only the M–M bonding orbital is occupied and there is an M–M bond order of one; upon protonation these electrons occupy the 3-center-2-electron M–H–M bonding orbital and the direct M–M bond is eradicated. Modified from reference 6

indicates that there is no 2-center-2-electron M–M interaction (Fig. 18). Indeed, early molecular orbital calculations on these complexes are in accord with the notion that there is no direct M–M bond and that the interactions are mediated by the hydride bridge [52]. Furthermore, recent experimental and theoretical studies also indicate that there is *no direct metal–metal bond path* in the chromium complex $\{[(CO)_5Cr]_2(\mu-H)\}^-$ [60,61].

In 1965 Dahl reported the first structure of a transition metal complex with a bridging hydride ligand, namely $[CpMo(CO)_2]_2(\mu-PM_e_2)(\mu-H)$ [12, 13]. Discussing the bonding in this complex, Dahl stated that “the bent, three-center Mo–H–Mo bond involving one electron from the two molybdenum atoms and one from the hydrogen accounts for the compound’s diamagnetism without the invoking of a separate Mo–Mo bond” [12]. Despite this early description of the bonding interaction, closely related $[CpMo(CO)_2]_2(\mu-PRR')(\mu-H)$ derivatives have been represented with direct Mo–Mo bonds [62–64]. Application of the μ -LX “half-arrow” electron-counting method, however, predicts an Mo–Mo bond (Fig. 17), in accord with Dahl’s description.

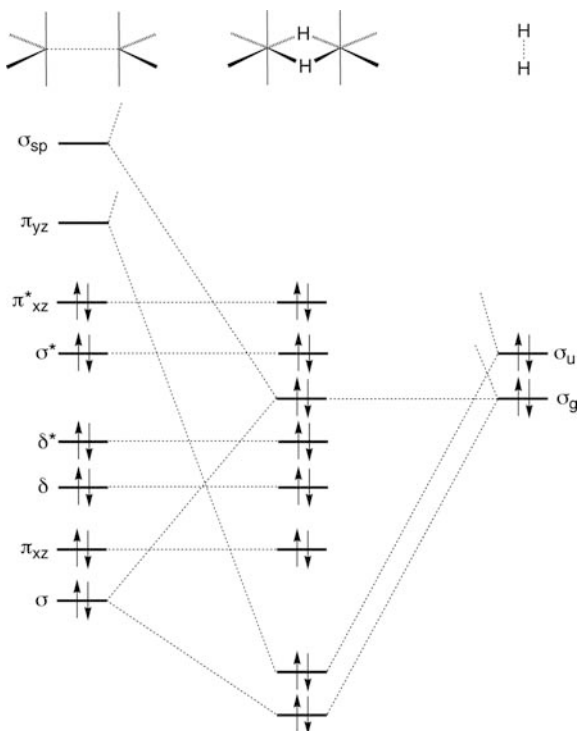


Fig. 15 Molecular orbital diagram for $[L_4M]_2(\mu-H)_2$, adapted from reference 52. The electron count shown corresponds to species such as $\{[(CO)_4W]_2(\mu-H)_2\}^{2-}$

$[CpMo(CO)]_2(\mu-PCy_2)(\mu-H)$ is a counterpart to $[CpMo(CO)]_2(\mu-PRR')(\mu-H)$ which features only a single carbonyl ligand on each molybdenum center and was described as possessing an $Mo \equiv Mo$ triple bond [65–70]. Application of the μ -LX “half-arrow” electron-counting method, however, predicts an $Mo=Mo$ double bond, a result that is in accord with density functional theory calculations which indicate that the bonding consists of one 3-center-2-electron $Mo-H-Mo$ interaction and two 2-center-2-electron $Mo-Mo$ bonds [65].

Other compounds that feature a single $M-H-M$ bridge and which have also been described as possessing $M \equiv M$ triple bonds include $[CpMo(CO)(SnPh_3)](\mu-H)-[CpMo(CO)(PHCy_2)]$ [71] and $\{[CpW(CO)]_2(\mu-H)(\mu-R_2PCH_2PR_2)\}^+$ [72, 73]. Each of these compounds, however, is predicted to possess an $M=M$ double bond according to the μ -LX “half-arrow” procedure. Likewise, $[M(CO)_2]_2(\mu-PBu_2^t)(\mu-dppm)_2(\mu-H)$ ($M = Fe, Ru$) are examples of compounds that were assigned $M=M$ double bonds [45], but subsequent calculations indicate that there is a single $M-M$ bond [74] in accord with that predicted by the μ -LX “half-arrow” procedure. The μ -LX “half-arrow” notation was also applied to $[Cp^*Ru]_2(\mu-H)(\mu-PHPh)(\mu-CO)$, which thereby predicts a direct $Ru-Ru$ single bond [75].

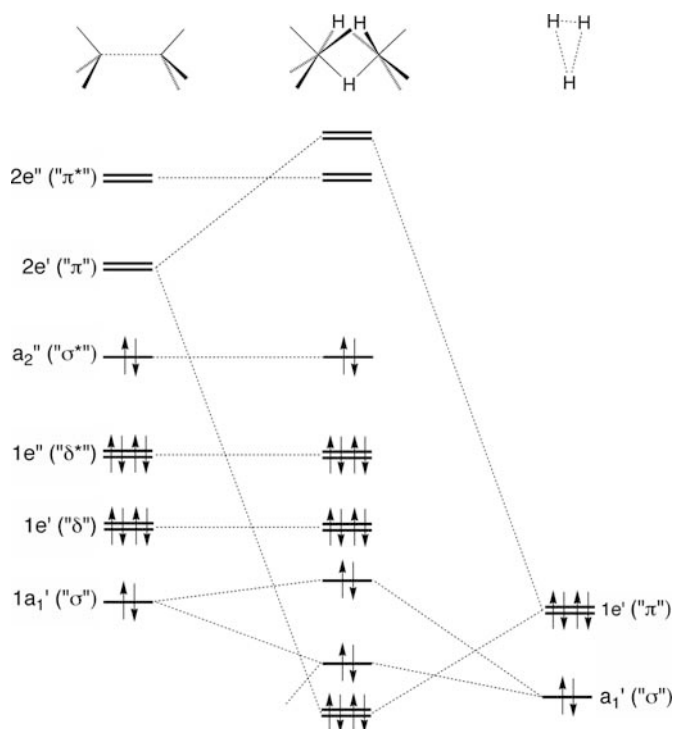


Fig. 16 Molecular orbital diagram for $[L_3M]_2(\mu-H)_3$. Adapted from references 15 and 53. The electron count shown corresponds to species such as $\{[(R_3P)_3Fe]_2(\mu-H)_3\}^+$ and $\{[(R_3P)_3Re]_2(\mu-H)_3\}^-$.

5.2 Dinuclear Compounds with Double Hydrogen Bridges

Consideration of compounds with two hydrogen bridges also provides support for the use of the “half-arrow” method in predicting M–M bond orders. For example, photoelectron spectroscopic studies on $Os_3(CO)_{10}(\mu-H)_2$, and related bridging hydride complexes, have been interpreted with the $M(\mu-H)M$ bonding orbital as being localized principally on the hydrogen atom, rather than on the metal atoms [76–78]. As such, it is not appropriate to view the interaction as comprising an $Os=Os$ double bond in which the electron density resides primarily between the osmium atoms. Indeed, calculations on $Os_3(CO)_{10}(\mu-H)_2$ are consistent with the major interaction between the two osmium centers being *via* the two 3-center-2-electron $Os-H-Os$ bonds [79]. The μ -LX “half-arrow” method predicts that there is no 2-center-2-electron $Os-Os$ interaction in $Os_3(CO)_{10}(\mu-H)_2$ (Fig. 1, E & F), a result that is much more in accord with the aforementioned experimental and theoretical studies than is the $Os=Os$ double bond (Fig. 1, A) that is predicted by the “half-electron” method.

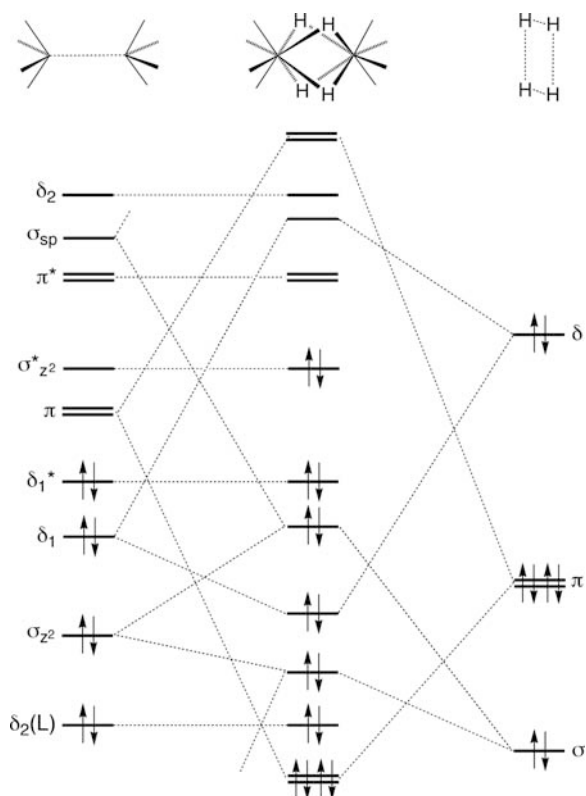


Fig. 17 Molecular orbital diagram for $[L_4M]_2(\mu-H)_4$, adapted from reference 15. The electron count shown corresponds to species such as $[(R_3P)_4Re]_2(\mu-H)_4$

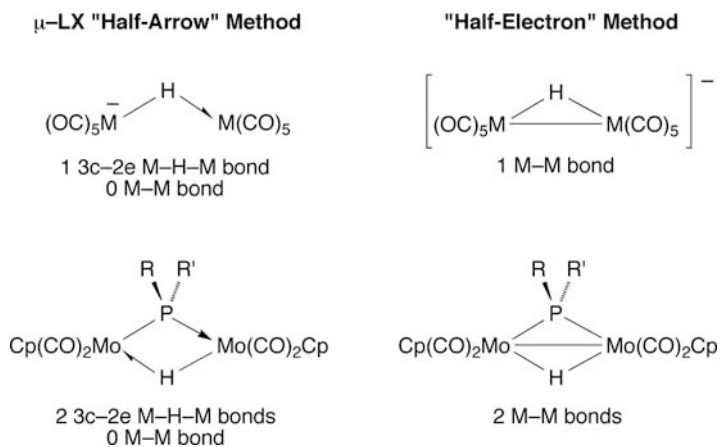


Fig. 18 Examples of dinuclear complexes with a single hydrogen bridge (M = Cr, Mo, W)

The cyclopentadienyl compound $[\text{Cp}^*(\text{CO})\text{Os}]_2(\mu\text{-H})_2$ contains a similar $[\text{Os}_2\text{H}_2]$ unit that has also been reported to have a $\text{Os}=\text{Os}$ double bond [80]; by analogy to $\text{Os}_3(\text{CO})_{10}(\mu\text{-H})_2$, however, the direct 2-center-2-electron $\text{Os}\text{-Os}$ bond order is reduced to zero upon consideration of the 3-center-2-electron nature of the two $\text{Os}\text{-H}\text{-Os}$ interactions. Likewise, the ruthenium counterpart $[\text{Cp}^*(\text{CO})\text{Ru}]_2(\mu\text{-H})_2$ is best represented as possessing two 3-center-2-electron $\text{Ru}\text{-H}\text{-Ru}$ interactions with no direct $\text{Ru}\text{-Ru}$ bond, rather than having an $\text{Ru}=\text{Ru}$ double bond [81]. Isoelectronic cyclopentadienyl tungsten dicarbonyl compounds, namely $[\text{Cp}^*\text{W}(\text{CO})_2]_2(\mu\text{-H})_2$ and $[\text{Cp}^*\text{W}(\text{CO})_2]_2(\mu\text{-H})_2$, have also been reported and were described as the first doubly hydrido-bridged neutral complexes which formally possess a $\text{W}=\text{W}$ double bond [82]. A better description, however, is that the bonding interaction simply consists of two 3-center-2-electron $\text{W}\text{-H}\text{-W}$ interactions with no direct $\text{W}\text{-W}$ bond. Correspondingly, rather than possessing an $\text{Mn}=\text{Mn}$ double bond [83], the manganese complex $[(\text{CO})_3\text{Mn}]_2(\mu\text{-dppm})(\mu\text{-H})_2$ is best described as possessing no direct $\text{Mn}\text{-Mn}$ bond.

$[(\text{Me}_2\text{PhP})_3\text{HOs}(\mu\text{-H})_2]$ provides another example of an osmium compound that was assigned an $\text{Os}=\text{Os}$ double bond [84, 85], but is better represented as possessing two 3-center-2-electron $\text{Os}\text{-H}\text{-Os}$ interactions. The ruthenium counterpart $[(\text{Me}_3\text{P})_3\text{HRu}]_2(\mu\text{-H})_2$ has also been reported [86], and although an $\text{Ru}\text{-Ru}$ bond order was not assigned, a direct bond order of zero would be predicted by the $\mu\text{-LX}$ “half-arrow” method. Moreover, calculations indicate that $[(\text{CO})_4\text{Re}]_2(\mu\text{-H})_2$ is predicted to have effectively no direct $\text{Re}\text{-Re}$ interaction [55], rather than the double bond that was initially reported in order to satisfy the 18-electron rule [25].

Compounds with two bridging hydrogen atoms have also been reported to have $\text{M}\equiv\text{M}$ triple bonds, e.g. $[\text{Cp}^*\text{Ru}]_2(\mu\text{-CO})(\mu\text{-H})_2$ [81, 89]. However, this complex is predicted to have an $\text{Ru}\text{-Ru}$ single bond according to the $\mu\text{-LX}$ “half-arrow” electron-counting method. Likewise, although an $\text{Re}\equiv\text{Re}$ triple bond was invoked for $[\text{CpReH}_2]_2(\mu\text{-H})_2$, calculations indicate that the electronic configuration is $(\sigma/\delta)^2(\pi^*)^2(\delta^*)^2$, i.e., a direct $\text{Re}\text{-Re}$ bond order of one [87].

An illustrative example of the confusion that may ensue when evaluating $\text{M}\text{-M}$ bond orders in the presence of bridging hydride ligands is provided by the descriptions that have been provided for the bonding in $[(\eta^6\text{-C}_6\text{H}_6)\text{Re}]_2(\mu\text{-H})_2(\mu\text{-CHR})$ [88]. This complex was originally assigned an $\text{Re}\text{-Re}$ single bond [88], a bond order assignment that takes fully into account the 3-center-2-electron nature of the interaction and was also supported by an MO analysis. Nevertheless, despite the theoretical basis for an $\text{Re}\text{-Re}$ single bond in this complex, a subsequent report refuted the assigned bond order and claimed that the correct bond order is actually three [89]. However, since the latter claim was not supported by theoretical calculations, there is no reason to accept the proposed modification and the original assignment of an $\text{Re}\text{-Re}$ single bond should be retained.

The $\text{Mo}\text{-Mo}$ distance (2.19 Å) in $[(\text{Me}_3\text{P})_3\text{HMo}]_2(\mu\text{-H})_2$ was described as being “well in the region of values found for quadruply bonded $\text{Mo}^{\text{II}}\text{-Mo}^{\text{II}}$ species” [90, 91]. Several descriptions of the bonding were evaluated for this molecule, but consideration of the 3-center-2-electron nature of the two $\text{Mo}\text{-H}\text{-Mo}$ interactions

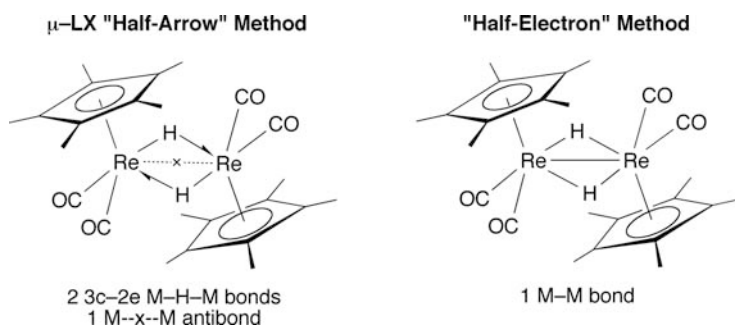


Fig. 19 $[\text{Cp}^*\text{Re}(\text{CO})_2]_2(\mu\text{-H})_2$, a compound that features an $\text{M}\text{-}\times\text{-}\text{M}$ antibonding interaction

[91] suggests that the compound is best described as possessing a direct $\text{Mo}=\text{Mo}$ double bond rather than a quadruple bond.

A particularly interesting situation arises when the “half-electron” method predicts an $\text{M}\text{-}\text{M}$ single bond for a compound with two bridging hydride ligands, as illustrated by $[\text{Cp}^*\text{Re}(\text{CO})_2]_2(\mu\text{-H})_2$ (Fig. 19). In this case, application of the $\mu\text{-LX}$ “half-arrow” method does *not* predict an 18-electron configuration for both metals. Specifically, neglecting the $\text{Re}\text{-}\text{Re}$ interaction, each rhenium center possesses a 19-electron configuration. Since the compound is diamagnetic, it is evident that the two 19-electron rhenium centers must interact, thereby resulting in a 20-electron configuration at each metal. Although transition metals with 20-electron configurations are known, they are not common and, on this basis, it could appear that the “half-electron” method provides a more reasonable answer. However, it must be emphasized that application of the formula $m = (18n - N)/2$ to predict the number of $\text{M}\text{-}\text{M}$ bonds *forces* each metal to have an 18-electron configuration, *regardless of the true electron configuration*. Thus, rather than being a failure of the method, the prediction of a 20-electron configuration is actually a strength of the $\mu\text{-LX}$ “half-arrow” electron counting since it indicates that a metal–metal *antibonding* orbital is occupied and, as a result, the $\text{M}\text{-}\text{M}$ bond order is reduced, a notion that has been discussed by Hoffmann [53], Dahl [13], Bursten [87] and Morokuma [92].

As a simple illustration, consider the hypothetical protonation of a dinuclear system in which there is no formal 2-center-2-electron $\text{M}\text{-}\text{M}$ bond because both bonding and antibonding components are occupied (Fig. 20). The hydrogen 1s orbital interacts specifically with the bonding component to form a 3-center-2-electron bond, thereby leaving a pair of electrons in an $\text{M}\text{-}\text{M}$ antibonding orbital. Casey has termed the resulting interaction an “antibond” [93]. The interaction may be depicted by using a crossed-dashed $\text{M}\text{-}\times\text{-}\text{M}$ representation, in which the cross emphasizes that the direct interaction is *antibonding*. Despite the presence of an “antibond,” the overall interaction may be favorable because of the stabilization resulting from the formation of the 3-center-2-electron bond [92].

The bonding situation within $[\text{Cp}^*\text{Re}(\text{CO})_2]_2(\mu\text{-H})_2$ has, therefore, been described by Casey as involving two 3-center-2-electron $\text{Re}\text{-}\text{H}\text{-}\text{Re}$ bonds and an $\text{Re}\text{-}\times\text{-}\text{Re}$ antibond, such that there is a *net* bond order of one [93]. While the

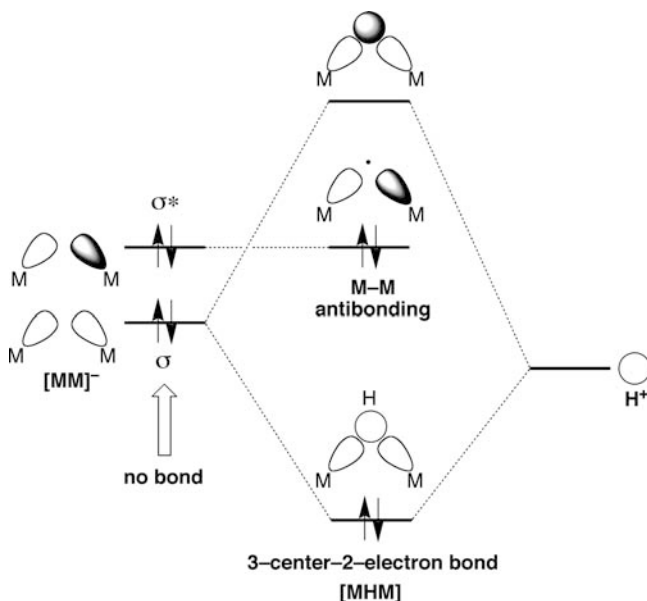


Fig. 20 Molecular orbital description of an M--x--M antibonding interaction in a [MHM] species derived by interaction of $[M_2]^-$ and H^+ fragments in which each atom uses a single orbital. Protonation of the $[M_2]^-$ fragment results in the interaction of the H 1s orbital with the M–M σ -bonding orbital, thereby forming a 3-center-2-electron M–H–M bonding orbital and leaving a pair of electrons in the M–M antibonding orbital. As such, the direct M–M interaction becomes repulsive, i.e. an *antibond*

notion of an M--x--M antibond may not be familiar, other compounds that feature M--x--M antibonds are known, as illustrated by $\{[(Ph_3P)_2HfIr]_2(\mu-H)_3\}^+$, $\{[MeC-(CH_2AsPh_2)_3Co]_2(\mu-H)_3\}^+$, $[(Et_2PhP)_2Re(H)_2]_2(\mu-H)_4$ and $[Cp^*Ru]_2(\mu-H)_4$, as discussed in more detail below.

Another example of a compound with two bridging hydride ligands that serves to point out the inadequacies of electron counting using the “half-electron” method is provided by $[Cp_2Zr(H)]_2(\mu-H)_2$, for which a Zr=Zr double bond is predicted. In contrast, the μ -LX “half-arrow” method indicates that each Zr center can attain an 18-electron configuration without forming two 2-center-2-electron Zr–Zr bonds (Fig. 21). The latter description is clearly preferable because the Zr center of mononuclear Cp_2ZrH_2 is d^0 and, as such, is incapable of forming a 2-center-2-electron Zr–Zr bond with the Zr center of another molecule.

5.3 Dinuclear Compounds with Triple Hydrogen Bridges

Compounds that feature three bridging hydride ligands are well precedented (Fig. 22) [53, 94] as illustrated by $\{[(Ph_3P)_2HfIr]_2(\mu-H)_3\}^+$, a compound that was originally described as possessing a direct $Ir \equiv Ir$ triple bond to satisfy the

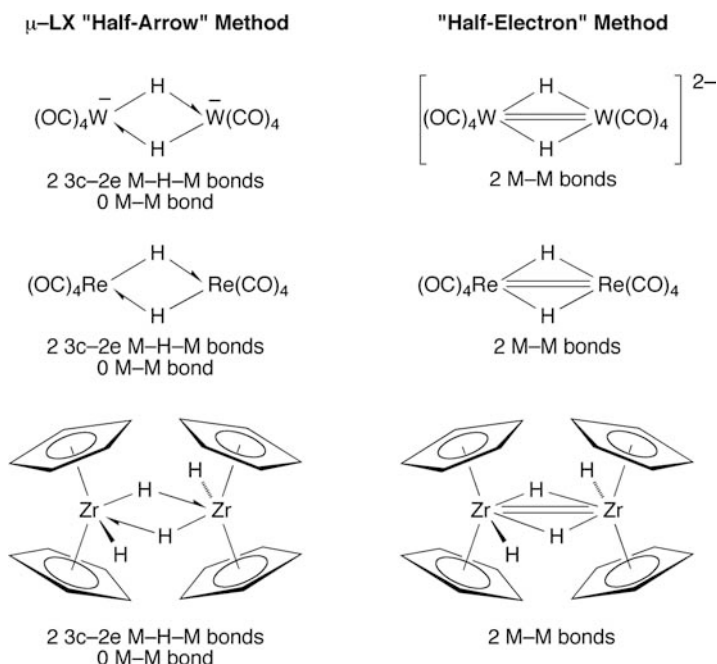


Fig. 21 Examples of dinuclear complexes with double hydrogen bridges

18-electron rule [95]. However, upon recognizing the 3-center-2-electron nature of the interaction, the compound was reformulated as having no direct Ir–Ir interaction and the shortness of the Ir···Ir separation is merely a consequence of there being three bridging hydrogen atoms [96]. In this regard, Bau provided a simple geometrical explanation for why $M\cdots M$ distances in $[M_2(\mu-H)_3]$ systems are invariably shorter than those in corresponding $[M_2(\mu-H)_2]$ systems. Specifically, if $[M_2(\mu-H)_3]$ and $[M_2(\mu-H)_2]$ correspond to two octahedra sharing a face and an edge, respectively, the centers of the two octahedra will be closer in the former case, assuming that the M–H distances are constant [94].

Compounds that are structurally related to bioctahedral $\{[(Ph_3P)_2HIr]_2(\mu-H)_3\}^+$ include isoelectronic $\{[(CO)_3Re]_2(\mu-H)_3\}^-$ [97], $\{[MeC(CH_2PPh_2)_3]Fe\}_2(\mu-H)_3\}^+$ [98], and $\{[(Me_2PhP)_3Os]_2(\mu-H)_3\}^+$ [85]. With three bridging hydride ligands, these compounds face the same bonding ambiguity noted for $\{[(Ph_3P)_2HIr]_2(\mu-H)_3\}^+$. For example, the iron complex $\{[MeC(CH_2PPh_2)_3]Fe\}_2(\mu-H)_3\}^+$ was reported to have an $Fe\equiv Fe$ triple bond [98], whereas the bonding in isoelectronic rhenium complex $\{[(CO)_3Re]_2(\mu-H)_3\}^-$ (which was actually the first dinuclear transition metal compound having three bridging hydride ligands) was described only in terms of 3-center-2-electron Re–H–Re bonds [97] in accord with the results of the μ -LX “half-arrow” electron-counting method.

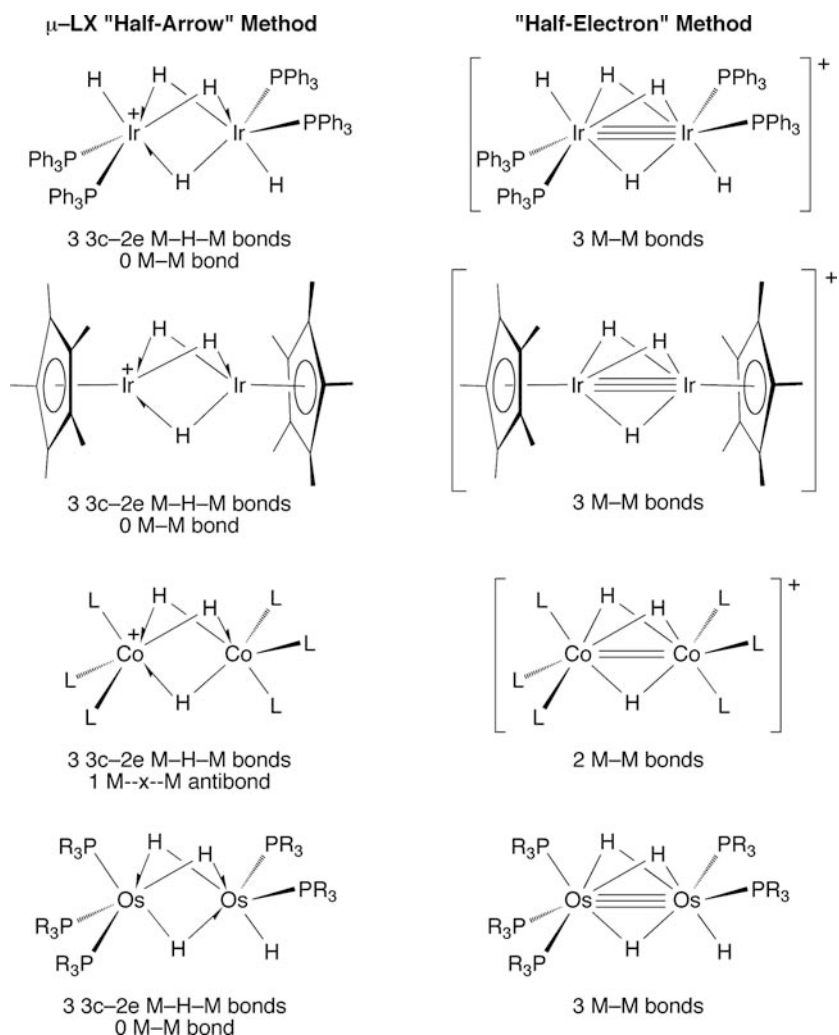


Fig. 22 Examples of dinuclear complexes with triple hydrogen bridges

Interestingly, $\{[(\text{Me}_3\text{P})_3\text{Ru}]_2(\mu\text{-H})_3\}^+$, which is isoelectronic with $\{[(\text{Me}_2\text{-PhP})_3\text{Os}]_2(\mu\text{-H})_3\}^+$ [84, 85], was originally suggested to have a possible Ru=Os double bond to achieve an 18-electron configuration [86], but it is not clear what electron-counting procedure would give this result. As a result, the Ru-Os interaction in this compound was subsequently reassigned to a triple bond [99], but it is actually best viewed as possessing only three 3-center-2-electron Ru-H-Os bonds.

The bonding in the arene complex $\{[(\eta^6\text{-C}_6\text{H}_6)\text{Ru}]_2(\mu\text{-H})_3\}^+$ has also been considered in terms of (1) an Ru \equiv Ru triple bond and (2) a situation involving 3-center-2-electron interactions [100, 101]. Of these, the latter was concluded to

be the more appropriate description on the basis of a comprehensive series of theoretical calculations which indicate that there is no direct bond between the two ruthenium atoms [100, 101]. Likewise, the isoelectronic cyclopentadienyl compound $\{[\text{Cp}^*\text{Ir}]_2(\mu\text{-H})_3\}^+$ does not possess a direct Ir–Ir bond, even though an Ir \equiv Ir triple bond was originally postulated [102].

For a similar reason to that described above for $[\text{Cp}^*\text{Re}(\text{CO})_2]_2(\mu\text{-H})_2$, an interesting situation arises when the “half-electron” method predicts an M=M double bond for a compound with three bridging hydride ligands. For example, the cobalt complex $\{[\text{MeC}(\text{CH}_2\text{AsPh}_2)_3\text{Co}]_2(\mu\text{-H})_3\}^+$ was originally proposed to have a Co=Co double bond [98], but application of the $\mu\text{-LX}$ “half-arrow” electron-counting method indicates that the cobalt centers of diamagnetic species would have 20-electron configurations, thereby indicating the occupation of a Co–Co *antibonding* orbital, a result that is in accord with theoretical calculations [52]. Thus, the bonding in $\{[\text{MeC}(\text{CH}_2\text{AsPh}_2)_3\text{Co}]_2(\mu\text{-H})_3\}^+$ is best described as comprising three 3-center-2-electron Co–H–Co interactions and a Co– \times –Co antibonding interaction.

While many compounds that feature three bridging hydride ligands are symmetric with respect to the nature of the metal center, asymmetric variants are also known, e.g., $\text{H}(\text{R}_3\text{P})_3\text{Re}(\mu\text{-H})_3\text{Re}(\text{PR}_3)_2\text{H}_2$ ($\text{PR}_3 = \text{PMe}_2\text{Ph}$) [84, 103] (Ph_3P)₂–(N_2)Ru($\mu\text{-H}$)₃Ru(PPh_3)₂H [99], and (R_3P)₃Os($\mu\text{-H}$)₃Os(PR_3)₂H($\text{PR}_3 = \text{PMe}_2\text{Ph}$ and PMePh_2) [84]. These compounds were proposed to have M \equiv M triple bonds, but application of the $\mu\text{-LX}$ “half-arrow” electron-counting method predicts that 18-electron configurations for these complexes can be obtained without any direct 2-center-2-electron bond in these complexes (Fig. 22). Furthermore, $[\text{Cp}^*\text{ReH}_2](\mu\text{-H})_3[\text{RuCp}^*]$ and $[\text{MeC}(\text{CH}_2\text{PPh}_2)_3\text{ReH}](\mu\text{-H})_3[\text{RuCp}^*]$ were described as possessing M \equiv M triple bonds to attain an 18-electron configuration [104], but 18-electron configurations can also be obtained by application of the $\mu\text{-LX}$ “half-arrow” electron-counting method, without the need for a direct metal-metal bond.

5.4 Dinuclear Compounds with Quadruple Hydrogen Bridges

The above discussion concerned with $[\text{Cp}^*\text{Re}(\text{CO})_2]_2(\mu\text{-H})_2$ and $\{[\text{MeC}(\text{CH}_2\text{AsPh}_2)_3\text{Co}]_2(\mu\text{-H})_3\}^+$ indicated that M– \times –M antibonding interactions result whenever the $\mu\text{-LX}$ “half-arrow” electron-counting method predicts both metal centers to have a 20-electron configuration. It is also evident that this situation will arise whenever there are more bridging hydride ligands than M–M bonds predicted by the “half-electron” method, a circumstance that is likely to occur whenever there are four bridging hydride ligands.

An excellent illustration is provided by the tetrahydride-bridged ruthenium complex $[\text{Cp}^*\text{Ru}]_2(\mu\text{-H})_4$ which, on the basis of electron counting according to the “half-electron” method, was proposed to have an Ru \equiv Ru triple bond (Fig. 23) [105]. This description of the bonding, however, was called into question by Morokuma who noted that “the Ru atoms do not have enough atomic orbitals to form so

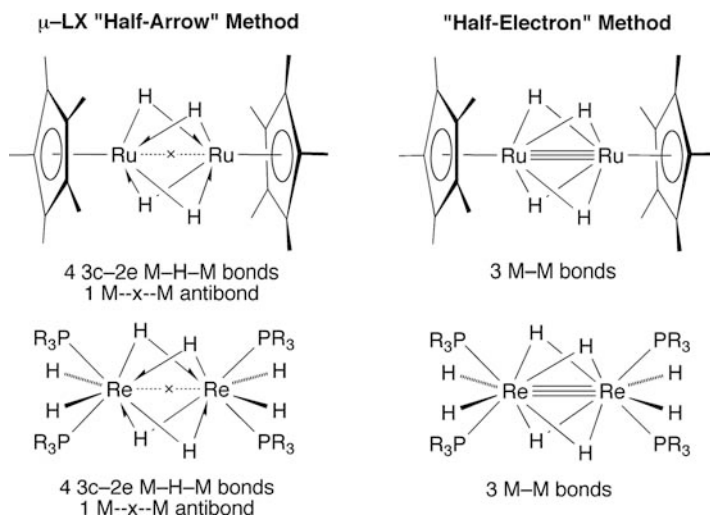


Fig. 23 Examples of dinuclear complexes with quadruple hydrogen bridges

many bonds as suggested by the 18-electron rule" [92]. Furthermore, Morokuma's calculations indicated that the direct Ru–Ru interaction is repulsive and that "[t]he four hydrides work as glue to connect the repulsive fragments" [92]. It is, therefore, evident that the bonding within $[\text{Cp}^*\text{Ru}]_2(\mu\text{-H})_4$ comprises four 3-center-2-electron Ru–H–Ru bonds and an Ru– \times –Ru antibond, a description that is predicted by the μ -LX "half-arrow" electron-counting procedure (Fig. 23). Importantly, this revised description of the bonding in $[\text{Cp}^*\text{Ru}]_2(\mu\text{-H})_4$ was subsequently accepted by the authors who first proposed the existence of an Ru \equiv Ru triple bond [106].

The bonding in the iron and osmium counterparts, $[\text{Cp}^*\text{Fe}]_2(\mu\text{-H})_4$ [107] and $[\text{Cp}^*\text{Os}]_2(\mu\text{-H})_4$ [108], has also been discussed and the possibility of the existence of M \equiv M triple bonds was discounted on the basis of the aforementioned theoretical study on the ruthenium analog. On the other hand, the heterobimetallic complex $[\text{Cp}^*\text{Ru}](\mu\text{-H})_4[\text{OsCp}^*]$ was described as having an Ru \equiv Os triple bond [109], which is a curious description considering that one of the authors acknowledged that the symmetric complex $[\text{Cp}^*\text{Ru}]_2(\mu\text{-H})_4$ does not possess an Ru \equiv Ru triple bond [106].

$[(\text{R}_2\text{PhP})_2\text{ReH}_2]_2(\mu\text{-H})_4$ (R = Me, Ph) belong to a category of complexes that were described as possessing a formal Re \equiv Re triple bond [84, 110], but the μ -LX "half-arrow" notation would indicate an Re– \times –Re antibonding interaction (Fig. 23). Indeed, the occurrence of an antibonding interaction is also in accord with the $\sigma^2(\delta^*)^2(\sigma^*)^2$ electronic configuration that was calculated for $[(\text{H}_3\text{P})_2\text{Re}(\text{H})_2]_2(\mu\text{-H})_4$ [52].

Furthermore, an Re \equiv Re triple bond was also invoked for $[\text{CpReH}]_2(\mu\text{-H})_4$, but theoretical calculations indicate that the rhenium-rhenium interaction is described by a $(\sigma/\delta)^2(\delta^*)^2(\delta^*)^2$ configuration [87] which corresponds to a direct Re– \times –Re antibond (Fig. 24). Thus, whenever there are more bridging hydride ligands than

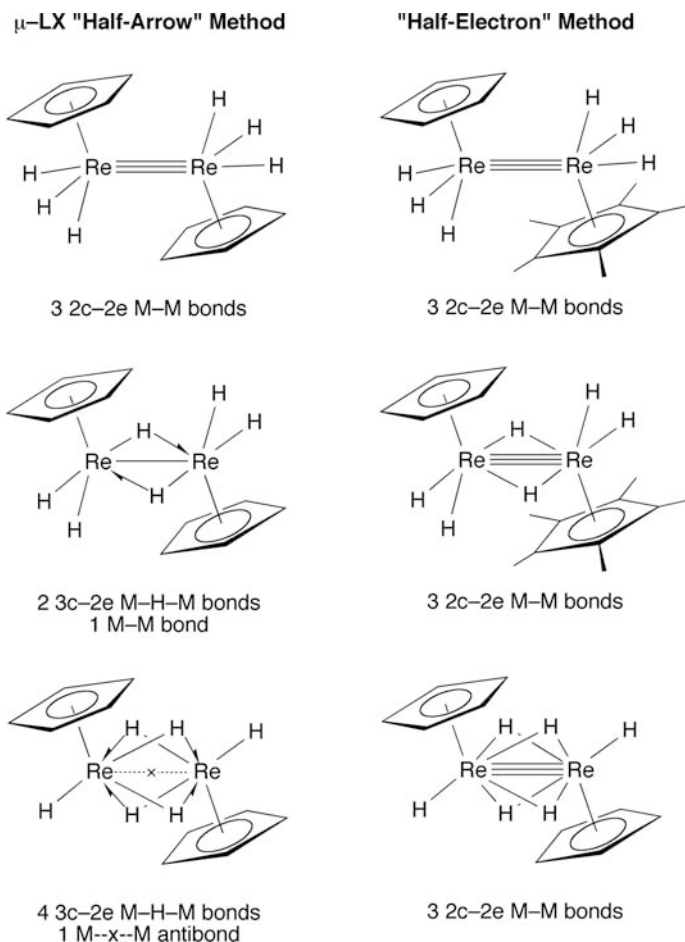


Fig. 24 Three postulated isomeric rhenium hydride complexes for which formal $\text{Re} \equiv \text{Re}$ triple bonds were invoked to satisfy the 18-electron rule (right hand side); the corresponding description of their bonding in terms of 3-center-2-electron bonds and direct $\text{Re}-\text{Re}$ bonds (left hand side)

$\text{M}-\text{M}$ bonds predicted by the “half-electron” method, the compound will actually possess an $\text{M}-\times-\text{M}$ antibonding interaction.

6 Conclusions

An analysis of the bonding in compounds with bridging hydrogen ligands demonstrates that, for every 3-center-2-electron $\text{M}-\text{H}-\text{M}$ interaction, the “half-electron” method over counts the $\text{M}-\text{M}$ bond order by one from the value predicted by the μ -LX “half-arrow” method. At one level, this is not really an issue once it

is recognized that the M–M bond orders derived by the two different electron-counting methods are merely *formalisms* and, as such, do not necessarily reflect reality. Problems of this type are commonplace in chemistry. For example, the formal charge [3] on an atom does not necessarily bear any relationship to the actual charge: the formal charge on nitrogen in NH_4^+ is + 1, whereas the actual charge is *negative* [111–113]. Likewise, it is well known that the charge on an atom generally bears no relationship to oxidation state [114]. At another level, however, the derivation of different M–M bond orders for the same compound is an issue from a pedagogical point of view because it causes confusion (as aptly demonstrated by the various descriptions of $\text{Os}_3(\text{CO})_{10}(\mu\text{-H}_2)$ shown in Fig. 1). Recognizing that both methods are formalisms, it is more appropriate to adopt the formalism that approximates more closely to the bond orders that are derived theoretically. For all of the examples discussed, the $\mu\text{-LX}$ “half-arrow” electron-counting method provides the best description of the bonding by clearly distinguishing between the number of 3-center-2-electron M–H–M interactions and direct 2-center-2-electron M–M interactions.

A good illustration of the inadequacy is provided by the fact that the M–M bond order predicted by the “half-electron” method is *independent* of whether or not the hydrogen atoms bridge the two metals. For example, the three isomers of $[\text{CpReH}_3]_2$ with (1) no bridging hydrogens, $[\text{CpReH}_3]_2$, (2) two bridging hydrogens, $[\text{CpReH}_2]_2(\mu\text{-H})_2$ and (3) four bridging hydrogens, $[\text{CpReH}]_2(\mu\text{-H})_4$ are each predicted by the “half-electron” method to have $\text{Re} \equiv \text{Re}$ triple bonds (Fig. 24) [82]. The notion that the Re–Re bond order would not be influenced by whether or not the hydrogen atoms bridge is far from intuitive. In contrast, the $\mu\text{-LX}$ “half-arrow” method for counting electrons predicts that the Re–Re bond order decreases from a triple bond in $[\text{CpReH}_3]_2$ to a single bond in $[\text{CpReH}_2]_2(\mu\text{-H})_2$, and to an “antibond” in $[\text{CpReH}]_2(\mu\text{-H})_2$ (Fig. 24), a result that is in accord with calculations [87].

As noted by Hoffmann for complexes with 3-center-2-electron bonds, “it is best not to argue over whether there is or is not metal–metal bonding in these molecules. The orbitals in question are delocalized and are used to bond a metal atom *both* to its metal partner and to the bridging group” [53]. Nevertheless, it must be emphasized that the “direct” $\text{M} \cdots \text{M}$ component for a 3-center-2-electron interaction *cannot* be viewed as equivalent to that of a normal 2-center-2-electron M–M bond. Furthermore, there may be additional direct M–M interactions that do not have a significant component from the bridging ligands. The “half-electron” method for counting electrons does not address these issues and merely applies a formula to predict the M–M bond order. Furthermore, application of the formula to predict the M–M bond order does not even require knowledge of whether or not the hydrogen atoms bridge, which is a rather unusual situation.

In contrast, the $\mu\text{-LX}$ “half-arrow” method requires one to consider the structure of the molecule prior to determining the M–M bond order. The $\mu\text{-LX}$ “half-arrow” method thus provides a more complete picture of the bonding by clearly distinguishing between (1) the number of 3-center-2-electron M–H–M interactions and (2) the number of direct 2-center-2-electron M–M interactions. A significant advantage of the $\mu\text{-LX}$ “half-arrow” method is that, by not forcing an 18-electron count on

a metal center (which is *explicitly* forced by the formula employed by the “half-electron” method), it provides a means of determining whether or not an M–x–M antibonding interaction could be present in a molecule. Thus, the μ -LX “half-arrow” method is recommended as the procedure of choice for counting electrons for complexes that possess 3-center-2-electron M–X–M interactions. In all cases evaluated, the μ -LX “half-arrow” method predicts M···M bond orders that are much more in accord with theoretical calculations than those obtained by the “half-electron” method.

Acknowledgements The U.S. Department of Energy, Office of Basic Energy Sciences (DE-FG02-93ER14339) is thanked for support.

References

1. Parkin G (2006) Comprehensive organometallic chemistry III, vol 1, Chap Crabtree RH and Mingos DMP (eds), Elsevier, Oxford
2. Jensen WB (2005) *J Chem Educ* 82:28
3. Parkin G (2006) *J Chem Educ* 83:791
4. Chisholm MH (1990) *Acc Chem Res* 23:419
5. Chisholm MH (1990) *J Organomet Chem* 400:235
6. Baik MH, Friesner RA, Parkin G (2004) *Polyhedron* 23:2879
7. Green MLH (1995) *J Organomet Chem* 500:127
8. DeKock RL, Bosma WB (1988) *J Chem Ed* 65:194
9. Bridgeman AJ, Empson CJ (2008) *New J Chem* 32:1359
10. Olsen JP, Koetzle TF, Kirtley SW, Andrews M, Tipton DL, Bau R (1974) *J Am Chem Soc* 96:6621
11. Bau R, Teller RG, Kirtley SW, Koetzle TF (1979) *Acc Chem Res* 12:176
12. Doedens RJ, Dahl LF (1965) *J Am Chem Soc* 87:2576
13. Petersen JL, Dahl LF, Williams JM (1974) *J Am Chem Soc* 96:6610
14. Dahl LF (1983) *Ann NY Acad Sci* 415:1
15. Parry RW, Kodama G (1993) *Coord Chem Rev* 128:245
16. Parry RW, Edwards LJ (1959) *J Am Chem Soc* 81:3554
17. Churchill MR, Ni S W-Y (1973) *J Am Chem Soc* 95:2150
18. Churchill MR, Chang SW-Y (1974) *Inorg Chem* 13:2413
19. Churchill MR, DeBoer BG, Rotella FJ (1976) *Inorg Chem* 15:1843
20. Churchill MR (1978) *Adv Chem Ser* 167:36
21. Berry M, Cooper NJ, Green MLH, Simpson SJ (1980) *J Chem Soc Dalton Trans* 29
22. Green MLH (1995) *J Organomet Chem* 500:127
23. Brookhart M, Green MLH, Parkin G (2007) *Proc Natl Acad Sci* 104:6908
24. Collman JP, Hegedus LS, Norton JR, Finke RG (1987) Principles and applications of organo-transition metal chemistry, University Science Books. Mill Valley, California, pp 24, 36
25. Owen SM (1988) *Polyhedron* 7:253
26. Housecroft CE, Sharpe AG (2001) *Inorganic chemistry*. Prentice Hall, New York, p 591
27. Bennett MJ, Graham WAG, Hoyano JK, Hutcheon WL (1972) *J Am Chem Soc* 94:6232
28. Shin JH, Parkin G (1998) *J Chem Soc Chem Commun* 1273
29. Sundermeyer J, Runge D, Field JS (1994) *Angew Chem Int Ed Engl* 33:678
30. Hwang JW, Kim J-H, Kim J, Uhm J-K, Do Y (2002) *Bull Kor Chem Soc* 23:1257
31. Chisholm MH, Kramer KS, Streib WE (1995) *Angew Chem Int Ed Engl* 34:891
32. Chisholm MH, Folting K, Kramer KS, Streib WE (1998) *Inorg Chem* 37:1549

33. Namorado S, Cui J, de Azevedo CG, Lemos MA, Duarte MT, Ascenso JR, Dias AR, Martons AM (2007) *Eur J Inorg Chem* 1103
34. Lopez LPH, Schrock RR, Müller P (2006) *Organometallics* 25:1978
35. Lopez LPH, Schrock RR (2004) *J Am Chem Soc* 126:9526
36. Cotton FA, Daniels LM, Hillard EA, Murillo CA (2002) *Inorg Chem* 41:2466
37. Cotton FA, Murillo CA, Walton RA (2005) *Multiple bonds between metal atoms*, 3rd edn, Chap 4-6. Springer Science and Business Media, New York
38. Bennett MJ, Brencic JV, Cotton FA (1969) *Inorg Chem* 8:1060
39. Cotton FA (1978) *Acc Chem Res* 11:225
40. Cotton FA, Walton RA *Multiple bonds between metal atoms*, 2nd edn. Oxford University Press, Oxford (1993)
41. Messerle L (1988) *Chem Rev* 88:1229
42. Handy LB, Ruff JK, Dahl LF (1970) *J Am Chem Soc* 92:7312
43. Elliot DJ, Vittal JJ, Puddephatt RJ, Holah DG, Hughes AN (1992) *Inorg Chem* 31:1247
44. Böttcher H-C, Hartung H, Krug A, Walther B (1994) *Polyhedron* 13:2893
45. Böttcher H-C, Grad M, Merzweiler K, Wagner C (2001) *J Organomet Chem* 628:144
46. Bo C, Poblet J-M, Costas M, Sarasa J-P (1996) *J Mol Struct (Theochem)* 371:37
47. Vahrenkamp H (1978) *Angew Chem Int Edit Engl* 17:379
48. Frenking G, Fröhlich N (2000) *Chem Rev* 100:717
49. Mayer I (1983) *Chem Phys Lett* 97:270
50. Bridgeman AJ, Cavigliasso G, Ireland LR, Rothery J (2001) *J Chem Soc Dalton Trans* 2095
51. Bridgeman AJ, Cavigliasso G (2001) *Polyhedron* 20:2269
52. Dedieu A, Albright TA, Hoffmann R (1979) *J Am Chem Soc* 101:3141
53. Summerville RH, Hoffmann R (1979) *J Am Chem Soc* 101:3821
54. Jezowska-Trzebiatowska B, Nissen-Sobocinska B (1987) *J Organomet Chem* 322:331
55. Jezowska-Trzebiatowska B, Nissen-Sobocinska B (1988) *J Organomet Chem* 342:215
56. Jezowska-Trzebiatowska B, Nissen-Sobocinska B (1988) *J Organomet Chem* 342:353
57. Jezowska-Trzebiatowska B, Nissen-Sobocinska B, Natkaniec L (1989) *J Organomet Chem* 376:67
58. Jezowska-Trzebiatowska B, Nissen-Sobocinska B (1989) *J Organomet Chem* 369:69
59. Nissen-Sobocinska B, Jezowska-Trzebiatowska B (1993) *J Organomet Chem* 452:277
60. Macchi P, Donghi D, Sironi A (2005) *J Am Chem Soc* 127:16494
61. Matito E, Solà M (2009) *Coord Chem Rev* 253:647
62. García ME, Riera V, Ruiz MA, Sáez D, Vaissermann J, Jeffery JC (2002) *J Am Chem Soc* 124:14304
63. García ME, Riera V, Ruiz MA, Rueda MT, Sáez D (2002) *Organometallics* 21:5515
64. Adams H, Bailey NA, Bisson AP, Morris MJ (1993) *J Organomet Chem* 444:C34
65. García ME, Ramos A, Ruiz MA, Lanfranchi M, Marchio L (2007) *Organometallics* 26:6197
66. García ME, Melón S, Ramos A, Riera V, Ruiz MA, Belletti D, Graiff C, Tiripicchio A (2003) *Organometallics* 22:1983
67. Alvarez MA, García ME, Ramos A, Ruiz MA, Lanfranchi M, Tiripicchio A (2007) *Organometallics* 26:5454
68. Alvarez MA, García ME, Ramos A, Ruiz MA (2007) *Organometallics* 26:1461-1472
69. Alvarez CM, Alvarez MA, García ME, Ramos A, Ruiz MA, Graiff C, Tiripicchio A (2007) *Organometallics* 26:321
70. Alvarez CM, Alvarez MA, García ME, Ramos A, Ruiz MA, Lanfranchi M, Tiripicchio A (2005) *Organometallics* 24:7
71. Alvarez MA, García ME, Ramos A, Ruiz MA (2006) *Organometallics* 25:5374
72. Alvarez MA, García ME, Riera V, Ruiz MA (1999) *Organometallics* 18:634
73. Alvarez MA, Bois C, García ME, Riera V, Ruiz MA (1996) *Angew Chem Int Ed Engl* 35:102
74. Philips AD, Ienco A, Reinhold J, Böttcher H-C, Mealli C (2006) *Chem Eur J* 12:4691
75. Takemoto S, Kimura Y, Kamikawa K, Matsuzaka H (2008) *Organometallics* 27:1780
76. Green JC, Mingos DMP, Seddon EA (1981) *Inorg Chem* 20:2595
77. Green JC, Mingos DMP, Seddon EA (1980) *J Organomet Chem* 185:C20
78. Hall MB, Green JC (1982) *Phil Trans Roy Soc London A* 308:85

79. Sherwood DE, Hall MB (1982) *Inorg Chem* 21:3458
80. Hoyano JK, Graham WAG (1982) *J Am Chem Soc* 104:3722
81. Forrow NJ, Knox SAR (1984) *J Chem Soc Chem Commun* 679
82. Alt HG, Mahmoud KA, Rest AJ (1983) *Angew Chem Int Ed Engl* 22:544
83. García Alonso FJ, Riera V, Ruiz MA, Tiripicchio A, Camellini MT (1992) *Organometallics* 11:370
84. Bruno JW, Huffman JC, Green MA, Zubkowski JD, Hatfield WE, Caulton KG (1990) *Organometallics* 9:2556
85. Green MA, Huffman JC, Caulton KG (1983) *J Organomet Chem* 243:C78
86. Jones RA, Wilkinson G, Colquhoun IJ, McFarlane W, Galas AMR, Hursthouse MB (1980) *J Chem Soc Dalton Trans* 2480
87. Bursten BE, Cayton RH (1988) *Organometallics* 7:1349
88. Green JC, Green MLH, O'Hare D, Watson RR, Bandy JA (1987) *J Chem Soc Dalton Trans* 391
89. See reference 13 in Kang B-S, Koelle U, Thewalt U (1991) *Organometallics* 10:2569
90. Jones RA, Chiu KW, Wilkinson G, Galas AMR, Hursthouse MB (1980) *J Chem Soc Chem Commun* 408
91. Chiu KW, Jones RA, Wilkinson G, Galas AMR, Hursthouse MB (1981) *J Chem Soc Dalton Trans* 1892
92. Koga N, Morokuma K (1993) *J Mol Struct* 300:181
93. Casey CP, Sakaba H, Hazin PN, Powell DR (1991) *J Am Chem Soc* 113:8165
94. Bortz M, Bau R, Schneider JJ, Mason SA (2001) *J Clust Sci* 12:285
95. Crabtree RH, Felkin H, Morris GE, King TJ, Richards JA (1976) *J Organomet Chem* 113:C7
96. Crabtree R (1979) *Acc Chem Res* 12:331
97. Ginsberg AP, Hawkes MJ (1968) *J Am Chem Soc* 90:5930
98. Dapporto P, Midollini S, Sacconi L (1975) *Inorg Chem* 14:1643
99. Chaudret B, Devillers J, Poilblanc R (1985) *Organometallics* 4:1727
100. Fowe EP, Therrien B, Süß-Fink G, Daul C (2008) *Inorg Chem* 47:42
101. Süß-Fink G, Therrien B (2007) *Organometallics* 26:766
102. Stevens RC, McLean MR, Wen T, Carpenter JD, Bau R, Koetzle TF (1989) *Inorg Chim Acta* 161:223
103. Green MA, Huffman JC, Caulton KG (1981) *J Am Chem Soc* 103:695
104. Ito J, Shima T, Suzuki H (2004) *Organometallics* 23:2447
105. Suzuki H, Omori H, Lee DH, Yoshida Y, Moro-oka Y (1988) *Organometallics* 7:2243
106. Suzuki H, Omori H, Lee DH, Yoshida Y, Fukushima M, Tanaka M, Morooka Y (1994) *Organometallics* 13:1129
107. Ohki Y, Suzuki H (2000) *Angew Chem Int Edit* 39:3120
108. Gross CL, Girolami GS (2007) *Organometallics* 26:160
109. Shima T, Suzuki H (2005) *Organometallics* 24:3939
110. Bau R, Carroll WE, Teller RG, Koetzle TF (1977) *J Am Chem Soc* 99:3872
111. Greenberg A, Winkler R, Smith BL, Liebman JF (1982) *J Chem Educ* 59:367
112. Wurthwein EU, Sen KD, Pople JA, Schleyer PV (1983) *Inorg Chem* 22:496
113. Sorensen JB, Lewin AH, Bowen JP (2003) *J Mol Struct (Theochem)* 623:145
114. Hoffmann R (2001) *Am Sci* 89:311

Structure and Bonding of Metal-Rich Coordination Compounds Containing Low Valent Ga(I) and Zn(I) Ligands

Sandra Gonzalez-Gallardo, Ganesan Prabusankar, Thomas Cadenbach, Christian Gemel, Moritz von Hopffgarten, Gernot Frenking, and Roland A. Fischer

Abstract Recent developments in the field of metal-rich low valent metal complexes with gallium(I)/zinc(I) ligands and their structural features are reviewed together with related theoretical calculations. Some emphasis is given to sterically encumbering NHC analogous ligands as well as the naked ions E^+ . The chemistry of organo Zn(I) ligands at transition metals is reviewed in the light of the recently discovered synthetic approach via suitable organo Ga(I) complexes as starting materials.

Keywords Main Group Chemistry · Metal-Metal Bond · Gallium(I) · Zinc(I) · Clusters

Contents

1	Introduction	148
2	Coordination Chemistry of Ga(I) Compounds	149
2.1	NHC analogue Ga(I) ligands	149
2.2	From GaCp* to the ‘Naked’ Ga ⁺ as Ligand	158
2.3	Quantum Chemical Calculations on the M–Ga Bonding in Complexes with Ga(I) Ligands	165
3	From Homoleptic GaCp* Complexes to Highly Coordinated Transition Metal Zinc Compounds	166
3.1	Synthesis and Molecular Structures of the Compounds [M(ZnR) _n]	168
3.2	Quantum Chemical Calculations of Highly Coordinated Transition Metal Zn(I) Complexes	170
4	Perspectives	183
	References	184

S.G.- Gallardo, G. Prabusankar, T. Cadenbach, C. Gemel and R.A. Fischer (✉)
Inorganic Chemistry II – Organometallics and Materials, Faculty of Chemistry
and Biochemistry, Ruhr University Bochum, D-44870 Bochum, Germany
e-mail: roland.fischer@rub.de

M.v. Hopffgarten and G. Frenking
Department of Chemistry, Philipps-University Marburg, D-35032 Marburg, Germany
e-mail: frenking@chemie.uni-marburg.de

1 Introduction

Synthetic strategies for a systematic construction of metal–metal bonded molecules and clusters have been a target for inorganic research over at least the last five decades, the development of which was particularly influenced by Cotton's pioneering work in the field of metal–metal multiple bonding and metal cluster chemistry [1,2]. Over this period, the size of the molecular ligand stabilized clusters in terms of aggregated metal atoms became larger and even giant metalloid clusters have been characterized [3–10], and simultaneously metal–metal bonds with non-classical electron structures became available and probed the limits of metal–metal bonding in molecules. Quite recent and spectacular reports such as the chromium–chromium quintuple bond [11], the zinc–zinc [12–25] and magnesium–magnesium [26] single bond show that there is still plenty of room for new discoveries. Within this context we wish to highlight most recent aspects of a particularly fruitful area of research which deals with metal–metal bonded systems of the general formula $[L_a M_b(ER)_c]$ involving carbenoid group 13 metal moieties ER (E=Al, Ga, In; R=bulky substituents) as typically very potent σ -donor ligands. The development of synthetic routes to sterically shielded and thus thermodynamically stable low valent group 13 metal compounds ER such as ECp^* (E = Al, Ga; R = Cp*) [27, 28, 28–31], Ga(DDP) (DDP = $\{[N(C_6H_3iPr_2-2, 6)C(Me_2)]_2CH\}$) [32] or the diazabutadienido compounds $[Ga\{N(R')C(H)\}_2]^-$ (R' = *t*Bu, C₆H₃*i*Pr₂-2, 6) [33, 34] and other related systems has been a big step towards the tailored synthesis of mixed metal coordination compounds. The other extreme in steric situations, i.e. the minimum limit in size of low valent group 13 ligands, is the substituent-free naked ions E⁺ (E = Ga [35, 36], In [37–39], Tl [40–46]) which show a coordination behaviour very different to all other low valent group 13 ligands. They behave as strong σ - as well as π -acceptors but have no donor properties at all. Originally, the work on the coordination chemistry of ER ligands focused on transition metal carbonyl fragments yielding very stable and kinetically inert complexes $[(CO)_a M_b(ER)_c]$ [47]. Much research has been expended within the past two decades for the exploration of related carbonyl-free complexes $[L_a M_b(ER)_c]$ (L other than CO) prepared by coordination of these low valent ER ligands to d-block, and more recently also s-, p- and f-block metal fragments, and quite a number of review articles are available [3–10, 48–50]. The coordination to very electrophilic metal centres such as Ca, Mg [51] or lanthanide centres [52, 53] has been accomplished by the use of anionic diazabutadienides $[Ga\{N(R)C(H)\}_2]^-$. The related, neutral Ga(DDP) [54–63] and Ga(Giso) [64] (Giso = $\{(2, 6 - iPr_2C_6H_3)NC(NCy_2)N(C_6H_3iPr_2-2, 6)\}$) have been shown to be suitable ligands for electronically strongly unsaturated complexes (14 or 16 VE species) by steric shielding of the complex periphery. However, most of the published (and reviewed) work still deals with synthesis, structural and bonding characterization. In general, not much is known about the *chemistry* of the new compounds containing the ER ligands. Only recently it has been shown that GaCp* and Ga(DDP) complexes of late transition metals show interesting reactivity patterns in comparison to classic organometallic reactions such as C–H [65–68], C–C [69, 70] or Si–H [65, 71] activation.

This review does not intend to give a detailed discussion on structure and bonding of all these types of complexes mentioned earlier. Most of the relevant aspects have been extensively reviewed before [3–12, 12–25, 48]. Rather, we will focus on very recent and novel developments with an emphasis on some unique features of the involved chemistry of gallium(I) and the related zinc(I) ligands, i.e. GaR and ZnR, which lead to novel structures and bonding situations. The first part will discuss typical examples for metal complexes of the bulky NHC analogue gallium ligands Ga(DDP), Ga(Giso) and the anionic $[\text{Ga}\{\text{N}(\text{R})\text{C}(\text{H})\}_2]^-$ and compare them to those of naked Ga^+ in particular. The second part will cover a newly discovered class of complexes which became available by using the special ligand properties of GaCp^* complexes towards zinc alkyls. Gallium and Zinc are neighbours in the periodic table and it was found that zinc can substitute gallium in the coordination sphere of d-block metal fragments under certain conditions. The treatment of homoleptic compounds $[\text{M}(\text{GaCp}^*)_n]$ ($n = 4-6$) with dimethyl zinc leads to the unusual zinc-rich transition metal compounds $[\text{M}(\text{ZnR})_a]$ ($a = 8-12$) with ZnR groups as one-electron ligands ($\text{R} = \text{Me}, \text{Cp}^*$) [49, 50].

2 Coordination Chemistry of Ga(I) Compounds

The variety of (organo) Ga(I) compounds known to date is rather large; however, only few of these compounds have been used as ligands for transition metals. The nature of the group R in compounds GaR determines the electronic properties of the coordination of the metal fragment to transition metal centres and is also responsible for its steric property. Thus, the steric encumbrance for Ga(I) ligands spans from virtually zero for ‘naked’ Ga^+ to a cone angle far beyond 180° for NHC analogous systems like Ga(DDP) (*vide infra*). As for the electronic properties, with the exception of Ga^+ (*vide infra*) all compounds represent strong σ -donors, with an ability to act as a weak π -acid, whose extent is dependent on the group R.

2.1 NHC analogue Ga(I) ligands

The chemistry of sterically demanding *N*-heterocyclic carbene (NHC) analogues of Ga(I) ligands with versatile electronic and steric properties has led to a variety of applications in synthesis and bond activation. Especially the neutral six-membered Ga(DDP) [32], the anionic five-membered diazabutadienido compounds $[\text{Ga}\{\text{N}(\text{R})\text{C}(\text{H})\}_2]^-$ [33, 34] and, very recently, the neutral four-membered guanidinate complexes Ga(Giso) [72] have been in the focus of recent research (Fig. 1). However, their electronic features are distinctly different not only from each other (*vide infra*) but also from their well-studied Cp^* congener. The metal centre in these Ga(I) heterocycles is isolobal to NHCs, the vacant p orbital not being stabilized by additional π electrons (as in the case of GaCp^* , which is stabilized by the strong

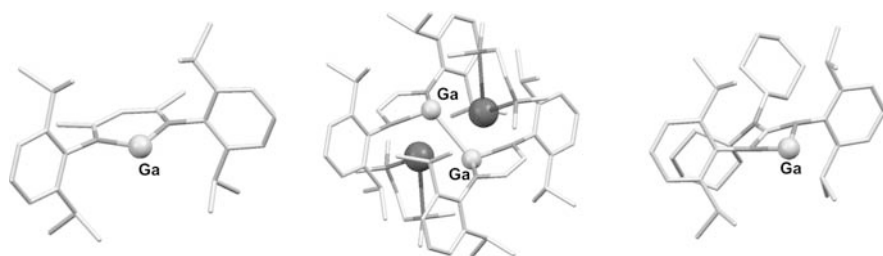


Fig. 1 Solid-state structures of Ga(DDP), {[K(tmeda)][(Diazabutadiene)Ga]}₂ and Ga(Giso)

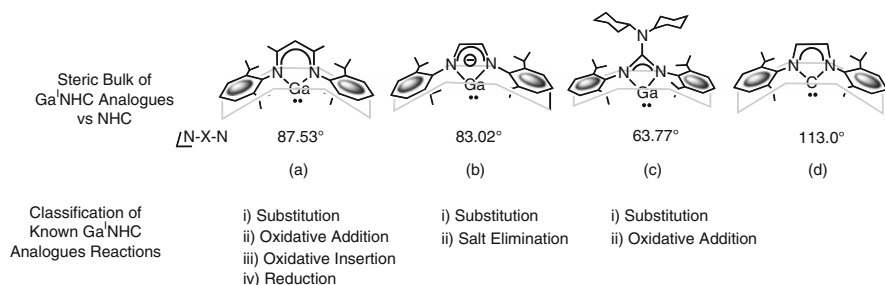
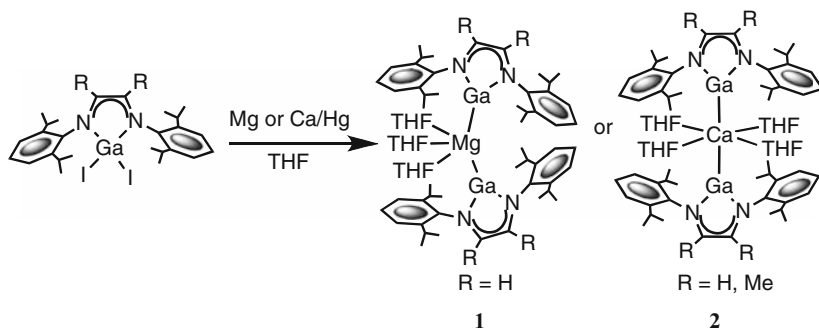


Chart 1 Comparison of (a) β -diketiminato, (b) diazabutadienido and (c) guanidinate Ga^IN-heterocyclic derivatives and (d) NHC

π -donor Cp^{*}) [73] leading to an increase in the electrophilicity of the metal centre on coordination to transition metals.

The presence of a directional lone pair (HOMO) and an empty p orbital (LUMO) at the Ga(I) centre of the heterocycles could principally lead to σ donor as well as π acceptor properties of the ligands in the respective transition-metal complexes. However, the NHC analogues of Ga(I) would be expected to have different magnitudes of σ donor and π acceptor nature as it is reflected by the large difference of HOMO–LUMO gaps of Ga(DDP) (ca. 100 kcal/mol) compared to the Ga(I) diazabutadienide and Ga(Giso) (ca. 60 kcal/mol). In addition, these species substantially differ from NHCs in terms of electron delocalization on the *N*-heterocyclic backbone and steric bulk (Chart 1) [48]. A fine-tuning in the steric and electronic properties of these ligands offers a significant variation in the N–X–N angle, which eventually results in a substantial change in their σ donor and π acceptor nature. Among the Ga(I) NHC derivatives, the neutral molecules Ga(DDP) and Ga(Giso) are very similar in their coordination properties; however, they are considerably different in their N–Ga–N angle and thus their steric encumbrance.

In general, the diazabutadienideo compound [Ga{N(R)C(H)}₂][–] undergoes substitution or salt elimination reactions with metal derivatives, while the main synthetic routes to Ga(Giso) and Ga(DDP) complexes are substitution or oxidative addition reactions [48].



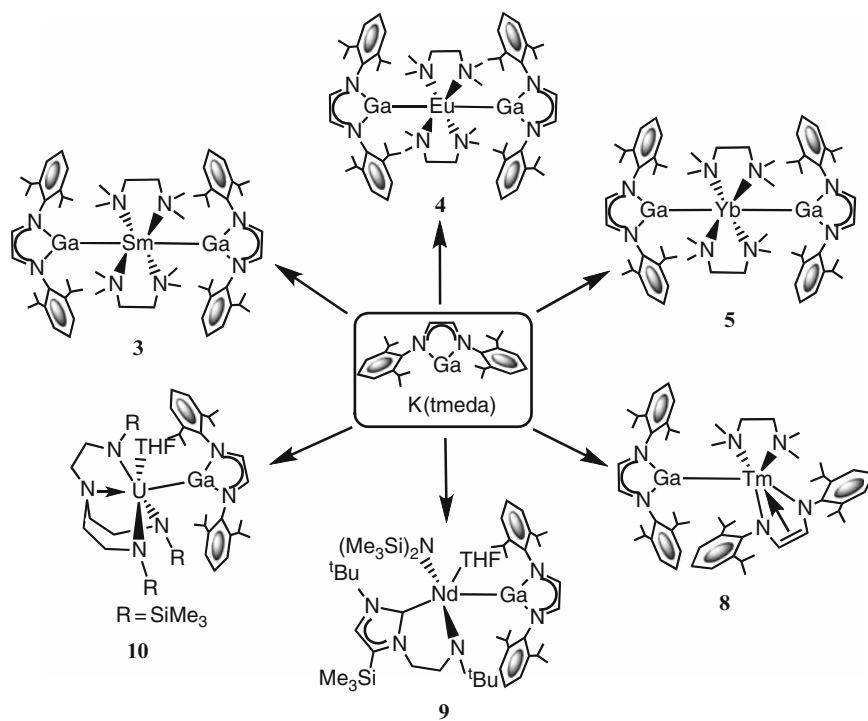
Scheme 1 Synthesis of Mg and Ca complexes **1** and **2** [51]

2.1.1 s- and f-Block Metal Complexes

s- or f-block elements of Ga(I) derivatives can be well stabilized by use of the charged diazabutadienideo ligand. For example, the in situ reduction of paramagnetic gallium(III) heterocycles by mercury in the presence of either magnesium or calcium metal resulted in the first structurally characterized gallium complexes of s-elements, i.e. $[\text{Mg}\{\text{Ga}(\text{ArNCH})_2\}_2(\text{THF})_3]$ (**1**) and $[\text{Ca}\{\text{Ga}(\text{ArNCR})_2\}_2(\text{THF})_4]$ (**2**) ($\text{R} = \text{H}$ or Me , $\text{Ar} = \text{C}_6\text{H}_3i\text{Pr}_2$, **6**) (Scheme 1) [51].

In **1**, the Mg centre is coordinated by two gallium heterocyclic ligands in equatorial sites and three THF molecules in a distorted trigonal-bipyramidal geometry. In contrast, the calcium centre in **2** shows an octahedral coordination environment with the gallium heterocyclic ligands *trans* to each other. This difference is explained by the greater covalent radius of the heavier metal. The Ga–Mg (2.7174 and 2.7269 Å) or Ga–Ca (3.1587 Å for $\text{R} = \text{H}$, 3.1988 Å for $\text{R} = \text{Me}$) bonds in these complexes are found to be slightly longer than the sums of the covalent radii for these element pairs (Ga–Mg 2.61 Å; Ga–Ca 2.91 Å). DFT calculations on the model complexes $[\text{Mg}(\text{OME}_2)_3\{\text{Ga}(\text{MeNCH})_2\}_2]$ (Ga–Mg mean distance: 2.715 Å) and $[\text{Ca}(\text{OME}_2)_4\{\text{Ga}(\text{MeNCH})_2\}_2]$ (Ga–Ca mean distance: 3.232 Å) lead to geometries similar to the crystal structures. Moreover, a significant ionic character for the group 2 metal–gallium interactions was confirmed from experimental as well as theoretical data.

More recently, the first examples of diazabutadienideo $[\text{Ga}\{\text{N}(\text{R})\text{C}(\text{H})\}_2]^-$ ligand supported f-element complexes with more polar Ga–M bonds were successfully realized. Salt elimination reactions of $[\text{K}(\text{tmeda})][\text{Ga}\{\text{ArNCH})_2\}]$ with $\text{LnI}_2(\text{THF})_n$ ($\text{Ln} = \text{Sm}$, Eu or Yb) in THF/tmeda (tmeda = tetramethylethylenediamine) give the iso-structural bis(gallyl) lanthanide(II) complexes, $[\text{Ln}^{\text{II}}\{\text{Ga}(\text{ArNCH})_2\}_2(\text{tmeda})_2]$ ($\text{Ln} = \text{Sm}$ (**3**), Eu (**4**) or Yb (**5**); $\text{Ar} = \text{C}_6\text{H}_3i\text{Pr}_2$, **6**) (Scheme 2, Fig. 2) [74]. In these complexes, the Ln centres are coordinated in a distorted octahedral geometry with the gallyl ligands *trans* to each other. The Ln–Ga distances in **3–5** follow the expected trend (Sm–Ga (3.3124 Å) \sim Eu–Ga (3.3124 Å) $>$ Yb–Ga (3.2050 and 3.2473 Å) based on the effective ionic radii for six-coordinate Ln^{2+} cations (Sm^{2+} 1.19 Å, Eu^{2+} 1.17 Å, Yb^{2+} 1.02 Å). Notably, the Ln–Ga distances in **3–5**



Scheme 2 Synthesis of f-element complexes of diazabutadienideo $[\text{Ga}\{\text{N}(\text{R})\text{C}(\text{H})\}_2]^-$

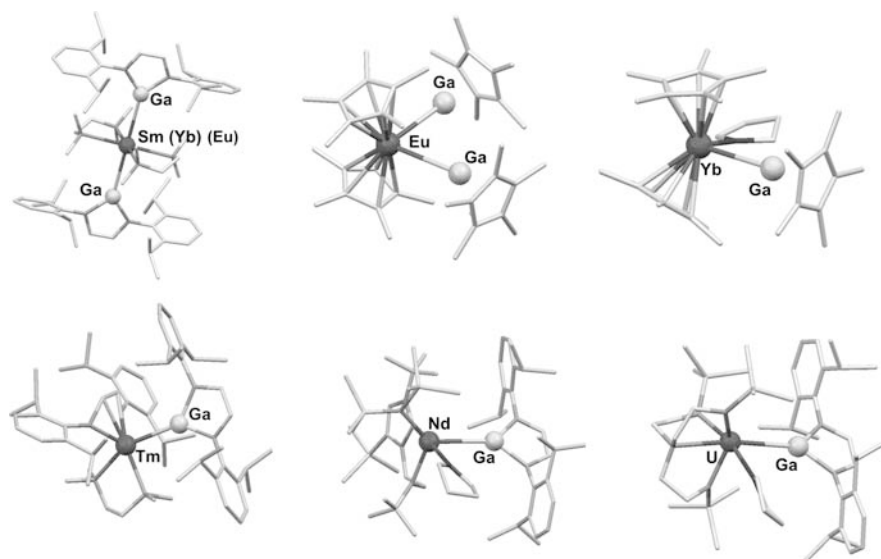


Fig. 2 Solid-state structures of the Ga-lanthanide complexes 3–10

are substantially longer than the sums of the covalent radii for the atom pairs (Sm–Ga 3.20Å, Eu–Ga 3.20Å or Yb–Ga 3.09Å). However the Eu–Ga distance is not shorter with respect to the Ga–Eu distances found in the GaCp* adduct $[\text{Cp}_2^*\text{Eu}(\text{GaCp}^*)_2]$ (**6**) (3.2499 and 3.3907Å), whereas the Yb–Ga distance is shorter than in $[\text{Cp}_2^*\text{Yb}(\text{GaCp}^*)(\text{THF})]$ (**7**) (3.2872(4)Å) [75]. Although the Ln–Ga bonds in **3–5** are very polar, the presence of some covalent character is proposed from theoretical studies based on **1** and **2** [51].

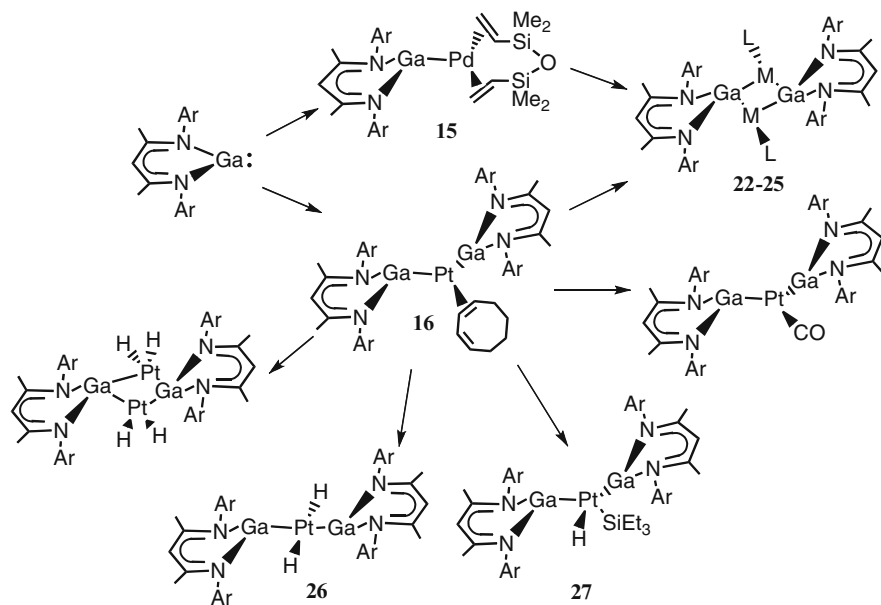
The reaction of $[\text{K}(\text{tmeda})][\text{Ga}\{\text{ArNCH}_2\}_2]$ with $\text{TmI}_2(\text{THF})_5$ in THF/tmeda yields $[\text{Tm}^{\text{III}}\{\text{Ga}\{\text{ArNCH}_2\}_2\}\{\text{ArNCH}_2\}(\text{tmeda})]$ (**8**) where the Tm centre is found in heavily distorted trigonal-bipyramidal coordination geometry (Scheme 2, Fig. 2) [74]. The Tm–Ga distance (2.9742Å) in **8** is considerably shorter than in the Ln–Ga distances in **3–5** and well within the sum of the covalent radii for Tm/Ga (3.12Å).

The reaction of $[\text{K}(\text{tmeda})][\text{Ga}\{\text{ArNCH}_2\}_2]$ and $[\text{Nd}(\text{L}')(\text{N}')(\mu\text{-I})_2[\text{L}' = t\text{BuNCH}_2\text{CH}_2\{\text{C}(\text{NCSiMe}_3\text{CHN}t\text{Bu})\}, \text{N}' = \text{N}(\text{SiMe}_3)_2]$ in THF results in the complex $[\text{Nd}(\text{L}')(\text{N}')(\text{Ga}\{\text{ArNCH}_2\}_2)(\text{THF})]$ (**9**) (Scheme 2, Fig. 2) [76]. The Nd centre in **9** adopts a distorted trigonal-bipyramidal geometry. The Nd–Ga bond length (3.2199Å) is slightly longer than the sum of the covalent radii (Nd–Ga = 2.89Å). NBO calculations on the model complex $[\text{Nd}(\text{L}'')(\text{NMe}_2)(\text{Ga}\{\text{MeNCH}_2\}_2)(\text{OMe}_2)][\text{L}'' = \text{HNCH}_2\text{CH}_2\{\text{C}(\text{NCHCHNMe})\}](\text{Nd-Ga distance: } 3.227\text{Å})$ shows that the bond is strongly polarized with 87% Ga and 13% Nd contribution to the MO.

The reaction of $[(\text{tren-TMS})\text{UCl}(\text{thf})](\text{tren-TMS} = [\text{N}(\text{CH}_2\text{CH}_2\text{NSiMe}_3)_3])$ and $[\text{K}(\text{tmeda})][\text{Ga}\{\text{ArNCH}_2\}_2]$ affords $[(\text{trenTMS})\text{U}\{\text{Ga}(\text{NArCH}_2)_2\}(\text{thf})]$ (**10**) (Scheme 2, Fig. 2) [77]. The uranium centres are found in a distorted octahedral geometry. However, the U–Ga bond lengths (3.2115 and 3.2983Å) in the two crystallographic non-equivalent molecules in the asymmetric unit are distinctly different. The U–Ga bond distances are comparable to the sum of the covalent radii (U–Ga = 3.18Å). It was stated that the existence of these two different U–Ga bond distances in the asymmetric unit could raise from crystal packing forces as well as known deviations of post-second-row elements from classic bond length–strength relationships. DFT calculations on **10** reproduced the structural features of the experimental results. Notably, **10** is the first example of a group 13/f element π donation in addition to σ donation where the U–Ga bond is of polar, covalent nature. Noteworthy this π acceptor or π donor nature is absent in U–Al [78] and Nd–Ga [76] bonds.

2.1.2 d-Block Metal Complexes

The first Ga(DDP) complex $[(\text{CO})_4\text{FeGa}(\text{DDP})]$ (**11**) was synthesized via a CO displacement reaction by treating $\text{Ga}^{\text{I}}(\text{DDP})$ with $\text{Fe}(\text{CO})_5$. The Ga–Fe distance (2.2851Å) in this complex is slightly longer than that of the related complexes $[\text{Ar}^*\text{GaFe}(\text{CO})_4]$ (**12**) (2.248Å) ($\text{Ar}^* = \text{C}_6\text{H}_3\text{-2, 6-}\{\text{C}_6\text{H}_2\text{-2, 4, 6-}i\text{Pr}_3\}_2$) [79] and $[\text{Cp}^*\text{GaFe}(\text{CO})_4]$ (2.2731Å) (**13**) [28] and also the IR spectrum suggests negligible π -back-bonding between the Fe and Ga centres.



Scheme 3 Reaction of GaDDP with Pt and Pd complexes [71]

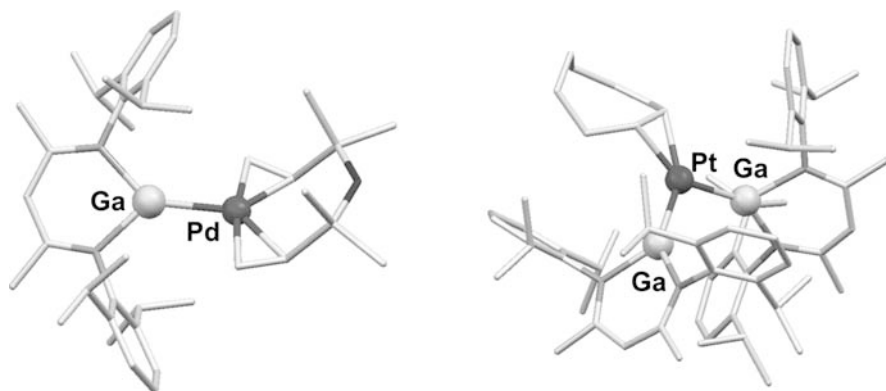
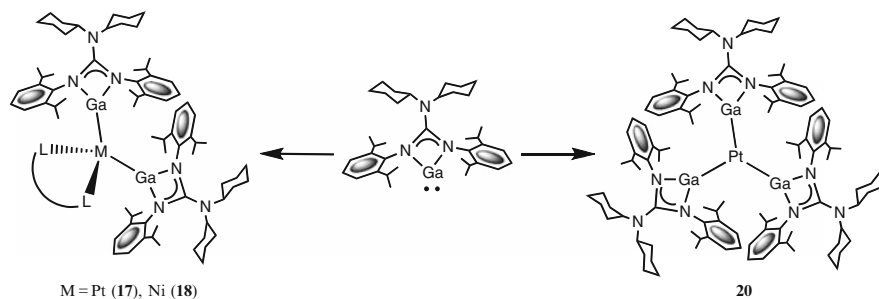


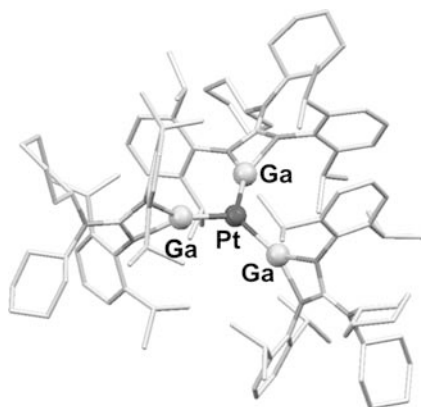
Fig. 3 Solid-state structures of Ga(DDP) stabilized olefin complexes of palladium (**15**) and platinum (**16**)

While the reaction of Ga(DDP) with excess $[\text{Ni}(\text{ethylene})_3]$ yields the trimeric C–H activated complex $[\{\mu^2\text{-Ga}(\text{DDP})\text{Ni}(\text{ethylene})\}_2\text{Ni}(\mu^2\text{-CH}=\text{CH}_2)(\text{H})]$ (**14**) as the thermodynamic product [80], the corresponding homoleptic palladium olefin complex $[\text{Pd}_2(\text{dvds})_3]$ (dvds = 1,1,3,3-tetramethyl-1,3-divinyldisiloxane) yields the simple substitution product $[(\text{dvds})\text{Pd}\{\text{Ga}(\text{DDP})\}]$ (**15**) (Scheme 3, Fig. 3). Partial substitution of COD from $[\text{Pt}(\text{COD})_2]$ by Ga(DDP) results in the monomeric complex $[\text{Pt}(\text{COD})\{\text{Ga}(\text{DDP})_2\}]$ (**16**) (Scheme 3). The Pt centre in **16** (Fig. 3) exhibits a trigonal planar 16VE Pt^0 centre with two Ga(DDP) moieties and one η^2 -coordinated



Scheme 4 Reaction of $\text{Ga}^{\text{I}}\text{Giso}$ with Ni and Pt complexes [64]

Fig. 4 Solid-state structure of $[\text{Pt}(\text{Ga}^{\text{I}}\text{Giso})_3](\mathbf{20})$



1,3-cod ligand. The Pt–Ga distances (2.342, and 2.346 Å) are quite similar than the Pt–Ga distances in the homoleptic complex $[\text{Pt}(\text{GaCp}^*)_4]$ (**40**) (2.335 Å) or the terminal Pt–Ga distances in the dimeric cluster $[\text{Pt}_2(\text{GaCp}^*)_5]$ (**41**) (2.326 and 2.331 Å) [81, 82]. Notably the higher degree of π -back-bonding to the olefins was observed in **15** and **16** than in its phosphane analogues which leads to the conclusion that the σ -donor properties of $\text{Ga}(\text{DDP})$ are more similar to those of NHCs than those of electron-rich phosphanes.

The reaction of $(\text{Ga}^{\text{I}}\text{Giso})$ with $[\text{Ni}(\text{COD})_2]$ ($\text{COD} = 1,5\text{-cyclooctadiene}$) or $[\text{Pt}(\text{dppe})(\text{C}_2\text{H}_4)]$ leads to complexes $[(\text{L}-\text{L})\text{M}(\text{Ga}^{\text{I}}\text{Giso})_2]$ ($\text{L}-\text{L} = \text{dppe}$, $\text{M} = \text{Pt}$ (**17**) or $\text{L}-\text{L} = \text{COD}$, $\text{M} = \text{Ni}$ (**18**)) where the metal centres are found in distorted tetrahedral geometries (Scheme 4) [64]. The Ni–Ga (2.2384 and 2.2401 Å) distances in **18** are slightly shorter than that of $[(\text{cdt})\text{Ni}\{\text{Ga}(\text{DDP})\}]$ (**19**) ($\text{cdt} = 1,5,9\text{-cyclododecatriene}$) (2.35 Å) [80], whereas the Pt–Ga distances (2.3549 and 2.3596 Å) in **17** are comparable to those in **16** (2.342 and 2.346 Å).

The reaction of $(\text{Ga}^{\text{I}}\text{Giso})$ and $[\text{Pt}(\text{norbornene})_3]$ gave the first homoleptic Pt complex $[\text{Pt}(\text{Ga}^{\text{I}}\text{Giso})_3]$ (**20**) supported by NHC– Ga^{I} analogues (Scheme 4) [64]. The trigonal-planar Pt centre in **20** (Fig. 4) is sterically overcrowded by three bulky $\text{Ga}(\text{Giso})$ ligands. The Pt–Ga (3-coordinate) bond lengths (2.3058, 2.3108 and 2.3118 Å) are in fact the shortest yet reported and slightly shorter than those

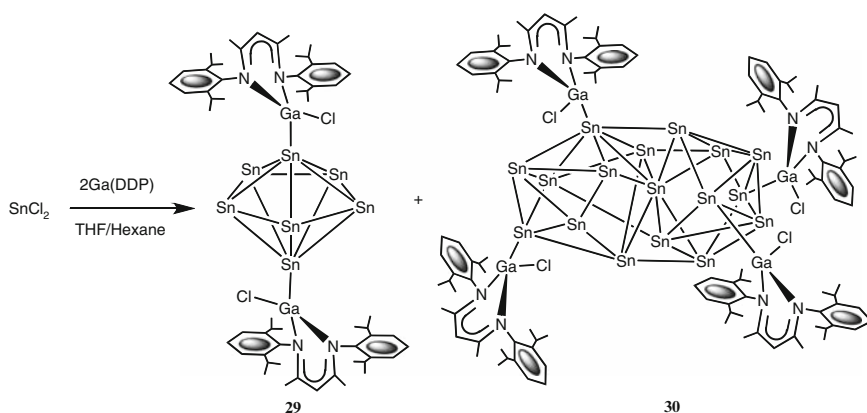
in $[\text{Pt}(\text{dcpe})\{\text{GaC}(\text{SiMe}_3)_3\}_2]$ (**21**) (Pt-Ga (2-coordinate): 2.315 and 2.318 Å) [dcpe = bis(dicyclohexylphosphino)ethane] [83]. Notably, a charge decomposition analysis (CDA) on $[\text{Pt}\{\text{Ga}[\text{N}(\text{C}_6\text{H}_3\text{Me}_2-2,6)]_2\text{CNMe}_2\}_3]$ indicated a significant (39.8% mean) π contribution of the covalent part of the Pt-Ga bonds.

Both **15** and **16** react readily with excess of strong π -acceptor ligands such as CO or tBuNC to give the dimeric cluster compounds $[\{M[\text{Ga}(\text{DDP})\text{L}\}_2]$ (M = Pd, L = CO (**22**); L = tBuNC (**23**); M = Pt; L = CO (**24**); L = tBuNC (**25**)) (Scheme 3) with considerable elongation of the Ga-M bond (Ga-Pt(CO), 2.4871 and 2.5207 Å; Ga-Pt(tBuNC), 2.4464 and 2.4741 Å; Ga-Pd(CO), 2.4875 and 2.5091 Å; Ga-Pt(tBuNC), 2.469 and 2.484 Å) [71].

In contrast to **15**, which proved to be completely inert towards H_2 and HSiEt_3 under various conditions, **16** was found to react readily with both reagents under ambient conditions to give *trans*- $[\text{Pt}\{\text{Ga}(\text{DDP})\}_2(\text{H})_2]$ (**26**) and *cis*- $[\text{Pt}\{\text{Ga}(\text{DDP})\}_2(\text{H})(\text{SiEt}_3)]$ (**27**) (Scheme 3), the latter of which interestingly shows H/D exchange with the solvent C_6D_6 [71]. The Pt-Ga distances in **27** are very similar (2.3694 and 2.3713 Å) and longer than in **26**. This experimental evidence strongly supports the potential of Ga(DDP) ligands to act as ancillary directing ligands similar to NHCs and phosphanes in classical organometallic chemistry.

2.1.3 p-Block Metal Complexes and Clusters

Among the NHC analogues of Ga(I), so far only Ga(DDP) has proved its potential to serve as a reducing agent for metal salts to produce metalloids clusters with strong metal-metal interactions. Earlier investigations on the reactions of Ga(DDP) with the main group metal halides GaX_3 (X = Me, Cl), Me_2SnCl_2 and SiCl_4 did not lead to reduction reactions but rather yielded insertion products [84]. However, more recently it has been shown that the reduction of SnCl_2 by Ga(DDP) gives the metalloids tin clusters $[\{(\text{DDP})\text{ClGa}\}_2\text{Sn}_7]$ (**29**) and $[\{(\text{DDP})\text{ClGa}\}_4\text{Sn}_{17}]$ (**30**) in



Scheme 5 Synthesis of Zintl-type anionic tin clusters $[\{(\text{DDP})\text{ClGa}\}_2\text{Sn}_7]$ and $[\{(\text{DDP})\text{ClGa}\}_4\text{Sn}_{17}]$ [85]

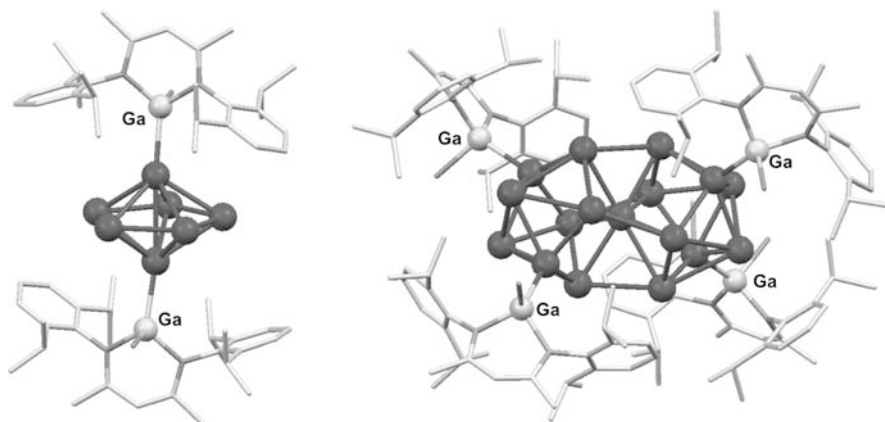
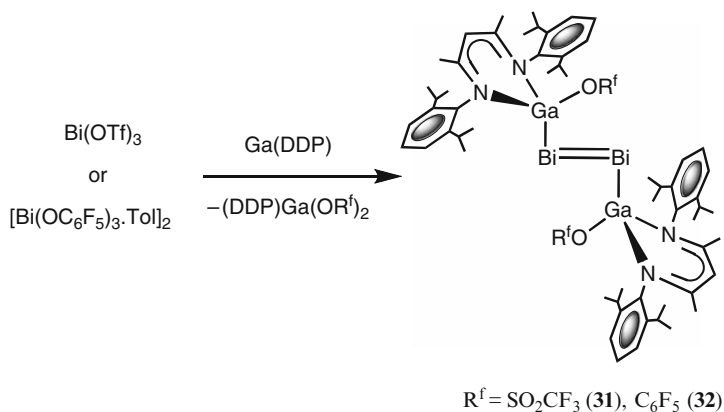


Fig. 5 Solid-state structures of $\{(\text{DDP})\text{ClGa}\}_2\text{Sn}_7$ (**29**) and $\{(\text{DDP})\text{ClGa}\}_4\text{Sn}_{17}$ (**30**)

unusually high yields (Scheme 5, Fig. 5) [85, 86]. The larger cluster **30**, consisting of an ellipsoid Sn_{17} core which is wrapped in a shell of four bulky $\text{GaCl}(\text{DDP})$ moieties, represents the largest metalloids tin cluster known till now. The Sn_{17} core is composed of two identical Sn_9 units sharing one common vertex. The $\text{Sn}-\text{Sn}$ bond distances found in the Sn_{17} core are in the range of 2.863–2.950 Å, but the bond distances around the common vertex in a pseudo-cubic environment are distinctly longer (3.073–3.124 Å). These bond lengths are quite close to the average value of 3.10 Å in grey tin (α -Sn, diamond lattice), and similar to those found in the cluster $[\text{Sn}_{15}\text{Z}_6]$ (average 3.15 Å; $\text{Z} = \text{N}(2, 6\text{-}i\text{-Pr}_2\text{C}_6\text{H}_3)(\text{SiMe}_2\text{X})$; $\text{X} = \text{Me, Ph}$) [87, 88]. The aspect of interest from a synthetic point of view is the unique combination of the smooth reducing power of the particular monovalent $\text{Ga}(\text{DDP})$ reagent together with its carbenoid ligand properties and steric bulk. This concept is quite different to the established synthesis protocols of ligand stabilized main group metalloids clusters $[\text{E}_a\text{R}_b]$.

In a similar manner, the reduction of $\text{Bi}(\text{OSO}_2\text{CF}_3)_3$ and $[\text{Bi}(\text{OC}_6\text{F}_5)_3 \cdot \text{toluene}]_2$ by $\text{Ga}(\text{DDP})$ gives the dibismuthenes $[(\text{R}^f\text{O})(\text{DDP})\text{Ga}-\text{Bi}=\text{Bi}-\text{Ga}(\text{DDP})(\text{OR}^f)]$ ($\text{R}^f = \text{SO}_2\text{CF}_3$ (**31**), C_6F_5 (**32**)) with a short $\text{Bi}=\text{Bi}$ bond (Scheme 6, Fig. 6) [89, 90]. This synthetic strategy falls under the same unique approach as for the Sn_{17} cluster and represents a ‘next generation’ of heavier main group multiple bonded systems with neutral (NHC, GaDDP) rather than anionic ligands, similar to the recent $\text{Si}(0)$ dimer with NHC stabilization by Robinson [91]. The $\text{Bi}=\text{Bi}$ bond lengths in **31** (2.8111 Å) and **32** (2.8182 Å) are slightly shorter in comparison to the known series of aryl dibismuthenes $\text{ArBi}=\text{BiAr}$ ($\text{Ar} = \text{C}_6\text{H}_2\text{-}2, 4, 6\text{-CH}(\text{SiMe}_3)_2$ [92]; $\text{C}_6\text{H}_2\text{-}2, 6\text{-CH}(\text{SiMe}_3)_2\text{-}4\text{-C}(\text{SiMe}_3)_3$ [93]; $\text{C}_6\text{H}_3\text{-}2, 6\text{-}(\text{C}_6\text{H}_2\text{-}2, 4, 6\text{-Me}_3)_2$ [94] (2.8206(8)–2.8699(6) Å). The $\text{Bi}=\text{Bi}$ bond lengths in **31** and **32** are nearly 0.17 Å shorter than the $\text{Bi}(\text{II})\text{-Bi}(\text{II})$ single bond in $\text{Ph}_2\text{Bi-BiPh}_2$ (2.990 Å) [95]. The Ga-Bi bond distances in **31** and **32** (2.655 Å for SO_2CF_3 and 2.693 Å for C_6F_5) are considerably shorter than the sum of the covalent radii for Ga/Bi (2.76 Å) and the covalently linked Ga/Bi molecule $[\text{Me}_2\text{GaBi}(\text{SiMe}_3)_2]_3$ (2.744–2.783 Å) [96]. DFT studies on the model dibismuthene



Scheme 6 Synthesis of dibismuthenes [89]

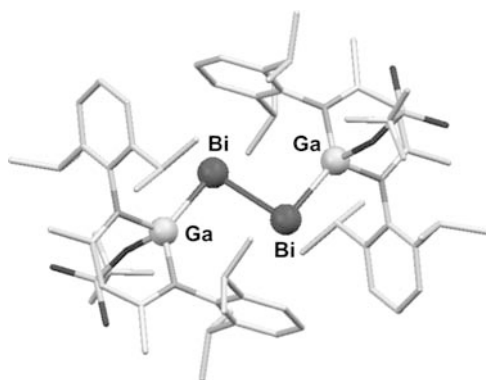


Fig. 6 Solid-state structures of $[(\text{SO}_3\text{CF}_3)(\text{DDP})\text{Ga}-\text{Bi}=\text{Bi}-\text{Ga}(\text{DDP})(\text{SO}_3\text{CF}_3)]$ (**31**)

$[(\text{C}_3\text{H}_5\text{N}_2)\text{Ga}(\text{F})\text{Bi}=\text{BiGa}(\text{F})(\text{C}_3\text{H}_5\text{N}_2)]$ show a typical covalent bonding situation between Ga and Bi and are not in favour of a description as contact ion pair $[\text{Bi}=\text{Bi}]^2[\text{Ga}(\text{OR}^f)\text{DDP}]^{2+}$ corresponding to a Bi(-I) vs. Ga(+III) formulation. Moreover the bismuth–bismuth bond is composed of $\sim 78\%$ σ and $\sim 22\%$ π bonding nature. Apart from the so far shortest and electron-rich dibismuthene bond, these new dibismuthenes demonstrate the unique synthetic potential of NHC analogous low coordinate group 13 compounds in main group chemistry.

2.2 From GaCp^* to the ‘Naked’ Ga^+ as Ligand

The coordination chemistry of GaCp^* has been studied rather extensively for the last decades and has been reviewed several times and will thus be summarized only shortly here. Since the first isolation of GaCp^* the investigation of its properties as ligand to transition metals mostly emphasized to metal carbonyl fragments. In

particular, the reaction of GaCp^* with homoleptic transition metal carbonyls was studied in detail. Hence, the complexes $[\text{Co}_2(\text{CO})_6(\mu^2\text{-GaCp}^*)_2]$ (**33**) [28, 31] or $[\text{Ni}_4(\mu^2\text{-GaCp}^*)_4(\text{CO})_6]$ (**34**) [28, 31] were obtained by reaction of the homoleptic metal carbonyl clusters with GaCp^* . The compounds $[\text{Cr}(\text{CO})_5(\text{GaCp}^*)]$ (**35**) [28, 31], $[(\text{GaCp}^*)_2\text{Mo}(\text{CO})_4]$ (**36**) [97] and $[\text{Fe}(\text{CO})_4(\text{GaCp}^*)]$ (**37**) [28, 31] were obtained by substitution of chelating olefin ligands such as cyclooctene, norbornadiene, cyclooctatetraene and cycloheptatriene, respectively. However, the coordination of the strong σ -donor ligand GaCp^* leads to a substantial strengthening of the M–CO bonds of the remaining carbonyl ligands, which means a strong limitation for the synthesis of gallium-rich coordination compounds.

Homoleptic GaCp^* transition metal complex $[\text{M}(\text{GaCp}^*)_4]$ ($\text{M} = \text{Ni}$ (**38**), Pd (**39**), Pt (**40**), Fig. 7) are accessible by ligand exchange reactions from transition metal olefins, e.g. $[\text{M}(\text{COD})_2]$ ($\text{M} = \text{Ni}$ [97], Pt [81]) or via a reductive route from $[\text{Pd}(\text{tmeda})(\text{CH}_3)_2]$ [98–101]. By slight change of the reaction conditions, also multinuclear homoleptic clusters are available, namely $[\text{Pt}_2(\text{GaCp}^*)_5]$ (**41**) [81, 82], $[\text{Pd}_2(\text{GaCp}^*)_5]$ (**42**) or $[\text{Pd}_3(\text{GaCp}^*)_8]$ (**43**) (Fig. 7) [98–101]. While the

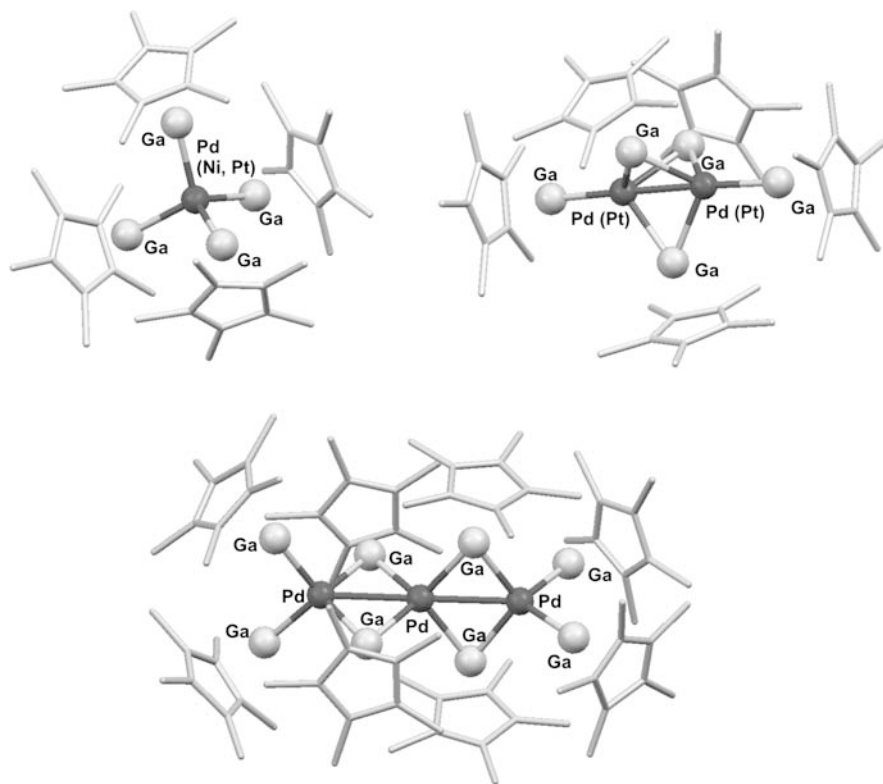


Fig. 7 Solid-state structures of $[\text{M}(\text{GaCp}^*)_4]$ (**38–40**), $[\text{M}_2(\text{GaCp}^*)_5]$ (**41**, **42**) and $[\text{Pd}_3(\text{GaCp}^*)_8]$ (**43**)

monomeric complexes are inert to ligand substitution reactions, the ligand sphere in the di- and trinuclear complexes is fluxional and the terminally bound GaCp^* ligands are exchanged when the complexes are treated with strong ligands (CO, isonitriles or phosphines) [98–101]. All complexes $[\text{M}_a(\text{GaCp}^*)_b]$ are sensitive to ZnMe_2 leading to homoleptic complexes $[\text{M}(\text{ZnR})_n]$ by a redox mechanism (*vide infra*).

2.2.1 Substituent-Free Gallium in d-Block Metal Carbonyl Complexes

While RE(I) (E = Al, Ga, In) units act as strong σ -donors, their π -acceptor properties depend largely on the nature of the R group. Thus, the ability of the ECp^* ligand to act as a π -acceptor in the M-E bond would be diminished by the presence of the strong π -donating ligand Cp^* [102], [103, 104]. Following this reasoning, the absence of ligands bound to the E^+ centre would allow the ‘naked’ cation to display π -acceptor properties in compounds featuring M-E bonds. Complexes of the type $[(\text{L}_n\text{M})_a\text{E}]$, exhibiting ‘naked’ main group 13 metals, are well known for $a = 2$ –4. But this series is restricted to carbonylmetallate fragments $[\text{L}_n\text{M}]$, E being in the oxidation state +III rather than +I, and displaying M–E–M bridging positions only [49, 50, 103–105]

A recent example of a transition metal carbonyl complex containing a ‘naked’ bridging Group 13 atom $[\text{Cp}^*\text{Fe}(\text{dppe})(\mu\text{-Ga})\text{Fe}(\text{CO})_4]$ (**44**) was reported in 2003 [106], followed by the related, symmetric cationic iron complexes $[\{\text{Cp}^*\text{Fe}(\text{CO})_2\}_2(\mu\text{-E})][\text{BAR}^{\text{F}}]$ (E = Ga (**45**), In (**46**)) (Fig. 8) [107, 108]. However, the gallium atoms in these compounds, and in all other compounds featuring $\text{M}(\text{CO})_x$ fragments, may be regarded as being in the oxidation state + III. Nevertheless, these complexes serve as key models for the importance of the π -donation contribution to the M-Ga bonds.

The symmetric complexes **45** and **46** feature quasi-linear Fe–E–Fe units ($178.99(2)^\circ$ and $175.32(6)^\circ$, respectively), in which the central group 13 atom does not engage in any other interaction. The Fe–E bond lengths for **45** (2.266(1), 2.272(1)Å) and **46** (2.460(2), 2.469(2)Å) are comparable to those found for the corresponding bridging halogallane- and haloindanediyl precursors $[\{\text{Cp}^*\text{Fe}(\text{CO})_2\}_2\text{EX}]$ (2.352(1), 2.513(3)Å and 2.509(3)Å) [108]. The Fe–Ga bond in **45** is distinctly

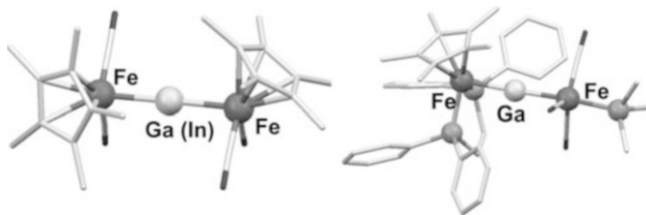
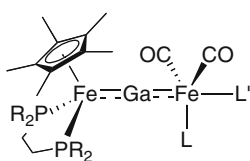


Fig. 8 Solid-state structures of $[\{\text{Cp}^*\text{Fe}(\text{CO})_2\}_2(\mu\text{-E})][\text{BAR}^{\text{F}}]$ (E = Ga (**45**), In (**46**)) and $[\text{Cp}^*\text{Fe}(\text{dppe})(\mu\text{-Ga})\text{Fe}(\text{CO})_3\text{PMe}_3]$ (**49**)

shorter than the typical Fe-Ga single bonds (2.36–2.46 Å) [105]. This shortening is consistent not only with the reduced steric demands around the gallium atom, but also with an increase of Fe→Ga π -donation. Most importantly, the Cp* centroid-Fe(1)–Fe(2)–Cp* centroid torsion angles observed for **45** (84.6(1)°) and **46** (86.8(3)°) reflect a relative alignment of the two [Cp*Fe(CO)₂] fragments, which allows for optimal Fe→Ga π -donation [109]. A bond population analysis derived from the DFT calculations carried out on compound **45** (BLYP/TZP level) reveals an important π contribution to the covalent Fe-Ga interaction ($\sigma:\pi = 61:38$), which is higher than that for the Fe-Ga single bond in the model compound CpFe(CO)₂GaCl₂ ($\sigma:\pi = 86:14$) [110]. An analogous analysis of **46** reflected a smaller π contribution in the case of the Fe-In bond ($\sigma:\pi = 74:26$), as expected for a heavier main-group element, due to its diminished π orbital overlap. In order to evaluate π -back-donation contribution to the Fe-Ga bond as a function of the π -basicity of the Fe fragments, Ueno and co-workers synthesized a series of asymmetric compounds (**44**, **47–52**), shown in Scheme 7 [106, 111, 112].

The effect of the systematic variation of the substituents on the Fe atoms is reflected on the Fe-Ga bond lengths of the structurally characterized compounds **44**, **47**, **48** and **49**. The four compounds feature linear trimetallic Fe–Ga–Fe units, as expected for a sp-hybridized gallium atom and all Fe-Ga bonds are markedly shorter than the usual corresponding single bonds, which indicates their multiple bonding character. As a more π -basic metal fragment is introduced, the corresponding Fe-Ga bond is shortened, while the other Ga-Fe bond length increases. This suggests a competition between both iron fragments for the π -back-bonding towards the gallium centre [111, 112]. Thus, the substitution of the dppe ligand on **44** with the more electron-donating ligand dmpe in **47** leads to the shortening of the corresponding Cp*(P2)Fe-Ga bond, while the Ga-Fe(CO)₄ bond is elongated. Similarly, the substitution of one of the CO ligands with a phosphorus-based donor leads to shorter Ga-Fe(CO)₃P bonds and longer Cp*(dppe)Fe-Ga bonds, as shown in Table 1.



- 44**; R = Ph, L = L' = CO
47; R = Me, L = L' = CO
48; R = Ph, L = CO, L' = P(OPh)₃
49; R = Ph, L = CO, L' = PMe₃
50; R = Ph, L = CO, L' = P(OMe)₃
51; R = Ph, L = L' = PMe₃
52; R = Ph, L = L' = P(OMe)₃

Scheme 7 Series of asymmetric Fe–Ga–Fe compounds **44**, **47–52** [106, 111, 112]

Table 1 Comparison of bond lengths for Ga bridged diiron complexes **44**, **47**, **48** and **49**

Complex	Cp*(P2)Fe-Ga (Å)	Ga-Fe(CO) ₂ LL' (Å)
[Cp*Fe(dmpe)(μ -Ga)Fe(CO) ₄] (47)	2.2409(5)	2.3205(5)
[Cp*Fe(dppe)(μ -Ga)Fe(CO) ₄] (44)	2.2479(10)	2.2931(10)
[Cp*Fe(dppe)(μ -Ga)Fe(CO) ₃ {P(OPh) ₃ }] (48)	2.2690(8)	2.2844(8)
[Cp*Fe(dppe)(μ -Ga)Fe(CO) ₃ (PMe ₃)] (49)	2.2769(5)	2.2686(5)

Furthermore, the first gallium-bridged heterobimetallic complexes $\text{Cp}^*(\text{dppe})\text{FeGaM}(\text{CO})_5$ ($\text{M} = \text{Cr}$ (**53**), W (**54**)) have been reported very recently [113]. The crystal structure analysis of complex **54** revealed a quasi-linear Fe-Ga-W unit ($173.78(4)^\circ$) and Fe-Ga and Ga-W bond lengths ($2.2687(12)\text{\AA}$ and $2.5861(8)\text{\AA}$) that are shorter than the corresponding single bonds (Fe-Ga : $2.36 - 2.46\text{\AA}$; Ga-W : $2.71 - 2.76\text{\AA}$) [105, 113, 114]. The Fe-Ga bond length is comparable to that in complex **48**, which suggests that the $\text{W}(\text{CO})_5$ fragment has a π -basicity similar to that of the $[\text{Cp}^*\text{Fe}(\text{dppe})(\mu\text{-Ga})\text{Fe}(\text{CO})_3\{\text{P}(\text{O}^i\text{Pr})_3\}]$ fragment [112].

2.2.2 Substituent-Free Gallium in All Gallium-Ligand Coordinated d-Block Metal Complexes

Until 2006, the only reported terminal complexes of the heavier Group 13 monocations were those of Tl^+ , whose bonds to d^8 or d^{10} centres are explained by dispersion interactions and long-range polarization effects without covalent contributions [41, 115, 116]. The recent availability of sources of E^+ ‘naked’ Group 13 cations, such as $[\{\text{Ga}_2\text{Cp}^*\}^+\{\text{BAR}_4^{\text{F}}\}^-]$ [117, 118], $[\{\text{In}_2\text{Cp}^*\}^+\{\text{BAR}_4^{\text{F}}\}^-]$ and $[\text{In}^+\{\text{BAR}_4^{\text{F}}\}^-]$, [38] (Fig. 9) has led to the preparation of the first examples of transition metal complexes featuring Ga^+ and In^+ cations as terminal ligands [38, 119]. The reaction of the suitable precursor with closed shell 18 VE complexes $[\text{Pt}(\text{GaCp}^*)_4]$ (**40**), $[\text{Pt}(\text{PPh}_3)_4]$ and $[\text{Ru}(\text{PCy}_3)_2(\text{GaCp}^*)_2(\text{H})_2]$ (**55**) yielded the ionic compounds $[\{\text{GaPt}(\text{GaCp}^*)_4\}^+\{\text{BAR}_4^{\text{F}}\}^-]$ (**56**), $[\{\text{InPt}(\text{PPh}_3)_3\}^+\{\text{BAR}_4^{\text{F}}\}^-]$ (**57**) [38] and $[\{\text{Ru}(\text{PCy}_3)_2(\text{GaCp}^*)_2(\text{Ga})\}^+\{\text{BAR}_4^{\text{F}}\}^-]$ (**58**), respectively (Fig. 10) [119].

Complex **56** exhibits a slightly distorted trigonal-bipyramidal structure with the Ga^+ ligand occupying an axial position. The $\text{GaCp}^*\text{-Pt-Ga}^+$ axis is almost linear ($176.83(3)^\circ$), while the GaCp^* equatorial ligands are bent towards the Ga^+ centre, with $\text{Cp}^*\text{Ga-Pt-Ga}^+$ angles closer to 80° than to 90° . As expected for this geometry, the equatorial Pt-Ga bonds are shorter (av. 2.352\AA) than the Pt-Ga axial bonds ($\text{Cp}^*\text{Ga-Pt}$, $2.444(1)\text{\AA}$ and Pt-Ga^+ $2.459(1)\text{\AA}$), and comparable to those observed in the parent complex $[\text{Pt}(\text{GaCp}^*)_4]$ (av. 2.335\AA). The formation

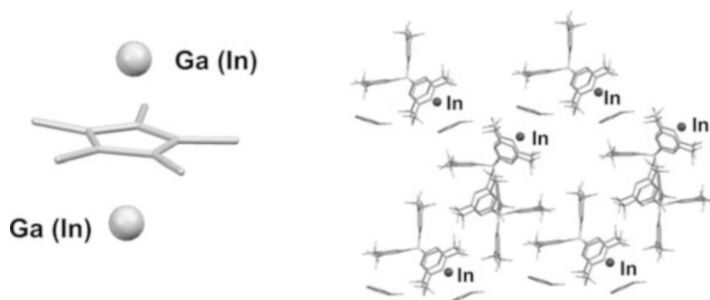


Fig. 9 Solid-state structures of the cation $[\{\text{E}_2\text{Cp}^*\}^+]$ and $[\text{In}^+\{\text{BAR}_4^{\text{F}}\}^-]$

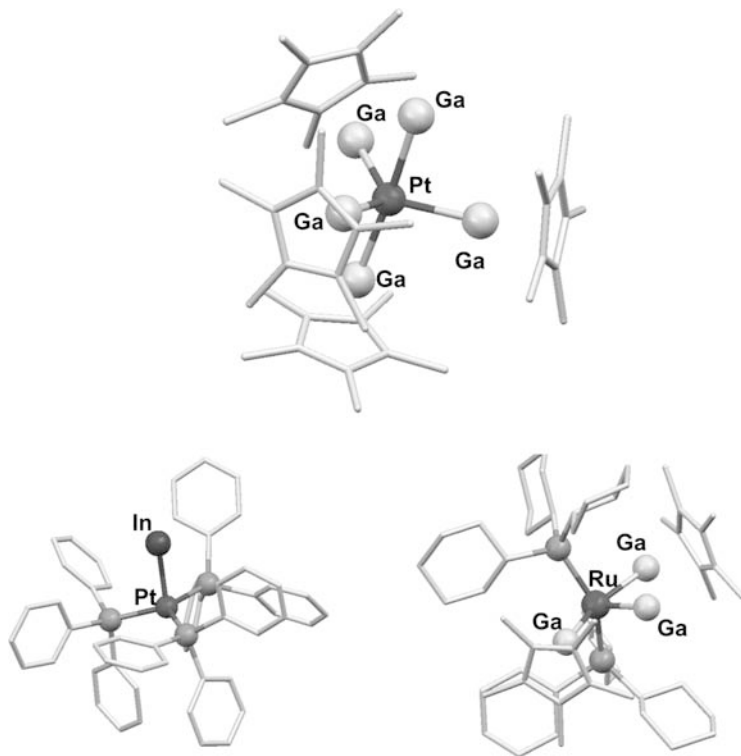


Fig. 10 Solid-state structures of the cations of $\{[\text{GaPt}(\text{GaCp}^*)_4]\}^+\{\text{BARf}_4\}^-$ (**56**), $[\text{InPt}(\text{PPh}_3)_3]^+\{\text{BARf}_4\}^-$ (**57**) and $\{[\text{Ru}(\text{PCy}_3)_2(\text{GaCp}^*)_2(\text{Ga})]\}^+\{\text{BARf}_4\}^-$ (**58**)

of complex **57** involves the loss of one phosphine ligand upon coordination of the low-valent cation, so that it features a trigonal-pyramidal geometry, in which the apical position is occupied by the In^+ ligand ($\text{Pt-In} = 2.580(1)\text{\AA}$). [38] Ru complex **58** exhibits a heavily distorted trigonal-bipyramidal coordination environment, where the equatorial positions are occupied by the Ga^+ ligand and, quite unexpectedly, by the bulky PCy_3 groups, while the two GaCp^* ligands are found at axial positions. As in the case of **56**, the GaCp^* ligands in **58** are significantly bent towards the terminal Ga^+ ligand, with $\text{Cp}^*\text{Ga-Ru-Ga}^+$ angles that are closer to 80° than to 90° , but no significant Ga-Ga interactions were observed. The average Ru-GaCp^* bond length (2.4236\AA) is comparable to the corresponding bonds in the starting material $[\text{Ru}(\text{PCy}_3)_2(\text{GaCp}^*)_2(\text{H})_2]$ (2.4017\AA). Interestingly, the Ru-Ga^+ bond length ($2.300(2)\text{\AA}$) is more than 5% shorter than that of the Ru-GaCp^* bonds and is the shortest Ru-Ga contact known to date [119].

In all cases, it is clear that the ‘naked’ E^+ ligand acts as a Lewis acidic centre, in contrast to the Lewis basic GaCp^* ligand. It has been shown by detailed bonding analysis that there is a substantial covalent contribution to the $\text{E}^+ - \text{M}$ interaction and that the contributions of σ and π orbitals are equally important. Thus, E^+ ligands

act as strong σ and π acceptors only, while the metal fragments $[\text{PtL}_n]$ and $[\text{RuL}_n]$ are pure donors. The formation of $[\{(\text{Cp}^*\text{Ga})_4\text{Pt}(\mu\text{-Ga})\text{Pt}(\text{H})(\text{GaCp}^*)_3\}^{2+}]$ (**59**) by selective protolysis of coordinated GaCp^* in $[\text{Pt}(\text{GaCp}^*)_4]$ helps to substantiate this analysis [38]. Moreover, the exceptionally short Ru-Ga bond length in **58** can then be explained by the higher basicity of the $[\text{Ru}(\text{PCy}_3)_2(\text{GaCp}^*)_2]$ fragment, compared to that of $[\text{Pt}(\text{GaCp}^*)_3]^+$ [119].

There is only one example of a true low-valent bridging Ga^+ complex, namely $[(\text{GaCp}^*)_4\text{Ru}(\text{H})(\mu\text{-Ga})\text{Ru}(\text{H})_2(\text{GaCp}^*)_3]$ (**60**) (Fig. 11) [120]. This compound was obtained by means of the hydrogenolysis of coordinated GaCp^* ligands. The structural parameters of the Ru and Ga atoms in the solid state suggest a hexacoordinate coordination environment for each Ru centre, which results in two different octahedral Ru fragments: $\{(\text{GaCp}^*)_4(\text{H})\text{Ru}(\mu\text{-Ga})\}$ (Ru1) and $\{(\text{GaCp}^*)_3(\text{H})_2\text{Ru}(\mu\text{-Ga})\}$ (Ru2). These two fragments are bound by a substituent free Ga atom in a linear arrangement (Ru1-Ga-Ru2 $178.0(1)^\circ$). The Ru-Ga⁺ bonds are $2.322(1)\text{\AA}$ (to Ru2) and $2.387(1)\text{\AA}$ (to Ru1), while the Ru-GaCp* bond lengths average to 2.365\AA and are thus comparable to those observed in related Ru-GaCp* complexes and clusters [121–123]. Like in the previous cases, the strong σ - and π -accepting abilities of the substituent-free Ga^+ account for the observed linear arrangement in **60** [120]. It has been shown so far that the coordination chemistry of the ‘naked’ E^+ ligands ($\text{E} = \text{Ga}, \text{In}$) is determined by the s character of its lone-electron pair, since it does not participate in coordinative bonding, but has strong σ/π -acceptor properties. Therefore, it can be said that in RE(I) species the substituents R^- ‘switch on’ the free electron pair on the electrophilic E^+ ligand, converting it into a strong σ -donor RE(I) ligand [38].

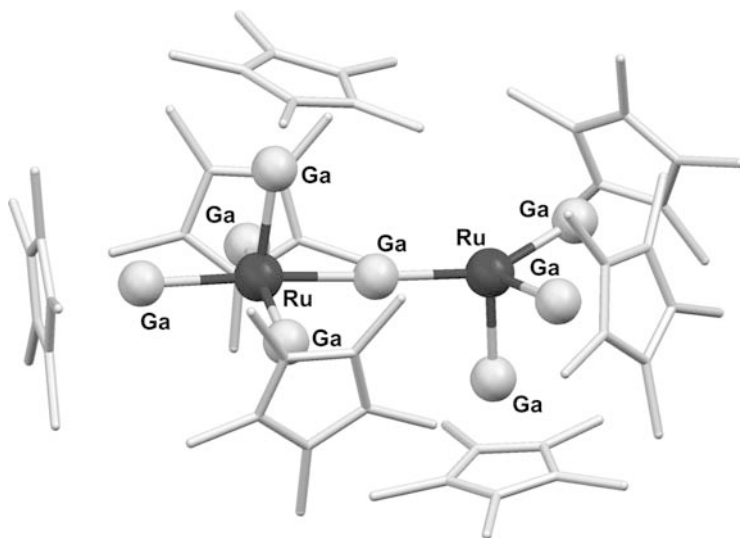


Fig. 11 Solid-state structures of $[(\text{GaCp}^*)_4\text{Ru}(\text{H})(\mu\text{-Ga})\text{Ru}(\text{H})_2(\text{GaCp}^*)_3]$ (**60**)

2.3 Quantum Chemical Calculations on the M–Ga Bonding in Complexes with Ga(I) Ligands

The nature of the bonding between a transition metal and a Ga(I) ligand in complexes [M]–GaR has been the topic of numerous theoretical studies [83, 102, 124–129]. Three reviews appeared which summarize the present knowledge in the field [130–132]. A particular focus of the work concerns the influence of the substituent R on the nature of the metal–GaR bonding. Early experimental work suggests [133–137] that π -donor groups R stabilize complexes [M]–GaR through charge donation into the formally empty p(π) valence orbitals of Ga and that the $M \rightarrow$ Ga π -back-donation is weak. The isolation of the complex $(\text{CO})_4\text{Fe–GaAr}^*$ with the bulky aryl ligand $\text{Ar}^* = 2,6\text{-(2,4,6-triisopropylphenyl)-phenyl}$ [138] and the synthesis of the homoleptic diyl complex $\text{Ni}(\text{Ga–C}(\text{SiMe}_3)_3)_4$ [102] were the first examples of stable complexes [M]–GaR where R is a weak π -donor. The rather short Fe–Ga bond in the former complex by Robinson et al. [138] let the authors suggest that there is strong $\text{Fe} \rightarrow$ Ga π -back-donation. A charge and energy decomposition analysis of the model complex $(\text{CO})_4\text{Fe–GaPh}$ (Ph = phenyl) showed that the π -back-donation is not much stronger than in $(\text{CO})_4\text{Fe–GaCp}$ and that the shorter and stronger Fe–Ga bond in the former species comes mainly from the stronger σ bond and from the increase in the electrostatic attraction [128].

Table 2 shows the results of an energy decomposition analysis (EDA) of the $(\text{CO})_4\text{Fe–GaR}$ bonds for R = Cp, $\text{N}(\text{SiH}_3)_2$, Ph, CH_3 in comparison with the data for the $\text{Fe}(\text{CO})_4\text{–CO}$ bond [128, 139]. It becomes obvious that the relative strength of the π -contribution to the $(\text{CO})_4\text{Fe–GaR}$ bond for the strong π -donor substituents R = Cp, $\text{N}(\text{SiH}_3)_2$ has comparable percentage values as for the weak π -donors Ph and CH_3 . For all systems $(\text{CO})_4\text{Fe–GaR}$ shown in Table 2 holds that the π -orbital contribution to ΔE_{orb} is much less than for the carbonyl bond in $\text{Fe}(\text{CO})_4\text{–CO}$.

Table 2 Energy decomposition analysis of the axial isomers of $\text{Fe}(\text{CO})_4\text{–GaR}$ (R = Cp), $\text{N}(\text{SiH}_3)_2$, Ph, CH_3 and $\text{Fe}(\text{CO})_5$ at BP86/TZP [kcal/mol]. The data are taken from references [128]

	$\text{Fe}(\text{CO})_4\text{–GaCp}$	$\text{Fe}(\text{CO})_4\text{–GaN}(\text{SiH}_3)_2$	$\text{Fe}(\text{CO})_4\text{–GaPh}$	$\text{Fe}(\text{CO})_4\text{–GaCH}_3$	$\text{Fe}(\text{CO})_4\text{–CO}$
ΔE_{int}	–31.7	–42.9	–61.0	–62.0	–54.6
ΔE_{Pauli}	69.8	95.2	129.5	133.4	134.8
$\Delta E_{\text{elstat}}^{\text{a}}$	–47.1 (46.6%)	–67.7 (49.1%)	–102.3 (53.7%)	–106.1 (54.3%)	–98.0 (51.7%)
$\Delta E_{\text{orb}}^{\text{a}}$	–54.4 (53.4%)	–70.4 (50.9%)	–88.2 (46.3%)	–89.3 (45.7%)	–91.4 (48.3%)
$\Delta E_{\sigma}^{\text{b}}$	–47.2 (86.8%)	–57.6 (81.8%)	–73.0 (82.8%)	–75.0 (84.0%)	–47.6 (52.1%)
$\Delta E_{\pi}^{\text{b}}$	–7.2 (13.2%)	–12.8 (18.2%)	–15.2 (17.2%)	–14.3 (16.0%)	–43.8 (47.9%)
ΔE_{prep}	8.7	8.4	8.7	8.2	8.1
$\Delta E (= -D_{\text{e}})$	–23.0	–34.5	–52.3	–53.8	–46.5

^a Values in parentheses give the percentage contribution to the total attractive interactions $\Delta E_{\text{elstat}} + \Delta E_{\text{orb}}$

^b Values in parentheses give the percentage contribution to the total orbital interactions ΔE_{orb}

Table 3 Energy decomposition analysis of the homoleptic complexes $\text{Fe}(\text{GaCH}_3)_5$ and $\text{M}(\text{GaCH}_3)_4$ ($\text{M} = \text{Ni}, \text{Pd}, \text{Pt}$) at BP86/TZP [kcal/mol]. The data are taken from references [128]

	$\text{Fe}(\text{GaCH}_3)_4-$ GaCH_3^a	$\text{Ni}(\text{GaCH}_3)_3-$ GaCH_3	$\text{Pd}(\text{GaCH}_3)_3-$ GaCH_3	$\text{Pt}(\text{GaCH}_3)_3-$ GaCH_3
ΔE_{int}	-67.0	-57.0	-46.7	-57.7
ΔE_{Pauli}	120.8	130.9	154.3	204.0
$\Delta E_{\text{elstat}}^b$	-115.2 (61.3%)	-123.7	-145.0	-187.1
ΔE_{orb}^b	-72.6 (38.7%)	-64.2 (34.2%)	-56.0 (27.9%)	-74.6 (28.5%)
ΔE_{σ}^c	-45.5 (62.7%)	-38.9	-34.0	-48.2
ΔE_{π}^c	-27.1 (37.3%)	-25.3 (39.4%)	-22.0 (39.2%)	-26.4 (35.3%)
ΔE_{prep}	2.9	3.6	4.7	7.4
$\Delta E_{\text{c}} (= -D_{\text{c}})$	-64.1	-53.4	-42.0	-50.3

^a Axial ligand^b Values in parentheses give the percentage contribution to the total attractive interactions $\Delta E_{\text{elstat}} + \Delta E_{\text{orb}}$ ^c Values in parentheses give the percentage contribution to the total orbital interactions ΔE_{orb}

The EDA results in Table 2 give the *relative* strength of the π -orbital contribution of the Ga(I) ligands with respect to the strong π -acceptor CO. What about the strength of the π -orbital interactions in systems where there is no competition with other ligands such as in homoleptic complexes $\text{M}(\text{GaR})_n$? The latter question has been addressed in theoretical studies of $\text{Fe}(\text{GaCH}_3)_5$ [128, 139] and $\text{M}(\text{GaCH}_3)_4$ [128, 139]. Table 3 shows the most important results. It becomes obvious that the π -orbital contribution to ΔE_{orb} in the homoleptic complexes is significantly stronger than in the complexes where the ligand GaCH_3 competes with CO for π -back-donation from the metal. It is interesting to note that the percentage contributions of the latter interactions are nearly the same for the metals Fe, Ni, Pd, Pt.

3 From Homoleptic GaCp^* Complexes to Highly Coordinated Transition Metal Zinc Compounds [12–25, 48, 140]

Zinc and Gallium are neighbours in the periodic table and have comparable atomic volumes and electronegativities (1.7 and 1.8 for Zn and Ga, respectively, on the Allred–Rochow scale). Some transition metal zinc complexes featuring covalent M–Zn bonds are known [12–25], but homoleptic zinc-rich compounds of the general type $[\text{M}_a(\text{ZnR})_b]$ similar to the earlier-mentioned gallium compounds $[\text{M}_a(\text{GaR})_b]$ do not exist. However, the recent discovery of Zn(I) compounds of the type $[\text{RZn}(\text{ZnR})]$ ($\text{R} = \text{Cp}^*, \text{DDP}, \text{etc.}$) suggested a rich chemistry of organometallic Zn(I) species [12–25]. From the viewpoint of the earlier-discussed chemistry of GaR groups as strong 2-electron donor ligands in coordination chemistry the question arises if a similar chemistry can be developed based on the analogous ZnR moieties which may act as one-electron ligands at transition metals. Taking into account the

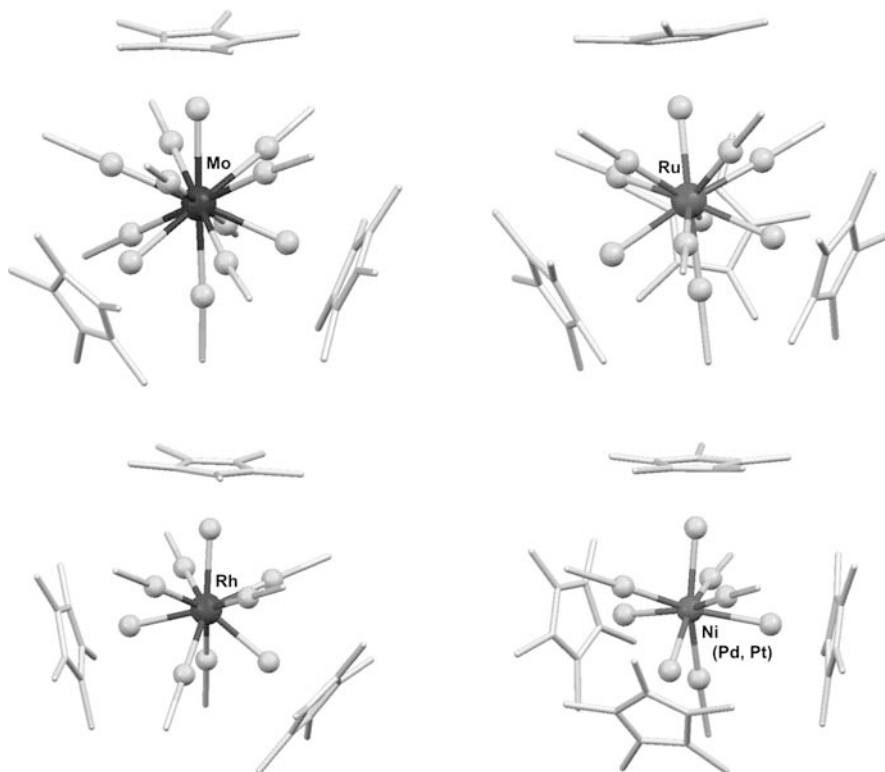


Fig. 12 Molecular structures of the homoleptic compounds $[M(\text{ZnCH}_3)_a(\text{ZnCp}^*)_b]$ ($M = \text{Mo}$, $a = 9$, $b = 3$ (**61**); $M = \text{Ru}$, $a = 6$, $b = 4$; (**65**), $M = \text{Rh}$, $a = 6$, $b = 3$ (**67**); $M = \text{Ni}$ (**69**), Pd (**70**), Pt (**71**), $a = 4$, $b = 4$)

soft and flexible binding properties of the Cp^* substituents and as well the inherent reducing power of the carbenoid gallium(I) compound we got curious to know of what would happen, if we treated $[\text{L}_m\text{M}(\text{GaCp}^*)_n]$ with ZnR_2 ($\text{L} = \text{CO}$ and/or all-hydrocarbon π -ligands; $\text{R} = \text{Me}$, Et). In the course of these studies we discovered the unusual very zinc-rich molybdenum compound $[\text{Mo}(\text{ZnCp}^*)_3(\text{ZnMe})_9]$ (**61**) [141]. The crystal structure of **61** exhibits an icosahedral closed packed MoZn_{12} core with a central Mo atom and a C_3 symmetric arrangement of the hydrocarbon substituents (Me , Cp^*) at the periphery (Fig. 12) [141]. The expansion to transition metal centres other than molybdenum obviously seems feasible, given the accessibility of (homoleptic) complexes such as $[\text{M}(\text{GaCp}^*)_n]$ for many transition metals M (see earlier). In the following section we will summarize the essentials of the synthesis and structural properties of the homoleptic compounds $[\text{M}(\text{ZnR})_n]$ ($n \geq 8$; $\text{R} = \text{Me}$, Et , Cp^*) for a selection of transition metals $\text{M} = \text{Mo}$, Ru , Rh , Ni , Pd and Pt (Table 4). Then, we will discuss the bonding situation of key examples of the series.

Table 4 Composition and numbering scheme of the compounds **61–72**

Number	Composition ^a	Core	c.n.	Symmetry ^b
61	[Mo(ZnCp [*]) ₃ (ZnMe) ₉]	MoZn ₁₂	12	C ₃
62	[Mo(ZnCp [*]) ₂ (ZnEt) ₁₀]	MoZn ₁₂	12	C _s
63	[Mo(GaMe) ₄ (ZnCp [*]) ₄]	MoGa ₄ Zn ₄	8	T _d
64	[Mo(GaMe) ₂ (ZnCp [*]) ₄ (ZnMe) ₄]	MoGa ₂ Zn ₈	10	C _s
65	[Ru(ZnCp [*]) ₄ (ZnMe) ₆]	RuZn ₁₀	10	C ₃
66	[Ru(ZnCp [*]) ₄ (ZnMe) ₄ (H) ₂]	RuZn ₈ H ₂	10	T _d
67	[Rh(ZnCp [*]) ₃ (ZnMe) ₆]	RhZn ₉	9	C ₃
68	[Rh(GaMe)(ZnCp [*]) ₄ (ZnMe) ₃]	RhGaZn ₇	8	C ₃
69	[Ni(ZnCp [*]) ₄ (ZnMe) ₄]	NiZn ₈	8	T _d
70	[Pd(ZnCp [*]) ₄ (ZnMe) ₄]	PdZn ₈	8	T _d
71	[Pt(ZnCp [*]) ₄ (ZnMe) ₄]	PtZn ₈	8	T _d
72	[Pt(ZnCp [*]) ₄ (ZnEt) ₄]	PtZn ₈	8	T _d

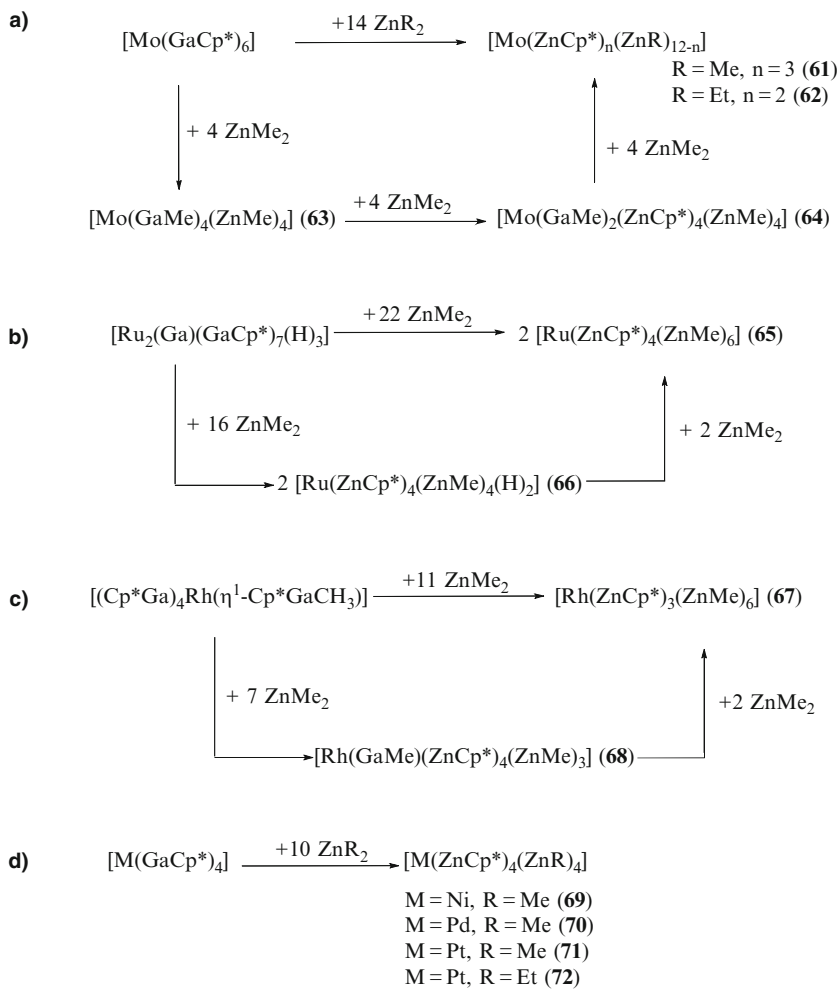
^aNote that all compounds **61–72** fulfil the eighteen-electron rule by counting the ZnR as one-electron and GaR as two-electron ligands at the metal centre M in oxidation state zero

^bThe symbols refer to the idealized (local) point group symmetry of the compounds

3.1 Synthesis and Molecular Structures of the Compounds [M(ZnR)_n]

The compounds **61–72** (Table 4) of the general formula [M(ZnR)_n] (*n* = 8–12; M = Mo, Ru, Rh, Ni, Pd, Pt; R = CH₃, Cp^{*}) are formed by the treatment of the all-gallium coordinated transition metal precursors [Mo(GaCp^{*})₆] (**73**), [Ru₂(Ga)(GaCp^{*})₇(H)₃] (**60**) [120] or [Ru(GaCp^{*})₆(Cl)₂] (**74**) [121] [(Cp^{*}Ga)₄RhGa(η¹-Cp^{*})Me] (**75**) [142] and [M(GaCp^{*})₄] (**38–40**; M = Ni, Pd, Pt) [81] with a suitably chosen excess of ZnMe₂ or ZnEt₂ in toluene solution at elevated temperatures of 80–110°C within a few hours of reaction time (Scheme 8). The isolated yields are usually quite good and the selectivity of the reactions is very high. The molecular structures (Fig. 12, 13) of all known compounds of this type (**61–72**) correspond to typical deltahedral coordination polyhedra, namely icosahedron, bicapped square antiprism, capped square antiprism and dodecahedron, in accordance with a straightforward deduction from the VSEPR concept. Note that exchange of the substituents R takes place which effectively leads to transfer of Cp^{*} from the gallium to the zinc to some extent. A detailed discussion of the NMR spectroscopic and structural properties is given in the original publication [140].

All compounds **61–72** fulfil the formal 18-electron rule in coordination chemistry [143]. This result is based on the treatment of the ZnR groups as 1-electron ligands and the GaR groups as 2-electron ligands. The synthesis of **61–72** involve reduction of Zn(II) to Zn(I) and a concomitant oxidation of Ga(I) to Ga(III). The corresponding by-products were Me₂GaCp^{*} (major) and GaMe₃. The driving force of the reaction is certainly connected with the facile oxidation of Ga(I) to Ga(III) combined with the very similar electronic and steric properties of the monovalent GaR and ZnR ligands at a given transition metal centre. However, the assignment



Scheme 8 Synthesis of the compounds 61–72

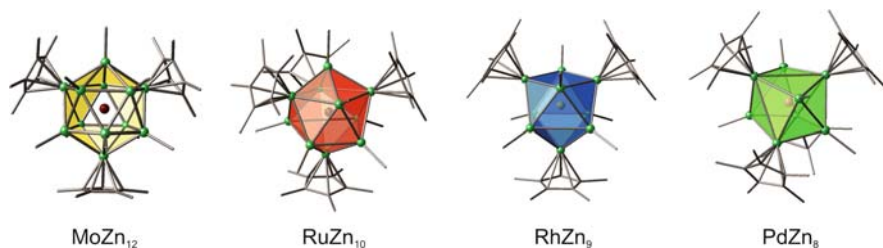


Fig. 13 Molecular structures of 61, 65, 67 and 70 as representative examples of the series of compounds listed in Table 4 showing the coordination polyhedron around the central metal M and the corresponding parent molecules

of oxidation states in the new compounds of Table 4 is not straightforward (see the bonding discussion later).

In the course of the overall redox and substituent exchange reactions, the resulting monovalent zinc fragments, ZnMe, ZnEt, and ZnCp* are efficiently trapped by binding to the transition metal centre resulting in rather strong covalent M–Zn bonds. Hence, the formal substitution of one GaR ligand always gives two ZnR ligands attached to the transition metal centre. As a reason for this the electron count of the product complexes does not change with the present amount of zinc in the ligand sphere and must sum up to 18 electrons in all cases. The total number of Zn ligands in the complexes is only dependent on the number of gallium ligands in the precursor as well as the amount of ZnMe₂ used in the reaction. Thus, treatment of the precursors [M(GaCp*)_n] with an excess ZnR₂ > 2n leads to the pseudo-homoleptic compounds [M(ZnCp*)_a(ZnR)_b] (*a* + *b* = 2*n*). Since the Cp* and the alkyl substituents R at gallium and zinc centres are known to be fluxional and/or transferable [38, 142], a further rise of the excess of ZnR₂ is likely to allow the formation of truly homoleptic compounds of the type [M(ZnR)_n] in case of a quantitative exchange of Cp* against R (see the compositions of compounds **1** and **2**). At this point, we like to note that a further extension of the synthesis concept to compounds [L_aM_b(GaR)_c] featuring substituents R other than Cp*, i.e. DDP, etc. (see the earlier section), certainly warrants to be explored as it is suggested for suitable MgR₂ compounds. In the following section we will focus on the bonding analysis using quantum chemical calculations on the representative examples **61**, and **65–72** of Table 4.

3.2 Quantum Chemical Calculations of Highly Coordinated Transition Metal Zn(I) Complexes

The bonding situation in the presented Zn(I) compounds **61** and **65–72** can be discussed by analysing the parent compounds **61H**, **65H**, **67H** and **69H–71H** where all the organic moieties are replaced by hydrogen. This is justified as the M–Zn-distances in these parent compounds only slightly differ from those in the synthesized molecules. The parent compounds have all minimum structures with high symmetries *I*_h (**61H**), *D*_{4d} (**65H** and **69H–71H**) and *D*_{3h} (**67H**) (See Table 5 for calculated geometry parameters and Fig. 14 for a graphical presentation of the minimum structures). A detailed discussion of the bonding situation in **61H**, using atoms-in-molecules-(AIM), molecular orbital-(MO) and energy decomposition analysis (EDA) is presented in the next paragraph. The bonding in **65H**, **67H** and **69H–71H** will be discussed in comparison with **61H**.

3.2.1 Bonding Situation in [Mo(ZnH)₁₂] (**61H**)

The highest occupied MOs (HOMO) in **61H** are the triply degenerated 12*t*_{1u} orbitals followed by quintuply degenerated 12*h*_g (HOMO-1) and the 9*a*_g (HOMO-2). The

Table 5 Calculated RI-BP86/def2-TZVPP metal–metal bond length of the model compounds **61H**, **65H**, **67H** and **69H–71H** where the organic moieties are replaced by hydrogen atoms. Distances in Å

Compound		Point group	M–Zn	Zn–Zn
Mo(ZnH) ₁₂	61H	<i>I</i> _h	2.684	2.822
Ru(ZnH) ₁₀	65H	<i>D</i> _{4d}	2.541; 2.584	2.740; 2.798
Rh(ZnH) ₉	67H	<i>D</i> _{3h}	2.497; 2.516	2.853; 3.044
Ni(ZnH) ₈	69H	<i>D</i> _{4d}	2.374	2.821; 2.993
Pd(ZnH) ₈	70H	<i>D</i> _{4d}	2.482	2.936; 3.149
Pt(ZnH) ₈	71H	<i>D</i> _{4d}	2.496	2.951; 3.172

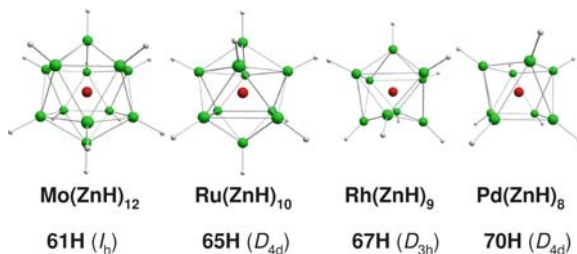


Fig. 14 Molecular structures of **1**, **5**, **7** and **10** showing the coordination polyhedron around the central metal M and the corresponding parent molecules [M(ZnH)_{*n*}] (**1H**, **5H**, **7H** and **10H** used for the quantum chemical calculations)

$12h_g$ MOs have large contributions from the 4d atomic orbitals (AO) and the $9a_g$ of the 5s AO of the molybdenum. The $12t_{1u}$ has only small contributions from the molybdenum's 5p AOs. Therefore, the $12h_g$ and $9a_g$ mainly describe bonding interactions of the Zn-atoms with the 4d AOs and 5s AOs of molybdenum while the Mo–Zn bonding contribution in the $12t_{1u}$ is negligible and these MOs describe Zn–Zn interactions.

Orbitals belonging to other irreducible representations of the *I*_h point group than a_g , t_{1u} and h_g cannot have contributions from s, p and d AOs of molybdenum and can only describe occupied ligand orbitals of the (ZnH)₁₂ cage-like icosahedral structure. Lower lying valence orbitals of a_g , t_{1u} and h_g symmetry give altogether three a_g , five sets of h_g and four sets of t_{1u} MOs (Fig. 15). Figure 15 shows all MOs representing adequate Mo–Zn interactions.

A topological analysis of the electron density of **61H** according to AIM theory gives twelve bond critical points and linear bond paths going from molybdenum to the zinc atoms indicating twelve Mo–Zn bonding interactions. While there are twelve additional bond paths describing zinc–hydrogen bonds there are no Zn–Zn bond paths (see Fig. 16).

To estimate the overall contributions of s, p and d orbitals of molybdenum to the Mo–(ZnH)₁₂ interactions, the results of an EDA are given in Table 6. The chosen fragments are the molybdenum atom in the configuration [Kr]4d⁵5s¹ and the (ZnH)₁₂ cage in a corresponding septet state. The total orbital interactions contribute 42.8% to the attractive interactions. While the strongest orbital interactions

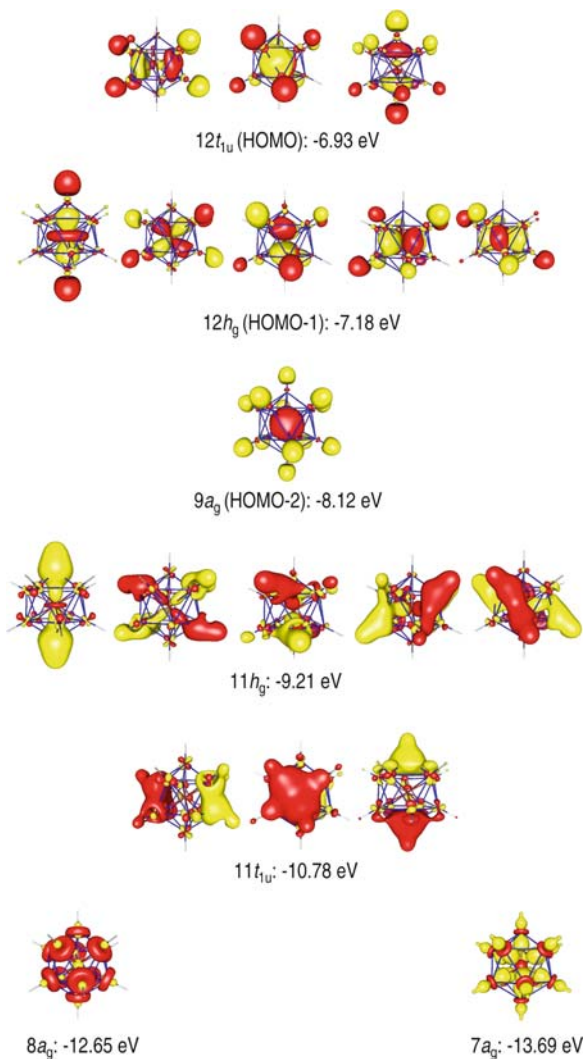


Fig. 15 Kohn–Sham molecular orbitals of $[\text{Mo}(\text{ZnH})_{12}]$ (**61H**) with significant coefficients at the molybdenum atom

come from orbitals in a_g and h_g irreducible representations (23.9% for a_g and 71.5% for h_g which gives 14.3% for every 5d AO of molybdenum) the contributions from t_{1u} MOs is only negligible (4.5%).

The EDA results suggest that only twelve of the 18 valence electrons are in the valence shell of the molybdenum atom [143], namely those in the 12 h_g and 9 a_g MOs. In terms of a valence bond model these twelve occupy six sd^5 hybrid orbitals, each of them building a three-centre two-electron bond stretching across the diagonals of the icosahedron. A schematic representation of six sd^5 hybrid orbitals is

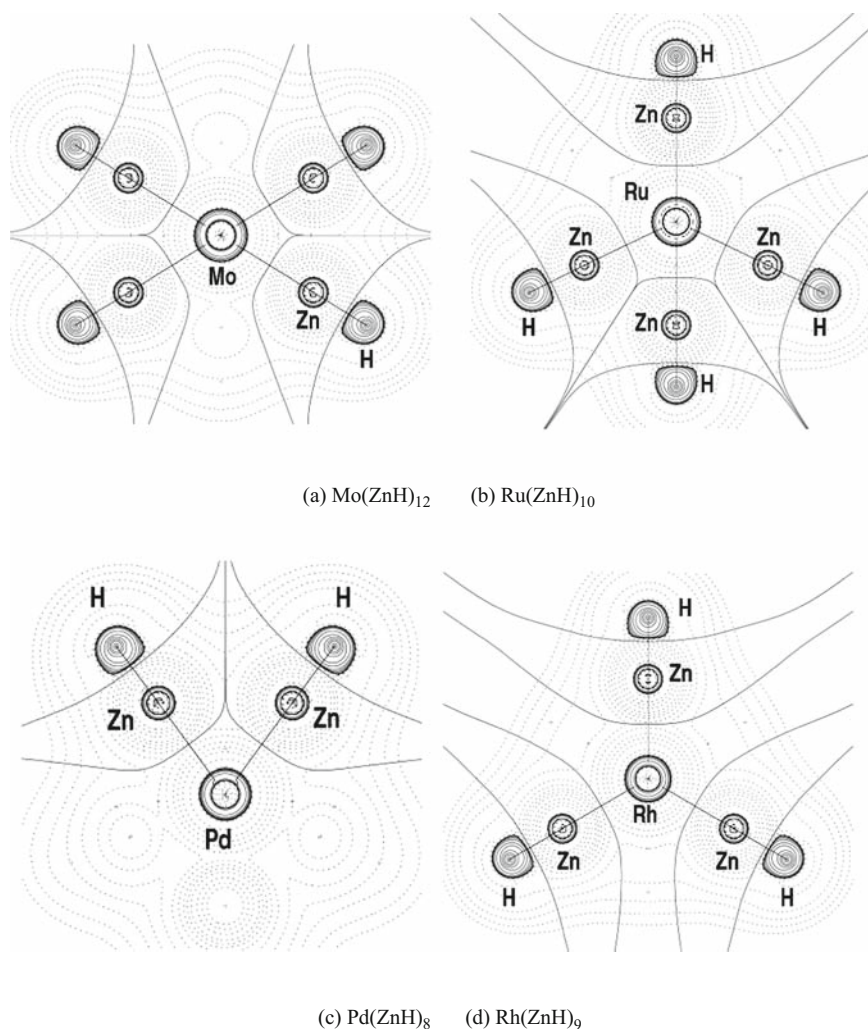


Fig. 16 AIM calculations for (a) **1H**, (b) **5H**, (c) **10H** and **7H** showing bond paths

given in Fig. 17. Every sd^5 hybrid orbital consists of two orbital lobes of equal size. Thus it is obvious that the sd^5 hybrid orbitals are ideally suited for σ -type orbital interactions in an icosahedral coordination sphere and do not prefer an octahedral environment.

The six remaining electrons, namely those in the $12t_{1u}$ orbitals, represent Zn–Zn interactions. With 30 equal Zn–Zn contacts in **61H** there is only 1/10 electron pair per Zn–Zn contact resulting only in weak Zn–Zn interactions. It is noteworthy that the $(\text{ZnH})_{12}$ cage without a central molybdenum is not a minimum on the potential

Table 6 EDA results of $[\text{Mo}(\text{ZnH})_{12}]$ at BP86/TZ2P+. The interacting fragments are $\text{Mo}(5s^1 4d^5)$ and $(\text{ZnH})_{12}$ with an electron configuration $a_g^1 h_g^5$. Energy values in kcal/mol

ΔE_{int}	-348.8
ΔE_{Pauli}	594.5
$\Delta E_{\text{elstat}}^{\text{a}}$	-540.1 (57.2%)
$\Delta E_{\text{Orb}}^{\text{a}}$	-403.2 (42.8%)
$\Delta E(a_g)^{\text{b}}$	-96.4 (23.9%)
$\Delta E(h_g)^{\text{b}}$	-288.0 (71.5%)
$\Delta E(t_{1u})^{\text{b}}$	-18.3 (4.5%)

^a The percentage values in parentheses give the contribution to the total attractive interactions $\Delta E_{\text{elstat}} + \Delta E_{\text{orb}}$

^b The percentage values in parentheses give the contribution to the total orbital interactions ΔE_{orb}

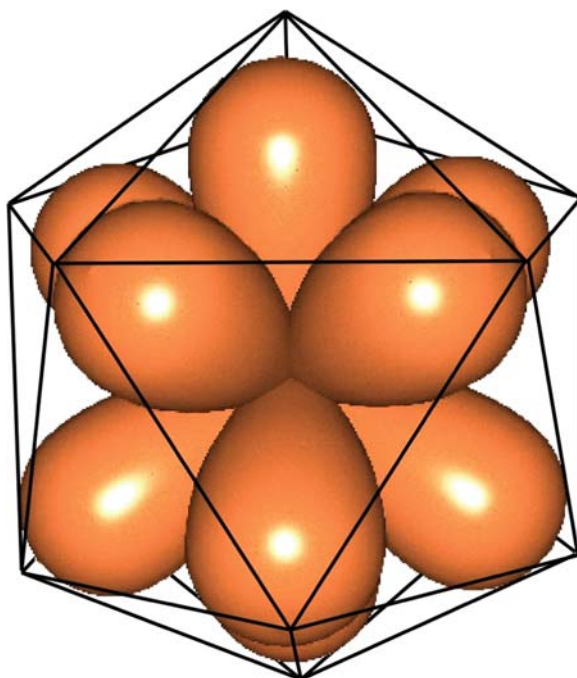


Fig. 17 Schematic representation of six sd^5 hybrid orbitals pointing to the twelve corners of an icosahedron

energy surface and that geometry optimization of this system in singlet or septet state results in decomposition. The weak Zn–Zn interactions are not sufficient to keep the Zn_{12} cage together, and the molybdenum atom plays an important role for the stability of the total system.

3.2.2 Bonding Situation in [Ru (ZnH)₁₀] (65H)

As the minimum geometry of [Ru (ZnH)₁₀] (**65H**) has D_{4d} symmetry (Fig. 14), the degeneracy of MOs involving valence d and p AOs of the ruthenium atom is lifted: The p-AO contributions from the central ruthenium atom are in b_2 (p_z) and e_1 (p_x , p_y) irreducible representations. Thus, MOs in b_2 and e_1 can describe interactions of the (ZnH)₁₀ fragment with p-AOs of the ruthenium atom. The d-AOs of Ru have e_2 (d_{xy} , $d_{x^2-y^2}$), e_3 (d_{xz} , d_{yz}) and a_1 (d_{z^2}) symmetry. As the s-AO is in the a_1 irreducible representation as well it is not possible to distinguish between bonding contributions of the d_{z^2} and the s AO with the EDA. The important valence molecular orbitals of **65H** containing contributions from the central ruthenium atom are presented in Fig. 18.

A visual inspection of the occupied MOs suggests a bonding pattern similar to that in the icosahedral **61H**: The $20e_1$ (HOMO) and $20b_2$ (HOMO-1) of **65H** have only small contributions from the p AOs of the ruthenium atom and thus mainly describe zinc–zinc and zinc–hydrogen bonding in the (ZnH)₁₀ fragment. These MOs are similar to the $12t_{1u}$ MOs in **61H**. The subsequent set of orbitals in **65H**, $19e_3$ (HOMO-2), $18e_2$ (HOMO-3) and $21a_1$ (HOMO-4), have significant d(Ru) contributions and therefore describe bonding orbital interactions between the (ZnH)₁₀ unit and d-AOs of Ru. These orbitals are analogue to the $12h_g$ MOs in **61H**. The next set of MOs of **65H** are $20a_1$, $18e_3$, $17e_2$ and $19a_1$ with d(Ru) contributions where the a_1 orbitals have also large coefficients from the s(Ru) AO. The following set, $19e_1$ and $18b_2$, containing small contributions from p(Ru) AOs are mainly cage orbitals. The $18a_1$, $10e_2$, $12e_3$, $15a_1$ and $14a_1$ have significant contributions from s- and d-AOs of the ruthenium atom while all other occupied MOs have only small coefficients at Ru.

Performing the EDA of the Ru-(ZnH)₁₀ interaction, the correct choice of electronic states of the fragments is not as clear as in **61H**. Numerical results of EDA calculations using different electronic states and charges of the fragments are presented in Table 7. The EDA results for the interaction of Ru^{2+} in s^1d^5 with the (ZnH)₁₂ fragment in the corresponding septet state give similar results as the presented EDA of **61H** and are best compared with that calculation as the Mo-fragment is isoelectronic to the Ru^{2+} fragment in **65H**. Thus, the following issue will be discussed in detail: Important bonding contributions, 88.6% in sum, come from those irreducible representations containing d(Ru) and s(Ru) orbitals, namely a_1 , e_2 and e_3 while orbital energies from b_2 and e_1 irreducible representations (representing orbital interactions with p(Ru) AOs) sum up to only 11.4% of the total orbital energy.

Table 7 shows that the numerical results of the EDA are strongly influenced by the choice of fragments. Using neutral Ru and (ZnH)₁₀ fragments in EDA decreases the total interaction energy as well as the total orbital interactions. Thus the relative contributions of the orbital energy and the electrostatic energy to the total attractive interactions change from $\Delta E_{\text{elstat}} : \Delta E_{\text{orb}} 37 : 63$ in the case of the charged fragments to roughly 60:40 for neutral species. The lowest total orbital contribution of the discussed fragmentations is yielded from the neutral triplet fragments. This

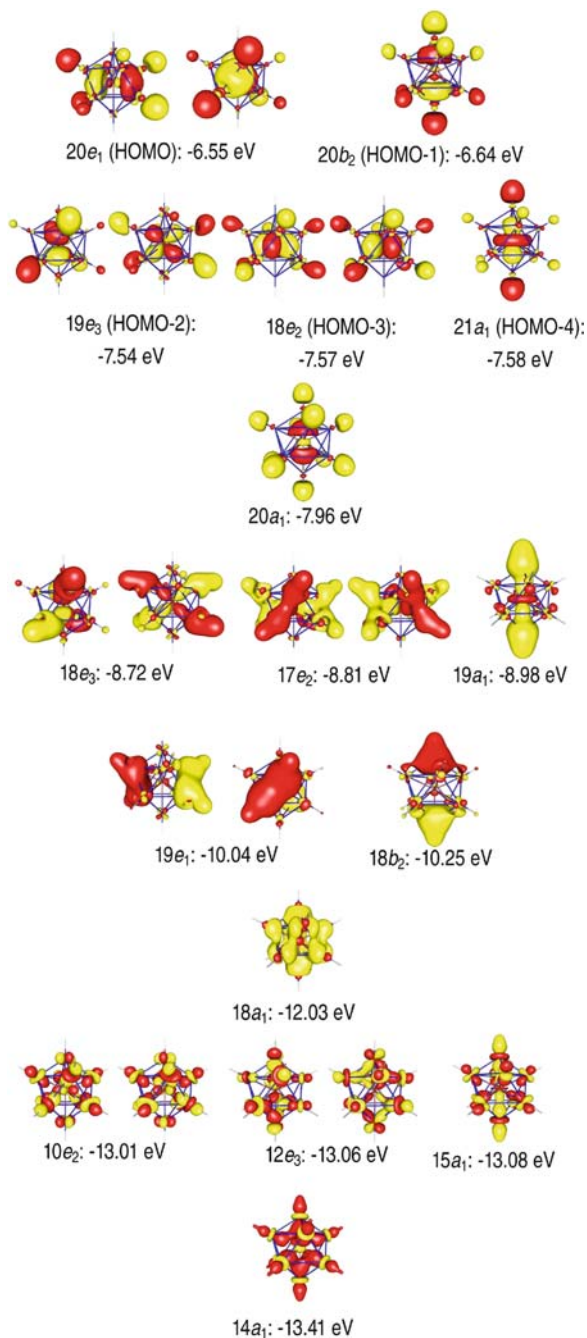


Fig. 18 Occupied Kohn–Sham molecular orbitals of [Ru(ZnH)₁₀] (**65H**) with coefficients at the central ruthenium atom

Table 7 Results of the EDA analyses of [Ru(ZnH)₁₀] (**65H**) at BP86/TZ2P+ with different electronic states of the fragments. Energies in kcal/mol

	Ru ²⁺ (s ¹ d ⁵) +(ZnH) ₁₀ ²⁻ (septet)	Ru(s ⁰ d ⁸) ^a +(ZnH) ₁₀ (triplet)	Ru(s ⁰ d ⁸) ^b +(ZnH) ₁₀ (singlet)
ΔE_{int}	-956.2	-342.3	-392.6
ΔE_{Pauli}	448.1	511.3	477.4
$\Delta E_{\text{elstat}}^{\text{c}}$	-518.0 (36.9%)	-542.0 (63.5%)	-531.1 (61.1%)
$\Delta E_{\text{orb}}^{\text{c}}$	-886.3 (63.1%)	-311.5 (36.5%)	-338.9 (39.0%)
$\Delta E(\text{a}_1)$ (s, d _{z²}) ^d	-212.2 (24.0%)	-78.6 (25.2%)	-94.1 (27.8%)
$\Delta E(\text{a}_2)$ ^d	-0.3 (0.1%)	-0.0 (0.0%)	-0.0 (0.0%)
$\Delta E(\text{b}_1)$ ^d	-0.5 (0.1%)	-0.0 (0.0%)	-0.0 (0.0%)
$\Delta E(\text{b}_2)$ (p _z) ^d	-35.2 (4.0%)	-4.2 (1.4%)	-5.2 (1.5%)
$\Delta E(\text{e}_1)$ (p _x , p _y) ^d	-65.4 (7.4%)	-7.0 (2.2%)	-7.7 (2.3%)
$\Delta E(\text{e}_2)$ (d _{x²-y²} , d _{xy}) ^d	-291.7 (32.9%)	-126.0 (40.5%)	-115.4 (34.1%)
$\Delta E(\text{e}_3)$ (d _{xz} , d _{yz}) ^d	-280.9 (31.7%)	-95.6 (30.7%)	-116.5 (34.4%)

^a In Ru(s⁰d⁸) (triplet) the valence d_{xz} and d_{yz}(e₃) AOs are singly occupied

^b In Ru(s⁰d⁸) (singlet) the valence d_{z²} AO is vacant

^c The percentage values in parentheses give the contribution to the total attractive interactions $\Delta E_{\text{elstat}} + \Delta E_{\text{orb}}$

^d The percentage values in parentheses give the contribution to the total orbital interactions ΔE_{orb}

indicates that the best choice for the description of the Ru–(ZnH)₁₀ interaction are neutral fragments in triplet states. The breakdown of the orbital interactions into relative contributions from the different irreducible representations gives similar results as discussed for the charged fragments: Most important orbital interactions arise from irreducible representations containing d and s AOs from the central Ru atom. Major outcome of the EDA investigations is thus that Ru–(ZnH)₁₀ bonding involves electron-sharing interactions of four unpaired electrons as well as donor acceptor interactions. Most important contributions come from bonding interactions of s(Ru) and d(Ru) atomic orbitals with the (ZnH)₁₀ fragment.

An AIM analysis of the electron density of **65H** also gives results comparable to those in **61H**. Figure 16 gives the contour map of $\nabla^2\rho$ and the molecular graph of **65H**. As in **61H**, only Ru–Zn and Zn–H bond paths exist while according to AIM there are no Zn–Zn bonds, although the Zn–Zn distances in **65H** (2.740 and 2.798Å) are even shorter than in **61H** (2.822Å). Thus, comparable to the situation in **61H**, the bonding analysis suggests a description of the Ru–Zn bonds including multi-centre Ru–Zn electron-sharing bonds as well as donor–acceptor interactions. Zn–Zn interactions seem to be only weak.

3.2.3 Bonding Situation in [Rh (ZnH)₉] (**67H**)

The minimum structure of the nine-coordinated compound [Rh(ZnH)₉] (**67H**) has D_{3h} symmetry (Fig. 14). The Zn–Zn distances of the closest neighbouring zinc atoms (2.853Å and 3.044Å) are longer than those in **61H** and **65H**. The resulting

molecular graph of an AIM analysis is presented in Fig. 16. There are no Zn–Zn but Rh–Zn and Zn–H bond paths.

In the D_{3h} point group, p and d AOs of the central rhodium atom mix in the e_1' irreducible representation that contains the $p_x, p_y, d_{xy}, d_{x^2-y^2}$ AOs of the central atom. As in **65H** both the s and the d_{z^2} AOs of Rh have a_1' symmetry. The d_{xz} and the d_{yz} AOs of Rh are in the e_1'' irreducible representation and p_z has a_2'' symmetry. The important occupied valence orbitals in these irreducible representations, i.e. those having significant coefficients on the central Rh atom, are shown in Fig. 19.

The $29e'$ (HOMO) and $16a_2''$ (HOMO-1) build a set of three nearly degenerate orbitals having coefficients from p(Rh) AOs. The $29e'$ also have small d(Rh) contributions. These orbitals are comparable to the $12t_{1u}$ MOs in **61H**. The next lower lying $22a_1'$ (HOMO-2) orbital has significant contributions from the s(Rh) AO and little mixing of d_{z^2} . The subsequent $28e'$ (HOMO-3), $21a_1'$ (HOMO-4) and $20e''$ (HOMO-5) build a set of five orbitals with large contributions from valence d(Rh) AOs. The set of orbitals from HOMO-2 to HOMO-5 in sum are comparable with the $12h_g$ and $9a_g$ MOs of **61H** but have reversed ordering. Lower lying molecular orbitals can be grouped into two additional sets of five MOs with significant coefficients of d(Rh) AOs (i.e., $20a_1', 27e', 19e''$ and $15a_1', 18e', 12e''$), two additional sets of three nearly degenerate MOs with small p(Rh) contributions (i.e. $16a_2'', 27e'$ and $11a_2'', 19e'$) and two additional MOs with significant contributions from the valence s(Rh) (i.e. $19a_1'$ and $14a_1'$).

EDA results of the Rh–(ZnH)₉ interaction in **7H** with charged species Rh^- (s^0d^{10}) and $(ZnH)_9^+$ in the singlet states as well as neutral species Rh (s^0d^9) and $(ZnH)_9$ in the doublet state as fragments are given in Table 8. In both fragmentations the electrostatic contributions to the total attractive interactions are larger than the orbital contributions. The smaller absolute value of the total orbital interactions in the calculation of the charged species -172.8 kcal/mol vs. -241.0 kcal/mol for neutral fragments) suggests that the bonding should be discussed in terms of these charged fragments Rh^- and $(ZnH)_9^+$. Largest contributions to ΔE_{orb} come from $\Delta E(e_1'')$ (d_{xz}, d_{yz}), $\Delta E(e_1')$ ($p_x, p_y, d_{xy}, d_{x^2-y^2}$) and $\Delta E(a_1')$ (s, d_{z^2}). As the $\Delta E(a_2'')$ (p_z) interactions are negligible it may be assumed that the $\Delta E(e_1')$ interaction comes mainly from contributions of the d_{xz}, d_{yz} AOs. Assuming that all d AOs contribute about equally to the total orbital interactions, the $\Delta E(a_1')$ orbital interaction comes mainly from the d_{z^2} orbital interaction with the $(ZnH)_9$ fragment.

3.2.4 Bonding Situation in $[Ni(ZnH)_8]$ (**69H**), $[Pd(ZnH)_8]$ (**70H**) and $[Pt(ZnH)_8]$ (**71H**)

As well as **65H**, the molecules $[Ni(ZnH)_8]$ (**69H**), $[Pd(ZnH)_8]$ (**70H**) and $[Pt(ZnH)_8]$ (**71H**) all have minimum structures in D_{4d} symmetry (Fig. 14). The distances between closest neighbouring Zn atoms in **69H–71H** range from 2.821\AA (shortest Zn–Zn distance in **69H**) to 3.172\AA (longest Zn–Zn distance in **71H**). In all cases

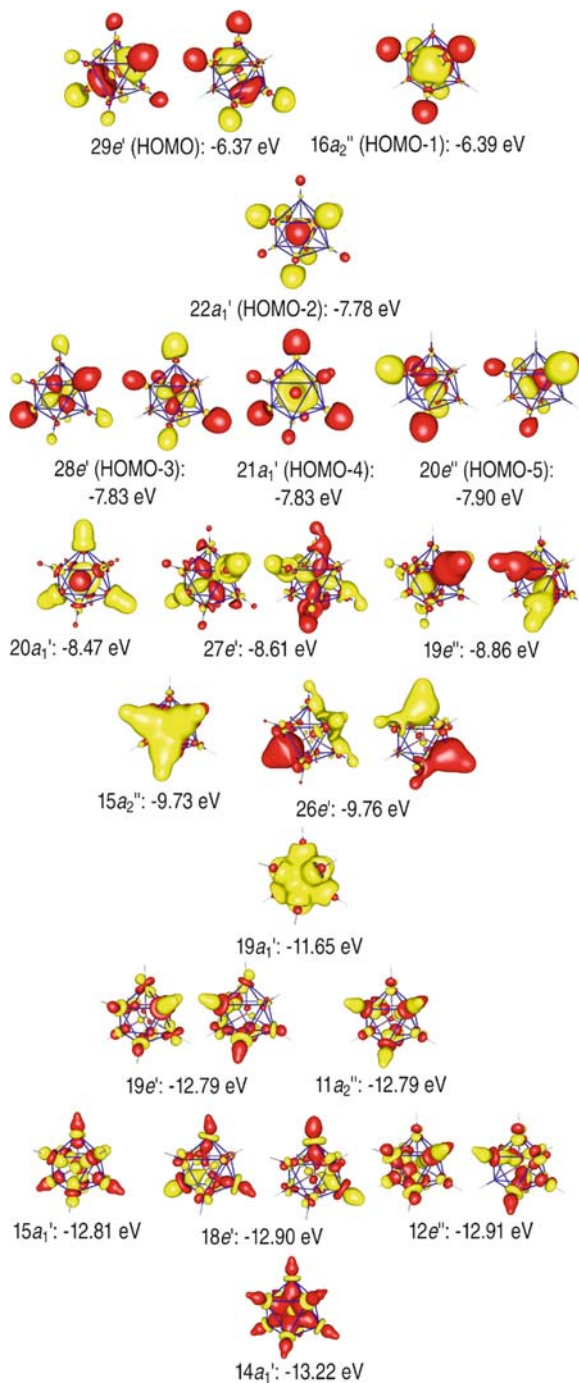


Fig. 19 Most important occupied valence MOs of **67H** which have coefficients at Rh

Table 8 Results of the EDA analyses of [Rh(ZnH)₉] in D_{3h} at BP86/TZ2P+ with different electronic states of the fragments. Energies in kcal/mol

	Rh ⁻ (s ⁰ d ¹⁰) + (ZnH) ₉ ⁺ (singlet)	Rh(s ⁰ d ⁹) + (ZnH) ₉ (doublet)
ΔE_{int}	-457.4	-294.5
ΔE_{Pauli}	598.4	465.1
$\Delta E_{\text{elstat}}^{\text{a}}$	-883.0 (83.6%)	-518.5 (68.3%)
$\Delta E_{\text{orb}}^{\text{a}}$	-172.8 (16.4%)	-241.0 (31.7%)
$\Delta E(a_{1'})$ (s, d _{z²}) ^b	-28.8 (16.7%)	-62.0 (25.7%)
$\Delta E(a_{2'})$ ^b	-0.2 (0.1%)	-0.3 (0.1%)
$\Delta E(e_{1'})$ (p _x , p _y , d _{xy} , d _{x²-y²}) ^b	-65.9 (38.2%)	-85.5 (35.5%)
$\Delta E(a_{1''})$ ^b	-0.1 (0.0%)	-0.0 (0.0%)
$\Delta E(a_{2''})$ (p _z) ^b	1.0 (-0.6%)	-5.2 (2.2%)
$\Delta E(e_{1''})$ (d _{xz} , d _{yz}) ^b	-78.8 (45.6%)	-88.1 (36.6%)

^aPercentage values in parentheses give the contributions to the total attractive energies $\Delta E_{\text{elstat}} + \Delta E_{\text{orb}}$

$\Delta E_{\text{elstat}} + \Delta E_{\text{orb}}$

^bPercentage values in parentheses give the contributions to the total orbital energy ΔE_{or}

and similar to the already discussed compounds **61H**, **65H** and **67H**, AIM gives bond path only connecting zinc atoms with the central atoms and with hydrogen but no zinc–zinc bonds (see Fig. 16).

The possible contributions of AOs of the central atom in MOs of different irreducible representations have been discussed in Sect. 3.2.2. Figure 20 shows the MOs of **70H** of with contributions from AOs at the Pd atom. These orbitals are discussed as representative examples for the homologue parent compounds **69H–71H**. As in all parent compounds discussed before, the three occupied orbitals of highest energy (12b₂, HOMO, and 17e₁, HOMO-1) have small p(Pd) contributions and resemble the 12t_{1u} set of **61H**. The next ten MOs lower lying in energy have large coefficients from s(Pd) and mainly d(Pd) AOs. Next lower lying 12b₂ and 16e₁ are mainly cage orbitals with only small contributions from p(Pd) AOs. The 12a₁ has large coefficients of the valence s(Pd) AO. It is followed by the five energetically close lying MOs 10a₁, 10e₂ and 10e₃ which have large d(Pd) contributions. The 9a₁ is the lowest valence orbital of **70H** with contributions from the s(Pd) AO.

EDA calculations were done with M–(ZnH)₈ fragments (M = Ni, Pd, Pt) in electronic singlet states (s⁰d¹⁰ at the central atom). The numerical results are given in Table 9. The main part of the total attractive interactions comes from the electrostatic interactions for all three compounds. The largest contributions to the orbital interactions come from donation of the doubly occupied d_{xy} and d_{x²-y²} AOs, as indicated by $\Delta E(e_2)$ and d_{xz} and d_{yz} AOs, as indicated by $\Delta E(e_3)$ to (ZnH)₈ fragment orbitals. $\Delta E(a_1)$, describing donations from d_{z²} to empty cage orbitals and from occupied cage orbitals to the empty s(Pd) AOs, contribute only 16% to the total orbital interactions which particularly suggests that the donation to the empty s(Pd) AO should give only small stabilization.

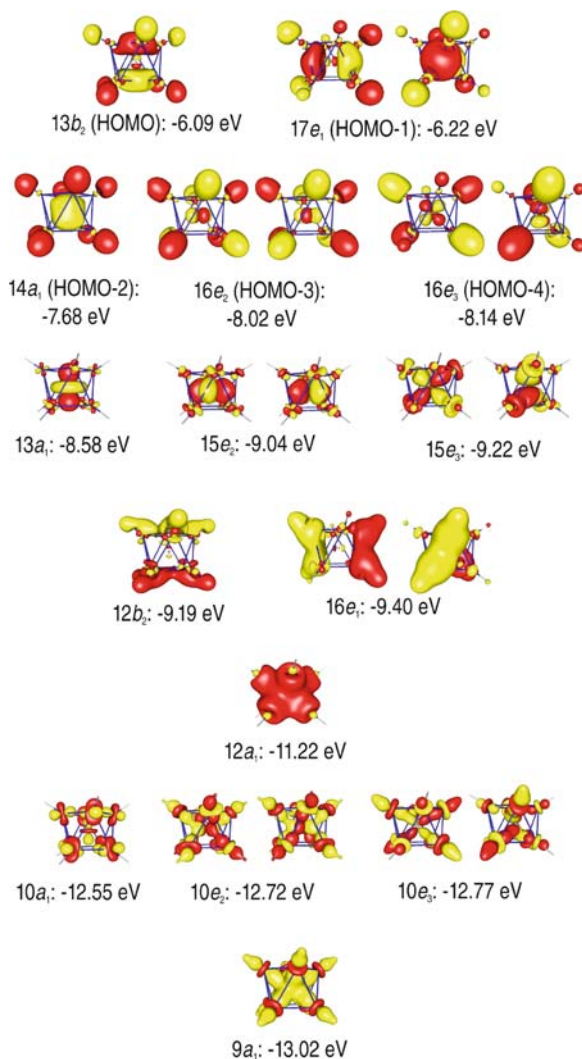


Fig. 20 Valence molecular orbitals of [Pd(ZnH)₈] (**70H**) with significant contributions at the central palladium atom

3.2.5 Comparison of the Systems [M(ZnR)_n]

From the earlier discussion it is evident that the bonding situation of the new compounds **61–72** is very different from typical clusters with strong tangential bonds. In particular, the compounds are different from endohedral Zintl-clusters of the general formula ME_n^{m-} . The analogy Au/ZnR or AuL/ZnR (L = phosphine, i.e. PPh₃, PEt₃) suggests a comparison with naked or ligand stabilized endohedral gold clusters (neutral or charged species) of the general formula MAu_n or M(AuL)_n

Table 9 EDA results at BP86/TZ2P for $[M(\text{ZnH})_8]$ ($M = \text{Ni, Pd, Pt}$) with the fragments $M(\text{s}^0\text{d}^{10})$ and $(\text{ZnH})_{10}$ in the singlet state. Energy values in kcal/mol

	Ni	Pd	Pt
ΔE_{int}	-246.3	-201.2	-279.0
ΔE_{Pauli}	208.1	402.4	486.0
$\Delta E_{\text{elstat}}^{\text{a}}$	-310.8 (68.4%)	-467.7 (77.5%)	-583.4 (76.3%)
$\Delta E_{\text{orb}}^{\text{a}}$	-143.6 (31.6%)	-135.8 (22.5%)	-181.6 (23.7%)
$\Delta E(\text{a}_1)$ (s, d_{z^2}) ^b	-23.4 (16.3%)	-21.7 (16.0%)	-43.8 (24.1%)
$\Delta E(\text{a}_2)$ ^b	0.0 (0.0%)	0.0 (0.0%)	0.0 (0.0%)
$\Delta E(\text{b}_1)$ ^b	0.0 (0.0%)	0.0 (0.0%)	0.0 (0.0%)
$\Delta E(\text{b}_2)$ (p_z) ^b	-5.9 (4.1%)	-5.4 (4.0%)	-8.2 (4.5%)
$\Delta E(\text{e}_1)$ (p_x, p_y) ^b	-12.0 (8.3%)	-11.0 (8.1%)	-16.7 (9.2%)
$\Delta E(\text{e}_2)$ ($\text{d}_{xy}, \text{d}_{x^2-y^2}$) ^b	-46.5 (32.4%)	-43.6 (32.1%)	-51.2 (28.2%)
$\Delta E(\text{e}_3)$ ($\text{d}_{xz}, \text{d}_{yz}$) ^b	-55.8 (38.9%)	-54.1 (39.8%)	-61.7 (34.0%)

^a Percentage values in parentheses give the contributions to the total attractive energy $\Delta E_{\text{elstat}} + \Delta E_{\text{orb}}$

$\Delta E_{\text{elstat}} + \Delta E_{\text{orb}}$

^b Percentage values in parentheses give the contributions to the total orbital energy ΔE_{orb}

(L = alkyl/aryl phosphane). For example, **61** or **61H** is related to the gas-phase species MAu_{12} ($M = \text{Mo, W}$) [144]. Autschbach et al. [145] discussed a closed-shell 18-electron bonding situation for the central tungsten atom with a significant population of the valence p orbitals. In addition, the relativistic aurophilic Au–Au interaction contributes substantially to the overall stability of the molecule MAu_{12} . These latter details, however, are clearly absent for **61H**. Zeng et al. performed a global search of highly stable endohedral gold clusters of the general formula $M@Au_n$ ($n = 8-17$) by DFT methods and found the central metal M prefers to be entirely covered by gold for $n \geq 9$, and the clusters $M@Au_n$ exhibit large HOMO–LUMO gaps suggesting chemical stability [146]. Note that the structures of the calculated species $\text{Ru}@Au_{10}$ (C_{2h}) and $\text{Rh}@Au_9$ (C_5) are very similar to $[\text{Ru}(\text{ZnH})_{10}]$ (**65H**, D_{4d}) and $[\text{Rh}(\text{ZnH})_9]$ (**67H**, D_{3h}) except for some differences in symmetry and corresponding details in the electronic properties [146]. But there are no structurally characterized and comparably close analogues for the series $[M(\text{ZnH})_8]$ ($M = \text{Ni, Pd, Pt}$; **69H–71H**) and their experimental counterparts **69–72** in endohedral gold cluster chemistry, so far. The well-known electronically unsaturated 16-electron clusters $[M(\text{AuL})_8]^{2+}$ ($M = \text{Pd, Pt}$) exhibit quite different, ellipsoidal structures [147]. Addition of 2-electron Lewis base ligand result in non-coordinated 18-electron spherical clusters, e.g. $[(\text{CO})\text{Pd}(\text{AuPPh}_3)_8]^{2+}$ [148]. The octa-coordinated neutral 18-electron cluster $[\text{Pt}(\text{AuPPh}_3)_8]$ is likely to have a similar structure as **61–72** and seems to be accessible by electrochemical reduction of $[\text{Pt}(\text{AuPPh}_3)_8]^{2+}$, but analytical details have not yet been published [149]. From these comparisons with homoleptic transition metal gold clusters also follows that even higher coordinated congeners of **61** might be a valid target for organometallic synthesis. The cited calculations of Zeng et al. revealed particular high binding energy per atom of $\text{Zr}@Au_{14}$, $\text{Sc}@Au_{15}$ and $\text{Y}@Au_{15}$ [146]. In fact, preliminary calculations show that $[\text{Zr}(\text{ZnH})_{14}]$ is a minimum on the potential energy

surface and adopts Frank–Kasper polyhedral structure of D_{6d} symmetry. Analysis of the bonding in $[\text{Zr}(\text{ZnH})_{14}]$ reveals an informative difference with regard to $[\text{Mo}(\text{ZnH})_{12}]$ (**61H**). There are 14 bond paths for the Zr–Zn interactions but now there are also Zn–Zn bond paths between the Zinc atoms of the planar Zn_6 moieties in $[\text{Zr}(\text{ZnH})_{14}]$ which means that there is *stronger* Zn–Zn bonding in the latter compound than in $[\text{Mo}(\text{ZnH})_{12}]$. This is quite reasonable because in the latter compound there are six electron pairs for Mo–Zn bonding and only three electron pairs for Zn–Zn bonding, while in $[\text{Zr}(\text{ZnH})_{14}]$ there are only four electron pairs for Zr–Zn bonding and five electron pairs for Zn–Zn bonding. We thus speculate that a stable compound of the type $[\text{Zr}(\text{ZnR})_{14}]$ might be accessible if a suitable Zr precursor such as $[\text{Zr}(\text{GaCp}^*)_7]$ or other related compounds similar to the transition metal precursors of Scheme 1 will be available, once.

4 Perspectives

The current progress on low valent group 13 metal coordination chemistry discussed earlier focused on gallium as the representative example. It was largely motivated by the investigation of the chemical properties group 13 and group 14 metal analogues of carbens or carbynes as metal analogues of nitrogen heterocyclic carbens (NHCs). A continuous issue of discussion has always been the question of σ -donor vs. π -acceptor properties of gallium centres in dependence of the substituents R on the one side and the coordinated metal fragment L_nM on the other hand. With our study herein, however, we emphasize other important and emerging aspects of this chemistry. In the first place, the GaR compounds provide a particular combination of classic ligand properties with reactive properties. The strong donor capability together with the steric bulk and the reducing power of Ga(DDP) in particular open new synthetic pathways to low coordinated homoleptic electron-rich metal centres and also to main group clusters and multiple bonded systems. Second, the unique properties of the Cp^* ligand as removable protecting group offers the option of novel chemistry at the group-13 centre. The transformation of coordinated GaCp^* ligands into substituents-free Ga^+ in terminal or bridging positions is possible. Likewise, the combination of reducing power with ligand and substituents exchange processes allows the synthesis of the homoleptic ZnR analoga $[\text{M}(\text{ZnR})_{2n}]$ of the known GaR compounds $[\text{M}(\text{GaR})_n]$ and as well Ga/Zn mixed systems. It will be interesting to probe similar metal exchange reactions with other substituents than Cp^* at the Ga centre. The related chemistry of aluminium and indium compounds and also the use of Mg or Cd reagents instead of Zn need to be investigated. This molecular chemistry appears to be related in some way to the chemistry of classic intermetallic Hume Rothery phases which are formed between (late) d-block metals and group-12 to group 14 metals [150–153]. Zinc, similar to aluminium and gallium, is an important metallurgical element and a component of classical alloy materials such as common brass. With transition metals it forms a rich variety of binary and ternary intermetallic solid-state

compounds of complex compositions and structures. For example, the metal atoms of the zinc-rich Hume Rothery γ -phase, Cu_5Zn_8 , are distributed over four distinct crystallographic sites, two exhibit an icosahedral local environment while the other two sites are surrounded by eleven and thirteen vertex polyhedra of lower symmetry [40–46]. Obviously the zinc-rich compounds **61–72** exhibit structural features similar to the coordination polyhedra found in related intermetallic phases. In this context we would like to mention that already some time ago, certain compounds featuring transition metal to group-13 metal bonds were studied as precursors for the soft chemical synthesis of the respective Hume–Rothery phases deposited as thin films on substrates (e.g. CoGa, NiIn) [154–161, 161, 162]. More recently, the earlier-discussed chemistry was the basis for the development of the synthesis intermetallic nanoparticles dispersed in non-aqueous colloidal solution (e.g. ‘nano-brass’ CuZn; ‘nano-bronze’ CuAl; NiAl) [163, 164]. In general, the mixed-metal compounds of the general formula $[\text{M}_a(\text{ER})_b]$ may be quite interesting within the scope of precursor chemistry for soft chemical synthesis of nanomaterials. So far, the Cp^* group was preferred over other possible substituents R because of its medium-scale steric bulk and soft binding properties which allows cleavage from the group 13 metal in a smooth and controlled way by hydrogenolysis, for example [35–37, 37–39]. However, the metal complexes of other GaR ligands such as the β -diketiminato, diazabutadienido and guanidinate Ga^1N -heterocycles (Chart 1) discussed in Sect. 2 may also be promising precursors for intermetallics since all these substituents R have been used in precursor chemistry of other materials (single metals and metal oxides and nitrides in particular) [165]. We thus suggest the family of compounds discussed in the earlier sections as precursors for novel nanoalloys and extending the scope of established concepts of nanometallurgy [154–167]. A door is opened into a new field of metal-rich molecules beyond the Zintl-boarder [168] filling the room between coordination compounds and clusters and linking the chemistry and physics of molecular compounds with intermetallic phases in a new way.

References

1. Cotton FA, Curtis NF, Harris CB, Johnson BFG, Lippard SJ, Mague JT, Robinson WR, Wood JS (1964) *Science* 145:1305
2. Cotton FA, Murillo LA, Walton RA (2005) *Multiple bonds between metal atoms*, 3rd edn. Springer, Berlin
3. Schnöckel H (2005) *Dalton Trans* 3131
4. Schnöckel H, Köhnlein H (2002) *Polyhedron* 21:489
5. Linti G, Schnöckel H, Uhl W, Wiberg N (2004) In: Driess M, Nöth H (eds) *Molecular clusters of the main group elements*. Wiley, Weinheim p 126
6. Koch K, Burgert R, Schnöckel H (2007) *Angew Chem* 119:5897
7. Koch K, Burgert R, Schnöckel H (2007) *Angew Chem Int Ed* 46:5795
8. Huber M, Schnepf A, Anson CE, Schnöckel H (2008) *Angew Chem* 120:8323
9. Huber M, Schnepf A, Anson CE, Schnöckel H (2008) *Angew Chem Int Ed* 47:8201
10. Linti G, Schnöckel H (2000) *Coord Chem Rev* 206–207:285
11. Nguyen T, Sutton AD, Brynda M, Fettinger JC, Long GL, Power PP (2005) *Science* 310:844
12. Resa I, Carmona E, Gutierrez-Puebla E, Monge A (2004) *Science* 305:1136

13. Kays DL, Aldridge S (2009) *Angew Chem Int Ed* 48:4109
14. del Río D, Galindo A, Resa I, Carmona E (2005) *Angew Chem* 117:1270
15. del Río D, Galindo A, Resa I, Carmona E (2005) *Angew Chem Int Ed* 44:1244
16. Zhu Z, Brynda M, Wright RJ, Fischer RC, Merrill WA, Rivard E, Wolf R, Fettinger JC, Olmstead MM, Power PP (2007) *J Am Chem Soc* 129:10847
17. Grirrane A, Resa I, Rodriguez A, Carmona E (2008) *Coord Chem Rev* 252:1532
18. Fedushkin IL, Skatova AA, Ketkov SY, Eremenko OV, Piskunov AV, Fukin GK (2007) *Angew Chem* 119:4380
19. Fedushkin IL, Skatova AA, Ketkov SY, Eremenko OV, Piskunov AV, Fukin GK (2007) *Angew Chem Int Ed* 46:4302
20. Wang Y, Quillian B, Wei P, Wang H, Yang X-J, Xie Y, King RB, Schleyer PVR, Schaefer HF III, Robinson GH (2005) *J Am Chem Soc* 127:11944
21. Schuchmann D, Westphal U, Schulz S, Florke U, Blaser D, Boese R (2009) *Angew Chem* 121:821
22. Schuchmann D, Westphal U, Schulz S, Florke U, Blaser D, Boese R (2009) *Angew Chem Int Ed* 48:807
23. Schulz S, Schuchmann D, Westphal U, Bolte M (2009) *Organometallics* 28:1590
24. Schulz S, Schuchmann D, Krossing I, Himmel D, Bläser D, Boese R (2009) *Angew Chem* 121, in press
25. Schulz S, Schuchmann D, Krossing I, Himmel D, Bläser D, Boese R (2009) *Angew Chem Int Ed* 48, in press
26. Green SP, Jones C, Stasch A (2007) *Science* 318:1754
27. Dohmeier C, Robl C, Tacke M, Schnöckel H (1991) *Angew Chem* 103:594
28. Jutzi P, Neumann B, Reumann G, Stammler H-G (1998) *Organometallics* 17:1305
29. Schulz S, Roesky HW, Koch HJ, Sheldrick GM, Stalke D, Kuhn M (1993) *Angew Chem* 105:1828
30. Schulz S, Roesky HW, Koch HJ, Sheldrick GM, Stalke D, Kuhn M (1993) *Angew Chem Int Ed Engl* 32:1729
31. Jutzi P, Schebaum LO (2002) *J Organomet Chem* 654:176
32. Hardman NJ, Eichler BE, Power PP (2000) *Chem Commun* 1991
33. Schmidt ES, Jokisch A, Schmidbaur H (1999) *J Am Chem Soc* 121:9758
34. Jin G, Jones C, Junk PC, Staschab A, Woodula WD (2008) *New J Chem* 32:835
35. Buchin B, Gemel C, Cadenbach T, Schmid R, Fischer RA (2006) *Angew Chem* 118:1074
36. Buchin B, Gemel C, Cadenbach T, Schmid R, Fischer RA (2006) *Angew Chem Int Ed* 46:1674
37. Jones JN, Macdonald CLB, Gorden JD, Cowley AH (2003) *J Organomet Chem* 666:3
38. Buchin B, Gemel C, Cadenbach T, Fernández I, Frenking G, Fischer RA (2006) *Angew Chem* 118:5331
39. Buchin B, Gemel C, Cadenbach T, Fernández I, Frenking G, Fischer RA (2006) *Angew Chem Int Ed* 45:5207
40. Janiak C (1997) *Coord Chem Rev* 163:107
41. Catalano VJ, Bennett BL, Muratidis S, Noll BC (2001) *J Am Chem Soc* 123:173
42. Gade LH (2003) *Dalton Trans* 267
43. Fernández I, Cerpa E, Merino G, Frenking G (2008) *Organometallics* 27:1106
44. Sarazin Y, Kaltsoyannis N, Wright JA, Bochmann M (2007) *Organometallics* 26:1811
45. Dias HVR, Singh S, Cundari TR (2005) *Angew Chem* 117:4985
46. Dias HVR, Singh S, Cundari TR (2005) *Angew Chem Int Ed* 44:4907
47. Weiss J, Fischer RA (1999) *Angew Chem Int Ed* 38:2830–2850
48. Baker RJ, Jones C (2005) *Coord Chem Rev* 249:1857
49. Gemel C, Steinke T, Cokoja M, Kempter A, Fischer RA (2004) *Eur J Inorg Chem* 4161
50. Fischer RA, Weiß J (1999) *Angew Chem Int Ed* 38:2830
51. Jones C, Mills DP, Platts JA, Rose RP (2006) *Inorg Chem* 45:3146
52. Roesky PW (2009) *Dalton Trans* 1887
53. Liddle ST (2009) *Proc R Soc A* 465:1673
54. Kempter A, Gemel C, Cadenbach T, Fischer RA (2007) *Inorg Chem* 46:9481

55. Wright RJ, Brynda M, Fettinger JC, Betzer AR, Power PP (2006) *J Am Chem Soc* 128:12498
56. Kempter A, Gemel C, Hardman NJ, Fischer RA (2006) *Inorg Chem* 45:3133
57. Kempter A, Gemel C, Fischer RA (2005) *Inorg Chem* 44:163
58. Hardman NJ, Wright RJ, Phillips AD, Power PP (2003) *J Am Chem Soc* 125:2667
59. Burford N, Ragogna PJ, Robertson KN, Cameron TS, Hardman NJ, Power PP (2002) *J Am Chem Soc* 124:382
60. Hardman NJ, Power PP (2001) *Inorg Chem* 40:2474
61. Hardman NJ, Cui C, Roesky HW, Fink WH, Power PP (2001) *Angew Chem Int Ed* 40:2172
62. Hardman NJ, Power PP (2001) *Chem Commun* 1184
63. Hardman NJ, Power PP, Gorden JD, Macdonald CLB, Cowley AH (2001) *Chem Commun* 1866
64. Green SP, Jones C, Stasch A (2006) *Inorg Chem* 46:11
65. Steinke T, Gemel C, Cokoja M, Winter M, Fischer RA (2004) *Angew Chem* 116:2349
66. Steinke T, Gemel C, Cokoja M, Winter M, Fischer RA (2004) *Angew Chem Int Ed* 43:2299
67. Steinke T, Cokoja M, Gemel C, Kempter A, Krapp A, Frenking G, Zenneck U, Fischer RA (2005) *Angew Chem* 117:3003
68. Steinke T, Cokoja M, Gemel C, Kempter A, Krapp A, Frenking G, Zenneck U, Fischer RA (2005) *Angew Chem Int Ed* 44:2943
69. Cadenbach T, Gemel C, Schmid R, Block S, Fischer RA (2004) *Dalton Trans* 3171
70. Cadenbach T, Gemel C, Schmid R, Fischer RA, (2005) *J Am Chem Soc* 127:17068
71. Kempter A, Gemel C, Fischer RA (2007) *Chem Eur J* 13:2990
72. Jones C, Junk PC, Platts JA, Stasch A (2006) *J Am Chem Soc* 128:2206
73. Kempter A, Gemel C, Fischer RA (2006) *Chem Commun* 1551
74. Jones C, Stasch A, Woodul WD (2009) *Chem Commun* 113
75. Wiecko M, Roesky PW (2007) *Organometallics* 26:4846
76. Arnold PL, Liddle ST, McMaster J, Jones C, Mills DP (2007) *J Am Chem Soc* 129:5360
77. Liddle ST, McMaster J, Mills DP, Blake AJ, Jones C, Woodul WD (2009) *Angew Chem Int Ed* 48:1077
78. Minasian SG, Krinsky JL, Williams VA, Arnold J (2008) *J Am Chem Soc* 130:10086
79. Ned JH, Robert JW, Andrew DP, Power PP (2003) *J Am Chem Soc* 125:2667
80. Kempter A, Gemel C, Cadenbach T, Fischer RA (2007) *Organometallics* 26:4257
81. Gemel C, Steinke T, Weiss D, Cokoja M, Winter M, Fischer RA (2003) *Organometallics* 22:2705
82. Weiss D, Winter M, Fischer RA, Yu C, Wichmann K, Frenking G (2000) *Chem Commun* 2495
83. Weiss D, Winter M, Merz K, Knüfer A, Fischer RA, Frölich N, Frenking G (2002) *Polyhedron* 21:535
84. Kempter A, Gemel C, Fischer RA (2008) *Inorg Chem* 47:7279
85. Prabusankar G, Kempter A, Gemel C, Schroeter M-K, Fischer RA (2008) *Angew Chem* 120:7344
86. Prabusankar G, Kempter A, Gemel C, Schroeter M-K, Fischer RA (2008) *Angew Chem Int Ed* 47:7234
87. Brynda M, Herber R, Hitchcock PB, Lappert MF, Nowik I, Power PP, Protchenko AV, Ruzicka A, Steiner J (2006) *Angew Chem* 118:4439
88. Brynda M, Herber R, Hitchcock PB, Lappert MF, Nowik I, Power PP, Protchenko AV, Ruzicka A, Steiner J (2006) *Angew Chem Int Ed* 45:4333
89. Prabusankar G, Gemel C, Parameswaran P, Flener C, Frenking G, Fischer RA (2009) *Angew Chem* 121:5634
90. Prabusankar G, Gemel C, Parameswaran P, Flener C, Frenking G, Fischer RA (2009) *Angew Chem Int Ed* 48:5526
91. Wang Y, Xie Y, Wei P, King RB, Schaefer HF III, Schleyer PVR, Robinson GH (2008) *Science* 321:1069
92. Tokitoh N, Arai Y, Okazaki R, Nagase S (1997) *Science* 277:78
93. Sasamori T, Arai Y, Takeda N, Okazaki R, Furukawa Y, Kimura M, Nagase S, Tokitoh N (2002) *Bull Chem Soc Japan* 75:661

94. Twamley B, Sofield CD, Olmstead MM, Power PP (1999) *J Am Chem Soc* 121:3357
95. Calderazzo F, Poli R, Pelizzi G (1984) *J Chem Soc Dalton Trans* 2365
96. Thomas F, Schulz S, Nieger M (2002) *Organometallics* 21:2793
97. Jutz P, Neumann B, Schebaum LO, Stammler A, Stammler H-G (1999) *Organometallics* 18:4462
98. Buchin B, Steinke T, Gemel C, Cadenbach T, Fischer RA (2005) *Z Anorg Chem* 631:2756
99. Steinke T, Gemel C, Winter M, Fischer RA (2005) *Chem Eur J* 11:1636
100. Cokoja M, Steinke T, Gemel C, Welzel T, Winter M, Merz K, Fischer RA (2003) *J Organomet Chem* 684:277
101. Steinke T, Gemel C, Cokoja M, Winter M, Fischer RA (2005) *Dalton Trans* 55
102. Uhl W, Benter M, Melle S, Saak W, Frenking G, Uddin J (1999) *Organometallics* 18:3778
103. Weiss J, Stetzkamp D, Nuber B, Fischer RA, Boehme C, Frenking G (1997) *Angew Chem* 109:95
104. Weiss J, Stetzkamp D, Nuber B, Fischer RA, Boehme C, Frenking G (1997) *Angew Chem Int Ed* 36:70
105. Compton NA, Errington RJ, Norman NC (1990) *Adv Organomet Chem* 31:91
106. Ueno K, Watanabe T, Tobita H, Ogino H (2003) *Organometallics* 22:4375
107. Bunn NR, Aldridge S, Coombs DL, Rossin A, Willock DJ, Jones C, Ooi L-L (2004) *Chem Commun* 1732
108. Bunn NR, Aldridge S, Kays DL, Coombs ND, Rossin A, Willock DJ, Day JK, Jones C, Ooi L-L (2005) *Organometallics* 24:5891
109. Schilling BER, Hoffmann R, Lichtenberger DL (1979) *J Am Chem Soc* 101:585
110. Aldridge S, Rossin A, Coombs DL, Willock DJ (2004) *Dalton Trans* 2649
111. Ueno K, Hirotsu M, Hatori N (2007) *J Organomet Chem* 692:88
112. Muraoka T, Motohashi H, Hirotsu M, Ueno K (2008) *Organometallics* 27:3918
113. Muraoka T, Motohashi H, Kazuie Y, Takizawa A, Ueno K (2009) *Organometallics* 28:1616
114. Conway AJ, Hitchcock PB, Smith JD (1975) *J Chem Soc Dalton Trans* 1945
115. Stork JR, Olmstead MM, Balch AL (2005) *J Am Chem Soc* 127:6512
116. Fernandez EJ, Lopez-de-Luzuriaga JM, Monge M, Olmos ME, Perez J, Laguna A, Mohamed AA, Fackler JP (2003) *J Am Chem Soc* 125:2022
117. Buchin B, Gemel C, Cadenbach T, Schmid R, Fischer RA (2006) *Angew Chem* 118:1703
118. Buchin B, Gemel C, Cadenbach T, Schmid R, Fischer RA (2006) *Angew Chem Int Ed* 45:1074
119. Cadenbach T, Gemel C, Bollermann T, Fernandez I, Frenking G, Fischer RA (2008) *Chem Eur J* 14:10789
120. Cadenbach T, Gemel C, Schmid R, Halbherr M, Yusenko K, Cokoja M, Fischer RA (2009) *Angew Chem Int Ed* 48:3872
121. Buchin B, Gemel C, Kempter A, Cadenbach T, Fischer RA (2006) *Inorg Chim Acta* 359:4833
122. Cokoja M, Gemel C, Steinke T, Schroder F, Fischer RA (2005) *Dalton Trans* 44
123. Cadenbach T, Bollermann T, Gemel C, Fischer RA (2009) *Dalton Trans* 322
124. Boehme C, Frenking G (1999) *Chem Eur J* 5:2184
125. Macdonald CLB, Cowley AH (1999) *J Am Chem Soc* 121:12113
126. Uddin J, Boehme C, Frenking G (2000) *Organometallics* 19:571
127. Weiss D, Steinke T, Winter M, Fischer RA, Fröhlich N, Uddin J, Frenking G (2000) *Organometallics* 19:4583
128. Uddin J, Frenking G (2001) *J Am Chem Soc* 123:1683
129. Doerr M, Frenking G (2002) *Z Anorg Chem* 628:843
130. Boehme C, Uddin J, Frenking G (2000) *Coord Chem Rev* 197:249
131. Frenking G, Wichmann K, Fröhlich N, Loschen C, Lein M, Frunzke J, Rayón VM (2003) *Coord Chem Rev* 238–239:55
132. Dykstra CE, Frenking G, Kim KS, Scuseria GE (2005) Theory and applications of computational chemistry: the first 40 years. In: Dykstra CE, Frenking G, Kim KS, Scuseria GE (eds). Elsevier, Amsterdam, p 1
133. Weiß J, Stetzkamp D, Nuber B, Fischer RA, Boehme C, Frenking G (1997) *Angew Chem* 109:95

134. Weiß J, Stetzkamp D, Nuber B, Fischer RA, Boehme C, Frenking G (1997) *Angew Chem Int Ed Engl* 36:70
135. Cowley AH, Lomeli V, Voigt A (1998) *J Am Chem Soc* 120:6401
136. Braunschweig H, Kollann C, Englert U (1998) *Angew Chem* 110:3355
137. Braunschweig H, Kollann C, Englert U (1998) *Angew Chem Int Ed Engl* 37:3179
138. Su J, Li X-W, Crittendon RC, Campana CF, Robinson GH (1997) *Organometallics* 16:4511
139. Doerr M, Frenking G (2002) *Z All Anorg Chem* 628:843
140. Major parts of this chapter are directly taken from the parallelly published original article: Cadenbach T, Bollermann T, Gemel C, Tombul M, Fernandez I, Hopffgarten MV, Frenking G, Fischer RA (2009) *J Am Chem Soc* 131, in press
141. Cadenbach T, Bollermann T, Gemel C, Fernandez I, Hopffgarten MV, Frenking G, Fischer RA (2008) *Angew Chem Int Ed* 47:9150
142. Cadenbach T, Gemel C, Zacher D, Fischer RA (2008) *Angew Chem Int Ed* 47:3438
143. Pyykkö P (2006) *J Organomet Chem* 691:4336
144. Li X, Kiran B, Li J, Zhai H, Wang L (2002) *Angew Chem Int Ed* 41:4786
145. Autschbach J, Hess B, Johansson MP, Neugebauer J, Patzschke M, Pyykkö P, Reiher M, Sundholm D (2004) *Phys Chem Chem Phys* 6:11
146. Gao Y, Bulusu S, Zeng XC (2006) *Chem Phys Chem* 7:2275
147. Ito LN, Johnson BJ, Mueting AM, Pignolet LH (1989) *Inorg Chem* 28:2026
148. Ito LN, Felicissimo AMP, Pignolet LH (1991) *Inorg Chem* 30:988
149. Vanderlinden JGM, Roelofsen AM, Ipskamp GHW (1989) *Inorg Chem* 28:967
150. Hume-Rothery W (1926) *J Inst Met* 35:295
151. Jones H (1937) *Proc Phys Soc* 49:250
152. Paxton A, Methfessel M, Pettifor D (1997) *Proc R Soc London Ser A* 453:1493
153. Ferro R, Saccone A (1993) *Materials science and technology In: Cahn RW, Haasen P, Kramer EJ (eds) The structure of solids. vol 1. VCH, Weinheim, pp 123*
154. Fischer RA, Kaesz HD, Khan SI, Muller HJ (1990) *Inorg Chem* 29:1601
155. Fischer RA, Scherer W, Kleine M (1993) *Angew Chem Int Ed* 32:748
156. Fischer RA, Priermeier T (1994) *Organometallics* 13:4306
157. Fischer RA, Miehr A, Schulte MM (1995) *Adv Mat* 7:58
158. Fischer RA, Miehr A (1996) *Chem Mater* 8:497
159. Fischer RA, Miehr A, Metzger T (1996) *Thin Solid Films* 289:147
160. Miehr A, Fischer RA, Lehmann O, Stuke M. (1996) *Adv Mat Optics Electr* 6:27
161. Fischer RA, Weiss J, Rogge W (1998) *Polyhedron* 17:1203
162. Fischer RA, Weiss D, Winter M, Muller I, Kaesz HD, Frohlich N, Frenking G (2004) *J Organomet Chem* 689:4611
163. Cokoja M, Jagirdar BR, Parala H, Birkner A, Fischer RA (2008) *Eur J Inorg Chem* 3330
164. Cokoja M, Parala H, Birkner A, Shekhah O, van den Berg MWE, Fischer RA (2007) *Chem Mater* 19:5721–5733
165. Edelman FT (2009) *Chem Soc Rev*. doi: 10.1039/b800100f
166. Cable RE, Schaak RE (2007) *Chem Mater* 19:4098
167. Cable RE, Schaak RE (2005) *Chem Mater* 17:6835
168. Fässler TF, Hoffmann SD (2004) *Angew Chem Int Ed* 43:6242

Homocatenation of Metal and Metalloid Main Group Elements

Michael S. Hill

Abstract Interest in poly(diorgano)silanes, catenated silicon compounds and heavier element analogues of alkanes has derived largely from their 1-dimensional delocalisation across the Si–Si σ framework, which affords similar properties observed for polyene and unsaturated “all organic” polymers. Although not so widely recognised or studied, similar “ σ -delocalised” activity may also be observed for homocatenated species of other p-block elements. In this study, a foundation for an understanding of the phenomenon of σ -delocalisation is provided through consideration of the structures, methods of synthesis and electronic behaviour of the well-established poly(diorgano)silanes. Synthetic and theoretical developments relating to analogous derivatives based upon silicon’s heavier group 14 congeners are then reviewed along with the more limited examples of catenated compounds among the heavier elements of groups 15 and 13. This coverage does not dwell upon detailed aspects of structure or electronic behaviour for the individual compounds and classes of compound included. Rather, the intention is to promote something of a phenomenological awareness of a series of superficially disparate chemical systems and to encourage a more widespread appreciation of the implication that, in not displaying σ -delocalisation, it is the elements of the first full period that display the more unusual or anomalous behaviour.

Keywords Catenation · P-block · Synthesis · Molecular Structure · Electronic Structure

Contents

1	Introduction	190
2	Group 14	191
2.1	Oligo and Polysilanes, a Historical Background	191
2.2	Synthesis of Oligo- and Polysilanes	193
2.3	Electronic Structure of Oligo- and Polysilanes.....	196
2.4	Applications of Polysilanes	198

3	Oligo- and Polygermanes, Stannanes and Plumbanes.....	199
3.1	Oligo- and Polygermanes	199
3.2	Properties of Oligo- and Polygermanes	201
3.3	Oligo- and Polystannanes	203
3.4	Oligoplumbanes	207
4	Catenation of Group 15 elements	207
5	Catenation of Group 13 Elements.....	209
6	Outlook	211
	References	212

1 Introduction

Carbon has an unsurpassed ability to form σ bonds to itself and its resultant capacity to form homologous families of compounds based upon extended homocatenated chains is the defining feature of organic chemistry. This is most clearly demonstrated by the structures of the linear n -alkanes whereby homologues, C_nH_{n+2} , may be constructed by addition of tetrahedral (sp^3) carbon centres with no detriment to the stability of the structure with increasing chain length. Although carbon's congeners in group 14, silicon, germanium, tin and lead also provide sufficient valence orbitals and electrons for the formation of analogous extended linear structures (Fig. 1), well-defined catenated compounds become increasingly uncommon with greater atomic weight.

A similar trend is observed across the entire p-block of elements where more diffuse valence orbitals and rising inner shell repulsion result, in general, in decreasing homonuclear sigma bond enthalpies, D_0 , as the groups are descended. The values illustrated in Table 1 describe a trend of decreasing values of D_0 both down and to either side of group 14.

Although the synthesis of defined oligomeric or polymeric systems is thus thermodynamically disfavoured, a wide variety of species containing chains of E–E

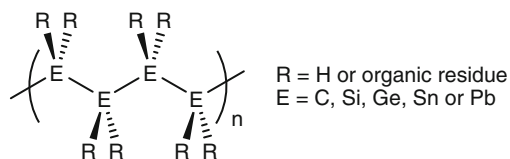


Fig. 1 Catenation in group 14 compounds

Table 1 Comparison of thermochemical single E–E bond dissociation energies, D_0 (kJ mol^{-1}), for the group 13–group 17 elements

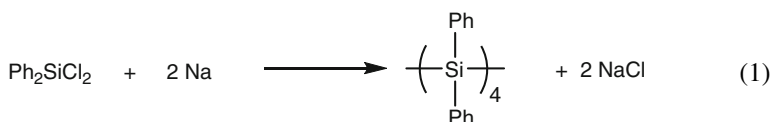
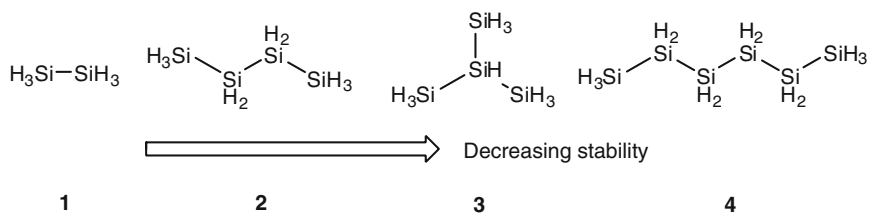
Group 13	B, 293	Al, 188	Ga, 113	In, 100
Group 14	C, 345	Si, 222	Ge, 188	Sn, 190
Group 15	N, 158	P, 198	As, 178	Sb, 141
Group 16	O, 142	S, 226	Se, 172	Te, 126
Group 17	F, 155	Cl, 239	Br, 190	I, 149

single bonds have been synthesised and characterised from across the entire p-block of elements. As well as having fundamental academic value, compounds of this type, particularly those of the heavier group 14 elements, display interesting and potentially technologically useful electro-optical properties that are not available to their saturated carbon-based counterparts. In this review, therefore, we shall attempt to provide a perspective upon the progress that has been made towards the elaboration of units containing more than one single E–E bond. To provide some level of coherence, this treatment will pay only scant regard to the formation of neutral molecular or charged clusters, typified by the Zintl ions [1, 2], the potential for the construction of element–element multiple bonds or questions arising from the ability of cyclic species to engage in pseudoaromatic behaviour. Although attention will, therefore, concentrate upon the formation of linear catenated species related to those illustrated schematically in Fig. 1 [3, 4], in the absence of authenticated examples of linear derivatives reference will also be made to cyclocatenated derivatives of specific elements. Although coverage of this type will be necessarily incomplete with regard to the most heavily represented compounds of this type, particularly the polysilanes for which the reader is directed to more specialised reviews [5–10], by providing breadth of coverage we shall attempt to illustrate parallels and contrasts between the behaviour of catenated species formed from the heavier group 14 elements as well as those elements of the neighbouring groups 15 and 13.

2 Group 14

2.1 *Oligo and Polysilanes, a Historical Background*

The multiplicity of structures available to the organic chemist is largely a result of the favourable thermodynamics involved in the formation of robust C–C linkages (Table 1). It is not surprising, therefore, that the potential to synthesise similar homologous compounds of the heavier elements of group 14 was apparent to chemists almost as soon as the electronic theories of valence and bonding were formulated. Although the silicon analogue of methane, monosilane SiH_4 , had been prepared by the action of HCl on Al/Si by Wöhler in the mid nineteenth century, it was not until 1902 that the first homologue, disilane Si_2H_6 , **1**, was identified by Moissan and Smiles [11]. The pyrophoric nature and thermal sensitivity of these compounds greatly hindered further progress until the pioneering studies of Stock who showed, in research simultaneous with his development of the boron hydrides, that higher homologues corresponding to silicon versions of *n*- and *iso*-butanes, **2**, **3**, and even hexanes, **4**, may be isolated by careful fractionation [12]. The thermal stability of these extended chain species was, however, seen to decrease rapidly with increasing chain length, such that the decomposition of even the tetrasilicon species was observed to be very rapid at room temperature.



The birth of organosilicon chemistry in the 1920s provided the first evidence that silicon could provide a much wider array of oligomeric and higher molecular weight catenated species. The initial reports of “silicohydrocarbons” were provided by Kipping through Wurtz-type coupling of diphenyldichlorosilane with sodium metal (1) [13, 14]. Via dark blue reaction intermediates, several colourless compounds of low molecular weight and containing no chlorine, most likely Si_4Ph_8 , were obtained. The intractable and insoluble nature of these materials did not arouse any further interest until Burkhard’s description of polydimethylsilane, $(\text{Me}_2\text{Si})_n$, prepared by a similar route in 1949 [15]. Again, however, this material was intractable and the area lay effectively dormant until Gilman reported UV spectral data for several oligosilanes, $\text{R}(\text{SiR}_2)_n\text{R}$ ($\text{R} = \text{Me}$ or Ph ; $n = 2-7$), and for some cyclosilane derivatives some 15 years later [16–19]. In contrast to alkanes, which show no electronic absorption beyond 160 nm, these compounds were observed to provide strong absorptions at wavelengths up to 250 nm. Within a given homologous series the spectra were seen to increase in complexity with extension of the chain length and to provide significant red shifts with phenyl substitution. These observations were the first indications that the electronic structures of these compounds were manifestly different from those of similarly homologated hydrocarbons and may be regarded as the origin of the continuing interest in catenated silicon species and, by extension, their heavier group 14 analogues. During the same period, the group of Kumada reported similar UV absorption behaviour and the syntheses of several well-defined permethylated linear polysilanes of the formula $\text{Me}(\text{SiMe}_2)_n\text{Me}$, where n was equal to 3–12 [20–22]. Kumada also provided the first reviews relating to the topic of catenated organosilicon compounds [23, 24]. Although several other reports of oligomeric and cyclosilanes were forthcoming in the intermediate time [25], the modern appreciation of the potential of polysilane research was initiated by almost simultaneous reports of the preparation of significantly soluble high molecular weight materials by the groups of West [26, 27], and of Wesson and Williams who showed that it is possible to modify the polymer structure through the introduction of less symmetrical dialkyl or alkylaryl monomer units [28–30]. Wurtz coupling of a 1:1 ratio of dimethyldichlorosilane and diphenyldichlorosilane,

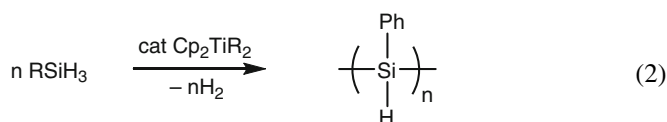
for example, resulted in a completely amorphous polymer which was highly soluble in many organic solvents [12]. These initial reports also highlighted the sigma delocalised character of the polymer chains and their conversion to semiconducting behaviour upon oxidation with quantities of SbF_5 .

2.2 Synthesis of Oligo- and Polysilanes

The most common method of synthesis of catenated silicon species involves the Wurtz coupling of dihalodiorganosilanes with sodium, potassium or Na/K alloy in an inert solvent such as toluene and at elevated temperatures. Under these conditions, the coupling reaction may be viewed as a condensation polymerisation occurring at the surface of the finely divided alkali metal [31–34]. This method, however, tends to be poorly reproducible and results in polymodal molecular weight distributions. The products of the reductive coupling with alkali metals typically consist of three fractions, a high molecular weight polymer ($M_w > 10^5$), a low molecular weight polymer ($M_w < 10^4$) and cyclic oligomers (Si_4 , Si_5 , and Si_6). A number of strategies have thus been devised which partly circumvent these difficulties. The addition of a catalytic amount of a crown ether, either 12-crown-4, 15-crown-5 or 18-crown-6, to the reaction mixture has been noted to increase the rate of disappearance of the monomer with increasing crown ether concentration suggesting that anionic species are involved in the polymerisation mechanism [35]. In this manner, higher yields of monomodal polymer relative to cyclic material and better reproducibility of yields and molecular weight of the polymers may be achieved. The presence of cryptand was found to have similar effects. Monomodal polysilanes with relatively narrow molecular weight distributions ($M_w/M_n < 1.5$) have also been prepared by the reductive coupling of methylphenyldichlorosilane and di-*n*-hexyldichlorosilane with alkali metals in toluene in the presence of ultrasound. Although sonochemical synthesis is accompanied by selective degradation, decreasing the molecular weight to an approximate limiting value of M_n of 50,000, polydispersities (M_w/M_n) are improved and are reduced to values less than 1.2 [36,37].

The relatively ill-defined nature of the Wurtz coupling procedure has given rise to variety of alternate stoichiometric and catalytic methods for silicon–silicon bond formation. Although limited in scope, the anionic ring opening polymerisation of a cyclic tetrasilane oligomer $(\text{PhMeSi})_4$ with *n*-BuLi or PhMe_2SiK as initiator produced a product with a molecular weight above 100,000. In this case, however, the small ring cyclic polymer precursors were still prepared by a Wurtz-type procedure [38,39]. Although alternative reagents for the reductive coupling of halosilanes have been assessed, for example Sm/SmI₂ [40], the method which seems to hold the greatest potential for future elaboration is the catalytic dehydrogenative coupling of primary and secondary organosilanes. Although an initial report of the condensation and disproportionation of various secondary and primary silanes promoted by Wilkinson's catalyst, $[(\text{Ph}_3\text{P})_3\text{RhCl}]$, appeared as early as 1973 [41], it was over

a decade later before any concerted interest was provoked by the researches of Harrod and co-workers who demonstrated the polymerisation of primary silanes, including PhSiH_3 and HexSiH_3 by the titanocene complexes Cp_2TiR_2 ($\text{R} = \text{CH}_3$, $\text{CH}_2\text{C}_6\text{H}_5$) (2) [42]. Since this time, a variety of early d^0 transition metal catalysts from groups 3 and 4 as well as later metal derivatives have given rise to a fascinating and mechanistically diverse research endeavour.



The initial work of Harrod utilising Cp_2TiMe_2 was characterised by an initiation period in which the reaction solution turned blue due to reduction to Ti(III). This inference was confirmed by the isolation of several intermediates, including a structurally characterised dimer of $\text{Cp}_2\text{TiSiHPh}$, **5** (Fig. 2a), in which dimerisation occurs through a pair of Ti–H–Si bridges, and which spontaneously decomposes into $[\text{Cp}_2\text{Ti}(\mu\text{-H})(\mu\text{-HSiHPh})\text{TiCp}_2]$, **6** (Fig. 2b), with production of poly(phenyl)silane. From these observations a mechanism (Scheme 1) involving polymer propagation by the repetitive insertion of a silylene moiety into a Ti–Si bond was proposed [43].

These discoveries stimulated a variety of researchers including Tilley who proposed an alternative mechanism for the polymerisation of primary organosilanes by group 4 metallocenes, including complexes of zirconium and hafnium, induced by σ -bond metathesis [44–47]. These systems produce relatively high molecular weight polymers with degrees of polymerisation as high as 7–100 monomer units and the catalytic cycle is believed to be initiated via the formation of a metallocene hydride which undergoes a σ -bond metathesis reaction with a Si–H bond to eliminate H_2 and form a metal silyl (Scheme 2) [46]. This latter species undergoes a second σ -bond metathesis, which results in the Si–Si coupling, which is particularly

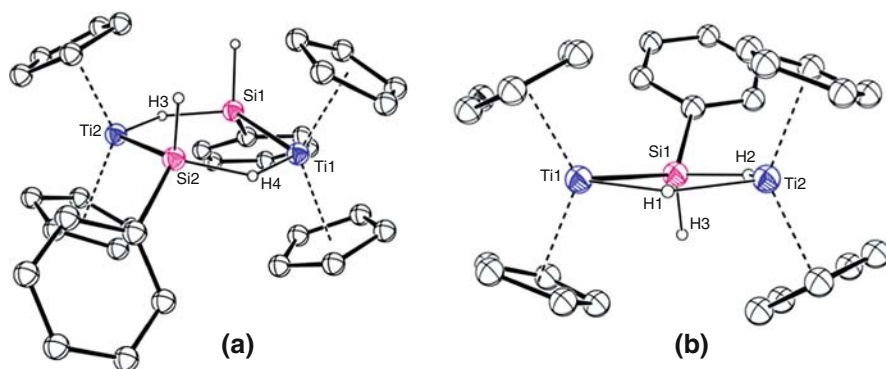
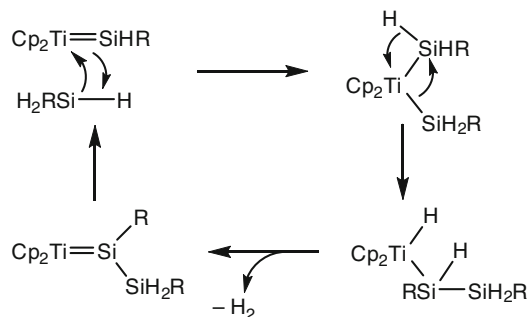
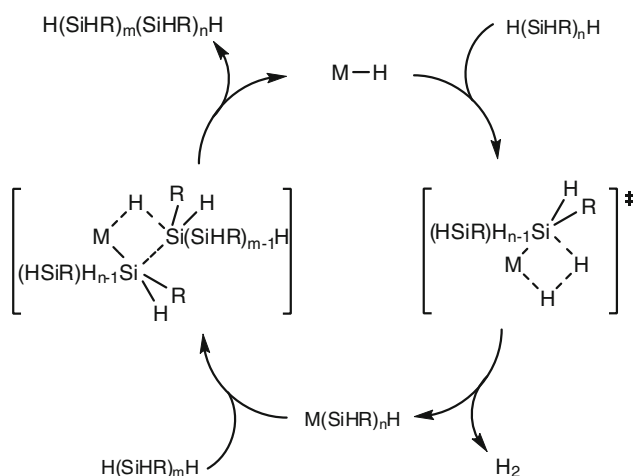


Fig. 2 Ti(III) intermediates isolated by Harrod and co-workers during titanocene-mediated dehydrocoupling of PhSiH_3



Scheme 1



Scheme 2

favoured for the coupling of primary silanes due to the crowding of the four-centred σ -bond metathesis transition states. The success of these procedures is dependent upon pushing the reactions to extremely high monosilane conversion, since it is only under such conditions that the requisite coupling of intermediate-length chains to give long chains will occur. Kinetic and structural studies provided evidence for this mechanism and it was demonstrated that reactions of Zr and Hf silyl complexes with hydrosilanes produce a variety of metal hydrido and silyl species such as compound **7** (Fig. 3) [48]. In closely related work Corey demonstrated that metallocene dichlorides may act as precatalysts when activated towards dehydropolymerisation of PhSiH_3 upon addition of two equivalents of $n\text{-BuLi}$. The mechanism was again believed to occur via a similar σ -bond metathesis mechanism [49–58]. Comparable findings for the dehydrogenative coupling of PhSiH_3 have been described for similarly d^0 organolanthanide metallocenes of the type $[\text{Cp}'_2\text{LnR}]$ [Cp' = substituted cyclopentadienyl; Ln = La, Nd, Sm, Y, Lu; R = H, $\text{CH}(\text{SiMe}_3)_2$] [59].

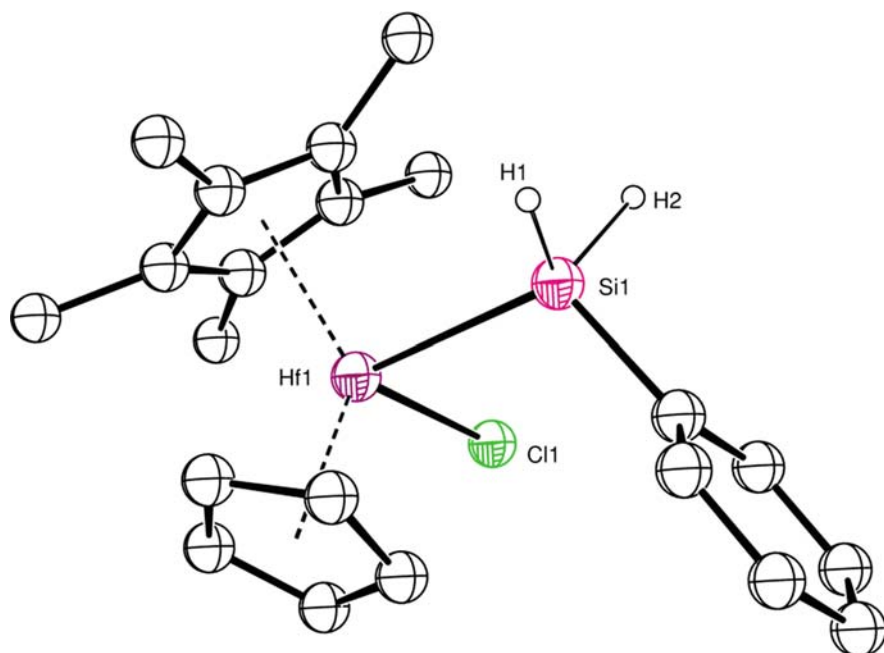


Fig. 3 Hafnium silyl species isolated by Tilley and co-workers during catalytic dehydrocoupling of PhSiH_3

A limited number of catalysts for dehydrogenative coupling of silanes based upon the later transition metals have also been described. A reinvestigation of the activity of Wilkinson's catalyst $[(\text{PPh}_3)_3\text{RhCl}]$ applied to the coupling of both secondary and primary organosilanes has been reported by Rosenberg. This work has established that secondary dialkyl- or alkarylsilanes may be coupled to produce a mixture of di- and trisilanes, contingent upon the efficient removal of H_2 from the reaction mixture [60]. Furthermore coupling occurs without any redistribution of the organic residues about the silicon centres and more reactive primary alkyl silanes, RSiH_3 ($\text{R} = n\text{-C}_{12}\text{H}_{25}$ or $n\text{-C}_8\text{H}_{17}$), provide chains of up to 5–6 silicon atoms in length [61]. Although apparently limited in terms of polymer formation, these latter studies, along with further reports that electron-rich complexes of Pt, Pd, Rh and Ir also catalyse the formation of Si–Si bonds from Si–H bonds in organosilanes, hint that a rich dehydrocoupling chemistry based upon these elements is waiting to be uncovered [62].

2.3 Electronic Structure of Oligo- and Polysilanes

Many of the proposed applications of organo(polysilanes) stem from their marked optoelectronic behaviour, which is proposed to result from delocalisation of the

Si–Si σ -electrons This is manifested in several ways, which parallel the behaviour delocalised cyclic, aromatic or linear polyenes. Although, as outlined earlier [17, 18, 20], these properties were first recognised through the observation of electronic transitions in the UV region, cyclic silane-based oligomers, such as $(\text{Me}_2\text{Si})_6$ or $(\text{Me}_2\text{Si})_5$ are also observed to form radical anions or cations upon reduction or oxidation. For linear permethylsilane oligomers, the lowest energy absorption shifts to longer wavelength with increasing chain length up to about 40 silicon atoms, beyond which λ_{max} becomes effectively constant at a value of the order of 310 nm [63].

This highly distinctive σ -delocalised behaviour may be satisfactorily described by a straightforward LCBO (linear combination of bonding orbitals) approach. The degree of σ -orbital delocalisation for alkanes and polysilanes has been determined on the basis of the Sandorfy C quantum chemical model and assessed by photoelectron spectroscopy [64–66]. A catenated polysilane chain may be propagated by overlap of approximately sp^3 hybridised valence orbitals (Fig. 4a). The resonance integral β_{vic} between adjacent silicons thus accounts for Si–Si σ bond formation with the resultant splitting of each pair of sp^3 atomic orbitals into a strongly bonding σ_{SiSi} and strongly antibonding σ_{SiSi}^* (Fig. 4b). The Sandorfy C model is an extension of the Hückel HMO-treatment of polyenes that includes geminal Si–Si–Si interactions, β_{gem} , as an additional resonance integral. This is a less strongly correlated integral between two sp^3 hybrids located on the same silicon atom. The manifold of mutually interacting localised orbitals that results from the both β_{vic} and β_{gem} interactions gives rise to a set of molecular orbitals that are delocalised over the entire silicon backbone and the degree of delocalisation is a function of the ratio $\beta_{\text{gem}}/\beta_{\text{vic}}$; the closer the value is to unity, the closer to perfection is the electronic delocalisation [66]. The nodal patterns that result are completely analogous to those in carbon-based polyenes (Fig. 4b). The HOMO contains a node at each silicon centre, while

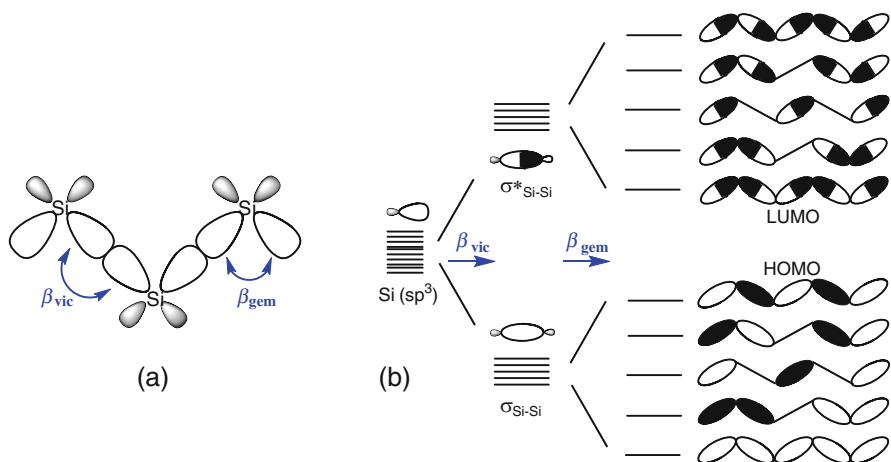


Fig. 4 (a) Overlap of sp^3 hybrid orbitals at Si to form an all *trans* σ -bonded catenated unit; (b) Schematic of the σ orbitals of an all *trans* oligosilane chain (after Michl) [5]

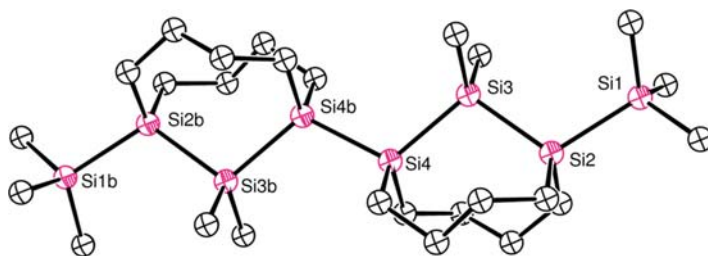


Fig. 5 A conformationally locked all-*anti* (tetramethylene)-tethered octasilane

the LUMO contains nodes only between the silicon centres. From this simple analysis it is also clear that secondary effects such as the identity of the organic silicon substituents and the conformation of the Si–Si bonded chain will have a profound effect upon the value of $\beta_{\text{gem}}/\beta_{\text{vic}}$ and, as a result, the delocalisation and absorption characteristics of a particular oligo- or polysilane. In an all *anti* (or *trans*) configuration the value of β_{vic} is maximised and has the effect of destabilising the HOMO and stabilising the LUMO of the chain with a concurrent red shift in the observed UV λ_{max} with the decreasing $\sigma\text{--}\sigma^*$ energy gap [67].

This latter effect is most clearly observed in the case of organosilane polymers which have been conformationally constrained to a transoid form by crystallisation. Poly(di-*n*-hexyl)silane has been reported to exhibit a typical absorption at 317 nm in solution but to display an anomalously long-wavelength absorption of 371 nm when spun from solution to the solid state [68, 69]. Similar solvatochromic transitions may be induced in polysilane polymers with oxygen atoms in the side chain upon addition of hexafluoro-2-propanol due to conformational ordering as a result of hydrogen bonding effects [70]. Similar effects also give rise to abrupt thermochromic behaviour with a shift of the position of the λ_{max} value for, in particular, long chain alkyl-substituted polysilanes to longer wavelength with decreasing temperature [71–73]. Polysilanes with all *anti* conformations of the main chain (i.e. SiSiSiSi dihedral angles of 180°) have been observed to provide the highest degree of σ -conjugation. A major step towards the realisation of an all-*anti*-polysilane was made with the synthesis of the (tetramethylene)-tethered octasilane, **8** (Fig. 5). This is the longest silicon chain where the silicon atoms are conformationally controlled to be in the all *anti* state. Remarkably, octasilane **8** exhibits a molar extinction coefficient three times larger than the unrestricted *n*-Si₈Me₁₈ at 0°C, consistent with increased σ -delocalisation [74, 75].

2.4 Applications of Polysilanes

Although a primary motivation towards the exploitation of polysilane compounds has been driven by their optoelectronic properties, much of the initial and continuing

interest has also centred upon their potential to act as lithographic precursors for semiconductor fabrication. Organosilane polymers are photoactive toward UV irradiation and photoscission and are commonly observed to photodegrade by either homolytic chain cleavage to silyl radicals or with the elimination of a diorganosilylene. Generally, photon energies are insufficient for the generation of two silyl radicals and a silylene by the cleavage of two adjacent SiSi bonds. Silylene elimination is not observed to occur for lower energy photons, however, and both processes may be viewed as being in competition [76, 77]. Although this instability is an issue for longer-term applications of polysilanes, the photodegradation behaviour has attracted attention in its own right as effective photoresist materials for microlithography when imaged by UV radiation [78]. The high mobility of the electrons within the σ framework results in large polarisabilities and, as a result, large nonlinear optical (NLO) effects have been measured for a variety of polysilanes with different side groups, and for composites of polysilanes and silver. The values of the third-order nonlinear susceptibilities, χ^3 , have been reported to vary substantially with changes in the side groups, backbone conformation, film thickness and orientation [79–81].

The discovery by West that insulating polysilanes may be rendered semiconducting upon exposure to oxidants such as AsF_5 and SbF_5 indicated that polysilanes resemble other polymers which can be made conducting in the presence of dopants, such as polyacetylene and poly(pyrrole) [82]. As is the case for such π -delocalised polymers, the dominant process of charge carrier transport in polysilanes involves the hopping of holes between localised states originating from domain-like subunits along the chain [83]. This behaviour has been recognised as holding potential for a variety of applications that have become the realm of π -conjugated polymers, but which exploit the σ -delocalised properties of the silicon-based polymer. Charge transfer from both linear and network polysilanes to C_{60} has been demonstrated to occur upon irradiation, and the resultant photoconducting materials may be employed in many applications, including photovoltaic cells [84–89]. In a complementary manner, polysilane-based structures also exhibit electroluminescence and have even been observed to display behaviour that is beyond the known capability of π -conjugated polymers [90]. For example, while most organic light-emitting diodes (OLEDs) are designed to emit in the visible region, a series of diode devices based upon poly(*n*-alkyl)silanes have been developed which are simultaneous UV emitters at room temperature [91, 92].

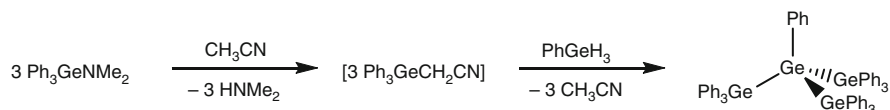
3 Oligo- and Polygermanes, Stannanes and Plumbanes

3.1 Oligo- and Polygermanes

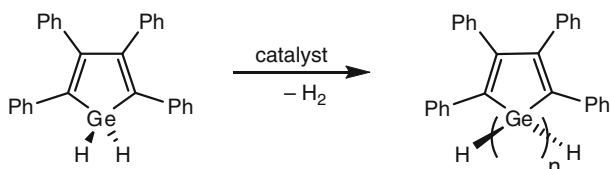
Although germanium lies below silicon in the periodic table and thus provides the most logical extension of the catenated behaviour outlined earlier, reports of truly catenated linear species beyond simple digermanes are relatively scarce. The

first extensive study of higher germanium hydrides appears to have been carried out in 1924 by Dennis and co-workers who prepared di- and trigermane, H_3GeGeH_3 and $\text{H}_3\text{Ge}(\text{GeH}_2)\text{GeH}_3$ via acid hydrolysis of magnesium germanide [93]. Although evidence for the existence of still higher hydrides was obtained in this study, it was not until 1959 that the presence of the higher homologues, Ge_4H_{10} and Ge_5H_{12} , from this reaction was confirmed [94]. As was the case for the corresponding silicon-based chemistry, more varied and versatile reaction products may be obtained in the presence of organic functional groups. The first compound of this type to be prepared was $\text{Ph}_3\text{GeGePh}_3$, which in contrast to the pyrophoric nature of the parent digermane is relatively tolerant of air and moisture [95]. Reflecting the syntheses of the majority of poly- and oligosilanes, the preparation of this latter compound involved the Wurtz coupling of Ph_3GeBr with sodium metal. Although a variety of oligomeric species corresponding to tri- [96–101], tetra- [97, 99, 102] and pentagermanes [103] have been synthesised, either by related germyl anion/halogermane metathesis, germylene insertion or ring opening of cyclic oligogermanes, routes to these compounds are generally unsatisfactory and low yielding. More recent research has been directed towards the development of milder and more selective methods of synthesis. Samarium diiodide has been employed as a single electron reductant in the coupling of halogermanium compounds resulting in the formation of di- and trigermanes [104, 105] and, most recently, an elegant method for the preparation of discrete oligogermanes has been introduced by Weinert and co-workers in which the Ge–Ge bonds are constructed sequentially through a hydrogermylation reaction. In this latter case, reaction of a germanium amide, R_3GeNMe_2 with acetonitrile solvent provided an α -germylated nitrile $\text{R}_3\text{GeCH}_2\text{CN}$, which underwent subsequent reaction with a germanium hydride to form the Ge–Ge bond (Scheme 3). [106, 107] The preparation of higher oligomers was also achieved by stepwise oligogermane chain construction. The ethoxyethyl-substituted compounds $\text{R}_2\text{Ge}(\text{NMe}_2)\text{CH}_2\text{CH}_2\text{OEt}$ ($\text{R} = \text{Et, Bu, Ph}$) were found to react with Ph_3GeH in CH_3CN to afford the corresponding digermanes. In the case of $\text{R} = \text{Et}$ and Bu these digermanes could also be reacted with di-*iso*-butylaluminium hydride to generate a digermane hydride which was subsequently coupled with the appropriate synthon to produce the corresponding trigermanes. Although this satisfyingly well-defined route may in principle be employed to construct longer homocatenated chains, the majority of higher molecular weight polygermane syntheses have, as is the case for polysilanes, been based around Wurtz coupling reactions of dichlorogermanes and sodium metal or by a metathesis method by reaction of dihalogermynes and Grignard reagents (or organolithiums) [108–110]. Most of the polygermanes prepared in this manner showed a narrow molecular distribution containing molecular weights 10^3 – 10^4 and provided characteristic electronic absorption bands at 300–350 nm and were strongly thermochromic for alkyl-substituted derivatives.

In contrast to the success of analogous procedures for the synthesis of high molecular weight polysilanes, attempted dehydrogenative coupling of organogermanes has only provided very limited success. In an extension of his polysilane work, Harrod reported that catalytic dehydrocoupling of Ph_2GeH_2 yielded



Scheme 3



Scheme 4

a tetrameric species as the only oligomerised product [111]. In contrast, Trogler has successfully applied either H_2PtCl_6 , $\text{RhCl}(\text{PPh}_3)_3$ or $\text{Pd}(\text{PPh}_3)_4$ to the polycondensation of dihydro(tetraphenyl)germole, perhaps indicating that this route is worthy of more intensive and focussed study (Scheme 4) [112]. In related but uniquely distinct work, Berry has shown that polygermanes with molecular weights of ca. 10^4 – 10^6 may be accessed via the demethanative coupling of methyl germanes such as Me_3GeH or Me_2PhGeH [113–115]. The resultant polymers were found to be highly branched and to vary in molecular weight dependent upon the identity of the ruthenium catalyst employed. Coupling of Me_3GeH with $[\text{Ru}(\text{PMe}_3)_4\text{Me}_2]$ was prefaced by a short induction period prior to methane evolution and it was suggested that the mechanism involves both α -methyl germyl to ruthenium migration and germyl to ruthenium-germylene migration within the coordination sphere of the metal (Scheme 5). Although this chemistry does not appear to have been further exploited, it, again, holds much promise particularly if further generalised and extended to other members of group 14.

3.2 Properties of Oligo- and Polygermanes

Like polysilanes, much of the impetus towards the synthesis of catenated germanium compounds has centred on their analogous σ -conjugated electronic structures. In solution, the polygermanes display characteristic electronic absorption bands at 300–350 nm and are strongly thermochromic for alkyl-substituted derivatives. The replacement of the silicon centres of an oligo- or polysilane with their heavier congener, thus, tends to result in a red shift to longer wavelength in the λ_{max} of the UV/vis spectrum. As early as 1969, Drenth and co-workers demonstrated that the UV absorption spectra of polymetal compounds, $\text{Me}(\text{SiMe}_2)_n\text{Me}$, $\text{Et}(\text{GeEt}_2)_n\text{Et}$ and $\text{Et}(\text{SnEt}_2)_n\text{Et}$, ($n = 2$ – 6) not only exhibit a bathochromic shift for increasing

regard. In common with the polysilanes discussed earlier, photolysis of polygermanes proceeds by both contraction of the chain with loss of diorganogermynes and homolytic scission of the germanium–germanium σ bond [109]. Although this instability may again provide a severe impediment to the application of polygermane compounds in device technologies, Berry and co-workers have shown that some of these problems may be circumvented by encapsulation of the Ge–Ge chains within a silica matrix formed by crosslinking of pendant ethoxy silanes prior to demethanative Ge–Ge coupling [115]. Under these conditions, both the thermal and the photochemical stability of the polygermane chains is enhanced due to an anchoring effect and subsequent recombination of the germynyl radicals formed under the higher energy conditions.

3.3 *Oligo- and Polystannanes*

Although the earliest examples of di-tin compounds containing an unsupported Sn–Sn bond can again be traced to the very earliest years of main group organometallic chemistry [118–121], the recognition that this catenated behaviour could be extended to cyclic or linear species of higher nuclearity was not reported until the work of Neumann in the early 1960s. These studies described the syntheses of a variety of di- and oligostannanes such as “diethyl tin”, which was reported to exist as a nine-membered cyclic species [122–128]. These compounds were generally prepared by either a simple pyridine-initiated dehydrocondensation reaction of diorganotinhydrides or an intermolecular amine elimination reaction between a diorganotinhydride and a diorganotin diamide. Prefacing the later interest in their absorption characteristics [116], the products resulting from these reactions were reported to exist as yellow, orange or even red waxy solids or oils. Although much of this early work was reviewed from the standpoint of diorganostannylene stability and formation, interestingly, these particular and simple methods of Sn–Sn bond formation do not seem to have been re-examined in more recent times (*vide infra*) [129]. Dräger’s demonstration that treatment of cyclotetrastannanes such as $(t\text{Bu}_2\text{Sn})_4$ [130] with iodine provided functionalised open chain species, $\text{I}(t\text{Bu}_2\text{Sn})_4\text{I}$, which could be further reacted with stannyl anions, for example Ph_3SnLi , provided the first example of a rational and directed tin-based homologation reaction [131, 132]. Apparently, solutions of $\text{I}(t\text{Bu}_2\text{Sn})_4\text{I}$ react as equilibrium mixtures of different diiodopolystannanes. Careful variation of the molar ratio of the starting materials as well as the solvents (toluene/THF) and concentration made it possible to isolate the tri- (**9**), tetra- (**10**), penta- (**11**) and hexastannanes (**12**). All four species were characterised by ^{119}Sn NMR and the X-ray analyses illustrated in Fig. 6. The UV spectra exhibited strong absorption maxima with a pronounced red-shift with increasing chain length and were correlated with a decreasing HOMO–LUMO energy difference based upon the linear σ -bonded chains.

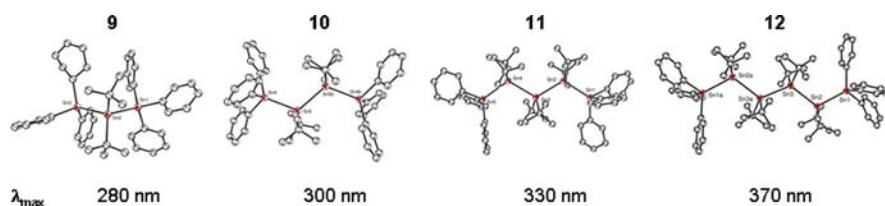
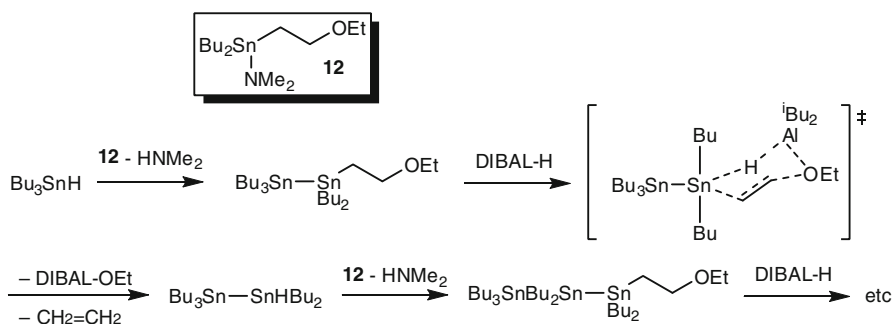


Fig. 6 Dräger's tri-, tetra-, penta- and hexastannanes and their absorption maxima

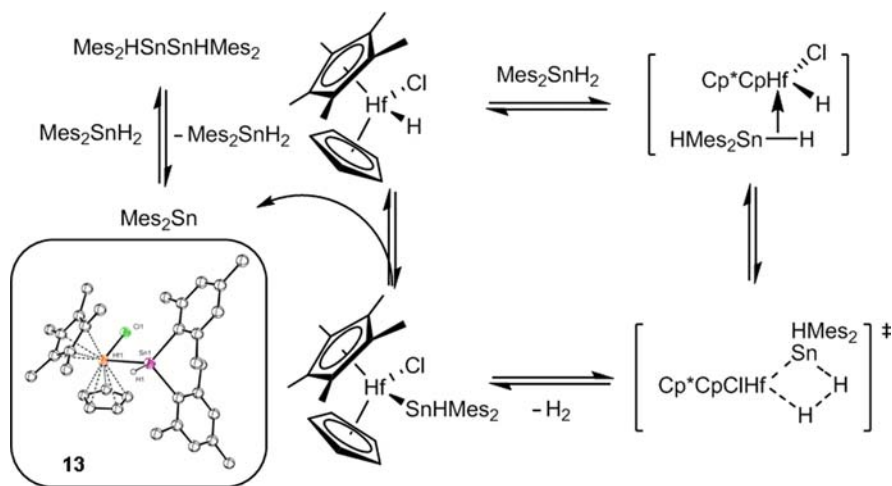


Scheme 6

Although such well-defined oligomeric species remain something of a rarity, Sita has provided an elegant stepwise synthesis of linear polystannane oligomers based upon a hydrostannolysis strategy reminiscent of that applied some two decades earlier by Neumann [133, 134]. In this case, utilisation of a β -alkoxy substituent was applied as a protecting group for the programmable stepwise synthesis of linear polystannanes. The key reagent $\text{Bu}_2\text{Sn}(\text{NMe}_2)\text{CH}_2\text{CH}_2\text{OEt}$ (**12**) was employed in reactions with appropriate tin hydrides before removal of the protecting group with DIBAL-H. The resulting Sn–H function was then employed in an iterative chain growth by repetition of the two-step sequence (Scheme 6) [133]. The electronic spectra of the resultant oligomers were, again, demonstrated to be dependent upon the Sn–Sn chain length as well as the specific placement of the organic residues. This work was continued in a subsequent report in which the synthesis and full characterisation of a series of oligostannanes $\text{X}(\text{}^n\text{Bu}_2\text{Sn})[\text{}^m\text{Bu}_2\text{Sn}]_m(\text{}^t\text{Bu}_2\text{Sn})[\text{}^n\text{Bu}_2\text{Sn}]_n(\text{Sn}^n\text{Bu}_2\text{CH}_2\text{CH}_2\text{OEt})$ (where m or $n = 0\text{--}3$), was described. This well-defined homologous series not only displayed the expected variations in their electronic spectra with varying chain length but also revealed quite dramatic perturbations in the $^1J(^{119}\text{Sn}\text{--}^{117}\text{Sn})$ coupling constants for the Sn–Sn bonds containing the more sterically demanding ${}^t\text{Bu}_2\text{Sn}$ unit [135].

Higher molecular weight and truly polymeric catenated tin species have also been prepared by transition metal catalysed dehydrocoupling of diorganotin dihydrides. Although dehydrogenative dimerisation or oligomerisation of stannanes has been achieved with a variety of transition metal complexes [136], the majority of catalytic polymerisation reactions have employed group 4-based reagents [137].

As an extension of his studies of polysilane synthesis [46, 47], Tilley reported that the addition of neat $n\text{-Bu}_2\text{SnH}_2$ to $[\text{Zr}(\text{C}_5\text{H}_5)(\text{C}_5\text{Me}_5)\{\text{Si}(\text{SiMe}_3)_3\}\text{Me}]$ resulted in instantaneous and vigorous evolution of hydrogen gas and the formation of a dark red poly(di- n -butyl)stannane, which, by gel permeation chromatography (GPC), was shown to contain a high molecular weight material ($M_w/M_n = 17,500/7,800$) along with small ring cyclic structures [138, 139]. This work was extended to a range of secondary stannanes and to several zirconocene catalyst structures [139]. The resultant alkyl polystannanes $\text{H}(\text{SnR}_2)_n\text{H}$ ($\text{R} = n\text{-butyl}, n\text{-hexyl}, n\text{-octyl}$) were observed to display λ_{max} values at ca. 380–400 nm, attributed to $\sigma\text{-}\sigma^*$ transitions. Although thermally stable, the polystannanes were photosensitive and it was demonstrated that $\text{H}(\text{Sn}^n\text{Bu}_2)_n\text{H}$ was photochemically depolymerised to a 2:1 mixture of *cyclo*-(Sn^nBu_2)₅ and *cyclo*-(Sn^nBu_2)₆. Thin films of $\text{H}(\text{Sn}^n\text{Bu}_2)_n\text{H}$ could also be doped by exposure to SbF_5 to produce material with vapour conductivities as high as 0.3 S cm^{-1} . Although initial mechanistic analysis of these reactions suggested that the dehydropolymerisation occurred by a σ -bond metathesis mechanism involving four-centre transition states analogous to that outlined for the dehydropolymerisation of primary silanes, later work deduced that reactions of hydrostannyl complexes such as $\text{CpCp}^*\text{Hf}(\text{SnHMes})_2\text{Cl}$ (**13**), with Ph_2SnH_2 or $n\text{-Bu}_2\text{SnH}_2$ to afford poly- and oligostannanes may involve R_2Sn insertions into $\text{M}\text{-}\text{Sn}$ bonds [140, 141]. This process is reported to occur via a mechanism involving initial σ -bond metathesis between the metal catalyst and the stannane substrate with elimination of a small stable molecule (e.g. H_2 , CH_4 , $\text{HSi}(\text{SiMe}_3)_3$, etc). This produces a hydrostannyl intermediate, which is unstable towards α -H-elimination and the formation of a transient stannylene (Scheme 7), which is then available to insert into $\text{M}\text{-}\text{Sn}$ or $\text{Sn}\text{-}\text{H}$ bonds as the primary $\text{Sn}\text{-}\text{Sn}$ bond forming reaction. Subsequent and similar observations of stibinidene formation during group 4-catalysed stibine



Scheme 7

dehydrocoupling lend weight to the view that α -H-abstraction and subsequent elimination and insertion of a low valent intermediate may be a common feature among the dehydrocoupling chemistries of the heavier p-block elements [142].

Later transition metals have also been employed for the catalytic dehydrocoupling of secondary diorganostannanes. Reactions of $(\text{PhMe}_2\text{P})_2\text{PtMe}_2$ or $[(\kappa^2\text{-P, N})\text{-Ph}_2\text{PC}_2\text{H}_4\text{NMe}_2]\text{PtMe}_2$ with an excess of ${}^n\text{Bu}_2\text{SnH}_2$ or Ph_2SnH_2 have been observed to result in the catalytic formation of *cyclo*-, *oligo*- and polystannanes. Only polystannanes were observed in the reaction of $[(\kappa^2\text{-P, N})\text{-Ph}_2\text{PC}_2\text{H}_4\text{NMe}_2]\text{PtMe}_2$ with H_2SnBu_2 . A series of reports describing the preparation of relatively high molecular weight poly(diorgano)stannane ($M_w = 20 \times 10^3 \text{g mol}^{-1}$) through dehydropolymerisation of R_2SnH_2 with $(\text{PPh}_3)_3\text{RhCl}$ have also recently appeared [143–146]. The mechanism in this case has again been proposed to occur via a sequence of α -hydrogen abstraction and stannylene elimination steps, combined with oxidative addition and reductive elimination from the catalytically active rhodium centre. An analogous catalyst system has also been employed in the polymerisation of a series of enantiomerically pure bis(myrtanyl)tin compds., *cis*- Myr_2SnH_2 and *trans*- Myr_2SnH_2 derived from (-)-1S- β -pinene to give a mixture of polystannanes, poly(*cis*- Myr_2Sn) $_n$ poly(*trans*- Myr_2Sn) $_n$ and oligomers that could not be separated. The CD spectra of these polystannanes revealed a positive Cotton effect at λ_{max} 422 and 425 nm, consistent with the idea that the chiral information is transferred from the UV-inactive myrtanyl groups to the polymer backbone, which most likely adopts a helical conformation with the right-handed screw sense being in excess [147].

This latter study also reported the reductive coupling of the corresponding bis(myrtanyl)tin dichlorides with magnesium metal. In these cases, reduction selectively produced pentastannane rings, *cyclo*-(*cis*- Myr_2Sn) $_5$ and *cyclo*-(*trans*- Myr_2Sn) $_5$. These failures to provide materials of high molecular weight notwithstanding, related Wurtz coupling procedures have been shown to yield high molecular weight polystannane materials under carefully controlled conditions.

Although Zou and Yang first reported higher molecular weight linear polymers, $({}^n\text{Bu}_2\text{Sn})_{\sim 60}$ by Wurtz coupling of ${}^n\text{Bu}_2\text{SnCl}_2$ using sodium dispersions in toluene catalysed by the addition of 15-crown-5 in 1992 [148], initial attempts to repeat this work were unsuccessful [139]. Subsequently it was discovered that the precise reaction conditions were critical to achieve maximum chain lengths [149]. During the first 2 h of the reaction very little polymer is formed, and most of the product is low molecular weight cyclic oligomers. The maximum yield of polymer was observed to occur after *ca.* 4 h when remarkably high molecular weight materials were formed ($M_n = \text{ca.} 1 \times 10^6$). These materials were also found to be extremely light sensitive, photobleaching within 1 to 2 min from brown polymer to pale yellow oligomer. Absorption maxima were also found to plateau at 380 nm even for the highest molecular weight polymer. These values are also consistent with UV/vis data obtained either from materials produced by SmI_2 reduction and electrochemically prepared polystannanes of lower molecular weights (10^4) [105, 150, 151], and indicate a similar σ -delocalised behaviour as that inferred for the electronic structures of polysilanes, albeit with diminished HOMO–LUMO band gaps.

The electronic properties of polystannanes have, as for their lighter congeners, been the focus of much attention. Poly(diaryl)stannanes, prepared by a dehydro-polymerisation route with a dimethylzirconocene catalyst, exhibited λ_{\max} values in the range 430–506 nm. These σ – σ^* transitions were seen to vary according to the polymer molecular weights and a sample of poly{bis(o-ethyl-p-n-butoxyphenyl)}stannane exhibited a strong absorption at 506 nm (tailing to ca. 550 nm). This latter value appears to be the smallest band gap yet observed for a group 14 σ -conjugated polymer and was attributed to the imposition of an all *trans* planar Sn backbone configuration by the steric demands of the *ortho*-ethyl substituents [152, 153]. Similar order–disorder phase transitions have also been attributed to changes in the absorption characteristics of oriented films of poly(dibutylstannane) under either variable temperature conditions or when placed under mechanical stress [146, 154]. Although further attempts to induce conformational ordering by adjustment of the organic residues directly attached to tin have been unsuccessful [155], these observations are consistent with the rather more well-developed studies of conformationally constrained polysilanes as well as density functional theoretical predictions of band gap variations in the parent polystannane $(\text{SnH}_2)_n$. [156].

3.4 Oligoplumbanes

Although reports of longer catenated species based upon the heaviest member of group 14 are yet to be authenticated, plausible syntheses of tetraorganodiplumbanes date from the early 1940s and a number of tetra-alkyl and tetra-aryl species have been structurally characterised [157–169]. The number of organometallic compounds containing more than a single Pb–Pb bond, however, is very small. Weidenbruch and co-workers reported an, as yet unique, example of a hexaaryl-cyclotriplumbane, **14**, in 2003 [170]. However, this compound is best described as being formed via weak interactions of plumbylene lone pairs with empty p orbitals of neighbouring lead atoms [171]. Of more relevance to the current discussion, therefore, are the two tris(triarylplumbyl)plumbate anions, including **15**, described by Weidenbruch and Robinson, respectively, and prepared by the disproportionation of lead dihalides during reactions with aryl Grignard reagents [172, 173]. Although the four lead atoms within the structures of both anions comprise a trigonal pyramid with the free electron pair at the apex, neither has been discussed from the context of possible delocalisation across the extended Pb–Pb σ -framework (Fig. 7).

4 Catenation of Group 15 elements

That phosphorus exhibits extensive catenation within its allotropes has long been rationalised as a consequence of its periodic diagonal relationship to carbon [174, 175]. Although, as typical non-metal and semi-metals, respectively, both phosphorus

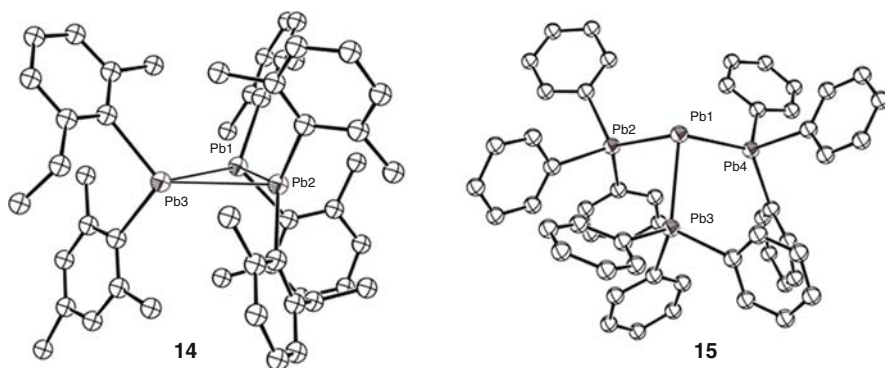
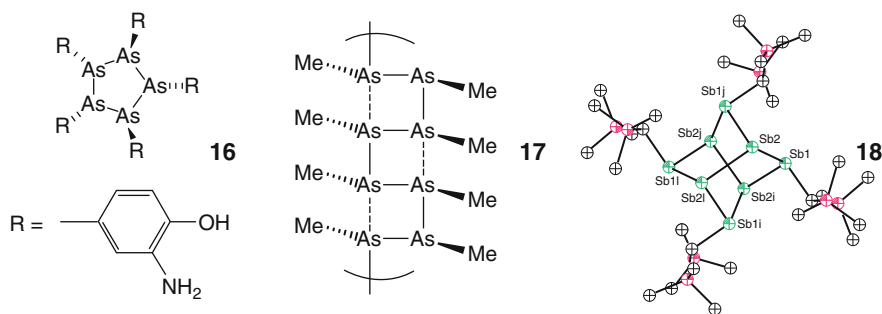
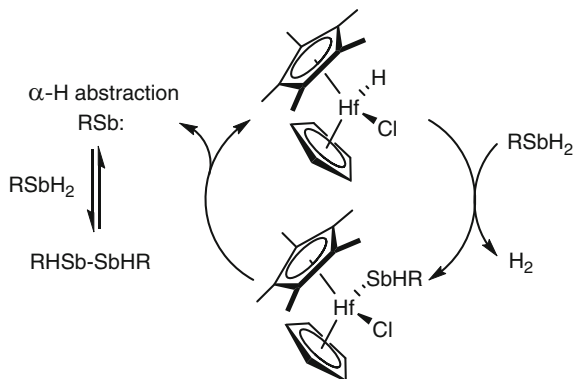


Fig. 7 Weidenbruch's hexaarylcyclotriplumbane and tris(triarylplumbyl)plumbate complexes

and arsenic lie outside the scope of this current review it is notable that a wide variety of open chain and cyclic molecular species based upon these elements have been reported [176–179]. Cyclic organoarsines hold a historically important position in organometallic chemistry as Ehrlich's “magic bullet” chemotherapeutic agents (Salvarsan, **16**) for the treatment of syphilis [180] and, in the current context, it is interesting to note that poly(metharsine), **17**, has been known and recognised as an intrinsic semiconductor for over 35 years [181–184]. In this latter case it was suggested that excitation of valence electrons from HOMO levels to LUMO levels was responsible for the electronic behaviour of this burgundy-coloured compound, primarily in the form of an n to d transition. Intriguingly, this observation does not appear to have been reinvestigated and, although this proposal may well be correct, it would be of interest to re-evaluate this work in the context of the potential for polysilane-analogous σ -delocalised behaviour.



Among the heaviest elements of group 15, a surprising number of organoantimony, $(RSb)_n$, and organobismuth, $(RBi)_n$ homocycles have been described [185–188]. Although the structures of a variety of both mono- and polycyclic species such as **18** have been reported [189], the chemistry of open chain *catena*-stibanes,



Scheme 8

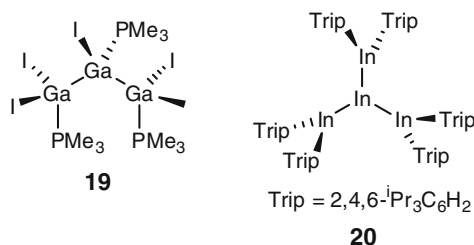
$R_{n+2}Sb_n$, and *catena*-bismuthanes, $R_{n+2}Sb_n$, beyond distibane and dibismuthane derivatives is much less developed and the majority of examples are ill-defined polymers or components of ring-chain equilibria where $n = 3$ or 4. The syntheses of the tri- and tetrastibanes, $(^tBu_2Sb)(SbMe)_n(Sb^tBu_2)$ [$n = 1$ or 2], $(Mes_2Sb)(SbPh)_n(SbMes_2)$, for example, have been achieved by reductive coupling of the appropriate organoantimony chlorides with magnesium [190]. Although such compounds were found to be unstable with respect to disproportionation to complex degradation products, the synthesis of a stable tristibane $[DmpSb(SbMe_2)_2]$ ($Dmp = 2, 6 - Mes_2C_6H_3$) has been achieved through the use of the more sterically protective Dmp substituent.

Despite such synthetic progress it is clear that this area is still ripe for development and requires the identification of suitable and flexible synthetic protocols. In research reminiscent of his work with stannane dehydrocoupling [140, 141], Tilley has reported that antimony-antimony bond formation may be catalysed by stibinidene elimination from zirconocene and hafnocene complexes (Scheme 8) [142]. Although, thus far, restricted to a very limited range of examples of stibane dehydrocoupling and to the formation of a single new Sb-Sb bond, this work demonstrates that, with imagination, a greater variety of catenated species based around this relatively understudied region of the periodic table may yet be forthcoming.

5 Catena-tion of Group 13 Elements

The identification of well-defined catenated species based upon the more electropositive elements of group 13 has a relatively recent history. For bonds between identical elements of group 13, the D_0 values are in general some 50 to 60 kJ mol^{-1} lower than those determined for their group 14 neighbours (Table 1). Possession

of only three valence electrons also commonly results in the adoption of aggregated structures and the formation of delocalised cluster molecular orbitals. Although both these factors mitigate against the routine formation of group 13 catenates, the possibility of more extended species was suggested for many years by the existence of molecular dihalides, X_2E-EX_2 (where E is a group 13 element and X is a halide) [191, 192]. More recent work has demonstrated that the maintenance of an unsupported two-electron E–E interaction in these compounds is far from unique, and a variety of larger cyclic and halide-bridged structures, such as the dialkyl dimetallanes $\{[(Me_3Si)_2CH]_2M_2\}$ (M = Al [193], Ga [194], In [195]), have also been reported for all the group 13 elements over the past 15 years [196, 197]. The observation of more than a single unsupported E–E interaction in a discrete molecule is, however, far from routine and for over a decade the only extended open chain complexes were the trigallium subhalide $[I_2(PET_3)GaGaI(PET_3)Ga(PET_3)I]$, **19** [198], and the crystallographically characterised trigonal complex $[In\{In(2,4,6-*i*Pr_3C_6H_2)_2\}_3]$, **20** [199].



The largest well-defined oligomer of this type is currently the linear hexa-indium complex, **21** (Fig. 8), supported by a single *ortho*-xylyl substituted β -diketiminato ligand at each four-coordinate In centre and terminated by two iodide substituents to maintain charge balance [200]. Compound **21** displayed an absorption maximum in hexane at ca. 349 nm, which was interpreted as evidence for the existence of electronic delocalisation across the indium σ framework analogous to that observed in isoelectronic catenated group 14 systems.

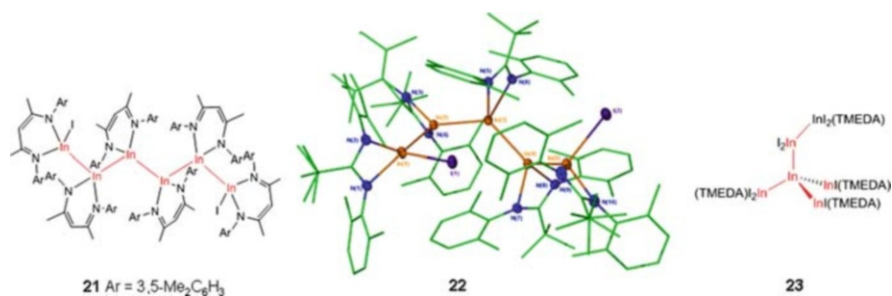
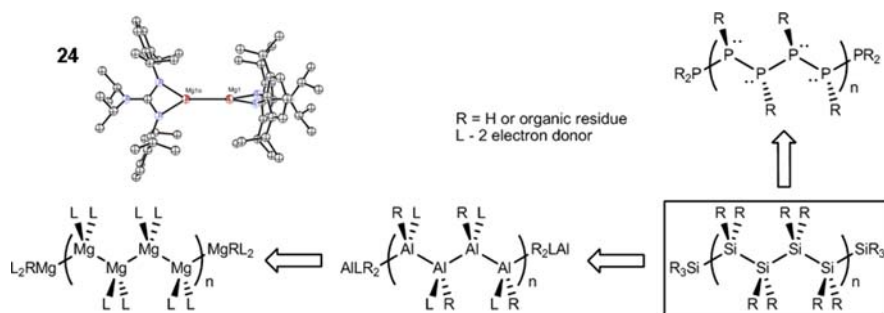


Fig. 8 Homocatenated indium complexes

Compound **21** was synthesised fortuitously as a product of disproportionation during a metathesis reaction between the monovalent indium halide, InI, and a potassium derivative of the supporting β -diketiminato. In subsequent work a similar reaction has provided the related amidinate-supported pentaindium derivative **22** [201]. Although a related disproportionation product of InI dissolution in the chelating amine TMEDA, **23**, has also been discussed from the context of σ -delocalisation [202], the phenomenon has not yet been widely recognised or indeed proven in group 13-based systems. In order for further progress it is apparent that more reliable and rational routes to oligomeric and truly polymeric species must be developed through, for example, examination of catalysed dehydrocoupling techniques related to those that have provided success in group 14 chemistry.

6 Outlook

The broad coverage provided by this chapter has tried to summarise the structures of and potential for homocatenated bonding within the metallic elements of the p-block of the periodic table. Although the chemistry of polysilanes has advanced to a somewhat sophisticated level, it is clear that there is still enormous potential for the elaboration of isoelectronic and related structures down both group 14 and to either side in groups 13 and 15. Indeed, complexes of the elements of these latter groups have only been seldom mentioned in the context of their potentially σ -delocalised electronic structures and it is, as yet, uncertain whether the noted behaviour of group 14 species may be so naively mapped onto their nearest neighbours in the periodic table. The rather empirical progress reported thus far has provided, however, a variety of intriguing observations that will encourage future synthetic and more applied investigations. Very few examples of either block or randomly copolymerised group 14 polymetallanes have appeared and, although the chemistry and the identification of suitable co-ligands appears to become more synthetically challenging with increasing element atomic weight and electropositivity, the prospect of materials with precisely tailored 1-dimensional band structures through judicious selection of catenated element identity is extremely appealing. The imaginative synthetic chemist has an effectively unexploited palette of building blocks available for the construction of novel oligo- and polymeric structures. This does not necessarily have to be limited to the subject of this chapter, the elements of the p-block of the periodic table. The first examples of molecular compounds containing unsupported E–E single bonds between two s-block elements, including the magnesium species **24** [203, 204], have very recently appeared and it is thus tempting to suggest that the isoelectronic relationships illustrated in Scheme 9 for catenated species of the second full period of the table may eventually be extended to the elements of group 2. Whatever the future holds, it is clear that surprises will continue to occur and that the discoveries are there to be made.



Scheme 9

References

1. Schnepf A (2007) *Chem Soc Rev* 36:745–758
2. Sevov SC, Goicoehea JM (2006) *Organometallics* 25:5678–5692
3. Power PP (1998) *J Chem Soc-Dalton Trans* 2939–2951
4. Power PP (2007) *Organometallics* 26:4362–4372
5. Miller RD, Michl J (1989) *Chem Rev* 89:1359–1410
6. Corey JY (2004) *Adv Organ Chem* 51:1–52
7. Tamao K, West R (2003) *J Organomet Chem* 685:1–2
8. West R (1986) *J Organomet Chem* 300:327–346
9. West R, Maxka J (1988) *ACS Symp Ser* 360:6–20
10. West R, Menescal R, Asuke T, Eveland J (1992) *J Inorgan Organomet Polym* 2: 29–45
11. Moissan H (1902) *Bulletin de la Société chimique de France* 27:1190
12. Stock AS, Paul Zeidler F (1923) *Berichte der Deutschen Chemischen Gesellschaft [Abteilung] B: Abhandlungen* 56B:11
13. Kipping FS (1924) *J Chem Soc Trans* 125: 2291–2297
14. Kipping FS, Sands JE (1921) *J Chem Soc Trans* 119:830–847
15. Burkhard CA (1949) *J Am Chem Soc* 71:963–964
16. Gilman H, Atwell WH, Cartledge FK (1966) *Adv Organomet Chem* 4:1–94
17. Gilman H, Atwell WH, Schwebke GL (1964) *J Organomet Chem* 2:369–371
18. Gilman H, Atwell WH, Schwebke GL (1964) *Chem Ind (London, UK)* 1063
19. Gilman H, Atwell WH, Sen PK, Smith CL (1965) *J Organomet Chem* 4:163–167
20. Sakurai H, Kumada M (1964) *Bull Chem Soc Jpn* 37:1894–1895
21. Kumada M, Ishikawa M (1963) *J Organomet Chem* 1:153–159
22. Kumada M, Ishikawa M, Maeda S (1966) *J Organomet Chem* 5:120–123
23. Kumada M (1966) *Pure Appl Chem* 13:167–187
24. Kumada M, Tamao K (1968) *Adv Organomet Chem* 6:19–117
25. Hasegawa Y, Iimura M, Yajima S (1980) *J Mater Sci* 15:720–728
26. Mazdiyasi KS, West R, David LD (1978) *J Am Ceram Soc* 61:504–508
27. West R, David LD, Djurovich PI, Stearley KL, Srinivasan KSV, Yu H (1981) *J Am Chem Soc* 103:7352–7354
28. Wesson JP, Williams TC (1979) *J Polymer Sci A Polym Chem* 17:2833–2843
29. Wesson JP, Williams TC (1980) *J Polymer Sci A Polym Chem* 18:959–965
30. Wesson JP, Williams TC (1981) *J Polymer Sci A Polym Chem* 19:65–72
31. Jones RG, Benfield RE, Cragg RH, Swain AC, Webb SJ (1993) *Macromolecules* 26:4878–4887
32. Jones RG, Holder SJ (2006) *Polym Int* 55:711–718
33. Gauthier S, Worsfold DJ (1990) *Adv Chem Series* 299–307

34. Miller RD, Thompson D, Sooriyakumaran R, Fickes GN (1991) *J Polymer Sci A Polym Chem* 29:813–824
35. Gauthier S, Worsfold DJ (1989) *Macromolecules* 22:2213–2218
36. Price GJ (1992) *J Chem Soc Chem Commun* 1209–1210
37. Matyjaszewski K, Greszta D, Hrkach JS, Kim HK (1995) *Macromolecules* 28:59–72
38. Cypryk M, Chrusciel J, Fossum E, Matyjaszewski K (1993) *Makromolekulare Chemie-Macromolecular Symposia* 73:167–176
39. Cypryk M, Gupta Y, Matyjaszewski K (1991) *J Am Chem Soc* 113:1046–1047
40. Li ZF, Iida K, Tomisaka Y, Yoshimura A, Hirao T, Nomoto A, Ogawa A (2007) *Organometallics* 26:1212–1216
41. Ojima I, Inaba S, Kogure T, Nagai Y (1973) *J Organomet Chem* 55:C7–C8
42. Aitken C, Harrod JF, Samuel E (1985) *J Organomet Chem* 279:C11–C13
43. Aitken C, Harrod JF, Gill US (1987) *Can J Chem Revue Canadienne De Chimie* 65: 1804–1809
44. Woo HG, Tilley TD (1989) *J Am Chem Soc* 111:8043–8044
45. Woo HG, Walzer JF, Tilley TD (1992) *J Am Chem Soc* 114:7047–7055
46. Tilley TD (1993) *Acc Chem Res* 26:22–29
47. Tilley TD (1990) *Comments Inorg Chem* 10:37–51
48. Woo HG, Heyn RH, Tilley TD (1992) *J Am Chem Soc* 114:5698–5707
49. Corey JY, Braddock-Wilking J (1999) *Chem Rev* 99:175–292
50. Corey JY, Huhmann JL, Shaltout RM, Kraichely DM (1993) 10th Jubilee International Symposium on Organosilicon Chemistry, Marciniak BCJ (ed) Poznan, Poland, pp 387–409
51. Corey JY, Huhmann JL, Zhu XH (1993) *Organometallics* 12:1121–1130
52. Corey JY, Rooney SM (1996) *J Organomet Chem* 521:75–91
53. Corey JY, Zhu XH (1992) *J Organomet Chem* 439:1–17
54. Corey JY, Zhu XH, Bedard TC, Lange LD (1991) *Organometallics* 10:924–930
55. Grimmond BJ, Corey JY (1999) *Organometallics* 18:2223–2229
56. Huhmann JL, Corey JY, Rath NP (1997) *J Organomet Chem* 533:61–72
57. Shaltout RM, Corey JY (1995) *Main Group Chemistry* 1:115–126
58. Shaltout RM, Corey JY (1995) *Tetrahedron* 51:4309–4320
59. Forsyth CM, Nolan SP, Marks TJ (1991) *Organometallics* 10:2543–2545
60. Rosenberg L, Davis CW, Yao J (2001) *J Am Chem Soc* 123:5120–5121
61. Rosenberg L, Kobus DN (2003) *J Organomet Chem* 685:107–112
62. Brown-Wensley KA (1987) *Organometallics* 6:1590–1591
63. De Mahieu AF, Daoust D, Devaux J, De Valck M (1992) *Eur Polym J* 28:685–687
64. Pitt CG, Jones LL, Ramsey BG (1967) *J Am Chem Soc* 89:5471–5472
65. Bock H, Ensslin W (1971) *Angew Chem Int Ed Engl* 10:404–405
66. Herman A, Dreczewski B, Wojnowski W (1985) *Chem Phys* 98:475–481
67. Tsuji H, Michl J, Tamao K (2003) *J Organomet Chem* 685:9–14
68. Miller RD, Hofer D, Rabolt J, Fickes GN (1985) *J Am Chem Soc* 107:2172–2174
69. Karikari EK, Greso AJ, Farmer BL, Miller RD, Rabolt JF (1993) *Macromolecules* 26:3937–3945
70. Oka K, Fujiue N, Dohmaru T, Yuan C-H, West R (1997) *J Am Chem Soc* 119:4074–4075
71. Kanai T, Ishibashi H, Hayashi Y, Ogawa T, Furukawa S, West R, Dohmaru T, Oka K (2000) *Chem Lett* 650–651
72. Kanai T, Ishibashi H, Hayashi Y, Oka K, Dohmaru T, Ogawa T, Furukawa S, West R (2001) *Journal of Polymer Science Part B-Polymer Physics* 39:1085–1092
73. Oka K, Fujiue N, Nakanishi S, Takata T, West R, Dohmaru T (2000) *J Organomet Chem* 611:45–51
74. Fukazawa A, Tsuji H, Tamao K (2006) *J Am Chem Soc* 128:6800–6801
75. Tsuji H, Fukazawa A, Yamaguchi S, Toshimitsu A, Tamao K (2004) *Organometallics* 23:3375–3377
76. Trefonas P, West R, Miller RD (1985) *J Am Chem Soc* 107:2737–2742
77. Karatsu T, Miller RD, Sooriyakumaran R, Michl J (1989) *J Am Chem Soc* 111:1140–1141

78. Kwark YJ, Bravo-Vasquez JP, Ober CK, Cao HB, Deng H, Meagley R (2003) 20th Annual Conference on Advances in Resist Technology and Processing, Fedynyshyn TH (ed) Santa Clara, CA, pp 1204–1211
79. Hamada T (1998) *J Chem Soc Faraday Trans* 94:509–517
80. Miller RD, Schellenberg FM, Baumert JC, Looser H, Shukla P, Torruellas W, Bjorklund GC, Kano S, Takahashi Y (1991) *ACS Symp Ser* 455:636–660
81. Shukla P, Cotts PM, Miller RD, Ducharme S, Asthana R, Zavislan J (1990) *Mol Cryst Liq Cryst* 183:241–259
82. West R, David LD, Djurovich PI, Stearley KL, Srinivasan KSV, Yu H (1981) *J Am Chem Soc* 103:7352–7354
83. Seki S (2007) *Polymer J* 39:277–293
84. Acharya A, Seki S, Koizumi Y, Saeki A, Tagawa S (2005) *J Phys Chem B* 109:20174–20179
85. Acharya A, Seki S, Saeki A, Tagawa S (2006) *Synth Met* 156:293–297
86. Kakimoto M, Kashiwara H, Kashiwagi T, Takiguchi T, Ohshita J, Ishikawa M (1997) *Macromolecules* 30:7816–7820
87. Kobayashi T, Shimura H, Mitani S, Mashimo S, Amano A, Takano T, Abe M, Watanabe H, Kijima M, Shirakawa H, Yamaguchi H (2000) *Angewandte Chemie Int Ed* 39:3110–3114
88. Ostapenko NI, Sekirin IV, Tulchynskaya DN, Suto S, Watanabe A (2002) *Synth Met* 129:19–24
89. Yu J, Zhang ZH, Ni Y, Lu YB, Xiong YQ, Xu WJ (2007) *J Appl Polymer Sci* 105:821–826
90. Suzuki H, Hoshino S, Furukawa K, Ebata K, Yuan CH, Bleyl I (2000) *Polym Adv Technol* 11:460–467
91. Sharma A, Katiyar M, Deepak, Seki S (2007) *J Appl Phys* 102
92. Sharma A, Katiyar M, Deepak, Seki S, Tagawa S (2006) *Appl Phys Lett* 88
93. Dennis LM, Corey RB, Moore RW (1924) *J Am Chem Soc* 46:657–674
94. Amberger E (1959) *Angew Chem* 71:372–373
95. Morgan GT, Drew HDK (1925) *J Chem Soc Trans* 127:1760–1768
96. Castel A, Riviere P, Saint-Roch B, Satge J, Malrieu JP (1983) *J Organomet Chem* 247:149–160
97. Roller S, Simon D, Draeger M (1986) *J Organomet Chem* 301:27–40
98. Draeger M, Simon D (1986) *J Organomet Chem* 306:183–192
99. Haeberle K, Draeger M (1986) *J Organomet Chem* 312:155–165
100. Weidenbruch M, Hagedorn A, Peters K, von Schnering HG (1995) *Angew Chem Int Ed Engl* 34:1085–1086
101. Weidenbruch M, Hagedorn A, Peters K, von Schnering HG (1996) *Chem Ber* 129:401–404
102. Draeger M, Simon D (1981) *Z Anorg Allg Chem* 472:120–128
103. Roller S, Draeger M (1986) *J Organomet Chem* 316:57–65
104. Yokoyama Y, Hayakawa M, Azemi T, Mochida K (1995) *J Chem Soc Chem Commun* 2275–2275
105. Azemi T, Yokoyama Y, Mochida K (2005) *J Organomet Chem* 690:1588–1593
106. Subashi E, Rheingold AL, Weinert CS (2006) *Organometallics* 25:3211–3219
107. Amadoruge ML, Gardinier JR, Weinert CS (2008) *Organometallics* 27:3753–3760
108. Miller RD, Sooriyakumaran R (1987) *Journal of Polymer Science Part a-Polymer Chemistry* 25:111–125
109. Mochida K, Chiba H (1994) *J Organomet Chem* 473:45–54
110. Hayashi T, Uchimaru Y, Reddy NP, Tanaka M (1992) *Chem Lett* 647–650
111. Aitken C, Harrod JF, Malek A, Samuel E (1988) *J Organomet Chem* 349:285–291
112. Toal SJ, Sohn H, Zakarov LN, Kassel WS, Golen JA, Rheingold AL, Trogler WC (2005) *Organometallics* 24:3081–3087
113. Reichl JA, Popoff CM, Gallagher LA, Remsen EE, Berry DH (1996) *J Am Chem Soc* 118:9430–9431
114. Katz SM, Reichl JA, Berry DH (1998) *J Am Chem Soc* 120:9844–9849
115. Huo YS, Berry DH (2005) *Chem Mater* 17:157–163
116. Drenth W, Noltes JG, Bulten EJ, Creemers HMJC (1969) *J Organomet Chem* 17:173–174
117. Pitt CG, Bursley MM, Rogerson PF (1970) *J Amer Chem Soc* 92:519–522

118. Gruttner G (1917) *Ber Dtsch Chem Ges* 50:1808–1813
119. Kraus CA, Bullard RH (1926) *J Am Chem Soc* 48:2131–2136
120. van der Kerk GJM, Luijten JGA (1954) *J Appl Chem* 4:301–307
121. Brown MP, Fowles GWA (1958) *J Chem Soc* 2811–2814
122. Neumann WP, Koenig K (1962) *Angew Chem* 74:215
123. Neumann WP, Pedain J (1964) *Justus Liebigs Ann Chem* 672:34–43
124. Neumann WP, Koenig K, Burkhardt G (1964) *Justus Liebigs Ann Chem* 677:18–20
125. Neumann WP, Schneider B (1964) *Angew Chem* 76:891
126. Sommer R, Neumann WP, Schneider B (1964) *Tetrahedron Lett* 3875–3878
127. Sommer R, Schneider B, Neumann WP (1966) *Justus Liebigs Ann Chem* 692:12–21
128. Creemers HMJC, Noltes JG (1965) *Recl Trav Chim Pays Bas* 84:382–384
129. Neumann WP (1978) *Organomet Coord Chem Germanium Tin Lead Plenary Lect Int Conf* 2:51–74
130. Puff H, Bach C, Schuh W, Zimmer R (1986) *J Organomet Chem* 312:313–322
131. Adams S, Drager M (1985) *J Organomet Chem* 288:295–304
132. Adams S, Draeger M (1987) *Angew Chem* 99:1280–1282
133. Sita LR (1992) *Organometallics* 11:1442–1444
134. Sita LR, Terry KW, Shibata K (1995) *J Am Chem Soc* 117:8049–8050
135. Shibata K, Weinert CS, Sita LR (1998) *Organometallics* 17:2241–2248
136. Braunstein P, Morise X (2000) *Chem Rev* 100:3541–3552
137. Woo H-G, Song S-J, Kim B-H (1998) *Bull Korean Chem Soc* 19:1161–1164
138. Imori T, Tilley TD (1993) *J Chem Soc Chem Commun* 1607–1609
139. Imori T, Lu V, Cai H, Tilley TD (1995) *J Am Chem Soc* 117:9931–9940
140. Neale NR, Tilley TD (2002) *J Am Chem Soc* 124:3802–3803
141. Neale NR, Tilley TD (2004) *Tetrahedron* 60:7247–7260
142. Waterman R, Tilley TD (2006) *Angewandte Chemie-International Edition* 45:2926–2929
143. Choffat F, Kaeser S, Wolfer P, Schmid D, Mezzenga R, Smith P, Caseri W (2007) *Macromolecules* 40:7878–7889
144. Choffat F, Smith P, Caseri W (2005) *J Mater Chem* 15:1789–1792
145. Choffat F, Fornera S, Smith P, Caseri W (2007) *Mater Res Soc Symp Proc 1007*, No pp given, Paper #: 1007-S10–03
146. Choffat F, Fornera S, Smith P, Caseri WR, Breiby DW, Andreasen JW, Nielsen MM (2008) *Adv Funct Mater* 18:2301–2308
147. Beckmann J, Duthie A, Grassmann M, Semisch A (2008) *Organometallics* 27:1495–1500
148. Zou WK, Yang NL (1992) *Polym Prepr (Am Chem Soc Div Polym Chem)* 33:188–189
149. Devylder N, Hill M, Molloy KC, Price GJ (1996) *Chem Commun (Cambridge)* 711–712
150. Yokoyama Y, Hayakawa M, Azemi T, Mochida K (1995) *J Chem Soc Chem Commun* 2275
151. Okano M, Matsumoto N, Arakawa M, Tsuruta T, Hamano H (1998) *Chem Commun (Cambridge)* 1799–1800
152. Lu V, Tilley TD (1996) *Macromolecules* 29:5763–5764
153. Lu VY, Tilley TD (2000) *Macromolecules* 33:2403–2412
154. Bukalov SS, Leites LA, Lu V, Tilley TD (2002) *Macromolecules* 35:1757–1761
155. Deacon PR, Devylder N, Hill MS, Mahon MF, Molloy KC, Price GJ (2003) *J Organomet Chem* 687:46–56
156. Takeda K, Shiraishi K (1992) *Chem Phys Lett* 195:121–126
157. Calingaert G, Soroos H, Shapiro H (1942) *J Am Chem Soc* 64:462–463
158. Arnold DP, Wells PR (1976) *J Organomet Chem* 111:269–283
159. Glockling F, Gowda NMN (1982) *Inorganica Chimica Acta-Articles* 58:149–153
160. Kleiner N, Drager M (1984) *J Organomet Chem* 270:151–170
161. Kleiner N, Draeger M (1985) *J Organomet Chem* 293:323–341
162. Kleiner N, Drager M (1985) *J Organomet Chem* 293:323–341
163. Kleiner N, Drager M (1985) *Zeitschrift Fur Naturforschung Section B-a J Chem Sci* 40:477–483
164. Schneider C, Drager M (1991) *J Organomet Chem* 415:349–362
165. Mallela SP, Geanangel RA (1993) *Inorg Chem* 32:602–605

166. Mallela SP, Myrczek J, Bernal I, Geanangel RA (1993) *J Chem Soc Dalton Trans* 2891–2894
167. Schneider-Koglin C, Mathiasch B, Draeger M (1993) *J Organomet Chem* 448:39–46
168. Koglin H-J, Behrends K, Draeger M (1994) *Organometallics* 13:2733–2742
169. Whittaker SM, Cervantes-Lee F, Pannell KH (1994) *Inorg Chem* 33:6406–6408
170. Stabenow F, Saak W, Marsmann H, Weidenbruch M (2003) *J Am Chem Soc* 125:10172–10173
171. Koch R, Bruhn T, Weidenbruch M (2005) *J Chem Theory Comput* 1:1298–1303
172. Stabenow F, Saak W, Weidenbruch M (2003) *Chem Commun* 2342–2343
173. Wang Y, Quillian B, Wei P, Yang X-J, Robinson GH (2004) *Chem Commun (Cambridge, UK)* 2224–2225
174. Baudler M (1982) *Angewandte Chemie Int (Ed: English)* 21:492–512
175. Baudler M (1987) *Angewandte Chemie Int (Ed: English)* 26:419–441
176. Baudler M, Glinka K (1993) *Chem Rev* 93:1623–1667
177. Baudler M, Glinka K (1994) *Chem Rev* 94:1273–1297
178. Smith LR, Mills JL (1975) *J Organomet Chem* 84:1–15
179. Dyker CA, Burford N (2008) *Chemistry-an Asian Journal* 3:28–36
180. Lloyd NC, Morgan HW, Nicholson BK, Ronimus RS (2005) *Angew Chem Int Ed* 44:941–944
181. Waser J, Schomaker V (1945) *J Am Chem Soc* 67:2014–2018
182. Rheingol AI, Lewis JE, Bellama JM (1973) *Inorgan Chem* 12:2845–2850
183. Burns JH, Waser Jr (1957) *J Am Chem Soc* 79:859–864
184. Daly JJ (1970) *Sanz Helvetica Chimica Acta* 53:1879
185. Breunig HJ, Rosler R (1997) *Coord Chem Rev* 163:33–53
186. Breunig HJ, Rosler R (2000) *Chem Soc Rev* 29:403–410
187. Balazs L, Breunig HJ (2004) *Coord Chem Rev* 248:603–621
188. Breunig HJ (2005) *Zeitschrift Fur Anorganische Und Allgemeine Chemie* 631:621–631
189. Breunig HJ, Rosler R, Lork E (1997) *Angewandte Chemie Int (Ed: English)* 36:2237–2238
190. Breunig HJ, Ghesner L, Ghesner ME, Lork E (2003) *J Organomet Chem* 677:15–20
191. Tuck DG (1990) *Polyhedron* 9:377–386
192. Tuck DG (1993) *Chem Soc Rev* 22:269–276
193. Uhl W (1988) *Zeitschrift Fur Naturforschung Section B-a J Chem Sci* 43:1113–1118
194. Uhl W, Layh M, Hildenbrand T (1989) *J Organomet Chem* 364:289–300
195. Uhl W, Layh M, Hiller W (1989) *J Organomet Chem* 368:139–154
196. Uhl W (1993) *Angewandte Chemie Int (Ed: English)* 32:1386–1397
197. Uhl W (2004) *Adv Organomet Chem* 51:53–108
198. Schnepf A, Doriat C, Mollhausen E, Schnockel H (1997) *Chem Commun* 2111–2112
199. Brothers PJ, Hubler K, Hubler U, Noll BC, Olmstead MM, Power PP (1996) *Angewandte Chemie Int (Ed: English)* 35:2355–2357
200. Hill MS, Hitchcock PB, Pongtavornpinyo R (2006) *Science* 311:1904–1907
201. Hill MS, Mahon MF, MacDougall DJ In Unpublished results
202. Green SP, Jones C, Stasch A (2007) *Angewandte Chemie Int Ed* 46:8618–8621
203. Green SP, Jones C, Stasch A (2007) *Science* 318:1754–1757
204. Green SP, Jones C, Stasch A (2008) *Angewandte Chemie Int Ed* 47:9079–9083

Aromaticity/Antiaromaticity in “Bare” and “Ligand-Stabilized” Rings of Metal Atoms

Constantinos A. Tsipis

Abstract During the last decade, the aromaticity/antiaromaticity of “bare” and “ligand-stabilized” rings of metal atoms has flourished reaching a high level of sophistication. Compared to the aromaticity/antiaromaticity encountered in organic rings, primarily being of the traditional π -type, “bare” and “ligand-stabilized” rings of metal atoms can exhibit a multifold aromaticity/antiaromaticity and conflicting aromaticity, arising from the electron delocalization of s, p, d, and even f orbitals of the ring atoms. In this context we can speak for σ -, π -, δ -, and φ -aromaticity/antiaromaticity as well as for double ($\sigma + \pi$) and even triple ($\sigma + \pi + \delta$) aromaticity (possible in rings of transition metal atoms) and any possible combination of the σ -, π -, δ -, and φ -types of aromaticity/antiaromaticity. The f-orbital and possibly φ -aromaticity can exist only in rings of lanthanide and actinide metal atoms. In view of these facts, in this review we have provided an overview and updated information about aromaticity/antiaromaticity of rings of metal atoms covering the most significant developments in this new emerging field.

Keywords All-metal aromatic rings · Aromaticity/antiaromaticity · DFT · Rings of metal atoms

Contents

1	Introduction	218
2	Magnetic and Electronic Aspects of Aromaticity/Antiaromaticity	219
	2.1 Magnetic Indicators of Aromaticity/Antiaromaticity	219
	2.2 Electronic Indicators of Aromaticity/Antiaromaticity	223
3	Aromatic/Antiaromatic Three-Membered Rings of Group 1 Metal Atoms	226
4	Aromatic/Antiaromatic Three-Membered Rings of Group 2 Metal Atoms	226
5	Aromatic/Antiaromatic Three-Membered Rings of Group 13 Metal Atoms	229
6	Aromatic/Antiaromatic Three-Membered Rings of Group 14 Metalloid and Metal Atoms	230

7	Aromatic/Antiaromatic Three-Membered Rings of group 15 Metalloid and Metal Atoms	231
8	Aromatic/Antiaromatic Three-Membered Rings of Transition Metal Atoms	234
9	Aromatic/Antiaromatic Four-, Five-, and Six-Membered Rings of Metal Atoms	252
10	Aromaticity/Antiaromaticity in Lanthanide and Actinide Chemistry (f-Orbital Aromaticity)	268
11	Epilog	269
	References	271

1 Introduction

To begin with, we comment on the concepts of aromaticity/antiaromaticity, which are so frequently used in the current chemical literature [1–9]. Aromaticity/antiaromaticity is one of the most general but at the same time one of the most vaguely defined chemical concepts. Even though this concept was introduced in 1865–1866 by Kekulé [10, 11] it has no precise and generally well-established definition yet. Despite the frequent use of the term “aromaticity” in the past and present literature, aromaticity is not a measurable quantity and must be defined by convention. However, because of its complexity and multiple manifestations, there is not yet any generally accepted single quantitative definition, and aromaticity still remains a vexing and nebulous chemical concept. With the advent of modern methods, algorithms, computer software, and hardware helping the theory of bonding, the concepts of aromaticity/antiaromaticity changed their status from the initial a priori explanatory virtues, expressing the active causal agents, to the rather passive role as subject of the eventual a posteriori recovery from the bare output of the electronic structure methods. The aromaticity/antiaromaticity is a dear keyword of the chemical language that has almost exclusively fallen within the domain of organic chemistry. But this organic boundary has become flexible in the past few years as several research groups have shown that inorganic clusters, homo- and bimetallic clusters either “bare” or “ligand-stabilized,” mononuclear and polynuclear coordination, and organometallic compounds can be aromatic. Timely exhaustive assessments of the aromaticity concept in the domain of the aforementioned classes of compounds have been covered in recent review articles [12–17].

As the collection of recent reviews in the topic shows [12–20], a rather large consensus appears in the computation or experimental tests for the diagnosis of the aromaticity/antiaromaticity (energetic, structural, magnetic, chemical reactivity, and electronic diagnostic tools), whereas the mechanisms themselves still remain open to the debate. The primary controversy in the area involves the questions of whether aromaticity/antiaromaticity can be quantified and, if so, which of the methods commonly used to evaluate aromaticity/antiaromaticity is most appropriate. The literature on aromaticity and its measure is so vast that I must be content here with outlining briefly only the aromaticity indicators which have been extensively used to diagnose aromaticity/antiaromaticity in the domain of “all-metal” aromatics.

2 Magnetic and Electronic Aspects of Aromaticity/Antiaromaticity

Various criteria have been used to judge aromaticity/antiaromaticity, but none is satisfactory, since no single property exists whose measurement could be taken as a direct, unequivocal measure of aromaticity; instead, it is better to use two or more criteria that are “orthogonal” to each other [21]. In “all-metal” aromatic molecules including “bare” or “ligand-stabilized” rings of metal atoms, mononuclear and polynuclear coordination and organometallic compounds and metallabenzenes the diagnosis of the aromatic/antiaromatic character was primarily based on the magnetic and electronic (molecular orbital pattern, electron delocalization, electronic excitations and orbital eigenvalues) criteria of aromaticity.

2.1 Magnetic Indicators of Aromaticity/Antiaromaticity

Magnetic criteria constitute the most frequently used aromaticity indices [3]. It is well known that aromatic molecules exhibit relatively strong diamagnetism when placed in a magnetic field, and this is due to induced ring currents that generate a magnetic field opposing the applied one. This “London diamagnetism” is detected readily in NMR chemical shifts and in diamagnetic susceptibility and diamagnetic anisotropy measurements. The magnetic criteria of aromaticity are based on the specific response of the aromatic compounds to externally applied uniform magnetic field perpendicular to the molecular plane. Several magnetic criteria have been put forward as measurements of the aromaticity of molecules [5, 22–27].

Magnetic aromaticity can be defined as the ability of a compound to sustain an induced ring current; these compounds are then called *diatropic*. Antiaromatic compounds are called *paratropic*. The ring current model (RCM) [24, 28] was proposed 60 years ago and is still widely used to rationalize the magnetic properties of aromatic molecules and as a criterion for determining the aromaticity of a wide range of cyclic molecules. Historically, characteristic proton NMR chemical shifts and the exaltation of magnetic susceptibility (Λ) have been important magnetic criteria for quantification of aromaticity. Mitchell has recently proposed measuring aromaticity by NMR spectroscopy [9, 29]. Concerning the diamagnetic susceptibilities, two factors are important when measuring a compound’s aromaticity: the anisotropy [30, 31] and the exaltation [32]. Aromatic molecules were found to possess high diamagnetic susceptibility anisotropies $\Delta\chi^m$, defined as:

$$\Delta\chi^m = \chi_{zz}^m - \frac{1}{2} \{ \chi_{xx}^m + \chi_{yy}^m \}$$

where χ_{zz}^m , χ_{xx}^m , and χ_{yy}^m are the three principal components of the diamagnetic susceptibility.

The magnetic exaltation is defined as the difference between the true mean molar magnetic susceptibility $\bar{\chi}^m$ and the one calculated by a hypothetical, additive incremental scheme by use of atom and bond increments χ_{calc}^m , according to the equation:

$$\Lambda^m = \bar{\chi}^m - \chi_{\text{calc}}^m$$

The exaltations are negative (diamagnetic) for aromatic compounds and positive (paramagnetic) for antiaromatic compounds.

An important aspect of magnetic susceptibility and nuclear magnetic shielding is that they can theoretically be expressed as sums of diamagnetic (diatropic) and paramagnetic (paratropic) current distributions. For a closed-shell molecule with N electrons, the total first-order induced current density at point \mathbf{r} is [33–35]:

$$\mathbf{j}^{(1)}(\mathbf{r}) = \frac{i e \hbar N}{m_e} \left[\int (\Psi_0 \nabla \Psi_0^{(1)} - \Psi_0^{(1)} \nabla \Psi_0) d\tau \right] \quad (1)$$

where Ψ_0 is the unperturbed wave function, and the first-order magnetically perturbed wave function $\Psi_0^{(1)}$ in an external magnetic field \mathbf{B} can be expressed as

$$\begin{aligned} \Psi_0^{(1)} &= \frac{e}{2m_e} \left[\sum_{l>0} \Psi_l \frac{\langle \Psi_l | \hat{\mathbf{L}}(\mathbf{0}) | \Psi_0 \rangle}{E_l - E_0} \right] \cdot \mathbf{B} + \frac{e}{2m_e} \left[\sum_{l>0} \Psi_l \frac{\langle \Psi_l | \hat{\mathbf{P}} | \Psi_0 \rangle}{E_l - E_0} \right] \cdot \mathbf{B} \\ &= \Psi_0^{(p)} + \Psi_0^{(d)} \end{aligned} \quad (2)$$

where $\hat{\mathbf{L}}(\mathbf{0})$ is the angular momentum operator for rotation around a global origin of coordinates, and $\hat{\mathbf{P}}$ is the translational angular momentum operator. Since $\hat{\mathbf{L}}$ and $\hat{\mathbf{P}}$ operators are sums of one-electron operators, the first-order wave function $\Psi_0^{(1)}$ becomes a sum over states (SOS) in which Ψ_l are the singly excited configurations $\Psi_n^{(p)}$ obtained from Ψ_0 by excitation of one electron from an occupied orbital ψ_n ($n \leq N/2$) to a virtual (unoccupied) orbital ψ_p ($p > N/2$). In this formulation, $\mathbf{j}^{(1)}$ can be written as a sum of occupied molecular orbital contributions:

$$\mathbf{j}^{(1)}(\mathbf{r}) = 2 \sum_{n=1}^{N/2} \mathbf{j}_n^{(1)}(\mathbf{r}) \quad (3)$$

where $\mathbf{j}_n^{(1)}(\mathbf{r})$ is the first-order induced current density for molecular orbital ψ_n , which is the sum of diamagnetic (diatropic) $\mathbf{j}_n^{(d)}$ and paramagnetic (paratropic) $\mathbf{j}_n^{(p)}$ induced current densities

$$\mathbf{j}^{(1)}(\mathbf{r}) = \mathbf{j}_n^{(d)} + \mathbf{j}_n^{(p)} \quad (4)$$

In the framework of the SOS approximation (2) may be expanded in terms of the occupied, ψ_n , and unoccupied, ψ_p , molecular orbitals and their orbital eigenvalues, ε_i .

$$\begin{aligned} \psi_n^{(1)}(\mathbf{r}; \mathbf{d}) = & \frac{e}{2m_e} \left[\sum_{p>n/2} \psi_p(\mathbf{r}) \frac{\langle \psi_p | \hat{\mathbf{I}}(\mathbf{0}) | \psi_n \rangle}{\varepsilon_p - \varepsilon_n} \right] \bullet \mathbf{B} \\ & + \frac{e}{2m_e} \left[\mathbf{d} \sum_{p>n/2} \psi_p(\mathbf{r}) \frac{\langle \psi_p | \hat{\mathbf{p}} | \psi_n \rangle}{\varepsilon_p - \varepsilon_n} \right] \bullet \mathbf{B} \end{aligned} \quad (5)$$

where the first-order wave function $\psi_n^{(1)}(\mathbf{r}; \mathbf{d})$ is a function of electron position \mathbf{r} and depends parametrically on the displacement \mathbf{d} .

For a symmetric molecule, it has been shown that consideration of the perturbed wave function in (5) allows us to simplify our understanding of which excitations will contribute to the total ring current; the paramagnetic current arises from $\psi_p^{(p)}$, its size depending on accessibility of states via the rotational operator (R_z) and the diamagnetic current from $\psi_p^{(d)}$, depending on accessibility of states via the translational ($T_{x,y}$) operator. Thus, an occupied-to-unoccupied transition $\psi_n \rightarrow \psi_p$ gives a *paramagnetic* contribution if the product of symmetries contains a match to R_z , and a *diamagnetic* ring current contribution if it contains a match to a translation $T_{x,y}$ [34, 36, 37].

The current density is a 3-D vector-field defined at any point in space. The topological analysis of the current fields has been used as a means of describing the calculated current fields, which are difficult to visualize in their full detail and complexity. The current density at a given point in space can be evaluated assuming that the same point lies at the origin of the coordinate system. To this end the CTOCD-DZ (continuous transformation of origin of the current density-diamagnetic zero) formulation of magnetic response, the so-called *ipsocentric* method, provides current density maps of high quality [38–42]. The ipsocentric distribution of origin of vector potential is the only distribution that gives rise to a clear physical separability of orbital contributions. Using the ipsocentric distributed gauge-origin formulation [38, 39], induced current density vector plots can be generated and the ring current circulations can be directly visualized [40]. The response of a molecule to an applied external magnetic field can also be evaluated by a graphical representation of the induced magnetic field [43]. It was shown that molecules that contain a π electron system possess a long-range magnetic response, while the induced σ magnetic field is short-range for molecules without π electron system.

More recently, a new and widely used index of aromaticity, the nucleus-independent chemical shift (NICS), has originally been proposed by Schleyer and coworkers [44, 45]. It is defined as the negative value of the absolute shielding computed at a ring center or at some other interesting points of the system. Negative NICS values correspond to aromaticity, while positive values are associated with antiaromaticity. There is a whole family of NICS methods, which include NICS computations at ring centers [43], NICS(0) and above [46], NICS(1) and NICS(2), dissected NICS values, i.e., the total NICS at a particular point in space may be dissected into paratropic and diatropic components, which mainly arise from the C-C σ and π multiple bonds, respectively [46, 47] and MO contributions to NICS,

MO–NICS, NICS $_{\pi}$ [22, 48]. NICS may be mapped in three-dimensional space [49–51].

The analytical capabilities of the NICS criterion continue to be enhanced and refined, with the out-of-plane zz -components of the shielding tensor elements NICS $_{zz}(0)$ and NICS $_{zz}(1)$ proposed to be a superior aromaticity measure index [1, 52]. Furthermore, the CMO–NICS criterion [52, 53] of aromaticity dissects the total shieldings calculated at ring or cage centers, into individual contributions from each canonical molecular orbital (CMO). The CMO–NICS analysis, however, does not provide a physical explanation for the magnitude of the individual molecular orbital contributions to the total NICS. More recently, it was established that the shapes of the NICS-scan profiles provide a clear picture of the type of the ring current in aromatic and antiaromatic systems [54, 55] and can be used to characterize unequivocally whether an inorganic system is aromatic, nonaromatic, and antiaromatic [56, 57]. Using the NICS criterion of aromaticity Hofmann and Berndt [58] investigated the type of aromaticity in a series of boron-containing molecules with two electrons delocalized cyclically over three centers and found that distinctly different patterns of NICS values characterize the π -, σ -, ($\pi + \sigma$)-double and π , σ -mixed aromatic character. More recently Boldyrev and coworkers [17] introduced the aromatic and antiaromatic concepts as useful tools for deciphering the chemical bonding in transition metal systems. However, no explanation is given whether aromaticity/antiaromaticity (cyclic delocalization/localization) tunes the chemical bonding in the transition metal systems or the particular chemical bonding (the occurrence of highly delocalized MOs introducing a ring current) tunes aromaticity/antiaromaticity.

As far as the most appropriate computational methodology to compute nuclear chemical shielding and NICS values is concerned, despite the considerable debate in the literature, the gauge including atomic orbital (GIAO) scheme was widely regarded as the most accurate when a large basis set is used [59].

Another magnetic indicator of aromaticity proposed by Herges et al. [60] is based on the anisotropy of the induced current density (ACID), $\Delta T_S^{(1)}$, which can also be computed from the current density tensor at each point as [35]:

$$\Delta T_S^{(1)}(\mathbf{r})^2 = \frac{1}{3} [(\mathbf{j}_{xx} - \mathbf{j}_{yy})^2 + (\mathbf{j}_{yy} - \mathbf{j}_{zz})^2 + (\mathbf{j}_{zz} - \mathbf{j}_{xx})^2] + \frac{1}{2} [(\mathbf{j}_{xy} + \mathbf{j}_{yx})^2 + (\mathbf{j}_{xz} + \mathbf{j}_{zx})^2 + (\mathbf{j}_{yz} + \mathbf{j}_{zy})^2] \quad (6)$$

The ACID is a scalar dimensionless quantity which is independent of the direction and magnitude of the magnetic field.

Finally, Sundholm and coworkers [61, 62] proposed two more magnetic indicators of aromaticity, the ring-current shielding (ARCS) and the gauge-including magnetically induced current. In the ARCS method, the strength of the induced ring current and the size of the current ring are obtained from nuclear magnetic shielding calculated in discrete points along a line perpendicular to the molecular plane starting at the ring center. Assuming that the induced ring current in an aromatic

molecule is cyclic, the induced magnetic field strength perpendicular to the loop is given by the expression [61]:

$$B(z)_{\text{ind}} = \frac{\mu_0 I_{\text{ring}}}{2} \frac{R^2}{(z^2 + R^2)^{3/2}} = -\sigma(z) B_{\text{ext}} \quad (7)$$

where R is the radius of the current loop, z is the perpendicular distance from the loop center, $\sigma(z)$ is the z -dependence of the isotropic nuclear magnetic shielding function, and B_{ext} is the applied magnetic field. By differentiating (7) with respect to the external magnetic field one obtains the relation between the isotropic nuclear magnetic shielding and the derivative of the induced current with respect to the applied magnetic field:

$$\sigma(z) = -\frac{\mu_0}{2} \frac{\partial I_{\text{ring}}}{\partial B_{\text{ext}}} \frac{R^2}{(z^2 + R^2)^{3/2}} \quad (8)$$

The strength of the induced ring current for a given magnetic field is given as

$$I_{\text{ring}} = \frac{\partial I_{\text{ring}}}{\partial B_{\text{ext}}} B_{\text{ext}} \quad (9)$$

By calculating $\sigma(z)$ for a number of z -values in the range $z = [0, z_{\text{max}}]$ and fitting (8) to the calculated $\sigma(z)$ values, the induced current derivative $\frac{\partial I_{\text{ring}}}{\partial B_{\text{ext}}}$ and the loops radii R can be deduced from the long-range part of the shielding function (typical values for z_{max} are 30–60 a_0 depending on the loop size). The loop radius R is determined by fitting $\log[\sigma(z)]$ as a function of $\log[R^2/(z^2 + R^2)]$. This was done by adjusting the loop radius R until the angular coefficient became 3/2. The current derivative is deduced from the intercept at $3/2\{\log[R^2/(z^2 + R^2)]\} = 0$.

2.2 Electronic Indicators of Aromaticity/Antiaromaticity

The electronic criteria of aromaticity/antiaromaticity are based on the electronic structure of the molecules. Molecular orbitals (MOs) that are highly delocalized over the entire cyclic nuclear framework support cyclic electron delocalization which characterizes aromaticity. Based on the symmetry of the highly delocalized MOs we can distinguish between the orbital-types of aromaticity, e.g., σ -, π -, δ -, and φ -aromaticity. Many planar cyclic clusters formulated as $c\text{-}E_n$ and $c\text{-}E_n L_n$ (E = element, L = H, C, O, NH, n = 3–6) exhibit the so-called *multifold* aromaticity, which arises from various combinations of the aforementioned orbital types. Molecular orbitals are multicenter mono-electronic wave functions constructed from the overlap of atomic orbitals (AOs) belonging to the nuclear centers. The σ -aromaticity is supported by delocalized σ -MOs, which can result from the linear combination of s-, p-, d-, or f-AOs. Similarly π -aromaticity is supported by delocalized π -MOs

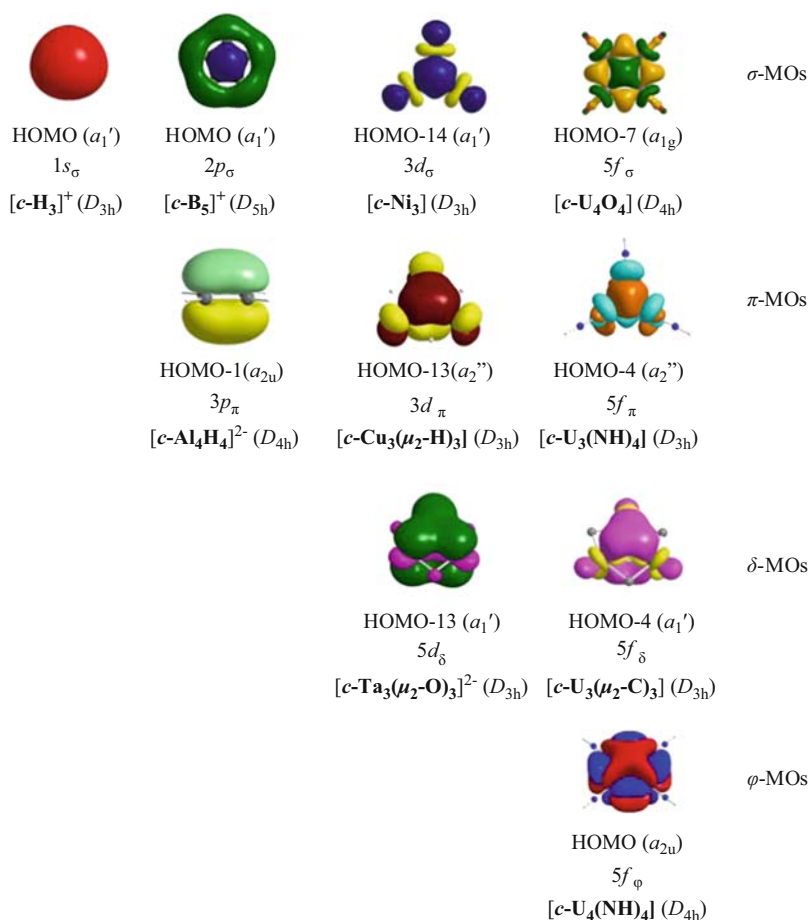


Fig. 1 Three-dimensional orbital plots of the delocalized σ -, π -, δ - and ϕ -MOs in selected $c\text{-E}_n$ and $c\text{-E}_n\text{L}_n$ clusters

constructed from the overlap of p-, d-, or f-AOs, while δ - and ϕ -aromaticity are supported by delocalized δ - and ϕ -MOs, respectively, constructed from the linear combination of d- or f-AOs and f-AOs, respectively. The 3-D orbital plots of the delocalized σ -, π -, δ -, and ϕ -MOs in selected “bare” and “ligand-stabilized” clusters are shown in Fig. 1. It is important to notice that the simple assignment of the delocalized MOs of an aromatic system does not provide a sufficient probe for the orbital type of aromaticity. One has also to check whether the delocalized MOs of any type are magnetically active participating in the translationally ($T_{x,y}$) allowed transitions leading to diatropic (diamagnetic) ring current which is associated with the aromaticity.

The topology of the electron density $\rho(\mathbf{r})$ of the aromatic systems has also been used to quantify aromaticity. An aromaticity index that takes account of the

topological properties of the electron density at ring-critical points of six-membered rings using Bader’s Atoms in Molecules (AIM) theory [63–65] has also been proposed [66]. An alternative approach, based on properties of the electron density probed by the electron localization function (ELF) [67] of Becke and Edgecombe [68], has been introduced to understand aromaticity [69–71]. A separation of the ELF in its σ - and π - components was shown to provide a useful scheme to discuss σ - and π - character in a molecular system [72].

The ELF is defined in terms of the excess of local kinetic energy density due to the Pauli exclusion principle $T(\rho(\mathbf{r}))$ and Thomas–Fermi kinetic energy density $T_h(\rho(\mathbf{r}))$

$$\text{ELF} = \left[1 + \left(\frac{T(\mathbf{r})}{T_h(\mathbf{r})} \right)^2 \right]^{-1}$$

For a monodeterminantal wave function these quantities are evaluated from the HF or the Kohn–Sham orbitals,

$$T(\rho(\mathbf{r})) = \frac{1}{2} \sum_i |\nabla \psi_i(\mathbf{r})|^2 - \frac{1}{8} \frac{|\nabla \rho(\mathbf{r})|^2}{\rho(\mathbf{r})}$$

and

$$T_h(\rho(\mathbf{r})) = \frac{3}{10} (3\pi^2)^{2/3} \rho(\mathbf{r})^{5/3}$$

$$\rho(\mathbf{r}) = \sum_i |\nabla \psi_i(\mathbf{r})|^2$$

The topological analysis of the ELF provides a picture in which the electron density is distributed and localized in different volumes called basins, thus enabling one to discuss the reliability of simplified representations of electron densities in terms of superposition of promolecular densities or resonant Lewis structures.

Furthermore, natural bond orbital (NBO) analysis of the first-order density has also been used to quantify aromaticity [73, 74]. More recently Boldyrev and Zubarev [75] developed the adaptive natural density partitioning (AdNDP) algorithm attempting to combine the ideas of Lewis theory and aromaticity. The results obtained by the application of the AdNDP algorithm to the systems with non-classical bonding can be readily interpreted from the point of view of aromaticity/antiaromaticity concepts.

Summarizing the probes of aromaticity it should be stressed that the concept of aromaticity must be analyzed in terms of a multiplicity of measures, since no single property exists whose measurement could be taken as a direct, unequivocal measure of aromaticity. This is especially true for the indicators, which are calculated from the differences of the properties of the parent and a reference system. In particular for the “all-metal” aromatic systems the use of both the magnetic and the electronic criteria of aromaticity is recommended.

3 Aromatic/Antiaromatic Three-Membered Rings of Group 1 Metal Atoms

The simplest three-membered metallic ring exhibiting aromatic character is the cationic $[c\text{-Li}_3]^+$ cluster. The $[c\text{-Li}_3]^+$ cluster adopts an equilateral triangular structure having D_{3h} symmetry as its global minimum [76]. The $[c\text{-Li}_3]^+$ cluster can be considered as a $2e\text{-}\sigma$ -aromatic prototype, since the delocalized MOs are constructed from the overlap of valence s -AOs. The σ -aromaticity/antiaromaticity of small alkali/alkaline earth clusters has recently been investigated by Alexandrova and Boldyrev [77]. The authors, based on orbital topology, simple electron count, and energetics, evaluated from a series of homodesmotic reactions at a high level of theory (B3LYP/6-311+G* and CCSD(T)/6-311+G*), concluded that $[c\text{-Li}_3]^+$ should be considered σ -aromatic. However, more recently Havenith et al. [78], based on computations of the ring current maps in the ab initio ipsocentric approach, raised a different opinion on the aromaticity of $[c\text{-Li}_3]^+$ cluster. In contrast to the marked σ -diatropic ring current showed by the $[c\text{-H}_3]^+$ cluster, the $[c\text{-Li}_3]^+$ cluster showed no global ring current and thus is nonaromatic on this magnetic criterion, despite its electron count and negative NICS values. We calculated the NICS_{zz}-scan curve for the $[c\text{-Li}_3]^+$ cluster [79], which showed all features of the NICS_{zz}-scan curves of pure σ -aromatic molecules, thus assuring its pure σ -aromaticity. Chi et al. [80] investigated the structures and aromaticities of the cationic $[c\text{-X}_3]^+$ ($X = \text{H, Li, Na, K, and Cu}$) clusters using various computational techniques and aromaticity criteria. They found that all $[c\text{-X}_3]^+$ clusters adopt the regular trigonal structure (D_{3h}) as the global minimum on the potential energy surface (PES) and are characterized by high degree of aromaticity originating only from s orbitals (σ -aromaticity).

4 Aromatic/Antiaromatic Three-Membered Rings of Group 2 Metal Atoms

The next three-membered metallic rings exhibiting aromatic/antiaromatic character are the neutral, cationic, and anionic alkaline earth metal $[c\text{-X}_3]^q$ ($X = \text{Be, Mg; } q = 0, -, 2-$ clusters [77, 81]. The anionic $[\text{Be}_n]^-$ ($n = 2, 3$) clusters have been observed experimentally [82], and their stability was explored theoretically [83]. Recently, the stability, reactivity, and aromaticity of the $[c\text{-Be}_3]^{2-}$ dianion and its bimetallic species $\text{M}[\text{Be}_3]^-$ and $\text{M}_2[\text{Be}_3]$ ($\text{M} = \text{Li, Na, Cu}$) were investigated by Roy and Chattaraj [84]. The aromaticity of these systems was analyzed in the light of the DFT-based reactivity descriptors, such as hardness (η), polarizability (α), electrophilicity (ω), molecular orbital analysis, and the NICS index. All of these molecules were found to be highly π -aromatic. Furthermore, the potency of the $[c\text{-Be}_3]^{2-}$ aromatic unit in stabilization of a direct Zn–Zn bond was investigated through the substitution reaction of cyclopentadienyl (Cp) ligands in the $[\text{CpZn}–\text{ZnCp}]$ compound by the $[c\text{-Be}_3]^{2-}$ unit affording the new sandwich-like $[(c\text{-Be}_3)\text{ZnZn}(c\text{-Be}_3)]^{2-}$ compound (Fig. 2).

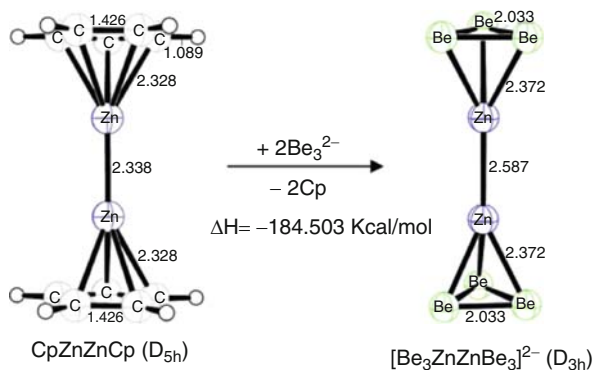


Fig. 2 Substitution reaction in $[\text{CpZnZnCp}]$ by $[\text{c-Be}_3]^{2-}$ to produce $[(\text{c-Be}_3)\text{ZnZn}(\text{c-Be}_3)]^{2-}$. Reprinted with permission from [84]. Copyright: ACS Journal Archives

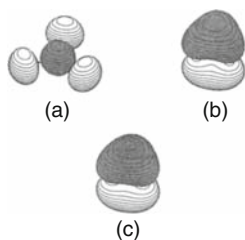


Fig. 3 Molecular orbitals plots of $[\text{c-Be}_3](^1\text{A}_1')$ and $[\text{c-Be}_3]^{-(2}\text{A}_2'')$. (a) $[\text{c-Be}_3]$ LUMO, $3a_1'$; (b) $[\text{c-Be}_3]$ LUMO + 1, $1a_2''$; (c) $[\text{c-Be}_3]^-$ SOMO, $1a_2''$. Reprinted with permission from [83]. Copyright: American Institute of Physics

Kaplan and coworkers [83] computed the electron affinities (EA) of beryllium clusters, $[\text{Be}_2]^-$ and $[\text{Be}_3]^-$, up to the CCSD(T) level using reasonable basis sets with many diffuse functions. The high values of EAs along with molecular orbital diagrams revealed that the clusters are valence bound. In the most stable $[\text{c-Be}_3]^-$ ($\text{D}_{3\text{h}}$) cluster the dominant contributions to the electron attachment energy are provided by the correlation and relaxation energies. Plots of the highest occupied molecular orbitals of the $[\text{c-Be}_3]^-$ ($\text{D}_{3\text{h}}$) anion shown in Fig. 3 disclose the dominant valence character of the change in electronic structure between neutral molecule and corresponding anion.

The lowest, virtual, canonical HF orbitals of the neutrals consist chiefly of valence s and p basis functions. Singly occupied spin orbitals that occur only in UHF calculations on the anion are composed of the same AOs. Both types of these one-electron wave functions may be considered approximations to the Dyson orbitals [85, 86] corresponding to the EAs of the beryllium clusters. In the framework of the electron propagator theory [85], the Dyson orbitals are overlaps between an N-electron reference state and final states with $N \pm 1$ electrons. They form an overcomplete set and are not necessarily normalized to unity.

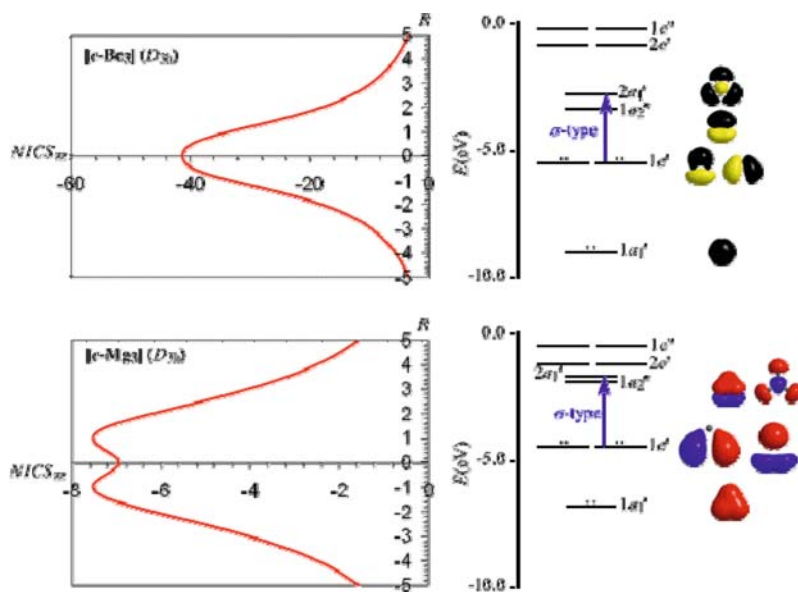


Fig. 4 NICS_{zz}-scan profiles (NICS_{zz} in ppm, R in Å) of the $[c\text{-Be}_3]$ (D_{3h}) cluster along with the molecular orbital energy level diagram, symmetries, 3-D molecular orbital pictures, and the significant translationally ($T_{x,y}$) allowed transition leading to the σ -diamagnetic ring current computed at the B3LYP/6-311+G(d,p) level

To the best of our knowledge the aromaticity/antiaromaticity of the $^1A_1'$ state of the $[c\text{-Be}_3]$ cluster has not been investigated so far. Therefore we calculated the NICS_{zz}-scan profile of the $[c\text{-Be}_3]$ cluster at the B3LYP/6-311+G(d) level (Fig. 4), which exhibits all features of the NICS_{zz}-scan curves typical of pure σ -aromatic molecules [79] and matches that of the $[c\text{-Li}_3]^+$ aromatic prototype.

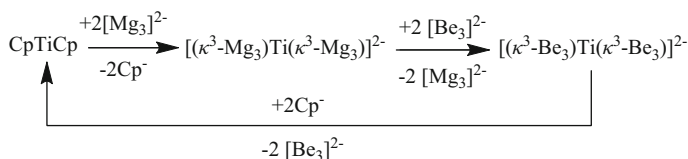
The ground-state $^1A_1'$ occupation in D_{3h} symmetry of six-valence electrons for the $[c\text{-Be}_3]$ cluster was found to be HOMO-3 (a_1'), HOMO-1,2 (e'). The most significant translationally ($T_{x,y}$) allowed transition HOMO-1,2 (e') \rightarrow LUMO+1 (a_1') with excitation energy of 2.617 eV introduces a σ -diatropic ring current.

The $[c\text{-Mg}_3]$ (D_{3h}) cluster was shown to be a weakly bound van der Waals complex with atomization energy 5.2 kcal/mol at the CCSD(T)/6-311+G(2df)//CCSD(T)/6-311+G(d) level [77, 81]. In $[c\text{-Mg}_3]$ (D_{3h}) cluster all bonding, non-bonding, and antibonding MOs constructed from the valence 3s AOs of Mg atoms are occupied, and therefore the net bonding effect should be close to zero. We calculated the interaction energy between the Mg₂ and Mg fragments and found to be only -2.98 kcal/mol at the B3LYP/6-311+G(d) level assuring the van der Waals nature of the bonding in $[c\text{-Mg}_3]$. Kuznetsov and Boldyrev [81] tested aromaticity in $[c\text{-Mg}_3]$ cluster using NICS calculations and found that it is a nonaromatic species. The calculated NICS_{zz}-scan profile of the $[c\text{-Mg}_3]$ cluster at the B3LYP/6-311+G(d) level (Fig. 4), assures that $[c\text{-Mg}_3]$ is a very

weak ($\text{NICS}_{zz}(0) = -6.9$ ppm; $\text{NICS}_{zz}^{\text{max}} = -7.5$ at 1.0 \AA) aromatic (almost a nonaromatic) molecule.

The $[\text{c-Be}_3]^{2-}$ and $[\text{c-Mg}_3]^{2-}$ clusters adopt also an equilateral triangular geometry having D_{3h} symmetry and $^1A_1'$ ground state. The occupation of eight-valence electrons was found to be HOMO-3 (a_1'), HOMO-1,2 (e'), HOMO (a_2''). Boldyrev et al. [77, 81] showed that the unusual $[\text{c-Mg}_3]^{2-}$ trigonal planar cluster exhibits an extraordinary type of aromaticity, where π -aromaticity occurs without initial formation of the σ -framework. In the $[\text{c-Be}_3]^{2-}$ and $[\text{c-Mg}_3]^{2-}$ clusters the most significant translationally ($T_{x,y}$) allowed transitions are the HOMO-1,2 (e') \rightarrow LUMO (a_1') and HOMO (a_2'') \rightarrow LUMO + 5, 6 (e''). In the first transition a σ -type (a_1') MO is involved in the excitation inducing a σ -diatropic ring current, while in the second transition a π -type (a_2'') MO is involved inducing a π -diatropic ring current. In the $[\text{c-Be}_3]^{2-}$ cluster the σ -diatropic ring current overwhelms the π -diatropic ring current because of the lower excitation energy (1.594 eV) of the first transition relative to the second one (1.668 eV). On the other hand, in the $[\text{c-Mg}_3]^{2-}$ cluster the π -diatropic ring current is much stronger than the σ -diatropic ring current, because of the much lower excitation energy (0.936 eV) of the π -type transition relative to the σ -type one (2.193 eV). It is important to notice that the estimated interaction energy between the Mg_2 and the Mg^{2-} fragments (-29.51 kcal/mol) is much smaller than the interaction energy between the Be_2 and the Be^{2-} fragments (-84.86 kcal/mol). Moreover, the Wiberg bond orders (WBO) between the fragments are 2.293 and 0.886, while the three-center bond orders are 2.293 and 0.373 for the $[\text{c-Be}_3]^{2-}$ and the $[\text{c-Mg}_3]^{2-}$ clusters, respectively, in line with the bonding scheme proposed by Boldyrev et al. [77, 81] for the $[\text{c-Mg}_3]^{2-}$ cluster.

Very recently Chattaraj and Giri [87] using various conceptual DFT based global reactivity indicators investigated the changes in the bonding, aromaticity, and reactivity behavior associated with the reaction cycle,



including all intermediate steps.

5 Aromatic/Antiaromatic Three-Membered Rings of Group 13 Metal Atoms

Another family of aromatic/antiaromatic three-membered rings of metal atoms concerns the 13 group elements (Al, Ga, In, and Tl). Kuznetsov and Boldyrev [88] reported theoretical evidence of double ($\sigma + \pi$) aromaticity in $[\text{c-X}_3]^-$ ($X = \text{B, Al, Ga}$) species. The $[\text{c-X}_3]^-$ clusters should be considered as earlier electron-deficient double aromatic systems, because their π -MOs are occupied earlier than in

the corresponding aromatic hydrocarbons. It was also found that the structural and electronic integrity of the $[c\text{-Al}_3]^-$ anion is maintained inside a $\text{Na}^+[c\text{-X}_3]^-$ salt-like molecule. The multiple aromaticity of the $[c\text{-Al}_3]^-$ cluster was recently verified by Boldyrev et al. [88, 89] through a molecular orbital analysis and by Dixon et al. [90] by estimating the resonance energy (RE) using high-level ab initio quantum chemical calculations.

The NICS_{zz}-scan curves of the $[c\text{-Al}_3]^-$, $[c\text{-Ga}_3]^-$, $[c\text{-In}_3]^-$ and $[c\text{-Tl}_3]^-$ clusters look like the mirror image of a typical scan of double ($\sigma + \pi$)-aromatic molecules. The ground-state ($^1A'_1$) occupation in D_{3h} symmetry of ten valence electrons for the $[c\text{-Al}_3]^-$, $[c\text{-Ga}_3]^-$ and $[c\text{-In}_3]^-$ clusters was found to be HOMO-4 (a'_1), HOMO-2,3 (e'), HOMO-1 (a''_2), HOMO (a'_1). In the $[c\text{-Tl}_3]^-$ cluster there is an inversion of the HOMO and HOMO-1. The most significant translationally ($T_{x,y}$) allowed transitions are the $a'_1 \rightarrow e'$ (σ -type) and $a''_2 \rightarrow e''$ (π -type). The coexistence of both the σ - and the π -type transitions accounts well for the double ($\sigma + \pi$)-aromatic character of the clusters. The extent of contribution of the two types of transitions to the induced diatropic ring current is determined by the excitation energies of the σ - and (π -type) transitions, estimated to be 1.581 (3.153), 1.500 (2.462), 1.113 (2.620), and 1.119 (2.446 eV) for the $[c\text{-Al}_3]^-$, $[c\text{-Ga}_3]^-$, $[c\text{-In}_3]^-$ and $[c\text{-Tl}_3]^-$ clusters, respectively [79].

6 Aromatic/Antiaromatic Three-Membered Rings of Group 14 Metalloid and Metal Atoms

The structural characteristics, thermodynamic properties, and bonding features of a number of binary Ge_nSi_m ($n + m = 5$) clusters including among others the GeSi_2 , Ge_2Si , and Ge_3 trimers have been investigated using the MP2//CCSD(T) and CCSD(T) computational techniques [91]. It was found that “mixed” clusters possess the same structure as corresponding “pure” moieties, with only little deformation due to the loss of symmetry and are stabilized by multicenter π bonding. The bonding properties of these species are discussed using their molecular orbital characteristics and analysis of NBO population data, but their magnetic properties related with the aromaticity/antiaromaticity are not discussed. Analogous results were reported almost simultaneously by Kuo et al. [92] on the ground-state structures, vibrational frequencies, HOMO–LUMO energy gap, electron affinities, and cluster mixing energy of binary semiconductor clusters Ge_nSi_m in the range $s = m + n \leq 7$ using the B3LYP-DFT and CCSD(T) methods with the 6–311+G(d) basis set. For the Ge_nSi_m ($m + n = 3$) binary clusters, the theoretically optimized ground states are the singlets with triangular shapes. When adding one electron to the neutral cluster, the bond angle becomes smaller and the bond length becomes longer. Both the HOMO–LUMO gaps and the calculated mixing energy show that binary clusters SiGe_2 , Si_2Ge_2 , Si_2Ge_3 , Si_2Ge_4 , and Si_2Ge_5 are species with high stability and more likely to be produced experimentally. It would be very interesting to understand the stability of the clusters in terms of the aromaticity/antiaromaticity concept.

The equilibrium geometries of the ground state of Ge_3 and its anion have been calculated at various levels of theory [93]. For the Ge_3 cluster the $^1\text{A}_1$ state with C_{2v} symmetry and the $^3\text{A}'_2$ state with D_{3h} symmetry are almost degenerate. On the other hand, the $[\text{Ge}_3]^-$ cluster adopt the $^2\text{A}_1$ state with D_{3h} symmetry as the ground state.

The electronic structure of mono-, di-, and trilitiated triatomic germanium (Ge_3Li_n) and their cations ($n = 0-3$) were investigated by Nguyen et al. [94] using a multiconfigurational quasidegenerate perturbation approach (MCQDPT2) based on complete active space CASSCF wave functions, MRMP2 and DFT. The computations revealed that Ge_3Li has a $^2\text{A}'$ ground state with a doublet-quartet gap of 24 kcal/mol, Ge_3Li_2 has a singlet ground state with a singlet-triplet ($^3\text{A}''-^1\text{A}_1$) gap of 30 kcal/mol, and Ge_3Li_3 a doublet ground state with a doublet-quartet ($^4\text{A}''-^2\text{A}'$) separation of 16 kcal/mol. The $^1\text{A}'$ ground state of the $[\text{Ge}_3\text{Li}]^+$ cation was found at 18 kcal/mol below the $^3\text{A}'$ state. The ELF and NBO analyses showed that the Ge–Li bond is predominantly ionic. The ELF isosurfaces and their cut planes of Ge_3 , $[\text{Ge}_3]^-$, and Ge_3Li are visualized in Fig. 5.

Boldyrev and coworkers [95] created the anionic mixed triatomic clusters, $[c\text{-AlGe}]^-$, $[c\text{-AlSi}_2]^-$, and $[c\text{-AlGe}_2]^-$, and studied their electronic structure and chemical bonding using photoelectron spectroscopy and ab initio calculations. Chemical bonding analysis revealed that the $[c\text{-AlSi}_2]^-$ and $[c\text{-AlGe}_2]^-$ clusters can be described as species with conflicting (σ -antiaromatic and π -aromatic) aromaticity. On the other hand, the $[c\text{-AlGe}]^-$ anion represents an interesting example of a chemical species which is between classical and aromatic. The authors have also calculated an isoelectronic $[c\text{-Si}_3]^{2+}$ cluster with D_{3h} symmetry and a $^1\text{A}_1$ ground state and assured its double aromaticity. Adding two electrons one obtains the neutral $[c\text{-Si}_3]$ cluster where a Jahn-Teller distortion occurs because only one of the doubly degenerate LUMOs is occupied. In $[c\text{-Si}_3]$ cluster four σ -electrons render its σ -antiaromaticity, which is resulting in the D_{3h} -to- C_{2v} structural distortion from the $[c\text{-Si}_3]^{2+}$ cluster.

More recently [79], we calculated the structures and magnetic response properties of the $[c\text{-Si}_3]^{2-}$ and $[c\text{-Ge}_3]^{2-}$ clusters and found that these 14 valence electron species exhibit double ($\sigma + \pi$) aromaticity, since both σ -type ($a'_1 \rightarrow e'$) and π -type ($a''_2 \rightarrow e''$) translationally ($T_{x,y}$) allowed transitions to contribute to the induced diatropic ring current. The estimated excitation energies for the σ -type (π -type) transitions of the $[c\text{-Si}_3]^{2-}$ and $[c\text{-Ge}_3]^{2-}$ clusters are 3.407 (3.608 eV) and 2.576 (3.029 eV), respectively.

7 Aromatic/Antiaromatic Three-Membered Rings of group 15 Metalloid and Metal Atoms

The molecular structures, electron affinities, and dissociation energies of the $[\text{As}_n]/[\text{As}_n]^-$ ($n = 1-5$) species have been examined using carefully selected DFT methods in conjunction with the DZP++ basis set [96]. Three different types of

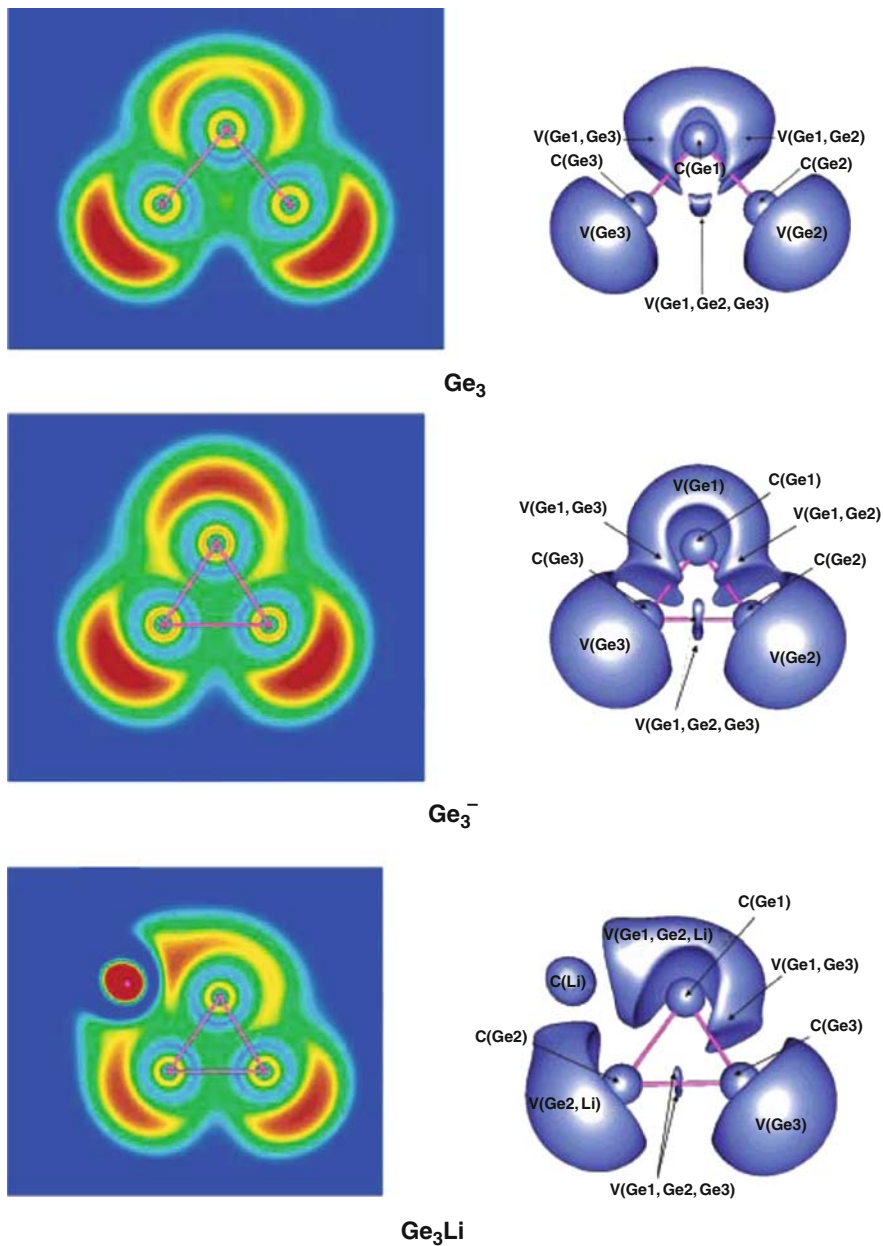


Fig. 5 Cut planes and ELF isosurfaces of Ge₃, [Ge₃]⁻ and Ge₃Li ($\eta = 0.6$). Reprinted with permission from [94]. *Copyright*: ACS Journal Archives

the neutral-anion energy separations were reported: the adiabatic electron affinity (EA_{ad}), the vertical electron affinity (EA_{vert}), and the vertical detachment energy. For the neutral As_3 cluster the 2A_2 state with C_{2v} symmetry is the global minimum. It is an isosceles (nearly equilateral) triangle. Its theoretical apex bond angle ranges from 64.9 to 65.4° , and the bond length for the two equal sides is in the range from 2.30 to 2.36 \AA . The isosceles triangular geometry of C_{2v} symmetry with apex angle $\alpha = 65.18^\circ$ and side length $r = 2.359 \text{ \AA}$ was found to be the ground-state structure of As_3 [97]. The energy of the isosceles triangle (C_{2v}) is lower than the equilateral triangle (D_{3h}) by 0.09 eV .

The negative ion photoelectron spectra of As^- , $[As_2]^-$, $[As_3]^-$, $[As_4]^-$ and $[As_5]^-$ have been also measured and calculations predicted that the ground state of As_3 has a D_{3h} equilateral triangle structure [98]. Density functional theory was used to study the electronic, geometric, and bonding properties of small Ga_n , As_m , and Ga_nAs_m clusters of up to eight atoms [99]. The As_3 and $GaAs_2$ trimers are predicted to have an isosceles triangular geometry.

Photoelectron spectroscopy has been performed on $[Sb_n]^-$ and $[Bi_n]^-$ cluster anions with photon energies of 4.03 eV and in some cases 5.0 eV [100]. For the small clusters, density functional theory calculations of the detachment energies are presented. The geometric structures of the small anionic antimony and bismuth clusters are similar, and similar to those of other group 15 elements. For the neutral and anionic trimers nonlinear geometries, in particular Jahn–Teller-distorted triangles were obtained.

More recently, the structural and electronic properties of Bi_n ($n = 2\text{--}14$) clusters have been systematically studied using gradient-corrected density-functional theory [101]. The lowest-energy structure found for the Bi_3 trimer is an isosceles triangle (C_{2v}) symmetry, with apex angle of 64.051° and side length of 2.915 \AA . The isosceles triangle is energetically lower than the equilateral triangle structure (D_{3h}) symmetry, side length 2.966 \AA , by 0.06 eV due to the Jahn–Teller effect. In the case of the $[Bi_3]^-$ trimer an equilateral triangle (D_{3h} symmetry) was found as the lowest-energy structure [101].

However, as far as we know, the bonding mechanism in relation with the aromaticity/antiaromaticity of the three-membered rings of group 15 metalloid and metal atoms has not been investigated up to now. Very recently [79] we reported on the electronic structure and aromaticity/antiaromaticity of the cationic Pnictogen $[c-Pn_3]^+$ ($Pn = N, P, As, Sb, \text{ and } Bi$) clusters. The $[c-Pn_3]^+$ clusters are 14 valence electron species, which adopt a triangular structure with D_{3h} symmetry. The ground-state (${}^1A'_1$) occupation in D_{3h} symmetry for the $[c-As_3]^+$, $[c-Sb_3]^+$, and $[c-Bi_3]^+$ clusters is HOMO-6 (a'_1), HOMO-4,5 (e'), HOMO-3 (a'_1), HOMO-2 (a''_2), HOMO,-1 (e'). For the cationic $[c-As_3]^+$, $[c-Sb_3]^+$, and $[c-Bi_3]^+$ clusters the most significant translationally allowed ($T_{x,y}$) transitions are the $a'_1 \rightarrow e'$ (σ -type) with excitation energies of 8.288 , 6.557 , and 6.272 eV , respectively, and the $a''_2 \rightarrow e''$ (π -type) with excitation energies of 4.627 , 3.748 , and 3.225 eV , respectively. According to the estimated excitation energies it was concluded that the $[c-As_3]^+$, $[c-Sb_3]^+$, and $[c-Bi_3]^+$ clusters are doubly ($\sigma + \pi$)-aromatic molecules with higher π - than σ -aromatic character.

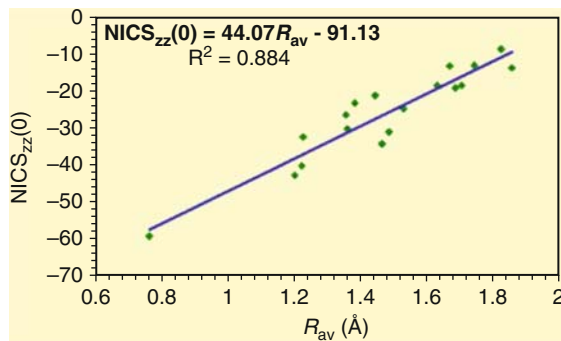


Fig. 6 Linear relationship between $\text{NICS}_{zz}(0)$ (in ppm) and R_{av} (in Å) for triangular (D_{3h}) main group double ($\sigma + \pi$)-aromatic clusters [79]

It is interesting to notice that for all three-membered rings of main group metalloid and metal atoms exhibiting double ($\sigma + \pi$) aromaticity there is an excellent linear correlation of the $\text{NICS}_{zz}(0)$ values with the R_{av} values of the rings (Fig. 6) [79].

8 Aromatic/Antiaromatic Three-Membered Rings of Transition Metal Atoms

The most comprehensive theoretical insight into the problem of aromaticity of cyclic transition metal systems was discussed in detail in a very recent review article published in *Phys Chem Chem Phys* by Boldyrev and coworkers [17]. In this article the multifold nature of aromaticity, antiaromaticity, and even conflicting aromaticity (σ -, π - and δ -aromaticity) has been analyzed in terms of the chemical bonding and electron counting rules. Therefore, we will discuss and comment herein on the latest developments in the field of stable aromatic three-membered rings of transition metal atoms.

In a three-membered ring of transition metal atoms, besides the ns AOs of the transition metal atoms, the $(n-1)d$ AOs can also participate in the chemical bonding of the rings forming delocalized σ -, π -, and δ -MOs. The 3-D plots of such MOs formed, for example, in the $[c\text{-Pt}_3]$ cluster are shown in Fig. 7.

Generally in transition metal trimers, the presence of open d shells and near degeneracies in $d^{n-2}s^2$ and $d^{n-1}s^1$ atomic states makes it likely that many molecular electronic states may also be close in energy and s - d orbital mixing may be important. Thus early transition metal trimers exhibit extensive d - d bonding interactions, while such interactions will be less dominant in late transition metal trimers, since the d orbitals in late transition metals are considerably smaller than in early transition metals.

Very recently Chi and Liu [102] calculated the equilibrium geometries for singlet, triplet, and quintet states of three all-metal $[c\text{-X}_3]^-$ ($X = \text{Sc}, \text{Y}, \text{and La}$) anions

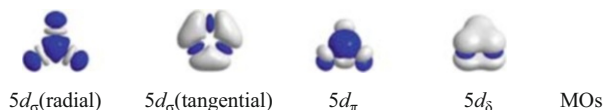


Fig. 7 Three-dimensional plots of the σ -, π -, and δ -MOs constructed from the overlap of 5d AOs of Pt atoms in the three-membered $[c\text{-Pt}_3]$ ring (D_{3h})

and nine relevant neutral singlet $M[c\text{-X}_3]$ ($M = \text{Li, Na, K; X} = \text{Sc, Y, and La}$) clusters using DFT (B3LYP, B3PW91) and ab initio methods (MP2, CCSD(T)). From a detailed molecular orbital analysis and the estimated REs and NICS values the authors provided an explicit theoretical evidence for the double ($\sigma + \pi$)-aromatic character of the singlet $[c\text{-X}_3]^-$ ($X = \text{Sc, Y, and La}$) clusters in D_{3h} symmetry originated primarily from the d–AO bonding interactions.

Moving across the transition metal series Averkiev and Boldyrev [103] predicted that the 12 valence electron $[c\text{-Hf}_3]$ (D_{3h}) cluster is triply (σ -, π -, and δ -) aromatic in the lowest $^1A'_1$ state. A similar aromaticity pattern ($\sigma + \pi + \delta$) was predicted by Wang et al. [104] for the 16 valence electron $[c\text{-Ta}_3]^-$ (D_{3h}) cluster in the quintet $^5A'_1$ ground state through a detailed molecular orbital analysis of its highly symmetric structure. However, it is dangerous to infer aromaticity of a molecular species based solely on the molecular orbital pattern and high symmetry of a species in particular for open-shell systems with high multiplicity. Moreover, the induced ring current (either diatropic or paratropic) by any occupied MO (bonding, nonbonding, or antibonding) cannot be related with its occupation, and the induced ring current by an antibonding MO by no means outweighs that induced by its bonding counterpart. It should be stressed that although the occupation of any bonding–antibonding MO pair leads to an almost zero bond order, the magnetic response of the occupied antibonding and bonding counterparts is not equal in magnitude and of opposite sign.

Recently Zhai et al. [105] using photoelectron spectroscopy and DFT calculations showed that $[c\text{-Ta}_3(\mu_2\text{-O})_3]^-$ cluster adopts a perfect planar triangular structure (D_{3h} symmetry) in its $^1A'_1$ ground state. From a detailed analysis of the MOs of $[c\text{-Ta}_3(\mu_2\text{-O})_3]^-$ cluster and electron counting rules the authors concluded that $[c\text{-Ta}_3(\mu_2\text{-O})_3]^-$ possesses two new types of d-bonding interactions that lead to π - and δ -aromaticity. The doubly ($\pi + \delta$)-aromatic molecule was found to serve as robust inorganic ligand yielding half-sandwich-type $C_{3v}[c\text{-Ta}_3(\mu_2\text{-O})_3]A$ ($A = \text{Li, Na, K}$) and full-sandwich-type $D_{3h}[c\text{-Ta}_3(\mu_2\text{-O})_3]B[c\text{-Ta}_3(\mu_2\text{-O})_3]$ ($B = \text{Ca, Sr, Ba}$) complexes [106]. These novel complexes shown in Fig. 8 are maintained by ionic interactions between the $[c\text{-Ta}_3(\mu_2\text{-O})_3]^-$ anion and the A^+ or B^{2+} cations.

Earlier Huang et al. [107] using photoelectron spectroscopy and DFT calculations observed d-orbital aromaticity in 4d and 5d transition metal-oxide clusters, $[M_3O_9]^-$ and $[M_3O_9]^{2-}$ ($M = \text{Mo, W}$). Molecular orbital analysis of the highly symmetric (D_{3h}) $[M_3O_9]^-$ and $[M_3O_9]^{2-}$ clusters along with the estimated negative NICS values showed that these clusters are unique in that they involve a single, fully delocalized meta–metal bond (Fig. 9) associated with σ -aromaticity due to the radial (inward) overlap of 4d and 5d AOs of the metal centers.

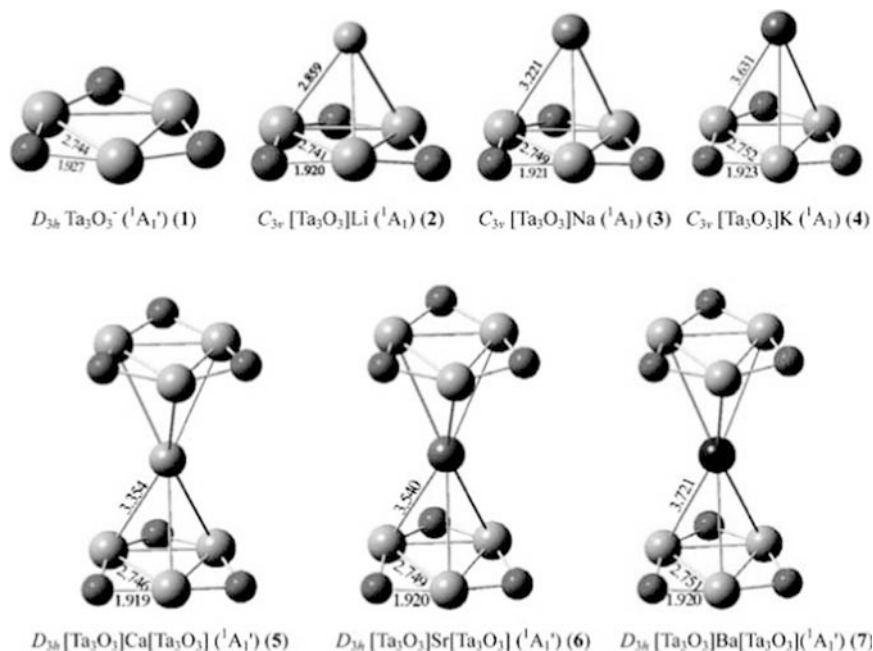


Fig. 8 Optimized structures of $C_{3v}[c-Ta_3(\mu_2-O)_3]A$ ($A=Li, Na, K$) and $D_{3h}[c-Ta_3(\mu_2-O)_3]B[c-Ta_3(\mu_2-O)_3]$ ($B=Ca, Sr, Ba$) compared with free $D_{3h}[c-Ta_3(\mu_2-O)_3]^-$ at the DFT-B3LYP level with necessary bond lengths indicated in Å. Reprinted with permission from [106]. Copyright: Wiley-VCH

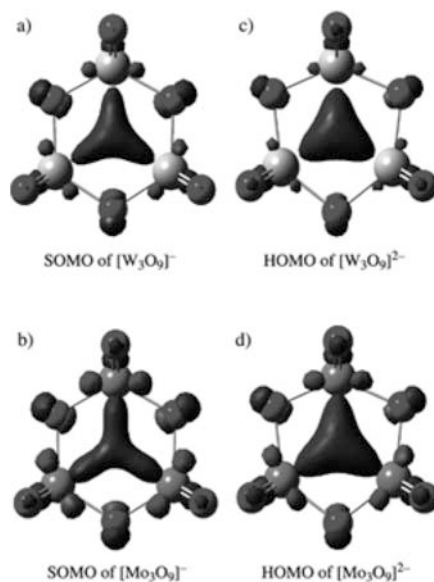


Fig. 9 The singly occupied molecular orbital (SOMO) for (a) $[W_3O_9]^-$ and (b) $[Mo_3O_9]^-$ clusters and the highest occupied molecular orbital (HOMO) of (c) $[W_3O_9]^{2-}$ and (d) $[Mo_3O_9]^{2-}$ clusters. Reprinted with permission from [107]. Copyright: Wiley-VCH

A number of transition metal trimers, including *c*-Sc₃ [108–110], *c*-Y₃ [108–110], *c*-Cr₃ [111, 112], *c*-Mn₃ [113], *c*-Fe₃ [114], *c*-Ni₃ [114–117], *c*-Pd₃ [117, 118], and *c*-Pt₃ [117, 119–121], have been examined using several experimental techniques and theoretical methods. *c*-Sc₃ and *c*-Y₃ have been isolated in rare gas matrices at temperatures near 4 K. ESR spectra established that the structure of *c*-Sc₃ is an equilateral triangle with a ²A₁' ground state. The unpaired electron has little s character and is delocalized in 3d orbitals of the three equivalent Sc atoms. On the other hand, Y₃ is not equilateral and is most probably a bent molecule with the spin again distributed over the 4d orbitals of Y atoms, but in ²B₂ ground state. La₃ was not observed and is therefore judged to be a linear orbitally degenerate molecule [108]. CASSCF/CI calculations on the low-lying states of *c*-Sc₃ and [*c*-Sc₃]⁺ showed that the good 3d bonding orbitals are of a₂' symmetry derived from 3d_π AOs and of a₁' symmetry derived from 3d_σ AOs. Moreover, the 3d_π AOs form also the e' MOs which are bonding between pairs of Sc atoms, while the 3d_δ AOs remain nonbonding [110].

c-Cr₃ immobilized in Ar and Xe matrices at different metal concentrations and thermal conditions can occur in a range of molecular geometries ranging from equilateral triangular to that of almost linear, thus having a rather shallow potential energy surface [112]. The resonance Raman and visible absorbance spectra of matrix isolated Mn₃ indicated that its structure belongs to a zero-order D_{3h} geometry subject to Jahn-Teller distortions [113]. Gutsev and Bauschlicher Jr [122] investigated the electronic and geometrical structures of the ground and excited states of Fe_n, [Fe_n]⁻ and [Fe_n]⁺ clusters using several different functionals in DFT calculations. It appeared that LSDA and B3LYP methods do not work well for iron clusters and should be avoided. The use of the Becke or the Perdew-Burke-Ernzerhof exchange functionals yielded essentially the same results as comparison of the BPBE or PBEPBE results showed. The BPW91, BPBE, and PBEPBE approaches provide nearly the same values for the bond lengths, the vibrational frequencies, and the electron affinities. Figure 10 shows the geometries and Mulliken open-shell occupation of the Fe₃, [Fe₃]⁻, and [Fe₃]⁺ clusters obtained at the BPW91 level. The atomic charges in neutral clusters are nearly zero and not shown in Fig. 10.

SCF/CCI calculations on four states of near equilateral triangle geometries of *c*-Ni₃ have been performed by Walch [115]. These states arise from three nickel atoms in the 4s¹3d⁹ state. The four states arise from two sets of 3d occupations. The first has all three 3d holes in δ'', while the second has two of the 3d holes in δ'' and the third in π'', where the sigma direction is taken along a line connecting a given atom with the center of the molecule (for D_{3h} symmetry). The first 3d shell occupation has ⁴A₂'' symmetry for equilateral triangle geometries. The trimer anions [*c*-Ni₃]⁻, [*c*-Pd₃]⁻, and [*c*-Pt₃]⁻ were prepared in a flowing afterglow ion source with a cold cathode dc discharge [117]. The bonding scheme in the anionic trimers is very similar to that of the neutrals, e.g., (d_A)⁹(d_B)⁹(d_C)⁹(sa₁')²(se')² for the equilateral triangle geometries.

To the best of our knowledge, the aromaticity/antiaromaticity of the aforementioned “bare” three-member rings of transition metal atoms has not been studied so far. However, the aromaticity/antiaromaticity of ligand-stabilized three-membered

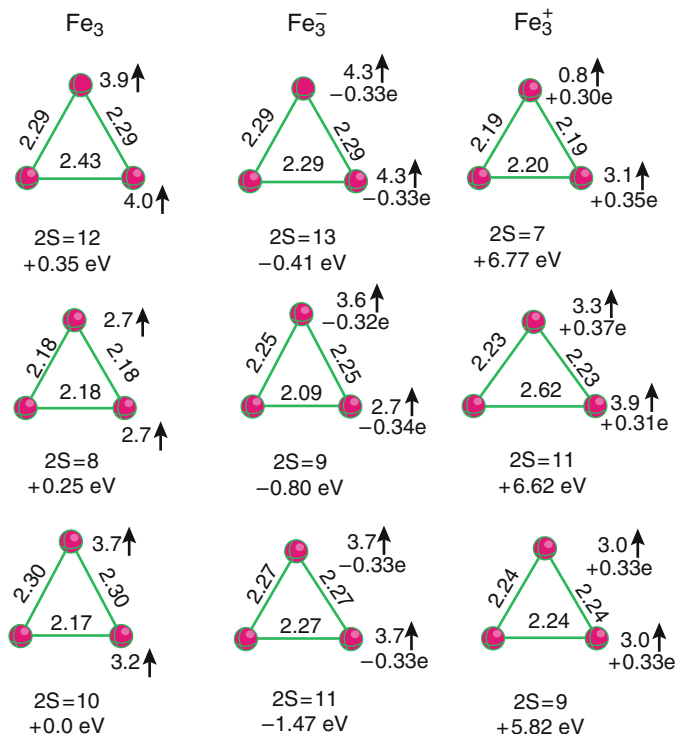


Fig. 10 Bond lengths and Mulliken atomic charges and open-shell occupation per atom obtained for Fe_3 , $[\text{Fe}_3]^-$ and $[\text{Fe}_3]^+$ clusters obtained at the BPW91 level. Reprinted with permission from [122]. Copyright: ACS Journal Archives

rings of transition metal atoms, namely the metal carbonyl triangles, such as $\text{M}_3(\text{CO})_{12}$ ($\text{M} = \text{Fe}, \text{Ru}, \text{Os}$) and $\text{Pt}_3(\text{CO})_3(\mu\text{-CO})_3$ clusters, has been investigated on the basis of structural, electronic, and magnetic criteria [123, 124]. Besides the simple edge-localized two-center two-electron ($2c\text{-}2e$) bonding model describing the bonding in M_3 triangles of the $\text{M}_3(\text{CO})_{12}$ ($\text{M} = \text{Fe}, \text{Ru}, \text{Os}$) clusters, King [123] developed an alternative model based on the concept of σ -aromaticity. Applying this to the triangular metal carbonyl partition the six orbitals and six electrons available for bonding within the M_3 triangle into a core $3c\text{-}2e$ bond of Hückel topology formed by radial hybrid orbitals and a surface $3c\text{-}4e$ bond of Möbius topology formed by tangential p-orbitals (Fig. 11).

More recently Corminboeuf et al. [124] based on structural and NICS analysis provided striking insights into the magnetic criteria for aromaticity in the group 8 metal carbonyl $[\text{M}_3(\text{CO})_{12}]$ ($\text{M} = \text{Fe}, \text{Ru}, \text{Os}$) clusters. Typically $[\text{Fe}_3(\text{CO})_{12}]$ (C_{2v}) exhibits the same type of diatropic behavior as D_{3h} cyclopropane arising from one $3c\text{-}2e$ radial Hückel orbital and the $3c\text{-}4e$ peripheral Möbius orbitals. The radial orbitals remain also diatropic in both $[\text{Ru}_3(\text{CO})_{12}]$ (D_{3h}) and $[\text{Os}_3(\text{CO})_{12}]$ (D_{3h}),

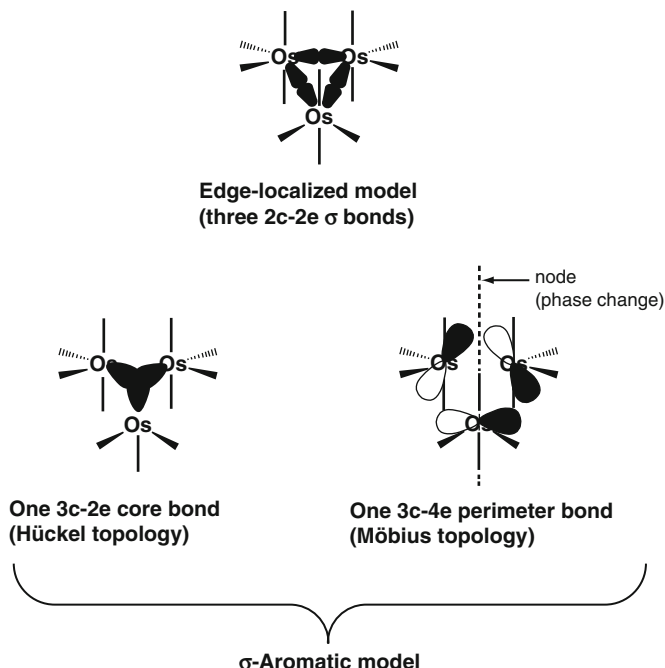


Fig. 11 The edge-localized bonding model for $\text{Os}_3(\text{CO})_{12}$ showing the three 2c–2e bonds along with the σ -aromatic model showing the 3c–2e core bond with Hückel topology and the 3c–4e perimeter bond with Möbius topology. Reprinted with permission from [123]. *Copyright*: Elsevier

while the degenerate set of peripheral MOs contribute positively to the NICS of $[\text{Os}_3(\text{CO})_{12}]$ cluster (Fig. 12).

Very recently [125] we investigated the molecular and electronic structures, stabilities, bonding features, and spectroscopic properties of prototypical ligand stabilized $[\text{cyclo-Ru}_3(\mu_2\text{-X})_3]^{0,3+}$ ($\text{X} = \text{H}, \text{BH}, \text{CH}_2, \text{NH}_2, \text{OH}, \text{Cl}, \text{NH}, \text{CO}, \text{O}, \text{PH}_2, \text{CF}_2, \text{CCl}_2, \text{CNH}, \text{N}_3$) clusters using electronic structure calculation methods at the DFT level of theory. It was found that all $[\text{cyclo-Ru}_3(\mu_2\text{-X})_3]^{0,3+}$ species, except $[\text{cyclo-Ru}_3(\mu_2\text{-H})_3]^{3+}$, exhibit aromatic character verified by the NICS(0), NICS(1), NICS(–1), NICS_{zz}(0), NICS_{zz}(1), NICS_{zz}(–1) negative values and the NICS scan profiles of the clusters. In contrast, the $[\text{cyclo-Ru}_3(\mu_2\text{-H})_3]^{3+}$ cluster exhibits high antiaromatic character (NICS(0) = 1032.8 ppm, NICS(1) = 299.8 ppm), which would be responsible for the well-established peculiar reaction field of the hydrido-bridged triruthenium core structure. The equilibrium geometries of the $[\text{cyclo-Ru}_3(\mu_2\text{-X})_3]^{0,3+}$ clusters computed at the B3P86/lan12dz(Ru)U6-31++G**(E)(E = nonmetal element) are shown in Fig. 13.

The $[\text{cyclo-Ru}_3(\mu_2\text{-X})_3]^{0,3+}$ clusters are predicted to be triply ($\sigma + \pi + \delta$) aromatic, since all types (σ -, π -, δ -) MOs participate in the most significant translationally allowed transitions inducing a diatropic ring current shown in Fig. 14.

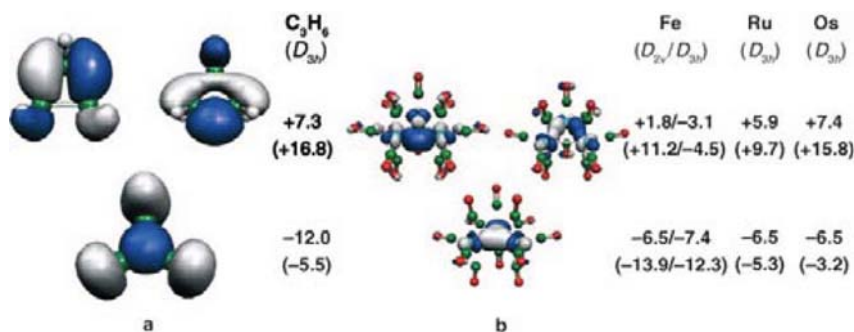


Fig. 12 Isotropic NICS ($NICS_{zz}$ given in parentheses) contributions at the ring center for the 3c–2e radial orbitals with Hückel topology and the 3c–4e peripheral orbitals with Möbius topology in a) cyclopropane and b) C_{2v}/D_{3h} [Fe₃(CO)₁₂], D_{3h} [Ru₃(CO)₁₂], and D_{3h} [Os₃(CO)₁₂]. Values are in ppm and the NICS contributions are summed for the set of degenerate MOs. Reprinted with permission from [124]. Copyright: Wiley-VCH

The NICS scan pictures shown in Fig. 15 indicated a dramatic change of aromaticity/antiaromaticity on the two sides of the Ru₃ ring, which can be explained on the grounds of the different coordination environment above and below the ring. In all [*cyclo*-Ru₃(μ_2 -X)₃]^{0,3+} clusters the bridging X ligands form an X₃ triangle parallel to the Ru₃ triangle at distances ranging from 0.748 up to 1.655 Å.

The versatile chemical reactivity of the antiaromatic [*cyclo*-Ru₃(μ_2 -H)₃]³⁺ cluster related with the activation of small molecules that leads to the breaking of various strong single and double bonds and the formation of face-capping moieties coordinated to the Ru₃ ring in μ_3 -fashion formulated as [*cyclo*-Ru₃(μ_2 -H)₃(μ_3 -Nuc)₃]^{0,1,2+} (Nuc = BH, BCN, BOMe, C⁴⁻, CH³⁻, CMe³⁻, N₃⁻, NCO⁻, OCN⁻, NCS⁻, O²⁻, S²⁻, OH⁻, P³⁻, POH²⁻, Cl⁻, O₂²⁻, NCH, AlMe, GaMe, C₆H₆, and *cyclo*-C₃H₂Me) has been explored by electronic structure computational methods. Generally, in the [*cyclo*-Ru₃(μ_2 -H)₃(μ_3 -Nuc)₃]^q clusters, the nucleophile Nuc is coordinated to the Ru₃ ring in a μ_3 -Nuc coordination mode, capping the face of the ring from the most antiaromatic side, which is the side opposite to that of the bridging hydride ligands.

Noble metal clusters, with valence electron configuration $(n-1)d^{10}ns^1$, differ from the simple s-orbital alkali metals [126, 127], but also present striking differences among Cu, Ag, and Au [128, 129]. Structural differences among [Au_n]^{0,±1} and [Ag_n]^{0,±1} or [Cu_n]^{0,±1} have been well established. Thus using nonrelativistic pseudopotentials, both the GGA and the LDA predict the onset of 3-D cluster structures already at $n = 6$ for Cu_n and Ag_n and at $n = 7$ for Au_n [130]. This result changes by considering scalar-relativistic pseudopotentials within the GGA, resulting in planar Au_n structures up to $n = 11$.

The recent computational studies of the dipole polarizabilities and optical absorption spectra of Ag_n ($n = 1-8$) and Au_n ($n = 1-3$) using the static and time-dependent versions of DFT were overviewed by Jellinek and coworkers [131]. The noble metal clusters are of special interest because the electronic properties are

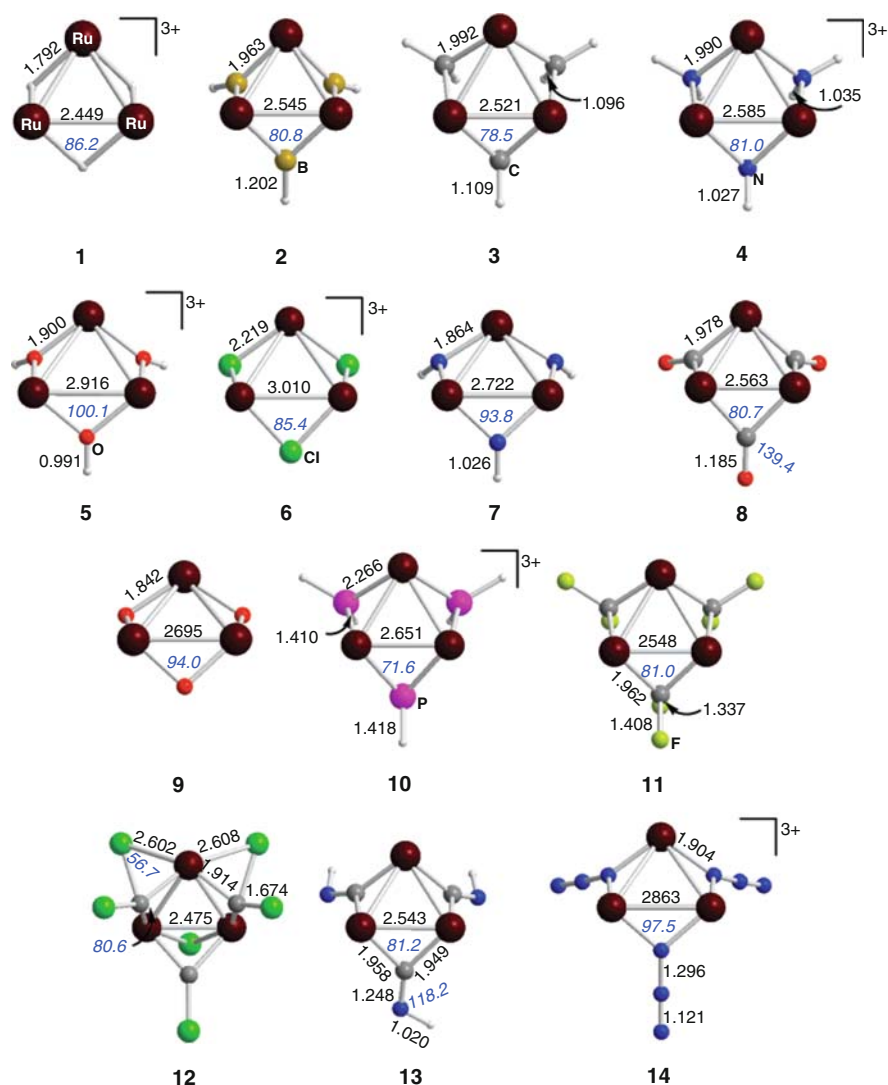


Fig. 13 Equilibrium geometries (bond lengths in Å, angles in degrees) of $[cyclo-Ru_3(\mu_2-X)_3]^{0.3+}$ ($X = H, BH, CH_2, NH_2, OH, Cl, NH, CO, O, PH_2, CF_2, CCl_2, CNH, N_3$) clusters computed at the B3P86/lanl2dz(Ru)U6-31++G**(E) (E=nonmetal element). Reprinted with permission from [125]. Copyright: ACS Journal Archives

influenced by the nearby d shell. Very recently $[Ag_3]^+$ clusters were efficiently trapped in argon matrix, and their absorption spectrum was recorded for the first time [132]. The spectroscopic pattern calculated for the D_{3h} structure of the cationic trimer [133] is characterized by three dominant transitions to $1^1E'$, $2^1A_2''$, and $6^1E'$ states located at ~ 4 , ~ 6 , and ~ 7 eV, respectively. The analysis of the leading

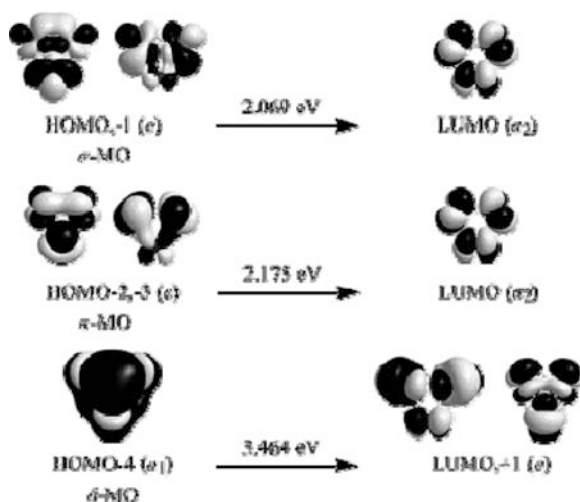


Fig. 14 The most significant translationally allowed transitions inducing a diatropic ring current in the $[\text{cyclo-Ru}_3(\mu_2\text{-X})_3]^{0.3+}$ ($X = \text{BH}, \text{CH}_2, \text{NH}_2, \text{OH}, \text{Cl}, \text{NH}, \text{CO}, \text{O}, \text{PH}_2, \text{CF}_2, \text{CCl}_2, \text{CNH}, \text{N}_3$) clusters. Reprinted with permission from [125]. *Copyright: ACS Journal Archives*

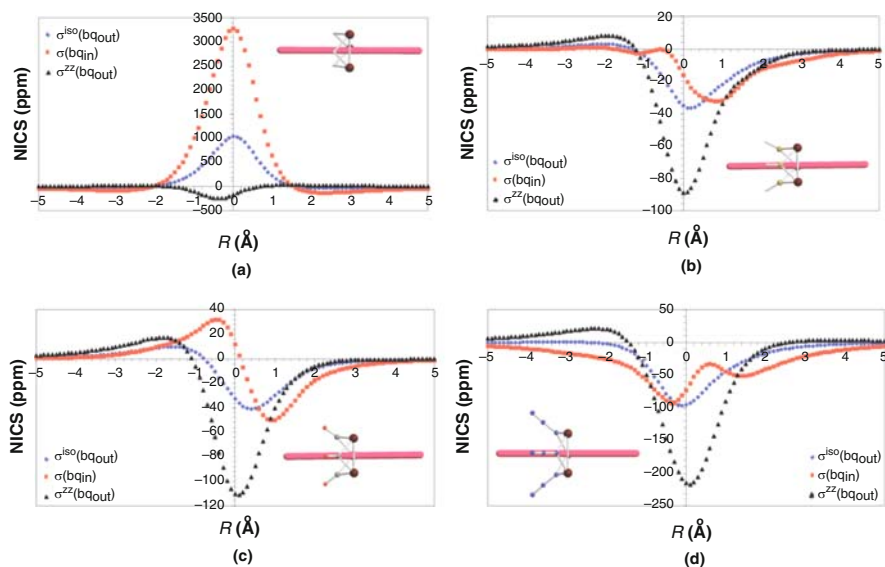


Fig. 15 NICS scan pictures for (a) $[\text{cyclo-Ru}_3(\mu_2\text{-H})_3]^{3+}$, (b) $[\text{cyclo-Ru}_3(\mu_2\text{-BH})_3]$, (c) $[\text{cyclo-Ru}_3(\mu_2\text{-CO})_3]$, and (d) $[\text{cyclo-Ru}_3(\mu_2\text{-N}_3)_3]^{3+}$ clusters. Reprinted with permission from [125]. *Copyright: ACS Journal Archives*

excitations responsible for the intense transition to the $1^1E'$ state at 4.1 eV indicates a dominant contribution from the HOMO (a'_1) to LUMO (e') as well as a considerably smaller but not negligible contribution from HOMO-1 (a'_2) to LUMO. In the HOMO, s-character prevails, while p-contributions act as polarization functions, but the HOMO-1 assumes d-character. Direct involvement of d-electrons in the leading excitations giving rise to the lowest energy intense transition of $[Ag_3]^+$ close to ~ 4 eV indicates that in this case the role of d-electrons seems to be important for all intense transitions.

Yong et al. [80] using electronic structure calculation methods (B3LYP, B3PW91, MP2, and CCSD(T)) investigated among others the structure and aromaticity of the $[c-Cu_3]^+$ cluster. They found that only the regular trigonal structure of D_{3h} symmetry is stable and according to the general criteria for aromaticity, including RE and NICS, $[c-Cu_3]^+(D_{3h})$ possesses high σ -aromatic character.

The aromaticity/antiaromaticity of an interesting class of three-membered rings of coinage metal atoms formulated as *cyclo*- $M_3(\mu-H)_3$ ($M = Cu, Ag, Au$) has been investigated by making use of several criteria for aromaticity, such as structural, energetic, magnetic, and chemical criteria [134–136]. In particular, the NICS parameter, the relative hardness $\Delta\eta$ and the electrophilicity index ω , and the chemical reactivity toward electrophiles are indicative for the aromaticity of the coinage metal clusters. These novel classes of inorganic compounds can be considered as the archetypes for the development of whole classes of new inorganic aromatic molecules (substituted derivatives) resulting upon substitution of the H atoms by other groups, such as alkyls (R) and aryls (Ar), halides (X), amido (NR_2), hydroxide (OH), and alkoxides (OR), etc. Our choice of the cyclic coinage metal hydrides (hydrocopper(I), hydrosilver(I), and hydrogold(I)) analogs of aromatic hydrocarbons was based on the well-known strong tendency of coinage metals to cluster together in a variety of organocopper(I) [see references given in [134]], organosilver(I) [see references given in [135, 136]] and organogold(I) [see references given in [136]] compounds with the general formula M_nL_n ($M = Cu, Ag, \text{ or } Au; L = \text{ a variety of bridging ligands}$).

All metallacycle three-membered rings of coinage metal atoms adopting a perfect planar geometry, with all M–M bonds equivalent (Fig. 16), exhibit a composite bonding mode involving σ , π , and δ components. Noteworthy is the presence of highly delocalized σ -, π -, and δ -MOs, for example, HOMO-8 (δ -MO), HOMO-13 (π -MO), and HOMO-15 (σ -MO) in *cyclo*- $Cu_3(\mu-H)_3$ and HOMO-2 (δ -MO), HOMO-13 (π -MO), and HOMO-14 (σ -MO) in *cyclo*- $Ag_3(\mu-H)_3$ and *cyclo*- Au_3H_3 (Fig. 17).

The delocalized σ -, π -, and δ -MOs in the rings of the coinage metal atoms account well for the observed equivalence of the M–M bonds. The most significant translationally allowed transitions contributing to the induced diatropic ring current in *cyclo*- $Cu_3(\mu-H)_3$ (D_{3h}), *cyclo*- $Ag_3(\mu-H)_3$ (D_{3h}), and *cyclo*- Au_3H_3 (C_{3h}) are the $e' \rightarrow a'_1$ (excitation energy: 5.578 eV), $a'_1 \rightarrow e'$ (excitation energy: 6.377 eV) and $e' \rightarrow a'$ (excitation energy: 4.496 eV), respectively. In all these transitions a δ -type MO is involved, thus giving rise to δ -aromaticity in the *cyclo*- M_3H_3 ($M = Cu, Ag, Au$) clusters.

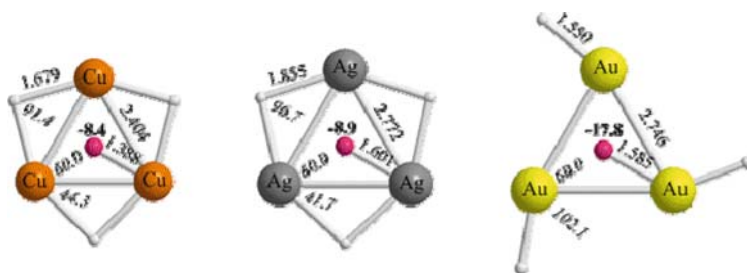


Fig. 16 Selected geometric parameters for the $cyclo-M_3(\mu-H)_3$ ($M = Cu, Ag, Au$) clusters computed at the B3LYP level using 6-311+G(d,p) basis set for Cu and H, the LANL2DZ basis set for Ag, the LANL2DZ basis set plus one f polarization function ($\alpha_f = 0.75$) for Au atoms, and the cc-pVQZ basis set for H atoms [134, 135]

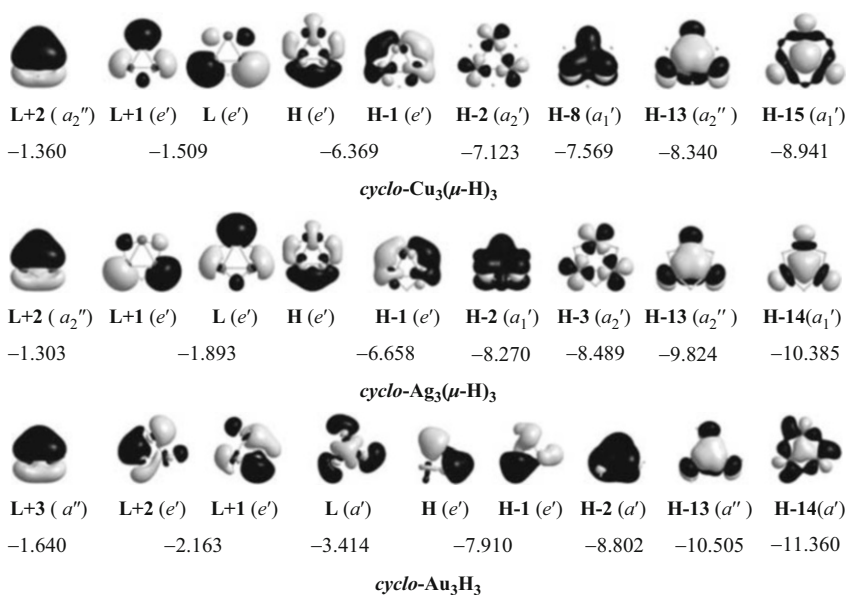


Fig. 17 The most relevant valence molecular orbitals of the $cyclo-M_3H_3$ ($M = Cu, Ag, Au$) (eigenvalues in eV) [134, 135]

Electronic structure calculations (DFT) indicated that ligand-stabilized three-membered gold(I) rings constituting the core structure in a series of $cyclo-Au_3L_nH_{3-n}$ ($L = CH_3, NH_2, OH$ and Cl ; $n = 1, 2, 3$) molecules (Fig. 18) exhibit remarkable aromaticity, which is primarily due to 6s and 5d cyclic electron delocalization over the triangular Au_3 framework (s- and d-orbital aromaticity) [136].

The aromaticity of the novel triangular gold(I) isocycles was verified by a number of established criteria of aromaticity, such as the NICS(0) parameter, the upfield

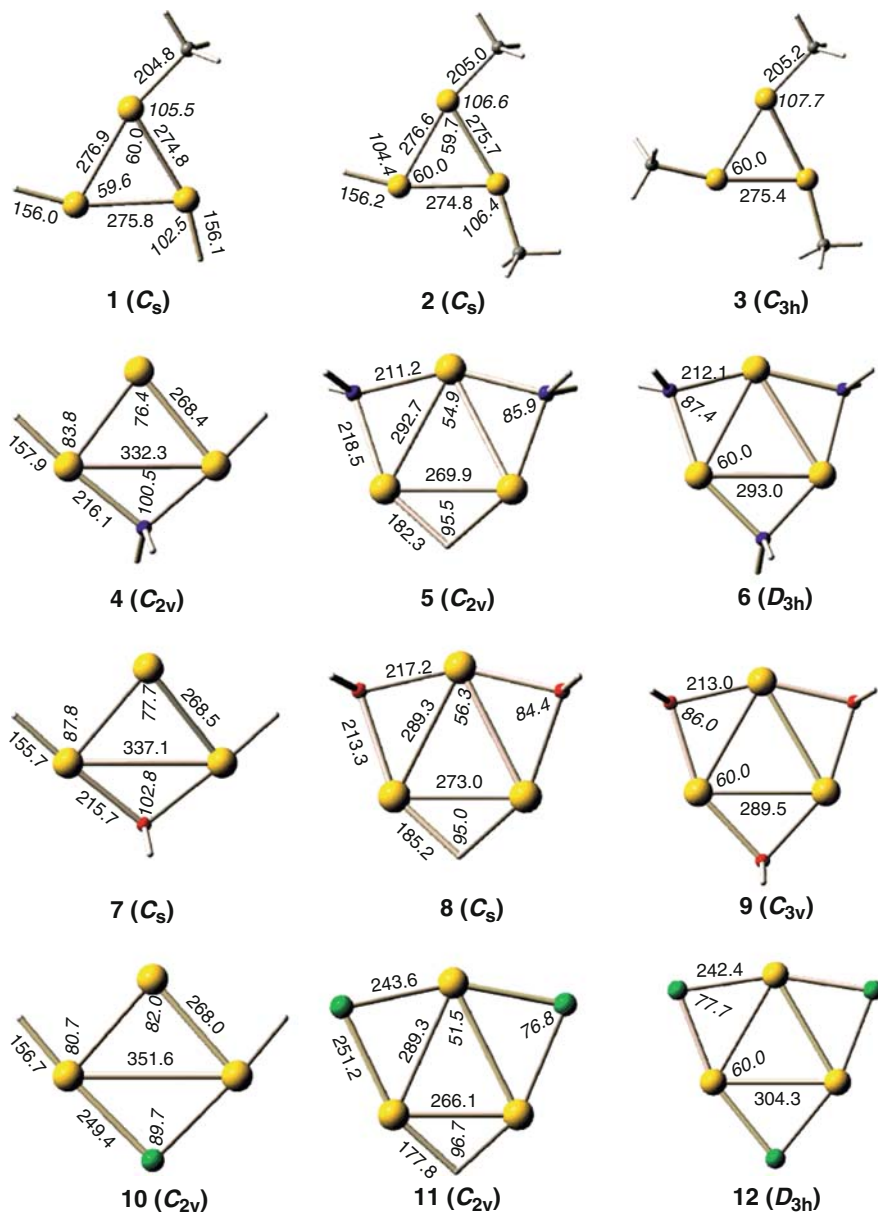


Fig. 18 Equilibrium geometries (bond lengths in pm, angles in degrees) of the *cyclo*-Au₃L_nH_{3-n} (L = CH₃, NH₂, OH, and Cl; n = 1, 2, 3) molecules corresponding to global minima in the PES computed at the B3LYP/LANL2DZ+f(Au)U6-31G** (L). Reprinted with permission from [136]. Copyright: ACS Journal Archives

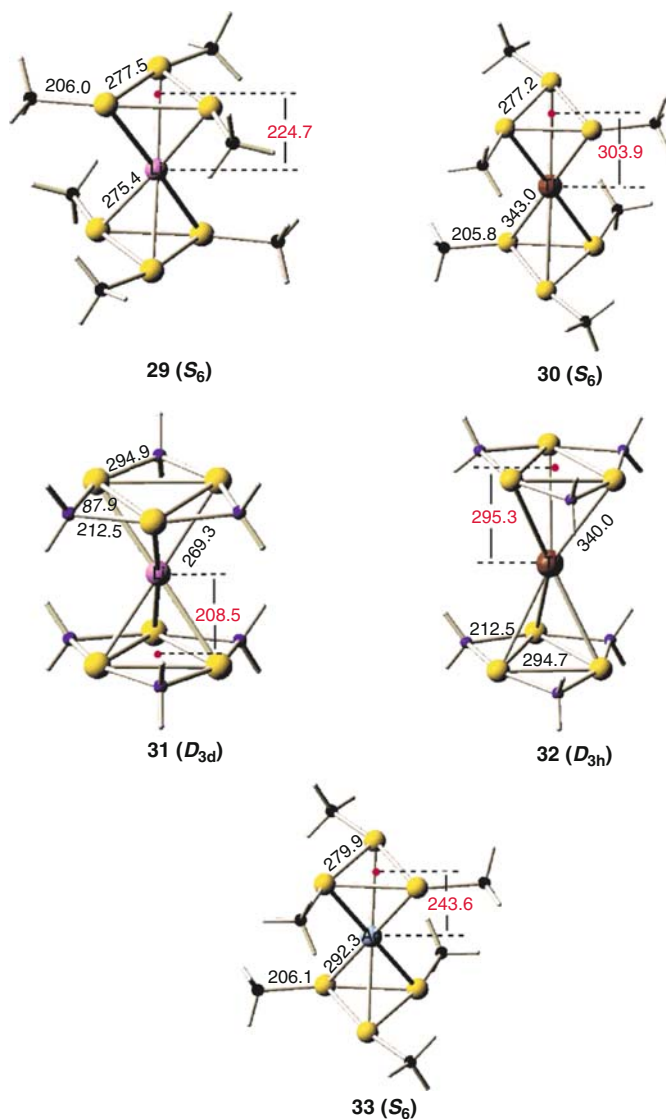


Fig. 19 Equilibrium geometries (bond lengths in pm, angles in degrees) of the $\{[cyclo-Au_3Me_3]_2M\}^+$ and $\{[cyclo-Au_3(NH_2)_3]_2M\}^+$ ($M=Li, Tl, Ag$) computed at the B3LYP/LANL2DZ+f(Au) U6-31G** (L). Reprinted with permission from [136]. *Copyright*: ACS Journal Archives

changes in the chemical shifts for Li^+ , Ag^+ , and Tl^+ cations over the Au_3 ring plane, and their interaction with electrophiles (e.g., H^+ , Li^+ , Ag^+ , and Tl^+) affording 1:1 and 1:2 sandwich-like complexes (Fig. 19) through cation- π interactions that are very common in aromatic organic molecules.

Regarding the bonding mechanism describing the cation- π interactions in the 1:1 and 1:2 complexes, it was found that covalent interactions play a prominent role in the π -complexes of H^+ and Ag^+ , while electrostatic interactions are dominant in the π -complexes of Li^+ and Tl^+ . The bonding in the three-membered gold(I) rings is characterized by a common ring-shaped electron density, more commonly seen in aromatic organic molecules and in “all-metal” aromatics, such as the $[c-Hg_3]^{4-}$ cluster [136].

More recently we addressed a number of points related to the ligand effects on the stability, conformational preference, and diatropic response of the aromatic $cyclo-Cu_3(\mu-H)_3L_n$ ($L = N_2, CO, CN^-, H_2O, NH_3,$ and $PH_3; n = 1-3$) [137]. The novel $[cyclo-Cu_3(\mu-H)_3L_n]$ molecules are predicted [137] to adopt planar structures, which are characterized by perfect equalization of all metal-metal bonds in the aromatic metallic rings for the fully substituted derivatives (Fig. 20).

The interaction energies between the parent $[cyclo-Cu_3(\mu-H)_3]$ fragments and the ligand L computed by means of CDA were found in the range of -7.2 to -56.2 kcal/mol. The bonding of the $[cyclo-Cu_3(\mu-H)_3L_n]$ molecules is described by highly delocalized σ -, π - and δ -MOs, which support a remarkable ring-shaped electron delocalization responsible for the aromaticity of the Cu_3 rings (s and d orbital aromaticity).

The existence of the sandwich compound with an Au monolayer sheet $[Au_3Tr_2Cl_3]^{2+}$ has been predicted at the ab initio level of theory and the scalar relativistic DFT [138]. The fully optimized geometry of $[Au_3Tr_2Cl_3]^{2+}$ shown in Fig. 21 is a triangular gold(I) monolayer sheet capped by chlorines and bounded to two cycloheptatrienyl (Tr) ligands.

The bonding between the Tr^+ ligands and the gold monolayer sheet is mainly governed by an electron back-donation interaction coming from the central gold sheet to the Tr^+ ligands with slight contributions originating from electron donation [138]. The Au-Au bond lengths inside the central gold sheet indicate that an intramolecular aurophilic interaction among the Au(I) atoms plays an important role in the bonding of the central Au_3 ring. Interestingly such bonding is ruled by d-d interactions where the 5d shell is no longer inert and the closed-shell structure of the Au(I) cations is broken, triggering the partial filling of the 6sp shell, contributing to the rise of the aurophilic bonding. NICS calculations showed a strong aromatic character in the gold monolayer sheet and Tr^+ ligands.

Even in the “free” $[c-Au_3]^{3+}$ fragment the breaking of the d^{10} structure in the gold atoms leads to d-d interactions that describe the bonding of the $[c-Au_3]^{3+}$ fragment. The latter is also inferred from the spatial representation of the frontier MOs shown pictorially in Fig. 22.

The HOMO is mainly made of the combination of the s and d_{z^2} orbitals of gold [138]. The LUMO is composed of antibonding d_{z^2} orbitals located at the Au2 and Au3 atoms, with a smaller contribution of a d_{xz} orbital on the Au1.

The concept of Au/H analogy is a general phenomenon in Au-alloy clusters adding new dimension to the expanding chemistry of Au [139]. Based on this concept we investigated bimetallic Cu_3Au_3 clusters using electronic structure calculation techniques (DFT) to understand their electronic, magnetic, and optical

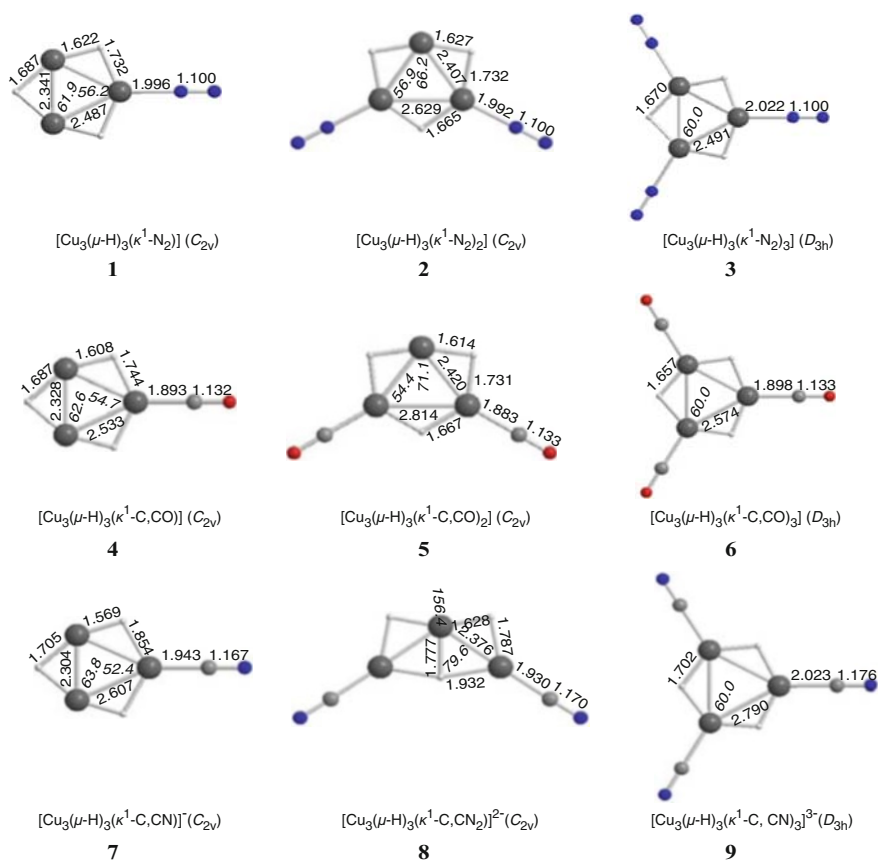


Fig. 20 Equilibrium geometries (bond lengths in Å, angles in degrees) of the $[cyclo-Cu_3(\mu-H)_3L_n]$ ($n = 1-3$; $L = N_2, CO, CN^-$) molecules corresponding to global minimum in the PES computed at the B3LYP/6-311+G** level. Reprinted with permission from [137]. Copyright: Nova Science Publishers

properties as well as the geometrical structures [140]. The most stable homotop is the planar $cyclo-[Cu_3(\mu-Au)_3]$ form consisting of a triangular positively charged Cu₃ structural core with negatively charged Au atoms located at the peripheral positions. It is clear that $cyclo-[Cu_3(\mu-Au)_3]$ is analogous to the $cyclo-[Cu_3(\mu-H)_3]$ cluster, thus demonstrating the concept of Au/H analogy. The bonding pattern along with the Density of States (DOS) plots of the $cyclo-[Cu_3(\mu-Au)_3]$ homotop are thoroughly analyzed and compared to those of the pure $cyclo-[Cu_3(\mu-Cu)_3]$ and $cyclo-[Au_3(\mu-Au)_3]$ clusters (Fig. 23). The bonding mode involves σ -, π -, and δ -type components, but having also significant ionic contribution due to the charge transfer from Cu to Au. The presence of π -type MOs resulting from the bonding interaction of the nd AOs of the Cu and Au atoms, delocalized over the entire bimetallic framework support a ring current, thus rendering the clusters aromatic.

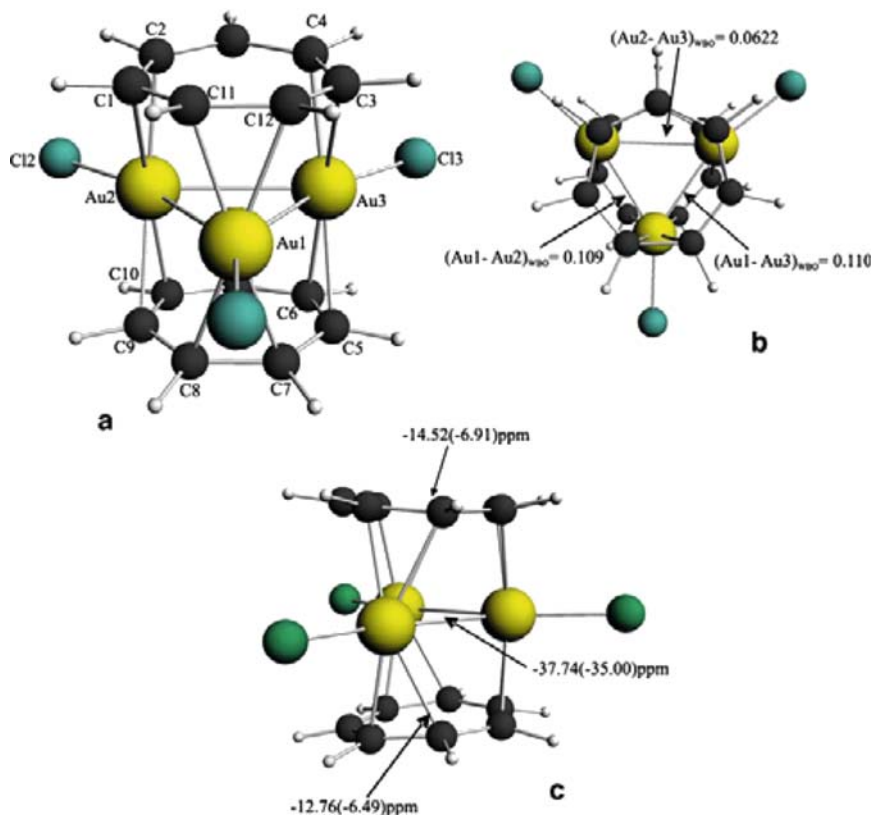


Fig. 21 (a) Ground-state geometry of $[\text{Au}_3\text{Tr}_2\text{Cl}_3]^{2+}$ complex; (b) Top view of $[\text{Au}_3\text{Tr}_2\text{Cl}_3]^{2+}$ and Wiberg bond orders computed with the MP2/B1 computational method; (c) Lateral view of $[\text{Au}_3\text{Tr}_2\text{Cl}_3]^{2+}$ and NICS values calculated with the MP2/B1 method; the values in parentheses were obtained at VWN/TZP level. Reprinted with permission from [138]. *Copyright*: Springer Science Publishers

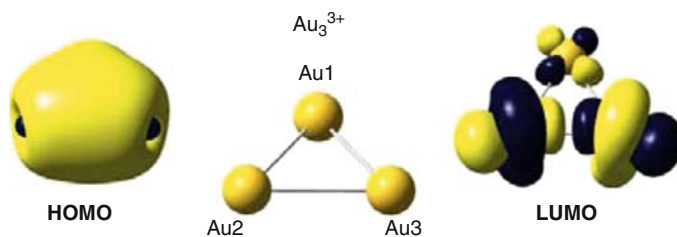


Fig. 22 Spatial representation of the frontier MOs for the $[\text{Au}_3\text{Tr}_2\text{Cl}_3]^{2+}$ complex; Top view of the $[\text{c-Au}_3]^{3+}$ fragment. Reprinted with permission from [138]. *Copyright*: Springer Science Publishers

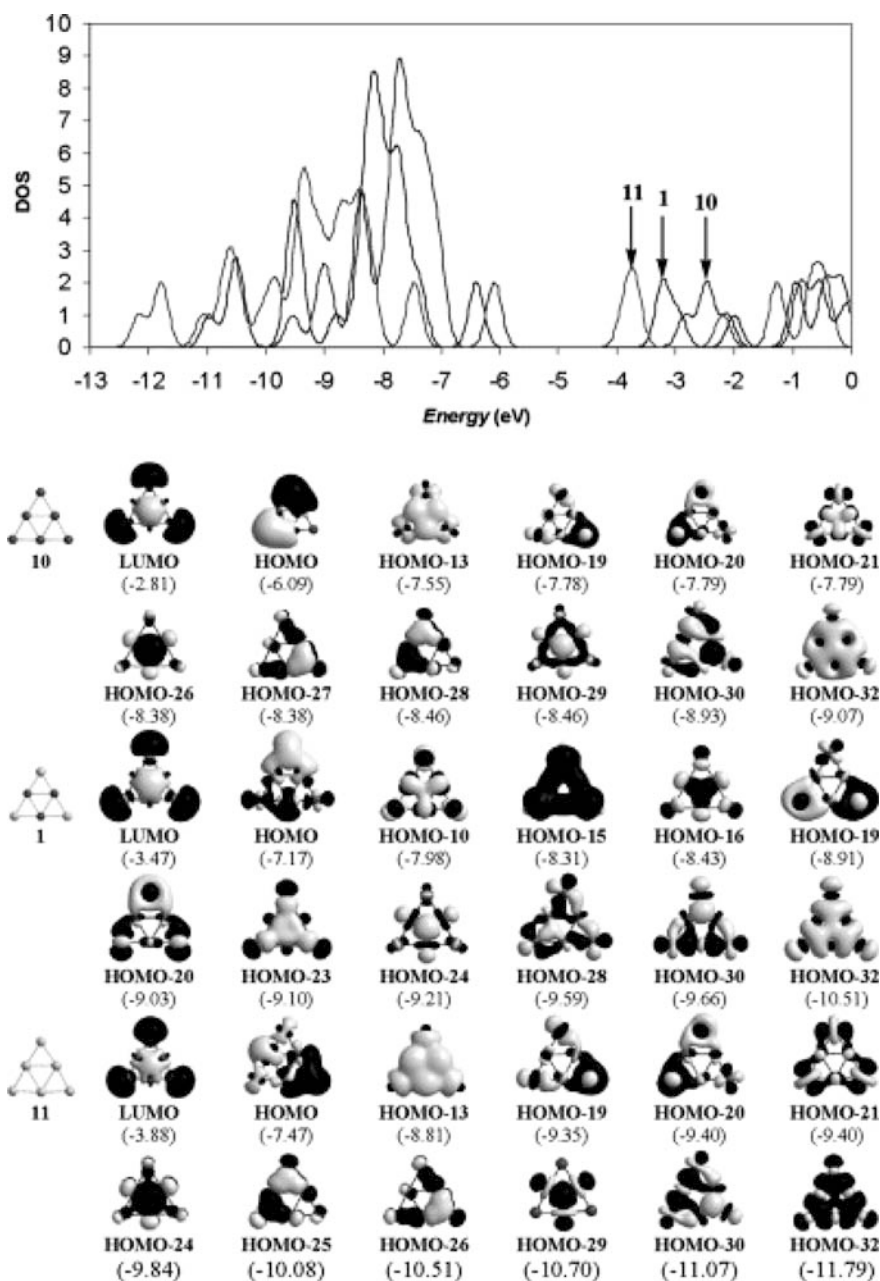


Fig. 23 DOS plots along with the shapes of the most relevant valence MOs of the most stable homotop $cyclo-[Cu_3(\mu-Au)_3]$, **1** and the pure $cyclo-[Cu_3(\mu-Cu)_3]$, **10** and $cyclo-[Au_3(\mu-Au)_3]$, **11** clusters computed at the B3P86/LANL2DZf(Au)UDGDZVP2(Cu). Reprinted with permission from [140]. Copyright: Wiley Periodicals Inc

The aromaticity of the bimetallic clusters was verified by structural, magnetic (NICS scan profiles), and out-of-plane ring deformability criteria. The 3-membered central metal cores in the *cyclo*-[Cu₃(μ-Au)₃] homotop and the pure *cyclo*-[Cu₃(μ-Cu)₃] and *cyclo*-[Au₃(μ-Au)₃] clusters exhibit negative NICS(0) values in the range of -19.4 to -28.0 ppm and therefore have significant aromatic character. Applying the magnetic criterion of aromaticity, namely, NICS, for the peripheral “all-metal” rings we have also diagnosed remarkable aromatic character.

Very recently DFT has been used by Cundari et al. [141] to assess the π-acidity and π-basicity of metallorganic trimetallic macromolecular complexes formulated as *cyclo*-[M(μ-L)₃] (M = Cu, Ag, Au; L = carbeniate, Cb, imidazolate, Im, pyridinate, Py, pyrazolate, Pz, triazolate, Tz). The π-basicity of the [M(μ-L)₃] clusters depends on the nature of the bridging ligand following the trend: [M(μ-Py)₃] > [M(μ-Cb)₃] > [M(μ-Pz)₃] > [M(μ-Tz)₃]. It was also predicted that the order of basicity is Au > Cu > Ag. Moreover electron-donating substituents (such as CH₃) on the bridging ligands produce strong π-basic trimers, while electron-withdrawing substituents (such as CF₃) produce strong π-acidic trimers. Molecular electrostatic potential (MEP) surfaces (Fig. 24) and positive charge attraction energy curves (Fig. 25) indicated that the metal-organic macromolecules show superior π-acidity and basicity compared to their organic counterparts.

We think that it would be advisable to explore the aromaticity/antiaromaticity of the aforementioned trimers and see how these properties are related with the opto-electronic properties, thus helping in designing metallorganic field-effect transistors and exciton blockers for organic light-emitting diode devices.

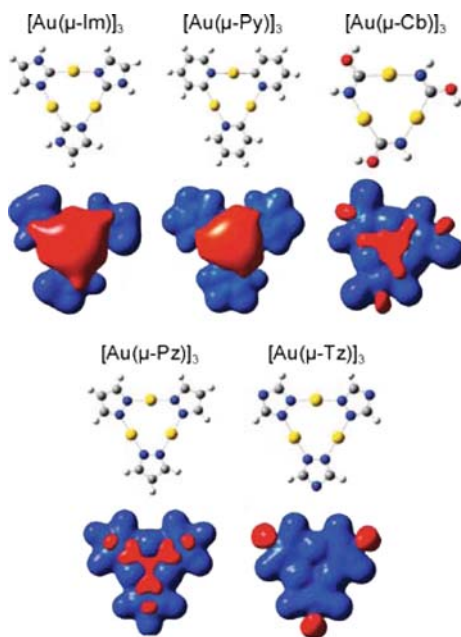


Fig. 24 MEP surfaces showing the relative π-basicity of *cyclo*-[M(μ-L)₃] trimers as a function of the bridging ligand (isosurface value = 0.02). Reprinted with permission from [141].
Copyright: ACS Journal Archives

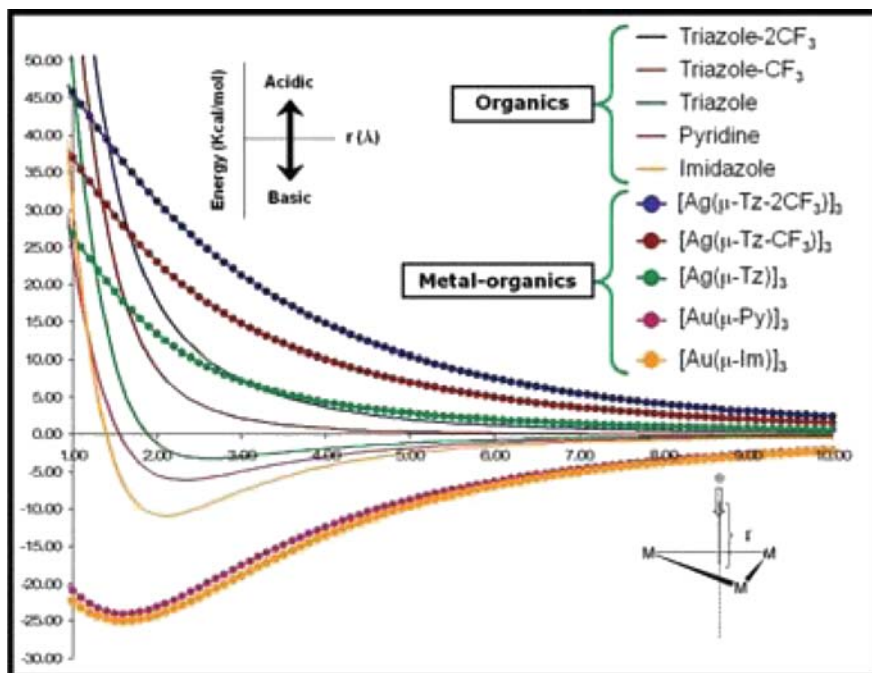


Fig. 25 Positive charge attraction energy illustrates examples of relative π -basicity of the organic compounds vs the metal–organic trimer complexes. Reprinted with permission from [141].
Copyright: ACS Journal Archives

Finally, Yong and Chi [142] performing comprehensive calculations (B3LYP, B3PW91, and CCSD(T)) on a series of dianionic $[c-M_3]^{2-}$ ($M = \text{Zn}, \text{Cd}, \text{Hg}$), anionic $\text{Na}[M_3]^-$, and neutral $\text{Na}_2[M_3]$ clusters, all having the $[c-M_3]^{2-}$ (D_{3h}) core, showed that the $[c-M_3]^{2-}$ in the $^1A'_1$ ground state is π -aromatic. The detailed molecular orbital analysis reveals that one highly delocalized π -type MO of a''_2 symmetry plays an important role in rendering the $[c-M_3]^{2-}$ clusters in pure π -aromaticity. Moreover, the estimated large negative NICS values and the computed RE for the $[c-M_3]^{2-}$ species further justified their π -aromatic character.

9 Aromatic/Antiaromatic Four-, Five-, and Six-Membered Rings of Metal Atoms

Chattaraj and coworkers [143] have very recently shown using DFT calculations that the M_6 ($M = \text{Na}, \text{K}$) rings in the chain present in 3-D $[\text{Na}_2\text{MoO}_3\text{L}(\text{H}_2\text{O})_2]_n$ and 2-D $[\text{K}_2\text{MoO}_3\text{L}(\text{H}_2\text{O})_3]_n$ are aromatic in character according to the nucleus independent chemical shift (NICS) and multicenter bond indices values. The NICS values at the center of the Na_6 rings and at the cage center of the K_6 rings are

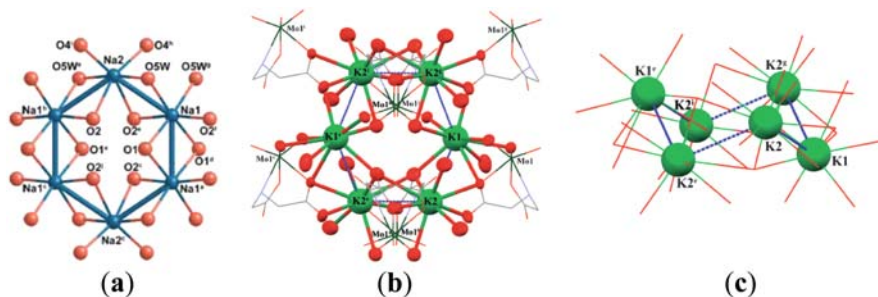


Fig. 26 (a) Core structure of the hexagonal Na_6 oxo cluster viewed along the crystallographic a -axis. (b) Structure of the hexagonal K_6 unit formed from metalloligands and bridging water molecules. (c) Another view of the K_6 unit which looks like the chair conformation of cyclohexane. Reprinted with permission from [143]. *Copyright:* the Owner Societies

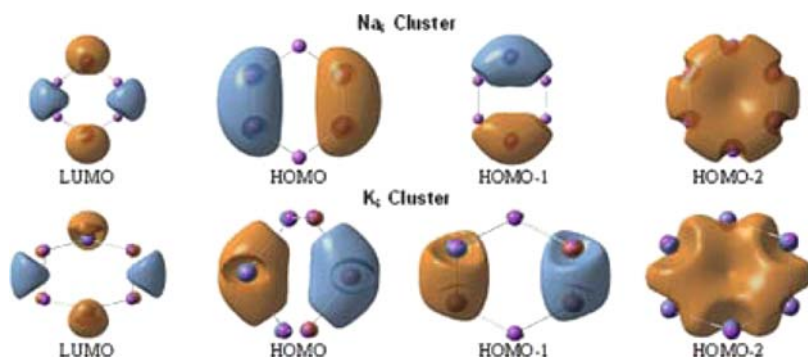


Fig. 27 Some frontier molecular orbitals of Na_6 and K_6 molecules. Reprinted with permission from [143]. *Copyright:* the Owner Societies

comparable to the corresponding values of their polyacene analogs in most cases. The stability and reactivity patterns of the M_6 rings also follow a similar trend as their organic analogs (Fig. 26).

Some pertinent frontier molecular orbitals of the Na_6 and K_6 clusters related with the aromaticity of the six-membered rings are shown in Fig. 27. Notice that the electron delocalization is observed in the HOMO-2 of both molecules.

The next species exhibiting pure σ -aromaticity are the $[\text{c-Mg}_4]^{2+}$ and $[\text{c-Li}_2\text{Mg}_2]$ clusters having six σ -electrons [144]. For the $[\text{c-Mg}_4]^{2+}$ and $[\text{c-Li}_2\text{Mg}_2]$ clusters where the occupation of six-valence electrons was found to be HOMO-1,2 (e_u) and HOMO (a_{1g}) for $[\text{c-Mg}_4]^{2+}$ (D_{4h}) and HOMO (b_{2u}), HOMO-1 (b_{1u}), and HOMO-2 (a_g) for $[\text{c-Li}_2\text{Mg}_2]$ (D_{2h}) the estimated excitation energies of the most significant translationally ($T_{x,y}$) allowed transitions found to be 1.121 eV for the σ -type HOMO,-1 (e_u) \rightarrow LUMO + 3(a_{1g}) in $[\text{c-Mg}_4]^{2+}$ (D_{4h}) and 2.062 eV for the σ -type HOMO (b_{2u}) \rightarrow LUMO + 1(a_{1g}) and 4.915 eV for the π -type HOMO-3 (a_g) \rightarrow LUMO(b_{3u}) in $[\text{c-Li}_2\text{Mg}_2]$ (D_{2h}) accounts well for the shape of the NICS_{zz}-scan curves (Fig. 28), which are typical for σ -aromatics [79].

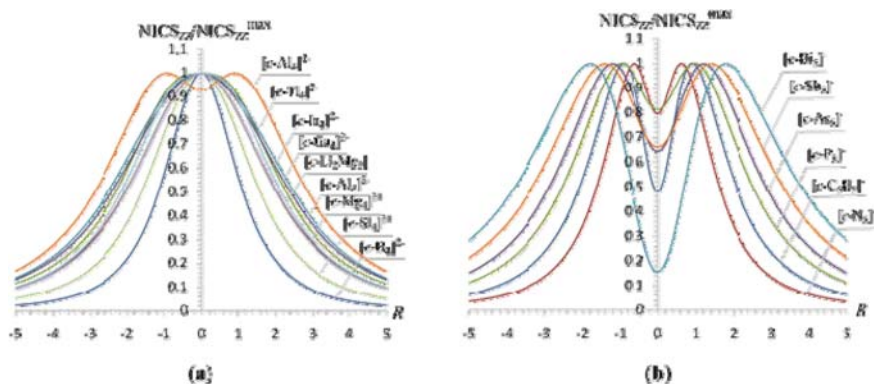


Fig. 28 The NICS_{zz} -scan profiles in the form of $\text{NICS}_{zz}/\text{NICS}_{zz}^{\max}$ vs R curves for selected four- and five-membered rings of main group atoms exhibiting double ($\sigma + \pi$) aromaticity [79].

The double ($\sigma + \pi$) aromaticity of the $[\text{c-Al}_4]^{2-}$ cluster was first introduced by Boldyrev et al. [145] and subsequently justified by the use of different criteria of aromaticity, such as the induced magnetic field analysis [146], the aromatic ring current shielding (ARCS) [147, 148], the ring current maps [149–152], NICS [153], RE estimations [154, 155], valence bond calculations [156], bifurcation analysis of electron localization function (ELF) [72], conceptual DFT descriptors [157], and quantum theory of atoms in molecules calculations [158]. It should also be noticed that Sundholm et al. [148] based on ARCS calculations on the $[\text{c-Al}_4]^{2-}$, $[\text{c-Ga}_4]^{2-}$, $[\text{c-In}_4]^{2-}$ and $[\text{c-Tl}_4]^{2-}$ indicated that all these species are aromatic, the calculated ring-current susceptibilities and the (ring radius) found to be 16.2 nA/T (194 pm), 17.2 nA/T (190 pm) 19.3 nA/T (210 pm), and 18.4 nA/T (241 pm), respectively, at the 3-VE+sp2df HF level.

The ground-state ($^1A_{1g}$) occupation in D_{4h} symmetry of 14 valence electrons for the $[\text{c-Al}_4]^{2-}$, $[\text{c-Ga}_4]^{2-}$, $[\text{c-In}_4]^{2-}$, and $[\text{c-Tl}_4]^{2-}$ clusters was found to be HOMO-6 (a_{1g}), HOMO-4,5 (e_u), HOMO-3 (b_{1g}), HOMO-2 (b_{2g}), HOMO-1 (a_{1g}), HOMO (a_{2u}). In $[\text{c-In}_4]^{2-}$ cluster there is an inversion of the HOMO and HOMO-1. The computed excitation energies of the $a_{1g} \rightarrow e_u$ (σ -type) and $a_{2u} \rightarrow e_g$ (π -type) translationally allowed ($T_{x,y}$) transitions of $[\text{c-Al}_4]^{2-}$, $[\text{c-Ga}_4]^{2-}$, $[\text{c-In}_4]^{2-}$ and $[\text{c-Tl}_4]^{2-}$ clusters found to be 2.001; **2.302**, 0.562; **1.165**, 1.919; **2.074**, and 1.962; **2.033** eV, respectively, are in support of the double ($\sigma + \pi$) aromaticity of the clusters with the σ -aromatic component overwhelming the π -aromatic one. The NICS_{zz} -scan curve along with the molecular orbital energy level diagram, symmetries, 3-D molecular orbital pictures, and the significant translationally ($T_{x,y}$) allowed transitions leading to the diamagnetic ring current of the prototype “all-metal” $[\text{c-Al}_4]^{2-}$ cluster computed at the B3LYP/6-311+G(d,p) level shown in Fig. 29 is typical for double ($\sigma + \pi$) aromatics exhibiting slightly higher σ -than π -aromatic character [79].

In contrast, the NICS_{zz} -scan curve of the $[\text{c-Al}_4]^{4-}$ (D_{2h}) cluster exhibits two maxima at a distance of 0.9 Å above and below the molecular plane (Fig. 29),

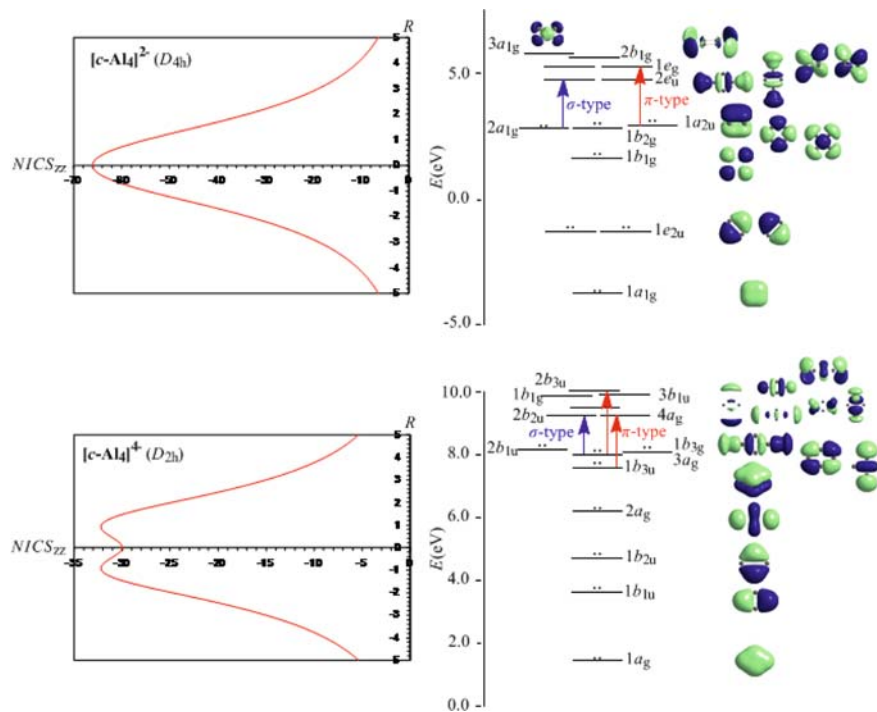


Fig. 29 The $NICS_{zz}$ -scan curves of the $[c-Al_4]^{2-}$ and $[c-Al_4]^{4-}$ clusters, along with the molecular orbital energy level diagram, symmetries, 3-D molecular orbital pictures, and significant translationally ($T_{x,y}$), allowed transitions leading to the diamagnetic ring current computed at the B3LYP/6-311+G(d,p) level

which is typical for double ($\sigma + \pi$) aromatics where the π -type diatropic ring current exceeds slightly the σ -type one. In effect, this is compatible with the estimated excitation energies of the most significant translationally ($T_{x,y}$) allowed transitions for the σ -type HOMO-2 (a_g) \rightarrow LUMO (b_{2u}) (1.272 eV) and the π -type HOMO-3 (b_{3u}) \rightarrow LUMO+1 (a_g) (1.582 eV) and HOMO-2 (a_g) \rightarrow LUMO+5 (b_{3u}) (2.051 eV). Notice the contribution of two translationally ($T_{x,y}$) allowed π -type transitions to the π -diatropic ring current in $[c-Al_4]^{4-}$ cluster.

Pati et al. [159, 160] calculated the structures of dimers of all-metal aromatic and antiaromatic molecules such as $[c-Al_4]^{2-}$ and $[c-Al_4]^{4-}$. They found that, unlike their organic benzene and cyclobutadiene counterparts which form π -stacked complexes, the $[c-Al_4]^{2-}$ and $[c-Al_4]^{4-}$ clusters form new extremely stable superclusters with no reminiscence of the original units. To this regard, the authors conjectured that the Al_6 clusters are aromatic and should be ideal candidates for experimental isolation through mass-spectrometric measurements or crystallization. In a more recent review article [160] the same authors presented computational strategies to unambiguously determine the aromaticity/antiaromaticity characteristics of “all-metal” Al_4M_4 ($M =$ alkali metal ion) clusters. The presented

methodology is based on the partition of the distortion energies belonging to σ and π electrons applicable for a large class of systems with closely spaced σ and π electronic levels. The Al_4M_4 clusters show a very large off-resonance third harmonic generation that is 10,000 times larger than their organic analogs. The authors have also proposed new strategies to stabilize all-metal antiaromatic Al_4M_4 species through complexation to low-valent transition metals, such as $\text{Fe}(0)$ and $\text{Ni}(0)$, yielding the half-sandwich $[(\text{Al}_4\text{M}_4)\text{Fe}(\text{CO})_3]$ and full-sandwich $[(\text{Al}_4\text{M}_4)_2\text{Ni}]$ complexes and discussed mechanisms for substitution reactions within the conventional organometallic systems by Al_4M_4 clusters.

The relative stabilities of the $[\text{MAl}_4]^-$ ($\text{M} = \text{Li}^+, \text{Na}^+, \text{K}^+, \text{Rb}^+, \text{Cs}^+, \text{Cu}^+, \text{Ag}^+, \text{Au}^+$) isomers have been investigated on the grounds of the minimum polarizability principle [161]. According to the minimum polarizability and maximum hardness principles, the stability of the pyramidal isomer decreases with the augmentation of the atomic number. It is no wonder that for the $[\text{AuAl}_4]^-$ the planar isomer is finally more stable than the pyramidal structure. The minimum polarizability and the maximum hardness principles have also been examined to describe the relative stability of various isomers of the $[\{c\text{-Cu}_4\}\text{Na}]^-$, $[\{c\text{-Cu}_4\}\text{Li}]^-$, $[\{c\text{-Al}_4\}\text{Cu}]^-$, $[\{c\text{-Ag}_4\}\text{Li}]^-$, $[\{c\text{-Au}_4\}\text{Li}]^-$, $[\{c\text{-Ag}_4\}\text{Na}]^-$, $[\{c\text{-Au}_4\}\text{Na}]^-$, $[\{c\text{-Al}_4\}\text{Ag}]^-$, and $[\{c\text{-Al}_4\}\text{Au}]^-$ using MP2 calculations [162]. The results showed that the pyramidal structures are more stable than the planar ones.

Satpati and Sebastian [163] demonstrated that all metal species such as Al_4Li_4 can be stabilized by capping with BH or C. The stabilization is due to suitable ring cap compatibility between the p_x and p_y orbitals of the capped atom and the HOMO and LUMO of Al_4Li_4 (Fig. 30).

Donation of two electrons to the ring by the cap atoms introduces aromatic character. It was also shown that Al_4Li_4 with a BH or C cap has very high binding energy, which suggests that these compounds should be considered as very good candidates for synthesis. Moreover, the very high rate of fluxional rearrangement at room temperature suggests that $\text{Li}_4[\{\text{Al}_4\}(\mu_4\text{-BH})]$ and $\text{Li}_4[\{\text{Al}_4\}(\mu_4\text{-C})]$ will show fluxionality.

The structure, dynamics, and electron delocalization of $[c\text{-Al}_4]^{2-}$ and $[c\text{-Al}_4]^{4-}$ based clusters were investigated by Merino et al. [164]. Gradient-corrected Density-Functional Born-Oppenheimer molecular dynamics simulations showed that the cations are relatively fixed for $\text{Li}[c\text{-Al}_4]^-$ and $\text{Li}_2[c\text{-Al}_4]$ but become more floppy for $\text{Li}_3[c\text{-Al}_4]^-$ and $\text{Li}_4[c\text{-Al}_4]$. For these molecules, any static structural representation is not realistic. The induced magnetic field analysis of the $[c\text{-Al}_4]^{2-}$ and $[c\text{-Al}_4]^{4-}$ species indicates that both systems have diatropic σ -systems, while the π -system is diatropic for $[c\text{-Al}_4]^{2-}$ and paratropic for $[c\text{-Al}_4]^{4-}$. The total magnetic response is diatropic for $[c\text{-Al}_4]^{2-}$ while $[c\text{-Al}_4]^{4-}$ is "bitropic": it has typical antiaromatic long-range cones, while the magnetic field in the $[c\text{-Al}_4]^{4-}$ ring plane is similar to that of aromatic annulenes. Magnetically, the induced magnetic field representation agrees with former investigations based on NICS and ring current calculations concerning the character of the σ - and π -systems. For the $[c\text{-Al}_4]^{4-}$ systems, the complete map of the induced magnetic field (Fig. 31) shows the "bitropic" character of the molecule, the diatropic contribution raised by the σ -electrons which

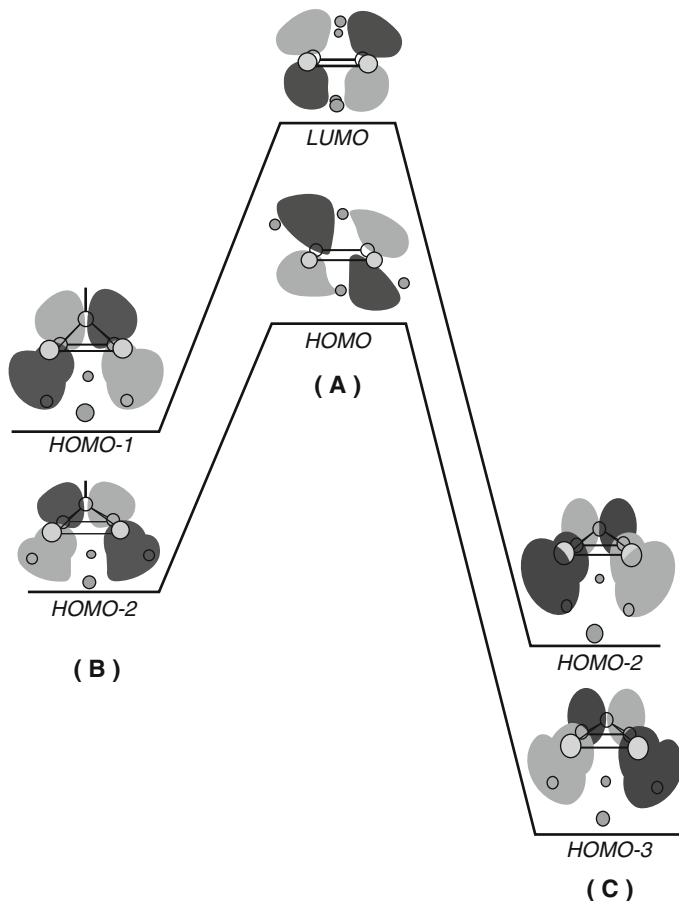


Fig. 30 (a) HOMO and LUMO of free Al_4Li_4 . (b) Resultant MOs formed by the interaction of the HOMO–LUMO of free Al_4Li_4 and p_x and p_y AOs of the BH cap. (c) Resultant MOs formed by the interaction of the HOMO–LUMO of free Al_4Li_4 and p_x and p_y AOs of the C cap LUMO of (a), HOMO-1 of (b), and HOMO-2 of (c) are rotated by 90° for clarity. Reprinted with permission from [163]. Copyright: ACS Journal Archives

dominates in the ring plane, and the paratropic part, induced by the π -system around the z-axis.

Wang et al. [165] using MP2 and HF nuclear magnetic resonance calculations compared the magnetic properties between spin singlet and triplet $[\text{Li}_3(c\text{-Al}_4)]^-$ clusters and confirmed the paramagnetism of the singlet and diamagnetism of the triplet $[\text{Li}_3(c\text{-Al}_4)]^-$ cluster. It was found that the paramagnetism of spin singlet $[\text{Li}_3(c\text{-Al}_4)]^-$ cluster originates from the paramagnetic ring current within the planar ring, which, in the central region of the ring, is at least partially produced with the localized diamagnetic current induced by external magnetic field perpendicular to the molecular plane. The origin is the orbital mixing of excited-state wave

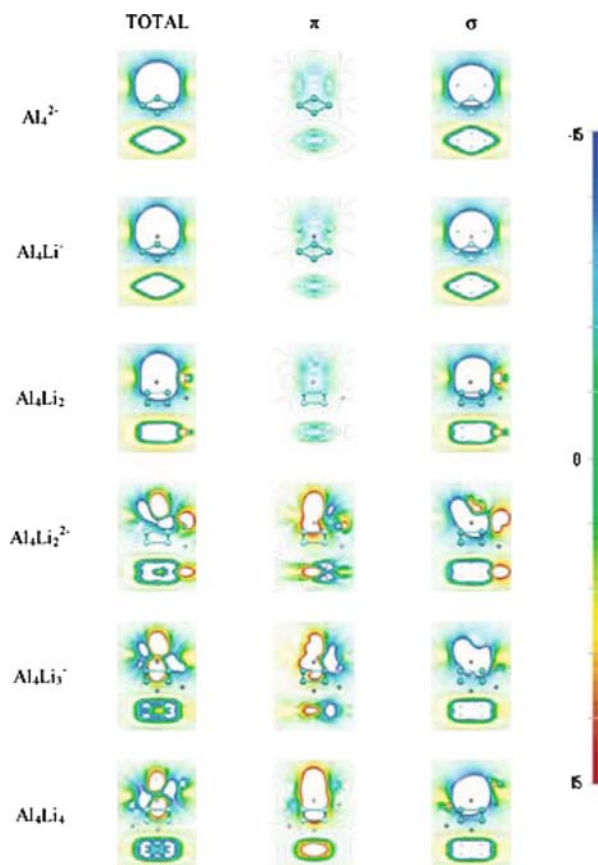
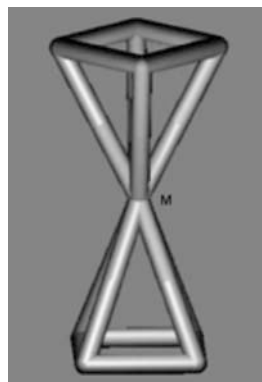


Fig. 31 Contour lines of the z -component of the induced magnetic field, \mathbf{B}^{ind} , in the molecular plane and perpendicular to the molecular plane through the origin. The scale is given in ppm or μT for an external field of 1T. Reprinted with permission from [164]. *Copyright*: ACS Journal Archives

function into ground-state one in external magnetic field and correlates with the localized electronic structure, low symmetry of geometric conformation, and narrow HOMO–LUMO gap. In the triplet $[\text{Li}_3(c\text{-Al}_4)]^-$ cluster the perturbation lifts the near degeneracy with a HOMO–LUMO gap that could modulate the magnitude of paramagnetic ring current to a small value, and therefore it may be easy for the unpaired electrons to contribute to the diamagnetic ring current. Consequently the diamagnetism surpasses the paramagnetism in the triplet $[\text{Li}_3(c\text{-Al}_4)]^-$ cluster.

The “all-metal” aromatic $[c\text{-Al}_4]^{2-}$ species has been proved to be a good ligand to form sandwich-type compounds analogous to the well-known metallocenes [166, 167]. Sandwich complexes based on the $[c\text{-Al}_4]^{2-}$ ligand were recently reported by Mercero et al. [166]. The authors using B3LYP calculations characterized the structures and properties of a series of $[\text{Al}_4\text{MAl}_4]^{q-}$ ($q = 2, 1, 0$; $\text{M} = \text{Ti}, \text{V}, \text{Cr}$,

Fig. 32 Staggered $[\text{Al}_4\text{MAl}_4]^{q-}$ ground-state structure (D_{4d} symmetry) for $\text{M} = \text{Ti}, \text{V}, \text{Cr}, \text{Zr}, \text{Nb}, \text{Ta}, \text{Mo}, \text{Hf}, \text{W}$ with charges $q = 2$, for Ti, Zr , and Hf , $q = 1$ for V, Nb , and Ta , and $q = 0$ for Cr, Mo , and W , respectively. Reprinted with permission from [166].
Copyright: Wiley-VCH



$\text{Zr}, \text{Nb}, \text{Ta}, \text{Mo}, \text{Hf}, \text{W}$) complexes. All the sandwich structures characterized adopt the staggered ground-state structure of D_{4d} symmetry (Fig. 32).

In all $[\text{Al}_4\text{MAl}_4]^{q-}$ sandwich structures the $[\text{c-Al}_4]^{2-}$ ligand keeps its geometric and aromaticity features essentially unchanged. Inspired by the aforementioned theoretical design of sandwich-type transition metal complexes, $[\text{Al}_4\text{MAl}_4]^{q-}$, Ding and coworkers [167] using DFT calculations (B3LYP/6-311+G*) designed a series of novel nontransition metal sandwich complexes based on the $[\text{c-Al}_4]^{2-}$ ligand and main-group metals M ($\text{M} = \text{Li}, \text{Na}, \text{K}, \text{Be}, \text{Mg}, \text{Ca}$). They found that the $[\text{c-Al}_4]^{2-}$ ligand seems unlikely to sandwich the main-group metal atoms in the *homo-decked* sandwich form. The authors proposed a new type of sandwich complexes, the *hetero-decked* $[\text{CpMAl}_4]^{q-}$ ones, where the presence of the rigid Cp partner, which cooperatively sandwiches alkali metal and alkaline-earth metal atoms, stabilizes the $[\text{c-Al}_4]^{2-}$ ligand which can act as a “superatom.”

Very recently Zeng et al. [168] reported the first evidence of a hexatomic species CAI_5 having a global-minimum structure with a planar pentacoordinate carbon. High-level ab initio computations and quantum molecular dynamics simulations at 300 and 400 K reveal that the most stable $[\text{CAI}_5]^+$ isomer has pentacoordinate D_{5h} symmetry and is ~ 3.80 kcal/mol lower in energy than the second most stable alternative. The latter has a nonplanar structure based on a tetrahedral CAI_4 moiety. The $[\text{CAI}_5]^+$ cluster has 18 valence electrons with the electronic configuration $(1a'_1)^2(1e'_1)^4(2a'_1)^2(1a''_2)^2(1e'_2)^4(2e'_1)^4$. The CMOs of the $[\text{CAI}_5]^+$ shown in Fig. 33 include a radial degenerate highest occupied MO of e'_1 symmetry (HOMO,-1), an occupied π -orbital of a''_2 symmetry (HOMO-2), a peripheral radial five-center MO of a'_1 symmetry (HOMO-3), and other σ -orbitals.

A significant contribution of the perpendicular $2p_z$ orbital of the central C atom to the π -orbital (HOMO-2) was found. In addition, the highly delocalized radial bonding HOMO-3 also favors the planar structure. Furthermore, the large HOMO–LUMO gap (1.65 eV at the PBEPBE/aug-cc-pVTZ level or 2.82 eV at the B3LYP/aug-cc-pVTZ level) also suggests high stability of the $[\text{CAI}_5]^+$ cluster. The CMO dissection of the out-of-plane tensor component of the NICS(1)_{zz} indicates that $[\text{CAI}_5]^+$ exhibits weak π -aromaticity (Fig. 33). The dissected NICS grid analysis further supports the CMO–NICS(1)_{zz} conclusions: the contribution to

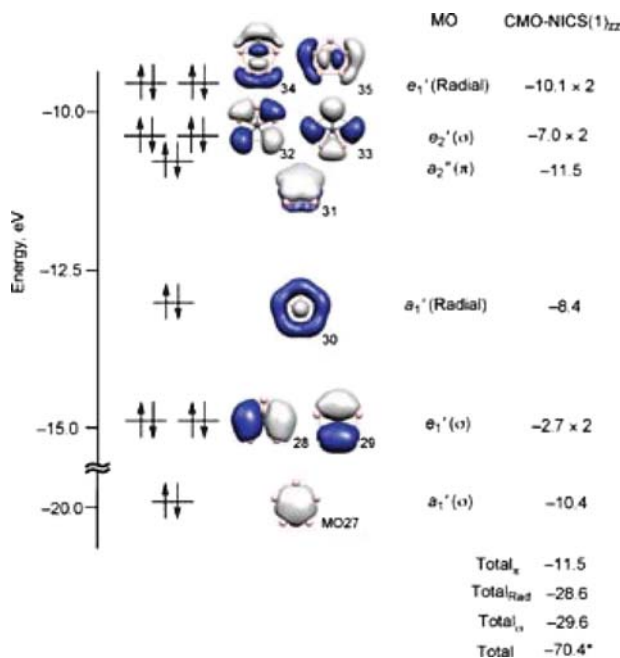


Fig. 33 Canonical molecular orbitals of D_{5h} $[\text{Al}_5]^+$ and their CMO-NICS(1)_{zz} contributions (in ppm) at PW91/IGLO-III level. Reprinted with permission from [168]. Copyright: ACS Journal Archives

the diatropic NICS tensor from the π MO is rather small relative to that of the radial MOs. Hence, the radial MOs are more important than the π MO in favoring the planar geometry of $[\text{Al}_5]^+$ (D_{5h}).

Todorov and Senov [169] recently reported the syntheses of six new compounds of four different structural types, $\text{Li}_{9-x}\text{CaSn}_{6+x}$, $\text{Li}_{9-x}\text{EuSn}_{6+x}$, $\text{Li}_5\text{Ca}_7\text{Sn}_{11}$, $\text{Li}_6\text{Eu}_5\text{Sn}_9$, $\text{LiMgEu}_2\text{Sn}_3$, and $\text{LiMgSr}_2\text{Sn}_3$, which together with three previously reported [170] isostructural compounds, Na_8BaSn_6 , Na_8BaPb_6 , and Na_8EuSn_6 , form a new class of compounds with heavy metal aromatic or conjugated systems. Most extraordinary in these compounds is the existence of one and the same structural feature for most of them, columns of stacked aromatic pentagonal rings of $[\text{c-Sn}_5]^{6-}$ (or $[\text{c-Pb}_5]^{6-}$) (Fig. 34a) that are analogous to the Cp ligand. The molecular orbital pattern of the $[\text{c-Sn}_5]^{6-}$ (or $[\text{c-Pb}_5]^{6-}$) aromatics (Fig. 34b) clearly resembles the π -manifold in the aromatic cyclopentadienyl anion, Cp.

Xu and Jin [171] investigated with DFT methods the geometrical and electronic structures and the vibrational frequencies of the low-lying states of alkali metal $\text{M}[\text{c-As}_4]^-$ ($\text{M} = \text{Li}, \text{Na}, \text{K}, \text{Rb}, \text{and Cs}$) clusters and alkaline earth metal $\text{M}'[\text{c-As}_4]$ ($\text{M}' = \text{Be}, \text{Ca}, \text{Sr}, \text{and Ba}$) clusters. The computational results showed that the square planar $[\text{c-As}_4]^{2-}$ dianion can coordinate with metal atoms forming pyramidal $\text{M}[\text{c-As}_4]^-$ and $\text{M}'[\text{c-As}_4]$ complexes. On the basis of structural and electronic criteria of aromaticity, along with the presence of six delocalized π -electrons

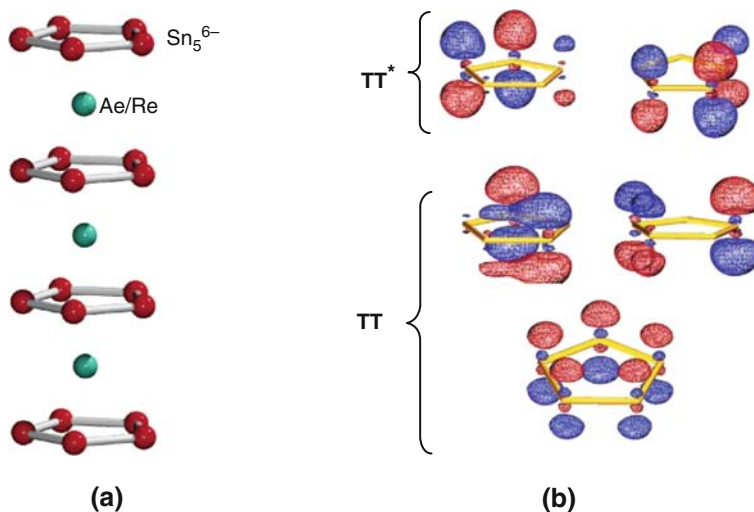


Fig. 34 (a) Column of eclipsed aromatic pentagons $[\text{c-Sn}_5]^{6-}$ separated by Ae or Re cations found in $\text{Li}_{9-x}\text{EuSn}_{6+x}$, $\text{Li}_{9-x}\text{CaSn}_{6+x}$, $\text{Li}_5\text{Ca}_7\text{Sn}_{11}$, $\text{Li}_6\text{Eu}_5\text{Sn}_9$. (b) Three π -bonding and two π -antibonding MOs in the aromatic $[\text{c-Sn}_5]^{6-}$ derived from single-point DFT calculations. Reprinted with permission from [169]. *Copyright*: ACS Journal Archives

(satisfying the $4n + 2$ electron counting rule) the square planar $[\text{c-As}_4]^{2-}$ dianion, keeping its integrity in the $\text{M}[\text{c-As}_4]^-$ and $\text{M}'[\text{c-As}_4]$ complexes, was found to exhibit characteristics of π -aromaticity.

Korber et al. [172] investigated the nature of the chemical bond in polypnictides. They synthesized novel compounds of the cyclotetrapnictide anion in a tripledecker-like coordination between two crown ether-coordinated alkali metal cations. The structure of one of the complexes studied is shown in Fig. 35.

With ab initio calculations at the HF level and by employing the concept of the electron localization function ELF, the authors established that the cyclotetraarsenide anion, $[\text{c-As}_4]^{2-}$, shows electron delocalization primarily through the lone pairs, and may consequently also be described as lone pair aromatic.

A series of alkali metal and alkaline earth metal–arsenic clusters formulated as $\text{M}[\text{c-As}_5]$ ($\text{M} = \text{Li}, \text{Na}, \text{K}, \text{Rb}, \text{Cs}$) and $\text{M}'[\text{c-As}_5]^+$ ($\text{M}' = \text{Be}, \text{Mg}, \text{Ca}, \text{Sr}, \text{Ba}$) were investigated by Xu and Jin [173] using DFT methods. All $\text{M}[\text{c-As}_5]$ and $\text{M}'[\text{c-As}_5]^+$ clusters adopt a pentagonal pyramidal structure with C_{5v} symmetry, its basal plane involving the planar pentagonal $[\text{c-As}_5]^-$ anion. From molecular orbital and NICS analysis, it was established that each of these species had three delocalized π MOs that satisfied the $4n + 2$ electron counting rule and therefore exhibit π -aromatic character.

The equilibrium geometries, electronic structures, harmonic vibrational frequencies, and NICS values of $[\text{c-Sb}_5]^-$ and $[\text{c-Sb}_5]\text{M}$ ($\text{M} = \text{Li}, \text{Na}, \text{and K}$) clusters were calculated at the B3LYP level [174]. The $[\text{c-Sb}_5]^-$ species adopt the aromatic planar cyclic D_{5h} structure, while the $[\text{c-Sb}_5]\text{M}$ species the pyramidal C_{5v} structures with

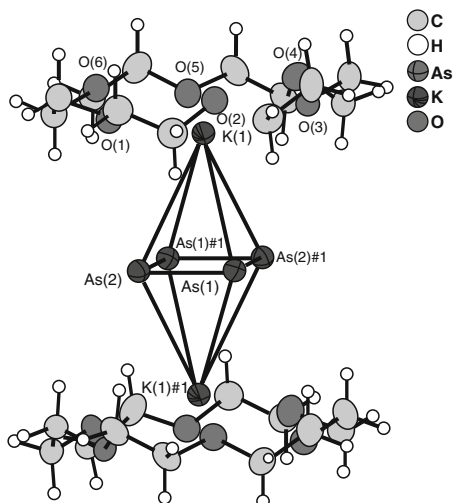


Fig. 35 Projection of the $(\text{K}@18\text{-crown-6})_2\text{As}_4$ molecule. Reprinted with permission from [172].
Copyright: ACS Journal Archives

the $[\text{c-Sb}_5]^-$ unit preserving its structural and electronic integrity in the $[\text{c-Sb}_5]\text{M}$ complexes. Molecular orbital analysis and NICS estimations indicated that the planar $[\text{c-Sb}_5]^-$ anion is aromatic exhibiting double ($\sigma + \pi$)-aromaticity. The same authors [175] extended their calculations on the $\text{M}[\text{c-Bi}_5]$ ($\text{M} = \text{Li}, \text{Na}, \text{K}$) and $\text{M}'[\text{c-Bi}_5]^+$ ($\text{M}' = \text{Be}, \text{Mg}, \text{Ca}$) clusters. The basal plane of the $\text{M}[\text{c-Bi}_5]$ and $\text{M}'[\text{c-Bi}_5]^+$ clusters having pyramidal structures of C_{5v} symmetry forms a perfect five-membered ring of bismuth atoms, $[\text{c-Bi}_5]^-$, with D_{5h} symmetry. Molecular orbital analysis and estimated NICS values indicate that the planar $[\text{c-Bi}_5]^-$ (D_{5h}) moiety exhibits double ($\sigma + \pi$) aromaticity.

The double ($\sigma + \pi$) aromaticity with the π -aromatic character surpassing, at a different extent, the σ -aromatic character is mirrored on the shape of the NICS_{zz} -scan curves and the excitation energies of the most significant translationally allowed σ - and π -type transitions of the five-membered pnictogen $[\text{c-Pn}_5]^-$ ($\text{Pn} = \text{N}, \text{P}, \text{As}, \text{Sb}, \text{Bi}$) clusters in D_{5h} symmetry [79].

Planar four-, five-, and six-membered rings of transition metal atoms are very rare. Planar transition metal carbonyls containing $\text{M}(\text{CO})_4$ groups are among planar transition metal clusters studied both experimentally and theoretically. Some representative examples are given in Fig. 36. It is interesting to explore the aromaticity/antiaromaticity of such planar transition metal clusters.

A quantitative evidence for the σ -antiaromatic nature of saturated tetranuclear metal-carbonyl clusters $[\text{M}_4(\text{CO})_{12}]$ ($\text{M} = \text{Fe}, \text{Ru}, \text{Os}$), which are similar metal-carbonyl analogs of cyclobutane was recently provided by Corminboeuf et al. [124]. The isotropic NICS of the C_{2v} $[\text{M}_4(\text{CO})_{12}]$ ($\text{M} = \text{Fe}, \text{Ru}, \text{Os}$) clusters are about one-third less negative than those of their trinuclear congeners. Some differences in the magnetic response between cyclobutane and transition metal four-membered rings were identified and analyzed in detail using CMO-NICS (Fig. 37).

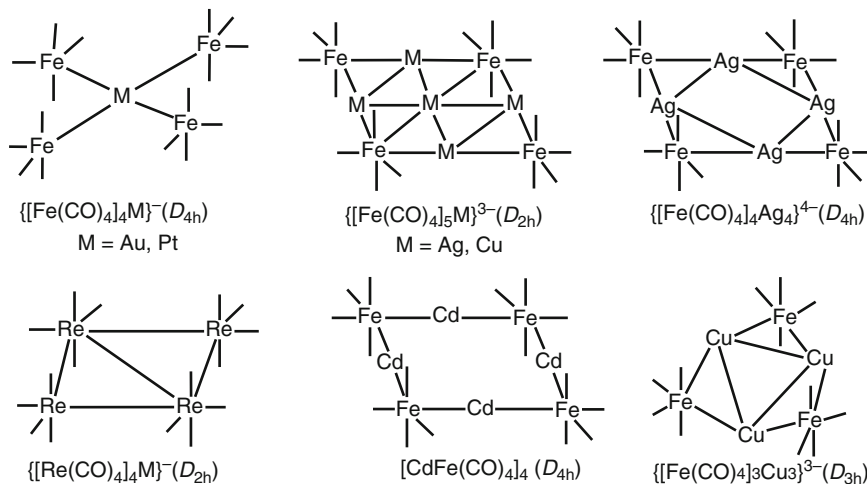


Fig. 36 Schematic structures of representative planar transition metal carbonyl clusters

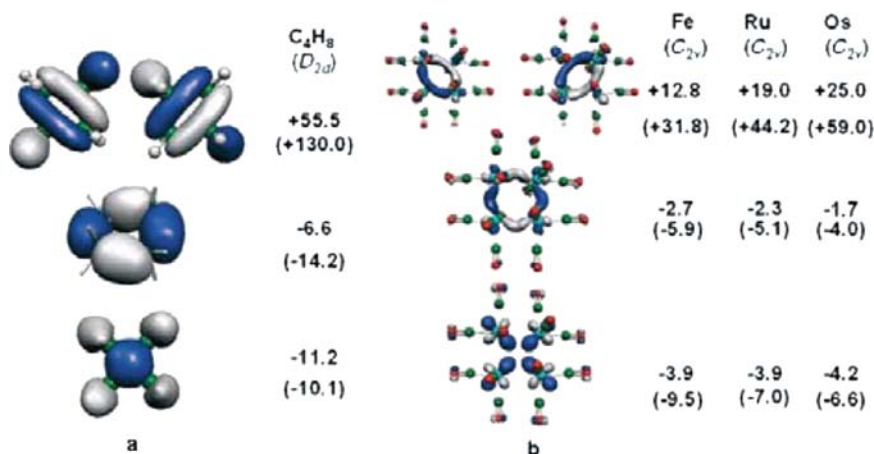


Fig. 37 Isotropic NICS ($NICS_{zz}$ are given in parenthesis) for the Walsh MOs of a) the D_{2d} isomer of C_4H_8 and b) C_{2v} $[M_4(CO)_{12}]$ ($M = Fe, Ru, Os$) clusters. Values are in ppm. The NICS contributions are summed for the degenerate set of MOs. Reprinted with permission from [124]. Copyright: Wiley-VCH

The highest set of σ -type degenerate occupied MOs is dramatically paratropic in D_{2d} cyclobutane (HOMO- $NICS_{zz} = +130.0$ ppm) and appreciably paratropic in the corresponding carbonyl $[M_4(CO)_{12}]$ ($M = Fe, Ru, Os$) complexes (HOMO- $NICS_{zz} = +31.8, +44.5$ and $+59.0$ ppm for $M = Fe, Ru,$ and Os , respectively).

An interesting ternary lanthanum bromide $La_8Br_7Ni_4$ cluster was recently synthesized and structurally characterized [176]. The structure showed condensed La_6

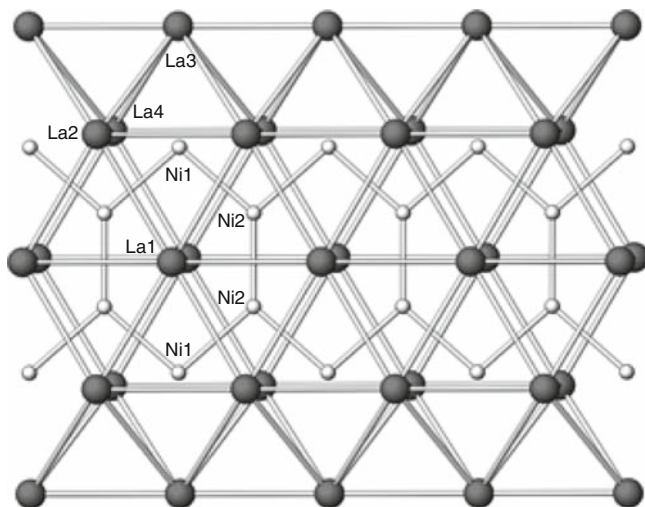


Fig. 38 A double trigonal prism chain with a Ni hexagon ribbon inside in the $\text{La}_8\text{Br}_7\text{Ni}_4$ crystal structure. Reprinted with permission from [176]. *Copyright: ACS Journal Archives*

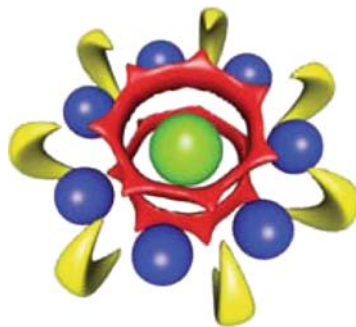
trigonal prisms with the Ni atoms bonded to each other forming ribbons of Ni hexagons (Fig. 38).

Considering that the hexagons of the Ni atoms propagate in the b direction similar to a polyacene ribbon it would be worthwhile to investigate the aromaticity/antiaromaticity of the six-membered rings of Ni atoms.

Two coinage and alkali metal mixed clusters, namely $\text{Na}[c\text{-Cu}_4]^-$ and $\text{Na}[c\text{-Au}_4]^-$, produced with laser vaporization have been characterized experimentally using photoelectron spectroscopy and computationally at correlated ab initio levels [177]. The observed $\text{Na}[c\text{-Cu}_4]^-$ and $\text{Na}[c\text{-Au}_4]^-$ clusters adopt the C_{4v} pyramidal and C_{2v} planar geometries, respectively. The related $\text{Li}[c\text{-Cu}_4]^-$, $\text{Li}[c\text{-Ag}_4]^-$, $\text{Na}[c\text{-Ag}_4]^-$, and $\text{Li}[c\text{-Au}_4]^-$ clusters as well as the neutral $\text{Li}_2[c\text{-Cu}_4]$ and $\text{Na}_2[c\text{-Cu}_4]$ clusters have also been studied computationally. Calculations of the magnetically induced current density in the pyramidal $\text{Li}[c\text{-Cu}_4]^-$ and bipyramidal $\text{Li}_2[c\text{-Cu}_4]$ clusters indicated that the strong ring current is sustained mainly by the HOMO dominated by Cu 4s character, and therefore the $[c\text{-Cu}_4]^{2-}$ ring exhibits pure σ -aromatic character. More recently Mang et al. [178] systematically assessed the minimum polarizability and maximum hardness principles in describing the relative stability of various isomers of all-metal $M[c\text{-MX}_4]^-$ ($\text{Na}[c\text{-Cu}_4]^-$, $\text{Li}[c\text{-Cu}_4]^-$, $\text{Cu}[c\text{-Al}_4]^-$, $\text{Li}[c\text{-Ag}_4]^-$, $\text{Li}[c\text{-Au}_4]^-$, $\text{Na}[c\text{-Ag}_4]^-$, $\text{Na}[c\text{-Au}_4]^-$, $\text{Ag}[c\text{-Al}_4]^-$, $\text{Au}[c\text{-Al}_4]^-$) clusters on the basis of MP2 calculations. According to the minimum polarizability principle the square-pyramidal structure (C_{4v}) is always more stable than the planar (C_{2v}) isomer at various computational levels.

Nguyen et al. [179] using DFT calculations demonstrated that the global minimum of the Cu_7Sc potential energy surface corresponds to a perfect planar geometry involving a seven-membered ring of copper atoms with scandium in its center.

Fig. 39 Map of the full electron localizability indicator for Cu_7Sc ; $\text{ELI-D} = 1.30$. Reprinted with permission from [179]. Copyright: Wiley-VCH



Nucleus-independent chemical shifts [$\text{NICS}(1)_{zz}$ and $\text{NICS}(2)_{zz}$] showed that the Cu_7Sc cluster exhibits aromatic character, which is consistent with the number of 4s electrons of Cu and Sc plus the 3d electrons of Sc satisfying Hückel's rule. According to a $\text{CMO-NICS}(R)_{zz}$ decomposition, the MOs consisting of the 4s AOs are mainly responsible for the aromatic behavior of the cluster. The electron localizability indicator (ELI-D) and its CMO decomposition (partial ELI-D) suggest that a localized basin is formed in Cu_7Sc by the Cu atoms, whereas the two circular localized domains are situated below and above the ring (Fig. 39). The planar Cu_7Sc cluster can thus be considered as an s-aromatic species. These findings agree with the phenomenological shell model.

A comprehensive DFT study of the structural, energetic, spectroscopic (IR, NMR, UV-Vis and photoelectron), electronic, and bonding properties of a new series of hydrocopper(I), hydrosilver(I), and hydrogold(I) analogs of aromatic hydrocarbons formulated as $\text{cyclo-M}_n\text{H}_n$ ($M = \text{Cu, Ag, Au}$; $n = 3-6$) has been reported recently by Tsipis et al. [134,135]. All $\text{cyclo-M}_n\text{H}_n$ molecules adopt structures analogous to the corresponding aromatic hydrocarbons (Fig. 40), which are characterized by perfect planarity, and equalization of all metal-metal bonds in the aromatic metallic rings.

The bonding of all $\text{cyclo-M}_n\text{H}_n$ molecules is characterized by a common ring-shaped electron density, which is constructed by highly delocalized σ -, π -, and δ - type MOs and associated with their aromatic character. The aromaticity of all $\text{cyclo-M}_n\text{H}_n$ ($M = \text{Cu, Ag, Au}$; $n = 3-6$) molecules was estimated by making use of several criteria for aromaticity, such as the $\text{NICS}(0)$ parameter, the relative hardness, $\Delta\eta$, and electrophilicity index, ω . It was further verified on the grounds of a chemical reactivity criterion of aromaticity, that of the interaction of the aromatics with electrophiles, such as Li^+ , Tl^+ , or Ag^+ .

Tsipis and Stalikas [180] using electronic structure calculation methods (DFT) investigated the structural, energetic, spectroscopic (IR, NMR, UV-Vis) and electronic properties of a novel series of hydrido-bridged binary coinage metal clusters with general formulae $\text{cyclo-Cu}_n\text{Ag}_{3-n}(\mu_2\text{-H})_n$ ($n = 1-3$), $\text{cyclo-Cu}_n\text{Ag}_{4-n}(\mu_2\text{-H})_n$ ($n = 1-4$), and $\text{cyclo-Cu}_n\text{Ag}_{5-n}(\mu_2\text{-H})_n$ ($n = 1-5$). The aromaticity of these bimetallic systems was explored by employing a number of established criteria such as the nucleus-independent chemical shift, the hardness,

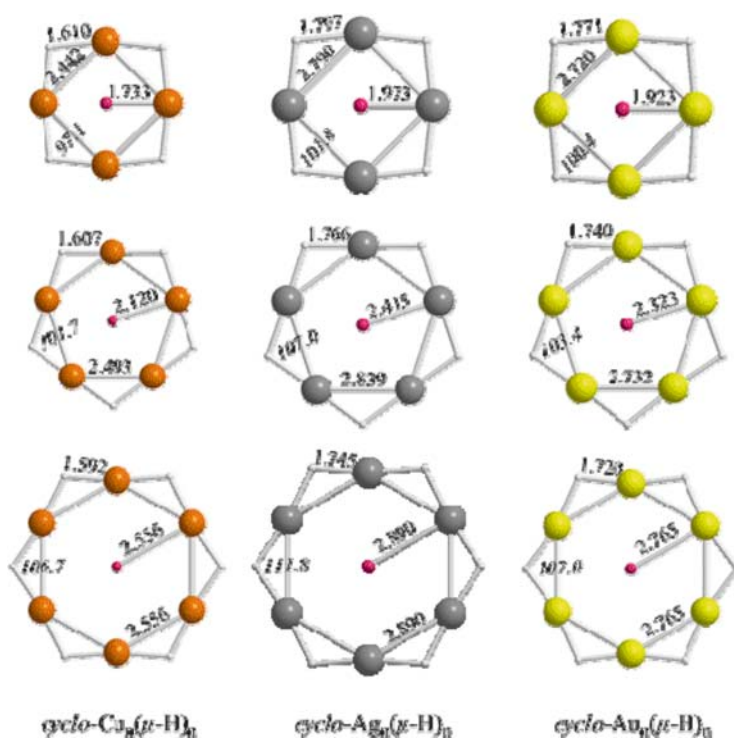


Fig. 40 Equilibrium geometries of the cyclic planar M_nH_n ($M = Cu, Ag, Au; n = 4-6$) molecules computed at the B3LYP level of theory. Reprinted with permission from [134, 135]. Copyright: ACS Journal Archives

η , and the electrophilicity index, ω . It was found that all clusters exhibit aromatic character, the aromaticity decreasing upon increasing the number of Cu atoms in the metallic ring core structure or increasing its size. The hydrido-bridged binary coinage metal clusters show a composite bonding mode involving σ -, π -, and δ -type components. The π -type MOs resulting from the bonding interaction of nd AOs of the metal atoms, delocalized over the entire metallic framework, are analogous to the π -type MOs of the aromatic hydrocarbons.

Li et al. [181, 182] using DFT computational methods predicted that the aromatic Cu_4H_4 and Cu_5H_5 hydrometals can host planar tetracoordinated and pentacoordinated nonmetals at the center of the rings forming perfect square planar and pentagonal complexes Cu_4H_4X and Cu_5H_5X ($X = B, C, N, O$).

Successive nucleophilic attack of the parent aromatic [$cyclo-Cu_4(\mu-H)_4$] molecules by a series of nucleophiles Nuc (Nuc = N_2, CO, H_2O, NH_3 , and PH_3) affords novel [$cyclo-Cu_4(\mu-H)_4Nuc_n$] clusters, which, depending on the nature of Nuc and the degree of substitution, adopt planar, bent, or 3-D tetrahedral geometries (Fig. 41) [183]. The 3-D structures are obtained for the higher degrees of substitution, that is in the [$cyclo-Cu_4(\mu-H)_4Nuc_3$] and [$cyclo-Cu_4(\mu-H)_4Nuc_4$] clusters.

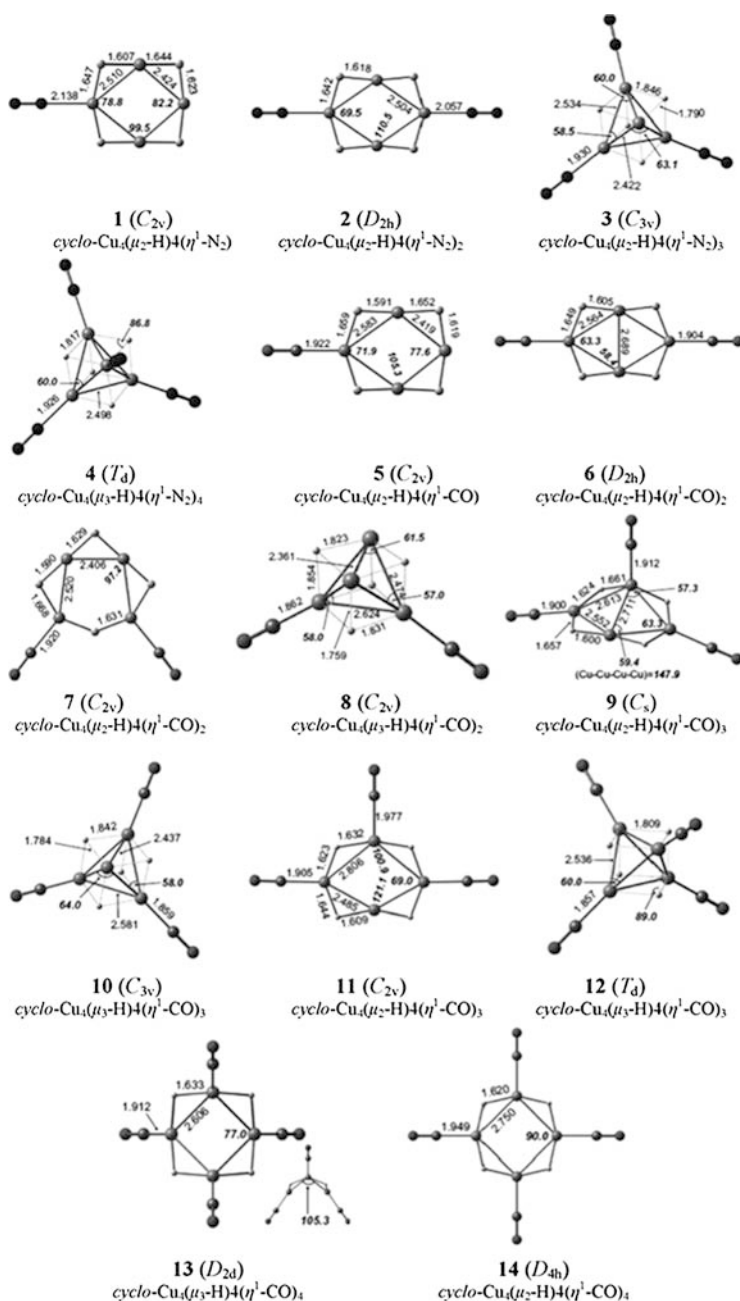


Fig. 41 Equilibrium geometries (bond lengths in Å, angles in degrees) of the stationary points located on the PES of the $[\text{cyclo-Cu}_4(\mu\text{-H})_4\text{Nuc}_n]$ ($n = 1-4$; Nuc = N₂, CO) molecules computed at the B3LYP/6-311+G** level. Reprinted with permission from [183]. Copyright: Bentham Science Publishers

The [*cyclo*-Cu₄(μ-H)₄Nuc_n] molecules exhibit aromatic character, which is primarily due to 4s and 3d cyclic electron delocalization over the Cu₄ framework (s and d orbital aromaticity). The aromaticity of the novel ligand-stabilized tetranuclear Cu₄ clusters was verified by the NICS(0), NICS(1), and their out-of-plane components NICS_{zz}(0), NICS_{zz}(1) along with the NICS scan pictures. Regarding the aromaticity of the [*cyclo*-Cu₄(μ-H)₄Nuc_n] it was found that increasing the number of the attacking nucleophiles increases the diatropic response of the aromatic tetranuclear Cu₄ clusters.

10 Aromaticity/Antiaromaticity in Lanthanide and Actinide Chemistry (f-Orbital Aromaticity)

Luo and Hou [184] performing ab initio MP2 calculations on binary lanthanide hydride clusters Ln₃H₉ and Ln₄H₁₂ (Ln = La, Gd, and Lu) predicted their stability and their possible existence, since their formation was found to be thermodynamically favorable. Among the binary clusters the cyclic pentacoordinated Ln₃H₉ one adopting an equilibrium geometry of D_{3h} symmetry in its ¹A₁' ground state (Fig. 41) was found to exhibit significant aromaticity. The estimated NICS(0) value of -8.0 ppm for the Ln₃H₉ (D_{3h}) cluster is comparable to that of benzene (-9.3 ppm). The aromaticity of Ln₃H₉(D_{3h}) cluster, arising primarily from highly delocalized MOs contributed from the overlap of Ln 5d and H 1s orbitals, suggests that the bridging hydride ligands play an important role in the electron delocalization of these systems.

Very recently we have communicated on the role of the 5f orbitals in bonding, aromaticity, and reactivity of planar isocyclic and heterocyclic uranium clusters [185]. Using electronic structure calculation methods (DFT) we demonstrated that the model planar isocyclic *cyclo*-U_nX_n (n = 3, 4; X = O, NH) and heterocyclic *cyclo*-U_n(μ₂-X)_n (n = 3, 4; X = C, CH, NH) clusters are thermodynamically stable molecules with respect to their dissociation either to "free" U and X moieties or to their monomeric UX species. The equilibrium geometries of the *cyclo*-U_nX_n and *cyclo*-U_n(μ₂-X)_n clusters are shown in Fig. 42.

The bonding in the *cyclo*-U_nX_n (n = 3, 4; X = OH, NH) and *cyclo*-U_n(μ₂-X)_n (n = 3, 4; X = C, CH, NH) clusters is characterized by a ring-shaped electron density. The U₃ and U₄ rings exhibit a composite bonding pattern involving highly delocalized σ-, π-, δ-, and φ-type MOs resulting from a completely bonding interaction of the 5f AOs of each U atom of the ring. The 3-D contour surfaces of the valence MOs describing the cyclic delocalization of the electron density in the *cyclo*-U_nX_n (n = 3, 4; X = OH, NH) clusters are visualized in Fig. 43.

It is evident that the 5f orbitals of the uranium metal centers play a key role in the bonding of the aforementioned f-block metal systems significantly contributing to the cyclic electron delocalization and the associated magnetic diatropic response. The aromaticity of the *cyclo*-U_nX_n (n = 3, 4; X = OH, NH) and *cyclo*-U_n(μ₂-X)_n (n = 3, 4; X = C, CH, NH) clusters was verified by the magnetic criterion of

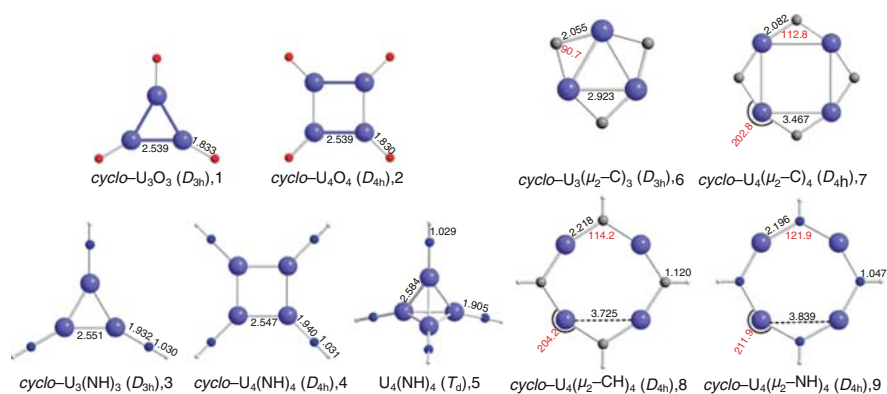


Fig. 42 Equilibrium geometries (bond lengths in Å, angles in degrees) of the U_nX_n ($n = 3, 4$; $X = OH, NH$) and $cyclo-U_n(\mu_2-X)_n$ ($n = 3, 4$; $X = C, CH, NH$) clusters computed at the BP86/SDD(U)6–31G** (X) level. Reprinted with permission from [185]. Copyright: ACS Journal Archives

aromaticity/antiaromaticity of a molecule, that of the nucleus-independent chemical shift, NICS(0), NICS(1), NICS_{zz}(0), and the most refined NICS_{zz}(1) index, along with the NICS scan profiles. According to the magnetic criterion all clusters exhibited high negative NICS_{zz}(0) and NICS_{zz}(1) values ranging from –135.2 to –359.9 ppm and from –40.1 to –170.6 ppm, respectively, and therefore are strongly aromatic. This type of aromaticity based on the electron delocalization of 5f orbitals of the U metal centers can be considered as the first example of the f-orbital aromaticity reported so far.

The size of the U_4 ring in the $cyclo-U_4(\mu_2-C)_4$ cluster can accommodate inside the ring center a planar tetracoordinate element E (E = H, C, Si) comfortably affording thermodynamically stable $E@[c-U_4(\mu_2-C)_4]$ molecules. The larger size of the ten-membered $cyclo-U_5(\mu_2-C)_5$ ring can capture at the center the bigger U atom in a pentacoordinate environment affording the thermodynamically stable $U@[c-U_5(\mu_2-C)_5]$ cluster. The $E@[c-U_4(\mu_2-C)_4]$ and the $U@[c-U_5(\mu_2-C)_5]$ clusters keep to some extent the aromatic character of the respective rings of the U atoms. Moreover, NBO analyses reveal significant electron transfer from the surrounding uranium atoms to the central E atoms, which acquire negative natural atomic charges and significantly increase the np_z orbital occupancies of the E atoms.

11 Epilog

In this study I reviewed the recent advances in the newly emerged interdisciplinary field of “bare” and “ligand-stabilized” rings of metal atoms with particular emphasis on the structural, energetic, electronic, and bonding properties of a variety of

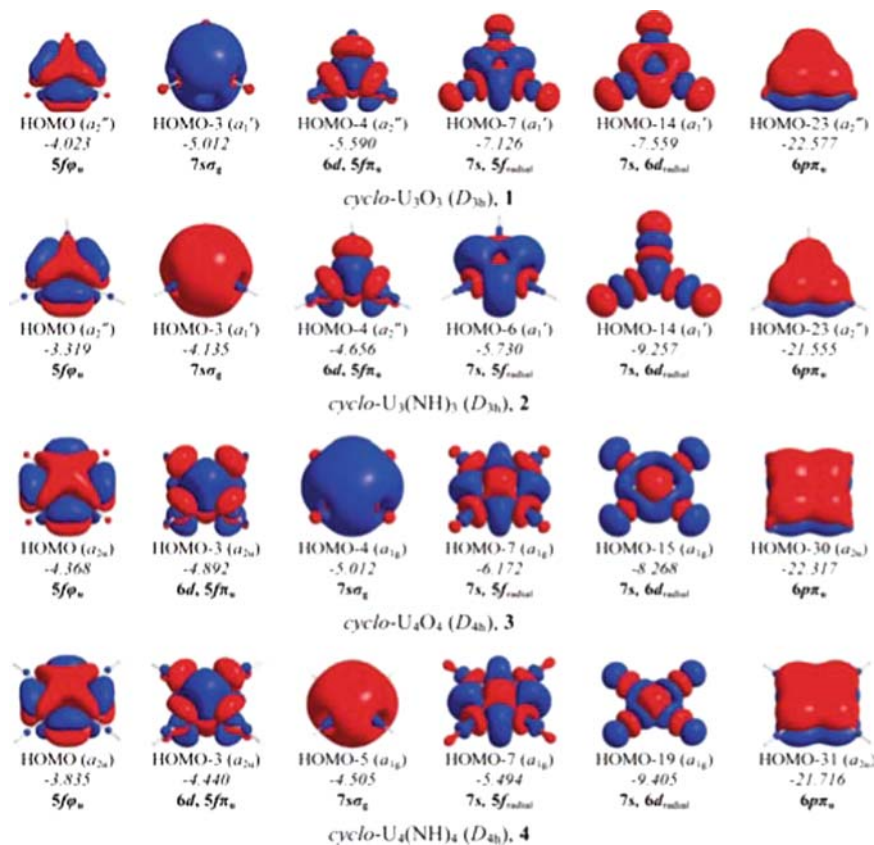


Fig. 43 Three-dimensional contour surfaces of the valence MOs responsible for the cyclic delocalization of the electron density in the U_3 and U_5 rings of the $cyclo-U_nX_n$ ($n = 3, 4$; $X = OH, NH$) clusters (figures in italics are the orbital energies, in eV). Reprinted with permission from [185]. Copyright: ACS Journal Archives

novel “all-metal” rings studied so far. Attempts have been made to throw light on the origin of aromaticity/antiaromaticity in these novel rings of metal atoms illustrating its multifold character. “Bare” and “ligand-stabilized” aromatic/antiaromatic “all-metal” systems represent one of the “new frontiers” that promise to keep aromatic/antiaromatic chemistry vibrant well into the twenty-first century. Apart from the aromaticity/antiaromaticity properties of the metallic rings, other physical, chemical, optical, biological, and technical properties are worth to be investigated in the future for finding applications as catalysts, drugs, and other materials of technological interest.

References

1. Fallah-Bagher-Shaidaei H, Wannere CS, Corminboeuf C, Puchta R, Schleyer PVR (2006) *Org Lett* 8:863
2. Wannere CS, Corminboeuf C, Allen WD, Schaefer HF, Schleyer PVR (2005) *Org Lett* 7:147
3. Chen Z, Wannere CS, Corminboeuf C, Puchta R, Schleyer PVR (2005) *Chem Rev* 105:3842
4. Faglioni F, Ligabue A, Pelloni S, Soncini A, Viglione RG, Ferraro MB, Zanasi R, Lazzarotti P (2005) *Org Lett* 7:3457
5. Lazzarotti P (2004) *Phys Chem Chem Phys* 6:217
6. Krygowski TM, Cyranski MK (2004) *Phys Chem Chem Phys* 6:249
7. Aihara J (2004) *Bull Chem Soc Jpn* 77:2179
8. Schleyer PVR (2001) *Chem Rev* 101:1115
9. Mitchell RH (2001) *Chem Rev* 101:1301
10. Kekulé A (1865) *Bull Chem Soc Fr* 3:98
11. Kekulé A (1866) *Justus Liebigs Ann Chem* 137:1866
12. Masui H (2001) *Coord Chem Rev* 219:957
13. Tsiapis CA (2005) *Coord Chem Rev* 249:2740
14. Boldyrev AI, Wang L-S (2005) *Chem Rev* 105:3716
15. Wang Y, Robinson GH (2007) *Organometallics* 26:2
16. Lee VYa, Sekiguchi A (2007) *Angew Chem Int Ed* 46:2
17. Zubarev DYU, Averkiev BB, Zhai H-J, Wang L-S, Boldyrev AI (2008) *Phys Chem Chem Phys* 10:257
18. Schleyer PVR (2001) Thematic issue “Aromaticity” *Chem Rev* 101:5
19. Schleyer PVR (2001) Thematic issue “Delocalization Pi and Sigma” *Chem Rev* 105:10
20. Special edition on New Perspectives on Aromaticity (2004) *Phys Chem Chem Phys* 6
21. Mirkin VI, Glukhovtsev MN, Simkin BY (1994) *Aromaticity and antiaromaticity: electronic and structural aspects*. Wiley, New York
22. Corminboeuf C, Heine T, Seifert G, Schleyer PVR, Weber J (2004) *Phys Chem Chem Phys* 6:273
23. Havenith RWA, Engelberts JJ, Fowler PW, Steiner E, van Lenthe JH, Lazzarotti P (2004) *Phys Chem Chem Phys* 6 289
24. Gomes JANF, Mallion RB (2001) *Chem Rev* 101:1349
25. Krygowski TM, Cyranski MK (2001) *Chem Rev* 101:1385
26. Katritzky AR, Jug K, Oniciu DC (2001) *Chem Rev* 101:1421
27. De Proft F, Geerlings P (2001) *Chem Rev* 101:1451
28. Lazzarotti P (2000) *Progr Nucl Magn Reson Spectrosc* 36:1
29. Williams RV, Armantrout JR, Twamley B, Mitchell RH, Ward TR, Bandyopadhyay S (2002) *J Am Chem Soc* 124:13495
30. Hutter DH, Flygare WH (1976) *Top Curr Chem* 63:89 and references therein
31. Flygare WH (1974) *Chem Rev* 74:653
32. Dauben HJ Jr, Wilson JD, Laity JL (1968) *J Am Chem Soc* 90:811
33. Lazzarotti P (2000) In: Emsley JW, Feeney J, Sutcliffe LH (eds) *Progress in nuclear magnetic resonance spectroscopy*. Elsevier, Amsterdam, The Netherlands p 1
34. Steiner E, Fowler PW (2001) *J Phys Chem A* 105:9553
35. Periyasamy G, Burton NA, Hillier IH, Thomas JMH (2008) *J Phys Chem A* 112:5960
36. Steiner E, Fowler PW (2001) *Chem Commun* 2220
37. Fowler PW, Steiner E, Havenith RWA, Jenneskens LW (2004) *Magn Reson Chem* 42:S68
38. Zanasi R, Fowler PW (1995) *Chem Phys Lett* 238:270
39. Fowler PW, Zanasi R, Cadioli B, Steiner E (1996) *Chem Phys Lett* 251:132
40. Keith TA, Bader RFW (1993) *Chem Phys Lett* 210:223
41. Keith TA, Bader RFW (1993) *J Chem Phys* 99:3669
42. Zanasi R, Lazzarotti P (1996) *Int J Quantum Chem* 60:249
43. Merino G, Heine T, Seifert G (2004) *Chem Eur J* 10:4367

44. Schleyer PVR, Maerker C, Dransfeld A, Jiao H, van Eikema Hommes NJR (1996) *J Am Chem Soc* 118:6317
45. Schleyer PVR, Jiao H (1996) *Pure Appl Chem* 68:209
46. Schleyer PVR, Manoharan M, Wang Z, Kiran XB, Jiao H, Puchta R, van Eikema Hommes NJR (2001) *Org Lett* 3:2465
47. Schleyer PVR, Jiao H, van Eikema Hommes NJR, Markin VG, Malkinba OL (1997) *J Am Chem Soc* 119:12669
48. Heine T, Schleyer PVR, Corminboeuf C, Seifert D, Reviakine R, Weber J (2003) *J Phys Chem A* 107:6470
49. Klod S, Kleinpeter E (2001) *J Chem Soc Perkin Trans 2*:1893
50. Klod S, Kleinpeter E (2002) *J Chem Soc Perkin Trans 2*:1506
51. Wodrich MD, Corminboeuf C, Park SS, Schleyer PVR (2007) *Chem Eur J* 13:4582
52. Bohmann JA, Weinhold F, Farrar TC (1997) *J Chem Phys* 107:173
53. Corminboeuf C, Heine T, Weber J (2003) *Phys Chem Chem Phys* 5:246
54. Stanger A (2006) *J Org Chem* 71:883
55. Stanger A (2006) *Chem Eur J* 12:2745
56. Poater J, Bofill JM, Alemany P, Solà M (2006) *J Org Chem* 71:1700
57. Jiménez-Halla JOC, Matito E, Robles J, Solà M (2006) *J Organometal Chem* 691:4359
58. Hofmann M, Berndt A (2006) *Heteroatom Chem* 17:224
59. Cheeseman JP, Trucks GW, Keith TA, Frisch MJ (1996) *J Chem Phys* 104:5497
60. Geuenich D, Hess K, Kohler F, Herges R (2005) *Chem Rev* 105:3758
61. Juselius J, Sundholm D (1999) *Phys Chem Chem Phys* 1:3429
62. Juselius J, Sundholm D, Gauss J (2004) *J Chem Phys* 121:3952
63. Bader RFW (1985) *Acc Chem Res* 18:9
64. Bader RFW (1991) *Chem Rev* 91:893
65. Bader RFW (1990) *Atoms in molecules: a quantum theory*, Oxford University Press, Oxford
66. Howard ST, Krygowski TM (1997) *Can J Chem* 75:117
67. Silvi B, Savin A (1994) *Nature* 371:683
68. Becke A, Edgecombe K (1990) *J Chem Phys* 92:5397
69. Chesnut DB, Bartolotti LJ (2000) *Chem Phys* 253:1
70. Fuster F, Savin A, Silvi B (2000) *J Phys Chem A* 104:852
71. Silvi B (2004) *Phys Chem Chem Phys* 6:256
72. Santos JC, Tiznado W, Contreras R, Fuentealba P (2004) *J Chem Phys* 120:1670
73. Bean GP (1998) *J Org Chem* 63:297
74. Sadlej-Sosnowska N (2001) *J Org Chem* 66:8737
75. Zubarev DYU, Boldyrev AI (2008) *Phys Chem Chem Phys* 10:5207
76. Bishop DM, Chaillet M, Larrieu K, Pouchan C (1984) *Mol Phys* 51:179
77. Alexandrova AN, Boldyrev AI (2003) *J Phys Chem A* 107:554
78. Havenith RWA, De Proft F, Fowler PW, Geerlings P (2005) *Chem Phys Lett* 407:391
79. Tsipis AC, Depastas IG, Tsipis CA (2010) *Symmetry, Special Issue Aromaticity and Molecular Symmetry*.
80. Yong L, Wu SD, Chi XX (2007) *Int J Quantum Chem* 107:722
81. Kuznetsov AE, Boldyrev AI (2004) *Chem Phys Lett* 388:452
82. Middleton R, Klein J (1999) *Phys Rev A* 60:3786
83. Kaplan IG, Dolgounitcheva O, Watts JD, Ortiz JV (2002) *J Chem Phys* 117:3687
84. Roy DR, Chattaraj PK (2008) *J Phys Chem A* 112:1612
85. Ortiz JV (1999) *Adv Quantum Chem* 35:33
86. Ortiz JV (2004) *Int J Quantum Chem* 100:1131
87. Chattaraj PK, Giri S (2008) *J Mol Struct (THEOCHEM)* 865:53
88. Kuznetsov AE, Boldyrev AI (2002) *Struct Chem* 13:141
89. Zhai H-J, Wang L-S, Alexandrova AN, Boldyrev AI, Zakrzewski VG (2003) *J Phys Chem A* 107:9319
90. Zhan C-G, Zheng F, Dixon DA (2002) *J Am Chem Soc* 124:14795
91. Wielgus P, Roszak S, Majumdar D, Saloni J, Leszczynski J (2008) *J Chem Phys* 128:144305
92. Bing D, Nguyen QC, Fan X-F, Kuo J-L (2008) *J Phys Chem A* 112:2235

93. Xu W, Zhao Y, Li Q, Xie Y, Schaefer HF III (2004) *Mol Phys* 102:579
94. Gopakumar G, Lievens P, Nguyen MT (2007) *J Phys Chem A* 111:4353
95. Zubarev DY, Boldyrev AI, Li X, Wang L-S (2006) *J Phys Chem* 110:9743
96. Zhao Y, Xu W, Li Q, Xie Y, Schaefer HF III (2004) *J Comput Chem* 25:907
97. Zhao J, Zhou X, Chen X, Wang J, Jellinek J (2006) *Phys Rev B* 73:115418
98. Lippa TP, Xu S-J, Lyapustina SA, Nilles JM, Bowen KH (1998) *J Chem Phys* 109:10727
99. BelBruno JJ (2003) *Heteroatom Chem* 14:189
100. Gausa M, Kaschner R, Seifert G, Faehrmann JH, Lutz HO, Meiwes-Broer K-H (1996) *J Chem Phys* 104:9719
101. Jia JM, Chen GB, Shi DN, Wang BL (2008) *Eur Phys J D* 47:359
102. Chi XX, Liu Y (2007) *Int J Quantum Chem* 107:1886
103. Averkiev BB, Boldyrev AI (2007) *J Phys Chem A* 111:12864
104. Wang B, Zhai HJ, Huang X, Wang L-S (2008) *J Phys Chem A* 112:10962
105. Zhai HJ, Averkiev BB, Zubarev DY, Wang L-S, Boldyrev AI (2007) *Angew Chem Int Ed* 46:1
106. Li S-D, Miao C-Q, Guo J-C (2008) *Eur J Inorg Chem* 1205
107. Huang X, Zhai HJ, Kiran B, Wang L-S (2005) *Angew Chem Int Ed* 44:7251
108. Knight LB Jr, Woodward RW, van Zee RJ, Weltner W Jr (1983) *J Chem Phys* 79:5820
109. Moskovits M, DiLella DP, Limm W (1984) *J Chem Phys* 80:626
110. Walch SP, Bauschlicher CW Jr (1985) *J Chem Phys* 83:5735
111. DiLella DP, Limm W, Lipson RH, Moskovits M, Taylor KV (1982) *J Chem Phys* 77:5263
112. Ozin GA, Baker MD, Mitchell SA, McIntish DF (1983) *Angew Chem Int Ed* 22:166
113. Bier KD, Haslett TL, Kirwood AD, Moskovits M (1988) *J Chem Phys* 89:6
114. Nour EM, Alfaro-Franco C, Gingerich KA, Laane J (1987) *J Chem Phys* 86:4779
115. Walch SP (1987) *J Chem Phys* 86:5082 and references therein
116. Woodward JR, Cobb SH, Gole JL (1988) *J Phys Chem* 92:1404
117. Ervin KM, Ho J, Lineberger WC (1988) *J Chem Phys* 89:4514
118. Balasubramanian K (1989) *J Chem Phys* 91:307
119. Eberhardt W, Fayet P, Cox DM, Fu Z, Kaldor A, Sherwood R, Sondericker D (1990) *Phys Lett* 64:780
120. Muller U, Sattler K, Xhie J, Venkataswaran N, Raina G (1991) *J Vac Sci Technol B* 9:829
121. Wang H, Carter EA (1992) *J Phys Chem* 96:1197
122. Gutsev GL, Bauschlicher CW Jr (2003) *J Phys Chem A* 107:7013
123. King RB (2003) *Inorg Chim Acta* 350:126
124. Corminboeuf C, Schleyer PVR, King RB (2007) *Chem Eur J* 13:978
125. Tshipis AC, Kefalidis CE, Tshipis CA (2007) *J Am Chem Soc* 129:13905
126. Pyykkö P (2004) *Angew Chem Int Ed* 43:4412
127. Pyykkö P (2005) *Inorg Chim Acta* 358:4113
128. Häkkinen H, Moseler M, Landman U (2002) *Phys Rev Lett* 89:033401
129. Fernández EM, Soler JM, Garzón IL, Balbás LC (2004) *Phys Rev B* 70:165403
130. Fernández EM, Soler JM, Garzón IL, Balbás LC (2006) *Phys Rev B* 73:235433
131. Öüt S, Idrobo JC, Jellinek J, Wang J (2006) *J Clust Sci* 17:609
132. Lecoultre S, Rydlo A, Félix C (2007) *J Chem Phys* 126:204507
133. Bonai-Koutecký V, Pittner J, Boiron M, Fantucci P (1999) *J Chem Phys* 110:3876
134. Tshipis AC, Tshipis CA (2003) *J Am Chem Soc* 125:1136
135. Tshipis CA, Karagiannis EE, Kladou PF, Tshipis AC (2004) *J Am Chem Soc* 126:12916
136. Tshipis AC, Tshipis CA (2005) *J Am Chem Soc* 127:10623
137. Tshipis CA, Kefalidis CE, Charistos ND (2007) In: Cartere TW, Verley KS (eds) *Coordination chemistry research progress*. Nova Science Publishers, New York, p 201–215
138. Muniz J, Sansores LE, Martinez A, Salcedo R (2008) *J Mol Model* 14:417
139. Kiran B, Li X, Zhai H-J, Wang L-S (2006) *J Chem Phys* 125:133204
140. Tshipis CA, Depastas IG, Kefalidis CE (2007) *J Comput Chem* 28:1893
141. Tekali SM, Cundari TR, Omary MA (2008) *J Am Chem Soc* 130:1669
142. Yong L, Chi X (2007) *J Mol Struct (THEOCHEM)* 818:93
143. Khatua S, Roy DR, Bultinck P, Bhattacharjee M, Chattaraj PK (2008) *Phys Chem Chem Phys* 10:2461

144. Alexandrova AN, Boldyrev AI (2003) *J Phys Chem A* 107:554
145. Li X, Kuznetsov AE, Zhang HE, Boldyrev AI (2001) *Science* 291:859
146. Islas R, Heine T, Merino G (2007) *J Chem Theory Comput* 3:775
147. Jusélius J, Straka M, Sundholm D (2001) *J Phys Chem A* 105:9939
148. Lin Y-C, Juselius J, Sundholm D (2005) *J Chem Phys* 122:214308
149. Fowler PW, Havenith RWA, Steiner E (2001) *Chem Phys Lett* 342:85
150. Fowler PW, Havenith RWA, Steiner E (2002) *Chem Phys Lett* 359:530
151. Havenith RWA, Fowler PW, Steiner E, Shetty S, Kanhere D, Pal S (2004) *Phys Chem Chem Phys* 6:285
152. Havenith RWA, Fowler PW (2006) *Phys Chem Chem Phys* 8:3383
153. Chen Z, Corminboeuf C, Bohmann J, Schleyer PVR (2003) *J Am Chem Soc* 125:13930
154. Zhan C-G, Zheng F, Dixon DA (2002) *J Am Chem Soc* 124:14795
155. Boldyrev AI, Kuznetsov AE (2002) *Inorg Chem* 41:532
156. Havenith RWA, van Lenthe JH (2004) *Chem Phys Lett* 385:198
157. Chattaraj PK, Roy DR, Elango M, Subramanian V (2006) *J Mol Struct (THEOCHEM)* 759:109
158. Mandado M, Krishtal A, van Alensoy C, Bultinck P, Hermida-Ramon IM (2007) *J Phys Chem A* 111:11885
159. Mallajosyula SS, Datta A, Pati SK (2006) *J Phys Chem B* 110:20098
160. Datta A, Mallajosyula SS, Pati SK (2007) *Acc Chem Res* 40:213
161. Mang C-Y, Liu C, Zhou J, Li Z, Wu K (2007) *Chem Phys Lett* 438:20
162. Mang C-Y, Zhao X, He L-X, Liu C-P, Wu K-C (2008) *J Phys Chem A* 112:1661
163. Satpati P, Sebastian KL (2008) *Inorg Chem* 47:2098
164. Islas R, Heine T, Merino G (2007) *J Chem Theory Comput* 3:775
165. Zhang RJ, Wang XQ, Cheng FL (2007) *J Clust Sci* 18:431
166. Mercero JM, Formoso E, Matxain JM, Eriksson LA, Ugalde JM (2006) *Chem Eur J* 12:4495
167. Yang L-M, Ding Y-H, Sun C-C (2007) *Eur J Chem* 13:2546
168. Pei Y, An W, Ito K, Schleyer PVR, Zeng XC (2008) *J Am Chem Soc* 130:10394
169. Todorov I, Senov SC (2005) *Inorg Chem* 44:5361
170. Todorov I, Senov SC (2004) *Inorg Chem* 43:6490
171. Xu WG, Jin B (2005) *J Mol Struct (THEOCHEM)* 731:61
172. Kraus F, Hanauer T, Korber N (2006) *Inorg Chem* 45:1117
173. Xu WG, Jin B (2005) *J Mol Struct (THEOCHEM)* 759:101
174. Li Z, Zhao C, Chen L (2007) *J Mol Struct (THEOCHEM)* 807:17
175. Li Z, Zhao C, Chen L (2008) *J Mol Struct (THEOCHEM)* 854:46
176. Zheng C, Mattausch H, Hoch C, Simon A (2008) *Inorg Chem* 47:10565
177. Lin Y-C, Sundholm D, Jusélius J, Cui L-F, Li X, Zhai H-J, Wang L-S (2006) *J Phys Chem A* 110:4244
178. Mang C-Y, Zhao X, He L-X, Liu C-P, Wu K-C (2008) *J Phys Chem A* 112:1661
179. Hölzl T, Janssens E, Veldeman, N, Veszprémi T, Lievens P, Nguyen MT (2008) *ChemPhysChem* 9:833
180. Tsipis AC, Stalikas AV (2007) 31:852
181. Li S-D, Miao C-Q, Ren G-M (2004) *Eur J Inorg Chem* 2232
182. Li S-D, Ren G-M, Miao C-Q, Jin Z-H (2004) *Angew Chem Int Ed* 43:1371
183. Tsipis CA, Charistos ND (2008) *Open Mech Eng J* 2:12
184. Luo Y, Hou Z (2008) *J Phys Chem* 112:635
185. Tsipis AC, Kefalidis CE, Tsipis CA (2008) *J Am Chem Soc* 130:9144

All-Transition Metal Aromaticity and Antiaromaticity

Alina P. Sergeeva, Boris B. Averkiev, and Alexander I. Boldyrev

Abstract Though aromaticity in compounds containing a transition-metal atom has already been discussed for quite a long time, aromaticity in all-transition metal systems have been recognized only recently. There are examples of σ -, π -, and δ -aromaticity based on s-, p-, and d-AOs. We derived the counting rules for σ -, π -, δ -, and ϕ -aromaticity/antiaromaticity for both singlet/triplet coupled model triatomic and tetratomic systems so that one could use those to rationalize aromaticity and antiaromaticity in all-transition metal systems. These rules can be easily extended for any cyclic systems composed out of odd or even number of atoms. We elucidated the application of these rules to the all-transition metal cyclic systems: $\text{Au}_3^+/\text{Au}_3^-$, Na_2Zn_3 , Hg_4^{6-} , $\text{Mo}_3\text{O}_9^{2-}$, Sc_3^- , Hf_3 , and Ta_3^- clusters. We believe that the use of concepts of aromaticity, antiaromaticity and conflicting aromaticity can be an important theoretical tool for deciphering chemical bonding in various known and novel chemical compounds containing transition metal atoms.

Keywords Adaptive natural density partitioning · All transition metal aromaticity · Chemical bonding · Cluster · Multifold aromaticity

Contents

1	Introduction	276
2	Model Consideration of σ -, π -, δ -, and ϕ -Aromaticity/Antiaromaticity	277
2.1	s-, p-, d-, f-AO Based σ -Aromaticity/Antiaromaticity	289
2.2	p-, d-, f-AO Based π -Aromaticity/Antiaromaticity	292
2.3	d-, f-AO Based δ -Aromaticity/Antiaromaticity	293
2.4	f-AO Based ϕ -Aromaticity/Antiaromaticity	294
3	Examples of Aromatic/Antiaromatic Transition Metal Systems	294
3.1	s-AO Based σ -Aromaticity and σ -Antiaromaticity	295
3.2	p-AO-Based Aromaticity and Antiaromaticity	296
3.3	d-AO Based Aromaticity and Antiaromaticity	298

4	Overview	301
	References	303

σ -	Sigma-
σ_r -	Sigma-radial-
σ_t -	Sigma-tangential-
π -	Pi-
π_r -	Pi-radial-
π_t -	Pi-tangential-
δ -	Delta-
δ_r -	Delta-radial-
δ_t -	Delta-tangential-
ϕ -	Phi-
AdNDP	Adaptive natural density partitioning
AO	Atomic orbital
AOs	Atomic orbitals
$ e $	Electron
MO	Molecular orbital
MOs	Molecular orbitals
nc-2e	n center two electron
ON	Occupation number

1 Introduction

Chemical bonding in transition metal compounds is more diverse and complicated compared to main group compounds due to participation of d- and f-atomic orbitals. In particular, in 1964, Cotton and coworkers published a milestone work on the $K_2[Re_2Cl_8] \cdot 2H_2O$ compound [1], in which they showed the presence of a new type of a chemical bond – δ -bond between two Re atoms. This finding was the first example of the bond order of four. This paper and follow-up works led to the establishment of a new branch of inorganic chemistry involving multiple metal–metal bonding [2] with bond orders higher than 3, the maximum allowed for main group molecules. Recently, Power and coworkers reported the synthesis of $Ar'CrCrAr'$ (where Ar' is the bulky aryl group $C_6H_3-2,6(C_6H_3-2,6-Pr_2^i)_2$) with a quintuple bond ($\sigma^2\pi^4\delta^4$) between two Cr atoms [3]. δ -bonds between two transition metal atoms suggests that there may exist multicenter transition metal species with completely delocalized cyclic δ -bond, thus raising the possibility of δ -aromaticity analogous to π - or σ -aromaticity in main group systems. Indeed, the first δ -delocalized bond and δ -aromaticity was recently discovered in the $Ta_3O_3^-$ cluster by Zhai et al. [4]. Averkiev and Boldyrev [5] theoretically predicted the first example of triple (σ -, π -, and δ -) aromaticity in Hf_3 cluster in the lowest singlet state. Tsipis, Kefalidis, and Tsipis showed that the delocalized ϕ electron density in the rings of planar isocyclic and heterocyclic uranium clusters could be associated with cyclic electron delocalization [6], which is a characteristic feature of aromaticity.

Thus, transition metal compounds have the striking feature of chemical bonding – the possibility of the multifold nature of aromaticity, antiaromaticity, and conflicting aromaticity [7]. When only *s*-atomic orbitals (AOs) are involved in chemical bonding, one may expect only σ -aromaticity or σ -antiaromaticity. If *p*-AOs are involved, σ -tangential (σ_t -), σ -radial (σ_r -), and π -aromaticity/antiaromaticity could occur. In this case, there can be multiple (σ - and π -) aromaticity, multiple (σ - and π -) antiaromaticity, and conflicting aromaticity (simultaneous σ -aromaticity and π -antiaromaticity or σ -antiaromaticity and π -aromaticity). If *d*-AOs are involved in chemical bonding, σ -tangential (σ_t -), σ -radial (σ_r -), π -tangential (π_t -), π -radial (π_r -), and δ -aromaticity/antiaromaticity could occur. In this case, there can be multiple (σ -, π -, and δ -) aromaticity, multiple (σ -, π -, and δ -) antiaromaticity, and conflicting aromaticity (simultaneous aromaticity and antiaromaticity among the three σ -, π -, and δ -types).

In the follow-up sections we discuss in detail these new types of bonding in model systems and also show examples of chemical species manifesting these types of aromaticity.

Summary: Though multiple bonding in transition metal compounds had been discussed in the literature for more than four decades, the discovery of aromaticity in all transition metal systems (cyclic systems composed out of transition metal atoms) was made only few years ago. In the compounds composed out of main group elements one may expect sigma- (σ -) and pi- (π -) aromaticity only. In all transition metal systems one may expect two new types of aromaticity: delta- (δ -) and phi- (ϕ -) in addition to σ - and π -aromaticity.

2 Model Consideration of σ -, π -, δ -, and ϕ -Aromaticity/Antiaromaticity

In order to develop a comprehensive understanding of chemical bonding in all-transition metal clusters we would like to present a concise picture of delocalized bonding including *s*-, *p*-, *d*-, *f*-AO based σ -, π -, δ -, and ϕ -aromaticity/antiaromaticity in model triatomic and tetraatomic systems. The σ -, π -, δ -, and ϕ -aromatic systems retain high symmetry structures whereas σ -, π -, δ -, and ϕ -antiaromatic systems should undergo Jahn–Teller distortion. When all bonding, partially bonding, and antibonding MOs composed out of a particular type of AOs (*s*-, *p*-, *d*-, or *f*-) are completely occupied, those MOs do not contribute to bonding anymore, because all bonding effects will be cancelled by corresponding antibonding effects.

In Table 1 we present schematic molecular orbital diagrams, possible electronic configurations and Huckel's rules for *s*-, *p*-, *d*-, and *f*-AO based σ -aromaticity/antiaromaticity, *p*-, *d*-, and *f*-AO based π -aromaticity/antiaromaticity, *d*-, and *f*-AO based δ -aromaticity/antiaromaticity, and *f*-AO based ϕ -aromaticity/antiaromaticity of a singlet/triplet model triatomic system as a general example of odd-number cyclic systems. The same information for a tetraatomic system as a general example of even-number cyclic systems is listed in Table 2. In Figs. 1–20 we give a

Table 1 Schematic molecular orbital diagrams, possible electronic configurations, and Huckel's rules for aromaticity/antiaromaticity of single/triplet model triatomic system as a general example of odd-number cyclic systems

	Schematic molecular orbital diagram		Huckel's rule for aromaticity		Huckel's rule for antiaromaticity	
			singlet coupling	triplet coupling	singlet coupling	triplet coupling
s-AO based σ -aromaticity	—	— $1e'$ — $1a_1'$	$4n+2$ { $1a_1^{(2)}$, $1e^{(0)}$ }	$4n$ { $1a_1^{(2)}$, $1e^{(2)}$ }	$4n$ { $1a_1^{(2)}$, $1e^{(2)}$ }	$4n+2$ { $1a_1^{(1)}$, $1e^{(1)}$ }
p-AO based σ -aromaticity	—	— $1a_2'$ — $2e'$ — $1e'$ — $1a_1'$	$4n+2$ { $1a_1^{(2)}$, $1e^{(0)}$ } { $1a_1^{(2)}$, $1e^{(4)}$ } { $1a_1^{(2)}$, $1e^{(4)}$, $2e^{(4)}$ }	$4n$ { $1a_1^{(2)}$, $1e^{(2)}$ } { $1a_1^{(2)}$, $1e^{(4)}$, $2e^{(2)}$ }	$4n$ { $1a_1^{(2)}$, $1e^{(2)}$ } { $1a_1^{(2)}$, $1e^{(4)}$, $2e^{(2)}$ }	$4n+2$ { $1a_1^{(1)}$, $1e^{(1)}$ } { $1a_1^{(2)}$, $1e^{(3)}$, $2e^{(1)}$ }
p-AO based π -aromaticity	—	— $1e''$ — $1a_2''$	$4n+2$ { $1a_2^{(2)}$, $1e^{(0)}$ }	$4n$ { $1a_2^{(2)}$, $1e^{(2)}$ }	$4n$ { $1a_2^{(2)}$, $1e^{(2)}$ }	$4n+2$ { $1a_2^{(1)}$, $1e^{(1)}$ }
d-AO based σ -aromaticity	—	— $1a_2'$ — $2e'$ — $1e'$ — $1a_1'$	$4n+2$ { $1a_1^{(2)}$, $1e^{(0)}$ } { $1a_1^{(2)}$, $1e^{(4)}$ } { $1a_1^{(2)}$, $1e^{(4)}$, $2e^{(4)}$ }	$4n$ { $1a_1^{(2)}$, $1e^{(2)}$ } { $1a_1^{(2)}$, $1e^{(4)}$, $2e^{(2)}$ }	$4n$ { $1a_1^{(2)}$, $1e^{(2)}$ } { $1a_1^{(2)}$, $1e^{(4)}$, $2e^{(2)}$ }	$4n+2$ { $1a_1^{(1)}$, $1e^{(1)}$ } { $1a_1^{(2)}$, $1e^{(3)}$, $2e^{(1)}$ }
d-AO based π -aromaticity	—	— $1a_1''$ — $2e''$ — $1e''$ — $1a_2''$	$4n+2$ { $1a_2^{(2)}$, $1e^{(0)}$ } { $1a_2^{(2)}$, $1e^{(4)}$ } { $1a_2^{(2)}$, $1e^{(4)}$, $2e^{(4)}$ }	$4n$ { $1a_2^{(2)}$, $1e^{(2)}$ } { $1a_2^{(2)}$, $1e^{(4)}$, $2e^{(2)}$ }	$4n$ { $1a_2^{(2)}$, $1e^{(2)}$ } { $1a_2^{(2)}$, $1e^{(4)}$, $2e^{(2)}$ }	$4n+2$ { $1a_2^{(1)}$, $1e^{(1)}$ } { $1a_2^{(2)}$, $1e^{(3)}$, $2e^{(1)}$ }

d-AO based δ -aromaticity	$\begin{array}{c} \text{---} \text{---} 1e' \\ \text{---} 1a_1' \end{array}$	$\begin{array}{c} 4n+2 \\ \{1a_1^{(2)}, 1e^{(0)}\} \end{array}$	$\begin{array}{c} 4n \\ \{1a_1^{(2)}, 1e^{(2)}\} \end{array}$	$\begin{array}{c} 4n+2 \\ \{1a_1^{(1)}, 1e^{(1)}\} \end{array}$
f-AO based σ -aromaticity	$\begin{array}{c} \text{---} 1a_2' \\ \text{---} 2e' \\ \text{---} 1e' \\ \text{---} 1a_1' \end{array}$	$\begin{array}{c} 4n+2 \\ \{1a_1^{(2)}, 1e^{(0)}\} \\ \{1a_1^{(2)}, 1e^{(4)}\} \\ \{1a_1^{(2)}, 1e^{(4)}\} 2e^{(4)} \end{array}$	$\begin{array}{c} 4n \\ \{1a_1^{(2)}, 1e^{(2)}\} \\ \{1a_1^{(2)}, 1e^{(4)}\} 2e^{(2)} \end{array}$	$\begin{array}{c} 4n+2 \\ \{1a_1^{(1)}, 1e^{(1)}\} \\ \{1a_1^{(2)}, 1e^{(3)}\} 2e^{(1)} \end{array}$
f-AO based π -aromaticity	$\begin{array}{c} \text{---} 1a_1'' \\ \text{---} 2e'' \\ \text{---} 1e'' \\ \text{---} 1a_2'' \end{array}$	$\begin{array}{c} 4n+2 \\ \{1a_2^{(2)}, 1e^{(0)}\} \\ \{1a_2^{(2)}, 1e^{(4)}\} \\ \{1a_2^{(2)}, 1e^{(4)}\} 2e^{(4)} \end{array}$	$\begin{array}{c} 4n \\ \{1a_2^{(2)}, 1e^{(2)}\} \\ \{1a_2^{(2)}, 1e^{(4)}\} 2e^{(2)} \end{array}$	$\begin{array}{c} 4n+2 \\ \{1a_2^{(1)}, 1e^{(1)}\} \\ \{1a_2^{(2)}, 1e^{(3)}\} 2e^{(1)} \end{array}$
f-AO based δ -aromaticity	$\begin{array}{c} \text{---} 1a_2' \\ \text{---} 2e' \\ \text{---} 1e' \\ \text{---} 1a_1' \end{array}$	$\begin{array}{c} 4n+2 \\ \{1a_1^{(2)}, 1e^{(0)}\} \\ \{1a_1^{(2)}, 1e^{(4)}\} \\ \{1a_1^{(2)}, 1e^{(4)}\} 2e^{(4)} \end{array}$	$\begin{array}{c} 4n \\ \{1a_1^{(2)}, 1e^{(2)}\} \\ \{1a_1^{(2)}, 1e^{(4)}\} 2e^{(2)} \end{array}$	$\begin{array}{c} 4n+2 \\ \{1a_1^{(1)}, 1e^{(1)}\} \\ \{1a_1^{(2)}, 1e^{(3)}\} 2e^{(1)} \end{array}$
f-AO based ϕ -aromaticity	$\begin{array}{c} \text{---} 1e'' \\ \text{---} 1a_2'' \end{array}$	$\begin{array}{c} 4n+2 \\ \{1a_2^{(2)}, 1e^{(0)}\} \end{array}$	$\begin{array}{c} 4n \\ \{1a_2^{(2)}, 1e^{(2)}\} \end{array}$	$\begin{array}{c} 4n+2 \\ \{1a_2^{(1)}, 1e^{(1)}\} \end{array}$

Table 2 Schematic molecular orbital diagrams, possible electronic configurations, and Huckel's rules for aromaticity/antiaromaticity of singlet/triplet model tetrameric system as a general example of even-number cyclic systems

	Schematic molecular orbital diagram	Huckel's rule for aromaticity		Huckel's rule for antiaromaticity	
		singlet coupling	triplet coupling	singlet coupling	triplet coupling
s-AO based σ -aromaticity	$\begin{array}{c} \text{---} 1b_u \\ \text{---} 1e_g \\ \text{---} 1a_u \end{array}$	$4n + 2$ $\{1a_{1g}^{(2)}1e_u^{(0)}\}$ $\{1a_{1g}^{(2)}1e_u^{(4)}\}$	$4n$ $\{1a_{1g}^{(2)}1e_u^{(2)}\}$	$4n$ $\{1a_{1g}^{(2)}1e_u^{(2)}\}$	$4n + 2$ $\{1a_{1g}^{(1)}1e_u^{(1)}\}$
p-AO based σ -aromaticity	$\begin{array}{c} \text{---} 1a_u \\ \text{---} 1b_u \\ \text{---} 2e_u \\ \text{---} 1e_u \\ \text{---} 1b_u \\ \text{---} 1a_u \end{array}$	$2, 4n + 4$ $\{1a_{1g}^{(2)}1b_{2g}^{(0)}\}$ $\{1a_{1g}^{(2)}1b_{2g}^{(2)}\}$ $\{1a_{1g}^{(2)}1b_{2g}^{(2)}1e_u^{(4)}\}$ $\{1a_{1g}^{(2)}1b_{2g}^{(2)}1e_u^{(4)}2e_u^{(4)}\}$	$4n + 2$ $\{1a_{1g}^{(1)}1b_{2g}^{(1)}\}$ $\{1a_{1g}^{(2)}1b_{2g}^{(2)}1e_u^{(2)}\}$ $\{1a_{1g}^{(2)}1b_{2g}^{(2)}1e_u^{(4)}2e_u^{(2)}\}$	$4n + 6$ $\{1a_{1g}^{(2)}1b_{2g}^{(2)}1e_u^{(2)}\}$ $\{1a_{1g}^{(2)}1b_{2g}^{(2)}1e_u^{(4)}2e_u^{(2)}\}$	$4n$ $\{1a_{1g}^{(2)}1b_{2g}^{(1)}1e_u^{(1)}\}$ $\{1a_{1g}^{(2)}1b_{2g}^{(2)}1e_u^{(3)}2e_u^{(1)}\}$
p-AO based π -aromaticity	$\begin{array}{c} \text{---} 1b_u \\ \text{---} 1e_g \\ \text{---} 1a_u \end{array}$	$4n + 2$ $\{1a_{2u}^{(2)}1e_g^{(0)}\}$ $\{1a_{2u}^{(2)}1e_g^{(4)}\}$	$4n$ $\{1a_{2u}^{(2)}1e_g^{(2)}\}$	$4n$ $\{1a_{2u}^{(2)}1e_g^{(2)}\}$	$4n + 2$ $\{1a_{2u}^{(1)}1e_g^{(1)}\}$
d-AO based σ -aromaticity	$\begin{array}{c} \text{---} 1a_u \\ \text{---} 1b_u \\ \text{---} 2e_u \\ \text{---} 1e_u \\ \text{---} 1b_u \\ \text{---} 1a_u \end{array}$	$2, 4n + 4$ $\{1a_{1g}^{(2)}1b_{2g}^{(0)}\}$ $\{1a_{1g}^{(2)}1b_{2g}^{(2)}\}$ $\{1a_{1g}^{(2)}1b_{2g}^{(2)}1e_u^{(4)}\}$ $\{1a_{1g}^{(2)}1b_{2g}^{(2)}1e_u^{(4)}2e_u^{(4)}\}$	$4n + 2$ $\{1a_{1g}^{(1)}1b_{2g}^{(1)}\}$ $\{1a_{1g}^{(2)}1b_{2g}^{(2)}1e_u^{(2)}\}$ $\{1a_{1g}^{(2)}1b_{2g}^{(2)}1e_u^{(4)}2e_u^{(2)}\}$	$4n + 6$ $\{1a_{1g}^{(2)}1b_{2g}^{(2)}1e_u^{(2)}\}$ $\{1a_{1g}^{(2)}1b_{2g}^{(2)}1e_u^{(4)}2e_u^{(2)}\}$	$4n$ $\{1a_{1g}^{(2)}1b_{2g}^{(1)}1e_u^{(1)}\}$ $\{1a_{1g}^{(2)}1b_{2g}^{(2)}1e_u^{(3)}2e_u^{(1)}\}$
d-AO based π -aromaticity	$\begin{array}{c} \text{---} 1a_u \\ \text{---} 1b_u \\ \text{---} 2e_u \\ \text{---} 1e_u \\ \text{---} 1b_u \\ \text{---} 1a_u \end{array}$	$2, 4n + 4$ $\{1a_{2u}^{(2)}1b_{1u}^{(0)}\}$ $\{1a_{2u}^{(2)}1b_{1u}^{(4)}\}$ $\{1a_{2u}^{(2)}1b_{1u}^{(2)}1e_g^{(4)}\}$ $\{1a_{2u}^{(2)}1b_{1u}^{(4)}2e_g^{(4)}\}$	$4n + 2$ $\{1a_{2u}^{(1)}1b_{1u}^{(1)}\}$ $\{1a_{2u}^{(2)}1b_{1u}^{(2)}1e_g^{(2)}\}$ $\{1a_{2u}^{(2)}1b_{1u}^{(2)}1e_g^{(4)}2e_g^{(2)}\}$	$4n + 6$ $\{1a_{2u}^{(2)}1b_{1u}^{(2)}1e_g^{(2)}\}$ $\{1a_{2u}^{(2)}1b_{1u}^{(4)}2e_g^{(2)}\}$	$4n$ $\{1a_{2u}^{(2)}1b_{1u}^{(1)}1e_g^{(1)}\}$ $\{1a_{2u}^{(2)}1b_{1u}^{(2)}1e_g^{(3)}2e_g^{(1)}\}$

d-AO based δ -aromaticity	$\begin{array}{c} \text{---}1b_{1g} \\ \text{---}1e_u \\ \text{---}1a_{1g} \end{array}$	$\begin{array}{c} 4n \\ \{1a_{1g}^{(2)}1e_u^{(2)}\} \end{array}$	$\begin{array}{c} 4n \\ \{1a_{1g}^{(2)}1e_u^{(2)}\} \end{array}$	$\begin{array}{c} 4n + 2 \\ \{1a_{1g}^{(1)}1e_u^{(1)}\} \end{array}$
f-AO based σ -aromaticity	$\begin{array}{c} \text{---}1a_{1g} \\ \text{---}1b_{1g} \\ \text{---}2e_u \\ \text{---}1e_u \\ \text{---}1b_{1g} \\ \text{---}1a_{1g} \end{array}$	$\begin{array}{c} 2, 4n + 4 \\ \{1a_{1g}^{(2)}1b_{2g}^{(0)}\} \\ \{1a_{1g}^{(2)}1b_{2g}^{(2)}\} \\ \{1a_{1g}^{(2)}1b_{2g}^{(2)}1e_u^{(4)}\} \\ \{1a_{1g}^{(2)}1b_{2g}^{(2)}1e_u^{(4)}2e_u^{(4)}\} \end{array}$	$\begin{array}{c} 4n + 2 \\ \{1a_{1g}^{(1)}1b_{2g}^{(1)}\} \\ \{1a_{1g}^{(2)}1b_{2g}^{(2)}1e_u^{(2)}\} \\ \{1a_{1g}^{(2)}1b_{2g}^{(2)}1e_u^{(4)}2e_u^{(2)}\} \end{array}$	$\begin{array}{c} 4n \\ \{1a_{1g}^{(2)}1b_{2g}^{(2)}1e_u^{(1)}\} \\ \{1a_{1g}^{(2)}1b_{2g}^{(2)}1e_u^{(3)}2e_u^{(1)}\} \end{array}$
f-AO based π -aromaticity	$\begin{array}{c} \text{---}1a_{1g} \\ \text{---}1b_{1g} \\ \text{---}2e_u \\ \text{---}1e_u \\ \text{---}1b_{1g} \\ \text{---}1a_{1g} \end{array}$	$\begin{array}{c} 2, 4n + 4 \\ \{1a_{2u}^{(2)}1b_{1u}^{(0)}\} \\ \{1a_{2u}^{(2)}1b_{1u}^{(2)}\} \\ \{1a_{2u}^{(2)}1b_{1u}^{(2)}1e_g^{(4)}\} \\ \{1a_{2u}^{(2)}1b_{1u}^{(2)}1e_g^{(4)}2e_g^{(4)}\} \end{array}$	$\begin{array}{c} 4n + 2 \\ \{1a_{2u}^{(1)}1b_{1u}^{(1)}\} \\ \{1a_{2u}^{(2)}1b_{1u}^{(2)}1e_g^{(2)}\} \\ \{1a_{2u}^{(2)}1b_{1u}^{(2)}1e_g^{(4)}2e_g^{(2)}\} \end{array}$	$\begin{array}{c} 4n \\ \{1a_{2u}^{(2)}1b_{1u}^{(2)}1e_g^{(1)}\} \\ \{1a_{2u}^{(2)}1b_{1u}^{(2)}1e_g^{(3)}2e_g^{(1)}\} \end{array}$
f-AO based δ -aromaticity	$\begin{array}{c} \text{---}1a_{1g} \\ \text{---}1b_{1g} \\ \text{---}2e_u \\ \text{---}1e_u \\ \text{---}1b_{1g} \\ \text{---}1a_{1g} \end{array}$	$\begin{array}{c} 2, 4n + 4 \\ \{1a_{1g}^{(2)}1b_{2g}^{(0)}\} \\ \{1a_{1g}^{(2)}1b_{2g}^{(2)}\} \\ \{1a_{1g}^{(2)}1b_{2g}^{(2)}1e_u^{(4)}\} \\ \{1a_{1g}^{(2)}1b_{2g}^{(2)}1e_u^{(4)}2e_u^{(4)}\} \end{array}$	$\begin{array}{c} 4n + 2 \\ \{1a_{1g}^{(1)}1b_{2g}^{(1)}\} \\ \{1a_{1g}^{(2)}1b_{2g}^{(2)}1e_u^{(2)}\} \\ \{1a_{1g}^{(2)}1b_{2g}^{(2)}1e_u^{(4)}2e_u^{(2)}\} \end{array}$	$\begin{array}{c} 4n \\ \{1a_{1g}^{(2)}1b_{2g}^{(2)}1e_u^{(1)}\} \\ \{1a_{1g}^{(2)}1b_{2g}^{(2)}1e_u^{(3)}2e_u^{(1)}\} \end{array}$
f-AO based ϕ -aromaticity	$\begin{array}{c} \text{---}1b_{1u} \\ \text{---}1e_u \\ \text{---}1b_{1u} \end{array}$	$\begin{array}{c} 4n \\ \{1a_{2u}^{(2)}1e_g^{(0)}\} \\ \{1a_{2u}^{(2)}1e_g^{(4)}\} \end{array}$	$\begin{array}{c} 4n \\ \{1a_{2u}^{(2)}1e_g^{(2)}\} \end{array}$	$\begin{array}{c} 4n + 2 \\ \{1a_{2u}^{(1)}1e_g^{(1)}\} \end{array}$

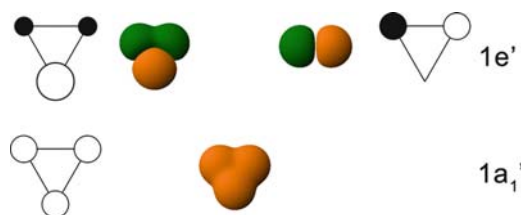


Fig. 1 s-AO based σ -MOs for model triatomic system plotted by Orbital Viewer 1.04

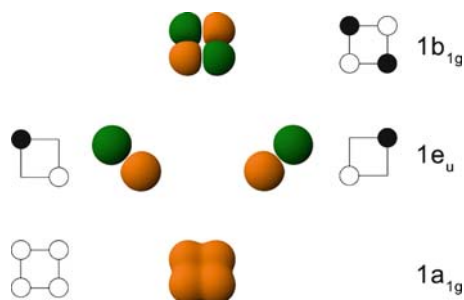


Fig. 2 s-AO based σ -MOs for model tetratomic system plotted by Orbital Viewer 1.04

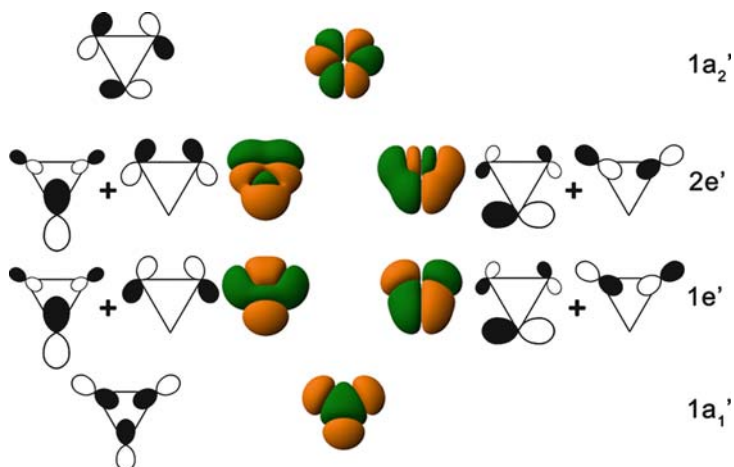


Fig. 3 p-AO based σ -MOs for model triatomic system plotted by Orbital Viewer 1.04. Here and elsewhere molecular orbitals which are composed of both radial and tangential AOs are symbolically shown as a sum of two hypothetical MOs built out of either radial or tangential AOs

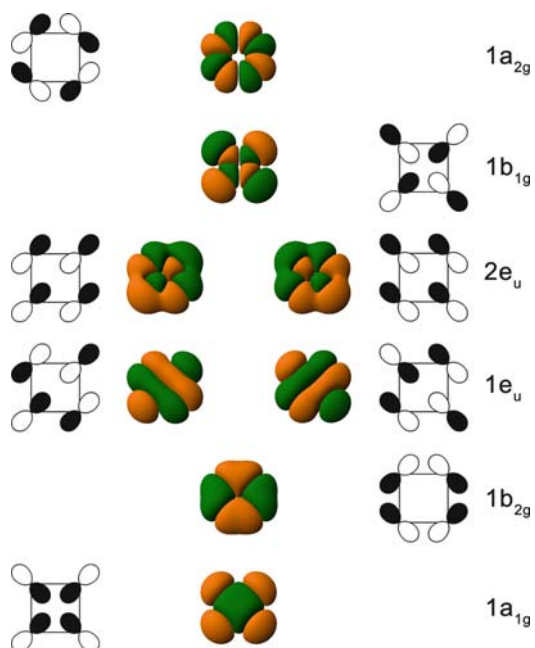


Fig. 4 p-AO based σ -MOs for model tetratomic system plotted by Orbital Viewer 1.04

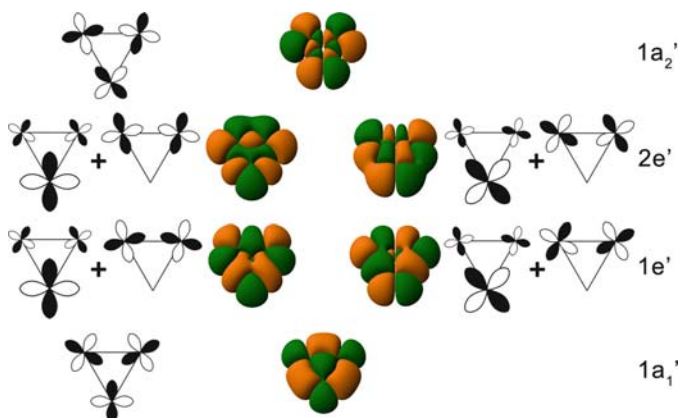


Fig. 5 d-AO based σ -MOs for model triatomic system plotted by Orbital Viewer 1.04

molecular orbital representation performed via Orbital Viewer 1.04 [8] that can be found in the centre of the corresponding figure and the schematic representation of those orbitals in terms of atomic orbitals (to the left and to the right from molecular orbital representation).

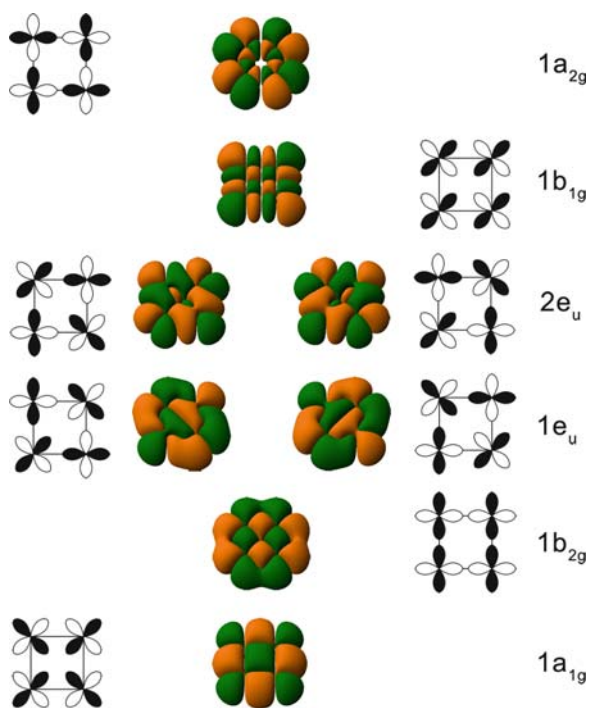


Fig. 6 d-AO based σ -MOs for model tetratomic system plotted by Orbital Viewer 1.04

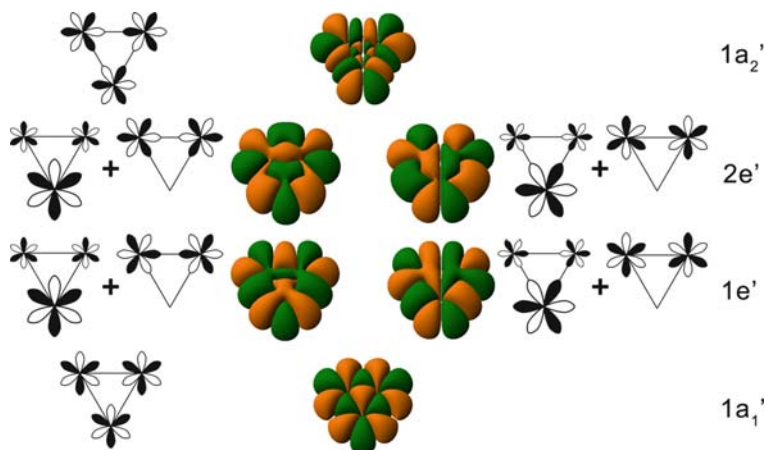


Fig. 7 f-AO based σ -MOs for model triatomic system plotted by Orbital Viewer 1.04

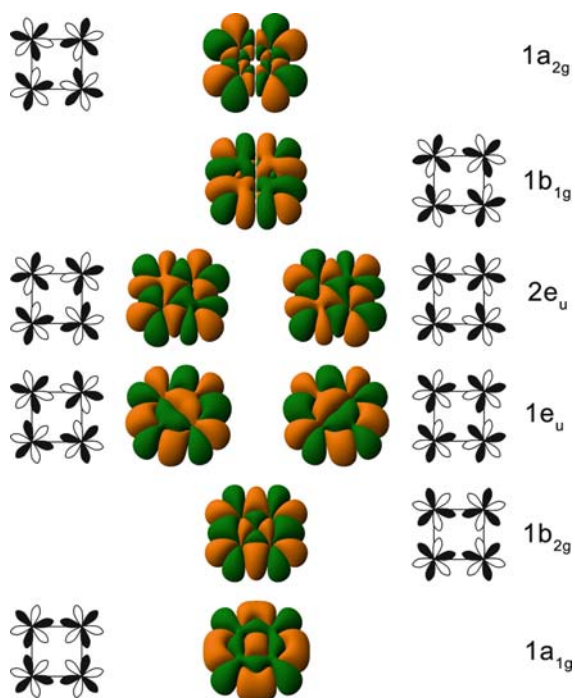


Fig. 8 f-AO based σ -MOs for model tetratomic system plotted by Orbital Viewer 1.04

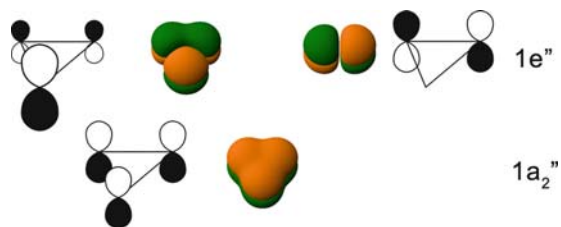


Fig. 9 p-AO based π -MOs for model triatomic system plotted by Orbital Viewer 1.04

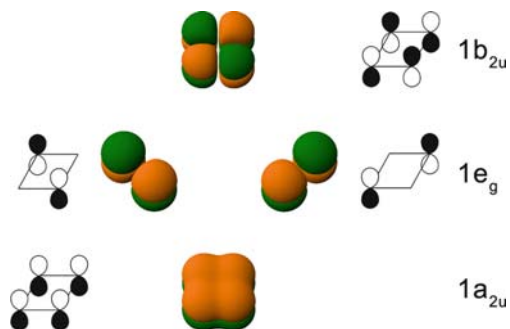


Fig. 10 p-AO based π -MOs for model tetratomic system plotted by Orbital Viewer 1.04

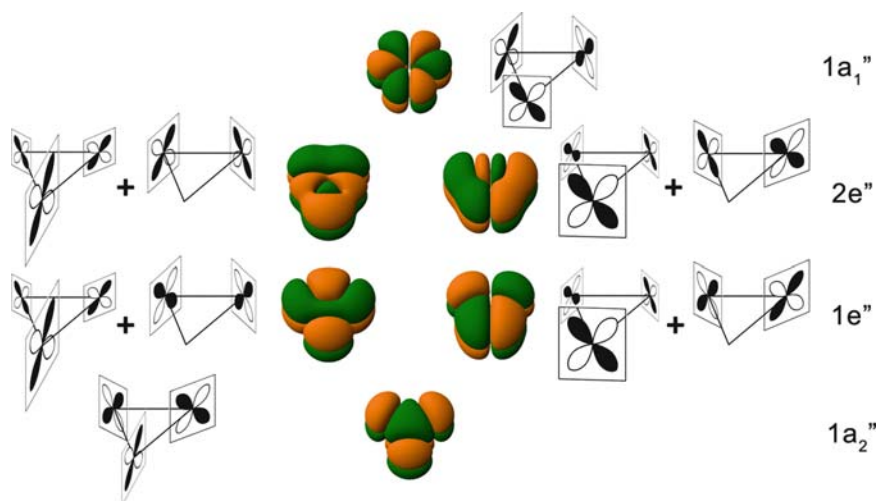


Fig. 11 d-AO based π -MOs for model triatomic system plotted by Orbital Viewer 1.04

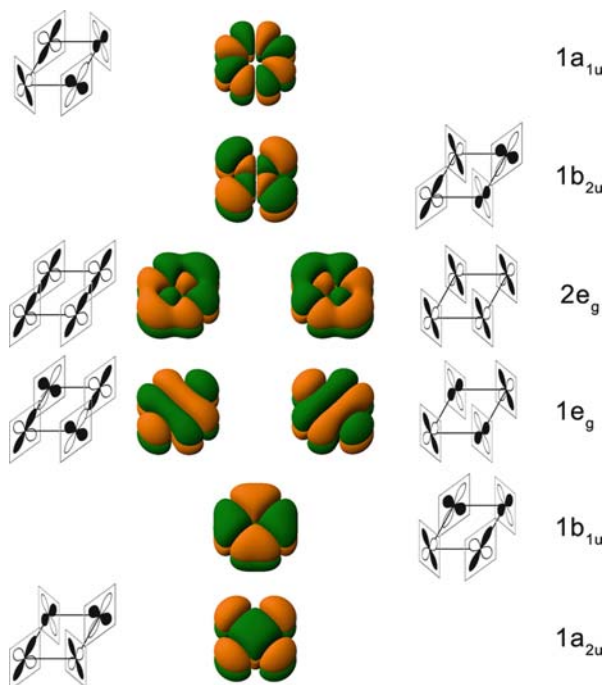


Fig. 12 d-AO based π -MOs for model tetratomic system plotted by Orbital Viewer 1.04

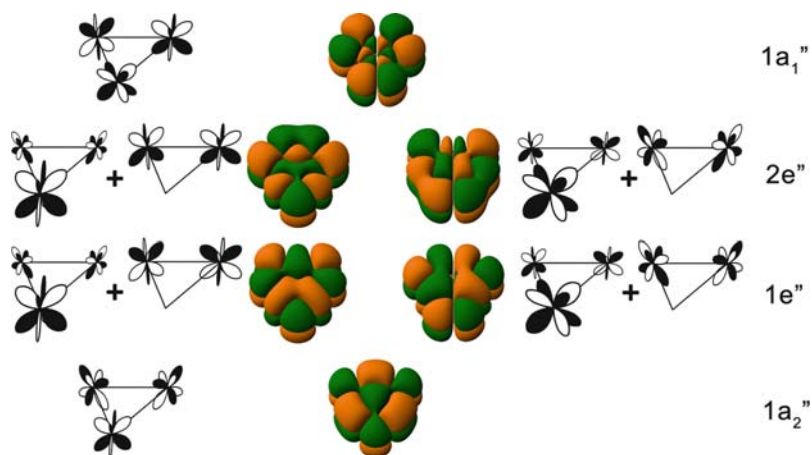


Fig. 13 f-AO based π -MOs for model triatomic system plotted by Orbital Viewer 1.04

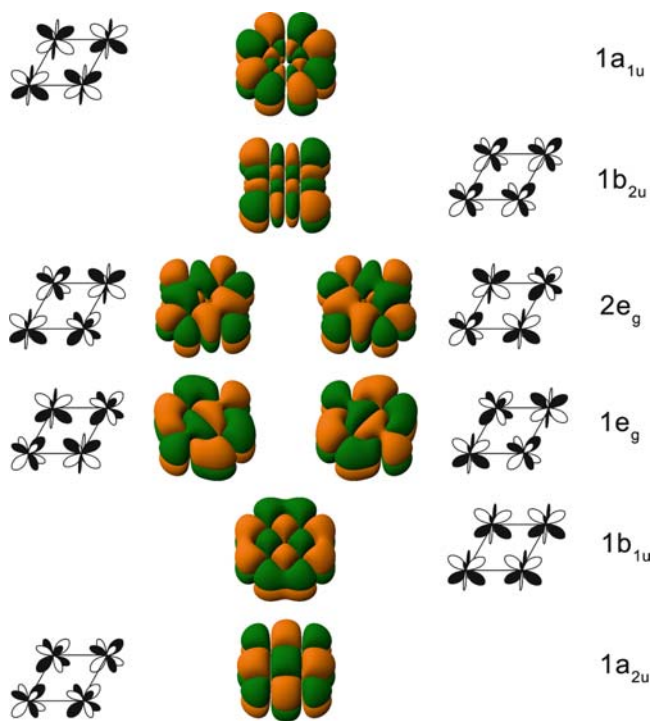


Fig. 14 f-AO based π -MOs for model tetraatomic system plotted by Orbital Viewer 1.04

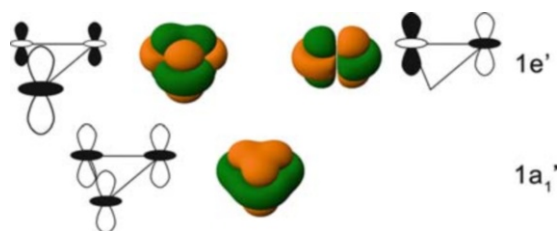


Fig. 15 d-AO based δ -MOs for model triatomic system plotted by Orbital Viewer 1.04

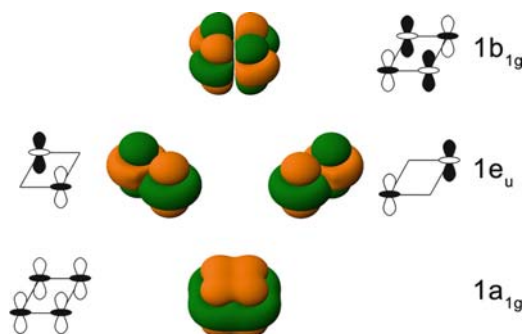


Fig. 16 d-AO based δ -MOs for model tetrahedral system plotted by Orbital Viewer 1.04

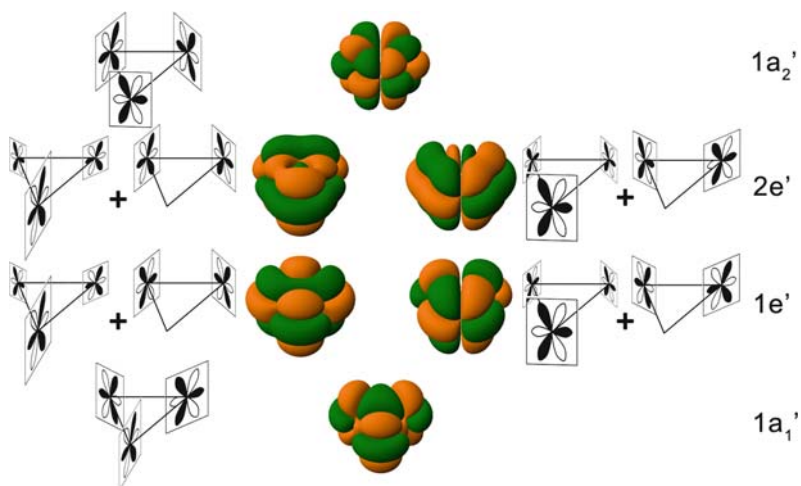


Fig. 17 f-AO based δ -MOs for model triatomic system plotted by Orbital Viewer 1.04

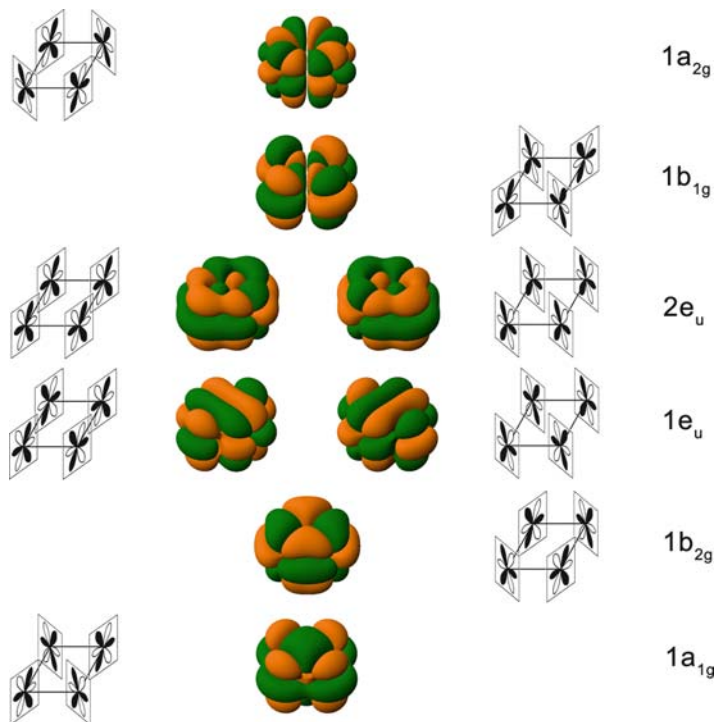


Fig. 18 f-AO based δ -MOs for model tetratomic system plotted by Orbital Viewer 1.04

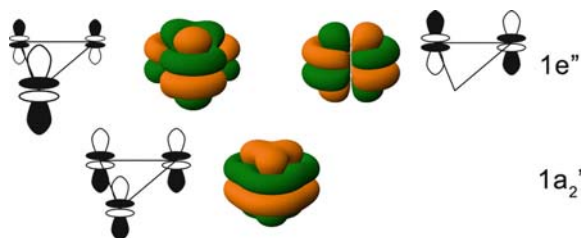


Fig. 19 f-AO based ϕ -MOs for model triatomic system plotted by Orbital Viewer 1.04

2.1 *s*-, *p*-, *d*-, *f*-AO Based σ -Aromaticity/Antiaromaticity

The simplest case is the *s*-AO based σ -aromaticity/antiaromaticity in a triatomic system. Out of three *s*-AOs (Fig. 1) one can compose a completely bonding $1a'_1$ -MO and two partially bonding/antibonding $1e'$ -MOs.

According to the $4n + 2$ Huckel's rule for aromaticity and the $4n$ Huckel's rule for antiaromaticity, triatomic systems with the electronic configuration $1a'_1^{(2)}1e'^{(0)}$ are σ -aromatic and with the electronic configuration $1a'_1^{(2)}1e'^{(2)}$ (singlet coupling) are

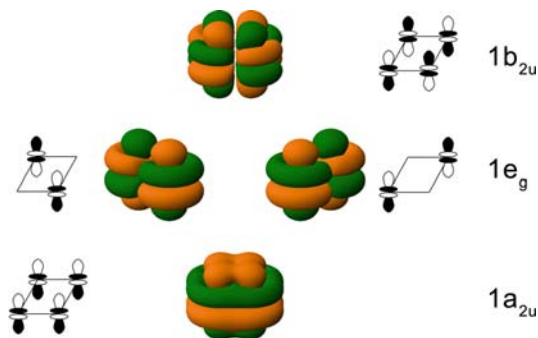


Fig. 20 f-AO based ϕ -MOs for model tetratomic system plotted by Orbital Viewer 1.04

σ -antiaromatic. On the other hand, triatomic systems with electronic configuration $1a_1^{(2)}1e'^{(2)}$ (triplet coupling) are σ -aromatic and with electronic configuration $1a_1^{(1)}1e'^{(1)}$ are considered σ -antiaromatic, thus satisfying the $4n$ Huckel's rule for triplet cases (Table 1).

In a tetratomic system out of four s-AOs (Fig. 2) one can compose a completely bonding $1a_{1g}$ -MO, two partially bonding/antibonding $1e_u$ -MOs, and one completely antibonding $1b_{1g}$ -MO.

Similar to the triatomic systems (see earlier), tetratomic systems with the electronic configurations $1a_{1g}^{(2)}1e_u^{(0)}1b_{1g}^{(0)}$, $1a_{1g}^{(2)}1e_u^{(2)}1b_{1g}^{(0)}$ (triplet coupling), and $1a_{1g}^{(2)}1e_u^{(4)}1b_{1g}^{(0)}$ are σ -aromatic, with the electronic configuration $1a_{1g}^{(2)}1e_u^{(2)}1b_{1g}^{(0)}$ (singlet coupling) are σ -antiaromatic, according to the counting rule $4n + 2/4n//4n/4n + 2$ (Table 2). Triplet coupling $1a_{1g}^{(1)}1e_u^{(1)}$ electronic configuration should be considered as being σ -antiaromatic.

In the case of p-AO based σ -aromaticity/antiaromaticity in a cyclic triatomic system there are two types of p-AOs: p-sigma-radial ($p_{\sigma-r}$)- and p-sigma-tangential ($p_{\sigma-t}$)- AOs participating in delocalized bonding (Table 1 and Fig. 3).

The lowest-lying σ -MO ($1a_1'$) is completely bonding formed out of $p_{\sigma-r}$ -AOs only, whereas the highest-lying one ($1a_2'$) is completely antibonding composed out of $p_{\sigma-t}$ -AOs. The doubly degenerate $1e'$ - and $2e'$ -MOs are composed out of both $p_{\sigma-r}$ - and $p_{\sigma-t}$ -AOs. This is the reason why $p_{\sigma-r}$ - and $p_{\sigma-t}$ -MOs are presented as one set in Fig. 3. The counting rules for aromaticity/antiaromaticity for σ -electrons in cyclic systems with the singlet/triplet coupling of electrons and odd number of vertices are $4n + 2/4n//4n/4n + 2$, respectively (Table 1).

For the cyclic tetratomic systems p-AO based σ -aromaticity/antiaromaticity is more complicated (Fig. 4, Table 2).

Now, the two lowest-lying σ -MOs ($1a_{1g}$ and $1b_{2g}$) are completely bonding and they are composed out of either $p_{\sigma-r}$ -AOs ($1a_{1g}$) or $p_{\sigma-t}$ -AOs ($1b_{2g}$). The highest-lying ones are completely antibonding and they are also composed out of either $p_{\sigma-r}$ -AOs ($1b_{1g}$) or $p_{\sigma-t}$ -AOs ($1a_{2g}$). The four MOs ($1e_u$ and $2e_u$) in the σ -set that are located in between the completely bonding and antibonding MOs are doubly

degenerate with bonding/antibonding characters. The $1e_u$ - and the $2e_u$ -MOs are composed of both $p_{\sigma-r}$ - and $p_{\sigma-t}$ -AOs. On the basis of this mixing of the $p_{\sigma-r}$ - and $p_{\sigma-t}$ -AOs the counting rule for σ -electrons for singlet/triplet coupling cyclic systems with even number of vertices should be $4n + 4/4n + 2//4n + 6/4n$ (Table 2) for aromaticity/antiaromaticity (in the simplest case of the occupation of just one $p_{\sigma-r}$ - or one $p_{\sigma-t}$ -MO the system is also aromatic).

d-AO based σ -aromaticity/antiaromaticity in a cyclic triatomic system is based on two types of d-AOs: $d_{\sigma-r}$ - and $d_{\sigma-t}$ -AOs participating in delocalized bonding (Fig. 5).

$d_{\sigma-r}$ -AOs participate in the formation of the completely bonding lowest-lying σ -MO ($1a'_1$), whereas $d_{\sigma-t}$ -AOs participate in the formation of the completely antibonding highest-lying σ -MO ($1a'_2$). Two doubly degenerate $1e'$ - and $2e'$ -MOs are composed out of both $d_{\sigma-r}$ - and $d_{\sigma-t}$ -AOs. The counting rules are $4n + 2/4n//4n/4n + 2$ for aromaticity/antiaromaticity for σ -electrons in cyclic systems with the singlet/triplet coupling of electrons and odd number of vertices (see Table 1).

There are also two types of d-AOs: $d_{\sigma-r}$ - and $d_{\sigma-t}$ -AOs participating in delocalized bonding which are responsible for d-AO based σ -aromatic/antiaromatic character in a cyclic tetratomic system (Table 2 and Fig. 6).

There are two lowest-lying completely bonding σ -MOs ($1a_{1g}$ and $1b_{2g}$) composed out of either $d_{\sigma-r}$ -AOs ($1a_{1g}$) or $d_{\sigma-t}$ -AOs ($1b_{2g}$). Similarly, there are two highest-lying completely antibonding σ -MOs ($1b_{1g}$ and $1a_{2g}$) composed out of either $d_{\sigma-r}$ -AOs ($1b_{1g}$) or $d_{\sigma-t}$ -AOs ($1a_{2g}$). The four MOs ($1e_u$ and $2e_u$) in the σ -set that are located in between the completely bonding and antibonding MOs are doubly degenerate with bonding/antibonding characters. The $1e_u$ - and the $2e_u$ -MOs are composed of both $d_{\sigma-r}$ - and $d_{\sigma-t}$ -AOs. The counting rules for σ -electrons for cyclic singlet/triplet coupling systems with even number of vertices should be $4n + 4/4n + 2//4n + 6/4n$ for aromaticity/antiaromaticity (in the simplest case of the singlet coupling occupation of just one $d_{\sigma-r}$ - or one $d_{\sigma-t}$ -MO the system is also aromatic).

Cyclic triatomic system exhibiting f-AO based σ -aromaticity/antiaromaticity involves $f_{\sigma-r}$ - and $f_{\sigma-t}$ -AOs in delocalized bonding (Fig. 7).

The lowest-lying completely bonding ($1a'_1$) and the highest-lying completely antibonding ($1a'_2$) σ -MOs are formed out of either $f_{\sigma-r}$ -AOs or $f_{\sigma-t}$ -AOs, respectively. $1e'$ - and $2e'$ -MOs are composed out of both $f_{\sigma-r}$ - and $f_{\sigma-t}$ -AOs. The counting rules for aromaticity/antiaromaticity for σ -electrons in singlet/triplet coupled cyclic systems with odd number of vertices are $4n + 2/4n//4n/4n + 2$, respectively (see Table 1 for details).

f-AO based σ -aromaticity/antiaromaticity in a cyclic tetratomic system involves $f_{\sigma-r}$ - and $f_{\sigma-t}$ -AOs in delocalized bonding (Table 2 and Fig. 8).

The two lowest-lying completely bonding ($1a_{1g}$ and $1b_{2g}$) and the two highest-lying completely antibonding ($1b_{1g}$ and $1a_{2g}$) σ -MOs are composed out of either $f_{\sigma-r}$ -AOs ($1a_{1g}$, $1b_{1g}$) or $f_{\sigma-t}$ -AOs ($1b_{2g}$, $1a_{2g}$). The four MOs ($1e_u$ and $2e_u$) in the σ -set have bonding/antibonding characters and are composed of both $f_{\sigma-r}$ - and $f_{\sigma-t}$ -AOs. The counting rules are $4n + 4/4n + 2//4n + 6/4n$ (Table 2) for σ -electrons for

cyclic singlet/triplet coupling systems with even number of vertices for aromaticity/antiaromaticity (the singlet coupled system is also aromatic in the simplest case of occupation of just one $f_{\sigma-r}$ - or one $f_{\sigma-t}$ -MO).

2.2 *p*-, *d*-, *f*-AO Based π -Aromaticity/Antiaromaticity

In a triatomic system with the *p*-AO based π -aromaticity/antiaromaticity (Fig. 9) there is one completely bonding $1a_2''$ -MO and two partially bonding/antibonding $1e''$ -MOs.

Singlet-coupled triatomic systems with the electronic configuration $1a_2''^{(2)}1e''^{(0)}$ are π -aromatic and systems with the electronic configuration $1a_2''^{(2)}1e''^{(2)}$ are π -antiaromatic (see Table 1). Triplet-coupled triatomic system with electronic configurations $1a_2''^{(2)}1e''^{(2)}$ and $1a_2''^{(1)}1e''^{(1)}$ are π -aromatic and π -antiaromatic, respectively (see Table 1).

The set of MOs composed out of four *p*-AOs in a tetratomic system is the following: a completely bonding $1a_{2u}$ -MO, two partially bonding/antibonding $1e_g$ -MOs, and one completely antibonding $1b_{2u}$ -MO (Fig. 10).

Similar to the triatomic systems (see earlier) tetratomic systems with the electronic configurations $1a_{2u}^{(2)}1e_g^{(0)}1b_{2u}^{(0)}$, $1a_{2u}^{(2)}1e_g^{(2)}1b_{2u}^{(0)}$ (triplet coupling), and $1a_{2u}^{(2)}1e_g^{(4)}1b_{2u}^{(0)}$ are π -aromatic, with the electronic configurations $1a_{2u}^{(2)}1e_g^{(2)}1b_{2u}^{(0)}$ (singlet coupling) and $1a_{2u}^{(1)}1e_g^{(1)}1b_{2u}^{(0)}$ (singlet coupling) are π -antiaromatic (Table 2).

In a cyclic triatomic system two types of *d*-AOs: $d_{\pi-r}$ - and $d_{\pi-t}$ -AOs are responsible for *d*-AO based π -aromaticity/antiaromaticity (Fig. 11).

The lowest-lying π -MO ($1a_1''$) is completely bonding formed out of only $d_{\pi-r}$ -AOs, the doubly degenerate $1e''$ - and $2e''$ -MOs are composed out of both $d_{\pi-r}$ - and $d_{\pi-t}$ -AOs, and the highest-lying one ($1a_1'$) is completely antibonding composed out of $d_{\pi-t}$ -AOs. See Table 1 for the counting rules and possible electronic configurations for aromaticity/antiaromaticity for π -electrons in cyclic systems with the singlet/triplet coupling of electrons and odd number of vertices.

Now, let us consider *d*-AO based π -aromaticity/antiaromaticity in cyclic tetratomic systems (Fig. 12).

Cyclic tetratomic systems have eight MOs corresponding to the *d*-AO based π -aromaticity/antiaromaticity: two completely bonding π -MOs ($1a_{2u}$ and $1b_{1u}$) composed out of either $d_{\pi-r}$ -AOs ($1a_{2u}$) or $d_{\pi-t}$ -AOs ($1b_{1u}$), set of two partially bonding/antibonding doubly degenerate MOs ($1e_g$ and $2e_g$) composed of both $d_{\pi-r}$ - and $d_{\pi-t}$ -AOs, and two completely antibonding MOs composed out of either $d_{\pi-r}$ -AOs ($1b_{2u}$) or $d_{\pi-t}$ -AOs ($1a_{1u}$). The counting rules and possible electronic configurations for *d*-AO based π -aromaticity/antiaromaticity can be found in Table 2.

In Table 1 and Fig. 13 we summarized the case of *f*-AO based π -aromaticity/antiaromaticity in a cyclic triatomic system.

There are six π -MO formed out of $f_{\pi-r}$ - and $f_{\pi-t}$ -AOs which are the following: completely bonding $f_{\pi-r}$ -AO based $1a_2''$, doubly degenerate bonding/antibonding

$f_{\pi-r}$ - and $f_{\pi-t}$ -AO based $1e''$ - and $2e''$, and finally completely antibonding $f_{\pi-t}$ -AO based $1a_1''$ (see Table 1 for the counting rules and possible electronic configurations for aromaticity/antiaromaticity).

Similar to cyclic triatomic systems there are two types of f-AOs: $f_{\pi-r}$ - and $f_{\pi-t}$ -AOs participating in delocalized bonding in the case of f-AO based π -aromaticity/antiaromaticity in a cyclic tetratomic system (Fig. 14).

This case is similar to d-AO based π -aromaticity/antiaromaticity (see Table 2 for the counting rules and possible electronic configurations for f-AO based π -aromaticity/antiaromaticity in a cyclic tetratomic system).

2.3 d-, f-AO Based δ -Aromaticity/Antiaromaticity

In the d-AO based δ -aromaticity/antiaromaticity in a triatomic system out of three d-AOs (Fig. 15) one can compose a completely bonding $1a_1'$ -MO and two partially bonding/antibonding $1e'$ -MOs.

The counting rules, symmetry of molecular orbitals and electronic configurations are like those in the case of s-AO based σ -aromaticity in a triatomic system (see Table 1, as well as Figs. 1 and 15).

Out of four d-AOs in a tetratomic system (Fig. 16) one can compose a completely bonding $1a_{1g}$ -MO, two partially bonding/antibonding $1e_u$ -MOs, and one completely antibonding $1b_{1g}$ -MO which participate in δ -aromaticity/antiaromaticity.

Tetratomic systems with the electronic configurations $1a_{1g}^{(2)}1e_u^{(0)}1b_{1g}^{(0)}$, and $1a_{1g}^{(2)}1e_u^{(4)}1b_{1g}^{(0)}$, as well as with electronic configuration $1a_{1g}^{(2)}1e_u^{(2)}1b_{1g}^{(0)}$ (triplet coupling) are δ -aromatic. Tetratomic systems with the electronic configurations $1a_{1g}^{(2)}1e_u^{(2)}1b_{1g}^{(0)}$ (singlet coupling), and $1a_{1g}^{(1)}1e_u^{(1)}$ (triplet coupling) are δ -antiaromatic (See Table 2 and Fig. 16 for details).

f-AO based δ -aromaticity/antiaromaticity in a cyclic triatomic system is based on $f_{\delta-r}$ - and $f_{\delta-t}$ -AOs (Table 1 and Fig. 17).

Similar to the cyclic triatomic systems exhibiting p-AO based σ -aromaticity/antiaromaticity, in case of f-AO based δ -aromaticity/antiaromaticity there are six δ -MOs: $1a_1'$, $1e'$ and $2e'$, and $1a_2'$ which are completely bonding, partially bonding/antibonding, and completely antibonding, respectively (see Table 1 and Figs. 3 and 17 for possible electronic configurations and the counting rules for aromaticity/antiaromaticity).

The $f_{\delta-r}$ - and $f_{\delta-t}$ -AOs are involved in f-AO based δ -aromaticity/antiaromaticity in cyclic tetratomic systems (Table 2 and Fig. 18).

There are eight δ -MOs, out of which $1a_{1g}$ and $1b_{2g}$ are completely bonding, $1e_u$ and $2e_u$ are partially bonding/antibonding, and $1b_{1g}$ and $1a_{2g}$ are completely antibonding. The counting rule for δ -electrons for singlet/triplet coupling cyclic systems with even number of vertices should be $4n + 4/4n + 2/4n + 6/4n$ for aromaticity/antiaromaticity (in the simplest case of the occupation of just one $f_{\delta-r}$ - or one $f_{\delta-t}$ -MO the system is also aromatic).

2.4 *f*-AO Based ϕ -Aromaticity/Antiaromaticity

Finally, the *f*-AO based ϕ -aromaticity/antiaromaticity in a triatomic system is based on completely ϕ -bonding $1a_2''$ -MO and two partially bonding/antibonding $1e''$ -MOs (Fig. 19).

Applying Huckel's rules for aromaticity/antiaromaticity in cyclic triatomic systems, one can say that the systems with the electronic configurations $1a_2''^{(2)}1e''^{(0)}$ and $1a_2''^{(2)}1e''^{(2)}$ (triplet coupling) are ϕ -aromatic, and with the electronic configurations $1a_2''^{(2)}1e''^{(2)}$ (singlet coupling) and $1a_2''^{(1)}1e''^{(1)}$ (triplet coupling) are ϕ -antiaromatic (Table 1).

As for *f*-AO based ϕ -aromaticity/antiaromaticity in tetratomic systems, there are four ϕ -MOs (Fig. 20): completely bonding $1a_{2u}$, two degenerate partially bonding/antibonding $1e_g$, and one completely antibonding $1b_{2u}$ -MO.

Having taken into account Huckel's rules for aromaticity/antiaromaticity in cyclic tetratomic systems, the systems with the electronic configurations $1a_{2u}^{(2)}1e_g^{(0)}1b_{2u}^{(0)}$, $1a_{2u}^{(2)}1e_g^{(2)}1b_{2u}^{(0)}$ (triplet coupling), and $1a_{2u}^{(2)}1e_g^{(4)}1b_{2u}^{(0)}$ can be said to be ϕ -aromatic, and the systems with the electronic configuration $1a_{2u}^{(2)}1e_g^{(2)}1b_{2u}^{(0)}$ (singlet coupling) – ϕ -antiaromatic (Table 2).

The above chemical bonding analysis on model triatomic and tetratomic systems can be used for assessing aromaticity/antiaromaticity in real molecules and clusters. However, hybridization may complicate this analysis. We will now present a few examples where aromaticity/antiaromaticity in transition metal systems allows us to rationalize chemical bonding.

Summary: Complicated nature of aromaticity in all transition metal cyclic systems can be understood more easily on simplified model cyclic triatomic and tetratomic systems as examples of cyclic systems composed out of odd or even number of atoms, respectively. Counting rules for σ -, π -, δ -, and ϕ -aromaticity/antiaromaticity for both singlet/triplet coupled triatomic and tetratomic systems depend on the nature of atomic orbitals involved in the formation of corresponding bonding/antibonding molecular orbitals.

3 Examples of Aromatic/Antiaromatic Transition Metal Systems

We performed chemical bonding analysis in a few representative transition metal clusters using recently developed Adaptive Natural Density Partitioning (AdNDP) method [9]. The AdNDP method is based on the concept of the electron pair as the main element of chemical bonding models. Thus, it represents the electronic structure in terms of $nc-2e$ bonds. With n spanning the interval from one to the total amount of atoms in the particular atomic assembly, AdNDP recovers both Lewis bonding elements ($1c-2e$ and $2c-2e$ objects, corresponding to the core electrons and lone pairs, and two-center two-electron bonds) and delocalized bonding

elements, which are associated with the concepts of aromaticity and antiaromaticity. From this point of view, AdNDP achieves seamless description of systems featuring both localized and delocalized bonding without invoking the concept of resonance. Essentially, AdNDP is a very efficient and visual approach to the interpretation of the molecular orbital-based wave functions.

3.1 *s*-AO Based σ -Aromaticity and σ -Antiaromaticity

There are a few works on the prototypical odd-number cyclic systems with *s*-AO based σ -aromaticity, namely the Li_3^+ [10–12] and the Cu_3^+ clusters [12]. In this chapter we would like to consider *s*-AO based σ -aromaticity/antiaromaticity in triatomic gold clusters Au_3^+ and Au_3^- , respectively.

Au_3^+ , similar to Li_3^+ and Cu_3^+ clusters, has a D_{3h} , $^1A_1'$ global minimum structure. Bonding in Au_3^+ is based on 6*s*-AOs of Au, because all the bonding and antibonding MOs composed out of 5*d*-AOs of Au are occupied; hence, the contribution to bonding from 5*d*-AOs of Au is negligible (according to NBO analysis natural electronic configuration of Au_3^+ cluster is: $6s^{(0.71)}5d^{(9.93)}$ at B3LYP/LANL2DZ). The AdNDP analysis reveals one 3*c*–2*e* σ -bond with occupation number (ON) of 2.00 electrons (2.00 |*e*|) composed out of 6*s*-AOs of three Au atoms (Fig. 21a). It is completely bonding and it is responsible for σ -aromaticity in Au_3^+ , according to the $4n + 2$ rule with $n = 0$ (for singlet coupling). The obtained 3*c*–2*e* σ -bond can be compared with the corresponding model molecular orbital $1a_1'$ (see Fig. 1 and Table 1).

For σ -antiaromatic species (with *ns*-AOs participating in bonding) the counting rule is $4n$ (singlet coupling). The Au_3^- anion is a good example of σ -antiaromatic system with four 6*s*-electrons. The electronic configuration for the singlet state of Au_3^- at the D_{3h} symmetry is $1a_1^{(2)}1e'^{(2)}$ (with the only contribution of 6*s* AOs to the bonding MOs, compared to Fig. 1 and Table 1), and the triangular structure with the singlet electronic state must undergo the Jahn–Teller distortion toward linear $D_{\infty h}$ structure with a $1\sigma_g^{(2)}1\sigma_u^{(2)}$ valence electronic configuration and that is exactly what we found in our calculations.

Two σ -delocalized MOs can be approximately localized into two 2*c*–2*e* bonds with ON = 2.00|*e*| and the linear structure of Au_3^- can be formally considered as a classical structure (Fig. 21b).

s-AO based σ -aromaticity in even-number cyclic systems namely M_4^{2-} (*M* = Cu, Ag, Au) dianions as parts of M_4Li_2 (*M* = Cu, Ag, Au) neutral species was studied

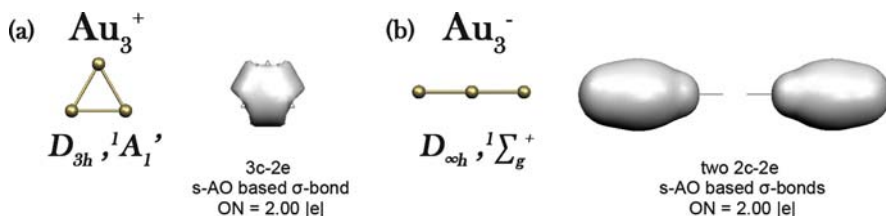


Fig. 21 (a) Geometric structure and 3*c*–2*e* *s*-AO based σ -bond of σ -aromatic Au_3^+ cluster; (b) Geometric structure and two 2*c*–2*e* *s*-AO based σ -bonds of σ -antiaromatic Au_3^- cluster

by Wannere et al. [13] and M_4X^- and M_4X_2 ($M = \text{Cu, Ag, Au}$; $X = \text{Li, Na}$) was studied by Lin et al. [14]. *s*-AO based σ -aromaticity in the *cyclo*- M_nH_n ($M = \text{Cu, Ag, Au}$; $n = 3-6$), *cyclo*- $\text{Au}_3L_nH_{3-n}$ ($L = \text{CH}_3, \text{NH}_2, \text{OH, and Cl}$; $n = 1-3$), *cyclo*- $\text{Cu}_n\text{Ag}_{k-n}H_n$ ($n = 1 - k, k = 3-5$) clusters was studied by Tsepis and Tsepis [15], Tsepis et al. [16], Tsepis and Tsepis [17], Tsepis and Stalikas [18]. We will not discuss these cases because their chemical bonding is similar to the earlier Au_3^+ case, and for those readers who would like to look into details we recommend consulting the original papers and the discussion in the recent review [7].

3.2 *p*-AO-Based Aromaticity and Antiaromaticity

p-AOs participation in delocalized chemical bonding may lead to the phenomenon of double (σ - and π -) aromaticity. Chandrasekhar et al. [19] introduced simultaneous presence of σ - and π -aromaticity to explain the properties of the 3,5-dehydrophenyl cation. Simultaneous presence of aromaticity and antiaromaticity was first used by Martin-Santamaria and Rzepa [20] to explain chemical bonding in small carbon rings. Later the simultaneous presence of aromaticity and antiaromaticity was named as conflicting aromaticity [21]. Alexandrova et al. [22] have also shown an example of a doubly σ - and π -antiaromatic species – the B_6^{2-} dianion. *p*-AO based σ -aromaticity/antiaromaticity and *p*-AOs based double σ - and π -aromaticity and antiaromaticity was also found in transition metal systems.

Yong and Chi [23] have recently shown that a series of M_3^{2-} , NaM_3^- , Na_2M_3 ($M = \text{Zn, Cd, Hg}$) clusters have the $M_3^{2-} D_{3h}, ^1A'_1$ core, which is *p*-AO-based π -aromatic. Thus, in all the M_3^{2-} , NaM_3^- , Na_2M_3 ($M = \text{Zn, Cd, Hg}$) systems bonding in the M_3^{2-} core is due to π -aromaticity only, without σ -bonding. Similar bonding pattern was previously reported for M_3^{2-} , NaM_3^- , Na_2M_3 ($M = \text{Be, Mg}$) systems by Kuznetsov and Boldyrev [24], Chattaraj and Giri [25], and Roy and Chattaraj [26]. We performed the AdNDP analysis of the Na_2Zn_3 cluster which revealed one $5c-2e$ π -bond composed out of $4p$ -AOs of three Zn atoms and $3s$ -AOs of two Na atoms with $\text{ON} = 2.00|e|$ (Fig. 22). The $5c-2e$ π -bond is similar to $3c-2e$ model molecular orbital $1a_2''$ if we exclude contribution from sodium atoms (Fig. 9 and Table 1).

$4s$ -AOs of Zn atoms are not responsible for bonding and they form three lone pairs (one per each Zn atom) with $\text{ON} = 1.90 |e|$. Thus, the Na_2Zn_3 species as well as Zn_3^{2-} (with $1a_2''$ occupied HOMO) and NaZn_3^- are all π -aromatic with no contribution from σ -bonding.

The first example of a solid compound (Na_3Hg_2 amalgam) containing doubly σ - and π -aromatic transition metal cluster Hg_4^{6-} was discovered by Kuznetsov et al. [27]. Formation of the Hg_4^{6-} cluster was puzzling since mercury has a closed shell electron configuration ($6s^{(2)}$), and therefore a neutral Hg_4 cluster is expected to be a van der Waals complex. The stability of the Hg_4^{6-} building block can be explained due to the fact that it is isoelectronic to the first all-metal aromatic cluster,

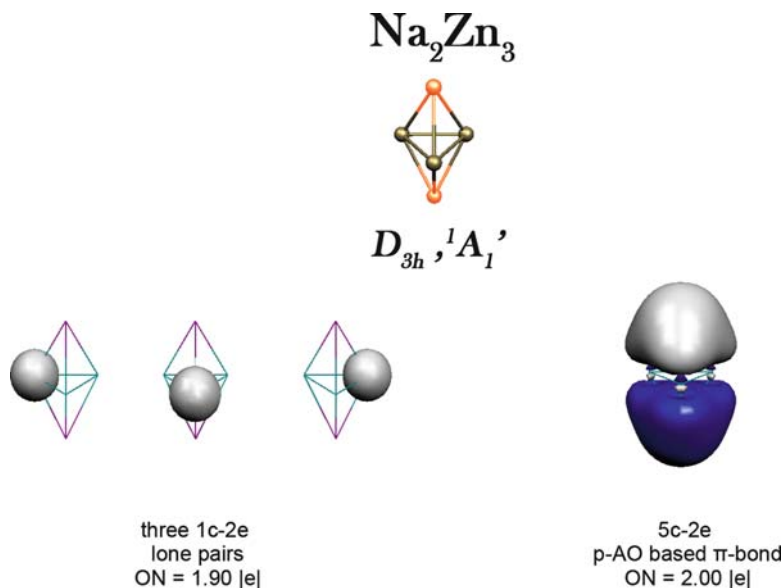


Fig. 22 Geometric structure, three 1c-2e lone pairs, and 5c-2e p-AO based π -bond of π -aromatic Na_2Zn_3 cluster

Al_4^{2-} [28]. Bonding in Hg_4^{6-} is due to Hg 6p-AO based MOs and the completely occupied d-AOs of mercury do not contribute to the bonding. Figure 23 displays the bonding pattern obtained via the AdNDP analysis of the square-planar Hg_4^{6-} .

The AdNDP analysis revealed four lone pairs on Hg atoms with ON = 1.94 |e|, as well as delocalized p-AO based 4c-2e σ -radial bond with ON = 2.00 |e|, p-AO based 4c-2e σ -tangential bond with ON = 2.00 |e|, and p-AO based 4c-2e π -bond with ON = 2.00 |e|. Thus Hg_4^{6-} should be considered as both p-radial-AO and p-tangential based σ -aromatic species. Therefore the Hg_4^{6-} cluster satisfies the $4n + 4$ counting rule for σ -aromaticity in cyclic systems with even numbers of atoms (see Table 2). In addition, Hg_4^{6-} should be considered as π -aromatic on the basis of the $4n + 2$ Huckel rule applied to its π -subsystem (see Table 2). Thus, Hg_4^{6-} is a doubly σ - and π -aromatic system.

The p-AO based 4c-2e σ -radial and 4c-2e σ -tangential bonds can be compared to model molecular orbitals $1a_{1g}$ and $1b_{2g}$, respectively (see Fig. 4). One can compare the p-AO based 4c-2e π -bond to the model molecular orbital $1a_{2u}$ (see Fig. 10).

The finding of the double aromaticity in Hg_4^{6-} establishes a solid bridge between our gas-phase studies of multiply aromatic clusters and bulk materials containing such species.

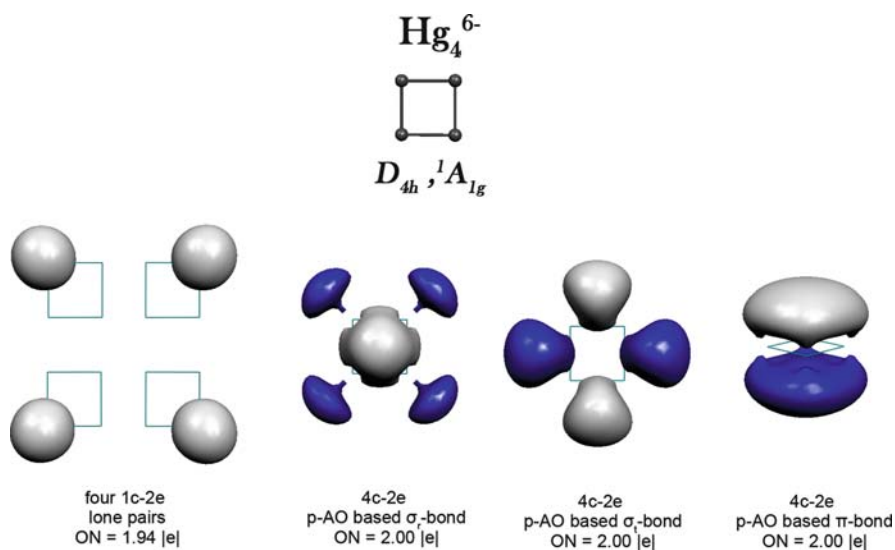


Fig. 23 Geometric structure, four 1c-2e lone pairs, 4c-2e p-AO based σ_r -bond, 4c-2e p-AO based σ_π -bond, and 4c-2e p-AO based π -bond of doubly σ - and π -aromatic Hg_4^{6-} cluster

3.3 d-AO Based Aromaticity and Antiaromaticity

Due to the more complicated nodal structure of d-AOs that can form δ -bond in addition to σ - and π -bonds, transition-metal systems can provide a more diverse array of aromaticity–antiaromaticity combinations. However, so far only few transition metal systems with d-AO based aromaticity have been reported.

The first cases of d-AO based σ -aromaticity were reported by Huang et al. [29] in 4d and 5d transition metal oxide clusters, Mo_3O_9^- and W_3O_9^- , by combining photoelectron spectroscopy and theoretical calculations. They found that the M_3O_9 , M_3O_9^- , and $\text{M}_3\text{O}_9^{2-}$ ($\text{M} = \text{Mo}, \text{W}$) clusters all have D_{3h} structures, and each metal atom is bonded to two bridged O atoms and two terminal O atoms. We performed the AdNDP analysis for $\text{Mo}_3\text{O}_9^{2-}$ cluster and the results are presented in Fig. 24.

The following bonding pattern is revealed for the $\text{Mo}_3\text{O}_9^{2-}$ cluster: six 2c–2e Mo–O_{terminal} σ -bonds with ON = 2.00 |e|, six 2c–2e Mo–O_{bridged} π -bonds with ON = 1.99 |e|, six 2c–2e Mo–O σ -bonds with ON = 1.92 |e|, and one completely delocalized 3c–2e d-AO based σ_r -bond. Thus, each terminal oxygen atom is bound to the closest molybdenum atom by both σ - and π -bonds, each bridged oxygen atom is bound to the neighboring molybdenum atoms by two σ -bonds, and the molybdenum atoms are bound to each other by completely bonding 3c–2e σ -bond. According to the performed AdNDP analysis, $\text{Mo}_3\text{O}_9^{2-}$ species is σ -aromatic. The 3c–2e d-AO based σ_r -bond in the Mo_3 kernel is similar to the 3c–2e model d-AO based $1a'_1\sigma$ -MO in Fig. 5.

The first systems with d-AO based double (σ - and π -) aromaticity have been reported recently by Chi and Liu [30]. They demonstrated that the D_{3h} (${}^1A'_1$)

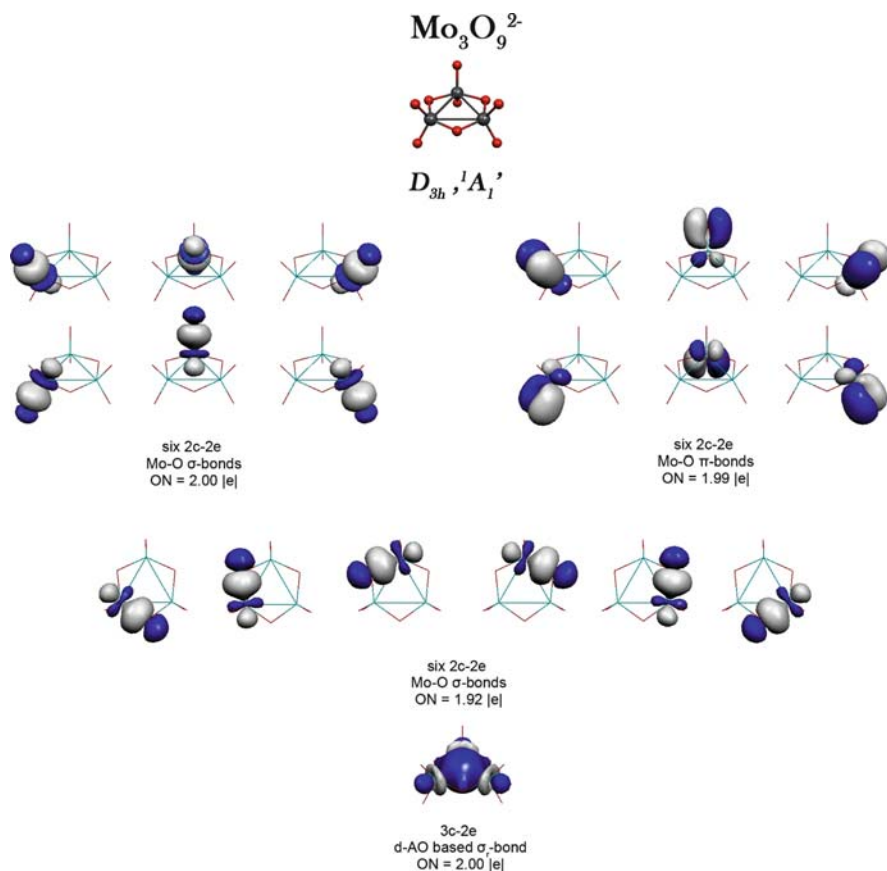


Fig. 24 Geometric structure, six 2c-2e Mo-O σ -bonds, six 2c-2e Mo-O π -bonds, six 2c-2e Mo-O σ -bonds, and 3c-2e d-AO based σ_r -bond of σ -aromatic $\text{Mo}_3\text{O}_9^{2-}$ cluster

structures are the global minimum structures for X_3^- ($\text{X} = \text{Sc}, \text{Y}, \text{La}$). All three species have the same valence electronic configuration $1a_1^{(2)}1e'^{(4)}1a_2''^{(2)}2a_1'^{(2)}$, though the order of the MOs varies. The AdNDP analysis of the Sc_3^- cluster reveals the following bonding pattern: there are three 2c-2e Sc-Sc σ -bonds with $\text{ON} = 1.99$ |e| composed out of hybrid 4s,3d-AOs of Sc, one completely bonding 3c-2e d-radial based σ -bond with $\text{ON} = 2.00$ |e|, and one completely bonding 3c-2e d-radial based π -bond with $\text{ON} = 2.00$ |e| (Fig. 25).

Therefore the X_3^- ($\text{X} = \text{Sc}, \text{Y}, \text{La}$) clusters satisfy the $4n + 2$ counting rule for σ -aromaticity and the $4n + 2$ Huckel rule for π -aromaticity in cyclic systems with odd numbers of atoms (see Table 1). Thus, all three anions are d-orbital based doubly (σ - and π -) aromatic systems. The obtained via the AdNDP method 3c-2e d-AO based σ_r -bond and 3c-2e d-AO based π_r -bond are similar to the 3c-2e $1a_1'$ and $1a_2''$ model molecular orbitals presented in Figs. 5 and 11, respectively.

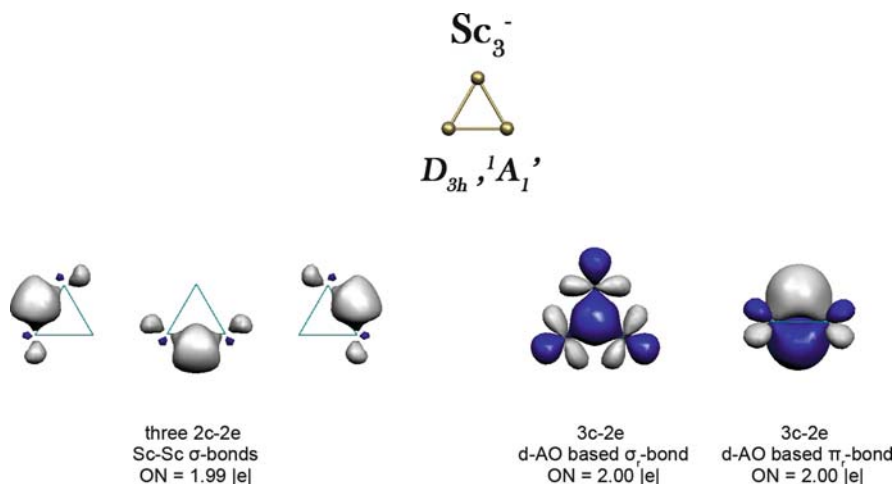


Fig. 25 Geometric structure, three 2c-2e Sc-Sc σ -bonds, 3c-2e d-AO based σ_r -bond, 3c-2e d-AO based π_r -bond of doubly σ - and π -aromatic Sc_3^- cluster

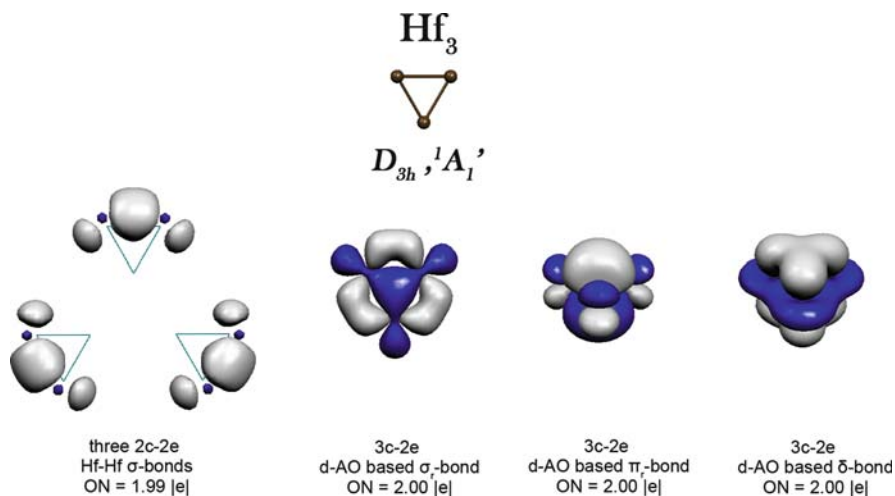


Fig. 26 Geometric structure, three 2c-2e Hf-Hf σ -bonds, 3c-2e d-AO based σ_r -bond, 3c-2e d-AO based π_r -bond, and 3c-2e d-AO based δ -bond of triply σ -, π - and δ -aromatic Hf_3 cluster

The first example of δ -aromaticity was found by Zhai et al. [4] in joint photoelectron spectroscopy and theoretical study. They showed that the Ta_3O_3^- cluster possesses a global minimum with a perfect D_{3h} ($^1A_1'$) planar triangular structure and that it's doubly π - and δ -aromatic species.

Averkiev and Boldyrev [5] theoretically predicted the first example of triple (σ -, π -, and δ -) aromaticity (Hf_3 in the D_{3h} , $^1A_1'$ $1a_1^{(2)}2a_1^{(2)}1e^{(4)}1a_2^{(2)}3a_1^{(2)}$ state).

The results of the AdNDP analysis for this system are presented in Fig. 26.

The following bonding pattern is revealed for the Hf_3 species: three 2c–2e Hf–Hf σ -bonds with $\text{ON} = 1.99 |e|$ formed out of hybrid 6s,5d-AOs of Hf atoms, and three completely delocalized bonds. They are: one completely bonding 3c–2e d-radial based σ -bond with $\text{ON} = 2.00 |e|$, one completely bonding 3c–2e d-radial based π -bond $\text{ON} = 2.00 |e|$, and one completely bonding 3c–2e d-AO based δ -bond $\text{ON} = 2.00 |e|$. Assignment of the triple (σ -, π -, and δ -) aromaticity can be made on the basis of the $4n + 2$ Huckel rule (odd number of atoms, see Table 1). One can find the correspondence between 3c–2e d-AO based σ_r -bond, 3c–2e d-AO based π_r -bond, 3c–2e d-AO based δ -bond and 3c–2e $1a'_1$, $1a''_2$, and $1a'_1$ model molecular orbitals shown in Figs. 5, 11 and 15, respectively.

Wang et al. [31] presented joint photoelectron spectroscopy and theoretical study of another example of transition metal Ta_3^- cluster with triple (σ -, π -, and δ -) aromaticity. They have shown that the lowest energy quintet state (D_{3h} , ${}^5A'_1$) has the following electronic configuration: $1a_1'^{(2)}2a_1'^{(2)}1a_2''^{(2)}1e'^{(4)}1e''^{(2)}3a_1'^{(2)}2e''^{(2)}$. Out of these MOs, $1a_1'$ and $1e'$ are the set of completely bonding and partially bonding/antibonding MOs formed out of primarily 6s-AOs of tantalum atoms and should not contribute to bonding significantly. $2a_1'$ is a completely bonding MO formed out of d-sigma-radial ($d_{\sigma-r}$)-AOs of tantalum atoms. The corresponding partially bonding/antibonding $2e'$ -MOs composed out of d-sigma-radial ($d_{\sigma-r}$)- and d-sigma-tangential ($d_{\sigma-t}$)-AOs of tantalum atoms. These doubly degenerate MOs are occupied by two electrons with triplet coupling, and together with two electrons on $2a_1'$ MO they satisfy the $4n$ rule for σ -aromaticity (triplet coupling) in odd number cyclic systems (see section 2.1 and Table 1). Similarly, $1a_2''$ is a completely bonding MO formed out of d-pi-radial ($d_{\pi-r}$)-AOs of tantalum atoms. The corresponding partially bonding/antibonding $1e''$ -MOs composed out of d-pi-radial ($d_{\pi-r}$)- and d-pi-tangential ($d_{\pi-t}$)-AOs of tantalum atoms. These doubly degenerate MOs are occupied by two electrons with triplet coupling, and together with two electrons on $1a_2''$ MO they satisfy the $4n$ rule for π -aromaticity (triplet coupling) in odd number cyclic systems (see Sect. 2.2 and Table 1). Finally, $3a_1'$ is a completely bonding δ -MO which is responsible for δ -aromaticity in this system (see Sect. 2.3 and Table 1).

Alvarado-Soto et al. [32], [33] have discussed the concept of aromaticity in Re_3Cl_9 , Re_3Br_9 , $\text{Re}_3\text{Cl}_9^{2-}$, and $\text{Re}_3\text{Br}_9^{2-}$ clusters.

Summary: There have been very few examples on the aromaticity/antiaromaticity in all-transition metal cyclic systems reported in the literature to this day. In the current section we give detailed discussion on antiaromaticity/antiaromaticity in $\text{Au}_3^+/\text{Au}_3^-$, Na_2Zn_3 , Hg_4^{6-} , $\text{Mo}_3\text{O}_9^{2-}$, Sc_3^- , Hf_3 , and Ta_3^- clusters.

4 Overview

Aromaticity in compounds containing a transition-metal atom has already had a long history. Initially, Thorn and Hoffmann [34] proposed six-membered ring metallocyclic compounds, derivatives of benzene with one C–H moiety replaced by an isolobal transition-metal fragment. Three years later the first example of a stable,

isolable metallobenzene – osmabenzene – was reported by Elliott et al. [35]. Since then a large family of metallobenzenes have been synthesized and characterized [36], [37], [38]. Profilet et al. [39] reported first synthesis of dimetallobenzenes with two metal atoms incorporated into the benzene ring. A thorough chemical bonding analysis of metallobenzene has been recently performed by Fernandez and Frenking [40]. However, in this review we demonstrated that aromaticity could be a powerful tool in explaining structure, stability, and other molecular properties in cyclic systems composed of transition-metal atoms only.

It is clear that aromaticity and antiaromaticity could be very useful concepts in explaining structure, stability, and other molecular properties of isolated and embedded clusters of transition metals and transition metal oxide clusters. The chemical bonding in transition metal clusters can come from s-AOs, p-AOs, and d-AOs, and can be expressed as a variety of multiple aromaticities and antiaromaticities as well as of conflicting aromaticities.

In Sect. 2 we considered models of σ -, π -, δ -, and ϕ -aromaticity/antiaromaticity based on a particular type (s-, p-, d-, or f-) of AOs in both even and odd number cyclic systems on an example of triatomic and tetratomic systems, respectively. One can compose σ -MOs out of s-AOs, as well as p-sigma-radial ($p_{\sigma-r}$)- and p-sigma-tangential ($p_{\sigma-t}$)-AOs, d-sigma-radial ($d_{\sigma-r}$)- and d-sigma-tangential ($d_{\sigma-t}$)-AOs, f-sigma-radial ($f_{\sigma-r}$)- and f-sigma-tangential ($f_{\sigma-t}$)-AOs participating in delocalized bonding. π -MOs can be composed out of p-AOs, as well as d-pi-radial ($d_{\pi-r}$)- and d-pi-tangential ($d_{\pi-t}$)-AOs, f-pi-radial ($f_{\pi-r}$)- and f-pi-tangential ($f_{\pi-t}$)-AOs participating in delocalized bonding. One can compose δ -MOs out of d-AOs, as well as f-delta-radial ($f_{\delta-r}$)- and f-delta-tangential ($f_{\delta-t}$)-AOs participating in delocalized bonding. Finally, ϕ -MOs can be composed out of f-AOs.

The counting rules for s-AO based σ -aromaticity, p-AO based π -aromaticity, d-AO based δ -aromaticity, and f-AO based ϕ -aromaticity are $4n + 2/4n//4n/4n + 2$ rules for aromaticity/antiaromaticity (singlet//triplet coupling, respectively) for all cyclic structures. The counting rules for p-AO based σ -aromaticity, d-AO based σ -aromaticity, d-AO based π -aromaticity, f-AO based σ -aromaticity, and f-AO based π -aromaticity are $4n + 2/4n//4n/4n + 2$ rules for aromaticity/antiaromaticity (singlet//triplet coupling, respectively) for cyclic structures with odd number of atoms. The counting rules for p-AO based σ -aromaticity, d-AO based σ -aromaticity, d-AO based π -aromaticity, f-AO based σ -aromaticity, and f-AO based π -aromaticity are $2, 4n + 4/4n + 2//4n + 6/4n$ rules for aromaticity/antiaromaticity (singlet//triplet coupling, respectively) for cyclic structures with even number of atoms.

This model chemical bonding analysis for odd/even-number cyclic systems can be used for assessing aromaticity/antiaromaticity in real molecules and clusters. However, hybridization may complicate this analysis. For instance, in planar cyclic boron clusters the peripheral boron atoms participate in localized $2c-2e$ B–B σ -bonding, and those bonds are formed out of hybridized $2p$ -sigma-tangential ($2p_{\sigma-t}$)- and $2s$ -AOs. Therefore, $2p_{\sigma-t}$ -AOs should be excluded from the delocalized σ -bonding. Thus, only $2p$ -sigma-radial ($2p_{\sigma-r}$)-AOs participate in the delocalized σ -bonding and the counting rule for σ -aromaticity becomes $4n + 2/4n$ for all cyclic boron systems [9, 41, 42].

In Sect. 3 of current work we presented a few examples of aromatic/antiaromatic transition metal systems. We have shown that triatomic gold clusters Au_3^+ and Au_3^- are s-AO based σ -aromatic and σ -antiaromatic, respectively. Na_2Zn_3 cluster was shown to have one $5c-2e$ π -bond composed out of 4p-AOs of three Zn atoms and 3s-AOs of two Na atoms; thus, it is a π -aromatic system with no contribution from σ -bonding in the Zn_3 kernel. The Hg_4^{6-} cluster is a doubly p-AO based both σ - and π -aromatic system. The $\text{Mo}_3\text{O}_9^{2-}$ species renders its d-radial-AO based σ -aromaticity. The Sc_3^- cluster is an example of a system with d-AO based double (σ - and π -) aromaticity with one completely bonding $3c-2e$ d-radial based σ -bond and one completely bonding $3c-2e$ d-radial π -bond.

The first cluster with δ -aromaticity was found via joint collaborative theoretical and photoelectron spectroscopic studies to be Ta_3O_3^- . The Hf_3 cluster was theoretically predicted to be the first example of triple (σ -, π -, and δ -) aromaticity in the lowest singlet state. The first experimentally observed triply aromatic system is Ta_3^- in the lowest quintet state.

Atomic f-AOs in lanthanide and actinide clusters offer additional possibility to form ϕ -bonds and thus could lead to systems with even richer variety of ϕ -aromaticity/antiaromaticity. Tsipis et al. [6] have recently presented the first evidence of f-AO participation in delocalized bonding.

We hope that the aromaticity, antiaromaticity, and conflicting aromaticity concepts would stimulate theoretical analysis of chemical bonding in other known and novel chemical compounds containing transition metal atoms in clusters, nanoparticles, solid compounds, and metallobiomolecules.

Acknowledgements The work done was supported by the National Science Foundation under Grant CHE-0714851. Computer time from the Center for High Performance Computing at Utah State University is gratefully acknowledged. The computational resource, the Uinta cluster supercomputer, was provided through the National Science Foundation under Grant CTS-0321170 with matching funds provided by Utah State University.

References

1. Cotton FA, Curtis NF, Harris CB, Johnson BFG, Lippard SJ, Mague JT, Robinson WR, Wood JS (1964) Mononuclear and polynuclear chemistry of rhenium (III): its pronounced homophilicity. *Science* 145:1305–1307
2. Cotton FA, Murillo CA, Walton RA (2005) Multiple bonds between metal atoms, 3rd edn. Springer, New York
3. Nguyen T, Sutton AD, Brynda M, Fettinger JC, Long GJ, Power PP (2005) Synthesis of a stable compound with fivefold bonding between two chromium(I) centers. *Science* 310:844–847
4. Zhai HJ, Averkiev BB, Zubarev DY, Wang LS, Boldyrev AI (2007) δ Aromaticity in $[\text{Ta}_3\text{O}_3]^-$. *Angew Chem Int Ed* 46:4277–4280
5. Averkiev BB, Boldyrev AI (2007) Hf_3 cluster is triply (σ -, π -, and δ -) aromatic in the lowest $D_{3h} \ ^1A_1'$. *State J Phys Chem A* 111:12864–12866
6. Tsipis AC, Kefalidis CE, Tsipis CA (2008) The role of the 5f orbitals in bonding, aromaticity, and reactivity of planar isocyclic and heterocyclic uranium clusters. *J Am Chem Soc* 130: 9144–9155

7. Zubarev DY, Averkiev BB, Zhai HJ, Boldyrev AI, Wang LS (2008) Aromaticity and antiaromaticity in transition-metal systems. *Phys Chem Chem Phys* 10:257–267
8. Manthey D (2004) Orbital viewer 1.04 <http://www.orbitals.com/orb/ov.htm>
9. Zubarev DY, Boldyrev AI (2008) Developing paradigm of chemical bonding: adaptive natural density partitioning. *Phys Chem Chem Phys* 10:5207–5217
10. Alexandrova AN, Boldyrev AI (2003) σ -Aromaticity and σ -antiaromaticity in alkali metal and alkaline earth metal small clusters. *J Phys Chem A* 107:554–560
11. Havenith RWA, De Proft F, Fowler PW, Geerlings P (2004) σ -aromaticity in H_3^+ and Li_3^+ : insights from ring-current maps. *Chem Phys Lett* 407:391–396
12. Yong L, Wu SD, Chi XX (2007) Theoretical study of aromaticity in small hydrogen and metal cation clusters X_3^+ ($X = H, Li, Na, K, \text{ and } Cu$). *Int J Quant Chem* 107:722–728
13. Wannere CS, Corminboeuf C, Wang ZX, Wodrich MD, King RB, Schleyer PVR (2005) Evidence for d orbital aromaticity in square planar coinage metal clusters. *J Am Chem Soc* 127:5701–5705
14. Lin YC, Sundholm D, Juselius J, Cui LF, Li X, Zhai HJ, Wang LS (2006) Experimental and computational studies of alkali-metal coinage-metal clusters. *J Phys Chem A* 110:4244–4250
15. Tsipis AC, Tsipis CA (2003) Hydrometal analogues of aromatic hydrocarbons: a new class of cyclic hydrocoppers(I). *J Am Chem Soc* 125:1136–1137
16. Tsipis CA, Karagiannis EE, Kladou PF, Tsipis AC (2004) Aromatic gold and silver ‘rings’: hydrosilver(I) and hydrogold(I) analogues of aromatic hydrocarbons. *J Am Chem Soc* 126:12916–12929
17. Tsipis AC, Tsipis CA (2005) Ligand-stabilized aromatic three-membered gold rings and their sandwichlike complexes. *J Am Chem Soc* 127:10623–10638
18. Tsipis AC, Stalikas AV (2007) A new class of all-metal aromatic hydrido-bridged binary coinage metal heterocycles. A DFT study. *New J Chem* 31:852–859
19. Chandrasekhar J, Jemmis ED, Schleyer PVR (1979) Double aromaticity: aromaticity in orthogonal planes. The 3,5-dehydrophenyl cation. *Tetrahedron Lett* 39:3707–3710
20. Martin-Santamaria S, Rzepa HS (2000) Double aromaticity and anti-aromaticity in small carbon rings. *Chem Commun* 16:1503–1504
21. Boldyrev AI, Wang LS (2005) All-metal aromaticity and antiaromaticity *Chem Rev* 105:3716–3757
22. Alexandrova AN, Boldyrev AI, Zhai HJ, Wang LS, Steiner E, Fowler PW (2003) Structure and bonding in B_6^- and B_6 : planarity and antiaromaticity. *J Phys Chem A* 107:1359–1369
23. Yong L, Chi XX (2007) Theoretical study on the aromaticity of dianions X_3^{2-} ($X = Zn, Cd, Hg$). *J Mol Struct THEOCHEM* 818:93–99
24. Kuznetsov AE, Boldyrev AI (2004) A single π -bond captures 3, 4 and 5 atoms. *Chem Phys Lett* 388:452–456
25. Chattaraj PK, Giri S (2008) Variation in aromaticity and bonding patterns in a reaction cycle involving Be_3^{2-} and Mg_3^{2-} dianions. *J Mol Struct: THEOCHEM* 865:53–56
26. Roy DR, Chattaraj PK (2008) Reactivity, selectivity, and aromaticity of Be_3^{2-} and its complexes. *J Phys Chem A* 112:1612–1621
27. Kuznetsov AE, Corbett JD, Wang LS, Boldyrev AI (2001) Aromatic mercury clusters in ancient amalgams. *Angew Chem Int Ed* 40:3369–3372
28. Li X, Kuznetsov AE, Zhang HF, Boldyrev AI, Wang LS (2001) Observation of all-metal aromatic molecules. *Science* 291:859–861
29. Huang X, Zhai HJ, Kiran B, Wang LS (2005) Observation of d-orbital aromaticity. *Angew Chem Int Ed* 44:7251–7254
30. Chi XX, Liu Y (2007) Theoretical evidence of d-orbital aromaticity in anionic metal X_3^- ($X = Sc, Y, La$) clusters. *Int J Quant Chem* 107:1886–1896
31. Wang B, Zhai HJ, Huang X, Wang LS (2008) On the electronic structure and chemical bonding in the tantalum trimer cluster. *J Phys Chem A* 112:10962–10967
32. Alvarado-Soto L, Ramirez-Tagle R, Arratia-Perez R (2008) Spin-orbit effects on the aromaticity of the Re_3Cl_9 and Re_3Br_9 clusters *Chem Phys Lett* 467:94–96
33. Alvarado-Soto L, Ramirez-Tagle R, Arratia-Perez R (2009) Spin-orbit effects on the aromaticity of the $Re_3X_9^{2-}$ ($X = Cl, Br$) cluster ions. *J Phys Chem A* 113:1671–1673

34. Thorn DL, Hoffmann R (1979) Delocalization in metallocycles. *Nouv J Chim* 3:39–45
35. Elliot GP, Roper WR, Waters JM (1982) Metallacyclohexatrienes or metallabenzenes. Synthesis of osmabenzene derivatives and X-ray crystal structure of $[\text{Os}(\text{CSCHCHCHCH}) (\text{CO})(\text{PPh}_3)_2]$. *J Chem Soc Chem Commun* 811–813
36. Bleeke JR (2001) Metallabenzenes *Chem Rev* 101:1205–1228
37. Wright LJ (2006) Metallabenzenes and metallabenzenoids *Dalton Trans* 1821–1827
38. Landorf WC, Haley MM (2006) Recent advances in metallabenzene chemistry. *Angew Chem Int Ed* 45:3914–3936
39. Profflet RD, Fanwick PE, Rothwell IP (1992) 1,3-Dimetallabenzene derivatives of niobium or tantalum. *Angew Chem Int Ed* 31:1261–1263
40. Fernandez I, Frenking G (2007) Aromaticity in metallabenzenes *Chem Eur J* 13:5873–5884
41. Alexandrova AN, Boldyrev AI, Zhai HJ, Wang LS (2006) All-boron aromatic clusters as potential new inorganic ligands and building blocks in chemistry. *Coord Chem Rev* 250:2811–2866
42. Zubarev DY, Boldyrev AI (2007) Comprehensive analysis of chemical bonding in boron clusters. *J Comput Chem* 28:251–268

Index

- Acetylides 80
- Adaptive natural density partitioning 294
- Alkyls 113
 - ligands 115
- All transition metal aromaticity 275
- All-metal aromatic rings 219
- Anisotropy of induced current density (ACID) 222
- 1,8-Anthracenedicarboxylic acid 34
- Antibonding 135
- ArMMAr (Cr, Fe, Co) 83
- Aromaticity, all transition metal 277
 - multifold 223, 277
- Aromaticity/antiaromaticity 217
 - d-AO-based 298
 - p-AO-based 296
 - s-AO-based 295
 - electronic indicators 223
 - four-/five-/six-membered rings 252
 - Group 1 metal atoms 226
 - Group 2 metal atoms 226
 - Group 13 metal atoms 229
 - Group 14 metalloid/metal atoms 230
 - Group 15 metalloid/metal atoms 231
 - lanthanides/actinides (f-orbital aromaticity) 268
 - magnetic indicators 219
 - transition metals 234, 296
- Aryl chromium halide 66
- 2,6-Azulenedicarboxylate 40

- Bismuth, dibismuthenes 157
- Bond length/order 123
- Bond stretch isomers 6

- Canonical molecular orbital (CMO) 222
- Carbenoid gallium(I) 167
- Carboxylate linkers 41
- Catenation 190

- Group 13 elements 209
- Group 15 elements 207
- 3-Center-2-electron interaction 118
- Charge resonance bands 47
- Chemical bonding 277
- Chromium, trichromium species 3
 - complexes, terphenyl ligand substituent effects 86
- Clusters 277
- Cobalt, tricobalt 5
- Cobalt(II) terphenylmetal halide 70
- Copper, organocopper(I) terphenyls 104
 - tricopper 10
- Cyanoorganocuprate 104
- Cyclooctatetraenyl terphenyl 62
- Cyclopentadienyl tungsten dicarbonyl compounds 134

- DFT 226
- N, N'*-Diaryloxamidate 42
- Dibismuthenes 157, 158
- Diborane 120
- 2,7-Dihydroxynaphthyridine 34
- Dimers of dimers 30
- Dinuclear compounds, double hydrogen bridges 132
 - quadruple hydrogen bridges 139
 - single hydrogen bridges 129
 - triple hydrogen bridges 136
- Dinuclear molybdenum, bonding, bridging methyl/hydride ligands 122
- Dioxalene dianions 32
- Dioxolene 43
- 3,6-Dioxypyridazine 35
- Di-2,2'-pyridylamine (Hdpa) 2

- Electronic coupling 29
 - frontier molecular orbital interactions 37

- Electronic structure 2, 3, 196
 EPR spectroscopy 45
 Extended metal atom chains (EMACs) 2, 12
 heterometallic 23
- Fe–Ga–Fe 161
 Formamidinates 36, 42
- Ga(I), coordination chemistry 149
 ligands, NHC analogue 149
 GaCp 158
 complexes, zinc compounds 166
 Ga(Giso) 149
 Gauge including atomic orbital (GIAO) 222
 Gold terphenyl 105
 Group 11 elements, terphenyl derivatives 102
 Group 14 elements 191
- Half-arrow method 120, 128
 Half-electron method 121, 128
 Heterometallic compounds 1
 Hume–Rothery phases 183
 Hydrides, bridging ligands 113, 115
- Iridium 136
 Iron triple bond 137
 Iron(II) terphenyl metal halide 70
 IVCT 47
- Ligands, axial/equatorial 14
 Loops 30, 52
 LX “half-arrow” electron-counting 128
- M–Ga bonding, Ga(I) ligands 165
 M–M bond order ambiguities 115
 M(ZnR)_n 168, 181
 Magnetic aromaticity 219
 Manganese halides, terphenyl 67
 Metal atoms, rings 217
 Metal(I) dimers, terphenyl stabilized 83
 Metal–GaR bonding 165
 Metal–metal bonds 1, 113
 Metals 113
 Metal-to-bridge charge transfer bands 48
 Mixed valence 30
 MM quadruple bonds 29
 Molecular conductance measurements 21
 Molecular wires 1
- Molybdenum 29, 125
 Mo(ZnH)₁₂ 172
 Multifold aromaticity 223, 277
- NHC (*N*-heterocyclic carbene) 149, 183
 Nickel, trinickel 9
 Ni(ZnH)₈ 178
 Nucleus-independent chemical shift (NICS)
 221
- O₂C–X–CO₂ bridges 39
 Oligogermanes 199
 Oligoplumbanes 199, 207
 Oligopyridylamine 2
 Oligosilanes 191
 electronic structure 196
 Oligostannanes 199, 203
 Optical spectra 47
 Osmium 114, 134
 Oxalate bridges 37
 Oxalic acid, dimetal pivalates 31
- P-block 190
 Paddle-wheel 83
 Pd(ZnH)₈ 178
 Pivalate 31, 44
 Polygermanes 199
 Polysilanes 191
 applications 198
 electronic structure 196
 Polystannanes 199, 203
 Pt(ZnH)₈ 178
- Quasi-two-coordinate amido complexes 73
- Resonance Raman 51
 Rhenium 140
 Rh(ZnH)₉ 177
 triple bond 140
 Ring-current shielding (ARCS) 222
 Ruthenium 11
 Ru(ZnH)₁₀ 175
 triruthenium 11, 138
- Silver terphenyl 105
 Single-molecule conductance 1
 Single-trimetal molecule transistor 23
 Squares 30, 52
 Steady-state emission spectroscopy 50

- Terphenyl metal halides 64, 83
 - chromium 64
 - cobalt 70
 - iron 70
 - manganese 67
 - PMe₃ 90
 - precursors 61
 - reactions with acetylides 80
- Terphenyl metals, arene complexed 93
 - transition metal complexes, amido coligands 73
 - dialkylamide-NMe₂ 77
 - homoleptic/two-coordinate 72
- Tetraazatetracene 32
- Thiocarboxylate linkers 41
- Transient absorption spectroscopy 50
- Transition metal, carbonyl 161
 - terphenyl metal halide derivatives 61
 - Zn(I) complexes 170
- Triangles 30, 52
- Trichromium species 3
- Tricobalt species 5
- Tricopper species 10
- Trinickel species 9
- Triruthenium species 11
- Tungsten 29
 - cyclopentadienyl tungsten dicarbonyl compounds 134
 - terephthalate 46
- Uranium clusters 268, 276
- Zinc 149, 166, 183
- Zintl-type anionic tin clusters 156
- Zirconium 136